Magnetic Nanostructures in Modern Technology

NATO Science for Peace and Security Series

This Series presents the results of scientific meetings supported under the NATO Programme: Science for Peace and Security (SPS).

The NATO SPS Programme supports meetings in the following Key Priority areas: (1) Defence Against Terrorism; (2) Countering other Threats to Security and (3) NATO, Partner and Mediterranean Dialogue Country Priorities. The types of meeting supported are generally "Advanced Study Institutes" and "Advanced Research Workshops". The NATO SPS Series collects together the results of these meetings. The meetings are co-organized by scientists from NATO countries and scientists from NATO's "Partner" or "Mediterranean Dialogue" countries. The observations and recommendations made at the meetings, as well as the contents of the volumes in the Series, reflect those of participants and contributors only; they should not necessarily be regarded as reflecting NATO views or policy.

Advanced Study Institutes (ASI) are high-level tutorial courses intended to convey the latest developments in a subject to an advanced-level audience

Advanced Research Workshops (ARW) are expert meetings where an intense but informal exchange of views at the frontiers of a subject aims at identifying directions for future action

Following a transformation of the programme in 2006 the Series has been re-named and re-organised. Recent volumes on topics not related to security, which result from meetings supported under the programme earlier, may be found in the NATO Science Series.

The Series is published by IOS Press, Amsterdam, and Springer, Dordrecht, in conjunction with the NATO Public Diplomacy Division.

Sub-Series

A.	Chemistry and Biology	Springer
B.	Physics and Biophysics	Springer
C.	Environmental Security	Springer
D.	Information and Communication Security	IOS Press
E.	Human and Societal Dynamics	IOS Press

http://www.nato.int/science
http://www.springer.com
http://www.iospress.nl

Series B: Physics and Biophysics

Magnetic Nanostructures in Modern Technology

Spintronics, Magnetic MEMS and Recording

edited by

Bruno Azzerboni
Università di Messina, Italy

Giovanni Asti
Università di Parma, Italy

Luigi Pareti
Consiglio Nazionale della Ricerche, Parma, Italy

and

Massimo Ghidini
Università di Parma, Italy

Springer

Published in cooperation with NATO Public Diplomacy Division

Proceedings of the NATO Advanced Study Institute on
Magnetic Nanostructures for Micro-Electromechanical
Systems and Spintronic Applications
Catona, Italy
2 – 15 July 2006

A C.I.P. Catalogue record for this book is available from the Library of Congress.

ISBN 978-1-4020-6337-4 (PB)
ISBN 978-1-4020-6336-7 (HB)
ISBN 978-1-4020-6338-1 (e-book)

Published by Springer,
P.O. Box 17, 3300 AA Dordrecht, The Netherlands.

www.springer.com

Printed on acid-free paper

CONTENTS

Preface xiii

Acknowledgements xv

List of Contributors xvii

1. John Slonczewski
Spin-Polarized Current and Spin-Transfer Torque in Magnetic Multilayers 1

1 Introduction 1
2 Two-channel spin-polarized transport 3
2.1 Suppression of transverse polarization 3
2.2 Half-pillar resistors 4
3 Effective circuit for a non-collinear all-metallic pillar 6
3.1 Spin polarization in a rotated reference frame 6
3.2 Spin-dependent electron distribution 7
3.3 Formulas for connecting channels across a spacer 9
4 Current-driven pseudo-torque 12
4.1 Torque mechanism 12
4.2 A general torque relation 14
5 Magnetoresistance and current-driven torque of a symmetric pillar 15
5.1 The magnetoresistance 15
5.2 Torques on a symmetric trilayer 17
6 Dynamics of magnetization driven by current 18
7 Quantum Tunneling Theory 21
7.1 Interaction picture 21
7.2 Tunneling rate 22
8 Currents and torques in magnetic tunnel junctions 24
8.1 Magneto-conduction and torques 24
8.2 Genesis of polarization factors 25
9 Junctions using MgO barriers 27
9.1 Magneto-conductance and torkance 29
9.2 Elastic tunneling 30
9.3 Inelastic tunneling 32
9.4 Observable signatures 33
References 34

2. Giorgio Bertotti
Spin-Transfer-Driven Magnetization Dynamics 37
1 Introduction 37
2 Equation for spin-transfer-driven magnetization dynamics 39
3 Magnetization dynamics and dynamical system theory 41
4 The role of thermal fluctuations 46
5 Uniaxial symmetry 50
References 57

3a. Giovanni Finocchio, Bruno Azzerboni, Luis Torres
Micromagnetic Modeling of Magnetization Dynamics Driven by Spin-Polarized Current: Basics of Numerical Modeling, Analysis of Confined Systems 61
1 Introduction 61
2 Numerical Modeling 62
3 Modeling of the Thermal Effect 65
References 66

3b. Giancarlo Consolo, Bruno Azzerboni, Luis Lopez-Diaz, Luis Torres
Micromagnetic Modeling of Magnetization Dynamics Driven by Spin-Polarized Current: Analysis of Nonconfined Systems 69
1 Introduction on nonconfined systems 69
2 Micromagnetic modeling of point-contact devices 71
2.1 The model 71
2.2 Boundary conditions 72
2.3 Results 73
References 75

3c. Mario Carpentieri, Bruno Azzerboni, Luis Torres
Micromagnetic Modelling of Magnetization Dynamics Driven by Spin-Polarized Current: Stability Diagrams and Role of the Non-Standard Effective Field Contributions 77
1 Introduction 77
2 Influence of the magnetostatic coupling 78
3 Effect of the Classical Ampere Field 80
4 Analysis of Persistent Dynamics Processes 81
References 83

4. Mathias Kläui
Magnetic Rings: A Playground to Study Geometrically Confined Domain Walls 85
1 Introduction 85
2 Fabrication 87
3 Measurement techniques 88

4 Head-to-head domain walls 89
4.1 Domain wall spin structures 89
4.2 Domain wall phase diagrams 89
4.3 Thermally activated domain wall transformations 91
4.4 Walls in thin and wide structures: Limits of the description 93
5 Domain wall coupling energetics 94
5.1 Coupling between adjacent domain walls 94
5.2 Direct observation of the domain wall stray field 96
6 Domain wall behaviour at constrictions 98
7 Conclusions 101
References 102

5. Orphée Cugat, Jérôme Delamare, Gilbert Reyne
Magnetic Microsystems: MAG-MEMS 105
1 Introduction 105
1.1 Mag-MEMS 105
2 Scale reduction laws 106
2.1 Historics 106
2.2 Magnetic interactions 107
2.3 Current density 110
2.4 Conclusions 111
3 Building blocks 112
3.1 μ-Coils 112
3.2 μ-Magnets 112
3.3 Exotic materials and hybridation 113
4 Additional features of Mag-MEMS 114
4.1 Permanent forces – bi-stability – suspensions 114
4.2 Long-range, remote, or wireless actuation 114
5 Design and optimization tools 114
6 Conclusion 115
7 Context 115
8 Prototypes 116
8.1 Planar synchronous μ-motors and μ-generators 116
8.2 μ-Switches with levitating mobile magnet 118
8.3 Optics 119
9 Other potential applications 120
10 Power supplies, control, cooling 121
11 Conclusion 121
References 122

6a. Martin A. M. Gijs
MEMS Inductors: Technology and Applications 127
1 Introduction 127
2 Inductor basics 128
3 Losses in inductors 128
3.1 Winding losses 129
3.2 Eddy current losses 129
3.3 Magnetic hysteresis losses 129
3.4 Ferromagnetic resonance losses 130
3.5 Choice of the core material 131
4 MEMS inductors: background 132
5 Radio frequency MEMS inductors 134
5.1 Embedded solenoidal inductors 135
5.2 Vertical spiral inductors 135
5.3 Horizontal spiral inductors over air cavities 139
5.4 Use of magnetic materials for RF inductors 139
6 Inductors using packaging technologies 141
6.1 Screen printed inductors 142
6.2 Magnetic printed circuit board inductors 143
7 MEMS power inductors 146
8 Conclusions 148
References 149

6b. Martin A.M. Gijs
Magnetic Particle Handling in Lab-on-a-Chip Microsystems 153
1 Introduction 153
2 Magnetic particle separation 155
3 Magnetic particle transport 155
4 Magnetic particles as labels for detection 157
5 Magnetic supraparticle structures 157
6 Magnetic particles as substrates for bio-assays 158
7 Magnetic beads in droplets 159
8 Conclusion 159
References 160

7. Oliver Gutfleisch, Nora M. Dempsey
High Performance μ-Magnets for Microelectromechanical Systems (MEMS) 167
1 Introduction 167
1.1 Basic principles of permanent magnet materials 169
1.2 Hard magnetic materials 173
2 μ-Permanent magnets 181
2.1 Top-down preparation techniques 183

2.2 Bottom-up preparation techniques 184
2.3 Patterning 187
3 Conclusions 189
References 189

8. Rostislav Grechishkin, Sergey Chigirinsky, Mikhail Gusev, Orphée Cugat, Nora M. Dempsey
Magnetic Imaging Films 195
1 Introduction 195
2 Nanoparticle films (Bitter method) 197
2.1 Liquid bitter films 197
2.2 Dried bitter films 197
2.3 Nanoparticle condensation ("smoke" method) 197
2.4 Magnetotactic bacteria 198
2.5 Solidified ferrofluid films 198
2.6 Micro-encapsulated ferrofluid containing films 199
2.7 Resume of and prospects for nanoparticle films 199
3 Ferrite garnet MO imaging films (MOIF) 200
3.1 Preparation and properties 200
3.2 Mo contrast and experimental setup 205
3.3 Comparison of uniaxial and planar MOIF 208
3.4 Intrinsic domain structure of planar MOIF 212
4 Amorphous metallic MOIF 214
4.1 Uniaxial low-coercivity films 214
4.2 Uniaxial high–coercivity films and thermomagnetic imprinting 215
5 Some application examples 216
5.1 Magnetic recording 216
5.2 Permanent magnets 216
5.3 Electric currents 218
5.4 Eddy current microscopy 218
5.5 Domain structure of wires 219
5.6 Spin reorientation transitions in multilayers 219
5.7 Hidden magnetic images in documents 219
5.8 Composition-spread studies 220
6 Summary 220
References 220

9. Giovanni Asti
Energy Exchanges of Magnets with the Environment 225
1 Introduction 225
2 Basic principles 226

2.1 Extrinsic representation 226
2.2 Intrinsic representation 227
2.3 The mechanical actions on magnetic bodies 228
3 Examples 231
3.1 Torque magnetometer 231
3.2 Calculation of the torque on a diamagnetic (or paramagnetic) substrate 234
Appendix: apparent susceptibility 236
References 236

10. Thomas Thomson, Leon Abelmann, Hans Groenland
Magnetic Data Storage: Past Present and Future 237
1 Introduction 237
2 Longitudinal recording on hard disc and tape 241
2.1 Media 241
2.2 Heads 248
2.3 Positioning 258
2.4 Signal processing/data encoding 261
3 Perpendicular recording 264
3.1 Media 265
3.2 Heads 270
3.3 Signal processing/data encoding 273
3.4 Intertrack interference (ITI) 274
4 Future recording technologies 274
4.1 Patterned media 274
4.2 Thermally assisted recording 284
4.3 Non-conventional media (nanoparticles) 291
4.4 Probe storage 295
4.5 Units 299
References 300

11. Salvatore Savasta
Quantum effects in interacting electron systems: The role of spin in the interaction and entanglement in mesoscopic systems 307
1 Introduction 307
2 Introduction to spin and entanglement 309
3 Electronic excitations in semiconductors 313
4 Of bulk excitonic- 317
5 Quantum complementarity of cavity polaritons 319
6 Spin entangled cavity polaritons 322
References 323

12. Pietro Gambardella
Magnetism in one-dimensional metal systems 325
1 Introduction 325
2 Epitaxial growth of one-dimensional atomic chains 328
3 Short- and long-range ferromagnetic order in one-dimension 330
3.1 Experiment 330
3.2 Magnetic behavior of Co monatomic chains 331
3.3 Spin block model 332
3.4 Heisenberg model 333
4 Dependence of the magnetic moment and anisotropy on the atomic coordination 336
5 Conclusions 338
References 339

Index 343

PREFACE

This book follows a NATO Advanced Study Institute on "Magnetic Nanostructures for Micro-Electromechanical Systems and Spintronic Applications" which has been held in Catona (Italy) from 2^{nd} to 15^{th} of July 2006. The objective of the school was to present the recent advances in the science of magnetic nanostructures and related developments in the field of nanotechnology for advanced magneto-electronic devices and magnetic micro-electromechanical systems. This goal was accomplished through a synergic junction between the characteristic expertise of the engineering and the knowledge of the basic science, thus favoring interdisciplinary enrichment and cross-cultural fertilization.

The Advanced Study Institute was held in the frame of the NATO initiative concerning the SECURITY THROUGH SCIENCE, that, among its objectives includes the addressing of the partner-country priorities in technology transfer. The contents of the School have indeed a strategic relevance in important fields such as information technology, micro-actuators and sensors. In addition the School contributed to the specific role of training young scientists in NATO counties.

The current volume is not merely intended as a proceeding of the School but it rather represents an articulate restructuring of the contributions in order to offer a real "state of the art" in the subject. It covers the period of the last decades during which fundamental discoveries such as giant magneto-resistance have been successfully transferred to industrial applications and new outcomes in spin-dependent processes, micromagnetic modeling, magnetic recording and innovative experimental techniques have been developed.

The book deals with the most advanced fields of modern magnetic nanotechnologies. It should be a significant source of up to date information for young physicists, chemists and engineers as well as a crucial reference for expert scientists and the teachers of advanced university courses.

The Editors wish to thank all the authors for their contributions. The cooperation of M. Carpentieri, G. Consolo and G. Finocchio is gratefully acknowledged.

Messina, January 2007
Bruno Azzerboni, Giovanni Asti, Luigi Pareti and Massimo Ghidini

ACKNOWLEDGEMENTS

The Organizing Committee of the School and the editors would like to acknowledge the sponsorship of the NATO Science Committee.

LIST OF CONTRIBUTORS

Leon Abelmann, Systems and Materials for Information Storage Group, Twente University, 7500AE Enschede, Netherlands. l.abelmann@utwente.nl

Giovanni Asti, Dipartimento di Fisica, Università di Parma, 43100, Italy. asti@unipr.it

Bruno Azzerboni, Dipartimento di Fisica della Materia e Tecnologie Fisiche Avanzate, Faculty of Engineering, University of Messina, Italy. azzerboni@ingegneria.unime.it

Giorgio Bertotti, Istituto Elettrotecnico Nazionale (IEN) Strada delle Cacce 91, 10135 Torino – Italy. bertotti@inrim.it

Mario Carpentieri, Dipartimento di Fisica della Materia e Tecnologie Fisiche Avanzate, Faculty of Engineering, University of Messina, Italy. carpentieri@ingegneria.unime.it

Sergey Ghigirinsky, Laboratory of Magnetoelectronics, Tver State University Zheliabova str., 33 170000 Tver, Russia. Sergey.Ghigirinsky@tversu.ru

Giancarlo Consolo, Dipartimento di Fisica della Materia e Tecnologie Fisiche Avanzate, Faculty of Engineering, University of Messina, Italy. consolo@ingegneria.unime.it

Orphée Cugat, Grenoble Electrical Engineering Lab UMR, 5529 INGP/UJF – CNRS ENSIEG – BP 46 – 38402 Saint-Martin-d'Hères, Cedex France. Orphee.Cugat@inpg.fr

Gerome Delamare, Grenoble Electrical Engineering Lab UMR 5529 INPG/UJF – CNRS ENSIEG – BP 46 – 38402 Saint-Martin-d'Hères Cedex, France. gerome.delamare@inpg.fr

Nora M. Dempsey, Institut Néel, CNRS/UJF, 25 rue des Martyrs, 38042, Grenoble, France. nora.dempsey@grenoble.cnrs.fr

Giovanni Finocchio, Dipartimento di Fisica della Materia e Tecnologie Fisiche Avanzate, Faculty of Engineering, University of Messina, Italy. gfinocchio@ingegneria.unime.it

Pietro Gambardella, LNS/EPFL Laboratory of Nanostructures at Surfaces Station 3 CH-1015 Lausanne, Switzerland. pietro.gambardella@epfl.ch

Martin Gijs, Ecole Polytechnique Fédérale de Lausanne, Institute of Microelectronics and Microsystems CH-1015 Lausanne, Switzerland. martin.gijs@epfl.ch

Rostislav Grechishkin, Laboratory of Magnetoelectronics, Tver State University Zheliabova Str., 33 170000 Tver, Russia. Rostislav.Grechishkin@tversu.ru

JPJ Groenland, Systems and Materials for Information Storage Group, Twente University, 7500AE Enschede, Netherlands. groenland@utwente.nl

Mikhail Gusev, Research Institute of Materials Science and Technology, 124460 Zelenograd, Russia

Oliver Gutfleisch, IFW, Institute for Metallic Materials, Dresden Helmholtzstr. 20 D-01069 Dresden Germany. P.O. Box 270016, D-01171 Dresden. o.gutfleisch@ifw-dresden.de

Mathias Klaeui, Department of Physics, University of Konstanz, Konstanz, Germany. mathias@klaeui.de

Luis Torres, Departmento de Fisica Aplicada, University of Salamanca, Plagade la Merced, 37008 Salamanca, Spain

Luis Lopez-Diaz, University of Salamanca, Departamento de Fisica Aplicada, Plaza de la Merced, 37008 Salamanca, Spain. lld@usal.es

Gilbert Reyne, Grenoble Electrical Engineering Lab UMR 5529 INPG/ UJF - CNRS ENSIEG – BP 46 – 38402 Saint-Martin-d'Hères Cedex France. gilbert.reyne@inpg.fr

Salvatore Savasta, Dipartimento di Fisica della Materia e Tecnologie Fisiche Avanzate – University of Messina Salita Sperone 31, 98166 Messina, Italy. Salvatore.Savasta@unime.it

John C. Slonczewski, IBM Watson Research Center, Box 218, Yorktown Heights, New York 10598, USA. john.slonczewski@verizon.net

Tom Thomson, Hitachi San Jose Research Center, San Jose, CA 95120, USA. thomas.thomson@hitachigst.com

SPIN-POLARIZED CURRENT AND SPIN-TRANSFER TORQUE IN MAGNETIC MULTILAYERS

JOHN SLONCZEWSKI*
IBM Research Division

Abstract. We expose the theory of quantized spin-polarized electron transport perpendicular to the plane of a magnetic multilayer with non-collinear magnetization vectors. The dependence of resistance and current-driven torque on relative angle between 2 magnetic moments of a multilayer pillar are derived. Spacers of both metallic and insulating tunnel-barrier types are considered. The classical Landau-Lifshitz equation describes the dynamics of the magnetization created by spin-transfer torque.

Keywords: Spin-polarized current, spin-transfer, magnetic multilayers, torque, pillar, metallic, tunneling

1. Introduction

In 1996, Luc Berger predicted that electric current flowing across a normal metal spacer between two magnets could excite forward-propagating spin waves in one of them.[1] In the same year, a ballistic WKB model predicted that a steady current may create a spin-transfer torque which would excite magnetic precession in one of two so seperated single-domain magnets having dimensions of order 100 nm.[2] If the sign of uniaxial anisotropy is negative, this precession may remain steady, making conceivable an RF oscillator. If the anisotropy is positive, magnetic reversal may ultimately occur, in which case writing magnetic memory is conceivable. Subsequent experiments supported these predictions and led to the vast array of new spin-transfer phenomena under investigation today.[3]

However, the first copious experimental evidence for any current-driven magnetic excitation was that of M. Tsoi et al in 1998,[4] who passed currents through mechanical point contacts into unpatterned (not single-domain) multilayers. In the absence of lithography, spin waves radiate energy transversally away from the contact region, greatly increasing the current required for excitation.[5] The year 1999 saw the beginning of mono-domain excitation in structures where the excited free magnet has dimensions of $\leq$ 150 nm. These included an oxide particle[6] and one layer of a lithographed all-metallic multilyer.[7]

* IBM RSM Emeritus

B. Azzerboni et al. (eds.), Magnetic Nanostructures in Modern Technology, 1–35.

Equivalent circuits of spin-polarized current play a large role in the theory of GMR and spin transfer torque.[8,9] Sections 2–4 present a *majority-spin transparency* model for diffusive non-collinear CPP-GMR and current-driven torque.[10] It takes explicit account of the band structures of the elements Co, Ni, and Cu used in many experiments. The question of torque is reduced to that of solving an effective circuit whose branches consist of the 4 spin-channel currents flowing in the 2 ferromagnets. The key formulas for cross-spacer connection of spin-channel voltages and currents enable algebraic solution of effective circuit equations. This theory predicts the currents and torques, requiring only the resistance and spin-relaxation parameters which govern, generally by linear coupled diffusion equations,[11] the current-voltage relations of the separate spin channels.

Section 5 presents the barest essentials of the magnetic dynamics resulting from spin-transfer torque. It assumes uniaxial anisotropy and illustrates both the switching and steady precession of a monodomain produced by a steady electric current.

Recently, spin-transfer switching was observed in magnetic tunnel junctions (MTJs). In 2004, two laboratories, at Grandis, Inc.[12] and Cornell U.,[13] reported it independently, thus making available higher signal voltages in memory elements. Sections 6–8 treats non-collinear magnetoresistance and spin transfer torque for the case of MTJs, employing Bardeen tunneling theory. For a quantum basis set, we take the eigenfunctions of any self-consistent field allowing any degree of atomic disorder in the magnetic electrodes (e.g. due to alloying) and magnet-barrier interface regions (e.g. due to roughness). This procedure is convenient, yet can reflect consequences of electron structure.

For a given voltage V, one has the known two-parameter formula $J = VG_0(1 + g\cos\theta)$ for the electric-current density versus the angle θ between the moments. Section 7 presents the theory for left- and right-torque densities $(\hbar/2e)VG_0\tau_{\mathrm{L,R}}\sin\theta$ with respective dimensionless coefficients τ_{L} and τ_{R}. Assuming the tunneling is elastic and validity of the polarization factors P_{L}, P_{R} for the two electrode-and-barrier compositional combinations, one has the mutual relation $g = \tau_{\mathrm{L}}\tau_{\mathrm{R}}$, with $\tau_{\mathrm{L}} = P_{\mathrm{R}}$ and $\tau_{\mathrm{R}} = P_{\mathrm{L}}$. Polarization factors are less convenient at the high voltages and small barrier thicknesses needed in practice where inelastic tunneling becomes more important. Responding to the recent advent of very highly magnetoresistive MTJs with MgO barriers, Sec. 8 describes an appropriate phenomenological model which concludes with predicted observational signatures of potential effects caused by special conditions at the F/I interfaces.

2. Two-channel spin-polarized transport

2.1. SUPPRESSION OF TRANSVERSE POLARIZATION

The internal exchange field giving rise to the spontaneous magnetization of a ferromagnet such as Fe, Co, or Ni is so strong that, in equilibrium, it creates a relative shift between spin-up and spin-down sub-bands amounting to about 2 eV for Fe and Co, and 1 eV for Ni. Consequently, if an additional out-of equilibrium electron should initially occupy a state in which the spin lies orthogonal to the spontaneous magnetization, then it precesses at this terrific frequency that is orders of magnitude greater than the frequencies encountered in the magnetic dynamics of nano-scale device elements described by classical Landau-Lifshitz equations.

More precisely, it is not exchange alone, but a *combination of three effects* which creates such a strong exchange splitting of those band regions near the Fermi surface which are important in electron transport. To begin, a free atom of Fe, Co, or Ni has the electron configuration $3d^n4s^2$ outside of an argon core. The values of n are 6 for Fe, 7 for Co, and 8 for Ni. When the atoms bond to form a pure metal, the strong spin-diagonal (non-exchange) crystalline electric field causes two effects. The first effect is that the electrostatic field of neighboring point-charge nuclei disrupts the atomic orbitals and "quenches" the atomic-orbital angular momentum. Secondly, it permits electron waves at the Fermi level to propagate with relative freedom through the lattice. Quantum-mechanically, both of these effects cause the atomic s($l = 0$) wave functions to mix strongly with p($l = 1$) and d($l = 2$) wave functions. Indeed, the sheer number of p(3) and d(5) states is so great compared to the one s state per atom, that none of the band states at the Fermi surface have predominantly s-character. (The one-electron V_{sd} matrix element in first-principle band-structure computations is of order 1–2 eV.) Thirdly, it follows that this mixing generally subjects the Fermi-energy electrons to the mean-field atomically *internal* d-d exchange interaction. This exchange is extremely large amounting to a level splitting of order $J_{dd} \approx$ 1–2 eV. Generally, very few of the wave functions approach the character of 4s or free-electron waves for which the exchange splitting would be smaller (≈ 0.1 eV). This fact accounts for the large Curie temperatures of these 3 ferromagnetic metals.

The physical consequence of this large exchange splitting is that an electron spin vector initially polarized transverse to $\mathbf{M}$ (which is collinear with the exchange field) must precess at a huge frequency characteristic of electronic energy levels. Consequently, the transverse polarization and its current are very strongly suppressed on the distance (>2 atomic layers) and time scales (>10 ps) of usual interest in magnetic memory.

Strong suppression of transverse spin components in a ferromagnet makes credible the *spin-channel model* of electron transport. Consider the layered

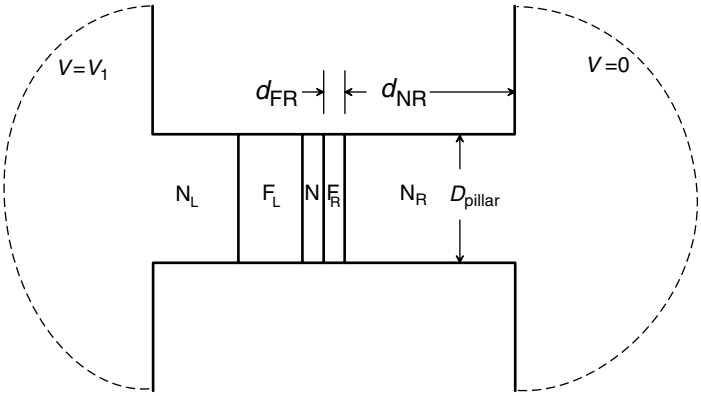

Figure 1. Magnetic-multilayer pillar laid sideways. N = normal metal, F = ferromagnet, L = left, R = right.

submicron metallic pillar joining two non-magnetic semi-infinite conductors of composition N shown in Fig. 1. It is rotated 90° so that the deposition plane is oriented vertically. The pillar includes left (F_L) and right (F_R) magnets separated by a very thin non-magnetic spacer. The cross-section in the plane parallel to the substrate is an ellipse with dimensions typically $100 \times 60\,\mathrm{nm}^2$.

Of interest is the resistance of this pillar to flow of electric current between the voltage $V = V_1$ deep within a bulky electric lead on the left and another voltage $V = 0$ deep within a similar bulky lead on the right. In metals a convenient measure of the relaxation is the characteristic so-called spin "diffusion" (relaxation, really) length (λ_N or λ_F) measuring the *spatial* decay of polarization described by the function $\exp(-x/\lambda_N)$ or $\exp(-x/\lambda_F)$.

The dimensions of experimental pillars often approach the condition that they are too small for relaxation to be of consequence. The thickness of each sublayer component must be less than the corresponding diffusion length. Sufficient such conditions for the pillar of Fig. 1 are

$$d_{NL}, d_{NR} \ll \lambda_N; \quad d_{FL}, d_{FR} \ll \lambda_F. \tag{1}$$

Our representation of spin relaxation in the external leads by means of the shorts shown in Fig. 2 requires an opposite sort of condition, namely that dimensions of the leads are greater than λ_N. If one of these conditions is violated, the problem requires solution of a two-component diffusion equation.

2.2. HALF-PILLAR RESISTORS

One may decompose each of the 4 *half-pillar* unit-area channel resistors $R_{L\pm}$ and $R_{R\pm}$ into terms in series arising from 2-channel bulk resistivity $\rho\pm$, from 2-channel unit-area interfacial resistance $r_\pm$, and from an end-effect term occurring

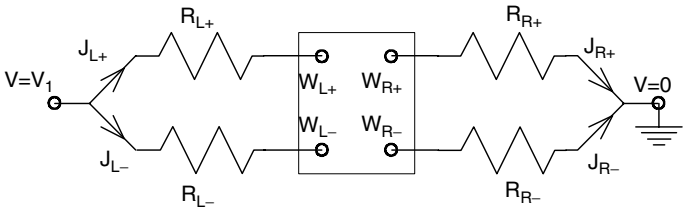

Figure 2. Equivalent two-channel circuit for a pillar containing a N/F/N multilayer.

at the pillar-lead connection. Thus the half-pillar unit-area resistances, with the subscripts R and L here elided, are

$$R_\pm = \rho_\pm d_\mathrm{F} + 2r_\pm + \rho_\mathrm{N}(2d_\mathrm{N} + \pi D_\mathrm{pil}/2) \tag{2}$$

where d_F and d_N are layer thicknesses and D_pil is the pillar diameter. (Remember the central spacer N is neglected.) The term $\pi\rho_\mathrm{N} D_\mathrm{pil}/2$ is due to the contact, approximated by half of a *constriction* resistance $\rho_\mathrm{N}/D_\mathrm{pil}$ derived long ago by James Clerk Maxwell. (The conducting constriction in Maxwell's case joins two semi-infinite conductors of homogeneous resistivity.)

A group at Michigan State University[14] made a series of systematic measurements of collinear CPP-GMR of magnetron-sputtered periodic N/F/N/F/N.. multilayers, numbering as many as 40 periods, at 4.2 K. This study established values of the resistance parameters appearing in Eq. (2). These values, as well as the spin diffusion distances λ_F and λ_N occurring in the conditions (1) are given in the table below.

The low-temperature resistivity of Cu and Ag varies with sputtering conditions but is typically about 3 times its 300K value given in the table. Sometimes the

TABLE I. Transport parameters for multilayers composed of sputtered Co, Cu, and Ag.

parameter	units	Co/Cu	Co/Ag
ρ_N(300 K)	nΩm	17	16
λ_F (4.2 K)	nm	50	50
λ_N (4.2,300 K)	nm	1500, 350	
from collinear	GMR experiments[14]	at 4.2K:	
ρ_+	nΩm	81	111
ρ_-	nΩm	220	320
r_+	$10^{-15}\Omega\mathrm{m}^2$	0.24	0.17
r_-	$10^{-15}\Omega\mathrm{m}^2$	1.8	2.1
G, Eq. (21)	$10^{15}\Omega^{-1}\mathrm{m}^{-2}$	1.32	1.04

magnet F_L is part of the substrate; then, in the limiting cases $\lambda_{FL} \ll D_{pil}$ and $\lambda_{FL} \gg D_{pil}$, this equation for L is replaced by the estimate

$$R_{L\pm} = r_\pm + \rho_\pm \cdot \min(\Lambda_{sf}, \pi D_{pil}/4), \tag{3}$$

where D_{pil} is the diameter of the pillar.

3. Effective circuit for a non-collinear all-metallic pillar

3.1. SPIN POLARIZATION IN A ROTATED REFERENCE FRAME

The term *spin accumulation,* or spin-polarization density, in a normal metal refers to the expectation value of σ_z for a set of electrons occupying a unit volume. Of course, its value depends on the quantization axis ζ considered. How it transforms in a spacer under coordinate-axis rotation is crucial to electron transport in non-collinear magnetic multilayers.

Consider n electrons occupying only given numbers $n_\pm$ of *pure* eigenstates $|\pm\rangle$ of $\sigma_z = \pm 1$, respectively, in our unprimed frame. The spin accumulation in a normal metal by definition is

$$\Delta n = n_+ - n_-. \tag{4}$$

Consider the primed frame, whose z'-axis lies in the xy-plane at an angle θ from the z-axis. The same electrons have the spin accumulation

$$\Delta n' = n'_+ - n'_- \tag{5}$$

where $n'_\pm$ is the expectation value of $\sigma_{z'}$. Applying the square-law of probability, n'_+ is obtained from the first column of the spin rotation matrix[23]

$$\langle \sigma | \sigma' \rangle' = \begin{pmatrix} \cos(\theta/2) & \sin(\theta/2) \\ -\sin(\theta/2) & \cos(\theta/2) \end{pmatrix}. \tag{6}$$

The result is

$$n'_+ = n_+ \cos^2 \frac{\theta}{2} + n_- \sin^2 \frac{\theta}{2}. \tag{7}$$

From the second column of (6), one finds

$$n'_- = n_+ \sin^2 \frac{\theta}{2} + n_- \cos^2 \frac{\theta}{2}. \tag{8}$$

After substitution of Eqs. (7), (8), and (4), Eq. (5) reduces to

$$\Delta n' = \Delta n \cos\theta. \tag{9}$$

Application of this equation requires caution because it involves no interaction, no physical change in the condition of the system during the transformation. The spins states remain pure eigenstates $|\pm\rangle$ of σ_z in the unprimed frame throughout.

3.2. SPIN-DEPENDENT ELECTRON DISTRIBUTION

Our treatment of non-colinear spin-dependent transport here totally neglects scattering within the spacer. It is equivalent to special cases of the computational drift-diffusion approach of M. Stiles and co-workers.[3] It is also a special case of independent circuit theory by X. Waintal et al.[16] It differs from arguments based on a general circuit theory (See Ref. 8 and Sec. 6.2 of 9). For the theoretical construct of a *node* having internal statistical equilibrium between different momentum directions in the latter references does not apply to the copper spacers of several nm thickness in usual spin-transfer experiments in which the mean free path at 300 K is about 40 nm. At much lower temperatures, where most magnetoresistance measurements are made, λ may be 3 times greater. Nonetheless, in the appropriate limit, the general theory reduces to our connection formulas given below.[17]

Figure 3 indicates a left ferromagnet F_L, having spontaneous magnetization $\mathbf{M}_L = -M_L\mathbf{l}$, separated from a right ferromagnet F_R, having spontaneous magnetization $\mathbf{M}_R = -M_R\mathbf{r}$, by a non-magnetic metal N. Here, $\mathbf{l}$ and $\mathbf{r}$ are unit spin-moment vectors forming the general mutual angle $\theta = \cos^{-1}(\mathbf{l}\cdot\mathbf{r})$. We assume the presence of steady-state spin-dependent currents within each

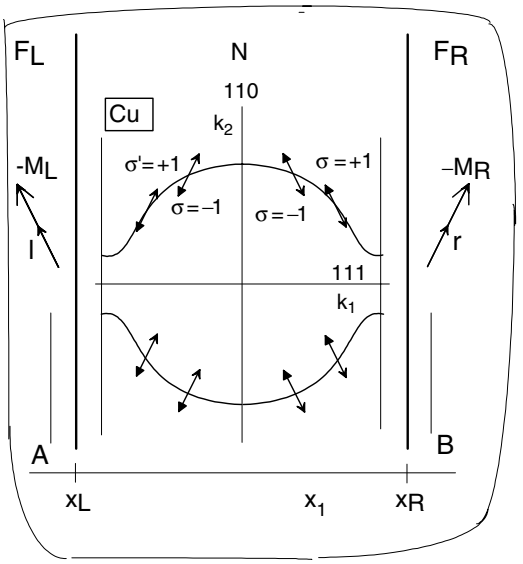

Figure 3. Notations for a metallic trilayer including ferromagnetic layers F_L with magnetization vector $\mathbf{M}_L$ at left and F_R with magnetization $\mathbf{M}_R$ at right, separated by a non-magnetic spacer N. Shown schematically is a $11\bar{2}$-section of the Fermi surface for a Cu spacer with 111-axis normal to the layer plane. Arrows on the surface depict spin polarization axes described in the text. The right (left) half of the Fermi surface is polarized parallel to the moment axis of the left (right) magnet.

ferromagnet The proximity of two different ferromagnetic polarization axes **l** and **r** implies the absence of any single axis of spin polarization appropriate to electrons within N. To deal with this situation, we describe the steady electron state within N that is consistent with the channel currents and potentials of the ferromagnets.

We distinguish alternative **l**− and **r**− quantization axes for Pauli spin with operators σ_1 and σ_r satisfying eigenstate equations $\sigma_1|\mathrm{L}, \sigma\rangle = \sigma|\mathrm{L}, \sigma\rangle$ ($\sigma = \pm 1$, sometimes abbreviated as $\sigma = \pm$) and $\sigma_r|\mathrm{R}, \sigma'\rangle = \sigma'|\mathrm{R}, \sigma'\rangle(\sigma' = \pm 1, \text{ or } \pm)$. The spin states satisfy

$$\langle i, \sigma | i, \sigma' \rangle = \delta_{\sigma,\sigma'} \quad (i = \mathrm{L}, \mathrm{R}) \tag{10}$$

and the plane spin rotation transformation:

$$\langle \mathrm{L}, \sigma | \mathrm{R}, \sigma' \rangle = \begin{pmatrix} \cos(\theta/2) & -\sin(\theta/2) \\ \sin(\theta/2) & \cos(\theta/2) \end{pmatrix}. \tag{11}$$

Total absences of exchange coupling and scattering within N are assumed. Whatever subregion within the spacer, adjoining $\mathrm{F_L}$ or $\mathrm{F_R}$, contains significant decaying exchange, or any interface-related scattering centers which may be present, is considered to belong to that magnetic region ($x_1 < x_\mathrm{L}$ or $x_1 > x_\mathrm{R}$) rather than to N.

Note, however that any electron within N ($x_\mathrm{L} < x_1 < x_\mathrm{R}$) moving *rightward*, thus satisfying $v_1(\mathbf{k}) > 0$ and represented by decoration with the symbol $\rightarrow$, last *either* passed through (transmitted), *or* back-scattered from, the *left* ($\mathrm{F_L/N}$) interface. If transmitted, its final polarization is clearly $|\mathrm{L}, +\rangle$ or $|\mathrm{L}, -\rangle$ according to the two-channel model of spin-polarized current flowing in $\mathrm{F_L}$. If backscattered, the electron spin has *the single polarization* $|\mathrm{L}, -\rangle$ under an assumed condition of *perfect majority-spin transmission* (PMST; see below.) through the interface. Therefore, a rightward moving electron [$\rightarrow$, with $v_1(\mathbf{k}) > 0$] has pure spin polarization $|\mathrm{L}, +\rangle$ or $|\mathrm{L}, -\rangle$, with no mixing that would describe a spin tilt away from this quantization axis. Similarly, a leftward moving electron [$\leftarrow$, with $v_1(\mathbf{k}) < 0$] has only pure spin polarization $|\mathrm{R}, +\rangle$ or $|\mathrm{R}, -\rangle$. This scheme for the case of a 111-textured multilayer is illustrated in the $11\bar{2}$-section of the copper Fermi surface sketched within Fig. 3.

The PMST condition is supported very well by the very small experimental values of interfacial resistance r_+ for Co/Cu and Co/Ag interfaces seen in Table 1 of the previous Section. (They are one order of magnitude smaller than the respective r_-). For they are consistent with a mean reflection coefficient of $\approx 5\%$. If this were 0% then reflected electrons could have only the minority-spin orientation and the polarization scheme in Fig. 3 would be exact. Therefore, for pillars composed of Co and Cu or Ag this electron distribution is well justified.

Why do the majority-spin electrons reflect so weakly? The answer lies in the following peculiarity of ferromagnetic electron structure: In experimental sputtered films, the metals Co, Ni, and Cu all have face-centered cubic (fcc) structure. As atomic number A increases in the sequence Co(A=27), Ni(28), Cu(29), each additional electron enters the minority band. In this range of A, the majority-spin electrons have the constant configuration $3d^5s^1$. Consequently, the majority-spin energy bands differ very little. As indicated in the schematic cross-section shown in Fig. 3, the majority-spin Fermi surface for Cu differs from a free-electron sphere mainly by the presence of small "necks" which lie along 111-axes and join the surface to the Brillouin-zone boundary. The diameter of the neck increases with increasing A, but otherwise the shape of the Fermi surface hardly changes. A majority-spin electron incident onto such an interface feels little change in potential. For this reason, majority-spin electrons reflect weakly at Co/Cu and Ni/Cu interfaces. Results of first-principle numerical computations[19] support this qualitative conclusion.

3.3. FORMULAS FOR CONNECTING CHANNELS ACROSS A SPACER

Spin channel currents are driven by a *chemical potential* in addition to the ordinary electrostatic potential. To illustrate this fact, consider $T = 0$K. Begin with states in the spacer having energy $\varepsilon \leq \varepsilon_{F0}$ at some point in the band channel $\sigma(= \pm)$ occupied up to the Fermi level ε_{F0}. First apply the electrostatic voltage V at this point. Clearly, the new Fermi level for each σ is $\varepsilon_F \to \varepsilon_{F0} - eV$ and the particle potential $-eV$ provides impetus to drive electrons away from (or attract them to) the given point. Suppose that some non-equilibrium process adds the number n_σ of electrons per unit volume to the channel σ at the same point. Because of the exclusion principle, the Fermi level must rise in first order approximation by the amount n_σ/n_F, where n_F is the electron density per unit energy and volume at $\varepsilon = \varepsilon_{F0}$, in order to make room for the added electrons. Clearly, now the Fermi level is spin-dependent and given by $\varepsilon_{F,\sigma} = \varepsilon_{F0} - eV + (n_\sigma/n_F)$. Surely, this chemical voltage $-n_\sigma/en_F$ is able to drive a channel current just as well as the equivalent amount of electric voltage V. It follows that transport in spin channels requires augmenting the electric voltage to form the total *electrochemical* voltage defined by

$$W_\sigma = V - n_\sigma/en_F. \tag{12}$$

One must hasten to add that in the absence of appreciable electrostatic capacitance, which we assume, charge neutrality is preserved. Thus, one has the condition $n_+ = -n_-$. It is easy to see that this expression for W_σ is correct at $T > 0$ K as long as kT is small compared to the width of the energy band.

So now we know that electric current density J_σ in a half-pillar spin channel $\sigma(= \pm)$ must be written $J_\sigma = W_\sigma/R_\sigma$, where R_σ is the unit-area resistance.

According to the laws of electric circuits, the ordinary *electric* voltage $V = (W_+ + W_-)/2$ and true *electric* current $J = J_+ + J_-$ must be continuous everywhere, and in particular across the central normal-metal spacer in Fig. 1. But we need 4 continuity relations altogether, so we must find two more in order to solve the complete circuit in Fig. 2. We attach the subscripts L and R to specify values for every quantity *evaluated within the spacer,* using the left and right spin-coordinate axes, respectively. Thus, left- and right-so-called *spin accumulation* or polarization densities are

$$\Delta n_{\mathrm{L}} \equiv n_{\mathrm{L},+} - n_{\mathrm{L},-} \text{ and } \Delta n_{\mathrm{R}} \equiv n_{\mathrm{R},+} - n_{\mathrm{R},-}. \tag{13}$$

Accordingly, we have

$$\Delta W_{\mathrm{L}} \equiv W_{\mathrm{L},+} - W_{\mathrm{L},-} = -(\Delta n_{\mathrm{L}}/en_{\mathrm{F}}) \text{ and } \Delta W_{\mathrm{R}} = -(\Delta n_{\mathrm{R}}/en_{\mathrm{F}}). \tag{14}$$

Finding two relations connecting ΔW_{R} and ΔJ_{R} to ΔW_{L} and ΔJ_{L} will suffice, together with continuity of V and J, to provide the four relations needed to solve the circuit of Fig. 2.

To proceed further, we need to parametrize the spin-polarization scheme shown in Fig. 4. For simplicity the Fermi surface is spherical. This figure indicates that the spin-polarization of electrons within N is concentrated within two hemispherical shells marked with scalar *partial spin accumulations* $\overleftarrow{\Delta n}$

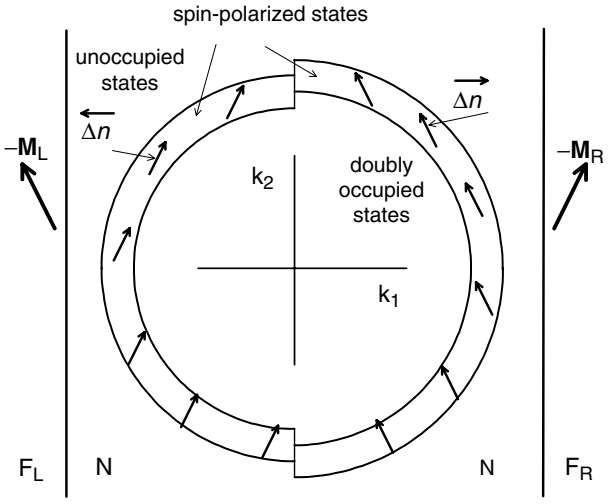

Figure 4. A special form of the previous Figure. It illustrates the parametrization of the non-equilibrium spin polarization of the Boch states in a metallic spacer having a spherical Fermi surface.

and $\overrightarrow{\Delta n}$. The thicknesses of these shells are infinitessimal for linear transport. The left- (right-) arrow above the symbol $\overleftarrow{\Delta n}(\overrightarrow{\Delta n})$ means that the electrons are moving leftward(rightward), $v_1 < (>)0$. In accord with our discussion connected with Fig. 3, the polarization axis for $\overleftarrow{\Delta n}(\overrightarrow{\Delta n})$ is $-\mathrm{M_R}(-\mathrm{M_L})$. The electron states outside of these shells are either doubly occupied or empty and therefore unpolarized in both cases.

To evaluate Δn_L, note that the shell marked $\overrightarrow{\Delta n}$ is already polarized along axis $-\mathrm{M_L}$ so it contributes to the total as it stands. But the one marked $\overleftarrow{\Delta n}$ is polarized along the other axis $-\mathrm{M_R}$ so its contribution must be projected upon the axis $-\mathrm{M_L}$. Therefore, one has from Eq. (9)

$$\Delta n_\mathrm{L} = \overrightarrow{\Delta n} + \overleftarrow{\Delta n}\cos\theta. \tag{15}$$

One then has from (14), and similarly using $\Delta n_\mathrm{R} = \overleftarrow{\Delta n} + \overrightarrow{\Delta n}\cos\theta$,

$$\Delta W_\mathrm{L} = -(\overrightarrow{\Delta n} + \overleftarrow{\Delta n}\cos\theta)/en_\mathrm{f},\ \Delta W_\mathrm{R} = -(\overleftarrow{\Delta n} + \overrightarrow{\Delta n}\cos\theta)/en_\mathrm{f}. \tag{16}$$

Evaluation of the current difference $\Delta J_{\mathrm{L(R)}} \equiv J_{\mathrm{L(R)}+} - J_{\mathrm{L(R)}-}$ is similar, except that to obtain current, one must weight the terms $\overleftarrow{\Delta n}(\overrightarrow{\Delta n})$ in Eq. (15) with $\pm e\overline{v}$, where $\overline{v}$ is the mean of v_1 over the right hemisphere of the Fermi surface. The current differences are

$$\Delta J_\mathrm{L} = e\overline{v}(\overleftarrow{\Delta n}\cos\theta - \overrightarrow{\Delta n}),\ \Delta J_\mathrm{R} = e\overline{v}(\overleftarrow{\Delta n} - \overrightarrow{\Delta n}\cos\theta). \tag{17}$$

From the four equations (16) and (17), one may eliminate the two variables $\overleftarrow{\Delta n}$, $\overrightarrow{\Delta n}$ to find the two desired connection equations:

$$\Delta J_\mathrm{R} = \left[\Delta J_\mathrm{L}(1+\cos^2\theta) - G\Delta W_\mathrm{L}\sin^2\theta\right]/2\cos\theta \tag{18}$$

$$\Delta W_\mathrm{R} = \left[-G^{-1}\Delta J_\mathrm{L}\sin^2\theta + \Delta W_\mathrm{L}(1+\cos^2\theta)\right]/2\cos\theta \tag{19}$$

where the single spacer-material parameter required is

$$G = e^2 n_\mathrm{F}\overline{v}/2. \tag{20}$$

These equations are verifiable by substitution of Eqs. (16) and (17).

Since the mean of v_1^2 equals $v_\mathrm{F}^2/3$ where v_F is the Fermi velocity of an assumed spherical Fermi surface of the spacer composition, the rms relation $\overline{v} \approx v_\mathrm{F}/3^{1/2}$ may be used to estimate $\overline{v}$. For a parabolic band this formula then becomes

$$G = e^2 k_\mathrm{F}^2/3^{1/2}\pi h \tag{21}$$

which is $2/3^{1/2}$ times the Sharvin ballistic conductance $G_{\rm Sh}$ (2 spins) per unit area of a constriction whose diameter is smaller in order of magnitude than the mean free path. (Note, however, that the ballistic resistance *phenomenon* itself plays no role in the present theory because all potentials and currents are independent of x_1 within the spacer region N.) Equation (21) gives $G = 1.32 \times 10^{15}\,\mathrm{Ohm}^{-1}\mathrm{m}^{-2}$ for a free-electron gas having the electron density of Cu. A computed value for $G_{\rm Sh}$ in Cu is $0.55 \times 10^{15}\ \Omega^{-1}\mathrm{m}^{-2}$/spin, in substantial agreement with the free-electron formula.

The crucial role of Eq. (15) in this derivation must be understood. Validity of the two-channel model of a ferromagnet does not require the spins within the adjoining spacer to occupy pure eigenstates of σ_ζ where ζ is parallel to **M** of the ferromagnet. One *does* need a correct electron distribution within the spacer as parametrized by the partial spin accumulations $\overleftarrow{\Delta n}$ and $\overrightarrow{\Delta n}$ indicated in Fig. 4. From these, one needs to evaluate only the *expectation* values of the properly evaluated *expectation* values of the accumulations to evaluate $\Delta W_{\rm L,R}$ and $\Delta J_{\rm L,R}$. The fact that not all spins are parallel to the same axis **1** or **r** does not matter.

The connection formulas (18) and (19) may reasonably be applied to Co, Ni, and alloys that lie on the negative-slope side of the Neel-Slater-Pauling curve[18] in which the majority-spin 3d-band is fully occupied. For then the majority-spin electrons at the Fermi level belong to the sp-band and therefore approach the condition of 100% transparency assumed in the derivation above. In particular, these formulas should not be applied when an electrode is composed of Fe.

4. Current-driven pseudo-torque

Our object is to calculate the electric resistance and current-driven torque for a pillar with non-collinear moments. The important thing is to solve the circuit equations for the non-collinear condition considered in the previous Section. As illustrated in the next Section, the connection formulas (18) and (19) are key to this solution. With this solution in hand, the resistance is simply

$$R(\theta) = V/(J_{\rm L,+} + J_{\rm L,-}) \text{ or } = V/(J_{\rm R,+} + J_{\rm R,-}). \tag{22}$$

But the current-driven torque needs the detailed discussion given in the present Section.

4.1. TORQUE MECHANISM

We explain first how the exchange-reaction torque created by scattering of preferentially polarized electrons incident from a normal metal onto a ferromagnet concentrates on the magnetization located within a distance equal to 2 or 3 atomic layers of the interface.

Figure 5 depicts schematically the local spin vector of the stationary-state wave-function for an electron incident rightward onto an N/F interface located at position $\xi \equiv x_1 = 0$. (The spin-coordinate axes η, ζ in Fig. 5 have no special relation to the position coordinates x_2, x_3 of the pillar illustrated in Fig. 1.) Within the region N, the local expectation of spin $\mathbf{s} = \hbar\sigma/2$ for the incident wave is a general constant. Dynamical reaction to the spin momentum scattered by the magnet causes a torque on **M**. Under the PMST assumption in Sec. 3.2 only minority spin $\sigma = -$ can scatter backwards into N. (This reflected wave is not indicated in Fig. 5.) But this *reflected* momentum is collinear with **M**, therefore its reaction does not contribute torque.

The local expectation of s for the wave component *transmitting* into the ferromagnet ($\xi > 0$) has an azimuthal angle with respect to the moment **M** of F given by

$$\varphi(\xi) = \varphi(0) + (k_{\xi+} - k_{\xi-})\xi, \quad (\xi > 0) \tag{23}$$

where $k_{\xi\pm}$ are the normal components of $\sigma = +$ and $\sigma = -$ Fermi vectors at $\varepsilon = \varepsilon_F$. (For graphical simplicity, Fig. 5 shows $\mathbf{M} \| \zeta$, but actually **M** may have any direction.) For a given Fermi energy, the two values of $k_{\eta\pm}(k_\zeta, k_\zeta)$ depend on the conserved transverse momentum components $\hbar(k_\eta, k_\zeta)$ and differ because of internal exchange.

In diffusive metallic transport, the wave vectors of all incident electrons having a given **s** lie very near all parts of the Fermi surface. Therefore the quantity $k_{\xi+} - k_{\xi-}$ varies over a great range. It follows that the averages of $s_\xi \propto \cos\varphi$ and $s_\eta \propto \sin\varphi$ at a given plane ξ approach 0 within an impact depth $\xi = d$ of a few atomic layers.[19,20] If the scale of micromagnetic homogeneity treated in the continuum representation with the Landau-Lifshitz equations is greater than

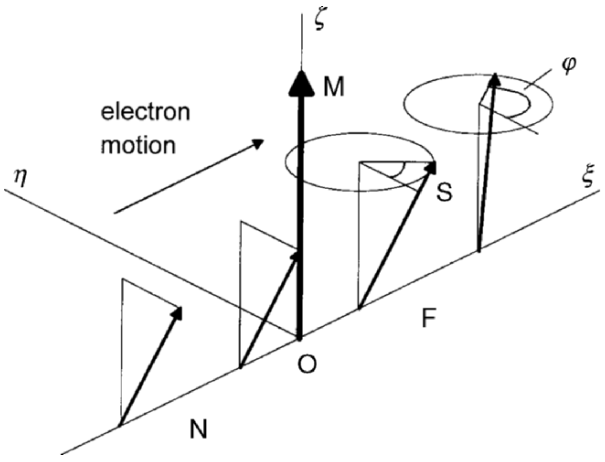

Figure 5. Illustration of spin precession for an electron passing from a nonmagnetic metal ($\xi < 0$) into a ferromagnetic metal ($\xi > 0$).

this impact depth d, as for the monodomain treated in Sec. 6 the reaction of this precession communicates to the magnet the net of the **s** components transverse to **M** of all of the electrons passing through the I/F interface into the magnet F. It follows also that the reactive momentum impulse given to F acts essentially at the interface and lies within the $\mathbf{M} - \mathbf{s}$ plane determined by the incident electrons.

Crucial is the principle of conservation of spin momentum which follows from absence of spin operators in the N-electron hamiltonian for a solid:

$$\mathcal{H} = \sum_i \frac{p_i^2}{2m} + \sum_{i<j} \frac{e^2}{|\mathbf{r}_i - \mathbf{r}_j|} - \sum_{i,l} \frac{e^2 Z_l}{|\mathbf{r}_i - \mathbf{R}_l|}. \tag{24}$$

The first of three terms above is kinetic energy with p_i the electron momentum operator, the second is coulomb interaction between electrons at positions $\mathbf{r}_{i,j}$, and the third is the coulomb interaction between electron i and atomic nucleus l carrying charge Z_l at fixed position $\mathbf{R}_l$. (Internal exhange coupling responsible for the formation of spontaneous magnetization of a ferromagnet arises from the antisymmetry priciple even though spin operators are absent from $\mathcal{H}$.)

Note that we neglect here the small spin-orbit effect. Spin-orbit coupling, in combination with interfacial and defect scattering, determines the spin relaxation lengths λ_N and λ_F tabulated in Table 1. Its neglect is valid within a pillar whose sublayers are thinner than their respective relaxation lengths, as is often the case experimentally. The opposite is true within the leads where this relaxation is represented by the shorts connecting the two spin channels indicated in Fig. 2. Physical effects of spin-orbit coupling are essential to current-induced torque, yet our equations do not necessarily need to include it.

4.2. A GENERAL TORQUE RELATION

Spin-momentum conservation causes the corresponding effective vectorial surface-torque densities $\mathbf{T}_L$ and $\mathbf{T}_R$ (with $\mathbf{l} \cdot \mathbf{T}_L = 0$ and $\mathbf{r} \cdot \mathbf{T}_R = 0$) to satisfy the vector equation

$$\mathbf{T}_L + \mathbf{T}_R = K_R \mathbf{r} - K_L \mathbf{l}. \tag{25}$$

Here

$$K_n \equiv \hbar(J_{n,-} - J_{n,+})/2e \tag{26}$$

is the rightward flowing *spin-momentum* current (or spin current for brevity) density within magnet $n(=$ L or R), $-e$ is the electron charge and $J_{n\pm}$ is the *electric* current density flowing in the majority-or-minority-spin channel of the respective magnet in the two-channel model of perpendicular magnetoresistance. By convention, both charge and momentum *current* directions are reckoned positive along the $+x_1$ direction in Fig. 3. (These densities ae assumed independent of x_2 and x_3.) Accordingly, the right-hand side of Eq. (25) represents the net rate of spin

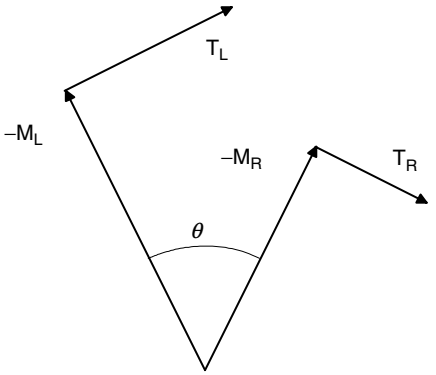

Figure 6. The torque vectors $\mathbf{T}_L$ and $\mathbf{T}_R$ lie within the plane containing the instantaneous magnetization vectors.

momentum flowing into the region enclosed by two geometric planes A and B (see Fig. 3) located inside the magnets at the distance d from the F/N interfaces; the left side gives the consequent sum of macroscopic torques concentrated on the magnets at these interfaces. The great strength of the internal exchange stiffness within the very thin (usually 1 to 3 nm) magnets insures that this torque is conveyed to their entire thickness as a whole.

As explained above, the coplanar orientations of $\mathbf{T}_L(t)$ and $\mathbf{T}_R(t)$ with the moments $\mathbf{M}_L$ and $\mathbf{M}_R$ displayed in Fig. 6 are general. Their scalar magnitudes are obtained by forming the scalar products of Eq. (25) alternatively with $\mathbf{M}_L$ and $\mathbf{M}_R$:

$$T_L = (K_L \cos\theta - K_R)/\sin\theta \tag{27}$$

$$T_R = (K_R \cos\theta - K_L)/\sin\theta, \tag{28}$$

where the sign convention for the scalars is indicated in the Fig. 6.

Equations (26), (27), and (28) are key to current-driven torque for, given the spin-channel currents obtained by solving the effective circuit, these equations predict the corresponding torques to be included in the Landau-Lifshitz equations used later to treat domain dynamics and switching. Thus both questions of magnetoresistance [See Eq. (22)] and torque are reduced to solution of the effective circuit equations introduced in the previous Section.

5. Magnetoresistance and current-driven torque of a symmetric pillar

5.1. THE MAGNETORESISTANCE

The two relations (18) and (19) provide the connection across spacers needed to complete the effective-circuit Kirchoff equations for angular dependence of

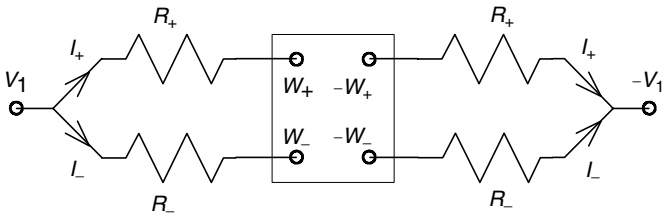

Figure 7. Effective circuit for the trilayer when magnets F_L and F_R are equal. $R_\pm$ are the channel resistances of each magnet and lead combination. Equations (18) and (19) connect the currents and voltages across the spacer and Eq. (32) gives the total resistance.

perpendicular magneto-resistance. Solutions for broad classes of pillars are published.[21] To take a simple example, the magneto-electronics of a trilayer $F_L/N/F_R$ is described by the circuit diagram of Fig. 7 in the special case that F_L and F_R have identical properties and thicknesses and spin relaxation can be neglected. The channel resistances $R_\pm$ should include both bulk and interfacial contributions given in Eq. (2).

To take advantage of the resulting odd voltage symmetry and even current symmetry, electric voltage V_1 is applied to the left contact and $-V_1$ to the right. Then symmetry permits omission of the subscripts L and R and dictates the disposition of current densities, $J_\pm \equiv J_{L\pm} = J_{R\pm}$, voltages $W_\pm \equiv W_{L\pm} = -W_{R\pm}$, shown in Fig. 7, as well as the relations $\Delta J \equiv J_+ - J_-$, $\Delta J_R = \Delta J_L$ and $\Delta W_R = -\Delta W_L$. The total unit-area resistance is

$$R = 2V_1/(J_+ + J_-). \tag{29}$$

($J_\pm$ is shown as $I_\pm$ in Fig. 7.) Our neglect of spacer resistance means $V_L = V_R = 0$, implying $W_+ = -W_-$ according to Eq. (12).

Each relation (18) and (19) now reduces to the single independent equation

$$(J_+ - J_-)(1 - \cos\theta)^2 = G(W_+ - W_-)\sin^2\theta. \tag{30}$$

Kirchoff's laws give the two relations

$$W_\pm = V_1 - R_\pm J_\pm \tag{31}$$

Simple elimination between Eqs. (29), (30), and (31) gives the result

$$R(\theta) = \frac{(R_+ + R_-)\sin^2(\theta/2) + 2GR_+R_-\cos^2(\theta/2)}{2\sin^2(\theta/2) + G(R_+ + R_-)\cos^2(\theta/2)}. \tag{32}$$

Experimental data is usefully reduced to the dimensionless variable

$$r = \frac{R(\theta) - R(0)}{R(\pi) - R(0)}. \tag{33}$$

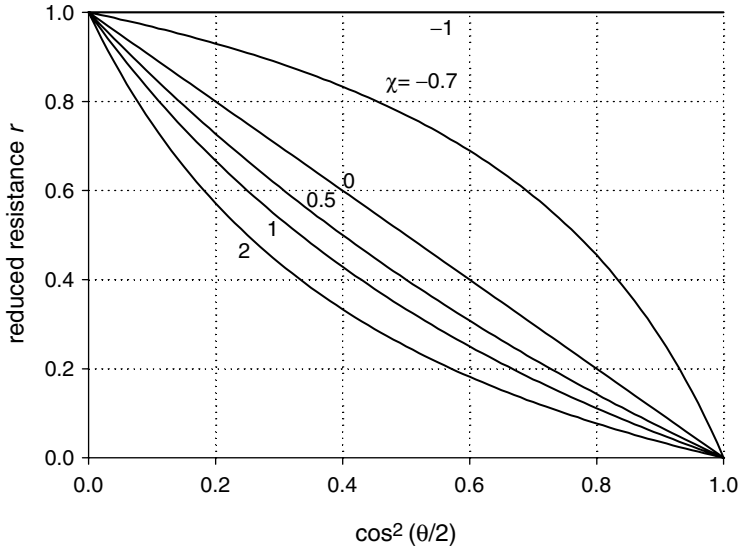

Figure 8. Angular dependence of reduced magnetoresistance on angle θ between magnetic moments defined by Eq. (33), according to Eqs. (34) and (35).

Interpretation of experiments sometimes centers on deviation of the r data from linearity with respect to the variable $\cos^2(\theta/2)$ as measured by the parameter χ in the formula

$$r = \frac{1 - \cos^2(\theta/2)}{1 + \chi \cos^2(\theta/2)}. \tag{34}$$

Figure 8 illustrates this relation. In these terms, the formulas (32) and (33) combine to give

$$\chi = \frac{1}{2} G(R_+ + R_-) - 1 \quad (> -1). \tag{35}$$

Experimental values of χ thus far are positive, including those for trilayers FeCo/Cu/FeCo and NiFe/Cu/NiFe having equal magnets. Application of the present theory to these experiments would require G to be about half of our expected $1.4 \times 10^{15}\,\mathrm{Ohm}^{-1}\,\mathrm{m}^{-2}$. However, the present theory takes no account of the anti-ferromagnetic and superconducting connecting layers used in the experiments. In addition, since the magnets are composed of alloys that include Fe, we do not know how well they satisfy the condition of negligible majority-spin interfacial reflection assumed by the theory (See Section 3.2).

5.2. TORQUES ON A SYMMETRIC TRILAYER

Specializing now to our above illustrative case of two identical magnets (See Fig. 7), application of the relations (30) and (31) reduces Eq. (28) to the new

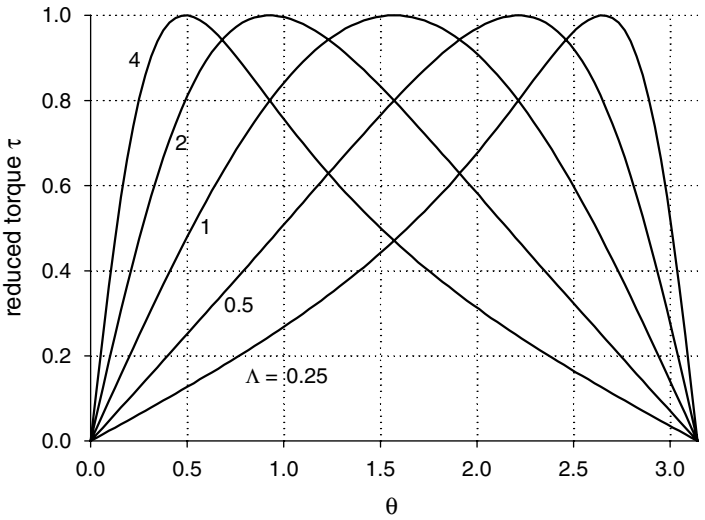

Figure 9. Dependence of reduced torque on angle θ for a trilayer with identical ferromagnetic sublayers. The parameter Λ is given by Eq. (37).

torque relation for either magnet:

$$T = \hbar J P_{\mathrm{r}} \Lambda \tau(\theta)/4e, \tag{36}$$

with

$$P_{\mathrm{r}} = (R_- - R_+)/(R_+ + R_-),\ \Lambda = [G(R_+ + R_-)/2]^{1/2} \tag{37}$$

and

$$\tau(\theta) = \frac{\sin\theta}{\Lambda \cos^2(\theta/2) + \Lambda^{-1} \sin^2(\theta/2)}. \tag{38}$$

The latter reduced torque relation is plotted in Fig. 9. The following Section treats the effect of such a current-driven torque on the dynamic behavior of a monodomain using the Landau-Lifshitz equation.

6. Dynamics of magnetization driven by current

For simplicity, consider a uniformly magnetized monodomain having uniaxial effective anisotropy field $H_{\mathrm{u}} = 2K_{\mathrm{u}}/M_{\mathrm{s}}$ where $K_{\mathrm{u}} \sin^2\theta$ is the total energy per unit volume, including material and shape terms. The free motion of the monodomain is a circular precession about the easy axis with constant θ and circular frequency $\omega = \gamma H_{\mathrm{u}} \cos\theta$.

In the presence of small damping and exchange torques, the time-dependence of the cone angle satisfies

$$d\theta/dt = \dot{\theta}_{\mathrm{damp}} + \dot{\theta}_{\mathrm{exch}} \text{ with} \tag{39}$$

$$\dot{\theta}_{\text{damp}} = -\frac{1}{2}\gamma\,\alpha\,H_{\text{u}}\sin 2\theta \quad \text{and} \tag{40}$$

$$\dot{\theta}_{\text{exch}} = \frac{\gamma\,\hbar J\,g(\theta)}{e M_{\text{s}} d_{\text{F}}}\sin\theta. \tag{41}$$

The latter three functions are plotted in Fig. 10 for three values of dimensionless current I. (Units for all physical quantities are arbitrary.) The function $g(\theta)$ employed is from an earlier theory and corresponds approximately to the

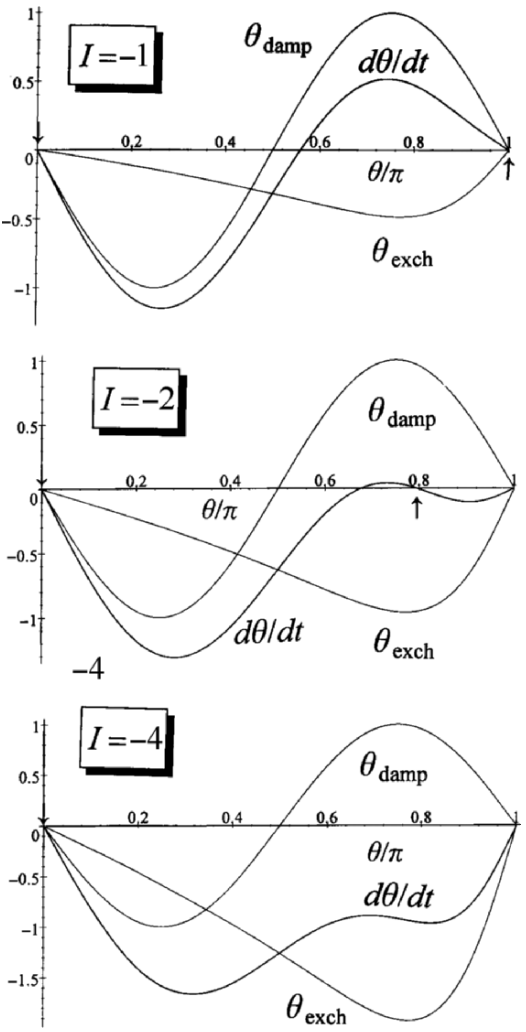

Figure 10. Instantaneous angular velocity versus angle θ of the precession cone for a uniaxial monodomain pillar magnet subject to viscous damping and three values of dimensionless current I, according to Eqs. (39). Points of stable dynamic equilibrium are indicated by ↑ or ↓.

symmetric pillar case $\Lambda = 0.4$ in Fig. 9. Obvious conditions for the stability of any cone angle are $d\theta/dt = 0$ (equilibrium) and $d[d\theta/dt]/d\theta < 0$ (stability).

For $I = -1$, the remanent states $\theta = 0, \pi$ satisfy both conditions, but the intermediate equilibrium point $\theta = 0.56\pi$ is not stable. Therefore the current value $I = -1$ does not excite either of the two remanent states. In the time domain, consider a small initial fluctuation (e.g. thermal) $\theta = 0.95\pi$ from one remanent state. Then, integration of Eq. (39) shows that the current $I = -1$ permits the moment to relax exponentially to the nearby remanent state as illustrated by the top curve in Fig. 11.

For $I = -2$, only two, ($\theta = 0, 0.79\pi$) of the four equilibrium states are stable. Therefore this value of current drives the moment out of the neighborhood of $\theta = \pi$ toward the first stable equilibrium $\theta = 0.79\pi$. (See Fig. 11.) After it relaxes to this point, the moment continues to precesses steadily at circular frequency $\omega = \gamma H_u \cos 0.79\pi$ as long as the constant current $I = -2$ is maintained. If the current is subsequently turned off, then the moment falls to the nearer remanent state, $\theta = \pi$ in this case. This example illustrates the fact that the criterion $d[d\theta/dt]/d\theta = 0$ for instability threshold does not necessarily imply a full moment reversal.

For $I = -4$, only one state has a stable equilibrium, so that a complete reverse switch from $\theta = \pi^-$ to $\theta = 0$ occurs. (See Fig. 11.) Note that the current speeds up the relaxation to the final state.

Clearly, positive I of sufficient magnitude will switch in the forward direction from $\theta = 0^+$ to $\theta = \pi$. In this case ($I > 0$) it happens that a steady precessing state does not exist and the threshold current for instability of $\theta = 0$ does also

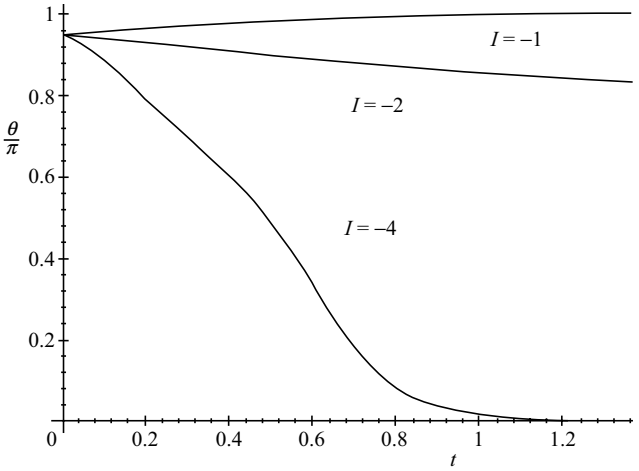

Figure 11. Dependence of precession-cone angle θ on time computed from Eq. (39) in arbitrary units. The initial state is $\theta = 0.95\pi$. The dimensionless current $I = -1$ causes no switch, $I = -2$ causes a partial switch to the precessing state $\theta = 0.79\pi$ and $I = -4$ causes a full switch to $\theta = 0$.

cause a full switch. Thus for $H_u > 0$, the possibility of a steady precessing state depends on the value of P and the sign of I. However, for $H_u < 0$ there exists a range including both signs of I supporting a steady precession.

7. Quantum Tunneling Theory

Beginning with this Section and in the remainder of this article, we replace the metallic spacer in the magnetic multilayer with a tunneling barrier. A facile and flexible way to treat tunneling is with the method of Bardeen, which uses Fermi's Golden Rule to describe the flow of electrons from one electrode to the other.[22] It is best derived together with the interaction picture for perturbation theory.[23] The argument in this Section establishes the special form of perturbation theory for tunneling.

7.1. INTERACTION PICTURE

Let ψ satisfy the Schroedinger wave equation

$$i\hbar\dot{\psi} = H\psi \tag{42}$$

for the one-particle hamiltonian

$$H = -(\hbar d/dx)^2/2m + V(x). \tag{43}$$

Let $\phi_n(x)(n = 0, 1, 2, \ldots)$ be a complete orthonormal set of basis functions in a one-dimensional x-space. A general wave function may be expanded thus:

$$\psi = \sum_n C_n(t)\phi_n(x) \tag{44}$$

The matrix equivalent of the Schroedinger equation is found as usual to be

$$i\hbar\dot{C}_n = \sum_{n'} H_{n,n'}C_{n'} \tag{45}$$

with $\dot{=} \, d/dt$ and the matrix form of the hamiltonian

$$H_{n,n'} = \langle\phi_n|H|\phi_{n'}\rangle. \tag{46}$$

Now let H' be a small general perturbation:

$$H = H_0 + H'. \tag{47}$$

Also, let $\lambda(x) \equiv \phi_0$ be single initial occupied unperturbed state having vanishing energy: $H_0\lambda = 0$. Each of the initially unoccupied remaining unperturbed states ϕ_n satisfy

$$(H_0 - \hbar\omega_n)\phi_n = 0(n = 1, 2, \ldots) \tag{48}$$

with energy $\hbar\omega_n$. Use the interaction picture[23]

$$C_n = a_n(t)e^{-i\omega_n t} \tag{49}$$

with initial values $a_0(0) = 1$ and $a_n(0) = 0$ for $n = 1, 2, \ldots$ For $n \neq 0$, consider $H'_{n,n'}$, a_n, and ω_n all to be first order quantities. Then upon substitution of Eq. (49) Eq. (45) reduces in first-order approximation to

$$\dot{a}_n = -i\,H'_{n,0}e^{i\omega_n t}(n = 1, 2\ldots) \tag{50}$$

These are the perturbation equations in the interaction picture. What remains now is to derive an expression for $H'_{n,0}$ for the case of tunneling.

7.2. TUNNELING RATE

To describe tunneling from left to right, specialize to the case of V approaching the constant barrier height B within much of the barrier (See Fig. 12). Let our $\lambda(x) \equiv \phi_0$ be one initial state localized within the *left* electrode having energy $E = 0$ by the potential $B + V_{\mathrm{L}}(x)$ where B is constant and $V_{\mathrm{L}} \leqslant 0$ for all x, and $V = 0$ for x $< a$. Let the remaining ϕ_n be localized on the right of the barrier by the potential $B + V_{\mathrm{R}}(x)$ where $V_{\mathrm{R}} \leqslant 0$ for all x, and $V_{\mathrm{R}} = 0$ for $x < b$. The total potential of the system is $V = B + V_{\mathrm{L}}(x) + V_{\mathrm{R}}(x)$. The basic approximation of the Bardeen method is to neglect the non-orthogonality of λ to $\phi_n(n = 1, 2, \ldots)$ due to the small wave-function overlap within the barrier.[22] (See Fig. 12)

Rewrite Eq. (44) in the interaction picture for tunneling

$$\psi = \lambda + \sum_n a_n(t)\varphi_n e^{-i\omega_n t}. \tag{51}$$

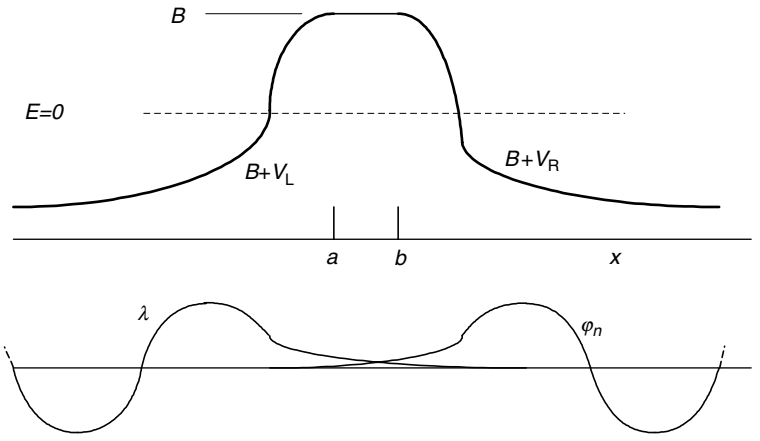

Figure 12. Potentials $V = B + V_{\mathrm{L}}$ and $V = B + V_{\mathrm{R}}$, plotted above, which define left $\lambda(x)$ and right $\varphi_n(x)$ electrode basis functions, plotted below, for Bardeen tunnel theory.

The probability P_n of occupation of the state φ_n and its rate of increase J_n (one-electron current through barrier) are

$$P_n = a_n^* a_n, \quad J_n = \dot{P}_n = \left(\dot{a}_n^* a_n\right) + \text{c.c.} \tag{52}$$

Let's calculate this current from perturbation theory. Substitute Eq. (50) into the current (52) and find

$$J_n = i\hbar H'_{0,n} a_n e^{-i\omega_n t} + \text{c.c.} \tag{53}$$

Note that we can assume that our basis states λ and φ_n are real, because we are free to use either the real or imaginary part of any complex unperturbed solution. Therefore, every matrix element $H'_{n,n'}$ is real and symmetric. Since the expectation of velocity $(-i\hbar d/dx)/m$ vanishes for a real wave function, the Bardeen method cannot describe flow of current through the electrodes.

Now calculate the one-electron current $J \equiv \sum_n J_n$ from the general expression for current[15]

$$J(c) = \dot{P} = \frac{i\hbar}{2}\left(\psi_x^*\psi - \psi^*\psi_x\right)_{x=c} = \frac{i\hbar}{2}\left(\psi_x^*\psi\right)_{x=c} + c.c., \tag{54}$$

at the point $x = c$, where $\psi_x \equiv \partial\psi/\partial x$.

Momentarily regard the system of linear equations (50) generally, admitting any sort of initial conditions. Assume, for example, that *only one* final-state amplitude a_n is not vanishing at some instant of time $t = t_1$ in the expansion (51). Then we let $x = c$ be a point within the barrier and (54) gives exactly

$$J = J_n(t_1) = \left[\frac{i\hbar}{2}(\lambda_x\varphi_n - \lambda\varphi_{n,x})_{x=c} a_n(t_1) e^{-i\omega_n t_1}\right] + \text{c.c.} \tag{55}$$

Now compare this with Eq. (53) and note the Bardeen transfer matrix element must be

$$H'_{0,n} = \frac{1}{2}(\lambda_x\varphi_n - \lambda\varphi_{n,x}). \tag{56}$$

We may take each value of n in turn and follow the same argument. Therefore Eq. (56) is valid for all n. This is the expression for the tunneling (transfer) matrix sought.

Fermi's Golden Rule for the transition rate gives:[23]

$$\frac{dP}{dt} = \frac{2\pi}{\hbar} H'^2_{n,0}\rho(E) \tag{57}$$

where $\rho \equiv \hbar(d\omega_n/dn)$ is the density of states assumed to be very closely spaced. This equation with the matrix element (56) substituted comprises the essential tool for calculating the tunneling rate through an insulating barrier.

8. Currents and torques in magnetic tunnel junctions

8.1. MAGNETO-CONDUCTION AND TORQUES

For adaptation[24] of the Bardeen method to the MTJ illustrated schematically Fig. 13 (a), a stationary basis state $|p, \sigma\rangle$ within the left ferromagnetic electrode F_L is assigned the orbital index p and majority/minority spin $\sigma = \pm$ quantized along axis **1**. It satisfies $(H + eV - \epsilon_{p,\sigma})|p, \sigma\rangle = 0$, and decays exponentially within the barrier, considered semi-infinite in width when defining the basis states. From this point forward, $-V$ is the external voltage applied to F_L. Here, $H = p^2/2m + \Sigma_\sigma |\sigma\rangle U_\sigma(x, y, z)\langle\sigma|$, where the potential U_σ depends on spin $\sigma(= \pm)$ within the ferromagnets but not within the barrier. Within F_R, a similar state satisfies $(H - \epsilon_{q,\sigma'})|q, \sigma'\rangle = 0$ with quantization axis **r**. Because the barrier is assumed to dominate all other resistances of this circuit, the spin channels are shown in Fig. 13 (b) as shorted in each magnet and/or external-contact region by spin lattice relaxation due to spin-orbit coupling. One may disregard *spin accumulation* and the related distinction between electric and electrochemical potentials which were important previously woth respect to metallic spacers.

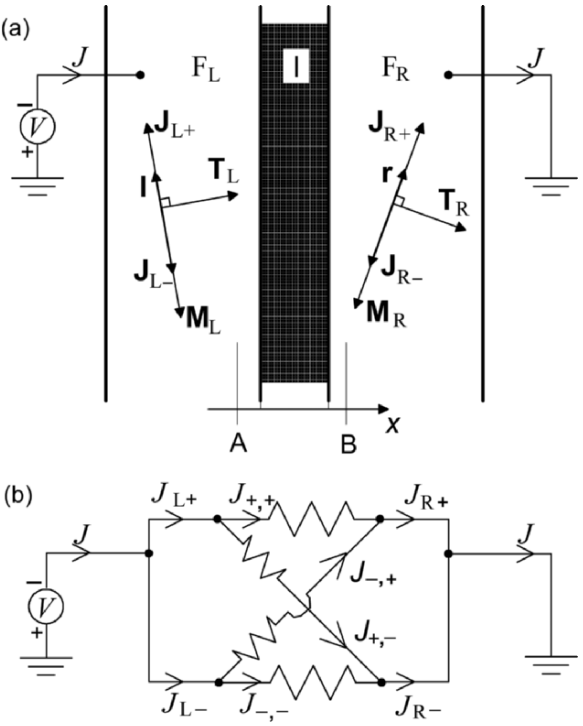

Figure 13. (a) Scheme of magnetic tunnel junction and key to notations. (b) Equivalent circuit for spin-channel currents and further key to notations.

U_σ includes all elastic terms arising from atomic disorder due to alloying, defects, interfacial atomic interdiffusion, etc. The state indices p, q simply enumerate the exact eigenstates $|p, \sigma\rangle$, $|q, \sigma'\rangle$ of H in the Bardeen basis. Each such state incorporates effects of all multiple elastic scatterings without limit.

Employing the spinor transformation connecting quantization axes **1** and **r**, the transfer matrix element takes the form

$$\langle p, \sigma | H - \varepsilon | q, \sigma' \rangle = \begin{bmatrix} \gamma_{p,+;q,+} \cos\frac{\theta}{2} & \gamma_{p,+;q,-} \sin\frac{\theta}{2} \\ -\gamma_{p,-;q,+} \sin\frac{\theta}{2} & \gamma_{p,-;q,-} \cos\frac{\theta}{2} \end{bmatrix} \quad (\sigma, \sigma' = \pm). \quad (58)$$

Here the purely orbital factor $\gamma_{p,\sigma;q,\sigma'}$ is evaluated by extending our tunnel matrix expression (56) to three dimensions. Then, inclusion of spin indices gives the expression

$$\gamma_{p,\sigma;q,\sigma'}(x) = \frac{-\hbar^2}{2m} \int dy dz (\psi_{p,\sigma} \partial_x \varphi_{q,\sigma'} - \varphi_{q,\sigma'} \partial_x \psi_{p,\sigma})_{x=c}. \quad (59)$$

Here the integral is over unit area with coordinate $x = a$ lying inside the barrier. The energies $\epsilon_{p,\sigma}$ and $\epsilon_{q,\sigma'}$ may differ only infinitesimally from a fixed value ε. The hamiltonian H, the left ($\psi_{p,\sigma}$) and right ($\psi_{q,\sigma'}$) orbital wave functions, and these matrix elements (59) are real.

Only the neglect of cross-barrier overlaps $\langle p, \sigma | q, \sigma' \rangle$ allows use of the Fermi golden rule (57) of perturbation theory which is strictly valid only for an orthonormal basis. Substitution of the perturbation (58) into this rule is followed by summation over the initial states in the energy band of width eV. Thus, for small V, the partial electric current density flowing between channel σ in F_L and channel σ' in F_R becomes

$$J_{\sigma,\sigma'} = \frac{-2\pi e^2 V}{\hbar} \sum_{p,q}{}' \langle p, \sigma | H - \varepsilon_F | q, \sigma' \rangle^2 \quad (60)$$

at $T = 0$ K. The $'$ in $\sum'_{p,q}$ imposes the conditions $\varepsilon_F < (\varepsilon_{p,\sigma}, \varepsilon_{q,\sigma'}) < \varepsilon_F + eV$.

8.2. GENESIS OF POLARIZATION FACTORS

Although MTJ relations depending on polarization factors are often used to interpret experiments, their validity is theoretically justified only under a severe restriction: The barrier is so thick that only a single basis function on each side penetrates it. To explain, consider the Schroedinger equation in two dimensions within the region of a flat barrier of height B:

$$\left[\frac{-\hbar^2}{2m} (\partial_x^2 + \partial_y^2) + B - E_F \right] \psi = 0 \quad (61)$$

A solution is

$$\psi \propto e^{-\kappa_x x}\cos(k_y y + \beta) \tag{62}$$

and the eigenvalue equation may be written

$$\kappa_x^2 = k_y^2 + 2m(B - E_{\rm F})/\hbar^2 \tag{63}$$

This equation says that the greater the y-momentum, the steeper the decay of ψ. Therefore the tunnel current concentrates in the single state $k_y = 0$. The barrier collimates the current. Under this extreme condition, drop the indices p and q. On both sides of the barrier, the wave functions $\psi_\sigma \propto e^{-\kappa x}$ and $\varphi_{\sigma'} \propto e^{\kappa x}$ are independent of y. The matrix element (59) reduces to

$$\gamma_{\sigma,\sigma'} = \frac{-\hbar^2}{m}\kappa \int dy\, \psi_\sigma \varphi_{\sigma'} \tag{64}$$

In the notation of Fig. 13(b), the total tunnel electric current density flowing from R to L is

$$J = \Sigma_{\sigma,\sigma'} J_{\sigma,\sigma'} \tag{65}$$

with

$$J_{\sigma,\sigma'} = c_1 \begin{pmatrix} \psi_+^2\varphi_+^2\cos^2(\theta/2) & \psi_+^2\varphi_-^2\sin^2(\theta/2) \\ \psi_-^2\varphi_+^2\sin^2(\theta/2) & \psi_-^2\varphi_-^2\cos^2(\theta/2) \end{pmatrix}. \tag{66}$$

Substitute the identities

$$2\cos^2(\theta/2) = 1 + \cos\theta \text{ and } 2\sin^2(\theta/2) = 1 - \cos\theta \tag{67}$$

to find

$$J = \frac{c_1}{2}\left[(\psi_+^2 + \psi_-^2)(\varphi_+^2 + \varphi_-^2) + (\psi_+^2 - \psi_-^2)(\varphi_+^2 - \varphi_-^2)\cos\theta\right]. \tag{68}$$

This may be written

$$J(\theta) = J_0(1 + \imath\cos\theta), \quad \imath = P_{\rm L}P_{\rm R} \tag{69}$$

where the right and left *tunnel-polarization* factors are

$$P_{\rm L} = \frac{\psi_+^2 - \psi_-^2}{\psi_+^2 + \psi_-^2}, \quad P_{\rm R} = \frac{\varphi_+^2 - \varphi_-^2}{\varphi_+^2 + \varphi_-^2}. \tag{70}$$

Note that the polarization factor relevant to tunneling is evaluated inside the barrier. We make no attempt here to evaluate the constant J_0. Its realistic evaluation generally requires *ab-initio* numerical computation. Experimental data for the resistance $R(\theta)$ are often summarized by the magnetoresistance ratio

$$\text{MR} \equiv \frac{R(\pi) - R(0)}{R(0)} = \frac{J(0) - J(\pi)}{J(\pi)}. \tag{71}$$

Whenever polarization factors are legitimate, this formula reduces to that of Julliere's model[31]

$$\mathrm{MR} = \frac{2P_\mathrm{L}P_\mathrm{R}}{1 - P_\mathrm{L}P_\mathrm{R}} \tag{72}$$

according to Eq. (69).

Apply the torque relations (27) and (28). Substitute the relations

$$J_{\mathrm{L},\sigma} = J_{\sigma,+} + J_{\sigma,-}, \quad J_{\mathrm{R},\sigma'} = J_{+,\sigma'} + J_{-,\sigma'}, (\sigma, \sigma' = \pm) \tag{73}$$

implied by the circuit diagram in Fig. 13. The torque on the right magnet is

$$T_\mathrm{R} = -(\hbar\tau_\mathrm{R}J_0/2e)\sin\theta \tag{74}$$

or, in coordinate-free form

$$\mathbf{T}_\mathrm{R} = (\hbar\tau_\mathrm{R}J_0/2e)\mathbf{r} \times (\mathbf{l} \times \mathbf{r}), \tag{75}$$

with the torque coefficient

$$\tau_\mathrm{R} = P_\mathrm{L}. \tag{76}$$

Similarly, the torque on the left magnet is

$$T_\mathrm{L} = -(\hbar\tau_\mathrm{L}J_0/2e)\sin\theta, \quad \tau_\mathrm{L} = P_\mathrm{R} \tag{77}$$

or, in coordinate-free form

$$\mathbf{T}_\mathrm{L} = \frac{\hbar\tau_\mathrm{L}}{2e}J_0\mathbf{l} \times (\mathbf{r} \times \mathbf{l}). \tag{78}$$

The Eqs. (69), (76), and (78) show the very close relation between current-driven torques and magneto-conduction at the same voltage, summarized by the relation $\imath = \tau_\mathrm{L}\tau_\mathrm{R}$ connecting observables in the limit of large barrier thickness.

9. Junctions using MgO barriers

At this time (2006), rapid improvements of magneto-resistance ratio (MR) and voltage-driven torque effects in MTJs using MgO barriers are taking place. Initially, first-principle computations by Mathon and Umerski[25] and by W. Butler et al[26] predicted enormous values of magneto-resistance ratio MR for epitaxial junctions of composition (001)Fe/MgO/Fe. The large MR is due to a selection rule prohibiting the transition of the minority-band Δ_5 wave function at transverse momentum $k_\parallel = 0$ to the most-slowly decaying Δ_1 wave function within the MgO barrier. Subsequently, Zhang and Butler[27] further predicted even greater ratios in such junctions with Co or ordered FeCo substituted for Fe.

Indeed, many experiments using compositions of the class $\mathrm{Fe}_x\mathrm{Co}_y\mathrm{B}_z/(001)\,\mathrm{MgO}/\mathrm{Fe}_x\mathrm{Co}_y\mathrm{B}_z$ reported MR as great as 270% at $T = 300\,\mathrm{K}$, but smaller than

predicted. The measured MR depends greatly on extrinsic conditions including annealing, dislocations, added elements inserted at interfaces, and sputtering conditions. It appears likely that details of microstructure at interfaces mix Δ_5 and Δ_1 states, thus permitting greater minority-spin current which decreases MR from its first-principle value.

Here we predict observable signatures of voltage-driven torque whose measurement could discriminate between various effects of the microstructural conditions mentioned above. As yet no experimental tests exist. Possibly applicable methods of directly measuring the current-driven torque have appeared recently in two reports: A. A. Tulapurkar et al[28] use an external field to orient the two magnetic moments at an angle of 30°. The torque created by an AC current flowing through the junction causes the free moment to oscillate. A voltmeter detects the DC magnetoresistive voltage proportional, by virtue of non-linearity, to the square of the oscillation amplitude. V. C. Sankey et al[29] similarly use current-driven torque to drive ferromagnetic resonance in the free magnet. They detect the output magnetoresistive voltage with low-frequency modulation and lock-in detection. These two techniques show promise for the experimental investigation of the torque signatures predicted below.

The previous two Sections assume the tunneling is elastic. Here we take advantage of the more general nature of the relations derived there. Our present model,[30] includes inelastic as well as elastic mechanisms of spin-polarized tunneling. It is inspired in part by awareness of conductance data for $Fe_xCo_yB_z/MgO/Fe_xCo_yB_z$ of the sort shown in Fig. 14. We find below that the anti-parallel conduction G_{AP} resembling the non-analytic function $a + b|V|$ for $|V| > 80\,\mathrm{mV}$

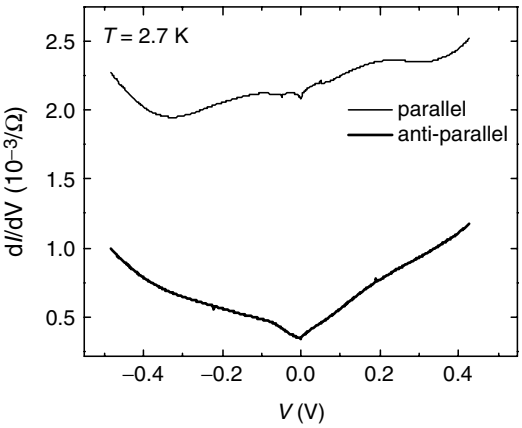

Figure 14. Measured conductance versus voltage for an MTJ having a very large MR. The parallel conductance G_P lies above, the antiparallel G_{AP} below. The composition is Co70Fe30/(8 Å)Mg-(26 Å)MgO/Co70Fe30. Junction dimensions are $240 \times 80\ \mu m^2$. Unpublished data, by courtesy of S. S. P. Parkin.

(which we call *pseudo-linear*), apparent in the lower curve of Fig. 14, does not arise from elastic tunneling. But *inelastic* tunneling theory can explain pseudo-linear voltage dependence observed for various non-MTJ tunneling-junction compositions.[32] Extention of the elastic theory to inelastic tunneling is a key feature of our model for MgO-based tunneling junctions.

9.1. MAGNETO-CONDUCTANCE AND TORKANCE

We employ notation compatible with the above-mentioned experimental techniques for measuring differential current- or voltage-driven torque.[28,29] In particular, we use the coefficients $G_{\sigma,\sigma'}$ of cross-channel *conductance amplitude*, defined below, for electric current flowing through any of the four spin channel combinations $\sigma, \sigma'(=\pm)$. Here $\sigma = \pm$ is the (majority/minority)-spin channel in the left (L) electrode, and similarly $\sigma' = \pm$ in the right (R) electrode. (See Fig. 13)

The *physical* electric conductance densities flowing between spin channel σ' (R) and σ (L) of the barrier (See Eq. (66)) are

$$dJ_{\sigma,\sigma'}/dV = G_{\sigma,\sigma'}(V)\langle\sigma|\sigma'\rangle^2, \quad (G_{\sigma,\sigma'}) \leq 0, \tag{79}$$

with the spin-coordinate transformation matrix elements $\langle\pm|\pm\rangle = \cos(\theta/2)$ and $\langle\pm|\mp\rangle = \pm\sin(\theta/2)$. The first-principle calculations for MTJs with (100)MgO barriers,[25,27] express, for $V = 0$, the conductance density for parallel and antiparallel moments with the formulas (in a different notation)

$$G_{\rm P} = G_{++} + G_{--}, \quad G_{\rm AP} = G_{+-} + G_{-+}. \tag{80}$$

These equations follow easily for any V from the condition of spin conservation.

Now we eschew polarization factors. Instead of Eq. (75), we introduce the following expression for what we may call *torkance*:

$$\frac{d\mathbf{T}_{\rm R}}{dV} = \frac{\hbar}{4e}(G_{++} - G_{--} + G_{+-} - G_{-+})\mathbf{r} \times (\mathbf{l} \times \mathbf{r}). \tag{81}$$

Here the factor $-\hbar/2e$ converts the electric current carried by a particle flux to the equivalent current of spin angular momentum.

Equation (81) follows from Eqs. (28) and (79). But to verify Eq. (81) more transparently for the special case $\mathbf{l} \perp \mathbf{r}$, define the vector spin moment per unit area of one metallic nano-magnet:

$$\mathbf{S} = (\hbar/2)(n_+ - n_-)\mathbf{s} \quad (n_+ > n_-) \tag{82}$$

where s is a unit vector, $n_\pm$ are total electron numbers for spin-polarized sub-bands $\sigma = \pm$. The spin-current density flowing rightward through the magnet is

$$\mathbf{K} = (K_+ - K_-)\mathbf{s} \equiv (\hbar/2)(\Sigma_i v_{i,+} - \Sigma_i v_{i,-})\mathbf{s} \tag{83}$$

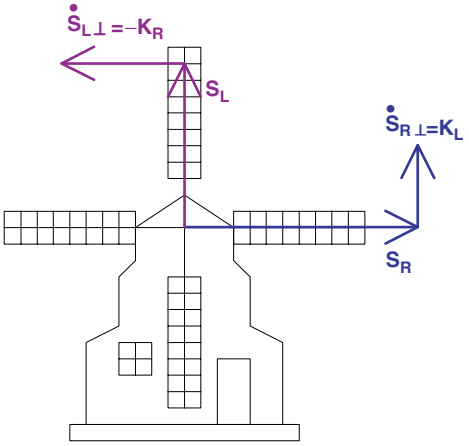

Figure 15. (Colored on-line) Illustrating relations between pseudo-torque and spin current vectors when moments are perpendicular. Assumed is the case in which each spin-current vector has the sense as the moment in each electrode.

where $v_{i,\sigma}$ is the velocity of an occupied state. Consider the volume Ω lying between the planes marked A and B in Fig. 13. Neglect all terms in the hamiltonian $\mathcal{H}$ except kinetic and coulomb energies. Since $\mathcal{H}$ contains no spin operators, the total vectorial spin $\mathbf{S}_{\rm tot}$ contained in Ω changes only by inward flow of vectorial spin currents. Then its time derivative satisfies the equations

$$\dot{\mathbf{S}}_{\rm tot} = \dot{\mathbf{S}}_{\rm L} + \dot{\mathbf{S}}_{\rm R} = \mathbf{K}_{\rm L} - \mathbf{K}_{\rm R} \tag{84}$$

The Bardeen method predicts only pseudo-torque vector components lying within the **l**—**r** plane. Now consider the special case $\mathbf{l} \perp \mathbf{r}$. Since $\dot{\mathbf{S}}_{\rm L} \bullet \mathbf{l} = \dot{\mathbf{S}}_{\rm R} \bullet \mathbf{r} = 0$, we have the cross-relations $\dot{\mathbf{S}}_{\rm L\perp} = -\mathbf{K}_{\rm R}$ and $\dot{\mathbf{S}}_{\rm R\perp} = \mathbf{K}_{\rm L}$. See Fig. 15. According to Eq. (79), the $\perp$ condition implies that $K_{\rm L\pm}$ in Eq. (83) has 1/2 the strength it would have for given $G_{\sigma,\sigma'}$ if the spin axes were optimally aligned:

$$dK_{{\rm L}\sigma}/dV = \left(\frac{1}{2}\right)\left(\frac{-\hbar}{2e}\right)(G_{\pm,+} + G_{\pm,-}). \tag{85}$$

The result of combining this with Eqs. (83) and substituting into $\dot{\mathbf{S}}_{\rm R\perp} = \mathbf{K}_{\rm L}$ agrees with Eq. (92).

9.2. ELASTIC TUNNELING

Consider a special model of an MTJ having symmetric chemical composition exemplified by the one whose conductances are plotted in Fig. 14. Compose each channel current density of elastic and inelastic terms: $J_{\sigma,\sigma'} = J^{\rm el}_{\sigma,\sigma'} + J^{\rm inel}_{\sigma,\sigma'}$.

Define a tunnel-rate coefficient $U_{\sigma,\sigma'}$ proportional to the mean-square matrix element for elastic tunneling between the orbital states of spin channels $\sigma(=\pm)$ and $\sigma'(=\pm)$. It is averaged over the index p of real Bardeen orbital basis states $|p,\sigma\rangle$ on the left and over q of $|q,\sigma'\rangle$ on the right, with the factor depending on θ omitted. Including all other factors in the conventional tunneling expression for current except the state densities ρ_σ, $\rho_{\sigma'}$, it may be written

$$U_{\sigma,\sigma'} = 2\pi e^2 \hbar^{-1} \overline{\langle p,\sigma|H|q,\sigma'\rangle^2}. \tag{86}$$

When fully evaluated, $U_{\sigma,\sigma'}(\geq 0)$ has the factor $e^{-2\kappa d}$ where κ is the decay coefficient for a real pseudo-Bloch function with $k_\parallel = 0$ and symmetry type Δ_1 having its energy within the forbidden band of MgO.[25,27] The predicted local density in the $\sigma = -$, Δ_5-propagation channel at ≥ 3 atomic layers of MgO from the initial F/I interface amounts to $\lessapprox 10^{-2}$ times that of the $\sigma = +$, Δ_1-channel. (See Fig. 7 of Ref.[26]) This prediction makes reasonable our neglect of tunneling via the Δ_5 channel in experimental MTJs. We assume that disorder or dislocations within the electrodes or interface regions enables the $\sigma = -$, Δ_5-state of an electrode to couple to the Δ_1-channel of MgO to an extent governed by details of the microstructure.

For finite V, we may integrate the transition rate of the golden rule (57) with respect to V. Then, in view of the relation (60), the current density due to elastic tunneling at $T = 0$ K reduces to

$$J^{\rm el}_{\sigma,\sigma'}(V,\theta) = U_{\sigma,\sigma'}\langle\sigma,\sigma'\rangle^2 \int_0^V d\upsilon \rho_\sigma(\upsilon - V)\rho_{\sigma'}(\upsilon). \tag{87}$$

Here, for convenience, we have replaced the energy ε argument in the state density ρ_σ, measured from the Fermi level $\varepsilon_{\rm F} = 0$, with voltage using $\varepsilon = eV$. We assume that, whatever lack of symmetry is present in this system, it will not be in the composition, therefore not in the state density ρ_σ. Rather it will lie in the coefficient $U_{\sigma,\sigma'}$, reflecting asymmetry of the concentration of defects or dopants in the interfacial microstructure; thus we omit the subscripts L and R from ρ_σ.

In many cases, as in Fig. 14, the relative dependence of $G_{\rm P}$ on V is much weaker than that of $G_{\rm AP}$. Thus, we take $G_{\rm P}$ constant and assume, to first order in υ,

$$\rho_+ = \text{const.}, \rho_- = \rho_{-,0} + \rho_{-,1}\upsilon. \tag{88}$$

Then in view of Eq. (79), Eq. (87) reduces in first order to

$$\begin{aligned} G^{\rm el}_{++} &= U_{++}\rho_+^2,\ G^{\rm el}_{+-} = U_{+-}\rho_+(\rho_{-,0} + \rho_{-,1}V) \\ G^{\rm el}_{-+} &= U_{-+}\rho_+(\rho_{-,0} - \rho_{-,1}V),\ G^{\rm el}_{--} = U_{--}\rho^2_{-,0}. \end{aligned} \tag{89}$$

Notice here that U_{+-} is distinct from U_{-+} because breaking of the selection rule forbidding coupling of a $k_\parallel = 0$ minority state in a magnetic electrode to Δ_1

in MgO is allowed only by disorder in the electrode or interface, or presence of a foreign interfacial layer. Thus U_{+-} and U_{-+} depend on microstructural conditions which may differ on the two sides of the barrier. In an MTJ having large MR, $G^{\rm el}_{--}$ is anyway small, so no correction is attempted.

Substitution of Eqs. (89) into (80), gives the functional form $G_{\rm AP} = a + bV$ and not the form $a+b|V|$ which would reasonably represent the data appearing in Fig. 14. To obtain a better representation of the data, we consider the possibility of inelastic tunneling below.

9.3. INELASTIC TUNNELING

The following argument sketches the crux of a theory[32] for the V-dependence of inelastic tunneling current $I^{\rm inel}$ at $T = 0\,{\rm K}$: For $V > 0$, write

$$I^{\rm inel} = \int_0^V d\upsilon \rho_{\rm L}(\upsilon - V) \int_0^\upsilon F^{\rm inel}(\upsilon - \upsilon')d\upsilon' \rho_{\rm R}(\upsilon'). \tag{90}$$

where the excitation, proportional to the spectral weight $F^{\rm inel}(\upsilon - \upsilon')(> 0)$ of excitation by some subsystem compensates for the difference $e(\upsilon - \upsilon')$ between initial and final energies in the electrodes. Then, assuming $F^{\rm inel}$, $\rho_{\rm L}$, $\rho_{\rm L}$ are constants, the result, written for both signs of V, is the pseudo-linear function $G^{\rm inel} = dI^{\rm inel}/dV = F^{\rm inel}\rho_{\rm L}\rho_{\rm R}|V|$ we seek. In the present case, the nature of this subsystem (maybe electron traps at oxygen vacancies or correlated Coulomb excitation of electrons) is not known.

In the case of a perfectly ordered, epitaxial crystalline MTJ having a composition in the class (Fe, Co, FeCo)/MgO/(Fe, Co, FeCo), a quantum-theoretical selection rule forbids mixing of the minority-spin Bloch waves at $k_\parallel = 0$, having little-group symmetry Δ_5, with the MgO gap wave function having the lowest decay coefficient κ.[25,27] An enormous magneto-conductance ratio is predicted from the consequently small values of G_{+-} and G_{-+} appearing in Eq. (80). We assume the inelastic mechanism provides channels additional to those of the defect-induced elastic coefficients U_{+-} and U_{-+} for breaking this selection rule. From the previous paragraph follow the formulas $G^{\rm inel}_{+-} = D_{\rm R}|V|$ and $G^{\rm inel}_{-+} = D_{\rm L}|V|$, where the adjustable coefficients satisfy $D_{\rm L} > D_{\rm R}$ or $D_{\rm L} < D_{\rm R}$ depending on which interface the inelastic mechanism favors. Since the $++$ connection does not involve the selection rule, and the $--$ involves it twice, we take $G^{\rm inel}_{++} = G^{\rm inel}_{--} = 0$.

Substitution of Eq. (89) into (80), with $G^{\rm inel}_{\sigma\sigma'}$ included, gives

$$\begin{aligned} G_{\rm AP} \;=\; & (U_{+-} + U_{-+})\rho_+\rho_{-,0} + (D_{\rm L} + D_{\rm R})|V| \\ & + (U_{+-} - U_{-+})\rho_+\rho_{-,1}V. \end{aligned} \tag{91}$$

By eliminating G_{++} between Eqs. (80) and (81), and including $G^{\text{inel}}_{\sigma\sigma'}$, one gets:

$$dT_R/dV = (\hbar/4e)[G_P + (U_{+-} - U_{-+})\rho_+\rho_{-,0} + (D_L - D_R)|V| + (U_{+-} + U_{-+})\rho_+\rho_{-,1}V]\sin\theta \quad (92)$$

where we have neglected G_{--} altogether.

9.4. OBSERVABLE SIGNATURES

With the aid of our Eqs. (91) and (92), combined observation of G_{AP} and dT_R/dV may serve to reflect interfacial microstructures of a compositionally symmetric MTJ having a large magneto-conductive ratio G_P/G_{AP}. To illustrate this, we assume G_P is constant and plot schematically G_{AP} and dT_R/dV in Fig. 16 for 5 special cases A—E reflecting terms in these equations:

A: **Symmetric reference case**, with $U_{+-} - U_{-+} = \rho_{-,1} = D_L - D_R = 0$: Here G_{AP} has the pseudo-linear dependence on $|V|$ due to inelastic scattering exemplified by the data in Fig. 14. The torkance $dT_R/dV = (\hbar/4e)G_P \sin\theta$ is constant. The remaining cases below illustrate possible changes from case A leaving the sums $U_{+-} + U_{-+}$ and $D_L + D_R$ unchanged:

B: **Asymmetry of elastic tunneling:** Let $U_{+-} > U_{-+}$, which reflects the difference in degrees of disorder or dislocation density at the two F/I interfaces. G_{AP} does not change. But now the torkance makes a constant shift amounting to $(U_{+-} - U_{-+})_{\rho+\rho-,0} \sin\theta$, according to Eq. (92).

C: **Dependence of state density on energy:** Let $\rho_{-,1} > 0$. This does not change G_{AP} but gives the torkance a true linear dependence.

D: **Asymmetry of distribution of inelastic tunneling centers:** Let $D_L > D_R$. This causes no change in G_{AP}, but gives pseudo-linear dependence to

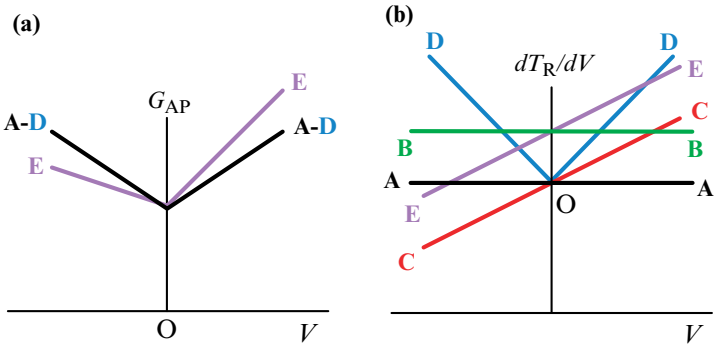

Figure 16. (Color on-line) Scheme of predicted anti-parallel conductance G_{AP} (a) and torkance dT_R/dV (b). The separate cases A—E are described in the text.

torkance. Depending on the sign of $D_{\rm L} - D_{\rm R}$, the torkance rises with $|V|$ as shown, or falls.

E: **Combine tunnel-matrix asymmetry with dependence of ρ_- on energy:** Let both $U_{+-} > U_{-+}$ *and* $\rho_{-,1} > 0$. This gives $G_{\rm AP}$ a true linear bias. The torkance acquires a superposition of the effects in cases B and C, namely a shift and a tilt.

Noteworthy is how much more information about spin-dependent tunnel transport observation of torkance is capable than the conductance. For example, any one of the cases A, B, C, or D could account for the data in Fig. 14. They are indistinguishable in Fig. 16 (a), but in panel (b) we see significant differences in the torkance signature, potentially enabling experimental discrimination between microstructural mechanisms.

Case E is particularly interesting because the dislocation densities at the two interfaces of epitaxial (001)Fe/MgO/Fe are known to differ markedly. This difference may cause the inequality $U_{+-} \neq U_{-+}$. Indeed, a plot of $G_{\rm AP}$ in sample B reported by C. Thiusan et al[33] reveals tilted-V behavior resembling that shown in case E of Fig. 16 (a). If the present model is correct, then the torkance should show, as a minimum, the shift and true linear tilt seen in panel (b), case E.

References

1. L. Berger, Phys. Rev. B 54, 9353 (1996).
2. J. C. Slonczewski, J. Magn. Magn. Mater. **159**, L1 (1996).
3. M. D. Stiles and J. Miltat, in *Spin Dynamics in Confined Magnetic Structures III,* edited by B. Hillebrands and A. Thiaville (Springer, Berlin, 2005).
4. M. Tsoi, A. G. M. Jansen, J. Bass, W. C. Chiang, M. Seck, V. Tsoi, and P. Wyder, Phys. Rev. Lett. **80**, 4281 (1998).
5. J. C. Slonczewski, J. Magn. Magn. Mater. **195**, L261 (1999).
6. J. Z. Sun, J. Magn. Magn. Mater. **202**, 157 (1999).
7. E. B. Myers, D. C. Ralph, J. A. Katine, R. N. Louie, R. A. Buhrman, Science **285**, 867 (1999).
8. A. Brataas, Y. V. Nazarov, and G. E. W. Bauer, Phys. Rev. Lett. **84**, 2481 2000
9. A. Brataas, G. E. W. Bauer, P. J. Kelly, Physics Reports **427** (2006) 157
10. J. C. Slonczewski, J. Magn. Magn. Mater. **247**, 324 (2002).
11. T. Valet and A. Fert, Phys. Rev. B, **48**, 7099 (1993).
12. Y. Huai, F. Albert, P. Nguyen, M. Pakala, and T. Valet, Appl. Phys. Lett. **84** (2003) 3118–3120.
13. G. D. Fuchs, N. C. Emley, I. N. Krivorotov, P. M. Braganca, E. M. Ryan, S. I. Kiselev, J. C. Sankey, D. C. Ralph, R. A. Buhrman, and J. A. Katine, Appl. Phys. Lett., 85, 1205 (2004).
14. J. Bass and W. P. Pratt, Jr., J. Magn. Magn. Mater. **200**, 274 (2001).
15. D. Bohm, *Quantum Theory,* (Prentice-Hall, New York, 1951), Sec. 17.7

16. X. Wainthal, E. B. Myers, P. W. Brouer, and D. C. Ralph, Phys. Rev. B, **62**, 12317 (2000).
17. G. E. W. Bauer, private communication.
18. Jürgen Kübler, *Theory of Itinerant Electron Magnetism,* Clarendon Press, Oxford, 2000, p. 234.
19. K. Xia, P. J. Kelly, G. E. W. Bauer, A. Brataas, and I. Turek, Phys. Rev. B **65**, 220401 (2002).
20. M. D. Stiles and A. Zangwill, Phys. Rev. **66**, 014407 (2002)
21. A. Manchon and J. C. Slonczewski, Phys. Rev. B **73**, 184429 (2006).
22. C. B. Duke, *Tunneling in Solids,* (Academic Press, New York, 1969)
23. J. J. Sakurai, *Modern Quantum Mechanics,* (Bemjamin/Cummings, Menlo Park, 1985), Secs. 5.5 and 5.6.
24. J. C. Slonczewski, Phys. Rev. B **71**, 024411 (2005)
25. J. Mathon and A. Umerski, Phys. Rev. B **63**, 220403 (2001)
26. W. H. Butler, X.-G. Zhang, T. C. Schulthess, and J. M. MacLaren, Phys. Rev. B **63**, 054416 (2001).
27. X.-G. Zhang and W. H. Butler, Phys. Rev. B **70**, 172407 (2004).
28. A. A. Tulapurkar, Y. Suzuki, A. Fukushima, H. Kubota, H. Maehara, K. Tsunekawa, D. D. Dajayapravira, N. Watanabe, and S. Yuasa, Nature, **438**, 339 (2005).
29. J. C. Sankey, P. M. Braganca, A. G. F. Garcia, I. N. Krivorotov, R. A. Buhrman, and D. C. Ralph, Phys. Rev. Lett. **96**, 227601 (2006).
30. J. Slonczewski, J. Sun, to be published in J. Magn. Magn. Mats. (2006)
31. M. Julliere, Phys. Lett. **54A**, 225 (1975)
32. J. R. Kirtley and D. J. Scalapino, Phys. Rev. B **65**, 798 (1990); and references therein.
33. C. Tiusan, M. Sicot, J. Faure-Vincent, M. Hehn, C. Belouard, F. Montaigne, S. Andrieu, and A. Schuhl, J. Phys.: Condens. Matter **18**, (2006) 941.

SPIN-TRANSFER-DRIVEN MAGNETIZATION DYNAMICS

GIORGIO BERTOTTI
Istituto Nazionale di Ricerca Metrologica, Torino, Italy

Abstract. Analytical methods are discussed for the study of spin-transfer-driven magnetization dynamics in nanomagnets. Particular emphasis is given to the case of uniformly magnetized systems, which is a key prerequisite before attempting any numerical computation of complex spin-transfer devices. The onset of current-induced microwave oscillations of the magnetization is analyzed in the frame of nonlinear dynamical system theory and bifurcation theory. Methods for the description of the effect of thermal fluctuations by appropriate Langevin or Fokker-Planck equations are also considered. It is shown that for systems exhibiting uniaxial symmetry the analytical treatment can be developed in considerable detail without introducing any approximation.

Keywords: Spin transfer, Landau-Lifshitz-Gilbert equation, microwave oscillations, nonlinear dynamical system

1. Introduction

Electrons exert a torque of quantum-mechanical origin, known as spin-transfer torque, when they flow across a ferromagnetic element. This effect is added to the magnetic torque that any electric current traversing a ferromagnetic element generates because of the Oersted field surrounding the current. When the current density is sufficiently large (of the order of 10^7–10^8 A cm^{-2}) and the ferromagnetic element is sufficiently small (lateral dimensions of the order of a few tens of nanometers), the spin-transfer torque exceeds the Oersted-field torque and a wealth of spin-transfer-driven effects appears in the magnetization dynamics of the ferromagnetic element. The basis for the interpretation of these effects was laid in the 1990s by Berger and Slonczewski (Berger, 1996; Slonczewski, 1996).

Spin-transfer effects are most often investigated in three-layer structures consisting of two ferromagnetic layers separated by a nonmagnetic metallic spacer. The observation and the interpretation of spin-transfer effects is greatly simplified when the magnetization in one of the magnetic layers is more or less independent of external actions due to large volume, large anisotropy, pinning to additional underlayers, and the like. Then that layer, commonly known as the "fixed" or the "pinned" layer, simply acts as the reference polarizer for the electron spins. The second layer, termed the "free" layer, is the one where various kinds of dynamic phenomena take place.

B. Azzerboni et al. (eds.), Magnetic Nanostructures in Modern Technology, 37–60.

The spin-transfer interaction between the electric current and the magnetization can give rise to two main types of magnetization motion (Sun, 2000; Zhang et al., 2002; Stiles and Zangwill, 2002; Li and Zhang, 2003; Bazaliy et al., 2004; Bertotti et al., 2006b): current-induced magnetization reversal; coherent magnetization oscillations or spin-wave emission at microwave frequencies. These types of magnetic response have potential applications in magnetic storage technology and spintronics, for novel types of current-controlled magnetic random access memory elements or current-controlled microwave oscillators integrable with semiconductor electronics.

Various experimental arrangements have been developed to observe spin transfer effects. Point-contact setups were initially proposed, where a sharpened tip is brought into electric contact with a layered structure consisting of a large number of alternating normal metal/ferromagnet sublayers (Tsoi et al., 1997, 1998, 2000). The point-contact method has then evolved into the preparation of nanocontact areas on top of three-layer structures (Myers et al., 1999; Rippard et al., 2004; Kaka et al., 2005; Mancoff et al., 2005). Finally, nanopatterning has been used to prepare "nanopillar" devices (Albert et al., 2000; Katine et al., 2000; Myers et al., 2002; Kiselev et al., 2003; Krivorotov et al., 2005), in which the device cross-section can be made noncircular in order to introduce in-plane shape anisotropy that leads to a better control of the orientation of the magnetization in the fixed layer and to more stable single-domain magnetization configurations in the free layer.

Current-induced switching of the magnetization was observed in point-contact configurations (Myers et al., 1999) and later in nanopillar devices (Albert et al., 2000; Myers et al., 2002; Grollier et al., 2001; Albert et al., 2002; Urazhdin et al., 2003; Krivorotov et al., 2004). More challenging has been the search for current-induced excitations of the magnetization at microwave frequencies. First results obtained for multilayers (Tsoi et al., 1998, 2000) were interpreted in terms of coherent magnon generation. Later studies on patterned nanocontacts (Rippard et al., 2004) gave evidence of excitations whose frequency could be a decreasing or increasing function of current, depending on field orientation. Similar results were obtained for nanopillar devices (Kiselev et al., 2003; Kiselev et al., 2004). Direct monitoring of these excitations in time (Krivorotov et al., 2005) permitted one to conclude that the excitations are associated with large-amplitude coherent precession of the magnetization in which spatial uniformity is largely preserved in time. Measurements on pairs of closely spaced point contacts on the same device (Kaka et al., 2005; Mancoff et al., 2005) have shown the appearance of frequency and phase locking in the magnetization oscillations with consequent enhancement of the total generated microwave power.

The magnetic volumes involved in spin-torque experiments are rather small, which means that thermal fluctuations can easily induce transitions from one dynamical regime to another. Such transitions and the associated random-telegraph

signals have been experimentally observed (Myers et al., 2002; Urazhdin et al., 2003; Krivorotov et al., 2004; Fabian et al., 2003). These effects can be described theoretically by adding, in analogy to what Brown proposed for the study of thermal switching in single-domain particles (Brown, 1963), a random torque to the equation for the magnetization dynamics (Li and Zhang, 2004; Li et al., 2005; Apalkov and Visscher, 2005b; Visscher and Apalkov, 2006; Bertotti et al., 2006a; Serpico et al., 2006). This leads to a Langevin-type stochastic differential equation for the magnetization and to a related Fokker-Planck equation for the magnetization probability distribution. On this basis, one can develop a thermal-activation-type approach, where the effective potential barrier controlling the transition between different dynamical regimes contains a nonequilibrium current-dependent part which cannot be expressed merely in terms of the system-free energy (Li et al., 2005; Visscher and Apalkov, 2006; Serpico et al., 2006). These aspects will be discussed in more detail in Section 4.

2. Equation for spin-transfer-driven magnetization dynamics

The effect of spin transfer on magnetization dynamics can be studied, quite independently of the details of the microscopic mechanism responsible for it, by adding an appropriate spin-transfer term to the other magnetic torques present in the Landau-Lifshitz-Gilbert (LLG) equation for the free-layer magnetization. In this respect, a first essential step before moving to the detailed micromagnetic simulation of complex spin-transfer devices is to study the ideal case where the magnetization in the free layer is assumed to be spatially uniform (Bazaliy et al., 2004; Bertotti et al., 2005, 2006b). In this case, the resulting equation for the magnetization dynamics in the free layer is (Slonczewski, 1996, 2002; Bertotti et al., 2005, 2006b):

$$\frac{d\mathbf{m}}{dt} - \alpha\,\mathbf{m}\times\frac{d\mathbf{m}}{dt} = -\mathbf{m}\times\mathbf{h}_{\text{eff}} + \beta\,\frac{\mathbf{m}\times\left(\mathbf{m}\times\mathbf{e}_p\right)}{1+c_p\,\mathbf{m}\cdot\mathbf{e}_p}\,, \tag{1}$$

where the last term is the spin transfer pseudotorque (Slonczewski, 1996; Slonczewski, 2002). Equation (1) is written in dimensionless form. Time is measured in units of $(\gamma M_s)^{-1}$, where M_s is the spontaneous magnetization and γ is the absolute value of the gyromagnetic ratio. The effective field $\mathbf{h}_{\text{eff}} = \mathbf{H}_{\text{eff}}/M_s$ and the magnetization $\mathbf{m} = \mathbf{M}/M_s$ are normalized by the spontaneous magnetization, α is Gilbert damping constant, the unit vector $\mathbf{e}_p$ identifies the magnetization direction in the fixed layer, and c_p is a model-dependent parameter discussed below. The strength of the spin-transfer effect is measured by the parameter β, proportional to the density of the electric current flowing through the device. One has:

$$\beta = b_p\,\frac{J_e}{J_p}\,, \tag{2}$$

where b_p is a second model-dependent parameter of the order of unity (see below), J_e is the current density, taken as positive when the electrons flow from the free into the fixed layer, while $J_p = \mu_0 M_s^2 |e| d/\hbar$ (e is the electron charge, $\hbar$ is the reduced Planck constant, and d is the free layer thickness). Typically, $J_p \sim 10^9$ A cm^{-2} for a free layer a few nanometers thick. Therefore, $J_e \ll J_p$ and consequently $\beta \ll 1$ even for the largest current densities applied to spin-transfer devices. Since $\alpha \ll 1$ as well, one concludes that both intrinsic damping and spin transfer act as small perturbations in Eq. (1). The physical consequences of this fact will be discussed in Section 3.

The coefficients b_p in Eq. (2) and c_p in Eq. (1) are model dependent. In the purely ballistic approach originally proposed by Slonczewski (1996) these coefficients are determined by the degree of spin polarization P in the ferromagnet ($0 < P < 1$):

$$b_p = \frac{4P^{3/2}}{3(1+P)^3 - 16P^{3/2}}\,, \tag{3}$$

$$c_p = \frac{(1+P)^3}{3(1+P)^3 - 16P^{3/2}}\,. \tag{4}$$

One finds that $0 < b_p < 1/2$ and $1/3 < c_p < 1$ when P is increased from 0 to 1. If one assumes for P the typical value $P = 0.3$, one finds $c_p \simeq 0.55$ and $b_p \simeq 0.17$. In subsequent extensions of the theory, where spin-diffusion effects are taken into account (Slonczewski, 2002), b_p and c_p are controlled by two parameters instead of P only. In the case of a symmetric three-layer structure with identical ferromagnetic layers, c_p is directly related to the deviation of the magnetoresistance of the device from a pure $(1 + \cos\theta)$ law and may attain positive as well as negative values in the interval $-1 < c_p < 1$.

The effective field $\mathbf{h}_{\text{eff}}$ appearing in Eq. (1) is given by $\mathbf{h}_{\text{eff}} = -\partial g_L/\partial \mathbf{m}$, where $g_L(\mathbf{m}; \mathbf{h}_a)$ is the normalized free energy of the free layer, measured in units of $\mu_0 M_s^2 S d$ (S is the free-layer surface area). In the case where both shape and crystal anisotropy have identical (ellipsoid-like) symmetry, the energy is expressed as:

$$g_L(\mathbf{m}; \mathbf{h}_a) = \frac{1}{2}\left(D_x m_x^2 + D_y m_y^2 + D_z m_z^2\right) - \mathbf{h}_a \cdot \mathbf{m}\,, \tag{5}$$

where $\mathbf{h}_a$ is the external field. In this case, the effective field takes the compact form $\mathbf{h}_{\text{eff}} = \mathbf{h}_a - D \cdot \mathbf{m}$, where the anisotropy tensor D has principal axes along the x, y, z directions. In terms of the energy g_L and of the additional function:

$$\Phi_{ST}(\mathbf{m}) = \frac{\ln(1 + c_p\, \mathbf{m} \cdot \mathbf{e}_p)}{c_p}\,, \tag{6}$$

one can express Eq. (1) as:

$$\frac{d\mathbf{m}}{d\,t} - \alpha\, \mathbf{m} \times \frac{d\mathbf{m}}{d\,t} = \mathbf{m} \times \frac{\partial g_L}{\partial \mathbf{m}} + \beta\, \mathbf{m} \times \left(\mathbf{m} \times \frac{\partial \Phi_{ST}}{\partial \mathbf{m}}\right). \tag{7}$$

It is evident from the structure of Eq. (7) that $\mathbf{m} \cdot d\mathbf{m}/dt = 0$. This means that the magnitude of the magnetization vector is preserved by the dynamics. In other words, the magnetization motion takes place on the surface of the unit sphere $|\mathbf{m}|^2 = 1$. On the other hand, written in this form the equation shows that the spin-transfer effect is inherently nonconservative and as such cannot be reduced to a correction to the free-layer energy. Competing spin-transfer models will result in different predictions for the functional form of $\Phi_{ST}(\mathbf{m})$.

We previously mentioned that we are interested in situations where both α and β are quantities much smaller than unity. To the first order in α and β, Eq. (7) becomes:

$$\frac{d\mathbf{m}}{d\,t} = \mathbf{m} \times \frac{\partial g_L}{\partial \mathbf{m}} + \alpha\, \mathbf{m} \times \left(\mathbf{m} \times \frac{\partial \Phi}{\partial \mathbf{m}} \right), \tag{8}$$

where:

$$\Phi\,(\mathbf{m}; \mathbf{h}_a, \beta/\alpha) = g_L\,(\mathbf{m}; \mathbf{h}_a) + \frac{\beta}{\alpha}\,\Phi_{ST}(\mathbf{m})\,. \tag{9}$$

Equation (8) has an interesting structure, with a clear-cut separation between the precessional contribution to the dynamics governed by g_L and the relaxation processes due to intrinsic damping and spin transfer, controlled by Φ.

Equation (1) describes the magnetization dynamics in the free layer under the assumption that this magnetization is spatially uniform. This is a natural and useful starting point, given the sub-micrometer lateral dimensions of typical spin-transfer devices. However, nonuniformities might become important under certain conditions, for example, in point-contact geometries where the spin-transfer-active region is a small part of a laterally unbounded medium. In such cases, one has to resort to the study of the complete space-dependent form of Eq. (1) (Slonczewski, 1999; Bazaliy et al., 1998; Hoefer et al., 2005). Appropriate numerical methods have been developed in order to carry out computer simulations of switching processes, magnetization oscillations, and thermal effects in nonuniformly magnetized devices (Miltat et al., 2001; Li and Zhang, 2003; Berkov and Gorn, 2005, 2006).

3. Magnetization dynamics and dynamical system theory

The equation governing the dynamics of the free-layer magnetic moment, Eq. (1), describes a nonlinear dynamical system with state vector $\mathbf{m}(t)$, driven far from equilibrium by the action of the spin-polarized electron flow. This suggests that the natural tools for the study of its properties should be nonlinear dynamical system theory and bifurcation theory (Perko, 1996; Kuznetsov, 1995; Hubbard and West, 1995). The dynamical-system perspective reveals certain physical aspects of the problem which are general and robust because they are topological in nature. In fact, when the external field $\mathbf{h}_a$ and the electric current, i.e., β, are

constant in time, Eq. (1) describes an autonomous (i.e., time-invariant) system whose state vector $\mathbf{m}(t)$ belongs to a two-dimensional state space, namely, the surface of the unit sphere $|\mathbf{m}|^2 = 1$. This immediately leads to stringent conclusions (Poincaré-Bendixson theorem) (Perko, 1996) about the admissible types of response to the field and current:

- *Chaos is precluded*
- The only possible types of steady-state magnetization response are:
  - *Stationary modes* associated with static solutions (fixed points) of Eq. (1)
  - *Self-oscillations* associated with periodic solutions (limit cycles) of Eq. (1)

The existence and stability of stationary modes can be analyzed with no particular difficulties (Bertotti et al., 2006b; Bazaliy et al., 2004). An example of this analysis is given in the Appendix. On the contrary, the study of self-oscillations (limit cycles) leads to one of the most difficult problems in dynamical system theory. The fact that the system may start to oscillate at some frequency even if the external driving forces (field and current) are constant in time is a typical property of nonlinear driven systems. However, in the case of LLG dynamics, this becomes possible only in the presence of the spin-polarized current. In fact, it is a general property of LLG dynamics under constant field and no current that:

$$\frac{dg_L}{dt} = -\alpha \left| \frac{d\mathbf{m}}{dt} \right|^2 . \tag{10}$$

Accordingly, magnetization processes are in the end all reduced to relaxation processes towards energy minima, for which no steady-state oscillations are possible. On the contrary, when spin transfer is active, the energy balance obtained from Eq. (7) becomes:

$$\frac{dg_L}{dt} = -\alpha\, \mathcal{P}(\mathbf{m}, \beta/\alpha) , \tag{11}$$

where:

$$\mathcal{P}(\mathbf{m}, \beta/\alpha) = \left| \frac{d\mathbf{m}}{dt} \right|^2 + \frac{\beta}{\alpha} \left(\mathbf{m} \times \frac{\partial \Phi_{ST}}{\partial \mathbf{m}} \right) \cdot \frac{d\mathbf{m}}{dt} , \tag{12}$$

Φ_{ST} is given by Eq. (6), and $d\mathbf{m}/dt$ must be expressed in terms of $\mathbf{m}$ by using the equations of motion. Depending on the sign of the current and the geometry of the magnetization trajectory, the function $\mathcal{P}(\mathbf{m}, \beta/\alpha)$ can be either positive or negative, which means that the free energy can be either decreasing or increasing during the magnetization motion. Therefore, magnetization oscillations become possible, in which energy dissipation through Gilbert damping and energy injection through spin transfer periodically balance each other.

A necessary condition for the existence of magnetization self-oscillations can be obtained as follows. Let us assume that the magnetization executes the periodic motion $\mathbf{m}_p(t)$. Then, $g_L(\mathbf{m}_p(t); \mathbf{h}_a)$ will be periodic as well, hence its time derivative will vanish when averaged over the period T_p of the motion. By using Eq. (11) one arrives at the conclusion that the periodic motion can exist only if:

$$I_{\mathcal{P}} = \int_0^{T_p} \mathcal{P}\left(\mathbf{m}_p(t), \beta/\alpha\right)\, dt = 0\,, \tag{13}$$

where $\mathcal{P}\left(\mathbf{m}_p(t), \beta/\alpha\right)$ is given by Eq. (12).

Much more difficult is the task of finding a sufficient, and if possible constructive, condition for the existence of self-oscillations. A fundamental role in this respect is played by the fact that both α and β are quantities much smaller than unity. Thus, we can study the spin-transfer-driven dynamics as a perturbation of the conservative dynamics corresponding to $\alpha = \beta = 0$ (Bertotti et al., 2005, 2006b):

$$\frac{d\mathbf{m}}{dt} = \mathbf{m} \times \frac{\partial g_L}{\partial \mathbf{m}}\,. \tag{14}$$

Solutions for the conservative dynamics can be obtained in closed analytical form thanks to the existence of two integrals of motion, namely, the magnetization magnitude $|\mathbf{m}|^2 = 1$ and the system energy $g_L(\mathbf{m}; \mathbf{h}_a) = g_0$ (Bertotti et al., 2004a, 2006b). The trajectories of the conservative dynamics are all periodic except few special trajectories, the separatrices, which are those trajectories starting from and ending on saddle equilibria. Each trajectory can be identified by the corresponding energy value g_0. We will use the notation $\mathbf{m}^c\,(t; \mathbf{h}_a, g_0)$ to denote the conservative motion of energy g_0. Explicit analytical expressions for $\mathbf{m}^c\,(t; \mathbf{h}_a, g_0)$ in the case where the external field is aligned along one of the symmetry axes of the problem have been presented and discussed elsewhere (Bertotti et al., 2006b).

The close connection between the properties of the conservative dynamics and the existence of self-oscillations is revealed by the following reasoning. Let us assume that a periodic motion exists in the dynamics. Then, Eq. (13) holds for that motion. Because of the smallness of α and β, the motion will be nearly coincident with one of the constant-energy orbits of the conservative dynamics. Let us denote this orbit and its energy by $C\,(g_0)$ and g_0, respectively. The integral $I_{\mathcal{P}}$ in Eq. (13) can then be calculated along $C\,(g_0)$ instead of the actual trajectory without significant error. By also taking into account that Eq. (14) holds along $C\,(g_0)$, one finds that $I_{\mathcal{P}} \simeq M\,(g_0, \mathbf{h}_a, \beta/\alpha)$, where:

$$M\,(g_0, \mathbf{h}_a, \beta/\alpha) = \oint_{C(g_0)} \left(\mathbf{m} \times \frac{\partial \Phi}{\partial \mathbf{m}}\right) \cdot d\mathbf{m}\,, \tag{15}$$

Φ is given by Eq. (9), and the orientation of $d\mathbf{m}$ is that of the conservative motion. Therefore, it is expected that $M\,(g_0, \mathbf{h}_a, \beta/\alpha) \simeq 0$ for self-oscillations. By applying Poincaré-Melnikov theory for slightly dissipative systems (Perko, 1996),

one transforms these heuristic considerations into the following fundamental result (Bertotti et al., 2005; Bertotti et al., 2006b).

Existence of limit cycles. In the limit $\alpha \to 0, \beta \to 0, \beta/\alpha \to const$, the equation $M(g_0, \mathbf{h}_a, \beta/\alpha) = 0$ represents the *necessary and sufficient* condition for the existence of a periodic solution (limit cycle) of Eq. (1). The limit cycle is asymptotically coincident with one of the trajectories of energy g_0 of the conservative dynamics, and is stable (unstable) when $\partial M(g_0, \mathbf{h}_a, \beta/\alpha)/\partial g_0 > 0 (< 0)$.

The Melnikov function $M(g_0, \mathbf{h}_a, \beta/\alpha)$ provides all the necessary information for the description of spin-transfer-induced microwave oscillations. This function depends on two basic features: the geometry of the trajectories $C(g_0)$ of the conservative dynamics and the functional form of the effective potential Φ. The fact that $M(g_0, \mathbf{h}_a, \beta/\alpha)$ is a line integral over $C(g_0)$ implies that $M(g_0, \mathbf{h}_a, \beta/\alpha) = 0$ also in correspondence of energy minima and maxima, where $C(g_0)$ is reduced to a point. These zeros do not represent real limit cycles and should not be included in the analysis. Let $\{g_i(\mathbf{h}_a, \beta/\alpha)\}$ be the set of energy roots of the equation $M(g_0, \mathbf{h}_a, \beta/\alpha) = 0$ after excluding those corresponding to energy minima and maxima. In addition, let $\mathbf{m}^c(t; \mathbf{h}_a, g_0)$ be the conservative motion along the orbit $C(g_0)$. Then, for each root $g_i(\mathbf{h}_a, \beta/\alpha)$ there exists a corresponding current-induced self-oscillation $\mathbf{m}^c(t; \mathbf{h}_a, g_i(\mathbf{h}_a, \beta/\alpha))$. The oscillation will be stable if $\partial M/\partial g_0|_{g_0=g_i} > 0$. From this knowledge of the self-oscillation time dependence, one can compute the corresponding frequency and the harmonic content. A complication is that in general there may be more than one conservative trajectory associated with the same value of energy. This fact is properly dealt with by describing energy dependencies in terms of a graph reflecting the topology of energy wells and barriers on the **m** sphere (Bertotti et al., 2006a).

A convenient way to visualize the overall properties of spin-transfer phenomena is through a stability diagram in the field-current control plane, in which one represents the location of the various dynamical regimes observed or computed, together with the lines (bifurcation lines) across which qualitative changes take place in the dynamics. These qualitative changes can be broadly classified as follows:

- Changes in the number of fixed points (saddle-node bifurcations)
- Changes in the stability of nonsaddle fixed points (Hopf bifurcations)
- Changes in the number of zeros of the Melnikov function (saddle-connection and semistable limit-cycle bifurcations)

The interplay between these various bifurcation conditions leads to stability diagrams of amazing richness (Bertotti et al., 2006b).

In the limit of small α, all the functions involved in the bifurcation analysis, for example, the Melnikov function defined by Eq. (15), do not depend on α and

β separately, but only on their ratio β/α. Once some critical condition $(\beta/\alpha)_{\text{crit}}$ is determined by solving the appropriate bifurcation equations, the corresponding critical current density will be (see Eq. (2)):

$$J_{\text{crit}} = \frac{\alpha \mu_0 \mathbf{M}_s^2 |e| d}{b_p \hbar} \left(\frac{\beta}{\alpha}\right)_{\text{crit}} . \tag{16}$$

This equation shows how the various physical parameters of the problem jointly determine the conditions leading to specific dynamic regimes. The proportionality of critical currents to the free-layer thickness d has been experimentally tested (Albert et al., 2002). The simple proportionality with respect to α is valid only in the limit of sufficiently small damping. Increasingly important deviations are expected under increasing α up to where additional bifurcations will introduce features not present in the $\alpha \to 0$ limit. The α threshold for these bifurcations is in general not known, a fact that should always be carefully considered in the comparison between theory and experiments.

The Poincaré-Melnikov theory shows that the system energy is the appropriate and natural state variable for the characterization of steady-state magnetization self-oscillations. As a matter of fact, the role of energy is even more general than that. Indeed, when α and β are small quantities, there exist two well-separated timescales in the dynamics: a fast one, where the magnetization precesses at virtually constant energy around the instantaneous effective field vector; and a slow one, where the energy of the system relaxes towards its steady-state value associated either with a stationary state or with self-oscillations. The magnetization will go through several precessional periods before its energy varies by a significant amount. In addition, during a single precessional period the magnetization motion will be very close to one of the trajectories of the conservative dynamics. This implies that no essential information on the long-time relaxation of the system is lost if one takes the average of Eq. (11) over one precessional period and assumes that the motion of the system coincides with the conservative one during that period (Bertotti et al., 2004b). This is precisely the assumption previously made in the derivation of the Melnikov function. Therefore, the resulting dynamical equation for the average of g_L over one precessional period will be:

$$\frac{dg}{dt} = -\alpha \frac{M(g, \mathbf{h}_a, \beta/\alpha)}{T(g)} , \tag{17}$$

where $M(g, \mathbf{h}_a, \beta/\alpha)$ is the Melnikov function defined by Eq. (15) and $T(g)$ is the period of the conservative motion of energy g. From Eq. (14) one finds:

$$T(g) = \oint_{C(g)} \frac{d\ell}{|\partial g_L / \partial \mathbf{m}|} , \tag{18}$$

where $d\ell$ represents the positive line increment along $C(g)$.

Equation (17) shows that the long-time behavior of the energy is governed by a viscous-type relaxation equation in which the ratio $-M/T$ acts as the driving force for the energy itself. This force can be thought of as the derivative with respect to the energy of the effective potential:

$$U(g) = \int_{g_0}^{g} \frac{M\,(u, \mathbf{h}_a, \beta/\alpha)}{T(u)}\, du + U_0\,, \tag{19}$$

where g_0 and U_0 are constants dependent on the properties of the graph describing the topology of energy wells and barriers on the $\mathbf{m}$ sphere (Bertotti et al., 2006a). In terms of U the equation for the energy becomes:

$$\frac{dg}{dt} = -\alpha\, \frac{\partial U}{\partial g}\,. \tag{20}$$

This approximate description will be more accurate, the smaller α, or, equivalently, the faster the magnetization precession period with respect to the timescale of energy relaxation. The U extrema where $\partial U/\partial g = 0$ for finite $T(g)$, that is where $M\,(g, \mathbf{h}_a, \beta/\alpha) = 0$, correspond to nonsaddle fixed points or to limit cycles of the dynamics, in agreement with Poincaré-Melnikov theory.

4. The role of thermal fluctuations

The effect of thermal fluctuations on spin-transfer-driven magnetization dynamics can be modeled by a method analogous to the one proposed by Brown for the study of thermally induced magnetization switching in small particles (Brown, 1963). One introduces thermal effects in Eq. (8) via a random magnetic torque $-\nu\, \mathbf{m} \times \mathbf{h}_N(t)$, where the components of $\mathbf{h}_N(t)$ are independent gaussian white-noise processes and the intensity of the thermal disturbance is measured by the parameter ν:

$$\frac{d\mathbf{m}}{d\,t} = \mathbf{m} \times \frac{\partial g_L}{\partial \mathbf{m}} + \alpha\, \mathbf{m} \times \left(\mathbf{m} \times \frac{\partial \Phi}{\partial \mathbf{m}}\right) - \nu\, \mathbf{m} \times \mathbf{h}_N(t)\,. \tag{21}$$

This is a Langevin-type stochastic differential equation in which the noise acts in a nontrivial multiplicative fashion, because of the presence of the $\mathbf{m} \times \ldots$ operation on $\mathbf{h}_N$. However, if one interprets the equation in the sense of Stratonovich (Kubo and Hashitsume, 1970; Gardiner, 1985), then the ordinary rules of calculus can be applied, which permits one to conclude that $\mathbf{m} \cdot d\mathbf{m}/dt = 0$. Hence, the magnitude of magnetization keeps on being preserved even after the introduction of noise and one can describe the magnetization dynamics as a stochastic process on the unit sphere $|\mathbf{m}|^2 = 1$, governed by the equation:

$$\frac{d\mathbf{m}}{d\,t} = \mathbf{m} \times \mathrm{grad}_{\Sigma}\, g_L - \alpha\, \mathrm{grad}_{\Sigma}\, \Phi + \nu\, \mathbf{h}_{\Sigma}(t)\,, \tag{22}$$

where grad_Σ represents the gradient operator on the sphere and $\mathbf{h}_\Sigma(t)$ is a homogeneous and isotropic process on the sphere characterized by independent gaussian white-noise components.

The value of the constant ν can be determined via the fluctuation-dissipation theorem in the particular case where the system is close to equilibrium and no current is injected ($\beta = 0$). One finds:

$$\nu^2 = \frac{2\alpha k_B T}{\mu_0 M_s^2 S d}\,, \tag{23}$$

where S and d are the free-layer surface area and thickness, respectively, whereas k_B represents Boltzmann constant. It is usually assumed as a first approximation that the statistical properties of the noise term in Eq. (22), and in particular, the value of ν expressed by Eq. (23) remain the same even when the spin-polarized current is injected into the system.

The Fokker-Planck equation on the sphere for the probability density $W(\mathbf{m}, t)$ associated with Eq. (22) is:

$$\frac{\partial W}{\partial t} + \mathrm{div}_\Sigma \mathbf{J} = 0\,, \tag{24}$$

where div_Σ is the divergence operator on the sphere and the probability current $\mathbf{J}$ is given by:

$$\mathbf{J} = W\,\mathbf{m} \times \mathrm{grad}_\Sigma\, g_L - \alpha\, W\, \mathrm{grad}_\Sigma\, \Phi - \frac{\nu^2}{2}\,\mathrm{grad}_\Sigma\, W\,. \tag{25}$$

The probability current $\mathbf{J}$ contains three terms: the first represents convective motion along the trajectories of the conservative dynamics; the second relaxation along the gradient lines of the potential Φ defined by Eq. (9); and the third isotropic diffusion on the sphere. Working out quantitative predictions about the time evolution of the probability density $W(\mathbf{m}, t)$ for this general case is a formidable task for which no general solutions have been found yet. Nevertheless, some interesting approximate results can be obtained in the limit of small damping and small fluctuations ($\alpha \ll 1$, $\nu \sim \sqrt{\alpha}$), thanks to the separation of timescales that exists in this case in the dynamics, as discussed at the end of the previous section. The presence of two distinct timescales is reflected by the fact that the second and third terms in Eq. (25), describing relaxation and diffusion, are of the order of α and thus much smaller than the first term, describing precession around the instantaneous effective field. We pointed out at the end of the previous section that energy is the natural state variable for the description of the system evolution on the long timescale. This suggests that, after some proper averaging of Eqs. (24) and (25) over fast precession, one should obtain a relaxation-diffusion equation on the long timescale involving only the system

energy and time (Apalkov and Visscher, 2005a; Li et al., 2005; Bertotti et al., 2006a; Serpico et al., 2006). This averaging can be carried out by assuming that on the long timescale the system is at each instant of time under stationary conditions with respect to the fast precessional motion, so that all the relevant information is carried by the probability density $W(g,t)$ of visiting different trajectories $C(g)$ of the precessional dynamics. The technical details of how the averaging can be performed in practice are discussed in the references cited above. The result is the following equation for $W(g,t)$:

$$T(g)\,\frac{\partial W}{\partial t}+\frac{\partial \bar{J}}{\partial g}=0\,, \tag{26}$$

$$\bar{J}=-\alpha\,M\,(g,\mathbf{h}_a,\beta/\alpha)\,W-\frac{\nu^2}{2}\,M^0\,(g,\mathbf{h}_a)\,\frac{\partial W}{\partial g}\,, \tag{27}$$

where $T(g)$ is the period of the conservative motion along $C(g)$, $M\,(g,\mathbf{h}_a,\beta/\alpha)$ is the Melnikov function defined by Eq. (15), and $M^0\,(g,\mathbf{h}_a)=M\,(g,\mathbf{h}_a,\beta/\alpha=0)$. From Eq. (15) one finds:

$$M^0\,(g,\mathbf{h}_a)=\oint_{C(g)}|\partial g_L/\partial\mathbf{m}|\;d\ell\,, \tag{28}$$

where $d\ell$ represents the positive line increment along $C(g)$. The normalization condition for W reads:

$$\int_{\mathcal{G}}W(g,t)\,T(g)\,dg=1\,, \tag{29}$$

where the symbol $\mathcal{G}$ indicates that the integral has to be carried out on the graph $\mathcal{G}$ describing the topology of energy wells and barriers on the **m** sphere (Bertotti et al., 2006a). As a matter of fact, it is Eq. (26) itself that must be solved on this graph, under the condition that W be continuous everywhere across the graph and that at each graph node the sum of all incoming probability currents be equal to zero.

According to Eq. (27), the stationary distribution $W^{\mathrm{eq}}(g)$ for which $\bar{J}=0$ is proportional to $\exp[-2\alpha V(g)/\nu^2]$, where:

$$V(g)=\int_{g_0}^{g}\frac{M\,(u,\mathbf{h}_a,\beta/\alpha)}{M^0\,(u,\mathbf{h}_a)}\,du+V_0\,, \tag{30}$$

while V_0 and g_0 are constants related to the properties of the graph $\mathcal{G}$. By also taking into account Eq. (23), one concludes that:

$$W^{\mathrm{eq}}(g)=\frac{1}{Z}\,\exp\left(-\frac{\mu_0 M_s^2 Sd\,V(g)}{k_B T}\right)\,, \tag{31}$$

where the normalization constant Z is set through Eq. (29):

$$Z = \int_{\mathcal{G}} \exp\left(-\frac{\mu_0 M_s^2 Sd\, V(g)}{k_B T}\right) T(g)\, dg\,. \tag{32}$$

Equation (31) is formally coincident with the Boltzmann distribution for a system with potential energy $\mu_0 M_s^2 Sd\, V(g)$, negligible kinetic energy, and density of states $T(g)$. However, the system is not in thermodynamic equilibrium but rather in a far-from-equilibrium stationary state driven by the injected current. The nonequilibrium character of the situation is revealed by the fact that the potential $V(g)$ depends on the current through the parameter β/α (Eq. (30)). Whenever the initial conditions in which the system is prepared are different from Eq. (31), it is expected that the rate of approach to the stationary state through thermally induced transitions between different dynamical regimes will be controlled by the distribution of wells and barriers in $V(g)$. In this sense $V(g)$ acts as a sort of effective potential for spin-transfer-driven relaxation and diffusion in the presence of thermal fluctuations.

In the previous section it was shown that the long timescale deterministic dynamics in the absence of thermal fluctuations is controlled by the effective potential $U(g)$ (Eq. (19)). If one compares Eq. (19) with Eq. (30) one finds that the potentials $U(g)$ and $V(g)$ do not coincide, so one might wonder how the stochastic dynamics will be reduced to the deterministic dynamics in the limit of low temperatures. The point is that the potentials U and V have the same distribution of maxima and minima, because:

$$\frac{\partial U}{\partial g} = \frac{M^0(g, \mathbf{h}_a)}{T(g)} \frac{\partial V}{\partial g}\,, \tag{33}$$

and $T(g)$ as well as $M^0(g, \mathbf{h}_a)$ are positive-definite quantities, as shown by Eqs. (18) and (28). This means that at low temperatures $W^{\mathrm{eq}}(g)$ will be peaked around the states for which $U(g)$ is minimum, as one would expect on physical grounds.

Another way to look at the problem is to discuss how the deterministic equation for the energy (Eq. (17)) should be modified in order to include the effect of thermal fluctuations. The difference between U and V suggests that this modification cannot be the simple addition of a white-noise term to Eq. (17). This aspect is conveniently discussed by first writing the Fokker-Planck equation for the probability density in energy $\rho(g, t)$, namely the function with the property that $\rho(g, t)\, dg$ represents the probability of finding the system in a state of energy in the interval $(g, g + dg)$. Equation (29) shows that:

$$\rho(g, t) = T(g)\, W(g, t)\,. \tag{34}$$

By rewriting Eqs (26) and (27) in terms of $\rho(g,t)$ one finds:

$$\frac{\partial\rho}{\partial t}=\frac{\partial}{\partial g}\left[\left(\alpha\,\frac{M}{T}-\frac{\nu^2}{2}\frac{1}{T}\frac{\partial M^0}{\partial g}\right)\rho+\frac{\nu^2}{2}\frac{\partial}{\partial g}\frac{\rho M^0}{T}\right], \tag{35}$$

where M and M^0 are the Melnikov functions previously introduced whereas T here represents the period of the precessional motion, not to be confused with temperature. The stochastic Ito equation corresponding to this Fokker-Planck equation is (Gardiner, 1985):

$$\frac{dg}{dt}=-\alpha\,\frac{M\,(g,\mathbf{h}_a,\beta/\alpha)}{T(g)}+\frac{\nu^2}{2}\frac{1}{T(g)}\frac{\partial M^0\,(g,\mathbf{h}_a)}{\partial g}+\nu\sqrt{\frac{M^0\,(g,\mathbf{h}_a)}{T(g)}}\,\mathrm{h}_N(t)\,, \tag{36}$$

where $\mathrm{h}_N(t)$ represents the gaussian white-noise process. We see that the connection between Eq. (17) and Eq. (36) is far from obvious. Equation (36) is reduced to Eq. (17) when thermal fluctuations vanish ($\nu\to 0$). On the other hand, when thermal fluctuations are important, a noise-induced drift appears in the equation in addition to the white-noise component, which has an energy-dependent intensity.

5. Uniaxial symmetry

When the spin-transfer problem exhibits uniaxial symmetry about the z-axis perpendicular to the free-layer plane, a detailed analytical treatment is possible and certain physical aspects of the dynamics emerge with particular evidence. Systems with this type of symmetry are of broad current interest because of their promising applications in data-storage technologies (Mangin et al., 2006), as discussed in other chapters of this volume.

Uniaxial symmetry is realized when the anisotropy coefficients appearing in Eq. (5) are such that $D_x=D_y=D_\perp$ and the external field is applied along the z-axis. It is convenient to use spherical coordinates (θ,ϕ) to identify points on $\mathbf{m}$ unit sphere: $m_x=\sin\theta\cos\phi$, $m_y=\sin\theta\sin\phi$, $m_z=\cos\theta$. Once expressed in terms of (θ,ϕ), both the system energy g_L (Eq. (5)) and the potential Φ (Eq. (9)) become functions of θ only. After dropping inessential constant offsets, one finds:

$$g_L\,(\mathbf{m};\mathbf{h}_a)=-\frac{k_{\mathrm{eff}}}{2}\cos^2\theta-h_a\cos\theta\,, \tag{37}$$

$$\Phi\,(\mathbf{m};\mathbf{h}_a,\beta/\alpha)=-\frac{k_{\mathrm{eff}}}{2}\cos^2\theta-h_a\cos\theta+\frac{\beta}{\alpha}\,\frac{\ln(1+c_p\,\cos\theta)}{c_p}\,, \tag{38}$$

where h_a is the z-directed amplitude of the external field, which can be positive or negative, whereas:

$$k_{\mathrm{eff}}=D_\perp-D_z \tag{39}$$

plays the role of effective anisotropy constant.

The physical consequences of the presence of rotational invariance in the problem are best revealed by considering the approximate, first-order equation for the magnetization dynamics, Eq. (8). By taking into account that g_L and Φ depend on θ only, one finds that the equations of motion for the spherical coordinates are:

$$\frac{d\theta}{dt} = -\alpha \frac{\partial \Phi}{\partial \theta}, \tag{40}$$

$$\frac{d\phi}{dt} = \frac{1}{\sin\theta} \frac{\partial g_L}{\partial \theta}. \tag{41}$$

Equation (40) shows that the polar angle θ follows a viscous-type relaxation dynamics in the effective potential Φ. The stationary states in which the system can live for indefinite time are the zeros of the force $\partial\Phi/\partial\theta$. From Eq. (38), one finds:

$$\frac{\partial \Phi}{\partial \theta} = \sin\theta \left(k_{\text{eff}} \cos\theta + h_a - \frac{\beta}{\alpha} \frac{1}{1 + c_p \cos\theta} \right). \tag{42}$$

The two states for which $\sin\theta = 0$, i.e. $\theta = 0$ and $\theta = \pi$, are fixed points of the dynamics that are always present whatever the field and current conditions. On the other hand, any zero θ_0 of the expression inside brackets in Eq. (42):

$$\frac{\beta}{\alpha} = (h_a + k_{\text{eff}} \cos\theta_0) \left(1 + c_p \cos\theta_0\right), \tag{43}$$

is a limit cycle of the dynamics, in which the magnetization precesses around the symmetry axis at the constant polar angle θ_0. The stability of both fixed points and limit cycles is controlled by the curvature of the effective potential. Physically observable regimes will be those for which $\partial^2\Phi/\partial\theta^2 > 0$.

Under varying field and current, one or the other of the fixed points at $\theta = 0$ and $\theta = \pi$ may pass from stable to unstable via a Hopf bifurcation entailing the creation or the destruction of a limit cycle. The Hopf bifurcation condition where the limit cycle is created or destroyed around $\theta = 0$ is obtained by setting $\cos\theta = 1$ in Eq. (43):

$$\frac{\beta}{\alpha} = (1 + c_p)(h_a + k_{\text{eff}}). \tag{44}$$

Analogously, the condition for the Hopf bifurcation around $\theta = \pi$ ($\cos\theta = -1$) is:

$$\frac{\beta}{\alpha} = (1 - c_p)(h_a - k_{\text{eff}}). \tag{45}$$

Equations (44) and (45) represent straight lines in the field-current $(h_a, \beta/\alpha)$ control plane. These lines identify the regions in the control plane where limit cycles exist. On this basis, one can construct the complete dynamical phase diagram for spin-transfer-driven magnetization dynamics in systems with uniaxial symmetry (Bazaliy et al., 2004).

A given stable limit cycle of polar angle θ_0 will result in observable magnetization oscillations. The frequency f_0 of these oscillations is determined by Eq. (41):

$$f_0 = \frac{1}{2\pi} \frac{1}{\sin\theta_0} \left.\frac{\partial g_L}{\partial \theta}\right|_{\theta_0} . \tag{46}$$

By using Eq. (37) one obtains:

$$f_0 = \frac{1}{2\pi} \left(h_a + k_{\text{eff}} \cos\theta_0\right) . \tag{47}$$

This frequency coincides with the Kittel frequency of free precession of an undamped system subject to no current, provided the amplitude of its motion coincides with the amplitude θ_0 of the limit cycle. This means that spin transfer does not affect the free precession of the system about the symmetry axis. What it does is to introduce a mechanism whereby one of the possible amplitudes of free precession is selected and elected to the status of stable limit cycle of the dissipative dynamics.

The effect of thermal fluctuations on uniaxial systems can be studied in great detail by taking advantage of rotational invariance. In fact, the long timescale relaxation-diffusion equation obtained in the previous section as an approximation valid in the limit of small α, can be derived for uniaxial systems without introducing any approximation. This can be shown by writing the Fokker-Planck equation for $W(\mathbf{m}, t)$ (Eqs. (24) and (25)) in terms of the spherical coordinates (θ, ϕ):

$$\frac{\partial W(\theta,\phi,t)}{\partial t} = -\frac{1}{\sin\theta} \frac{\partial}{\partial\theta} \left(\sin\theta\, J_\theta\right) - \frac{1}{\sin\theta} \frac{\partial J_\phi}{\partial\phi} , \tag{48}$$

$$J_\theta = -\frac{W}{\sin\theta} \frac{\partial g_L}{\partial\phi} - \alpha W \frac{\partial\Phi}{\partial\theta} - \frac{\nu^2}{2} \frac{\partial W}{\partial\theta} , \tag{49}$$

$$J_\phi = W \frac{\partial g_L}{\partial\theta} - \frac{\alpha W}{\sin\theta} \frac{\partial\Phi}{\partial\phi} - \frac{\nu^2}{2} \frac{1}{\sin\theta} \frac{\partial W}{\partial\phi} . \tag{50}$$

By integrating Eq. (48) with respect to ϕ and by taking into account that g_L and Φ are independent of ϕ, one obtains the following equation in θ only:

$$\frac{\partial\rho}{\partial t} = \frac{\partial}{\partial\theta} \left[\left(\alpha \frac{\partial\Phi}{\partial\theta} - \frac{\nu^2}{2} \cot\theta \right) \rho + \frac{\nu^2}{2} \frac{\partial\rho}{\partial\theta} \right] , \tag{51}$$

where:

$$\rho(\theta, t) = \sin\theta \int_0^{2\pi} W(\theta,\phi,t)\, d\phi \tag{52}$$

is the probability density with respect to θ, in the sense that $\rho(\theta, t)\, d\theta$ represents the probability that the system be found in a state with polar angle in the interval

$(\theta, \theta + d\theta)$. Equation (51) is analogous to Eq. (35), since constant θ trajectories coincide with constant energy trajectories. However, we stress once more that Eq. (51) has been obtained without introducing any approximation and in particular is not limited to small values of α. The Ito stochastic equation corresponding to Eq. (51) is:

$$\frac{d\theta}{dt} = -\alpha \frac{\partial \Phi}{\partial \theta} + \frac{\nu^2}{2} \cot\theta + \nu \, \mathrm{h}_N(t) \,, \tag{53}$$

where $\mathrm{h}_N(t)$ represents the gaussian white-noise process. This equation is the stochastic extension of Eq. (40) and shoud be compared with Eq. (36).

Finally, the stationary probability distribution obtained from Eq. (51) is $\rho^{\mathrm{eq}}(\theta) \propto \sin\theta \, \exp[-2\alpha \, \Phi(\theta)/\nu^2]$. This result and Eq. (40) show that in the case of uniaxial symmetry the role of the potentials U and V discussed in the previous section is played by the single potential Φ given by Eq. (38).

Appendix

In this appendix, we give an example of analysis of the properties of the fixed points of Eq. (1) in a particular case. We assume that the anisotropy coefficients appearing in Eq. (5) obey the ordering $D_x < D_y < D_z$, which means that the free-layer easy axis is along the x-axis. We discuss the case, of interest to spin-transfer experiments in nanopillars (Kiselev et al., 2003), where both the applied field and the spin-polarization are aligned along the easy axis of the free layer: $\mathbf{h}_a = h_{ax}\mathbf{e}_x$, $\mathbf{e}_p \equiv \mathbf{e}_x$.

Stationary states are represented by the fixed points of the dynamics, obtained by imposing $d\mathbf{m}/dt = 0$ in Eq. (1). One finds that the fixed-point magnetization $\mathbf{m}_0$ is the solution of the equation:

$$\mathbf{h}_{\mathrm{eff}}(\mathbf{m}_0) - \beta \frac{\mathbf{m}_0 \times \mathbf{e}_p}{1 + c_p \, \mathbf{m}_0 \cdot \mathbf{e}_p} = \lambda \, \mathbf{m}_0 \,, \tag{54}$$

where λ is an unknown parameter to be determined. By using Eq. (5) and by taking into account that $\mathbf{h}_a = h_{ax}\mathbf{e}_x$, $\mathbf{e}_p \equiv \mathbf{e}_x$, Eq. (54) is reduced to the set of equations:

$$(\lambda + D_x) \, m_{0x} = h_{ax} \,, \tag{55}$$

$$\big(\lambda + D_y\big) \, m_{0y} + \beta_x \, m_{0z} = 0 \,, \tag{56}$$

$$\beta_x \, m_{0y} - (\lambda + D_z) \, m_{0z} = 0 \,, \tag{57}$$

where:

$$\beta_x = \frac{\beta}{1 + c_p \, m_{0x}} \,. \tag{58}$$

Equations (55)–(57) consist of an equation for m_{0x} and a set of two coupled equations for (m_{0y}, m_{0z}). Therefore the fixed points can be classified as follows.

– Fixed points with $m_{0y} = m_{0z} = 0$.
There are two such fixed points:

$$m_{0x} = \pm 1, \;\; m_{0y} = m_{0z} = 0\,. \tag{59}$$

These two fixed points are always present and never destroyed whatever the field and current conditions. The corresponding values of λ and β_x are:

$$\lambda = \lambda_\pm = -D_x \pm h_{ax}, \quad \beta_x = \beta_\pm = \frac{\beta}{1 \pm c_p}\,. \tag{60}$$

– Fixed points with $m_{0y} \neq 0, m_{0z} \neq 0$.
This solution will exist only if the determinant of Eqs. (56)–(57) is equal to zero:

$$\left(\lambda + D_y\right)\left(\lambda + D_z\right) + \beta_x^2 = 0\,. \tag{61}$$

This gives two solutions for λ:

$$\lambda = \lambda'_\pm = -\frac{D_z + D_y}{2} \pm \sqrt{\frac{\left(D_z - D_y\right)^2}{4} - \beta_x^2}\,. \tag{62}$$

By inserting $\lambda'_\pm$ into Eq. (55) one finds:

$$\left(\lambda'_\pm + D_x\right) m_{0x} = h_{ax}\,. \tag{63}$$

This is an equation for m_{0x}, because $\lambda'_\pm$ depends on m_{0x} through β_x. By rearranging terms, squaring, and taking into account that $\lambda'_\pm + D_x < 0$ as a consequence of the fact that $-D_z \leq \lambda'_\pm \leq -D_y < -D_x$ (see Eq. (62)), one obtains:

$$\left(\frac{h_{ax}}{m_{0x}} + D_z - D_x\right)\left(\frac{h_{ax}}{m_{0x}} + D_y - D_x\right) + \beta_x^2 = 0\,. \tag{64}$$

To the first order in β, this equation can be solved under the approximation $\beta_x^2 = 0$. This is acceptable whenever $\beta_x^2 \ll \left(D_z - D_y\right)^2/4 - D_x^2$. This requirement is usually satisfied in spin-torque experiments, where $\beta \ll 1$ (current limit), $D_z \approx 1$ (thin-film geometry), and $c_p \approx 0.5$ (level of spin polarization). Equation (64) gives two solutions for m_{0x}. Each of these solutions gives two fixed points with opposite values of m_{0y} and m_{0z}, obtained by imposing $m_{0y}^2 + m_{0z}^2 = 1 - m_{0x}^2$ and by using Eq. (56) or (57). The result is the following two pairs of fixed points.

- Fixed points which coincide with g_L maxima when $\beta = 0$.

$$m_{0x} = -\frac{h_{ax}}{D_z - D_x}\,, \tag{65}$$

$$\lambda = \lambda'_- \ , \quad \beta_x = \beta'_- = \frac{\beta}{1 - c_p\, h_{ax} / \left(D_z - D_x\right)} , \tag{66}$$

$$m_{0y} \ = \ \mp\beta'_- \sqrt{\frac{1 - m_{0x}^2}{\left(\lambda'_- + D_y\right)^2 + \beta'^2_-}} \tag{67}$$

$$m_{0z} \ = \ \pm\left(\lambda'_- + D_y\right) \sqrt{\frac{1 - m_{0x}^2}{\left(\lambda'_- + D_y\right)^2 + \beta'^2_-}} . \tag{68}$$

These fixed points exist only in the field interval $|h_{ax}| \leq D_z - D_x$. This condition is found by imposing $m_{0x}^2 \leq 1$ in Eq. (65).

- Fixed points which coincide with g_L saddles when $\beta = 0$.

$$m_{0x} = -\frac{h_{ax}}{D_y - D_x} \tag{69}$$

$$\lambda = \lambda'_+ \ , \quad \beta_x = \beta'_+ = \frac{\beta}{1 - c_p\, h_{ax} / \left(D_y - D_x\right)} , \tag{70}$$

$$m_{0y} \ = \ \pm\left(\lambda'_+ + D_z\right) \sqrt{\frac{1 - m_{0x}^2}{\left(\lambda'_+ + D_z\right)^2 + \beta'^2_+}} , \tag{71}$$

$$m_{0z} \ = \ \pm\beta'_+ \sqrt{\frac{1 - m_{0x}^2}{\left(\lambda'_+ + D_z\right)^2 + \beta'^2_+}} . \tag{72}$$

These fixed points exist only in the field interval $|h_{ax}| \leq D_y - D_x$.

In conclusion, the number of fixed points is as follows.

- 6 fixed points for $|h_{ax}| < D_y - D_x$
- 4 fixed points for $D_y - D_x < |h_{ax}| < D_z - D_x$
- 2 fixed points for $|h_{ax}| > D_z - D_x$

The number and/or the stability of these fixed points change in correspondence of saddle-node or Hopf bifurcations (Hubbard and West, 1995). In a saddle-node bifurcation, the number of fixed points is increased or decreased by 2 via the creation or annihilation of a saddle-node pair. In our case, this occurs for $|h_{ax}| = D_y - D_x$ and $|h_{ax}| = D_z - D_x$. The current does not appear in these expressions, which means that this type of instability can be produced only by varying the external field. On the contrary, the current plays a central role in Hopf bifurcations, where a nonsaddle fixed point changes from the stable to unstable with the simultaneous appearance or disappearance of a limit cycle.

Hopf bifurcations are studied by linearizing Eq. (1) around the fixed point of interest and by imposing that the trace of the stability matrix controlling the dynamics of the linear perturbation be equal to zero. To this end, let us consider one of the fixed-point solutions $\mathbf{m}_0$ of Eq. (54), and let us introduce the perturbed magnetization $\mathbf{m}(t) = \mathbf{m}_0 + \delta\mathbf{m}(t)$. The perturbation must be such that $\mathbf{m}_0 \cdot \delta\mathbf{m} = 0$, as a consequence of the fact that the magnetization magnitude must be preserved. By inserting $\mathbf{m}(t)$ in Eq. (1), one obtains the following linearized LLG equation for $\delta\mathbf{m}$:

$$\frac{d\,\delta\mathbf{m}}{d\,t} - \alpha\,\mathbf{m}_0 \times \frac{d\,\delta\mathbf{m}}{d\,t} = \mathbf{m}_0 \times \left[\lambda\,\delta\mathbf{m} + D\cdot\delta\mathbf{m} + \beta_x\left(\delta\mathbf{m}\times\mathbf{e}_x - c_p\,\frac{\mathbf{m}_0\times\mathbf{e}_x}{1+c_p\,m_{0x}}\,\delta\mathbf{m}\cdot\mathbf{e}_x\right)\right], \tag{73}$$

where λ and β_x have the same meaning as before. The stability analysis is conveniently carried out by introducing the vector basis $(\mathbf{e}_1, \mathbf{e}_2, \mathbf{m}_0)$, where $\mathbf{m}_0$ is the fixed point under consideration, whereas $(\mathbf{e}_1, \mathbf{e}_2)$ identify the plane perpendicular to $\mathbf{m}_0$. Indeed, the perturbation lies in the plane $(\mathbf{e}_1, \mathbf{e}_2)$ by construction:

$$\delta\mathbf{m} = \delta m_1\,\mathbf{e}_1 + \delta m_2\,\mathbf{e}_2\,. \tag{74}$$

Accordingly, Eq. (73) can be reduced to a two-dimensional equation in this plane:

$$\frac{d}{d\,t}\begin{pmatrix}\delta m_1\\ \delta m_2\end{pmatrix} = A_0\begin{pmatrix}\delta m_1\\ \delta m_2\end{pmatrix}, \tag{75}$$

where the matrix A_0 controls the stability of the fixed point. In particular, the equation $\mathrm{tr}A_0 = 0$ will describe Hopf bifurcations provided that the fixed point considered is not a saddle. After some algebra one finds:

$$\mathrm{tr}A_0 = -\frac{2\alpha}{1+\alpha^2}\left[\lambda + \frac{D_p}{2} - \frac{\beta}{\alpha}\,\frac{1}{1+c_p\,m_{0x}}\left(m_{0x} + \frac{c_p}{2}\,\frac{1-m_{0x}^2}{1+c_p\,m_{0x}}\right)\right], \tag{76}$$

where:

$$D_p = D_x\left(1-m_{0x}^2\right) + D_y\left(1-m_{0y}^2\right) + D_z\left(1-m_{0z}^2\right)\,. \tag{77}$$

These results permit one to determine the Hopf bifurcation conditions for all the nonsaddle fixed-point solutions previously obtained.

– Fixed points $m_{0x} = \pm 1$, $m_{0y} = m_{0z} = 0$.
  For these fixed points, $\lambda = -D_x \pm h_{ax}$ and $D_p = D_z + D_y$. By using these relations in Eqs (76) and (77), one obtains the following bifurcation conditions.
  - $m_{0x} = 1$

This fixed point may undergo a Hopf bifurcation only for $h_{ax} \leq -(D_z - D_x)$ or $h_{ax} \geq -\left(D_y - D_x\right)$. The fixed point is a saddle of the dynamics when $-(D_z - D_x) \leq h_{ax} \leq -\left(D_y - D_x\right)$. The Hopf bifurcation occurs for:

$$\frac{\beta}{\alpha} = \left(1 + c_p\right)\left[h_{ax} + \left(\frac{D_z + D_y}{2} - D_x\right)\right]. \tag{78}$$

- $m_{0x} = -1$
  This fixed point may undergo a Hopf bifurcation only for $h_{ax} \leq D_y - D_x$ or $h_{ax} \geq D_z - D_x$. The fixed point is a saddle of the dynamics when $D_y - D_x \leq h_{ax} \leq D_z - D_x$. The Hopf bifurcation occurs for::

$$\frac{\beta}{\alpha} = \left(1 - c_p\right)\left[h_{ax} - \left(\frac{D_z + D_y}{2} - D_x\right)\right]. \tag{79}$$

– Fixed points which coincide with g_L maxima when $\beta = 0$.
  For these fixed points one has that, to the first order in β: $m_{0x} = -h_{ax}/(D_z - D_x)$, $m_{0y} = 0$, $\lambda = -D_z$, $D_p = D_x + D_y + (D_z - D_x)\, m_{0x}^2$. The corresponding bifurcation line is:

$$\frac{\beta}{\alpha} = -\frac{\left[\left(D_z - D_y\right) + \left(D_z - D_x\right)\left(1 - m_{0x}^2\right)\right]\left(1 + c_p\, m_{0x}\right)^2}{2m_{0x} + c_p\left(1 + m_{0x}^2\right)}, \quad m_{0x} = -\frac{h_{ax}}{D_z - D_x}. \tag{80}$$

Acknowledgements

The ideas presented in this paper are the result of close joint effort by Claudio Serpico, Issak D. Mayergoyz, and the author. The author wishes to thank also Roberto Bonin and Massimiliano d'Aquino, who contributed to significant parts of the technical analysis.

References

Albert, F. J., Emley, N. C., Myers, E. B., Ralph, D. C., and Buhrman, R. A. (2002) Quantitative Study of magnetization reversal by spin-polarized current in magnetic multilayer nanopillars, *Phys. Rev. Lett.* **89**, 226802.

Albert, F. J., Katine, J. A., Buhrman, R. A., and Ralph, D. C. (2000) Spin-polarized current switching of a Co thin film nanomagnet, *Appl. Phys. Lett.* **77**, 3809–3811.

Apalkov, D. M. and Visscher, P. B. (2005a) Slonczewski spin-torque as negative damping: Fokker-Planck computation of energy distribution, *J. Magn. Magn. Mater.* **286**, 370–374.

Apalkov, D. M. and Visscher, P. B. (2005b) Spin-torque switching: Fokker-Planck rate calculation, *Phys. Rev. B* **72**, 180405(R).

Bazaliy, Y. B., Jones, B. A., and Zhang, S. C. (1998) Modification of the Landau-Lifshitz equation in the presence of a spin-polarized current in colossal- and giant-magnetoresistive materials, *Phys. Rev. B* **57**, R3213–R3216.

Bazaliy, Y. B., Jones, B. A., and Zhang, S. C. (2004) Current-induced magnetization switching in small domains of different anisotropies, *Phys. Rev. B* **69**, 094421.

Berger, L. (1996) Emission of spin waves by a magnetic multilayer traversed by a current, *Phys. Rev. B* **54**, 9353–9358.

Berkov, D. and Gorn, N. (2005) Transition from the macrospin to chaotic behavior by a spin-torque driven magnetization precession of a square nanoelement, *Phys. Rev. B* **71**, 052403.

Berkov, D. and Gorn, N. (2006) Micromagnetic simulations of the magnetization precession induced by a spin-polarized current in a point-contact geometry, *J. Appl. Phys.* **99**, 08Q701.

Bertotti, G., Mayergoyz, I. D., and Serpico, C. (2004a) Analytical solutions of Landau-Lifshitz equation for precessional dynamics, *Physica B* **343**, 325–330.

Bertotti, G., Mayergoyz, I. D., and Serpico, C. (2004b) Averaging technique for the analysis of magnetization relaxations, *J. Appl. Phys.* **95**, 6598–6600.

Bertotti, G., Mayergoyz, I. D., and Serpico, C. (2006a) Analysis of random Landau-Lifshitz dynamics by using stochastic processes on graphs, *J. Appl. Phys.* **99**, 08F301.

Bertotti, G., Mayergoyz, I. D., and Serpico, C. (2006b) Nonlinear magnetization dynamics. Switching and relaxation phenomena, In: G. Bertotti and I. D. Mayergoyz (eds), *The Science of Hysteresis. Volume II: Physical Modeling, Micromagnetics, and Magnetization Dynamics*, Oxford, Elsevier, pp. 435–566.

Bertotti, G., Serpico, C., Mayergoyz, I. D., Magni, A., d'Aquino, M., and Bonin, R. (2005) Magnetization switching and microwave oscillations in nanomagnets driven by spin-polarized currents, *Phys. Rev. Lett.* **94**, 127206.

Brown, W. F. (1963) Thermal fluctuations of a single-domain particle, *Phys. Rev.* **130**, 1677–1686.

Fabian, A., Terrier, C., Serrano-Guisan, S., Hoffer, X., Dubey, M., Gravier, L., and Ansermet, J. P. (2003) Current-induced two-level fluctuations in pseudo-spin-valve (Co/Cu/Co) nanostructures, *Phys. Rev. Lett.* **91**, 257209.

Gardiner, C. W. (1985) *Handbook of Stochastic Methods*, Berlin, Springer-Verlag.

Grollier, J., Cros, V., Hamzic, A., George, J. M., Jaffres, H., Fert, A., Faini, G., Youssef, J. B., and le Gall, H. (2001) Spin-polarized current induced switching in Co/Cu/Co pillars, *Appl. Phys. Lett.* **78**, 3663–3665.

Hoefer, M. A., Ablowitz, M. J., Ilan, B., Pufall, M. R., and Silva, T. J. (2005) Theory of magnetodynamics induced by spin torque in perpendicularly magnetized thin films, *Phys. Rev. Lett.* **95**, 267206.

Hubbard, J. H. and West, B. H. (1995) *Differential Equations: A Dynamical Systems Approach*, New York, Springer-Verlag.

Kaka, S., Pufall, M. R., Rippard, W. H., Silva, T. J., Russek, S. E., and Katine, J. A. (2005) Mutual phase-locking of microwave spin torque nano-oscillators, *Nature* **437**, 389–392.

Katine, J. A., Albert, F. J., Buhrman, R. A., Myers, E. B., and Ralph, D. C. (2000) Current-driven magnetization reversal and spin-wave excitations in Co/Cu/Co pillars, *Phys. Rev. Lett.* **84**, 3149–3152.

Kiselev, S. I., Sankey, J. C., Krivorotov, I. N., Emley, N. C., Rinkoski, M., Perez, C., Buhrman, R. A., and Ralph, D. C. (2004) Current-induced nanomagnet dynamics for magnetic fields perpendicular to the sample plane, *Phys. Rev. Lett.* **93**, 036601.

Kiselev, S. I., Sankey, J. C., Krivorotov, I. N., Emley, N. C., Schoelkopf, R. J., Buhrman, R. A., and Ralph, D. C. (2003) Microwave oscillations of a nanomagnet driven by a spin-polarized current, *Nature* **425**, 380–383.

Krivorotov, I. N., Emley, N. C., Garcia, A. G. F., Sankey, J. C., Kiselev, S. I., Ralph, D. C., and Buhrman, R. A. (2004) Temperature dependence of spin-transfer-induced switching of nanomagnets, *Phys. Rev. Lett.* **93**, 166603.

Krivorotov, I. N., Emley, N. C., Sankey, J. C., Kiselev, S. I., Ralph, D. C., and Buhrman, R. A. (2005) Time-domain measurements of nanomagnet dynamics driven by spin-transfer torques, *Science* **307**, 228–231.

Kubo, R. and Hashitsume, N. (1970), *Progr. Theor. Phys. Suppl.* **46**, 210.

Kuznetsov, Y. A. (1995) *Elements of Applied Bifurcation Theory*, New York, Springer-Verlag.

Li, Z., He, J., and Zhang, S. (2005) Stability of precessional states induced by spin-current, *Phys. Rev. B* **72**, 212411.

Li, Z. and Zhang, S. (2003) Magnetization dynamics with a spin-transfer torque, *Phys. Rev. B* **68**, 024404.

Li, Z. and Zhang, S. (2004) Thermally assisted magnetization reversal in the presence of a spin-transfer torque, *Phys. Rev. B* **69**, 134416.

Mancoff, F. B., Rizzo, N. D., Engel, B. N., and Tehrani, S. (2005) Phase-locking in double-point-contact spin-transfer devices, *Nature* **437**, 393–395.

Mangin, S., Ravelosona, D., Katine, J. A., Carey, M. J., Terris, B. D., and Fullerton, E. E. (2006) Current-induced magnetization reversal in nanopillars with perpendicular anisotropy, *Nature Mater.* **5**, 210–215.

Miltat, J., Albuquerque, G., Thiaville, A., and Vouille, C. (2001) Spin transfer into an inhomogeneous magnetization distribution, *J. Appl. Phys.* **89**, 6982–6984.

Myers, E. B., Albert, F. J., Sankey, J. C., Bonet, E., Buhrman, R. A., and Ralph, D. C. (2002) Thermally activated magnetic reversal induced by a spin-polarized current, *Phys. Rev. Lett.* **89**, 196801.

Myers, E. B., Ralph, D. C., Katine, J. A., Louie, R. N., and Buhrman, R. A. (1999) Current-induced switching of domains in magnetic multilayers devices, *Science* **285**, 867–870.

Perko, L. (1996) *Differential Equations and Dynamical Systems*, New York, Springer-Verlag.

Rippard, W. H., Pufall, M. R., Kaka, S., Russek, S. E., and Silva, T. J. (2004) Direct-current induced dynamics in CoFe/NiFe point contacts, *Phys. Rev. Lett.* **92**, 027201.

Serpico, C., Bertotti, G., Mayergoyz, I. D., d'Aquino, M., and Bonin, R. (2006) Thermal stability in spin-torque-driven magnetization dynamics, *J. Appl. Phys.* **99**, 08G505.

Slonczewski, J. C. (1996) Current-driven excitation of magnetic multilayers, *J. Magn. Magn. Mater.* **159**, L1–L7.

Slonczewski, J. C. (1999) Excitation of spin waves by an electric current, *J. Magn. Magn. Mater.* **195**, L261–L268.

Slonczewski, J. C. (2002) Currents and torques in metallic magnetic multilayers, *J. Magn. Magn. Mater.* **247**, 324–338.

Stiles, M. D. and Zangwill, A. (2002) Anatomy of spin-transfer torque, *Phys. Rev. B* **66**, 014407.

Sun, J. Z. (2000) Spin-current interaction with a monodomain magnetic body: a model study, *Phys. Rev. B* **62**, 570–578.

Tsoi, M., Jansen, A. G. M., and Bass, J. (1997) Search for point-contact giant magnetoresistance in Co-Cu multilayers, *J. Appl. Phys.* **81**, 5530–5532.

Tsoi, M., Jansen, A. G. M., Bass, J., Chiang, W. C., Seck, M., Tsoi, V., and Wyder, P. (1998) Excitation of a magnetic multilayer by an electric current, *Phys. Rev. Lett.* **80**, 4281–4284.

Tsoi, M., Jansen, A. G. M., Bass, J., Chiang, W. C., Tsoi, V., and Wyder, P. (2000) Generation and detection of phase-coherent current-driven magnons in magnetic multilayers, *Nature* **406**, 46–48.

Urazhdin, S., Birge, N. O., Pratt, W. P., and Bass, J. (2003) Current-driven magnetic excitations in permalloy-based multilayer nanopillars, *Phys. Rev. Lett.* **91**, 146803.

Visscher, P. B. and Apalkov, D. M. (2006) Non-Boltzmann energy distributions in spin-torque devices, *J. Appl. Phys.* **99**, 08G513.

Zhang, S., Levy, P. M., and Fert, A. (2002) Mechanisms of spin-polarized current-driven magnetization switching, *Phys. Rev. Lett.* **88**, 236601.

MICROMAGNETIC MODELING OF MAGNETIZATION DYNAMICS DRIVEN BY SPIN-POLARIZED CURRENT: BASICS OF NUMERICAL MODELING, ANALYSIS OF CONFINED SYSTEMS

GIOVANNI FINOCCHIO, BRUNO AZZERBONI
Dipartimento di Fisica della Materia e Tecnologie Fisiche Avanzate.
Faculty of Engineering, University of Messina.
Salita Sperone 31, 98166, Messina, Italy

LUIS TORRES
University of Salamanca, Departamento de Fisica Aplicada,
Plaza de la Merced, 37008 Salamanca, Spain

Abstract. In this chapter will be presented the numerical details necessary to model the magnetization dynamics driven by a spin-polarized current (SPC) of a ferromagnet in a confined system, spin valves, or magnetic tunnel junctions (MTJs).

Keywords: Magnetic tunnel junctions; magnetization dynamics; spin torque; spin valves

1. Introduction

A sufficiently large spin-polarized current (SPC) can apply a torque to a nanoscale ferromagnet that is able to invert the magnetization of the ferromagnet or excite persistent magnetic dynamics.[1,2] These behaviors have been experimentally observed in both spin valves (SVs)[3] and magnetic tunnel junctions (MTJs).[4] These devices are composed of two ferromagnetic layers separated by a normal metal or thin insulator, respectively. One of the ferromagnetic layers (pinned or fixed layer, PL) is either thicker than the other (free layer, FL) or exchanged biased with an antiferromagnetic material.[5,6] The resistance of the device depends on the relative orientation of the magnetization of the ferromagnets; there is a low resistance state when the magnetization of the two layers are aligned (parallel state, PS) and a high resistance state when they are anti-aligned (antiparallel state, APS). This property is a key point in the design of magnetoresistive random access memory (MRAM). A main application of a SPC is the possibility to use it as a mechanism for MRAM, in particular; from the technological point of view, the MTJs show promise as high-performance MRAM with respect to the SVs.

B. Azzerboni et al. (eds.), Magnetic Nanostructures in Modern Technology, 61–67.

While the SPC necessary to invert the APS to PS and *vice versa* for the MTJs is comparable with that of SVs, there is a more restrictive physical limit on the maximum value of applied current due to the breakdown voltage of the barrier.[4]

From the theoretical point of view, both macrospin[7,8] and a full micromagnetic model[12–14] can be used to explain the results of experiments related to the magnetization dynamics driven by a SPC in a ferromagnet. Although macrospin models are useful to understand the general trends of the behavior of these devices (either numerically or analytically),[7,8] in some experimental works, multiple domain configurations and domain wall motion are invoked as the underlying cause of the observed magnetization dynamics.[3,4] In this case, a micromagnetic approach is necessary to obtain spatial information about the magnetization configuration and a deeper understanding of the magnetization processes. In this chapter will be presented the numerical details of micromagnetic modeling of the magnetization dynamics driven by a SPC in MTJs and SVs considering a zero temperature model first, then a brief description about the inclusion of the thermal effect will be discussed.

The methodology which will be treated in this chapter has been applied to several systems.[9] Furthermore, some "state-of-the-art" examples can be found in other two chapters of this book (M. Carpentieri et al., G. Consolo et al.). The first one deals mainly with the effect of nonuniform contributions to the effective field in dynamical magnetization processes while the second one focuses on the modeling of nonconfined point-contact systems.

2. Numerical Modeling

The magnetization dynamics of a FL can be described by the Landau-Lifshitz-Gilbert (LLG) equation which includes the term for the spin-transfer torque deduced by Slonczewski. In general, it is possible to solve this nonlinear equation numerically only, this implies to change the continuous problem where the magnetization is a vector field $\mathbf{M}(\mathbf{r}, t)$ to a discrete problem in both space and time. From numerical point of view, it is possible to use either finite elements or finite differences (FD) approach; here we will present the numerical details of the FD. The FL is discretized considering cubic (or prismatic) cells (an example of discretization of a rectangular FL is shown in Fig. 1), the size has to ensure enough precision in the solution according to the standard criterion in micromagnetics which consist of using cell sizes smaller than the exchange length of the material of the FL (e.g. 6 nm for Py, 4 nm for Co) and big enough in order to define the magnetization (1–1.5 nm).

In our analysis, we also consider the following hypotheses: the current density is spatially uniform, no RKKY coupling between ferromagnets is taken into account, the magnetization configuration of the PL is spatial uniform and constant, the physical parameters (damping, saturation magnetization, polarization)

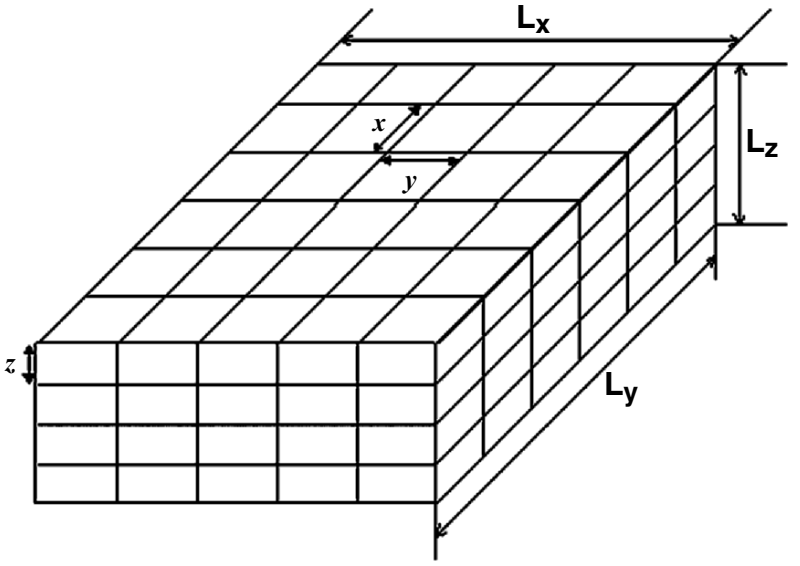

Figure 1. Example of discretization of a rectangular shape considering cubic cells

are uniform and constant, concerning the MTJ, there are no pinholes in the isolator, and the boundaries between the isolator and the ferromagnets are flat in order that the Orange-Peel coupling is negligible. The numerical LLG-Slonczewski (LLGS) equation has to be solved for each cell, its expression is reported in the following:

$$\frac{d\mathbf{M}(i,j,k)}{dt} = -\gamma_0\,\mathbf{M}(i,j,k)\times\mathbf{H}_{eff}(i,j,k) + \frac{\alpha}{M_s}\left(\mathbf{M}(i,j,k)\times\frac{d\mathbf{M}(i,j,k)}{dt}\right) - \frac{g\mu_B J}{L_z\,|\mathrm{e}|\;M_s^3}\,g(\mathbf{M}(i,j,k)\cdot\mathbf{P},\eta)\mathbf{M}(i,j,k)\times(\mathbf{M}(i,j,k)\times\mathbf{P}) \tag{1}$$

where $(i,\ j,\ k)$ are the indexes of the cell considering x, y, and z axes respectively, g is the gyromagnetic splitting factor, γ_0 is the gyromagnetic ratio, μ_B is the Bohr's magneton, α is the damping parameter, J is the applied current density (here we consider positive when flows are from the PL to the FL), $g(\mathbf{M}(i,j,k)\cdot\mathbf{P},\eta)$ is the polarization function, η is the polarization, L_z is the thickness of the FL, e is the electron charge, $\mathbf{M}$ is the magnetization of the FL, $\mathbf{P}$ is the magnetization of the PL, M_S is the saturation magnetization of the FL, and $\mathbf{H}_{eff}$ is the effective field. The effective field ($\mathbf{H}_{eff} = \mathbf{H}_{ext} + \mathbf{H}_{exch} + \mathbf{H}_M + \mathbf{H}_{ani} + \mathbf{H}_{AF} + \mathbf{H}_{Amp}$) is the sum of the four standard micromagnetic contributions for the external, exchange, magnetostatic, and magneto-crystalline anisotropy fields; furthermore, it includes the magnetostatic

coupling between PL and FL and the Ampere field due to the current. These two last contributions play a crucial role in the magnetization dynamics, but being not uniform, they can not be taken into account in a macrospin model correctly.[9]

The magnetostatic coupling is computed solving the 3D magnetostatic problem for the whole nanostructure before starting the simulations, its value is constant and added to the effective field of each cell.[10] The Ampere field is computed by adequate numerical techniques developed to evaluate solenoidal fields.[9] The numerical expression of the effective field (considering uniaxial magneto-crystalline anisotropy and cubic computational cell[11]) is the following:

$$\begin{aligned} \boldsymbol{H}_{eff}(i,j,k) = & \frac{2A}{\Delta^2 \mu_0 M_s} \sum_{(i',j',k')=1}^{6} \boldsymbol{m}\left(i',j',k'\right) + \frac{2K}{M_s \mu_0} \left(\boldsymbol{m}(i,j,k) \cdot \boldsymbol{u}_i\right) \boldsymbol{u}_i \\ & + \boldsymbol{H}_M(i,j,k) + \boldsymbol{H}_{ext}(i,j,k) + \boldsymbol{H}_{AF}(i,j,k) + \boldsymbol{H}_{Amp}(i,j,k) \end{aligned} \tag{2}$$

where Δ is the side of the computational cell, A is the exchange constant, $\boldsymbol{m}$ is the normalized magnetization of the FL, K, and $\boldsymbol{u}_i$ are the constant and the unit vector of the easy axis of magneto-crystalline anisotropy. The first term is the exchange field, its value is related to the magnetization of the six nearest neighbor cells, the magnetostatic coupling is a nonlocal term and it depends on the magnetization configuration of the whole layer, lastly the Ampere field depends on the current and the shape of the layer.

The expression of the polarization function, for the SVs, was computed for the first time by Slonczewski in 1996[1] considering just the ballistic contribution to the torque due to a SPC and the macrospin approximation $\left(g_1(\mathbf{M},\mathbf{P}) = \left[-4+(1+\eta)^3\left(3+\mathbf{M}\cdot\mathbf{P}/M_S^2\right)/4\eta^{3/2}\right]^{-1}\right)$. In 2002, the expression was computed considering the two-channel diffusive transport model for symmetric systems[1] $\left(g_2(\mathbf{M},\mathbf{P}) = \left(1-\cos^2(\theta/2)\right)/\left(1+\chi\cos^2(\theta/2)\right)\right)$, where $\cos(\theta) = \mathbf{M}\cdot\mathbf{P}/{M_S}^2$. This expression was generalized for asymmetric structures by Xiao et al.[12] $\left(g_3(\mathbf{M},\mathbf{P}) = \frac{q_+/2}{A+B\mathbf{M}\cdot\mathbf{P}/M_S^2} + \frac{q_-/2}{A-B\mathbf{M}\cdot\mathbf{P}/M_S^2}\right)$ (the parameters of $g_2(\mathbf{M},\mathbf{P})$ and $g_3(\mathbf{M},\mathbf{P})$ are related to the resistances of the layers of the structure). In 2005, a polarization function for the MTJs has been also computed, it is $g_T(\mathbf{M},\mathbf{P}) = 0.5\,\eta_T\left(1+{\eta_T}^2\mathbf{M}\cdot\mathbf{P}/{M_S}^2\right)^{-1}$ where η_T depends on the applied voltage. Differently by the macrospin, the polarization function in micromagnetics has to be computed in each computational cells ($g(\mathbf{M}(i,j,k),\mathbf{P})$). In a different way, it is possible to identify numerically the polarization function by fitting the experimental data.

One more interesting aspect of the micromagnetic is the possibility to perform a study of the effect of the nonidealities of the shape of a sample with respect to an ideal case. For example, Fig. 2 (bottom) shows an example of a nonideal shape computed directly by a SEM image, Fig. 2 (top) shows the shape

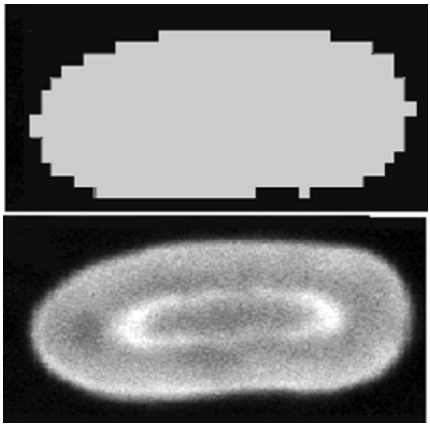

Figure 2. (*bottom*) An example of a nonideal shape computed directly by a SEM image, (*top*) the same shape discretized

discretized. A systematic study performed to determine the effect of the nonidealities of the shape of the magnetization reversal reveals that the mechanism of inversion changes qualitatively depending on the shape. These nonidealities can either increase or decrease the switching time.[14]

3. Modeling of the Thermal Effect

In order to take into account the effect of the temperature, we consider that the experimental data are well described by current dependent activation barriers that agrees with prediction of the LLG-based models.[15,16] We include in our micromagnetic simulations a thermal field as an additive random field to the deterministic effective field for each cell, which leads to a definition of the stochastic Langevin-Landau-Lifshitz-Gilbert (LLLG) equation.[17] In order to take into account the SPC terms in this formulation, we assume that the spin torque does not contain a fluctuating field, the fluctuating field is independent of the spin torque, and the magnetization configuration of the PL does not depend on the temperature. The thermal field, $\mathbf{H}_{th}$, is a random fluctuating 3D vector quantity given by:

$$\mathbf{H}_{th} = \xi \sqrt{2 \frac{\alpha K_B T_S}{\mu_0 \gamma_0 \, \Delta V \, M_s \, \Delta t}} \tag{3}$$

where K_B is the Boltzmann constant, $\Delta V$is the volume of the computational cubic cell, Δt is the simulation time step, T_S is the true temperature of the sample,[16,18] and ξ is a Gaussian stochastic process. The thermal field $\mathbf{H}_{th}$ satisfies the following statistical properties:

$$\begin{cases} \langle \mathbf{H}_{th,k}(t) \rangle = 0 \\ \langle \mathbf{H}_{th,k}(t), \mathbf{H}_{th,l}(t') \rangle = D\delta_{kl} \quad \delta(t - t') \end{cases} \tag{4}$$

where k and l represent the Cartesian coordinates x, y, z. According to this expression, each component of $\mathbf{H}_{th} = (\mathbf{H}_{th,x}, \mathbf{H}_{th,y}, \mathbf{H}_{th,z})$ is a space and time independent random Gaussian distributed number (Wiener process) with zero mean value. The constant D measures the strength of thermal fluctuations and its value is obtained from the Fokker-Planck equation.[17] A second order Heun scheme is used to solve numerically the LLLG equation so that the solution converges to the Stratonovich interpretation directly.[17]

An important point is to use the right temperature for the simulations: the temperature of the sample. It is related to the bath temperature, for the SVs all the details are reported in Ref. 16. In the case of a MTJ an interesting results is reported by Fuchs et al.,[19] where it is shown that the relationship between the temperature of the sample and of the bath is a simple expression:

$$T_S = \sqrt{T_B^2 + \beta I^2} \tag{5}$$

where the T_B is the bath temperature, I is the current, and β is a parameter which depends on the experimental data.

Acknowledgements

The authors are grateful to M. Carpentieri, G. Consolo, L. Lopez-Diaz, E. Martinez, J. Sankey, G. Fuchs, I. Krivorotov, and O. Ozatay, for the helpful discussions.

References

1. J. Slonczewski, *J. Magn.Magn. Mater.* **159**, L1 (1996); *J. Magn. Magn. Mat.* **195**, L261 (1999); *J. Magn. Magn. Mater.* **247**, 324 (2002).
2. L. Berger, *Phys. Rev. B* **54**, 9353 (1996).
3. J.A. Katine, F.J. Albert, R.A. Buhrman, E.B. Myers, and D.C. Ralph, *Phys. Rev. Lett.* **84**, 3149 (2000); J. Grollier, V. Cros, H. Jaffres, A. Hamzic, J.M. George, G. Faini, J.B. Youssef, H. Le Gall, and A. Fert, *Phys. Rev. B* **67**, 174402 (2003); M. AlHajDarwish et al., *Phys. Rev. Lett.* **93**, 157203 (2004). S.I. Kiselev, J.C. Sankey, I.N. Krivorotov, N.C. Emley, R.J. Schoelkopf, R.A. Buhrman, and D.C. Ralph, *Nature* **425**, 380 (2003). I. Krivorotov et al., *Science* **307**, 228–231 (2005). T. Devolder et al., *App. Phys. Lett.*, **86**, 062505 (2005).
4. G.D. Fuchs, N.C. Emley, I.N. Krivorotov, P.M. Braganca, E.M. Ryan, S.I. Kiselev, J.C. Sankey, D.C. Ralph, R.A. Burman, and J.A. Katine, *Appl. Phys. Lett.* **85**, 1205 (2004); J.S. Moodera and G. Mathon, *J. Magn. Magn. Mater.* **200**, 248 (1999); Z. Diao, D. Apalkov, M. Pakala, Y. Ding,

A. Panchula, Y. Huai, *Appl. Phys. Lett.* **87**, 232502 (2005). J. Vogel, W. Kuch, R. Hertel, J. Camarero, K. Fukumoto, F. Romanens, S. Pizzini, M. Bonfim, F. Petroff, A. Fontaine, and J. Kirschner, *Phys. Rev. B* **72**, 220402(R) (2005).

5. A.A. Tulapurkar, et al., *Nature* **438**, 339 (2005).
6. G.D. Fuchs, J.A. Katine, S.I. Kiselev, D. Mauri, K.S. Wooley, D.C. Ralph, and R.A. Buhrman, *Phys. Rev. Lett.*, 96, 186603 (2006).
7. J. Z. Sun, *Phys. Rev. B* **62** 570 (2000).
8. G. Bertotti et al., *Phys. Rev. Lett.* **94**, 127206 (2005).
9. L. Torres, L. Lopez-Diaz, E. Martinez, M. Carpentieri, and G. Finocchio, *J. Magn. Magn. Mater.* **286**, 381 (2005). M. Carpentieri et al., *J. Appl. Phys.* **97**, 10C713 (2005). E. Martinez, et al., *J. Appl. Phys.* **97**, 10E302 (2005).
10. It is possible to consider the magnetization of the PL no constant and no uniform in this case it is necessary to simulate the whole structure. The solution of the magnetostatic problem includes also the magnetostatic coupling between the ferromagnets.
11. If the computational cells are not cubic, the exchange field has to be computed introducing scale factors which depend on the shape of the cell itself.
12. J. Xiao, A. Zangwill, M.D. Stiles, *Phys. Rev. B* **70** 172405 (2004).
13. J. Slonczewski, *Phys. Rew. B*, **71**, 024411 (2005).
14. G. Finocchio, et al., J. Appl. Phys. 101, 063914 (2007).
15. Y. Zhang, Z. Zhang, Y. Liu, B. Ma, and Q. Y. Jin, J. *Appl. Phys.* 99, 08G515 (2006).
16. I. N. Krivorotov et al., *Phys. Rev. Lett.* **93**, 166603 (2004).
17. J. L. Garcia-Palacios and F. J. Lazaro, *Phys. Rev. B* **58**, 14937 (1996).
18. Z. Li and S. Zhang, *Phys. Rev. B* **69**, 134416 (2004).
19. G.D. Fuchs, I.N. Krivorotov, P.M. Braganca, N.C. Emley, A.G.F. Garcia, D.C. Ralph, and R.A. Buhrman, *Appl. Phys. Lett.* **86**, 152509 (2005).

MICROMAGNETIC MODELING OF MAGNETIZATION DYNAMICS DRIVEN BY SPIN-POLARIZED CURRENT: ANALYSIS OF NONCONFINED SYSTEMS

GIANCARLO CONSOLO, BRUNO AZZERBONI
Dipartimento di Fisica della Materia e Tecnologie Fisiche Avanzate, Faculty of Engineering, University of Messina, 98166 Vill.S.Agata, Messina, Italy

LUIS LOPEZ-DIAZ, LUIS TORRES
University of Salamanca, Departamento de Fisica Aplicada, Plaza de la Merced, 37008 Salamanca, Spain

Abstract. We present a brief overview of the magnetization dynamics driven by a spin-polarized current in nonconfined ferromagnetic multilayers when a point-contact setup is used. The possibility to sustain persistent oscillations in these systems could be employed in the design of current-controlled microwave oscillators on nanometric scale. The attempt to reproduce the main experimental results by means of both macrospin and micromagnetic models encounters many difficulties. We have focused on the latter, summarizing the state-of-art and pointing out the still unsolved methodological problems arising from such a modeling.

Keywords: Micromagnetic modeling; point contact; spin-transfer effects; absorbing boundary conditions

1. Introduction on nonconfined systems

It has been proved both experimentally[1,6,9,10] and theoretically[2–5,7] that the spin-transfer torque exerted by a spin polarized current (SPC) on the magnetic moment of a ferromagnet can produce persistent magnetization dynamics in the ferromagnet, which could be used for developing technological applications, such as oscillators and resonators.[8] Different geometries and materials have been proposed to explore this effect. In this report we will focus on the "point contact" system where, differently from a classical nanopillar structure (see the previous chapters by G. Finocchio et al. and M. Carpentieri et al. of this book), the current flows only through a confined region at the center of the structure, whereas the lateral size of the device is about two orders of magnitude larger. Such systems could be used in current-controlled oscillators at RF frequency with very narrow linewidths (more than five times than in pillar devices). In addition, the large distance between the excited area and the boundaries (about 10 μm or

B. Azzerboni et al. (eds.), Magnetic Nanostructures in Modern Technology, 69–75.

more) strongly reduces the influence of edge defects and also yields less artifacts, no magnetostatic anisotropies, less current-induced instabilities, and noise. Furthermore, these high symmetric geometries are quite simple to fabricate, suitable for making coupled arrays, and also present high contact resistances.[4]

Regarding the direction of the applied field with respect to the device plane, different possibilities have been investigated so far.[1–6,9,10] These studies have shown that the applied field orientation substantially affects the most relevant spin waves properties, e.g. propagating character, frequency, magnetization trajectory, and current dependence.

The relevance of these effects was first detected experimentally[1] and later on justified analytically by means of a single-domain approach[2] and a subsequent nonlinear correction.[3] In particular, the results presented by Tsoi et al.[1] show that, when the applied field direction is perpendicular to the plane, (i) the excitation of standing spin-waves in the thinner layer is symmetric with respect to the field but asymmetric in current (excitation occurs when electrons flow from the free layer into the fixed layer only); (ii) there exists a critical current below which the emission of spin waves is not possible, and (iii) the excitation frequency exhibits a linear blue-shift when the applied field is increased, a behavior later confirmed in another experimental work.[6]

In the first theoretical work,[2] the possibility of exciting spin-waves was confirmed and an analytical expression for the threshold current was derived. The latter consisted of two terms: the classical local viscous spin precession damping inside the contact area and a radiative loss due to the spin waves propagation outside the contact. Although the slope of the current vs field was validated experimentally in the out-of-plane configuration, the initial current value was in disagreement with the experiments made by both Tsoi et al.[1] and Rippard et al.[6] In those cases, the experimental value was roughly ten times lower than the predicted one. The nonlinear approach presented by Slavin[3] solved this problem for the in-plane case, considering nonpropagating evanescent waves as a solution for this geometry. As first pointed out by Slonczewski,[2] this theory could also explain the disagreement between the analytical prediction and the experimental results presented by Tsoi et al.[1] In fact, the contact tip used in that experimental setup could be the main responsible for damages induced in the free-layer. In this case, the damages act as barriers for the spin-waves propagation and, consequently, the contribution due to the spin waves radiation outside the contact is absent, thus reducing the initial current value. However, the solution proposed by Slavin suggests the necessity of nonlinear corrections in some parameters of the Landau-Lifshitz-Gilbert-Slonczewski (LLGS) equation, such as the introduction of a nonlinear phenomenological dissipation.[3]

Nevertheless, because such systems are characterized by a large number of degrees of freedom, most understanding of their dynamics could be clarified from an accurate micromagnetic model and extensive micromagnetic simulations.[4–6,9]

2. Micromagnetic modeling of point-contact devices

Recent theoretical works based on a macrospin approach[6] showed the impossibility to accurately reproduce some experimental features, such as the abrupt jumps occurring in the spin-waves spectrum when increasing the current density.[6] On the other hand, micromagnetic simulations seem to be a more accurate framework to study some of these features (e.g. nonuniform spin-waves properties) and to explore dynamics occurring at frequencies higher than those experimentally accessible. However, as it has been already presented in literature,[4,5] a micromagnetic approach encounters several difficulties arising from constrains in both memory allocation and computational times, which preclude the possibility to simulate the real sizes of the devices under investigation. These constrains impose a trade-off between computational times and accuracy. Another crucial point is the identification of both geometrical and material parameters required to build up a micromagnetic model. In addition, for the specific "point contact" geometry, some further artificial effects (which will be discussed below) arise from: the relatively low damping (for Permalloy, in the order of $10^{-2} \div 10^{-3}$), the proximity of computational boundaries and the very large dimensions of the structures under investigation. Considering that we are forced to simulate a computational region smaller than the physical one, it is necessary to introduce some sort of *ad hoc* perfect-absorbing boundary conditions to avoid artificial spurious effects, like interferences between the waves traveling towards the computational boundaries and the waves reflected from them. As a consequence, the duration of the persistent excited oscillations is strongly shortened.[4,5] Furthermore, another difficulty originates from the implementation of absorbing boundary conditions without the knowledge of any analytical solution, as it happens in all the numerical techniques used to integrate nonlinear differential equations.[5,12] On the other hand, the solution presented by Berkov[5] should be considered as a partial one because of many artificial assumptions, such as the spatial dependence of the damping constant and the use of periodic boundary conditions.

2.1. THE MODEL

The starting point of our micromagnetic approach is the LLGS equation, whose details are available in the previous chapters by G. Finocchio et al. and M. Carpentieri et al. of this book.

In order to enable a comparison with experimental spectra, we have chosen the system parameters as close as possible to the experimental ones presented by Rippard et al.[6] In particular, the spin-valve structure under investigation is composed by a trilayer $Co_{90}Fe_{10}$ (20 nm)/Cu (5 nm)/$Ni_{80}Fe_{20}$ (5 nm), whose lateral dimensions, for the computational reasons cited above, have been set as 600 nm $\times$ 600 nm, whereas the real dimensions are 8 μm $\times$ 12 μm.[6] The point contact area

is assumed to be circular in shape with a 40 nm diameter. The following saturation magnetization values for the PL and FL have been used: $M_{SPL} = 1.5 \times 10^6$ A/m, $M_{SFL} = 640 \times 10^3$ A/m. Other parameters are: exchange constant $A = 1.3 \times 10^{-11}$ J/m, damping $\alpha = 0.015$, and no crystalline anisotropy for the FL, while a cubic anisotropy constant of $k_{\text{aniPL}} = 5.6 \times 10^4$ J/m^3 for the PL has been considered. The computational region is discretized in a 2D mesh of 4 nm × 4 nm × 5 nm prismatic cells in order to integrate the LLGS numerically.

Our first goal was to reproduce results presented in Fig. 4 of the Ref. 6 where an out-of-plane field $H_{\text{ext}} = 0.9$ T is applied to the system. As predicted by Rippard et al.,[6] it has been checked that this field tilts the magnetization of the PL about 30° out of the film plane. The measurements reported by Rippard et al.[6] were performed at room temperature, but in our simulations we have not considered the random fluctuating field representing thermal noise since its effect is found to be negligible in the case under study. By geometrical considerations, the magnetostatic field arising from the coupling with the PL is assumed to be uniform and due to the out-of-plane component of the PL magnetization only.

Regarding the polarization function $g(\boldsymbol{M}(i, j, k), \boldsymbol{P}, \eta)$, which modulates the strength of the spin-transfer torque, we started from the expression derived by Slonczewski for a macrospin model[7] which, in normalized terms, can be described as follows:

$$g(\mathbf{m}, \mathbf{p}, \eta) = c \cdot u(\mathbf{m}, \mathbf{p}, \eta) = c \cdot \left[-4 + (1+\eta)^3 (3 + \mathbf{m} \cdot \mathbf{p}) / 4\eta^{3/2}\right]^{-1} \quad (1)$$

When considering this expression within a micromagnetic framework one could assume a constant in time and uniform in space value ($g(\mathbf{m},\mathbf{p},\eta) = c, u(\mathbf{m},\mathbf{p},\eta) = 1$) or, alternatively, allow for a time and space variation ($g(\mathbf{m},\mathbf{p},\eta) = u(\mathbf{m},\mathbf{p},\eta)$, $c = 1$).[11] In our model, the efficiency value at time t is the average over the contact area of the efficiencies found evaluating Eq. (1) locally at the previous computational time $t - \Delta t$. According to our simulations, these different interpretations of the efficiency factor lead to slight differences in both the trajectory of the average magnetization and the high harmonics filtering effect.[13]

2.2. BOUNDARY CONDITIONS

The absorbing boundary conditions (ABC) introduced by Berkov et al.[5] were based on three main assumptions: (i) the dissipation within and nearby the contact area must be equal to its physical value; (ii) dissipation far from the contact area and close to the simulated boundaries must be large enough to ensure the wave energy absorption; and (iii) the spatial variation between these two values must be smooth enough to prevent wave reflection at the boundary. Contrarily to this last assumption, we found that the introduction of an abrupt profile in the damping guarantees the expected stable magnetization precession. In particular, leaving

the previous first two assumptions mentioned above unchanged, we base our proposal on the following further requirements: (i) to create a nonphysical absorbing medium surrounding the FD-TD mesh boundaries, (ii) to consider a damping coefficient two orders greater than the physical one just in the boundary cells, and (iii) the computational area must entirely preserve its physical properties.

Another issue involves the choice of the boundary conditions for the exchange field. As reported by Berkov et al.,[5] the use of "periodic" boundary conditions (PBC) does not represent the optimal solutions for three main reasons. First, PBC do not represent physical or geometrical properties. Second, an interference between waves is however present, due to the waves traveling inwards coming from the neighbor periodic images. Third, in an implicit manner, the implementation of PBC is equivalent to the simulation of a matrix of point-contacts. In our approach, NBCs have been implemented in the usual manner:

$$\left.\frac{\partial m}{\partial n}\right|_{\text{boundaries}} = 0 \tag{2}$$

where n is the direction normal to the boundaries.

2.3. RESULTS

Results of simulations using a current $I = 8$ mA and a constant efficiency $g(\mathbf{m}, \mathbf{p}, \eta) = c = 0.21$ are shown in Fig. 1.

As can be observed, a stable magnetization precession is obtained over a temporal window of 30 ns. No disruptive interference between incident and reflected waves has been detected, which instead occurs after 1 ns when no absorbing boundary conditions are considered. Moreover, a sharp peak of about 23 GHz has been found in very good agreement with the experiment. Further smaller peaks at higher frequencies have been detected in our simulations, which are expected

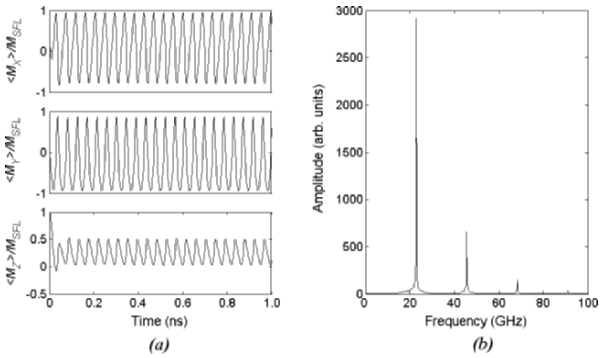

Figure 1. (a) Time-evolution of the normalized magnetization components with a framework including abrupt ABC, (b) the corresponding spectrum of the GMR signal.

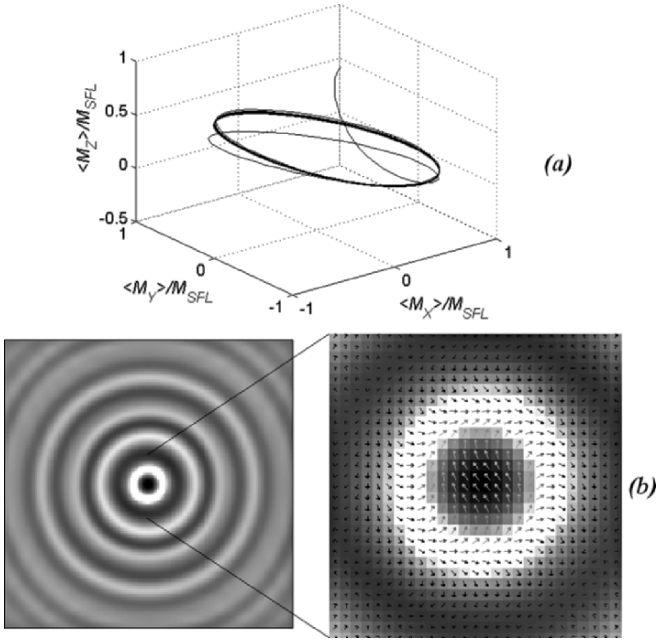

Figure 2. (a) 3D trajectory of the contact-averaged magnetization during the precession; (b) snapshot of the spatial magnetization configuration (the greyscale map is representative of the x-component of the magnetization).

wherever an abrupt change of a physical property is considered.[5,13] In any case, these high frequency peaks were not experimentally accessible, since the oscilloscope bandwidth used by Rippard et al.[6] was 40 GHz, so it is not fully clear whether then harmonics are pure numerical artifacts or not.

The 3D trajectory followed by the average magnetization and a snapshot of the spatial magnetization configuration are shown in Fig. 2. As reported in previous works,[6,10] the magnetization in the FL precesses in a nearly circular orbit around the direction of the external field.

A duality in the relationship frequency *versus* current is observed between the in-plane and perpendicular field orientations. In fact, while a red-shift is characteristic of the former, a blue-shift is typical of the latter.[3,6] For intermediate field orientations,[9] the precessional frequency and device output power show complicated dependencies on current, e.g. abrupt jumps, existence of multiple stable precessional states, etc. Attempts to reproduce these features are still under investigation.

Acknowledgements

The authors are grateful to Prof. Andrei N. Slavin for fruitful discussions.

References

1. M. Tsoi et al., *Phys. Rev. Lett.* 80(19), 4281–4284 (1998).
2. J.C. Slonczewski, *J. Magn. Magn. Mater.* 195, L261–L268 (1999).
3. A. Slavin et al., *Phys. Rev. Lett.* 95, 237201 (2005).
4. S.E. Russek et al., *Proc. of MMM 2005 Conference*.
5. D.V. Berkov et al., *J. Appl. Phys.* 99, 08Q701 (2006).
6. W.H. Rippard et al., *Phys. Rev. Lett.* 92(2), 027201 (2004).
7. J.C. Slonczewski, *J. Magn. Magn. Matert.* 159, L1–L7 (1996).
8. M. Tsoi et al., *Nature* 406, 46–48 (2000); S. Kaka et al., *Nature* 437, 389–392 (2005).
9. W.H. Rippard et al., *Phys. Rev. B* 70, 100406(R) (2004).
10. W.H. Rippard et al., *Phys. Rev. Lett.* 95, 067203 (2005).
11. M. Carpentieri et al., *J. Magn. Magn. Matert.* 316, 488 (2007).
12. B. Engquist and A. Majda, *Math. Comp.* 31, 629–651 (1977); X. Feng, *Math. Comput.* 68(225), 145–168 (1999); J.P. Berenger, *J. Computat. Phys.* 114, 185–200 (1994).
13. G. Consolo L. Torres, L. Lopez-Diaz, and B. Azzerboni, *IEEE Trans. Magn*. 43, 2827 (2007); G. Consolo, L. Lopez-Diaz, L. Torres, and B. Azzerboni, *IEEE Trans. Magn*. 43, 2974 (2007); G. Consolo et al. *Journ. Appl. Phys*. 101, 09C108 (2007); G. Consolo et al., *Phys. Rev. B*, 75, 21 (2007).

MICROMAGNETIC MODELLING OF MAGNETIZATION DYNAMICS DRIVEN BY SPIN-POLARIZED CURRENT: STABILITY DIAGRAMS AND ROLE OF THE NON-STANDARD EFFECTIVE FIELD CONTRIBUTIONS

MARIO CARPENTIERI, BRUNO AZZERBONI
Dipartimento di Fisica della Materia e Tecnologie Fisiche Avanzate, Faculty of Engineering, University of Messina, Salita Sperone 31, 98166 Messina, Italy

LUIS TORRES
Departamento de Fisica Aplicada, University of Salamanca, Plaza de la Merced, 37008 Salamanca, Spain

Abstract. The spin-polarized current can exert a torque on the magnetization and if it is large enough can induce reversal or even excite persistent dynamical regimes. Micromagnetic models can be used to describe the general features of the magnetization dynamics driven by the coexistence of an applied field and a spin-polarized current. In particular, magnetostatic coupling (MC) between ferromagnets and also the classical Ampere field have to be taken into account. A systematic study of the effect of these two contributions will be presented. The main results are that the MC always helps the switching from parallel state (PS) to anti-parallel state (APS) and, more precisely, the application of a current, which gives rise to the switching (PS→APS or vice versa), results in a faster process with MC than without it. Differently, the role of the Ampere field depends on the physical and geometric properties of the system under investigation and it has to be investigated in each case. The simulations reveal a complex switching behaviour that involves highly inhomogeneous magnetization configurations with multiple domains. Lastly, in order to describe the full behaviour of the magnetization dynamics in these multilayer structures, some complete dynamical stability diagrams have been computed.

Keywords: Micromagnetic simulations; spin-polarized current; magnetic switching; precessional states

1. Introduction

The theoretical demonstration by Slonczewski[1,2] that a spin-polarized current (SPC) flowing through a ferromagnetic conductor exerts a torque on its magnetic moment opened new ways for manipulating magnetization dynamics. These experimental results are usually interpreted assuming that each magnetic layer is uniformly magnetized[5–8] although some experimenters claimed that multiple

B. Azzerboni et al. (eds.), Magnetic Nanostructures in Modern Technology, 77–84.

domains and possibly domain wall motion may be involved.[5,8] This point is difficult to verify experimentally in patterned nanostructures, but it can be investigated by means of micromagnetic modelling.[9,10] The SPC is generating interest as an alternative to the use of the magnetic field for switching elements in Magnetic Random Access Memory (MRAM). The interaction between MC and Slonczewski torque produces more symmetric switching processes from PS to APS and vice versa, yielding approximately the same absolute values of critical current as shown by the experimental data.

In this work, we discuss about micromagnetic simulations in multilayer devices; numerical details can be found in the previous chapter by Finocchio et al. Throughout this work, in the case of Permalloy samples no magnetocrystalline anisotropy is included. On the other hand, the anisotropy of thin Cobalt nanostructures is not well known, so we used the anisotropy field obtained by Kiselev et al.[8] fitting the frequency of microwave oscillations in similar nanopillars, yielding an anisotropy constant of $k_u = 1.37\ 10^5$ J/m^3 which is of the order of the anisotropy constants found in literature.[11] Computational cubic cells of 2.5 nm side and time step of 40 fs were used.

2. Influence of the magnetostatic coupling

In this section, we present a micromagnetic study of the MC on the magnetization reversal dynamics of the free layer, pointing out the obtained results about one spin valve where the non-ferromagnetic layer thickness is between 2.5 and 10 nm. The MC was computed by a 3D micromagnetic simulation of the whole structures. The nanostructures under investigation are nanopillars of Permalloy (Py) pinned layer (PL) (10 nm)/Cu (x)/Py free layer (FL) (2.5 nm) with rectangular section of $60 \times 20 \times 2.5$ nm^3 ($x = 2.5$, 5, 7.5, and 10 nm). The PL is exchange-biased with the bottom layer by using a 8 nm thick anti-ferromagnetic layer of $Ir_{20}Mn_{80}$; thus we can consider the magnetization of the fixed layer along the positive x-direction.[12,13] The simulations demonstrate the presence of the MC field influences the behaviour of the dynamics in the nanostructure when a uniform electric current is applied along the z-axis. Furthermore, the same dynamics depends on the distance between the two ferromagnetic layers. Figure 1 (left panel) shows the configuration of the MC field ($\mathbf{H}_{AF}$) between fixed (10 nm) and FL (2.5 nm) for different copper spacers, 2.5, 5, 7.5, and 10 nm, respectively. As can be observed, the $\mathbf{H}_{AF}$ is uniform in the central region and there are inhomogeneities in the lateral regions of the nanorectangle. Obviously, the magnetostatic effect becomes smaller with increasing the distance between the ferromagnetic layers.

Figure 1 (right panel) shows the average of the absolute value of the MC versus the non-metallic spacer to the FL due to a PL of 10 (a), 20 (b), and 40 (c) nm of thickness, respectively. The y and z components of MC have zero mean value, but they play a crucial role in the magnetization dynamics as will be shown by

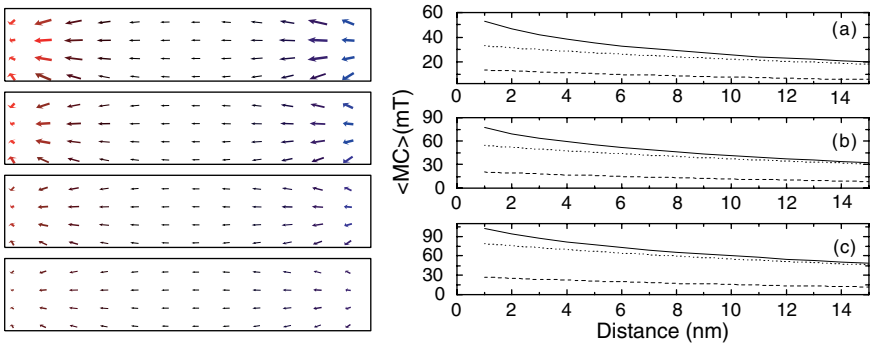

Figure 1. (*Left panel*) Field pattern for antiferromagnetic coupling and for different distances (2.5, 5, 7.5, and 10 nm respectively) between the ferromagnetic FL and PL. (*Right panel*) Average of the absolute value of the MC versus the non-metallic spacer thickness, for three different PL thicknesses, (a) 10 nm, (b) 20 nm, and (c) 40 nm.

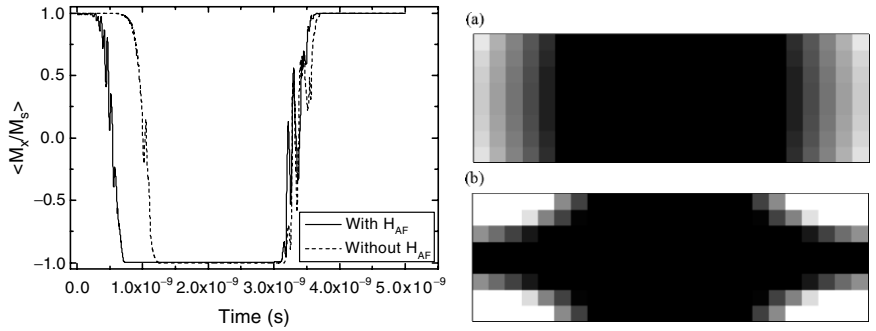

Figure 2. (*Left panel*) Temporal evolution of M_x for a rectangle nanostructure of Py/Cu/Py during the switching processes from PS to APS and backwards, with $\mathbf{H}_{AF}$ (*solid line*) and without $\mathbf{H}_{AF}$ (*dashed line*). (*Right panel*) Spatial distribution of the main modes excited for the simulation of the left panel (a) with MC (b) without MC.

the micromagnetic model. This is principally due to the non-uniform distribution in the structure. The non-uniformity degree can be checked in Figure 1 (right panel), observing the ratio between the x component and the y and z components, respectively. The MC along the x-axis detains the greatest value (solid line); MC along the y-axis has a smaller value (dashed line) and MC along the z-axis has an intermediate value (dotted line). Naturally, in all cases, the values of the MC decrease with the distance from the PL. In particular, the MC is able to speed the switching PS→APS (see Fig. 2 left panel, solid line). On the other hand, the MC delays the switching APS→PS for short pulse of current, but it does not change the critical current for the long ones.

However, by applying a current pulse of such amplitude to give the switching both with and without the MC, a faster switching process either PS→APS or

APS→PS is observed with MC (see Fig. 2 left panel). The interpretation of this effect can be found in the inhomogeneities of the MC in the lateral region of the rectangle which are the cause of the accelerated reversal of the switching. In order to explain this kind of behaviour, the excited spatial modes configuration has been studied. This is achieved by means of a micromagnetic spectral mapping technique similar to that used in Refs. 13–15. The procedure consists in performing the Fourier transform of the magnetization temporal evolution for each computational cell and then plotting the 2D spatial distribution of the spectral power at the specific frequency of the mode to be analyzed.[15–17] In particular, for the simulation of Figure 2 (left panel) the main mode (12 GHz) excited in the first 0.25 ns of the structures is mapped in Figure 2 (right panel), (a) with MC and (b) without MC. It can be seen how the MC helps the formation of a uniform distribution of the main excited modes at the boundary of the structure. Similar configurations of the excited modes can be seen for APS→PS switching process. In conclusion, we can affirm that the MC has to be taken into account in order to carry out micromagnetic computations correctly. Furthermore, the distance between the two ferromagnetic layers (FL and PL) has to be considered. Lastly, our results demonstrate that the switching process in a ferromagnetic coupled system is faster than that in an uncoupled one; this is useful in order to design MRAM devices with smaller writing times.

3. Effect of the Classical Ampere Field

The investigated nanopillars are circular multilayer of 10 nm Co (PL)/6 nm Cu/2.5 nm Co (FL) with a radius of 65 nm.[18] We applied an external uniform and constant field ($\mathbf{H}_{ext}$ = 1,400 A/m) in order to maintain fixed the magnetization of the thick Co layer and the maximum negative current is $J_0 = 2.7 \cdot 10^8$ A/cm^2. In this case, the Ampere field contribution is able to trigger the switching to the PS→APS transition and the passage occurs in a time of around 1 ns (see Fig. 3 left panel, solid line). On the other hand, when we carry out the simulation without the Ampere contribution and for the same applied field and current, the switching does not occur and the magnetization has a noisy, non-uniform configuration (see Fig. 3 left panel, dashed line). In Figure 3 (centre panel) we show also the behaviour of the same multilayer but using Py as ferromagnetic material. In this case, the influence of the $\mathbf{H}_{Amp}$ is similar. In fact, it is able to speed the switching process, anticipating the PS→APS transition which takes place in about 0.7 ns. Figure 3 (right panel) shows some snapshots of the magnetization configuration at the beginning of the switching from PS to APS including the Ampere's field, for the nanostructures of Co/Cu/Co and Py/Cu/Py marked in the left and centre panels. The first thing to be noted is that, in all cases, the configurations are highly non-uniform, confirming the assertions of experimentalists who claimed that multiple domains and possibly domain wall motion were involved in their results.[5,8] This

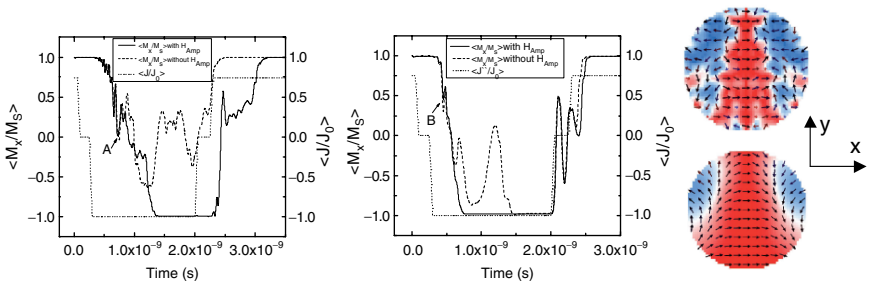

Figure 3. Temporal evolution of M_x together with the applied current for a circular nanostructure of Co/Cu/Co (*left panel*) Py/Cu/Py (*centre panel*) during the switching processes from PS to APS and backwards, with $\mathbf{H}_{\text{Amp}}$ (*solid line*) and without $\mathbf{H}_{\text{Amp}}$ (dashed line). Snapshots of the magnetization configuration marked with the letters 'A' and 'B' respectively. (From [18]. With permission.)

point is difficult to verify directly by the experimentalists but our micromagnetic computations confirm it. It is also to be noted how the $-M_x$ domains which start to form in the states shown in Figure 3 (A) and (B) follow the symmetry of the Ampere field created by electrons flowing downwards and therefore $\mathbf{H}_{\text{Amp}}$ triggers and helps the switching. It has to be noted that, these results cannot be generalized to every geometry, thickness of the layers, materials, etc. Each particular nanostructure has to be analyzed in detail to find the spin polarized current values needed for the switching and to describe the dynamics of the magnetization and the influence of the several contributions of the effective field.

4. Analysis of Persistent Dynamics Processes

Figure 4 (left panel) shows the phase stability diagram of the dynamical modes related to the structure of Py-10 nm-(PL)/Cu-5 nm-/Py-2.5 nm-(FL) with two different cross-sections: $60 \times 20 \times 2.5$ nm^3 ($120 \times 40 \times 2.5$ nm^3) for PS a(c) and APS b(d) configuration as initial state between the ferromagnetic layers. The regions labelled 'PS' and 'APS' denote the zones where the magnetization either remains or switches (depending on the initial state) to one of the two stable static states ('fixed points' of the dynamics[18]). The zone 'PS/APS' is characterized by a noisy oscillation of the magnetization between the stable PS and APS states. No characteristic frequencies arise in the Fast Fourier Transform (FFT) power spectrum in this zone, neither clear traces of telegraph noise were observed (Fig. 4b right panel). Finally the regions marked as 'W' presented characteristic frequencies in the FFT (Fig. 4a right panel) indicating a self-oscillation of the magnetization. This oscillations could be thought to correspond to periodic solutions like the ones found in uniform magnetization models,[19] but the micromagnetic computations show that, in this case, they are associated to a non-uniform persistent oscillation involving the formation of '$-M_x$' domains. It has to be taken

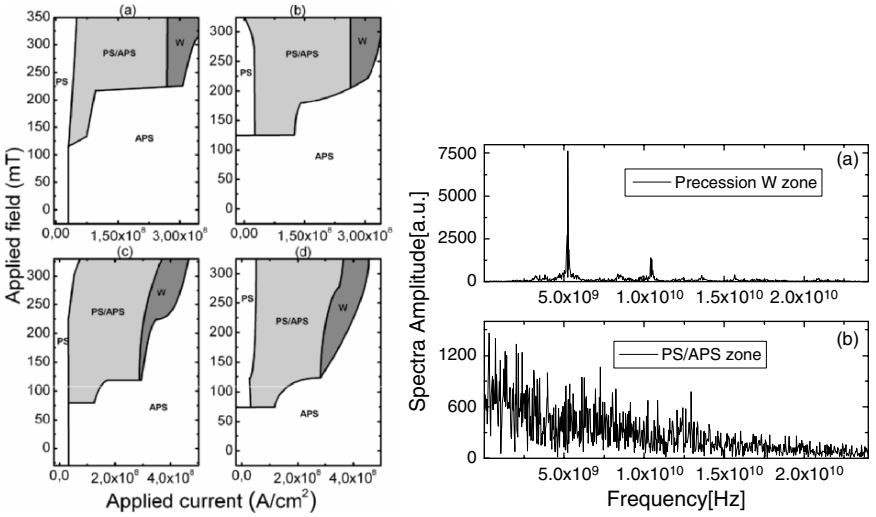

Figure 4. (*Left panel*) Micromagnetic dynamical stability diagram of the structure $60 \times 20 \times 2.5\,nm^3$ (*top*) and $120 \times 40 \times 2.5\,nm^3$ (*bottom*) starting from PS(a, c) and APS configurations (b, d). (*Right panel*) FFT of the magnetization for the structure $60 \times 20 \times 2.5\,nm^3$ (a) $\mathbf{H_{ext}} = 300\,\mathrm{mT}$ and $J_{\mathrm{app}} = -3\ 10^8 \mathrm{A/cm^2}$ (b) $\mathbf{H_{app}} = 300\,\mathrm{mT}$ and $J_{\mathrm{app}} = -1.5\ 10^8 \mathrm{A/cm^2}$.

into account that in our micromagnetic computations the non-uniformities in the magnetization dynamics come mainly from the magnetostatic coupling (MC), the Ampere field and also from the spatial dependence of the polarization function '$g(\mathbf{M}(i, j, k), \mathbf{P})$'.

Figure 5 (left panel) shows the 3D magnetization orbits related to the W zone dynamics of the stability diagram, where non-uniform patterns of the magnetization are evident.

In the computation of the present phase diagrams, the polarization function was computed for each individual cell considering the angular dependence as computed by Slonczewski in 1996 and reported in the previous chapter of this book by Finocchio et al. When a non-uniform pattern of the magnetization (Fig. 5, left panel) is present, this angular dependence is different for each computational cell so that for calculating the phase diagrams the spatial and angular dependence of '$g(\mathbf{M}(i, j, k), \mathbf{P})$' has been employed.

In order to check the effect of such dependences, the magnetization dynamics shown in Figure 5 (left panel) has been recomputed in the following way: (i) using a constant value of '$g(\mathbf{M}, \mathbf{P}) = \max_i(g(\mathbf{M}_i, \mathbf{P}))$' (the maximum) and (ii) using a value of '$g(\mathbf{M}, \mathbf{P}) = g(< \mathbf{M} >, \mathbf{P})$' constant for each cell, (but including the angular dependence calculated at any time 't' with the averaged value of the magnetization found at the previous computational time '$t-\Delta t$'). The computed frequency spectra are shown in the right panel of Figure 5. It can be observed how both the angular and the spatial dependence of the polarization functions lead

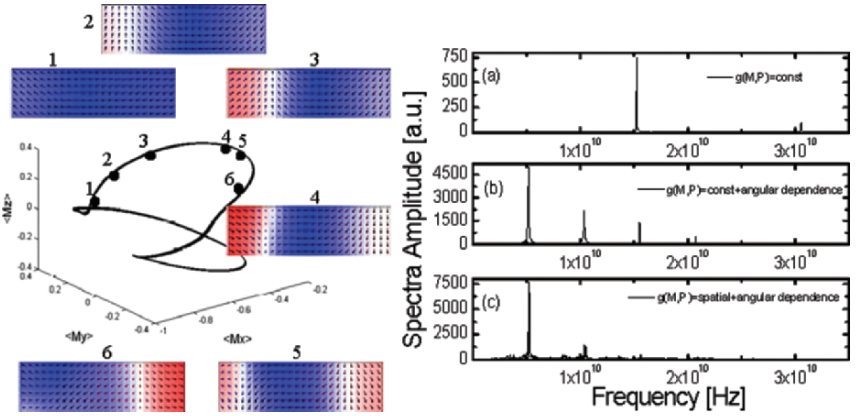

Figure 5. (*Left panel*) W precession magnetization orbits plotted in 3D together with snapshots of the magnetization configuration corresponding approximately to the points marked in the 3D trajectory. (Right panel) FFT of the magnetization for (a) g(**M**, **P**) constant, (b) g(**M**, **P**) constant and angular dependence, (c) g(**M**, **P**) spatial and angular dependences.

to the presence of oscillation modes with characteristic frequencies in the FFT spectrum. Some of these modes, present in the 'W' zone could be identified with those observed experimentally.[8] This fact reveals that a full micromagnetic model including the non-uniformities of MC, Ampere field and Slonczewski's polarization function can give rise to complex oscillation modes without considering artificial anisotropies or microstructures.[20]

References

1. J. C. Slonczewski, *J. Magn. Magn. Mater.* 159 (1996).
2. J. C. Slonczewski, *J. Magn. Magn. Mater.* 247, 324 (2002).
3. L. Berger, *Phys. Rev. B* 54, 9353 (1996).
4. L. Berger, *J. Appl. Phys.* 91(10), 6795 (2002).
5. J. A. Katine et al., *Phys. Rev. Lett.* 84, 3149 (2000).
6. J. Grollier et al., *Phys. Rev. B* 67, 174402 (2003).
7. F. B. Mancoff et al., *Appl. Phys. Lett.* 83(8), 1596 (2003).
8. S.I. Kiselev et al., *Nature* 425, 380 (2003).
9. S. Urazhdin, H. Kurt, W. P. Pratt Jr., and J. Bass, *Appl. Phys. Lett.* 83, 114 (2003).
10. S. Urazhdin, W. P. Pratt Jr., and J. Bass, *Appl. Phys. Lett.* 84, 1516 (2004).
11. Bertotti, G., *Hysteresis in Magnetism: For Physicists, Materials Scientists, and Engineers,* Academic Press, New York, 1998.
12. I. N. Krivorotov et al., *Science* 307, 228 (2005).
13. P. Lubitz, M. Rubistein, J.J. Krebs, and S.F. Cheng, *J. Appl. Phys.* 89, 6901 (2001).

14. L. Torres, L. Lopez-Diaz, M. Carpentieri, and G. Finocchio, *J. Magn. Magn. Mater.* 286, 381 (2005).
15. M. Grimsditch et al., *Physica B* 354, 266 (2004).
16. R. D. McMichael and M. D. Stiles, *J. Appl. Phys.* 97, 10J901 (2005).
17. D. V: Berkov and N. L. Gorn, *Phys. Rev. B* 71, 052403 (2005).
18. M. Carpentieri, G. Finocchio L. Torres et al., *J. Appl. Phys.* 97, 10C713 (2005).
19. G. Bertotti, C. Serpico et al., *Phys. Rev. Lett.* 94(12), 127206 (2005).
20. D. V. Berkov and N. L. Gorn, *Phys. Rev. B* 72, 094401 (2005).

MAGNETIC RINGS: A PLAYGROUND TO STUDY GEOMETRICALLY CONFINED DOMAIN WALLS

MATHIAS KLÄUI
Fachbereich Physik, Universität Konstanz,
Universitätsstr. 10, 78457 Konstanz, Germany

Abstract. Geometrically confined domain walls are comprehensively investigated using a range of magnetometry and imaging techniques. The spin structures of head-to-head domain walls are systematically determined and a quantitative domain wall type phase diagrams for NiFe and Co are obtained and compared with available theoretical predictions and micromagnetic simulations. Differences to the experiment are explained taking into account thermal excitations. Thermally induced domain wall type transformations are observed, from which a vortex core nucleation barrier height is obtained. The stray field of a domain wall is mapped directly with sub-10 nm resolution using off-axis electron holography, and the field intensity is found to decrease as $1/r$ with distance. The magnetic dipolar coupling of domain walls in NiFe and Co elements is studied using x-ray magnetic circular dicroism photoemission electron microscopy. We observe that the spin structures of interacting domain walls change from vortex to transverse walls, when the distance between the walls is reduced. Using the measured stray field values, the energy barrier height distribution for the nucleation of a vortex core is obtained. Finally the pinning behaviour at constrictions is determined.

Keywords: Micromagnetic simulations; spin-polarized current; magnetic switching; precessional states

1. Introduction

The physics of surfaces, interfaces, and nanostructures has become one of the main areas of research in the last few decades, due to the trend in science and technology towards miniaturization of physical systems into the nanoscale. The miniaturization trend demands as complete an understanding as possible of the physical properties of systems whose boundaries constitute an appreciable portion of the overall system. From a technological point of view, some of the properties exclusive of mesoscopic systems (thin films, multilayers, fine particles, patterned elements, etc.) hardly need to be emphasized, so obvious and conspicuous have been their practical applications, and this is particularly true of magnetism (e.g. sensors, storage, etc.[1]). From the scientific viewpoint, such systems pose a whole new set of problems, both theoretical and experimental, that have stimulated a growing number of researchers to dedicate their efforts to this branch of science,

B. Azzerboni et al. (eds.), Magnetic Nanostructures in Modern Technology, 85–104.

especially now that a reasonably good understanding of the bulk properties of materials has been achieved. The rapid development of thin-film fabrication technology together with the improvement of in situ surface characterization techniques has led to substantial improvements in surface preparation techniques and epitaxial growth of thin films. This has created the possibility of achieving very high quality surfaces with procedures that have become standard and accessible in any modern growth system. Apart from the improvement in the quality of the films, significant development of lithography techniques has occurred (electron beam, x-ray, etc.,[2] allowing the patterning of well-defined structures with sub-100 nm resolution. Together with the high quality of the magnetic films, this leads to structures, which behave closely to the theoretical predictions for perfect magnetic elements.

Particularly exciting areas are magnetic domain walls, which constitute the boundaries between magnetic domains.[3] A magnetic domain is an area of uniform magnetization, and the idea of ferromagnetic domains was put forward already in by Weiss last century. When the magnetization points in two different directions in two domains, the magnetic spins have to change their orientation at the interface between the two domains and this interface is called a domain wall. In Fig. 1, two examples of such domain walls between domain 1 where the spins of the magnetization are pointing right and domain 2, where the spin are pointing left, are shown. Such domain walls, which separate two domains with antiparallel magnetization pointing towards or away from one another are commonly called head-to-head domain walls or tail-to-tail domain walls.

In contrast to bulk materials, domain walls can be easily manipulated in small magnetic structures and exhibit unique quasi-particle behaviour. Domain walls in nanoscale ferromagnetic elements are also in the focus of interest because of their potential for applications in a variety of fields such as magnetic logic,[4] as well as data storage.[1,5]

Fundamental physical effects associated with domain walls occur since their dimensions in nanostructures become comparable to fundamental physical length scales, such as the exchange length, the Fermi wavelength, the spin diffusion

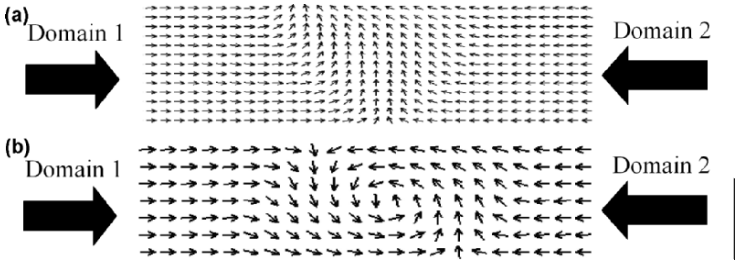

Figure 1. Micromagnetic simulations of head-to-head domain wall spin structures. (a) Shows a transverse wall and (b) a vortex wall.

length, etc.[3] The quasi-particle behaviour becomes obvious, when the motion of domain walls induced by external fields is studied[6,7,8] and wall mobilities and depinning fields[9] are determined.

The interaction of domain walls with spin-polarized currents has been the focus of research recently and one resulting effect is domain wall magneto-resistance, where electrons are scattered from domain walls leading to a change of resistance.[10–14] Here, a detailed knowledge of the domain wall spin structures is necessary, since the effects have been predicted to depend on the wall spin structure, in particular the wall width.[10,11]

The inverse effect, namely the motion of domain walls induced by electrons impinging on a domain wall (current induced domain wall motion – CIDM) and the underlying spin torque effect have been the subject of rising interest,[15–19] and critical current densities as well as domain wall velocities have been measured.

Due to the high-current densities involved in this field of research, temperature and heating effects play a key role.[16,19,20] In particular, the wall spin structure was predicted to depend on the temperature,[20] which calls for studies at variable temperatures.

Thus the resistivity of a domain wall, its mobility, the depinning fields, and critical propagation currents due to the spin torque effect depend critically on the wall spin structure, which serves as a motivation to study these wall spin structures in detail.

Ring elements have proven to be a useful geometry for the investigation of domain walls since they can easily be created and positioned by applying an external uniform magnetic field. Ferromagnetic rings can be in the flux closure vortex state or in the onion state characterized by 180° head-to-head and tail-to-tail domain walls.[21] A strong influence of domain wall interaction on the switching of magnetic elements was found recently, when interaction-induced collective switching of adjacent elements was observed for small spacings.[22,23] Such switching is dominated by domain wall motion and can only be understood with a detailed knowledge of the interacting domain walls' spin structures. Theoretically, the energies of the two wall types are different when interacting with an external field. We therefore expect the dipolar coupling to affect the two wall types in different ways and coupling-induced transitions from one domain wall type to another may occur.[24] A deeper understanding of the energetics involved is only possible if the stray fields of domain walls are determined quantitatively. For all these studies, high quality magnetic nanostructures have to be fabricated.

2. Fabrication

Arrays of polycrystalline Co and NiFe rings with different thicknesses and widths have been fabricated.[25,26] Electron-beam lithography was used to define magnetic rings. This involves the manufacture of a patterned polymer resist mask followed

by transfer of the pattern into the magnetic material. In the first step, a poly methyl-methacrylate (PMMA) resist, spin-coated on a naturally oxidized Si (001) substrate, is patterned using a Leica LION LV1 electron-beam writer. To write the rings, the electron beam follows a circular single pixel path along the ring and the linewidth is determined by the electron-beam dose.[27] The electron-beam energy is set to 2.5 keV to minimize the proximity effect. For pattern transfer, a lift-off process is used. Here, different thickness polycrystalline permalloy ($Ni_{80}Fe_{20}$) films, with a 2 nm thick gold capping layer to prevent oxidation of the magnetic film, are deposited on the patterned resist on silicon by molecular-beam epitaxy (MBE) evaporation in a ultra-high vacuum deposition chamber (base pressure 3×10^{-10} mbar). The unwanted resist and magnetic material is then removed in acetone.[26]

For one set of samples, the edge-to-edge spacing between adjacent rings was more than twice the diameter to prevent dipolar interactions, which might otherwise influence the domain wall type. Arrays of rings with edge-to-edge spacings down to 10 nm were fabricated to investigate different dipolar coupling strengths between domain walls in adjacent rings and resulting domain wall types. For the transmission off-axis electron holography experiments, 3/4-rings were patterned on 50 nm thick SiN membranes as detailed by Heyderman et al.[28] Open rings rather than full rings were grown on the fragile membranes in order to facilitate the lift-off process which cannot be assisted by ultrasound.

3. Measurement techniques

To determine the spin structure of the domain walls as a function of the ring geometry, the samples were imaged using x-ray magnetic circular dichroism photoemission electron microscopy.[29,30]

The non-intrusive technique of XMCD-PEEM was used to image the magnetization state in remanence after saturation in an external magnetic field. In PEEM, the yield of electrons is proportional to $P \times M$ where P is the helicity of the elliptically polarized synchrotron radiation and M the sample magnetization. The yield difference between the helicities can be seen as magnetic contrast in the image.[30]

In order to obtain quantitative information about stray fields, which are not accessible by XMCD-PEEM, samples were investigated by off-axis electron holography.[31,32] Co was chosen rather than NiFe for this investigation due to its higher saturation magnetization and therefore higher stray field. Electron waves passing through the sample gain a phase shift, which results from the interaction with electric and magnetic fields. The phase shift is determined using a biprism, which interferes the transmitted electron wave and a wave crossing only the membrane. This phase shift is then evaluated to obtain the magnetic induction direction and strength.

4. Head-to-head domain walls

4.1. DOMAIN WALL SPIN STRUCTURES

In a thin film strip-wire (length >> width (W) >> thickness (t)) two types of head-to-head domain wall spin structures were predicted to occur[24,33]: (i) transverse walls and (ii) vortex walls. In Fig. 1a, the simulated spin structure of a transverse wall is shown. In this case the spins rotate in the plane, similar to a Néel wall in a continuous film.[3] A characteristic triangular structure can be observed, which leads to a large stray field, since significant magnetization is pointing perpendicular to the wire edge. In Fig. 1b, the spin structure of a vortex wall is shown. Here the spins rotate in a vortex structure. This leads to a vortex core, where the magnetization is pointing out of the plane and this vortex core leads to a high exchange energy.

4.2. DOMAIN WALL PHASE DIAGRAMS

In Fig. 2, we present PEEM images of (c) a thick and wide NiFe ring, (d) a thin and narrow ring, and (e) an ultra-thin ring measured at room temperature. The domain wall type was systematically determined from PEEM images for more than 50 combinations of ring thickness and width for both NiFe and Co and the quantitative phase diagrams shown in Figs. 3a, c were extracted. The phase diagrams exhibit two phase boundaries indicated by solid lines between vortex walls (thick and wide rings, squares), transverse walls (thin and narrow rings, circles), and again vortex walls for ultra-thin rings.

Now we first discuss the upper boundary shown in Figs. 2a, c. Theoretically this phase boundary was investigated by McMichael and Donahue.[24] They calculated the energies for a vortex and a transverse wall, and determined the

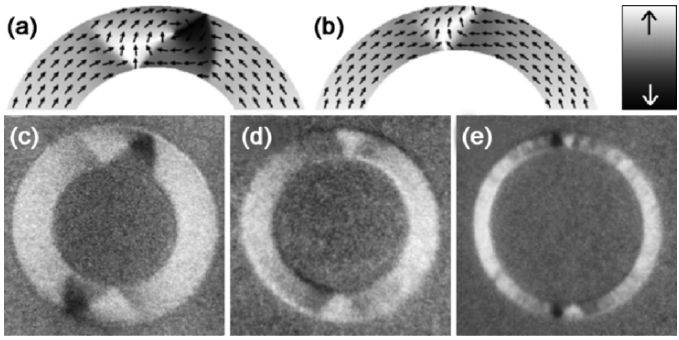

Figure 2. Spin structure of (a) a vortex and (b) a transverse wall simulated using OOMMF. PEEM images of (c) 30 nm thick and 530 nm wide (outer diameter $D = 2.7\,\mu$m), (d) 10 nm thick and 260 nm wide ($D = 1.64\,\mu$m), and (e) 3 nm thick and 730 nm wide ($D = 10\,\mu$m) NiFe rings. The grey scale indicates the direction of magnetic contrast. (From Laufenberg et al.[34])

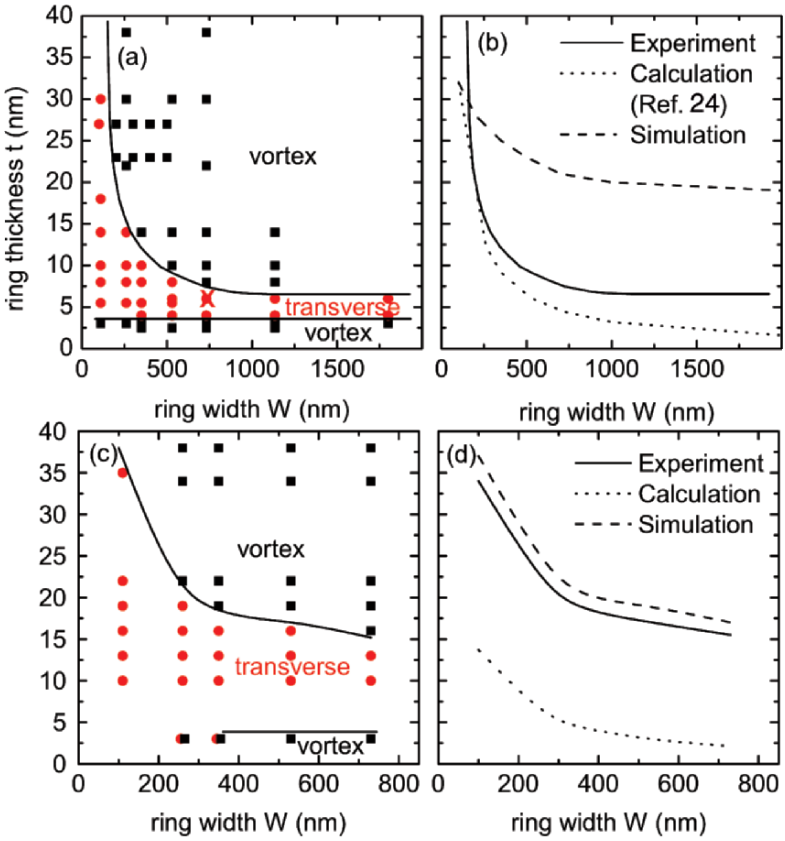

Figure 3. Experimental phase diagrams for head-to-head domain walls in (a) NiFe and (c) Co rings at room temperature. Black squares indicate vortex walls and red circles transverse walls. The phase boundaries are shown as solid lines. (b, d) Comparison of the upper experimental phase boundary (*solid lines*) with results from calculations (*dotted lines*) and micromagnetic simulations (*dashed lines*). The thermally activated wall transitions shown were observed for the ring geometry marked with a red cross in (a) ($W = 730$ nm, $t = 7$ nm). (Adapted from Laufenberg et al.[34] Kläui et al.[35])

phase boundary by equating these two energies. The calculated phase boundary (dotted lines in Figs. 2b, d) is of the form $t \times W = \mathrm{C} \times \delta^2$ where δ is the exchange length and C a universal constant. It is shifted to lower thickness and smaller width compared to the experimental boundary (solid lines in Figs. 2b, d). This discrepancy can be understood by taking into account the following: The calculations[24] compare total energies and therefore determine the wall type with the absolute minimum energy as being favourable. In the experiment, the wall type was investigated after saturation of the ring in a magnetic field and relaxing the field to zero. During relaxation, first a transverse wall is formed reversibly.[35] For the formation of a vortex wall, an energy barrier has to be overcome to nucleate

the vortex core. So the observed spin structure does not necessarily constitute the absolute minimum energy, but transverse walls can be observed for combinations of thickness and width where they constitute local energy minima even if a vortex wall has a lower energy for this geometry. To shed further light onto this, we have simulated the experiment by calculating the domain wall spin structure after reducing an externally applied field stepwise using the OOMMF code (available at: gams.nist.gov) (for NiFe: $M_s = 800 \times 10^3$ A/m, $A = 1.3 \times 10^{-11}$ J/m; for Co: $M_s = 1,424 \times 10^3$ A/m, $A = 3.3 \times 10^{-11}$J/m; for both: damping constant $\alpha = 0.01$, cell size 2–5 nm). The simulated boundary is shifted to higher thickness and larger width compared to the experiment. This we attribute to the fact that thermal excitations help to overcome the energy barrier between transverse and vortex walls in case of the room temperature experiment, while they are not taken into account in the 0 K simulation. So we can expect that for temperatures above room temperature the upper phase boundary is shifted to lower thickness, in other words, that transverse walls formed at room temperature change to vortex walls with rising temperature. This means that with rising temperature the experimental phase boundary approaches the theoretical one since the walls attain the energetically lower spin structure.

4.3. THERMALLY ACTIVATED DOMAIN WALL TRANSFORMATIONS

In order to corroborate this explanation for the difference between the experiments on the one hand and calculations and simulations on the other, we have performed temperature dependent XMCD-PEEM studies. Figure 4 shows an image series

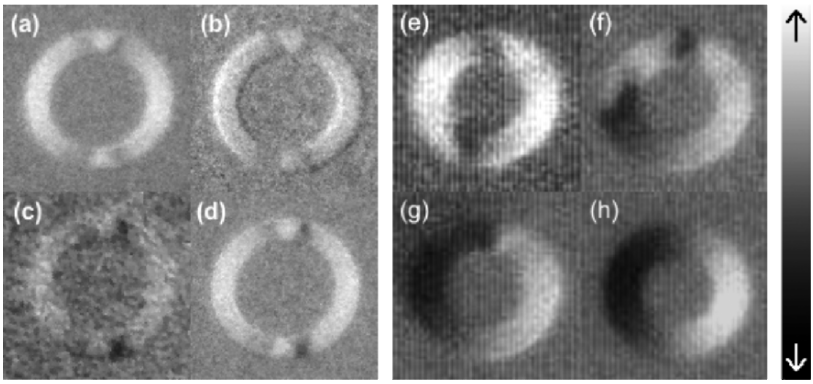

Figure 4. PEEM images of a 7 nm thick and 730 nm wide ring imaged during a heating cycle at temperatures of (a, d) $T = 20°$C (before and after heating, respectively), (b) $T = 260°$C, and (c) $T = 310°$C (estimated errors are ± 10 K). Due to heating, rings (here (e): 7 nm thick, 1,135 nm wide with two vortex walls) can attain either (g) a vortex state with a 360° domain wall or (h) the vortex state. The intermediate state, where one wall is displaced, is shown in (f). The grey scale indicates the direction of magnetic contrast. (Adapted from Laufenberg et al.[34])

of a 7 nm thick and 730 nm wide NiFe ring (geometry marked by a cross in Fig. 3a) for different temperatures of (a, d) $T = 20°C$ (before and after heating), (b) $T = 260°C$, and (c) $T = 310°C$. Transverse walls are formed (a) during saturation in a magnetic field and relaxation before imaging. At first, heating does not influence the spin structure of the domain walls as shown in (b), only the image contrast becomes weaker because imaging is more difficult at higher temperatures due to drift problems and decreasing magnetization. At a transition temperature between $T = 260°C$ and $T = 310°C$ corresponding to a thermal energy between 6.7×10^{-21} J and 8.0×10^{-21} J, the transverse walls change to vortex walls (c), so that a domain wall spin structure was created which is not accessible for the same ring geometry by only applying uniform magnetic fields. Figure 4d confirms that the vortex wall is stable during cooling down. This means that both domain wall types are (meta-)stable spin configurations and therefore constitute local energy minima at room temperature for this geometry. These PEEM experiments directly show that the position of the upper experimental phase boundary is temperature dependent and is shifted to lower thickness and width with increasing temperature. These results thus confirm the hypothesis about the discrepancy between experiment and theory put forward before: both domain wall types constitute local energy minima, with the transverse wall attained due to the magnetization process, even if a vortex wall has a lower energy. Experimentally, we directly observe thermally activated crossing of the energy barrier between high-energy transverse and low-energy vortex walls. It should be mentioned, however, that the flux closure vortex state of the ring without any domain walls and with the magnetization aligned everywhere along the ring perimeter is the energetically most favourable state. Many rings attain this state when the temperature is increased as shown in Figs. 4e–h. In order to observe the wall type transformations shown in Figs. 4a–d, it is therefore necessary, that the energy barrier between transverse and vortex walls is lower than the barrier for the transition to the vortex state of the ring. This critically depends on imperfections of the ring microstructure, which can serve as pinning centres and stabilize a domain wall.

It can be seen by comparing the boundaries for NiFe and Co in Fig. 3, that for NiFe, the calculations[24] fit the experiment better than the simulations, while for Co the opposite is true. The energy barrier between a transverse and a vortex wall can be overcome more easily in the case of NiFe rather than Co, so that transverse walls created are more likely to be retained at a certain temperature in a Co ring than in a NiFe ring with analogous dimensions. This is consistent with the observation that in NiFe there is a more abrupt change between transverse and vortex walls with varying geometry than in Co.

4.4. WALLS IN THIN AND WIDE STRUCTURES: LIMITS OF THE DESCRIPTION

We turn now to the discussion of the low thickness regime of the phase diagrams shown in Fig. 3, where a second phase boundary between 3 and 4 nm is found both for NiFe and for Co. In terms of energetics, this is not expected because the calculations[24] show that a transverse wall has a lower energy than a vortex wall in this thickness regime. But these calculations assume a perfect microstructure and do not take into account morphological defects such as the surface roughness. Holes, which might serve as nucleation centres for the vortex wall formation, were not observed in atomic force microscopy images. However, this does not exclude a spatial modulation of magnetic properties such as the exchange or the saturation magnetization, which could locally allow for a stronger twisting of adjacent spins. Thus a vortex wall would be energetically more favourable in this thickness regime due to imperfections of the microstructure or the morphology.

In the thin samples investigated, a ripple domain formation[3] is observed as shown in Figs. 5a, b (see also Fig. 2e). This can be attributed to statistical variations of the anisotropy of individual grains. Consequently, this phenomenon is more pronounced in the polycrystalline Co structures, in which individual grains exhibit a non-negligible anisotropy compared to the weak anisotropy in NiFe.

The description in the frame of these phase diagrams is, however, limited by the width and thickness of the structure. In rings wider than $\approx$1.5 μm, we observe more complicated domain wall spin structures like distorted transverse walls (Fig. 5c). Wide rings with a small hole in the centre exhibit a disc-like behaviour with a triangle state as shown in Fig. 5d. This type of structure is discussed in more detail in.[36,37] In very thick elements, double vortex walls with two vortices with opposite sense of rotation were reported recently,[38] which can also constitute (meta-)stable configurations in the thickness regime investigated here (Fig. 6a). As it turned out from experiments on current-induced domain wall transformations,[39] other spin structures are stable as well, as shown in Fig. 6. Recent theoretical calculations[33] propose to distinguish between symmetric and

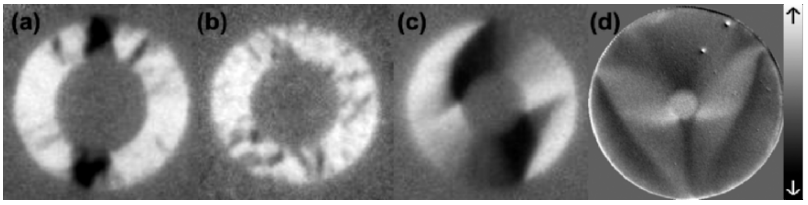

Figure 5. Limiting cases of the structures investigated: 3 nm thick and 1.8 μm wide (a) NiFe and (b) Co rings showing ripple domain formation, (c) 6 nm thick and 3 μm wide ring with distorted transverse walls, and (d) 10 nm thick and 2.1 μm wide disc-like NiFe ring with 700 nm inner diameter in the triangle state (For detailed explanations of the contrast see [36,37]). The grey scale indicates the direction of magnetic contrast.

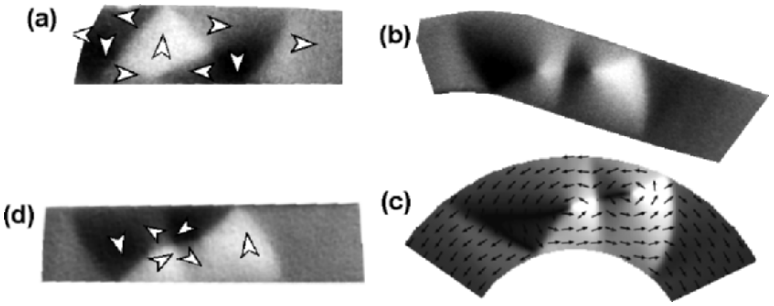

Figure 6. Other domain wall spin structures, which constitute (meta-) stable magnetization configurations in 28 nm thick and 1 μm wide Py structures: (a) double vortex wall with two vortices with different sense of rotation; (b) double vortex wall with two vortices with the same sense of rotation and a cross-tie structure at the centre; (c) micromagnetic simulation of such a double vortex wall; (d) extended vortex wall. (Adapted from Kläui et al.[39])

asymmetric transverse walls which is not done here, because both types are difficult to distinguish experimentally and sample irregularities can influence the detailed wall spin structure.

5. Domain wall coupling energetics

5.1. COUPLING BETWEEN ADJACENT DOMAIN WALLS

After saturating with a magnetic field and relaxing the field, rings attain the onion state characterized by two head-to-head domain walls as shown before (see also Fig. 7a). An array of 25 rings in the onion state exhibits 50 walls in total. The domain walls inside the array interact with adjacent walls via their stray fields. Only 10 walls, which are located at the two opposite edges (top and bottom edges in Figs. 7b and c) of the array and therefore have no neighbouring rings, are not significantly influenced by stray fields of an adjacent wall. For all experiments, ring thickness and width were chosen such that isolated rings of this geometry exhibit vortex walls according to the phase diagram presented above.

Figure 7 shows XMCD-PEEM images of arrays of 27 nm thick NiFe rings with (b) 40 nm and (c) 500 nm edge-to-edge spacing, respectively, as well as a high-resolution image (a) presenting both wall types. Vortex walls can be easily identified by black and white contrast which occurs because all magnetization directions corresponding to the full greyscale are present in a vortex (Fig. 7a, top). In contrast, transverse walls exhibit the characteristic grey–white–grey contrast with the triangular spin structure in their centre (Fig. 7a, bottom).

In Fig. 8a, we show the percentage of transverse walls inside the array as function of the edge-to-edge spacing for 27 nm thick NiFe rings (black squares) extracted from images of the type shown in Fig. 7. A decreasing number of transverse walls is found with increasing spacing. Domain walls at the edges of the

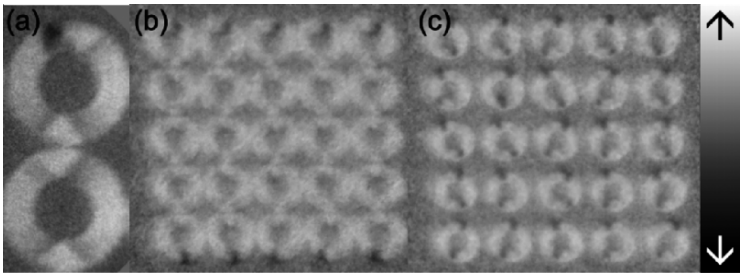

Figure 7. (a) A high-resolution XMCD–PEEM image of two rings in the onion state after saturation with an external field in the vertical direction and relaxation. White and black contrasts correspond to the magnetization pointing up and down, respectively. A non-interacting vortex wall (*top*) and three interacting transverse walls are visible. Overview images of an array of 27 nm thick and 350 nm wide NiFe rings with an edge-to-edge spacing of (b) 40 nm and (c) 500 nm, respectively. The transition from 100% transverse walls inside the array for narrow spacings (b) to close to 0% for large spacings (c) can be clearly seen. Since domain walls at the top and bottom edges of the array do not interact with adjacent walls, they are vortex walls for all spacings investigated. (From Laufenberg et al.[40])

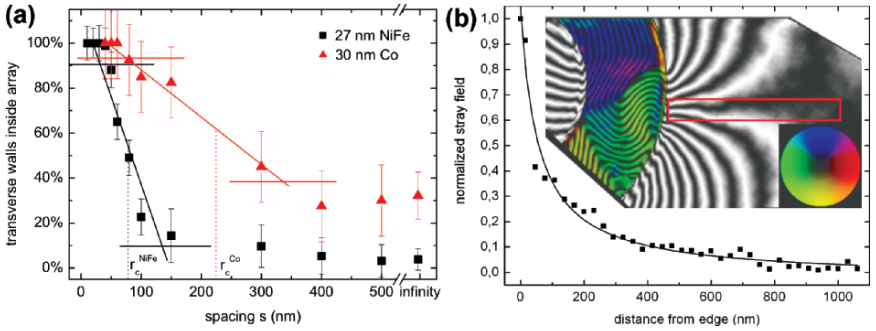

Figure 8. (a) Percentage of transverse walls inside a ring array as function of edge-to-edge spacing. Black squares are for 27 nm NiFe, and red triangles for 30 nm Co, respectively. The error bars represent the absolute statistical error $1/\sqrt{n}$ due to the finite number n of domain walls investigated. The horizontal lines show the 10–90% levels of the transition from a transverse to a vortex domain wall. (b) The inset shows an off-axis electron holography image of a transverse wall in a 27 nm thick Co 3/4-ring. The colour code indicates the direction of the in-plane magnetization and the black lines represent directly the stray field. The stray field strength was measured at several distances inside the marked area. The data points show the stray field normalized to the saturation magnetization as a function of the distance r from the ring edge for the wall shown in the inset. The line is a $1/r$-fit. (From Laufenberg et al.[40])

arrays are vortex walls irrespective of the spacing due to the absence of dipolar coupling with adjacent walls. The data points for infinite spacings in Fig. 8a result from these domain walls. The transverse to vortex transition is characterized by a (10–90%)-width of the switching distribution of $w = 65 \pm 9$ nm and a centre at $r_c = 77 \pm 5$ nm. In Fig. 8a, red triangles show a similar transition for 30 nm thick Co rings with $w = 328 \pm 130$ nm and $r_c = 224 \pm 65$ nm.

In order to explain these results, we first consider the process of domain wall formation in an isolated ring. When relaxing the applied external field from saturation, transverse walls are initially formed. In order to create a vortex wall, a vortex core has to be nucleated. This hysteretic transition from one wall type to the other involves overcoming a local energy barrier,[35,41] since the nucleation of the vortex core is associated with a strong twisting of the spins in the core region.[42] In arrays of interacting rings, the edge-to-edge spacing dependent stray field stabilizes transverse walls so that for small spacings (corresponding to a strong stray field from the adjacent domain wall) transverse walls are favoured (Fig. 7b). For increasing spacing, the influence of the stray field from an adjacent wall is reduced, until vortex walls are formed in the rings with the lowest energy barrier for the vortex core nucleation. The further the spacing increases the more rings nucleate vortex walls (Fig. 7c). Thus the spacing at which a wall switches from transverse to vortex is related to the nucleation barrier, which depends on local imperfections such as the edge roughness. So the number of domain walls that have switched from transverse to vortex as a function of the edge-to-edge spacing is a measure of the distribution of energy barriers for the vortex core nucleation.

For NiFe, a relatively sharp transition occurs from all walls being transverse to all walls being vortex walls. This corresponds to a narrow energy barrier distribution, while the domain walls in Co rings exhibit a much wider transition. This difference is thought to result from the different polycrystalline microstructures of the NiFe (magnetically soft fcc crystallites with negligible anisotropy) and the Co (hcp crystallites with strong uniaxial anisotropy leading to a larger number of pinning sites). Furthermore, this results in the presence of transverse walls in our Co sample even at infinite spacings. Thus, we chose Co for the electron holography measurements rather than NiFe in order to be able to observe a transverse wall and its stray field in an isolated structure.

5.2. DIRECT OBSERVATION OF THE DOMAIN WALL STRAY FIELD

This spacing-dependent distribution for the vortex core nucleation needs to be transformed to a distribution as a function of the stray field strength, which is in a first approximation proportional to the energy. To do this, the stray field as well as the magnetization of the domain wall was imaged using off-axis electron holography. The inset of Fig. 8b shows an image of the in-plane magnetic induction integrated in the electron beam direction, obtained from a transverse wall in a 27 nm thick isolated Co 3/4-ring designed with the same width as that of the rings imaged by XMCD-PEEM. The stray field was measured along the length of the region indicated in the image, and is shown as a function of the distance r from the ring edge in Fig. 8b, normalized to the saturation magnetization of Co. The line is a $1/r$-fit which can be expected for the distance dependence of the stray field

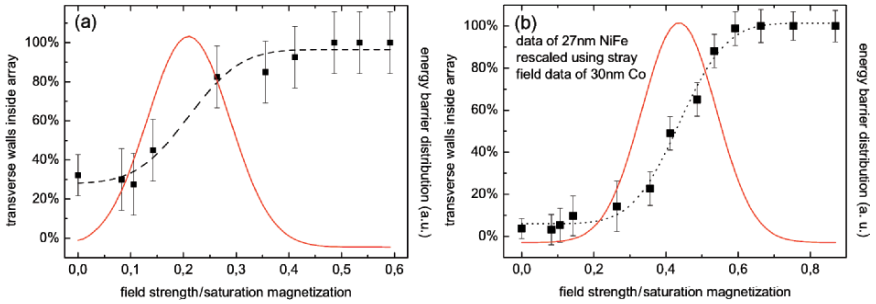

Figure 9. (a) Black squares represent the same data points as shown in Fig. 8a for the 30 nm thick Co sample, but as a function of the normalized field strength. The black dashed line shows a fit with the error function. The corresponding Gaussian distribution of the energy barriers is shown as a full red line. (b) Corresponding data for the 27 nm thick NiFe sample rescaled using the stray field measurement of a domain wall in 30 nm thick Co. (Adapted from Laufenberg et al.[40])

created by an area of magnetic poles for small r.[43] This dependence also confirms earlier results from indirect Kerr effect measurements.[23] In order to obtain the stray field of one single domain wall acting on an adjacent wall, the stray field of an isolated wall was imaged.

The spacing-dependent energy barrier distribution is now rescaled to a field-dependent distribution using the measured stray field decay of Fig. 8b and presented in Fig. 9a. The rescaled data can be fitted with the error function erf(x), which is the integral of a Gaussian distribution. Assuming a similar dependence of the stray field for NiFe like measured for Co, a Gaussian distribution is also obtained for the energy barrier height distribution for NiFe as presented in Fig. 9b. Thus a Gaussian distribution for the energy barriers is found, which is in agreement with the presence of independent local pinning centres at the particular wall position that determine the nucleation barrier. The position of the maximum is $H_{\max}/M_s = 0.21 \pm 0.10$ and the full width at half maximum $w/M_s = 0.16 \pm 0.05$, where M_s is the saturation magnetization. Using $E_{\max} = 1/2\,\mu_0 M_s H_{\max}$, an energy density of $E_{\max} = 8.4 \pm 4.0 \times 10^4$ J/m^3 equivalent to the field $H_{\max}$ can be obtained for the 30 nm thick Co sample.

Figure 8a shows that the transition for the Co sample saturates at a finite value for large spacings. In terms of the model described above, which explains how vortex walls are formed during relaxation from saturation, this means that an additional effective field would be needed to overcome the pinning of the remaining transverse walls at structural imperfections and to allow the vortex core nucleation and formation of an energetically favourable vortex wall. Since the pinning is much stronger in our Co sample than in the NiFe sample, this occurs here only for Co.

6. Domain wall behaviour at constrictions

As the spin structure and the resulting energy of domain walls depends on the geometry, we can engineer a potential landscape for the domain walls by varying the geometry. In earlier work on rings, we observed that constrictions create an attractive potential well for transverse walls, but vortex walls are repelled from a constriction.[9,44] Qualitatively the potential landscape for the two types of domain walls is presented in Fig. 10. In general, the depth of the potential well and thus the depinning field increases with decreasing constriction width, indicating that walls in narrower constrictions are more strongly pinned. Qualitatively this behaviour is expected, since the energy of the domain wall scales with the size, so that smaller domain walls in narrower constrictions are more energetically favourable and thus more strongly pinned. But this simple picture does not do justice to the more sophisticated aspects of domain wall behaviour; in particular for the two domain wall types (transverse and vortex) very different behaviour at constrictions was predicted: Transverse walls should be attracted into constrictions (as confirmed by MR measurements in[44]). In contrast, vortex walls should be repelled at the precise location of the constriction but pinned close by with a definite sense of rotation (clockwise or anticlockwise depending on which side of the constriction the wall is located).[9]

We now employ direct imaging of domain walls to reveal the details of the interaction of domain walls with constrictions. In Fig. 11 we present high spatial resolution magnetic induction maps of domain walls at various constrictions, which were prepared by saturating the sample with a field along the notch position

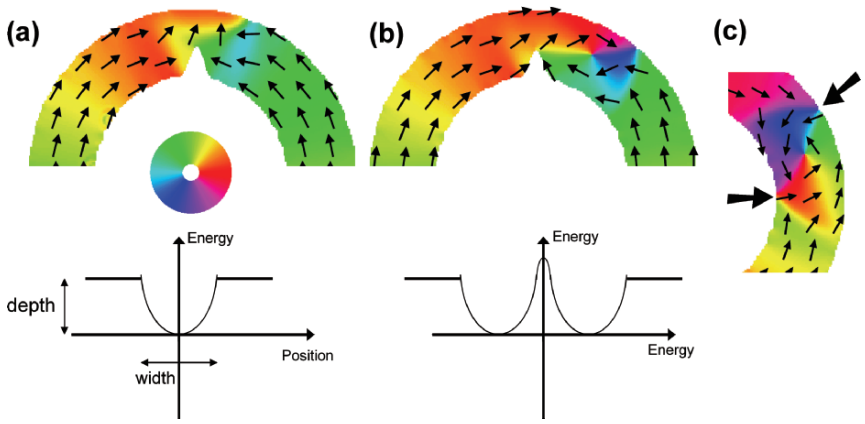

Figure 10. Simulated behaviour of a transverse and a vortex wall at a constriction. (a) shows a transverse domain wall inside a constriction and below the corresponding potential landscape schematically (single potential well at the notch position). In (b) this is shown for a vortex wall, which is pinned adjacent to the constriction. The potential landscape exhibits a double well. The black arrows in (c) point to the positions, where stray field enters or leaves a vortex wall.

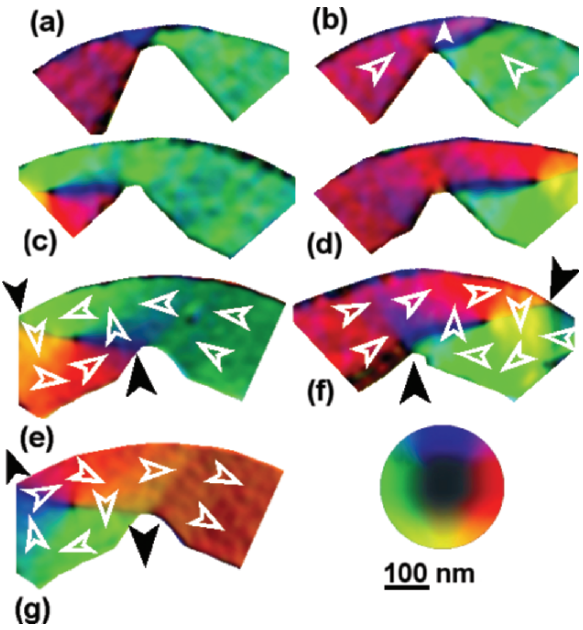

Figure 11. High spatial-resolution electron holography images of sections of 27 nm thick, 200 nm wavy line structures with different constriction widths: (a) 35 nm, (b) 60 nm, (c) 100 nm, (d) 110 nm, (e) 140 nm, (f) 160 nm, and (g) 140 nm. The walls in constrictions (a) and (b) are transverse walls, (c) and (e) exhibit vortex head-to-head walls to the left and (d) and (f) vortex head-to-head walls to the right of the constriction; (e) and (g) show the same constriction with (e) a head-to-head and (g) a tail-to-tail vortex wall. The magnetization directions are indicated in (b), (e), (f), and (g) by white arrows. Areas where stray field occurs are denoted with black arrows in (e), (f), and (g). The colour code indicating the magnetization direction is also shown. (From Kläui et al.[9])

and then relaxing the field to zero. For narrow constrictions (Fig. 11a, b) transverse walls can be discerned inside the constrictions, while for larger constrictions (Fig. 11c–g) vortex walls are located at positions adjacent to the constrictions (on the left or right hand side depending on slight geometrical asymmetries in the notch with respect to the applied field direction). We can now directly correlate the sense of rotation with the position with respect to the notch, which is not possible using magnetoresistance measurements. We see that the head-to-head walls to the left of the constriction have anticlockwise sense of rotation (Fig. 11c, e), while the walls to the right of the notch have a clockwise sense of rotation (Fig. 11d, f). When the field is reversed to create tail-to-tail walls, the vortex wall sense of rotation is reversed. This can be seen by comparing the vortex walls to the left of the notch in Figs. 11e and g, which show the same notch after applying opposite fields. The head-to-head domain wall in (e) has a anticlockwise sense of rotation, while the tail-to-tail wall in (g) has a clockwise sense of rotation. This is a universal behaviour, which we observed for all vortex walls at constrictions for

all film thicknesses. To understand this behaviour, we have to take into account the fact that a vortex wall has two areas where a stray field occurs. In Fig. 11, the positions at which the stray field enters (Fig. 11e, f) or leaves (Fig. 11g) the vortex wall are marked by two black arrows. In order to minimize the stray field associated with the vortex wall, the lower of the two stray field areas is always located inside the notch, which determines the sense of rotation of the vortex wall. As a result the wall is actually pinned in the location directly adjacent to the notch (even though it is repelled from the constriction). This behaviour explains the fact that a significant depinning field is necessary to displace the vortex walls as well as the transverse walls.[9]

In order to probe the pinning strength, we have measured the external magnetic fields necessary to depin a domain wall from the constriction as a function of the constriction width.[9] The depinning field of the narrowest constrictions (335 Oe) is about six times the field needed to move a wall in a ring without a constriction (60 Oe), where the depinning field is governed by material imperfections and the edge roughness. Therefore the geometrically-induced pinning is by far stronger than the pinning due to natural imperfections, which means that the pinning strength can be tailored over a wide range of values by adjusting the notch geometry. Comparison to micromagnetic simulations and quantitative calculations of the depth of the potential well show good agreement (Fig. 12). Similar results have also been obtained by other groups.[45]

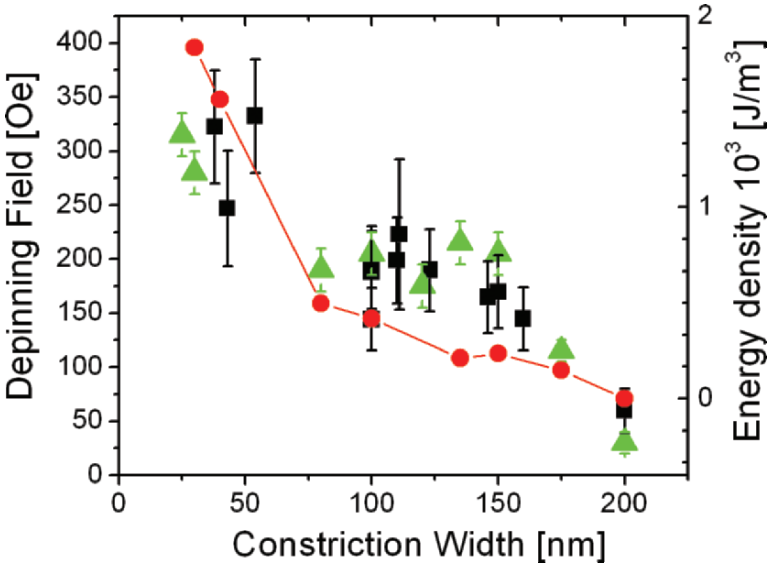

Figure 12. Experimental depinning field (*left ordinate*) vs constriction width in 200 nm wide permalloy ring structures with triangular constrictions and a film thickness of 34 nm (*black squares*); numerical simulations (*green up triangles*). The calculated energy density differences show the same trend (*red disks, right ordinate*). (From Kläui et al.[9])

The width (the spatial extent) of a potential well was measured in,[44] and was found to extend far beyond the physical size of the notch due to the size of the domain wall.

So using different types of domain walls and constrictions with different geometries, we can engineer well-defined pinning potentials, which can then act as stable positions for domain walls in applications.

7. Conclusions

In conclusion, we have comprehensively investigated the properties of head-to-head domain walls in thin film nanostructures.

We have determined the spin structure of domain walls in NiFe and Co and extracted the corresponding room temperature phase diagrams with two phase boundaries between vortex walls for thick and wide as well as ultra-thin rings and transverse walls for thin and narrow rings.

Using temperature-dependent XMCD-PEEM imaging, we have observed a thermally activated switching from transverse walls established at room temperature to vortex walls at a transition temperature giving direct experimental evidence for the fact that transverse and vortex walls are separated by an energy barrier, which can be overcome thermally. The low thickness regime of the phase diagrams revealed a second phase boundary which we attribute to spatial modulations of the magnetic properties in our thinnest samples.

Furthermore, we have mapped the stray field of a domain wall directly using off-axis electron holography with sub-10 nm resolution, and we find that the field strength falls off with a $1/r$-dependence. For interacting domain walls in 350 nm wide ring structures we observe a transition from a transverse to a vortex spin structure with increasing edge-to-edge spacing. By correlating this transition with the measured stray field, we are able to obtain the energy barrier height distribution for vortex core nucleation.

Introducing constrictions, we create a potential landscape for the domain walls and find that transverse walls are attracted into the constriction, while vortex walls are repelled from constrictions. Vortex walls are pinned at a position adjacent to a constriction, which is due to a lowering of the stray field energy. As a consequence, the sense of rotation of the pinned vortex wall is directly determined by the position of the wall with respect to the constriction.

Acknowledgements

M. Laufenberg, D. Backes, L. J. Heyderman, D. Bedau, F. Nolting, S. Cherifi, A. Locatelli, R. Belkhou, S. Heun, C. A. F. Vaz, J. A. C. Bland, T. Kasama, R. Dunin-Borkowski, and in particular U. Rüdiger are gratefully acknowledged

for help, discussions, and support. Financial support is acknowledged from the Deutsche Forschungsgemeinschaft through SFB 513, the Landesstiftung Baden-Württemberg, the EPSRC (UK), the Royal Society (UK), the EC through the 6th Framework Programme, and by the EU through the European Regional Development Fund (Interreg III A Program). Part of this work was carried out at the Swiss Light Source, Villigen (Switzerland) and at Elettra, Trieste (Italy).

References

1. Prinz, G.A., Magnetoelectronic applications, *J. Magn. Magn. Mater.* 200, 57 (1999).
2. Martín, J.I. et al., Ordered magnetic nanostructures: fabrication and properties, *J. Magn. Magn. Mater.* 256, 449 (2003).
3. Hubert, A. and Schäfer, R., *Magnetic Domains*. Springer-Verlag, Berlin (1998).
4. Allwood, D.A. et al., Magnetic domain-wall logic, *Science* 309, 1688 (2005).
5. Parkin, S.S.P., Magnetic shift register with shiftable magnetic domains between two regions, US Patent Application 20050094427 (2005).
6. Atkinson, D. et al., Magnetic domain-wall dynamics in a submicrometre ferromagnetic structure, *Nature Mat.* 2, 85 (2003).
7. Nakatani, Y. et al., Faster magnetic walls in rough wires, *Nature Mat.* 2, 521 (2003).
8. Beach, G.S.D. et al., Dynamics of field-driven domain-wall propagation in ferromagnetic nanowires, *Nature Mat.* 2, 741 (2005).
9. Kläui, M. et al., Direct observation of domain-wall pinning at nanoscale constrictions, *Appl. Phys. Lett.* 87, 102509 (2005).
10. Levy, P. M. and Zhang, S., Resistivity due to domain wall scattering, *Phys. Rev. Lett.* 79, 5110 (1997).
11. Viret, M. et al., Spin scattering in ferromagnetic thin films, *Phys. Rev. B* 53, 8464 (1996).
12. Rüdiger, U. et al., Negative domain wall contribution to the resistivity of microfabricated Fe wires, *Phys. Rev. Lett.* 80, 5639 (1998).
13. Kent, A.D. et al., Domain wall resistivity in epitaxial thin film microstructures, *J. Phys.: Condens. Matter* 13, R461 (2001).
14. Ebels, U. et al., Spin accumulation and domain wall magnetoresistance in 35 nm Co wires, *Phys. Rev. Lett.* 84, 983 (2000).
15. Yamaguchi A. et al., Real-space observation of current-driven domain wall motion in submicron magnetic wires, *Phys. Rev. Lett.* 92, 77205 (2004).
16. Yamaguchi A. et al., Effect of Joule heating in current-driven domain wall motion, *Appl. Phys. Lett.* 86, 12511 (2005).
17. Kläui, M. et al., Controlled and reproducible domain wall displacement by current pulses injected into ferromagnetic ring structures, *Phys. Rev. Lett.* 94, 106601 (2005).
18. Kläui, M. et al., Direct observation of domain-wall configurations transformed by spin currents, *Phys. Rev. Lett.* 95, 26601 (2005).

19. Laufenberg, M. et al., Temperature dependence of the spin torque effect in current-induced domain wall motion, *Phys. Rev. Lett.* 97, 46602 (2006).

20. Kazantseva, N. et al., Transition to linear domain walls in nanoconstrictions, *Phys. Rev. Lett.* 94, 37206 (2005).

21. Rothman, J. et al., Observation of a bi-domain state and nucleation free switching in mesoscopic ring magnets, *Phys. Rev. Lett.* 86, 1098 (2001).

22. Zhu X. et al., Construction of hysteresis loops of single domain elements and coupled permalloy ring arrays by magnetic force microscopy, *J. Appl. Phys.* 93, 8540 (2003).

23. Kläui, M. et al., Domain wall coupling and collective switching in interacting mesoscopic ring magnet arrays, *Appl. Phys. Lett.* 86, 32504 (2005).

24. McMichael, R.D. and Donahue M.J., Head to head domain wall structures in thin magnetic strips, *IEEE Trans. Mag.* 33, 4167 (1997).

25. Kläui, M. et al., Vortex formation in narrow ferromagnetic rings, *J. Phys.: Condens. Matter* 15, R985 (2003).

26. Heyderman, L.J. et al., Nanoscale ferromagnetic rings fabricated by electron-beam lithography, *J. Appl. Phys.* 93, 10011 (2003).

27. David, C. and Hambach, D., Line width control using a defocused low voltage electron beam, *Microelectron. Eng.* 46, 219 (1999).

28. Heyderman, L.J. et al., Fabrication of magnetic ring structures for Lorentz electron microscopy, *J. Magn. Magn. Mater.* 290, 86 (2005).

29. Stoehr, J. et al., Element-specific magnetic microscopy with circularly polarized x-rays, *Science* 259, 658 (1993).

30. Locatelli, A. et al., X-ray magnetic circular dichroism imaging in a low energy electron microscope, *Surf. Rev. Lett*. 9, 171 (2002).

31. Tonomura, A., Electron-holographic interference microscopy, *Adv. Phys.* 41, 59 (1992).

32. Dunin-Borkowski, R.E., Off-axis electron holography of patterned magnetic nanostructures, *J. Microsc.* 200, 187 (2000).

33. Nakatani, Y. et al., Head-to-head domain walls in soft nano-strips:a refined phase diagram, J. Magn. Magn. Mater. 290, 750 (2005).

34. Laufenberg, M. et al., Observation of thermally activated domain wall transformations, *Appl. Phys. Lett.* 88, 52507 (2006b).

35. Kläui, M. et al., Head-to-head domain-wall phase diagram in mesoscopic ring magnets, *Appl. Phys. Lett.* 85, 5637 (2004).

36. Vaz, C.A.F. et al., Multiplicity of magnetic domain states in circular elements probed by photoemission electron microscopy, *Phys. Rev. B* 72, 224426 (2005).

37. Kläui, M. et al., Magnetic states in wide annular structures, *J. Appl. Phys.* 99, 08G308 (2006).

38. Park, M. H. et al., Vortex head-to-head domain walls and their formation in onion-state ring elements, *Phys. Rev. B* 73, 94424 (2006).

39. Kläui, M. et al., Current-induced vortex nucleation and annihilation in vortex domain walls, *Appl. Phys. Lett.* 88, 232507 (2006).

40. Laufenberg, M. et al., Quantitative determination of domain wall coupling energetics, *Appl. Phys. Lett.* 88, 212510 (2006a).

41. Lau, J. W. et al., Energy barrier to magnetic vortex nucleation, *Appl. Phys. Lett.* 88, 12508 (2006).

42. Cowburn, R. P. et al., Single-domain circular nanomagnets, *Phys. Rev. Lett.* 83, 1042 (1999).

43. McCaig, M., *Permanent Magnets in Theory and Practice*, Pentech, London (1977).

44. Kläui, M. et al., Domain wall pinning in narrow ferromagnetic ring structures probed by magnetoresistance measurements, *Phys. Rev. Lett.* 90, 97202 (2003).

45. Faulkner, C.C. et al., Artificial domain wall nanotraps in $Ni_{81}Fe_{19}$ wires, *J. Appl. Phys.* 95, 6717 (2004).

MAGNETIC MICROSYSTEMS: MAG-MEMS

ORPHÉE CUGAT, JÉRÔME DELAMARE, GILBERT REYNE
Laboratoire de Génie Electrique de Grenoble LEG / G2ε-Lab, BP46, 38402 St Martin d'Hères, Cedex, France

Abstract. Magnetic interactions offer outstanding performances and provide the base for powerful and efficient Magnetic Micro-Electro-Mechanical Systems (Mag-MEMS). The strong points of magnetic interactions are presented: high energy density and force density, stable forces without power supply, remote actuation, levitation, high-efficiency electrical generation, etc. In the first section, the scale reduction laws are described: in general they are highly favourable to magnetic interactions, particularly, where permanent magnets are involved. As an added bonus, extreme current densities are admissible in integrated μ-coils: this further improves force density in current-driven devices. In the second section, the basic components of Mag-MEMS are reviewed; technological processes and specifications are only briefly explored here, as they are fully covered in other chapters (μ-magnets, μ-coils, 'active' magnetic materials). In the third section, a panorama of applications of Mag-MEMS is explored: switches, motors, generators, commutators, scanners, sensors, etc. Illustrative examples are taken from state-of-the-art research prototypes and preindustrial devices, developed within the Grenoble MEMS and magnetism community.

Keywords: Magnetic microsystems; MEMS, Mag-MEMS; Power-MEMS; scale reduction laws; electromagnetic forces; μ-motor, μ-generator; μ-switch

PART I: BASIC PRINCIPLES AND SCALING LAWS FOR MAG-MEMS

1. Introduction

1.1. MAG-MEMS

Magnetic interactions offer outstanding performances and provide the base for powerful and efficient Magnetic Micro-Electro-Mechanical Systems (Mag-MEMS). This work first explains how the main types of magnetic interactions evolve as dimensions are reduced. These interactions involve permanent magnets, electrical currents, and various magnetic materials. Many remain very effective during downscaling, a few are badly degraded, but most interestingly some of them improve greatly. Mag-MEMS therefore exhibit outstanding performances for powerful integrated electrical-to-mechanical energy conversion, and belong to the family of Power-MEMS. We have published detailed work on this topic in several publications.[1–4]

The main components of Mag-MEMS are μ-coils and μ-magnets. The μ-coils are well mastered by many laboratories around the world, and they come in

B. Azzerboni et al. (eds.), Magnetic Nanostructures in Modern Technology, 105–125.

numerous shapes and sizes (planar, spiral, multi-layered, solenoid, meander, etc). A full review of μ-coils is given in a further chapter by Gijs.

The main revolution will certainly be triggered by the rapid progress which we are currently witnessing in integrated, patterned thick-film permanent magnets compatible with MEMS technologies. Exciting developments are happening both in Europe and Japan, which will allow the fabrication of fully integrated Mag-MEMS with many potential applications. Gutfleish describes μ-magnets and their fabrication in a further chapter.

In addition to coils and magnets, a range of advanced magnetic materials, both passive (soft ferromagnetic alloys) and active (magnetostrictive, thermo-magnetic, multi-ferroic) allow for innovative configurations. Some of these exotic materials are dealt with in a further chapter by Grechishkine.

The diversity of structures and possible range of applications, including actuation through membranes, explains the many recent publications and the large scope of researches in the field, ranging from electrical μ-sources to μ-motors, μ-actuators, μ-switches, levitation, remote-controlled μ-objects. These projects promise applications to optical, electrical, RF, Telecom, fluidics or bio-medical, automotive and aerospace devices.

Some of the work developed in Grenoble with our local partners is described in the third section. These Mag-MEMS include planar μ-turbo-generators and μ-motors, ultrafast bistable μ-switches and deformable μ-mirrors for adaptive optics. One important characteristic of these novel devices is the use of integrated permanent magnets; another key feature is the very high current densities achievable in integrated μ-coils.

2. Scale reduction laws

2.1. HISTORICS

In this section, attention will be focused on downscaling laws.

MEMS, having originated from microelectronics, the first actuation of thin beams was electrostatic, aluminium conductors and electrodes being standard. Thermal bimorph actuation came later. Development of other actuation principles (electromagnetism, piezoelectricity, magnetostriction, SMA, etc.) was slower because basic components and specific materials are not standard. Magnetic interactions for MEMS were already mentioned in 1959 and 1983.[5,6]

As soon as MEMS were emerging, however, many articles stated boldly that electromagnetism had no future in the world of MEMS. Alas for Mag-MEMS, they were not written by electrical engineers, and were not even based on the direct and homothetic scale reduction of the most appropriate electrical machines which power our everyday macroscopic world. These articles referred to basic interactions between conductors in air or between a conductor in air and a piece of

iron. This gives easy theory, but in these specific instances downscaling effectively proves catastrophic, and even more so considering that the drastic evolution of essential parameters such as field gradients or current densities was not considered! Many recently published 'downscaling laws' still obviously favour electrostatics, considering electromagnetism in its less appropriate and less downscalable configurations.

However, in the past decade several articles have listed and compared the existing actuation principles for MEMS. Many general downscaling of different actuation for MEMS were neutral or pessimistic for magnetism while a rigorous electrical engineering approach did lead to very positive conclusions.[7] In the late 1980s, the first teams designed and promoted magnetic μ-actuators.[8,9] They wisely remarked that permanent magnets are vital to magnetic actuation but that unfortunately their integration yet needed to be mastered.[10] This is still one of the main obstacles today. Nevertheless the pertinence of magnetic interactions for MEMS has been progressively explored and demonstrated: many other works deserve to be read.[11–18]

Due both to the recently available permanent magnets and the dramatic increase in admissible current density in μ-coils, it is now demonstrated that downscaling actually results in more effective electromagnetic converters.

The mere idea that magnetic interactions could actually improve when downscaling is quite new and goes against the generally received dogma.

2.2. MAGNETIC INTERACTIONS

Simple calculations can be done for the downscaling of magnetic interactions involving permanent magnets, coils and soft ferro-magnetic materials, and currents induced by time-varying fields.[19] The results of these calculations are summarized in the sub-sections below, which list the effects of a scale reduction of factor 1/k on the basic magnetic interactions per unit volume (or per unit mass), and for a constant, conservative current density in the conductors.

2.2.1. *Interactions and downscaling at constant current density δ*

Electrical engineering clearly indicates, for simple energy considerations, that macroscopic devices (electrical engines and actuators which dominate the macroscopic world) are mainly composed of ferromagnetic materials (either iron or magnets). Hence, focus is put on scale reduction laws applied to such structures.

2.2.2. *Magnetic field radiated by magnets*

A magnet of volume v_1 and magnetic polarisation J_1 generates a scalar potential V in any point P located at a distance r. The magnetic field H is the local gradient

of the scalar potential V:

$$V_{(P)} = \frac{\nu_1}{4\pi\,\mu_0}\frac{\vec{J}_1.\vec{r}}{r^3} \qquad \overrightarrow{\mathrm{H}} = \overrightarrow{\mathrm{gradV}} \tag{1}$$

Homothetic miniaturisation (all dimensions reduced by the same factor $k = 10, 100, 1000$, etc) of a given magnet (constant material and polarisation J_1), conserves the magnetic field H generated by the magnet while the scalar potential $V(P)$ is divided by k. The relative geometrical distribution and the magnitude of the field map around a magnet are conserved after a scale reduction. The direct and remarkable consequence is that field gradients are multiplied by k! This has tremendous impact on interaction forces.

2.2.3. *Interactions between magnets and conductors*

Intuitively, one considers magnet forces on conductors. Homothetic downscaling of magnets conserves the field maps and amplitudes, and thus leaves Lorenz volume forces on conductors unchanged.

Obviously equivalent is to consider the forces of current-carrying conductors on magnets. The Biot and Savart law states that the magnetic field H created in a point P by a conductor of length dl and section S, carrying a current density δ (current I = δ.S) is:

$$\overrightarrow{\mathrm{H}}(\mathrm{P}) = \frac{1}{4\pi}\cdot\frac{\delta\cdot\mathrm{S}\cdot\overrightarrow{\mathrm{dl}}\wedge\overrightarrow{\mathrm{r}}}{\mathrm{r}^3} \tag{2}$$

Hence, a scale reduction of 1/k divides by k the field H generated by the conductors. The magnetic force F on the magnet derives from their magnetic interaction energy W_i:

$$\mathrm{W_i} = -\overrightarrow{\mathrm{J}}\cdot\mathrm{v}\cdot\overrightarrow{\mathrm{H}} \qquad \overrightarrow{\mathrm{F}} = -\overrightarrow{\mathrm{gradW_i}} \tag{3}$$

Scale reduction divides the energy W_i by k^4, and divides the force F by k^3: thus the force to weight (or force to volume) ratio does not change.

The direct consequence is that any device using a conductor/magnet interaction therefore works as well at small dimensions as it does at macroscopic dimensions. Please consider that most loudspeakers and many permanent magnet actuators fall in this category!

2.2.4. *Torque on a magnet due to an external field*

The torque experienced by a magnet of polarization J and volume v immersed in a homogeneous field H is proportional to M and H (where the magnetic moment $M = \nu \cdot J$). During the homothetic $1/k$ reduction, both H and J remain constant, thus the torque to volume ratio also remains constant.

2.2.5. *Interactions between magnets and magnets or iron*
As we have seen earlier, the magnetic field from a magnet downscales unchanged in amplitude and geometrical distribution. Hence, for magnet–magnet or magnet–iron interactions, Eq. (3) shows a decrease of the interaction energy W_i by k^3, but a decrease of the force F by k^2 only, which implies a relative increase by k of the force to volume ratio. This means that systems using the attractive or repulsive forces between magnets will greatly benefit from being downscaled: this includes latching, bearings, suspensions etc.

2.2.6. *Other magnetic interactions*
Similar calculations can be done for the magnetic interactions involving soft ferromagnetic materials combined to currents, interactions between conductors (including induction machines), and time-variation induced currents. They are described in detail by Delamare et al.[19] and in the upcoming, updated English version of Cugat.[1]

2.2.7. *Diamagnetism*
Diamagnetism and its associated effects such as passive, stable levitation are among the great winners of miniaturization.[20] The volumic forces generated by a permanent magnet on a magnetized element are proportional to the local field gradient multiplied by the magnetisation of the body. For diamagnetic bodies (such as a piece of carbon or a drop of water for example), the magnetisation is induced by the magnetic field to which it is submitted. This induced magnetisation is directly proportional to the field. We have seen earlier that when a permanent magnet is downscaled by a factor 1/k, the magnitude of the field around it is conserved, but the gradients are multiplied by k. Therefore, in a downscaled permanent magnet/diamagnetic body configuration, the associated diamagnetic body keeps the same induced magnetisation because it is submitted to the same magnetic field, but it experiences a force which is multiplied by k because the field gradients themselves are multiplied by k!

2.2.8. *Intermediary conclusions*
The first conclusions, for a scale reduction of 1/k, and keeping a conservative constant current density, are as follows:

- The main magnetic interactions benefit from scale reduction
- Most efficient magnetic interactions involve permanent magnets
- Magnet–magnet or magnet–iron volume forces increase as k
- Diamagnetic forces increase as k

- Magnet-currents interactions, when effective on a macroscopic scale, remain as effective once miniaturized
- Inductive effects are to be avoided

2.3. CURRENT DENSITY

In the macroscopic world, the current density in conductors is limited to 3–5 A/mm^2, and about 50 A/mm^2 for short-time use (starter motors of cars for example). This is mainly due to thermal overheating and limitations in cooling. In the microscopic world, however, thermal downscaling allow densities of 10^3–10^5 A/mm^2, and sometimes up to10^6 A/mm^2. Indeed, while Joule conduction losses are intrinsically volumic, the heat flow (used for cooling) is proportional to the exchange surfaces and inversely proportional to the distances through which the heat flows. Hence, heating scales as k^3, while heat flow dissipated by conduction scales as k^2/k, i.e. as k. For a same temperature, volumic Joule losses can therefore theoretically increase by $k^3/k = k^2$. These Joule losses being proportional to the square of the current density, the admissible current density can theoretically increase as k. Hence downscaling a μ-coil by 1/k can be done with an increase of k in the admissible current density.

It is worth noting that this is equivalent to a constant surface current density or, in other words, that both magnets and coils can downscale the same way. Since forces and energies are proportional either to this density or to the square of this density, this deeply boosts scale reduction laws.

Furthermore, additional positive factors contribute to increase even further the admissible DC current densities:[21]

- The small volume to surface ratio of μ-coils (planar geometry)
- The direct contact with good heat-conducting substrates (Si)
- The use of pulsed currents

As a consequence, μ-coils can withstand very high current densities: generally between $10^3$and 10^5 A/mm^2, while some extreme cases report up to 1 million A/mm^2 for very short pulses.[22]

However, despite the huge benefits that can be extracted from this fact, it remains that such increases of current densities and the associated thermal losses reduce the overall efficiency and the device, thus reducing its autonomy (if used on batteries), and requires adapted heat sinks. These by-effects are the practical limiting parameters in the design and operation of real-life Mag-MEMS.

The actual increase in admissible current density is therefore very variable and depends greatly on the real working conditions.

2.4. CONCLUSIONS

With admissible current densities increasing as k, and μ-magnets as good as macroscopic magnets, the conservative downscaling laws are thus significantly modified. The conclusions are outstanding:

- All magnetic interactions benefit from scale reduction
- Efficient magnetic interactions in small-dimension devices generally involve permanent magnets
- Magnet/magnet (and magnet/iron) force per volume increases as k
- Current–magnet interactions remain as effective in MEMS as at the macroscopic scale
- Admissible current densities can theoretically increase by k
- Current/magnet force per volume can be increased by k
- Magnet-to-coil induction benefits from the increase of speed and frequencies when downscaling
- Coil/coil inductive effects decrease, resistances increase and inductances decrease, and thus inductive machines without permanent magnets should be avoided.

Summary of downscaling for various types of forces

Down-scaling:	/k
Volume, mass, or gravity force	$/k^3$
Heat flow dissipated by conduction	/k
Electrostatic forces	$1/k^2$
Admissible current density (at constant temperature)	X k
Most magnetic interactions	$1/k^2$
Force/volume for most magnetic interactions	X k

PART II: BUILDING BLOCKS FOR MAG-MEMS

3. Building blocks

3.1. μ-COILS

Many magnetic μ-sensors, as well as RF transmission antennae, use μ-coils; similarly, Mag-MEMS require them to generate variable fields and forces. A first panorama is given in;[24] a full review of μ-coils is given in a further chapter by Gijs.

3.1.1. *Equivalence between a permanent magnet and a coil*

A permanent magnet is equivalent to a coil with a constant surface current density (Amperian current model). In other words, if you want to produce the same magnetic field as a permanent magnet but using a coil instead, you need to inject a volumic current density in the coil which is inversely proportional to its dimension. This means that, the equivalent volumic current density in the competing μ-coil must increase as k in order to keep up with permanent μ-magnets which magnetisation would be as good as in bulk (i.e. about 1 Tesla for rare-earth magnets in general).[3,21] Although we have seen that the admissible current density in coils actually does increase in the same proportion, this means that μ-coils can theoretically compete with μ-magnets. However, keep in mind that this must be paid for by an increase in thermal losses and a decrease in energy efficiency. As a consequence, μ-magnets will be favoured every time that it is not necessary to use a coil, i.e. for the generation of static magnetic fields and forces.

3.2. μ-MAGNETS

Efficient Mag-MEMS require the integration of high quality permanent magnets. The most common and most powerful μ-magnets currently used in Mag-MEMS are individually μ-machined from bulk Nd-Fe-B or Sm-Co magnets (generally using wire electro-discharge machining). However, this method is hardly compatible with full integration or batch fabrication.

Many other ways to obtain μ-magnets for Mag-MEMS are being developed. These methods all provide good results, but each suffers from some limitation.[25]

Some techniques are well adapted to μ-fabrication (electroplating of Co-Pt, screen-printing of bonded powders) but the resulting magnetic properties are relatively poor compared to bulk REPMs.[26] Other techniques give excellent magnetic properties as sputtering,[27] pulsed laser deposition,[28] low pressure plasma spraying,[29] or direct sintering,[30] but either the thickness of the deposited layer is too thin, or the process is difficultly adaptable to micro-technology and batch fabrication (high deposition temperature, chemical pollution, slow deposition rate, small deposition surface, etc.). An important aspect currently emerging is the patterning

of thick magnet films.[31,32] Optimal magnetic orientation of μ-magnets is also studied.[17] Is the dream of low temperature electroplated high quality rare-earth permanent magnets achievable?[33] However, the perfect candidate for cheap, compatible and fast integration of thick patterned layers of good quality μ-magnets remains to be found. Recently, technologies have improved rapidly and breakthroughs in this critical field are at last on their way.[34]

Based on the outstanding potential of the sputtering process developed by the Moscow Institute of Steel and Alloys (MISA) to produce high quality magnets for Mag-MEMS,[35,36] a triode sputtering machine with a high deposition rate (≈20 μm/h) has been recently developed at Laboratoire Louis Néel (LLN) by Kornilov and Dempsey.[34] In preliminary experiments, some of the main results of the MISA group have been reproduced: coercive, highly anisotropic NdFeB thick films of up to 100 μm have been deposited.

A full review of μ-magnets is given in a further chapter by Gutfleish.

3.3. EXOTIC MATERIALS AND HYBRIDATION

The major drawbacks of magnetic actuation are the by-effects arising from the relatively high currents involved in conventional magnetic actuation: the Joule losses in conductors imply overheating which may call for cooling techniques, but also energy wastage. One may dream to overpass these problems by exploring other ways to modify magnetic fields in order to obtain magnetic actuation. This may be achieved by using exotic materials:

- Thermal demagnetization of a ferromagnetic material[37]
- Magnetic 'reprogramming' of semi-hard materials by demagnetization and remagnetization[38]
- Thermal switching of ferrimagnetic and anti-ferromagnetic materials[39]
- Thermal reorientation of permanent magnets[39]
- Strain-induced modulation of the magnetization of a magnetostrictive material, by hybridization with a voltage-actuated piezoelectric element[40]
- Superconducting films can be used for levitation (Meissner diamagnetic effect) and HTSC may be a future possible solution for magnetizing Mag-MEMS for specific applications (space, cryogenic systems, etc.),[41]

Nevertheless, the use of specific magnetic materials in thin or thick films and their integration is quite new, and only a handful of articles report experimenting with the potential application to Mag-MEMS. Many specific challenges still lay ahead. Materials scientists should continue to develop and improve thick-film patterned permanent magnets and other relevant materials, which must be compatible with integrated microtechnologies.

4. Additional features of Mag-MEMS

In addition to high energy and force densities, electromagnetism presents other advantages (and obviously drawbacks) for the actuation of MEMS.[3]

4.1. PERMANENT FORCES – BI-STABILITY – SUSPENSIONS

Permanent magnets provide constant magnetic fields. Hence, simple latching or bi-stability is achievable without the need for any power supply. This ensures energy savings while it also guarantees safety in case of power failure.[42,43] Bi-stability combines particularly well with pulsed-switching currents. Such permanent forces can also be implemented into passive magnetic suspensions/bearings, providing an elegant solution to the problem of friction in MEMS.[44,46]

4.2. LONG-RANGE, REMOTE, OR WIRELESS ACTUATION

- Magnetic fields and gradients can be effective over long distances relatively to the size of MEMS. This allows large-throw and/or wide-angular actuators.
- Contactless magnetic interaction allows remote actuation through sealed interfaces allowing wireless actuation or vacuum packaging of resonant systems for high Q factors (no air viscosity dampening). Furthermore, remote actuation through sealed interfaces makes magnetic actuators very well suited to harsh environment (e.g. ABS sensors) or for medical applications, through the skin.
- External magnets or macro-coils can be added to power the microsystem thus avoiding integration of supply and most by-effects such as embedded batteries or wire connections. In some cases, this considerably simplifies fabrication.[47]
- This latter characteristic is unique and deserves to be used for medical applications with implanted wireless Mag-MEMS actuated at a distance by external fields which can be generated by classical electromagnets or hand-held permanent magnets.[48]

5. Design and optimization tools

Electromagnetism cannot be handled intuitively, especially at very low scales for which expertise is only presently being capitalized. For this reason, design and optimisation tools must provide rapid and adaptive solutions to the many potential devices needed: this implies analytical models and derivation tools which take into account the exact models of electromagnetic actuation (field, gradient, force, torque, stiffness, etc.), as well as the specificity of the planar

dimensions of MEMS. All the Mag-MEMS presented in the last section of this chapter have largely benefited from specific design and optimisation tools (mainly CDI_Optimizer and pro@Design) developed in LEG.[49–51]

The need for such specific tools cannot be over-emphasized. Furthermore, they provide automatic programming of dedicated design/optimisation software specifically generated for each new idea or structure.

6. Conclusion

Electromagnetic interactions deserve a larger interest from the MEMS community. Mag-MEMS offer large forces, large strokes, remote or distance control, bi-stability, robustness, high energy conversion efficiency, etc. all with great potential for new devices in many domains of applications.

The huge current densities experimentally reported at small scales (10^4 to 10^6 A/mm^2) have been theoretically justified. These, together with the recent development of high-performance magnet thick films, and specific power supplies, may soon greatly promote the development of Mag-MEMS and convince the industry to rely on them.

The old controversy on downscaling has dramatically changed, due to progress in μ-fabrication technologies, new available μ-magnets, and recent breakthroughs on the sustainable current densities at the micro-scale: not only does magnetism already dominate the macro-world, but it scales down very well to the micro-world and, possibly, the nano-world.

PART III: EXAMPLES OF MAG-MEMS PROTOTYPES

7. Context

In the previous sections we have described the downscaling laws for magnetic interactions, the basic principles of actuation, and the building blocks for Mag-MEMS.

Magnetic μ-sensors are already well established in commercial products (HDD read heads, fluxgates, RF transmission coils, ABS sensors, etc.). However, despite their growing visibility only a handful of Mag-MEMS have so far reached industrial production. Laboratory-developed prototypes include RF μ-switches for mobile phones, read/write heads and μ-position systems, optical μ-cross-connect for fibre optic networks, μ-scanners, μ-motors for less-invasive surgery or μ-robotics, μ-pumps or μ-valves for lab-on-chip and μ-fluidic devices, electrical μ-generators for autonomous power supplies, μ-mirrors for adaptive optics, μ-scanners for retinal scanning displays, magnetic suspensions for hard disk drives, etc.

8. Prototypes

A few Mag-MEMS are now briefly presented. They were developed in Grenoble, benefiting from the rich academic and R&D environment and our close partnership with LETI-CEA and Institut Néel and within MINATEC among others. The full details can be found in the associated bibliography.

8.1. PLANAR SYNCHRONOUS μ-MOTORS AND μ-GENERATORS

A family of rotating synchronous μ-motors and μ-generators has been developed, based on highly-efficient three-phase Si, double layers of 20 μm thick Cu coils realized in LETI[52] (Fig. 1). The disk rotors are micro-machined from bulk SmCo magnet and magnetized into 8 or 15 pairs of poles[53] (Fig. 2).

In motor mode with ruby bearings; about 100 μNm is available at 100,000 rpm. The μ-motors were driven at over 275,000 rpm in brushless mode on hybrid magneto-pneumatic bearings.[54]

In generator mode, the planar machine (driven by a dentist turbine) converts about 5 W of electrical power at 400,000 rpm,[55] with an efficiency conversion of over 66% (Fig. 3).

The dedicated low-voltage electrical rectifier and converter was integrated into a fully integrated CMOS chip.[56]

The low output torque of the integrated etched turbine greatly limits the speed and the output power of the all-in-one turbo generator. For high-speed trials a dentist turbine was used. In collaboration with ONERA and Silmach, work is in

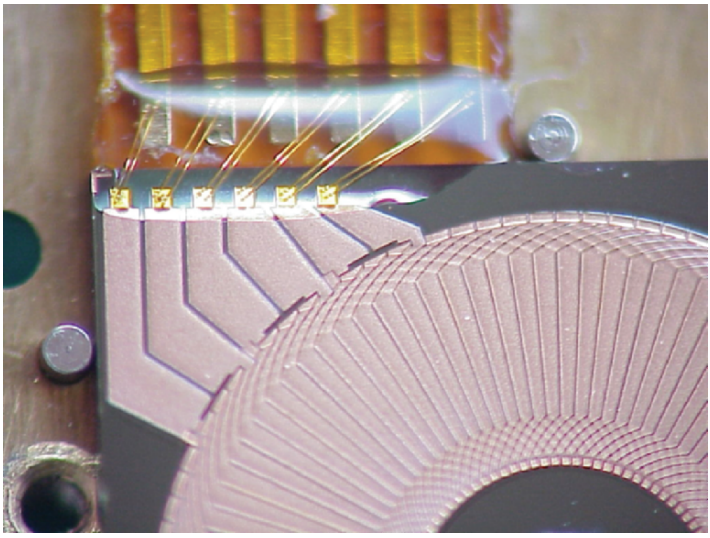

Figure 1. Three-phase Si integrated ø 8 mm stator coils (fab. LETI)

Figure 2. Bulk micro-machined NdFeb rotor with etched planar turbine

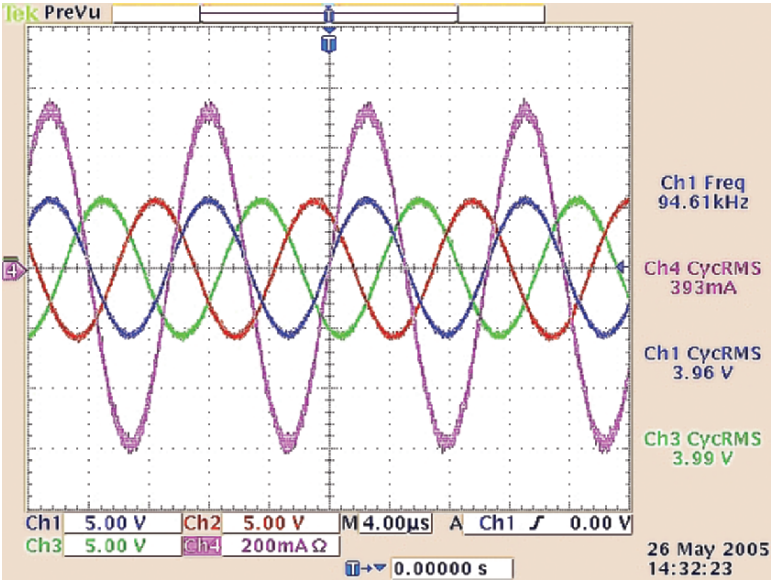

Figure 3. Three-phase output signals at 385 000 rpm on a 5 W electric load

progress to integrate a high-efficiency Si-machined planar turbine into the prototype, which will use combustion gases from a low-temperature burner.

Other μ-generator projects include Prof. MG Allen's team at Georgiatech[57] for high-power levels, as well as Holmes's at Imperial College London[58] for low power.

8.2. μ-SWITCHES WITH LEVITATING MOBILE MAGNET

This novel family of devices was developed by LEG and LETI.[59] It is an innovative principle exploiting fully integrated, mobile permanent magnets.

8.2.1. *Ultra-fast planar bistable μ-switch*

The switching magnet is free-levitating (no mechanical guide or spring) between a pair of fixed magnets. The use of permanent magnets ensures both its bi-stability (without power supply) and the magnetic guidance during switching, which is controlled by low-voltage (<1 V) current pulses (Lorenz forces). Depending on the dimensions and due to the high force to volume ratio, the system can withstand shocks of up to a few thousand G. It may be used as an electrical μ-switch, as well as in MOEMS, RF, or μ-fluidic applications. Transformation into a bi-stable electrical switch configuration only requires an additional layer of Cu conductors connecting the pairs of fixed magnets which also act as open/closed contact areas (Fig. 4). The CoPtP alloy μ-magnets are patterned during electroplating. First trials indicate switching times of 30 μs and actuation energy of 50 μJ per pulse.

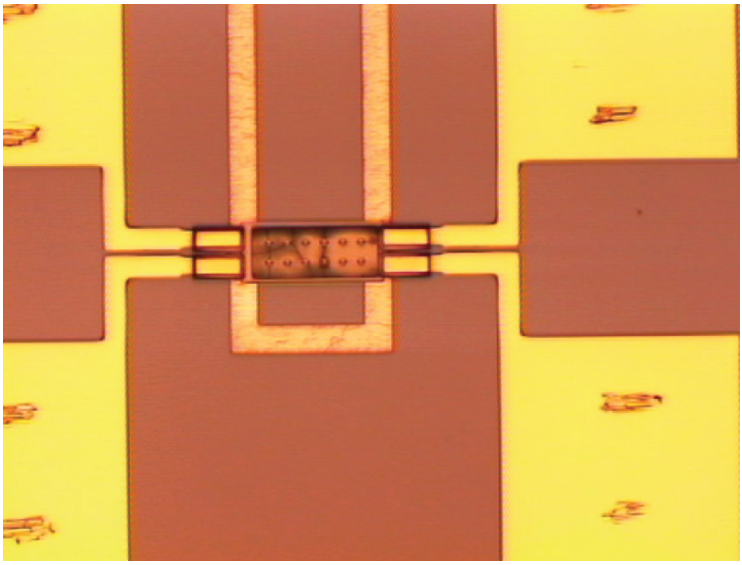

Figure 4. Top view of bi-stable μ-switch for electrical signals. Mobile length ca. 250 μm

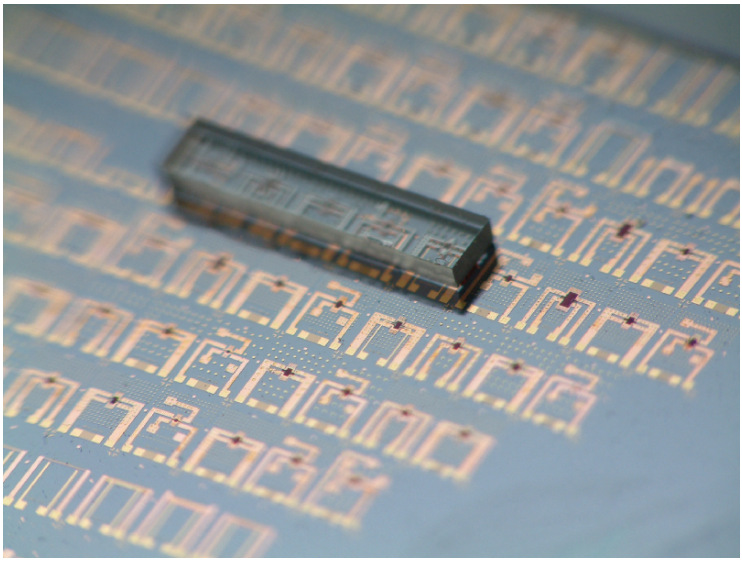

Figure 5. Out-of-plane bi-stable μ-switch – bottom waffer = Si; top waffer = glass. Glass waffer dimensions 5 × 1.5 × 0.5 mm

8.2.2. *Out-of-plane bistable μ-switch*

A patented, out-of-plane version of this bi-stable μ-switch has also been designed and built. The out-of-plane configuration allows for larger displacements (>100 μm). The bottom wafer is similar to the previous in-plane prototype; a glass wafer containing symmetrical conductors and fixed magnets is assembled on top of the bottom wafer, thus encapsulating the mobile magnet (Fig. 5).

The geometry and thus the technological fabrication steps are more complex, as well as the design and optimisation which take into account the stability. Full details of the flip-chip design are provided in the full paper.[60]

Specific conductor geometry allows for pulsed switching currents of up to 30,000 and 90,000 A/mm^2; however, great reductions in the required switching currents were obtained using the optimisation software CDI_Optimizer and pro@Design,[49,50] and switching occurs within 300 μs with current pulses as low as 300 mA.

8.3. OPTICS

8.3.1. *Deformable magnetic mirror for astronomy and ophthalmology*

Ground-based telescopes suffer from atmospheric turbulences which perturb the quality of the light arriving from space. Astronomers use adaptive optics in order to correct the wavefront of oncoming light. In this context, a first prototype of electromagnetic miniature (ø 50 mm) deformable mirror was developed, using micro-technologies available at IEMN in Lille and LPMO in Besançon.[61]

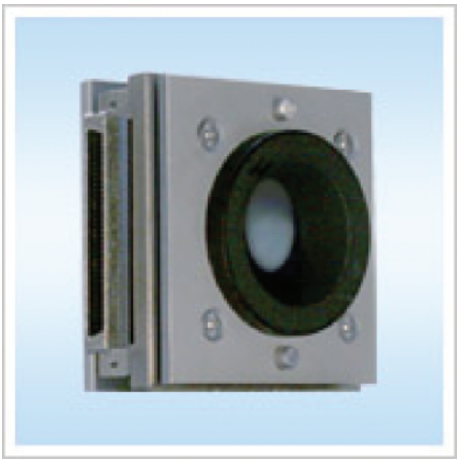

Figure 6. Prototype 50 mm deformable mirror for ophtalmology and astronomy

The first mirrors were composed of a thin polymer membrane (2–5 μm) onto which was glued a matrix of permanent μ-magnets, and an array of planar μ-coils on a ø 50 mm substrate facing the membrane. The second generation of mirrors uses 10 μm thick Si membranes developed at LETI, and mechanically wound coils (Fig. 6).

The behaviour of the mirror allows deformations of up to 100 μm with currents in the range 1 ± 3 A. Good linearity of the deformation is observed up to 200 Hz, and best-flat down to a few nanometre is achieved. The devices are now commercialized by Imagine-Optics and Imagine-eyes, for both astronomy and ophthalmology applications.[62,63] The magnetic actuation allows for smaller pixels and more compact mirrors with huge dynamics and fast response.

8.3.2. *Other Mag-MEMS*

Many other optical Mag-MEMS can be found in the literature. Most of them are magnetically activated mirrors for scanners and fibre optic switching.[64–66]

9. Other potential applications

We have described here only the Mag-MEMS developed in Grenoble. Within the last decade, a great number of articles have been published describing many prototypes of Mag-MEMS with applications in a wide range of domains. The reader is encouraged to explore in depth and width the many excellent journals and conference proceedings, among which the following ones are noteworthy:

Journals:

- Journal of Micro Electro-Mechanical Systems (JMEMS)
- Journal of Microsystems and Microtechnology
- Sensors and Actuators A

Conferences:

- MEMS
- Actuator
- Transducers
- Intermag
- MME, EMSA, Mecatronics

10. Power supplies, control, cooling

While electrostatic actuators use 'high' voltages and low currents, Mag-MEMS require 'high' currents and low voltages. Current pulses, if used, need faster control. Hence, final performances highly rely on working conditions and development of appropriate integrated supplies and coolers.

Also, for μ-sources, specifically dedicated power-electronics is required in order to make use of the often low-voltage, sometimes erratic energy and power levels produced by μ-generators. Recent work on a converter for the above mentioned μ-turbo generator has yielded excellent results.[56]

11. Conclusion

Electromagnetic interactions deserve a larger interest from the MEMS community. Mag-MEMS offer large forces, large strokes, remote or distance control, bi-stability, robustness, etc. all with great opportunities for new devices in many domains of applications. The fantastic current densities available at small scales, together with the development of magnet thick films, specific supplies and coolers should soon greatly promote the development of Mag-MEMS.

Acknowledgement

This work was mainly funded by the CNRS and the French Ministry for Higher Education and Research, the French Ministry for Defense DGA, and the ELESA Federation of INPG laboratories.

References

1 μ-ACTUATORS, MAG-MEMS, AND SCALING LAWS

1. O. Cugat (ed.), *Microactionneurs electromagnétiques - MAGMAS*, Hermès/Lavoisier, (in French), ISBN 2-7462-0449-5 (2002).
2. O. Cugat, J. Delamare, and G. Reyne, MAGnetic Micro-Actuator & Systems MAGMAS, *IEEE Trans. Magnetics,* 39(6), 3608–3612 (2003).
3. G. Reyne, J. Delamare, and O. Cugat, Magnetic μ-actuators (Mag-MEMS), *Encyclopedia of Materials: Science and Technology Update Online (EMSAT)*, Elsevier, ISBN: 0-08-043152-6 (2004).
4. O. Cugat, G. Reyne, J. Delamare, and H. Rostaing, Novel magnetic μ-actuators and systems (MAGMAS) using permanent magnets, *Sensors Actuators A* 129, 265–269 (2006).
5. R.P. Feynman, There's plenty of room at the bottom, *American Phys. Soc*. 26 December 1959, reprint *J. MEMS,* 1(1), 60–66 (1992).
6. R.P. Feynman, Infinitesimal machinery, Jet Propulsion Lab., 23 February 1983, *J. of MEMS,* 2, 4–14 (1993).
7. M. Jufer, Size limits and characteristic influence of electro-magnetic actuators, *Proc. 4th International Conference on New Actuators*, Bremen, Germany, pp. 390–393, (1994).
8. B. Wagner and W. Benecke, Magnetically driven μ-actuators: design considerations. *Microsystem Technologies*, Springer-Verlag, Berlin (1990), p. 838.
9. H. Guckel et al., Fabrication and testing of the planar magnetic micromotor.*J. Micromech. Microeng*. 1, 135–138 (1991).
10. H. Guckel, Progress in electromagnetic actuators, *Proc. 4th International Conference on New Actuators*, Bremen, Germany, 45–48 (1996).
11. Z. Nami, C. Ahn, and M.G. Allen, An energy-based design criterion for magnetic micro-actuators. *J. Micromech. Microeng.* 6, 337–344 (1996).
12. I.J. Busch-Vishniac, The case for magnetically-driven micro-actuators, *Sensors Actuators A* 33, 207–220 (1992).
13. W. Trimmer, Microrobots and micromechanical systems, *Sensors Actuators A* 19(3), 267–287 (1989).
14. J.H. Fluitman and H. Guckel, Micro-actuator principles, *Proc. 4th International Conference on New Actuators*, Bremen, Germany, 23–28 (1996).
15. D.K. MacKay and R.D. Findlay, An examination of the scaling properties of electric micromotors and their magnetic duals, *IEEE 5th International Conference on Electrical Machines and Drives, London, UK, 11–13 September* 170–174 (1991).
16. W. Benecke, Scaling behavior of μ-actuators, *Proc. 4th International Conference on New Actuators, Bremen, Gemany*, 19–24 (1994).
17. A. Kruusing, Actuators with permanent magnets having variable in space orientation of magnetization. *Sensors Actuators A* 101, 168–174 (2002).
18. G. Reyne, J. Delamare et al., Chapter 1 in ref. 1.
19. J. Delamare, G. Reyne et al., Chapter 2 in ref. 1.
20. G. Reyne et al., Diamagnetism and MEMS (in preparation).

2 μ-COILS AND CURRENT DENSITY

21. G. Reyne et al., Chapter 3 in ref. 1
22. H. Rostaing, J. Stepanek, M. Audoin, C. Dieppedale, and O. Cugat, High Current Densities in Magnetic μ-Actuators, *Journal of MEMS* (submitted).
23. K. MacKay, M. Bonfim, D. Givord, and A. Fontaine, 50 T pulsed magnetic fields in microcoils, *J. Appl. Phys*. 87(4), 1996–2002 (2000).
24. S. Basrour, Chapter 4 in ref. 1.

3 μ-MAGNETS

25. N. Kornilov et al., Chapter 5 in ref. 1.
26. G. Zangari et al., Magnetic properties of electroplated Co-Pt films. *J. Mag. Mag. Mat.* 157–158, 256–257 (1996).
27. Y.L. Linetsky and N. Kornilov, Structure and magnetic properties of sputtered Nd-Fe-B alloys. *J. Mat. Eng. Perform.* 4(2), 188–195 (1995).
28. F.J. Cadieu et al., High coercivity Sm-Co based films made by pulsed laser deposition. *J. Appl. Phys.* 83–11, 6247–6249 (1998).
29. G. Rieger et al., Nd-Fe-B permanent magnet (thick films) produced by a vacuum-plasma-spraying process, *J. Appl. Phys*. 87(9), 5329 (2000).
30. F. Yamashita et al., Preparation of thick-film Nd-Fe-B magnets by direct Joule heating, *Proc. REM XVII* 668–674 (2002).
31. T. Budde and H.H. Gatzen, Patterned sputter deposited Sm-Co films for MEMS applications. *J. Magn. Magn. Mater.* (April 2002).
32. B. Pawlowski and J. Töpfer, Permanent magnetic NdFeB thick films, *J. of Mater. Sci.* 39(4), 1321–1324 (2004).
33. M. Schwartz et al., Thin film alloy electrodeposits of transition rare-earth metals from aqueous media. *Electrochem. Soc. Proc*. 98(20), 646–659 (1998).
34. N.M. Dempsey, N.V. Kornilov, and O. Cugat, Thick hard magnetic films for Mag-MEMS: some key issues, *High Performance Magnets & Applications - Mag-MEMS, Annecy, France, September 2004*, pp. 779–782 (2004).
35. N.V. Kornilov, Sputtered Nd-Fe-B Thick Films: Technology, Properties, Texture, *La Revue de Métallurgie, SF2M - JA 99 Paris*, 85–90 (1999).
36. A.S. Lileev, A.A. Parilov, and V.G. Blatov, Properties of hard magnetic Nd-Fe-B films vs different sputtering conditions, *J. Magn. Magn. Mater.* 242–245, 1300–1303 (2002).

4 EXOTIC MATERIALS

37. Hashimoto et al., Thermally controlled magnetization actuator using thermosensitive magnetic materials, *MEMS*, 108 (1994).
38. Nagaoka et al., Micro-magnetic alloy tubes for switching and splicing single mode fibres, *MEMS*, 86 (1991).
39. R.M. Grechishkin, M.S. Kustov, O. Cugat, J. Delamare, G. Poulin, D. Mavrudieva, and N.M. Dempsey, Thermo-reversible permanent magnets in the quasi-binary GdCo5-xCux system, *Appl. Phys. Rev.* (2006).

40. T. Ueno, J. Qiu, and J. Tani, Self-sensing magnetic force control by composite element of giant magnetostrictive and piezoelectric materials, *Movic, Saitama, Japan*, August (2002).
41. T. Iizuka and H. Fujita, Precise positioning of a micro-conveyer based on superconducting magnetic levitation, *IEEE Symp. on Micromechatronics and Human Sci.* 131–135 (1997).

5 LATCHING, REMOTE ACTUATION, LEVITATION

42. K. Fisher et al., A latching bistable optical fiber switch combining LIGA technology with micro-machined permanent magnets. *Proc. Transducers*'01 (2001).
43. M. Ruan, J. Shen, and C.B. Wheeler, Latching micromagnetic relays. *J. MEMS* 10(4), 511–517 (2001)
44. M. Klöpzig, A novel linear μ-machined electromagnetic actuator including magnetic suspension, *Proc. 4th International Conference on New Actuators* 548–551 (1998).
45. O. Cugat, V. Fernandez, D. Roy, G. Reyne, and J. Delamare, Miniature permanent magnet bearings: application to planar micromotors. *Proc. Europe-Asia Conference Mecatronics* (1996).
46. J. Stepanek, H. Rostaing, S. Lesecq, J. Delamare, O. Cugat, Position control of a levitating magnetic actuator. Applications to microsystems, *Proc. Prague World Conf. Intl. Feder. Automatic Control* (2005).
47. C.H. Ji, Y.K. Kim, Experiments on electromagnetic micromirrorArray with Bulk Silicon Mirror Plate and Aluminum Spring, *Proc. Transducers* (2001).
48. W. Lüdemann, S.K. Rosahl, J. Kaminsky, and M. Samii, Reliability of a new adjustable shunt device without the need for readjustment following 3-Tesla MRI, *Childs Nerv. Syst.* 21(3), 227–229 (2005).

6 DESIGN AND OPTIMIZATION

49. B. Delinchant, J. Stepanek, L. Rakotoarison, J. Delamare, O. Cugat, and F. Wurtz, Capitalizing on computation tools to improve design and knowledge sharing of magnet-based devices, *High Perf. Magnets & Appl. - Mag-MEMS*, *Annecy, France, September 2004*, pp. 900–903, (2004).
50. B. Delinchant, F. Wurtz, and E. Atienza, Reducing sensitivity analysis time cost of compound model, *IEEE Trans. Magn. MAG* 40(2), 1216–1219 (2004).
51. H.L. Rakotoarison, F. Wurtz, J. Stepanek, B. Delinchant, and O. Cugat, Integration of the volume segmentation method into an optimization process. Application to the sizing of a micro-actuator for deformable mirrors, *IEEE Trans. Magn. MAG* - 42(4), 1163–1166 (2006).

7 MOTORS

52. P-A. Gilles, O. Cugat, J. Delamare, C. Divoux, and V. Fernandez , Three-phase coil for planar brushless μ-motor, *Actuator* 181–184 (2000).
53. P-A. Gilles, J. Delamare, and O. Cugat, Rotor for a brushless micromotor, *J. Magn. Magn. Mater.* 1186–1189 (2000).
54. N. Achotte, P.-A. Gilles, O. Cugat, J. Delamare, P. Gaud, and C. Dieppedale, Planar brushless magnetic μ-motors, *J. MEMS* 15(4), 1001–1014 (2006).

8 GENERATORS

55. H. Raisigel, O. Cugat, and J. Delamare, Permanent magnet planar μ-generators, *Sensors Actuators A*, 130–131, 438–444 (2006).
56. H. Raisigel, J.-C. Crébier, Y. Lembeye, O. Cugat and J. Delamare, Integrated μ-rectifier for μ-sources, *Proc. ISPS 2006, Prague, Sept. 2006*.
57. D.P. Arnold, S. Das, F. Cros, I. Zana, M.G. Allen, and J.H. Lang, Magnetic induction machines integrated into bulk-micromachined silicon, *J. of MEMS* 406–414 (2006).
58. A.S. Holmes, Guodong Hong, and K.R. Pullen, Axial-flux permanent magnet machines for μ-power generation, *J. MEMS* 54–62 (2005).

9 SWITCHES

59. C. Dieppedale, B. Desloges, H. Rostaing, J. Delamare, O. Cugat, and J. Meunier-Carus, Magnetic bistable μ-actuator with integrated permanent magnets, *IEEE Sensors 2004, Vienna, October 2004* 493–496.
60. Rostaing H, Stepanek J, Cugat O, Dieppedale C, and Delamare J, Magnetic, Out-of-plane, Totally integrated bistable μ-actuator, *Proc. Transducers* '05, 2, 1366–1370 (2005).

10 OPTICAL

61. O. Cugat, S. Basrour, C. Divoux, P. Mounaix, and G. Reyne, Deformable magnetic mirror for adaptive optics: technological aspects, *Sensors Actuators A* 89, 1–9 (2001).
62. Available at: www.imagine-optics.com
63. Available at: www.imagine-eyes.com
64. G. Reyne, Electromagnetic actuation for MOEMS, Examples, advantages and drawbacks of Mag-MEMS. *J. Magn. Magn. Mater.* 242–245, 1119–1125 (2002).
65. J. Bernstein, and W. Taylor et al., Electromagnetically actuated mirror arrays for use in 3D optical switching applications, *J. of MEMS* 13(3), 526–535 (2004).
66. Y. Jun, S. Luanava, and V. Casasanta, Magnetic actuation for MEMS scanners for retinal scanning displays, *SPIE Proc. 4985 MOEMS Displays and Imaging Systems* (2004).

MEMS INDUCTORS: TECHNOLOGY AND APPLICATIONS

MARTIN A. M. GIJS
Ecole Polytechnique Fédérale de Lausanne,
Institute of Microelectronics and Microsystems,
CH-1015 Lausanne, Switzerland

Abstract. We expose the past and present state-of-the-art of Micro-ElectroMechanical System (MEMS) inductors. Starting from the basic inductor equations, we discuss the various material and frequency-dependent loss mechanisms that contribute to a decreasing quality factor of an inductive component. We then discuss the most commonly developed inductor geometries: the planar, solenoidal, and stripe inductor. Subsequently, we highlight various techniques to realize RF inductors for operation at GHz frequencies and their integration directly on silicon substrates. We also explain how cheap packaging technologies can be used to realize inductive components that interface directly with silicon chips or can be used for high-sensitivity magnetic field and current sensors. We finally discuss technologies for the realization of power inductors.

Keywords: Inductor; RF-MEMS; inductor losses; solenoid; technology; silicon; Printed Circuit Board; magnetic material; ferrite; quality factor; power inductor; fluxgate; current sensor; magnetic field sensor; transformer

1. Introduction

An increasing number of today's electronic applications require reduced-size electronic devices and components. The basic electronic component that is least compatible with miniaturization and integration often is the inductor. An appreciable inductance can only be realized by allocating a sufficiently large chip area to it, or by combining current carrying wires or circuits with low-loss high-permeability magnetic materials, a process that may not be compatible with standard CMOS technology. Applications having on-board inductive sensors, filter circuits, and integrated power handling devices require small inductors with high inductance value, a high saturation current and a high-quality factor. For inductive switch mode power converters of high efficiency and small size, switching frequencies in the MHz range are common, posing stringent requirements on the losses in magnetic materials that are used in the inductive components. Today's boom in communication products at radio frequencies (RF) has strongly motivated research on integration of low-loss inductors directly on low-resistivity silicon substrates.

B. Azzerboni et al. (eds.), Magnetic Nanostructures in Modern Technology, 127–152.

2. Inductor basics

Inductance is the ratio of the amount of magnetic flux that is produced for a given current. When a conductor is coiled upon itself N number of times around the same axis, the current i required to produce a given amount of flux is reduced by a factor N compared to a single turn of wire. The inductance of a coil of wire of N turns is therefore given by

$$L = N\frac{\Phi}{i} \tag{1}$$

with L the inductance and Φ the magnetic flux. Faraday's law gives for the coil voltage v that is induced upon a current change:

$$v = \frac{d\,(N\Phi)}{dt} = L\frac{di}{dt} \tag{2}$$

saying that a current changes in a linear manner at a rate proportional to the applied voltage and inversely proportional to L. As the magnetic flux produced by a current depends on the permeability of the surrounding medium $\mu = \mu_0\mu_r$, with μ_0 the permeability in vacuum and μ_r the relative permeability, incorporation of magnetic materials in the inductor design is the natural way to decrease the space needed to realize a given inductance value.

When an electrical current is flowing in an inductor, there is energy stored in the magnetic field. The instantaneous power that must be supplied to initiate the current in the inductor is:

$$P = iv = Li\frac{di}{dt} \tag{3}$$

which, after time integration, gives the total energy input needed to build a final current I in the inductor:

$$E = \frac{1}{2}LI^2 \tag{4}$$

This energy storage concept is the basis for transformers and switch mode power supply applications. The application field for inductors is tremendous and includes magnetic (micro-)actuators, electrical machines, and mini-motors; we will focus in this chapter on MEMS technologies and the way they are used to realize inductors for sensor applications, filter and oscillator circuits, RF- and miniaturized power applications.

3. Losses in inductors

An ideal inductor or transformer would have no losses and would therefore be 100% efficient. In reality, energy is dissipated due to the resistance of the windings

(often referred to as copper losses), and to magnetic losses that are associated with the magnet materials used within the inductors (referred to as core or iron losses). Depending on the magnetic material used and the frequency of operation, losses can be of either origin. Understanding the losses is of primary importance for the realization of high-quality inductors, which is the reason why we will review in some detail the various loss mechanisms.

3.1. WINDING LOSSES

Current flowing through the windings of an inductor causes resistive heating of the winding material. Due to its low resistivity $\rho = 2\ \mu\Omega$ cm, copper is often chosen. At high frequencies f, the current moves away from regions in the conductor with the strongest magnetic field and the current will be distributed on the outer side of the winding, typically over a distance given by the skin depth $\delta = \sqrt{\rho/\pi f \mu}$. For copper at 1 MHz, the skin depth is about 6 μm. Hence, at high frequencies, the effective cross-section of the current carrying wire will be reduced, resistance goes up and winding losses will increase.

3.2. EDDY CURRENT LOSSES

Eddy current losses occur whenever the core material is electrically conductive and subjected to time-dependent magnetic fields. To reduce eddy current losses, a method is to increase the resistance of the core without inhibiting the magnetic flux. In classical transformer applications, this can be done by alloying the iron with about 3% of silicon, which lifts the resistivity to 45 $\mu\Omega$ cm.

In any resistive circuit with resistance R, the power is proportional to the square of the applied voltage $P = v^2/R$. In an inductor core material, the induced voltage is itself proportional to $f \times B$, with B the magnetic induction, so that eddy current losses are given by

$$P_{\text{eddy}} = K_{\text{e}} \frac{d^2}{\rho} (f B_{\max})^2 \left[\text{W/m}^3\right] \tag{5}$$

Here, K_e is a core-dependent prefactor and d the so-called lamination thickness. Indeed, to decrease eddy current losses, a common practice is to replace a monolithic magnetic core by a set of laminated sheets of thickness d, which enhances quadratically the resistance to be taken into account for the calculation of the eddy current losses.

3.3. MAGNETIC HYSTERESIS LOSSES

The total work that has to be done to change the magnetic state of the magnetic core material of an inductor over one complete cycle of the magnetic hysteresis

loop is proportional to the area within the hysteresis loop. The hysteresis losses are roughly proportional to the square of the working induction, in general to B^n, with n the Steinmetz exponent, which is specific for a given material. Moreover the loss rate is proportional to the number of times the hysteresis loop is completed per unit time, giving for the magnetic hysteresis losses:

$$P_{\text{hyst}} = K_{\text{h}} f B_{\text{max}}^{\text{n}} \left[\text{W/m}^3\right] \tag{6}$$

with K_{h} a core-dependent prefactor.

3.4. FERROMAGNETIC RESONANCE LOSSES

Generally, permeability drops off and magnetic loss increases in the very high-frequency (MHz–GHz) region because of the occurrence of a magnetic resonance. The Landau-Lifshitz equation has to be solved when the magnetization changes are studied in a high-frequency magnetic field.[1] This differential equation describes the change in magnetization as a function of the magnetization itself and the magnetic field. In an alternating magnetic field, the magnetization will show a damped precession motion around the easy axis. The damping is responsible for the losses.

As the complex impedance of an inductor can be written as $Z = R + i\omega L$, losses can be described by the imaginary part of the complex permeability $\mu_{\text{r}} = \mu' - \text{i}\mu''$. Figure 1 shows the frequency dependence of μ' and μ''as observed for Ni-Zn ferrites with various compositions.[2,3] Snoek[4] explained these curves in terms of the natural resonance or the resonance of rotation magnetization under the action of the anisotropy field. For example, for the ferrite 4F1 of Ferroxcube,[5] having an anisotropy constant $K_1 = -5 \times 10^2$ W/m^3, the resonance frequency is given by

$$\omega_{\text{res}} = 2\pi f_{\text{res}} = \frac{2\gamma K_1}{\mu_0 M_{\text{s}}} \tag{7}$$

with M_s the saturation magnetization and $\gamma = 1.105 \times 10^5$ g m/A the gyromagnetic constant. Combining Eq. (7) with the expression for the permeability of a rotational magnetization process, $\mu' = \dfrac{(\mu_0 M_s)^2}{3K_1}$, results in the equation

$$f_{\text{res}}\mu' = \frac{2}{3}\gamma\,\mu_0 M_{\text{s}} \approx 5\ \text{GHz} \tag{8}$$

The broken line in Fig. 1 is obtained by connecting the points where μ' drops off to one half the maximum value. The condition given by Eq. (8) coincides approximately with this line. No ferrites could attain points higher than this line, as long as the presence of cubic magnetic anisotropy was assumed. An important message of Fig. 1 is that a low-loss high-frequency magnetic material should not have a too high permeability at low frequencies.

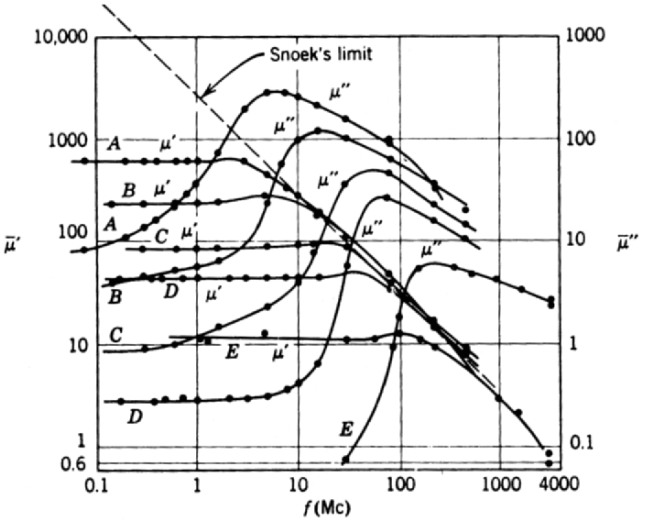

Figure 1. Frequency dependence of the real and imaginary parts of the initial permeability for polycrystalline Ni-Zn ferrite (compositional ratio NiO:ZnO = 17.5:33.2 (A), 24.9:24.9 (B), 31.7:16.5 (C), 39.0:9.4 (D), 48.2:0.7 (E), remaining part, Fe_2O_3). (Reprinted from Smit and Wijn.[2] With permission.)

For metallic ferromagnets, a similar behaviour can be observed, although the situation is more complex due to the importance of eddy currents at high frequencies.[6]

3.5. CHOICE OF THE CORE MATERIAL

In the previous section, we have briefly summarized the most important loss mechanisms and materials in inductors. The choice of a particular material depends on the frequency of the application, as in general one is interested in an inductor with highest possible quality factor $Q \equiv \dfrac{\omega L}{R}$; in practice, for a high-quality factor MEMS inductor, $Q > 10 - 20$. A small value for R is a prerequisite for a high-quality factor. Table 1 summarizes the three most important materials that are used in inductors: ferrites, which are high-resistivity magnetic oxides, metallic ferromagnets, and air. From a magnetic point of view, a metallic ferromagnet presents the best option, as it has the highest saturation induction and a very high permeability. However, due to the metallic character, eddy current losses become important at high frequencies, which is the reason why the majority of applications of a metallic ferromagnet are at frequencies below 50–100 kHz. Ferrites are inferior magnetic materials from a magnetic point of view, as the magnetic structure is 'diluted' by the oxygen atoms, but on the other hand, they do not show eddy current losses or chemical degradation. This explains the interest of

	Ferrite	Metal	Air
Permeability	1000	10^5	1
B_{sat}(Tesla)	0.45	1.5	–
Magnetic losses at low f (< 50 kHz)	f × A = high 	f × A = low 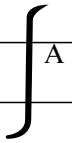	0
Resistivity (Ω m)	10^5 [0.1 MHz] 10^3 [100 MHz]	135×10^{-8}	–
Skin depth	15 m [0.1 MHz] 1.6 m [100 MHz]	18 μm [10 kHz] 1.8 μm [100 kHz]	–
Eddy current losses at high f (>100 kHz)	low	high	0
Ferromagnetic resonance losses at MHz-GHz frequencies	high	high	0

Table 1. Comparison of the magnetic properties and losses of the most frequently used materials in miniaturized inductors: ferrites (magnetic oxides), metallic magnetic materials, and air.

ferrites for use in high-frequency applications (0.1–10 MHz), especially for switch mode power supplies. Finally, air is a third material that can be used. It has a low permeability ($\mu_r = 1$), but there are no material losses, which makes air one of the best options for very high-frequency inductors (0.1–10 GHz). This explains the numerous efforts to realize RF inductors on Si substrates by removing part of the Si underneath a coil and replacing it by air.

Another important quantity characterizing an inductor is its self-resonant frequency. Self-resonance describes the way in which the electrical characteristics of an inductor deviate at high frequencies from that of an ideal inductor. At high frequencies, a stray capacitance between the windings and the substrate and/or core material will dominate over the inductive behaviour and limit the useful frequency range of the inductor.

4. MEMS inductors: background

Soohoo was the first to bring the subject of miniaturized integrated inductors to the magnetism community.[7] He gave a theoretical analysis for a magnetically sandwiched spiral and a magnetic core solenoid. He presented also an experimental inductor consisting of copper wire windings around a Permalloy film that was deposited on a glass or Si substrate. Hereafter, Kawabe et al.[8] have studied a number of miniaturized inductive structures, like planar coils embedded in evaporated SiO layers and sandwiched between two sputtered Permalloy films. A schematic diagram of the microfabrication process is shown in Fig. 2. Planar inductors also have been studied, both theoretically and experimentally, by Oshiro et al.[9]

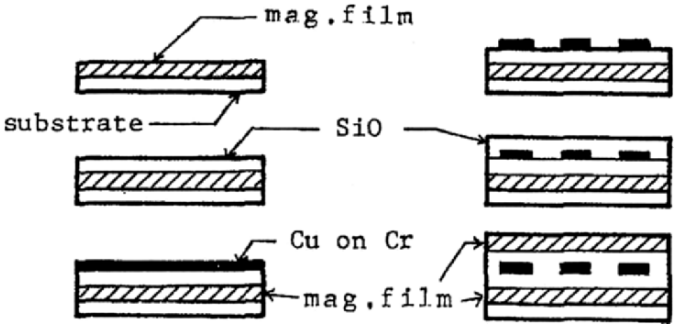

Figure 2. Schematic fabrication process of a planar inductor consisting of a planar Cu coil sandwiched between two magnetic films. (Reprinted from Kawabe.[8] With permission.)

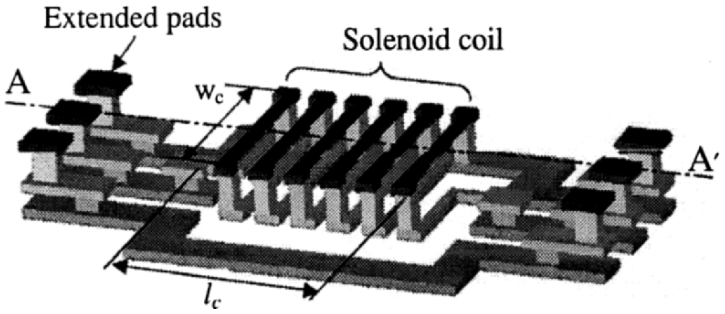

Figure 3. Schematic diagram of a solenoid inductor realized using three successive electroplating steps. (Reprinted from Yoon and Allen.[20] With permission.)

The planar spiral geometry is far from being solenoidal and the inductance does not scale efficiently with the number of turns. A thorough discussion of all possible inductor designs is out of the scope of this chapter. Details can be found in the paper of Korenivski.[10] A first class of devices is formed by planar inductors where a microfabricated planar coil is realized on a substrate and eventually sandwiched between magnetic films to enhance the coil inductance. While the coil fabrication is compatible with a planar microfabrication process, a spiral shape for the coil is not the most efficient way of obtaining a high inductance. Technologically, the combination of the coil with magnetic and insulating films above and below the coil is nontrivial.

Another approach is to build a miniaturized solenoid,[11–15] for example, using electroplating techniques for the coil and the magnetic material, but such process is more complex than that of realizing a planar coil. However, solenoids with magnetic cores have superior inductance-per-area characteristics. Figure 3 is a schematic diagram of a solenoid (without magnetic core) that is microfabricated using a sequence of three electroplating steps.

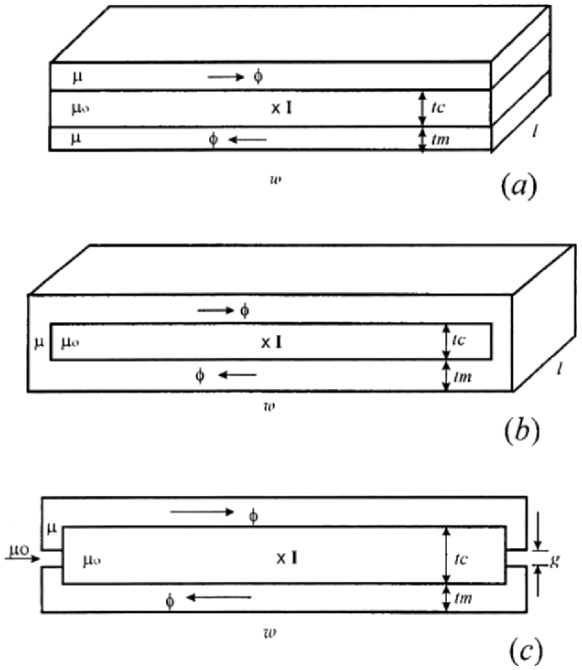

Figure 4. Schematic of a magnetic stripe inductor: (a) a trilayer without magnetic flanges; (b) an enclosed stripe inductor; (c) a magnetic stripe inductor with gaps. (Reprinted from Korenivski and vanDover.[16] With permission.)

Magnetic stripe inductors present another less exploited option.[16] A sandwich stripe inductor is a thin film multilayer having a conductor stripe made of Cu or Al, sandwiched in between two magnetic films, with optional insulation layers between the conductor and the magnetic films. Figure 4 shows three options for a magnetic stripe inductor, which differ by the way magnetic flux is closed at the outer side of the structure. In general, when a magnetic material is present all around the conductor, flux closure, and inductance are maximized.

5. Radio frequency MEMS inductors

Wireless communication products have triggered a large demand for low-cost on-chip RF devices. An important factor limiting integrated solutions is the achievement of a high Q-factor inductor, preferably realized on a low-resistivity silicon chip that contains the active circuits. Conventionally RF inductors are planar structures fabricated on the silicon surface.[17] The increase of the quality factor of those planar inductors has been limited by eddy current loss of the conductive substrate and ohmic loss of the metal windings. In order to improve the quality factor, a number of techniques to reduce substrate and winding losses have been

proposed, such as the use of high-resistivity silicon or silicon-on-insulator substrates,[18] removal of part of the substrate under the spiral metals or employing thick dielectric layers underneath the coils.[19] We will now discuss four different approaches for obtaining RF inductors with enhanced quality factor.

5.1. EMBEDDED SOLENOIDAL INDUCTORS

Due to their advantageous inductance per surface ratio, several attempts to realize miniaturized solenoids have been reported[12–15,20–22] Recently, a surface micromachined epoxy-embedded conductor fabrication process for high-aspect ratio vertical interconnect and lateral conductors was presented. The aim is to realize solenoid structures of the form of Fig. 3. The embedded vertical interconnect process used a high-aspect ratio via mold formation from photosensitive SU-8 epoxy and subsequent conformal plate-through-mold metallization. The SU-8 mold was retained as a part of the substrate for both subsequent processing steps and ultimate packaging. Via fabrication techniques that are currently used for both backend IC processes, as well as other MEMS processes were used.

The process is attractive for two reasons. First, the embedded nature of the interconnects and inductors allows conventional handling and packaging of inductor/interconnect/chip systems without additional mechanical precautions for the inductor structure and without significant electrical degradation after further packaging. Second, since the embedding material forms a permanent structural feature of the device, SU-8, which is a resist that is known to be very hard to remove, presents an advantage here. Moreover, the epoxy-based implementation of this technology is low-temperature and compatible with post-processing on CMOS chips.

Multiple solenoid-type inductors with varying numbers of turns and air core widths were realized. Figure 5a represents a Scanning Electron Microscopy (SEM) graph of the embedded inductor, showing the exposed metal probe pads and the upper metal of the coil. Figure 5b shows a SEM view of the device after the embedding epoxy has been etched away for clarity. It shows that the solenoid coil is about 25 μm above the substrate. Figure 6 shows the measured inductance and Q-factor of an embedded test inductor with six turns and a core width of 400 μm. The peak Q-factor and inductance at 4.5 GHz are 20.5 and 2.6 nH, respectively. These results clearly show the good performance of ‘air’ (SU-8) as core material at GHz frequencies.

5.2. VERTICAL SPIRAL INDUCTORS

When placed on a low-resistivity substrate, planar geometries present both a desired inductance and a parasitic capacitance. Reducing the size of the conducting elements brings about a reduction in parasitic capacitance and self-resonance

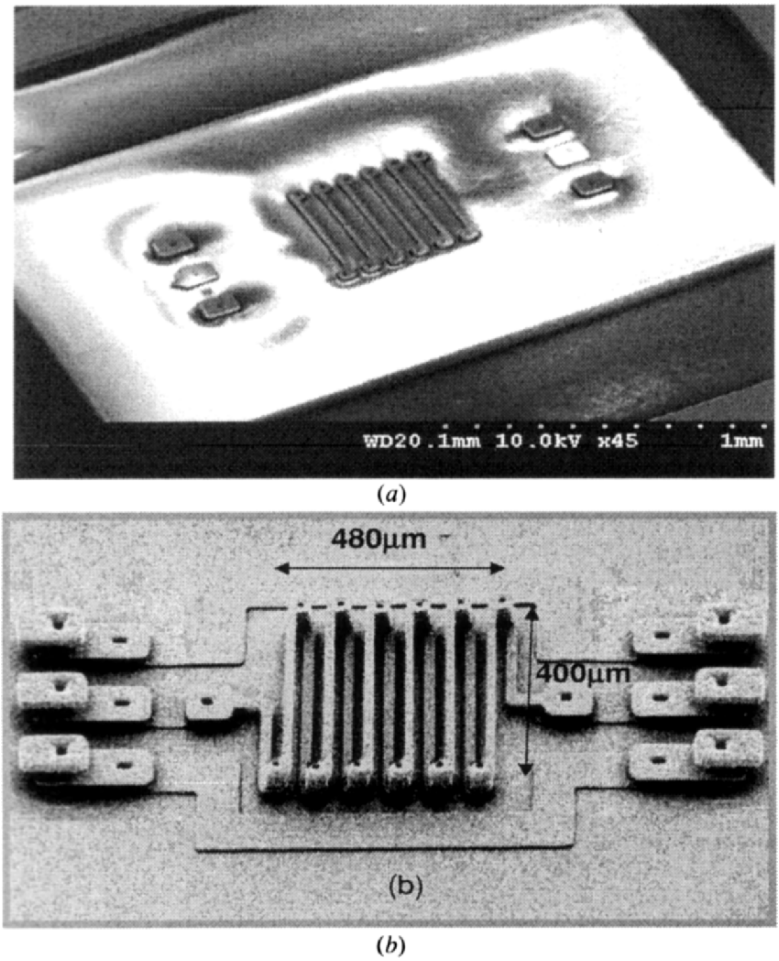

Figure 5. SEM images of a microfabricated six-turn embedded inductor: (a) embedded in SU-8 epoxy material; (b) after removal of the SU-8. (Reprinted from Yoon and Allen.[20] With permission.)

frequency, but also increases the resistive loss. An approach for improving this situation is lifting the coil structure off the substrate plane into a vertical position to reduce the capacitance without increasing the resistance. In addition, it is avoided that magnetic flux along the centre of the coil passes through the substrate causing thereby eddy current losses.

In a first type of vertical coil structure, the inductors assemble out of the plane by means of an interlayer stress that causes portions of the inductor to bend away from the substrate in a controllable manner.[23] The simplest way of doing this is to fabricate the inductor in the substrate plane over a sacrificial layer, with anchor points at both ends connecting to the substrate. By using two or more material layers deposited with different stresses, the inductor can be made to curl away

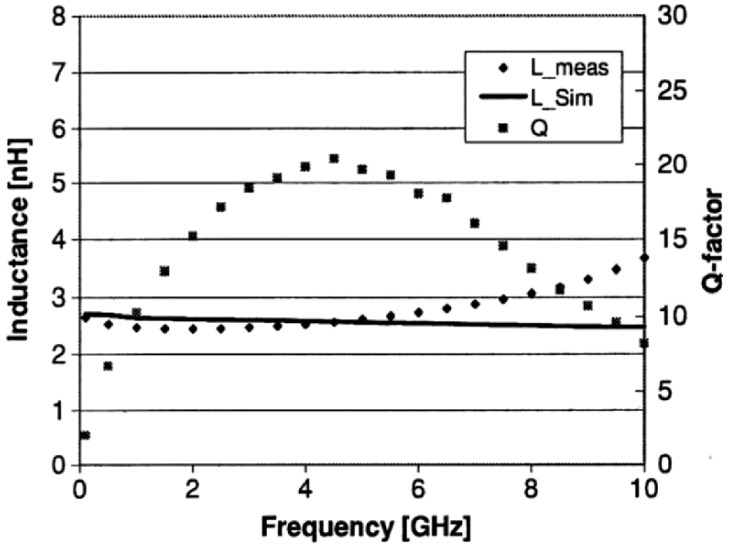

Figure 6. Measured inductance (*diamonds*) and Q-factor (*squares*) of the fabricated embedded inductor (six turns and 400 μm core width). The solid line is a simulation of the inductance. (Reprinted from Yoon and Allen.[20] With permission.)

from the substrate when the sacrificial layer is removed. Inductance values of a few nH and a Q-factor up to 13 have been obtained at a few GHz.

A second type of approach involves lifting a planar inductor out of the substrate using so-called Plastic Deformation Magnetic Assembly (PDMA)[24,25] This process is illustrated in Fig. 7. First, a planar structure with a piece of magnetic material attached to its top surface is released from the substrate by etching away the sacrificial layer beneath (Fig. 7a). Next, a magnetic field H_{ext} is applied, the magnetic material piece is magnetized, and the planar structure will be rotated off the substrate by the magnetic torque generated in the magnetic material piece (Fig. 7b). If the structure is designed properly, this bending will create a plastic deformation in the flexible region. The planar structure will then be able to remain at a certain rest angle ϕ above the substrate even after H_{ext} is removed (Fig. 7c). By using a ductile metal like Au in the flexible region, a good electrical connection between the assembled structure and the substrate can be easily achieved. Au can also be used as the material for the bottom inductor of the coil. For the actuation layer, a Permalloy film can be directly electroplated on the conductor windings. Figure 8 shows a vertical inductor lifted out of the plane by PDMA. When the planar inductor is in the silicon substrate, it has a peak Q-factor of 3.5 and a self-resonant frequency of 1 GHz. When the inductor is in the vertical position after the PDMA assembly, the peak Q-factor increases to 12 and the self-resonant frequency goes well above 4 GHz.

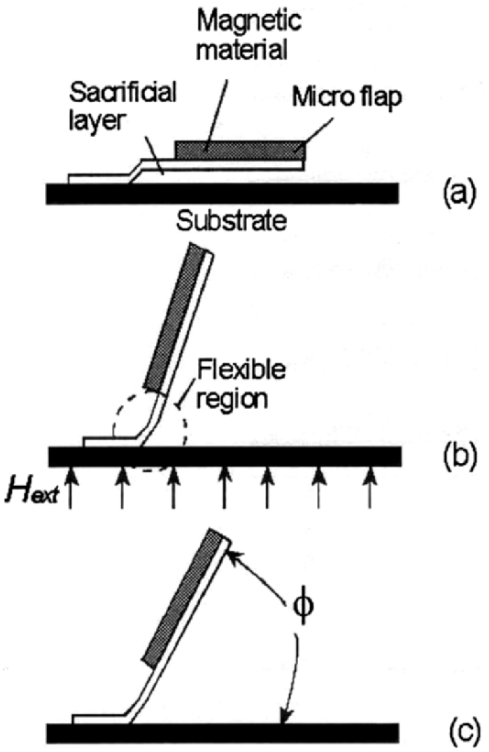

Figure 7. Schematic diagram of the Plastic Deformation Magnetic Assembly (PDMA) process for the realization of out-of-plane components. (Reprinted from Chen et al.[24] With permission.)

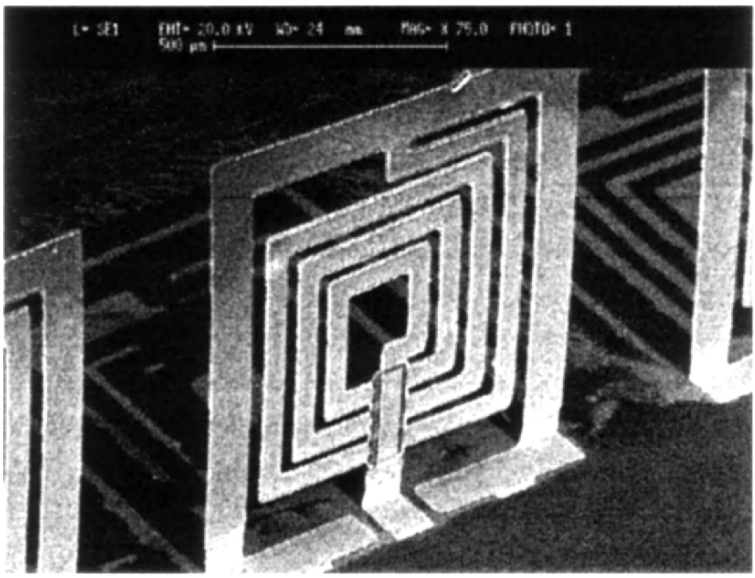

Figure 8. SEM image of a planar inductor lifted out-of-the plane by the PDMA process. (Reprinted from Chen et al.[24] With permission.)

5.3. HORIZONTAL SPIRAL INDUCTORS OVER AIR CAVITIES

Another method to minimize the substrate loss and the parasitic capacitance and thereby realize a high-quality factor inductor is to remove the silicon substrate beneath the inductor.[26] However, in this case the mechanical robustness of the inductor structure is a concern and additional fabrication steps, such as bonding a low-loss superstrate to the circuit area, may be required to improve the mechanical strength. Metal ground lines can also be placed around the inductors in these methods. Also a patterned metal shield can be inserted beneath the inductor to provide an electromagnetic shield and to reduce the crosstalk between devices.

In one of the approaches, a suspended inductor was built over a cavity whose bottom plane and sidewalls were metallized with copper.[27] The deep cavity substantially reduces the electromagnetic coupling and the parasitic capacitance between the inductor and the silicon substrate, thus increasing the quality factor and the self-resonance frequency. The polysilicon spiral inductor was electrolessly plated with Cu for obtaining a small series resistance. The same plating process coats the silicon bottom plane and sidewalls of the cavity with Cu as well. Provided that the cavity is deep enough, the eddy currents induced in the metal shield by the magnetic field generated by the inductor will be small, and so is the power loss. The way to realize the cavity was etching deep (30 μm) narrow beam-and-trench structures out of bulk silicon and subsequently transforming such silicon structures to silicon oxide. After microfabrication of the polysilicon inductor structures, the deep sacrificial oxide block underneath was removed by wet etching. Figure 9 is a SEM image of a suspended rectangular spiral inductor. Figure 10 shows the quality factor of three inductors, with inductance values in the nH range, versus frequency. High quality factors over 30 and self-resonant frequencies higher than 10 GHz have been achieved. Moreover, the suspended inductors withstood large shocks and vibrations. Also other work on the realization of spiral inductors over air cavities has been reported.[28–31]

5.4. USE OF MAGNETIC MATERIALS FOR RF INDUCTORS

Previously discussed approaches for realization of an inductor with high Q-factor on a low-resistivity silicon substrate involved the replacement of the silicon material close to the coil by air. An original approach to tackle the same problem is to apply ferromagnetic thin films to the RF integrated inductor.[33–37] The idea is to enhance the magnetic flux associated with the coil current and accordingly to enhance the inductance and quality factor of the inductor. To be able to use ferromagnetic films up to GHz frequencies, highly resistive $Co_{85}Nb_{12}Zr_3$ amorphous films ($\rho = 120\ \mu\Omega$cm) were sputtered on both sides of the planar coil structure. A schematic section of the coil with magnetic films is shown in Fig. 11. Moreover,

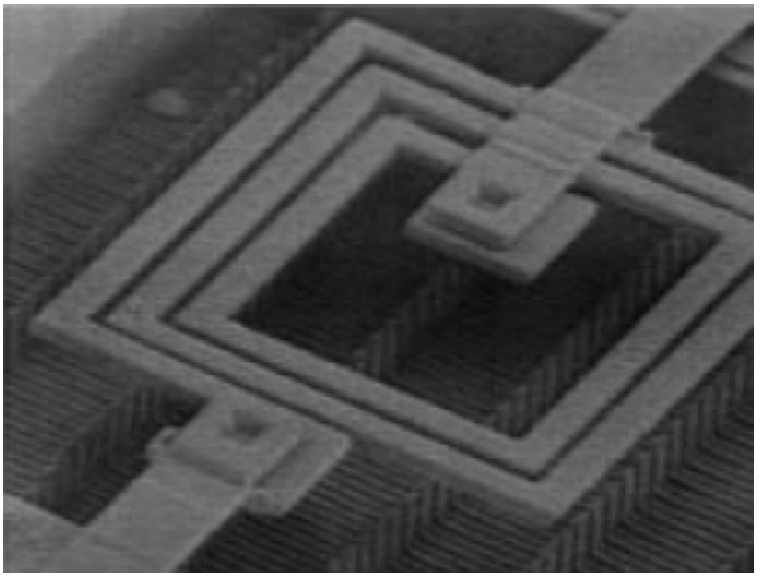

Figure 9. SEM image of a rectangular spiral inductor suspended over an air cavity. (Reprinted from Jiang et al.[32] With permission.)

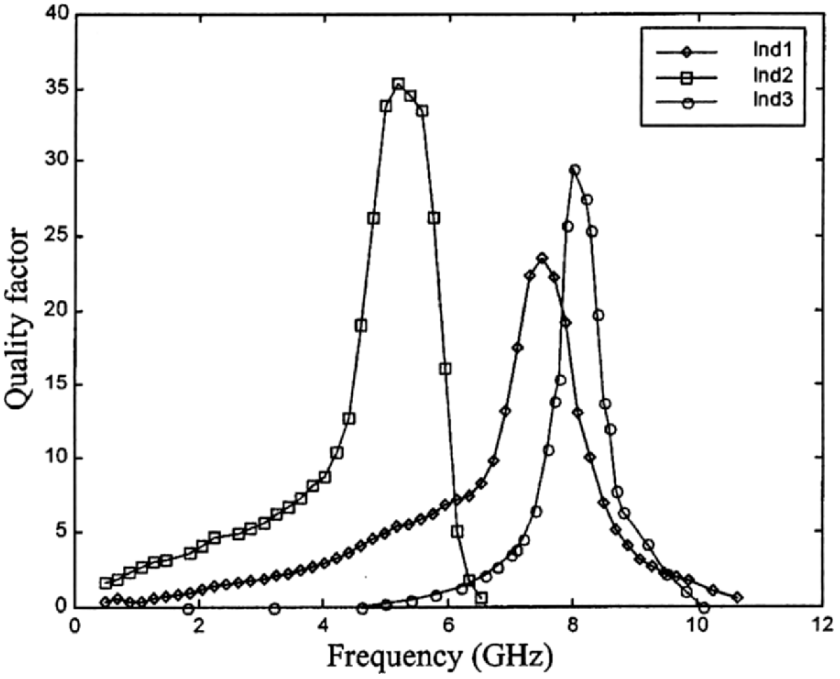

Figure 10. Measured Q-factors of inductors suspended over an air cavity. (Reprinted from Jiang et al.[32] With permission.)

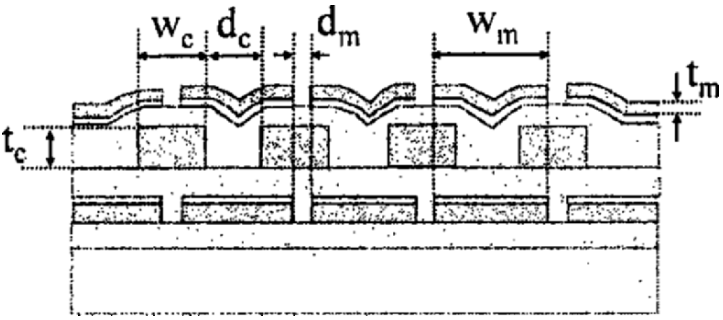

Figure 11. Cross-sectional view of a sandwich-type planar inductor with segmented high-resistivity magnetic films for RF applications. (Reprinted from Yamaguchi et al.[34] With permission.)

to reduce eddy current loss and to impose a certain magnetic anisotropy, the magnetic film has been microstructured into small segments. An inductance of about 8 nH and a Q-factor of 12.7 was obtained at 2 GHz.

It is clear that, in this context, high-resistivity Ni-Zn ferrites ($\rho \sim 10^7$ $\mu\Omega$cm) may present an interesting option for use as a magnetic material. Sputtering, spin coating, or plating techniques have been proposed for the realization of ferrite films, but such films often require a post-deposition annealing up to 1000°C, which is not compatible with Integrated Circuit (IC) post-processing. Pulsed laser deposition of high-quality (Mn-Zn)Fe ferrite films, having bulk magnetic properties, was achieved at 400–600°C by a careful selection of buffer layers.[38] However, there appears to be no readily available technique for fabrication of ferrite films with the desired magnetic properties at a sufficiently low temperature compatible with an IC-based process. To resolve this problem, one has realized polyimide embedded Cu coils on top of normal Si substrates and assembled these coils with magnetic cover plates of commercially available bulk Ni-Zn ferrites of high resistivity.[39] The hybrid combination of state-of-the-art ferrites with post-processed coils on Si enabled to evaluate the ultimate potential of ferrite-based inductors for RF applications. Using the magnetic flux-amplifying ferrite plates, a 40% enhancement of the inductance and a 25% enhancement of the quality factor was obtained with respect to the simple coil, for frequencies up to 0.2 GHz.

6. Inductors using packaging technologies

Integration of high-performance active transistors with high-quality factor passive components is a subject of increasing interest today. Among the passive components, inductors are maybe the most studied because of their important role in affecting the performance of RF/microwave circuits such as voltage-controlled oscillators, filters, and impedance matching networks. A system-on-chip approach,

which intends to integrate the passive components with the active transistors, has its own drawbacks. The system-in-package solution emerges now as a promising integration scheme, owing to its low cost, flexibility in combination with different device technologies, and the saving of precious chip area. We will discuss here two packaging technologies that have been used to realize miniaturized inductors: screen printing technology and a magnetic Printed Circuit Board (PCB) technology.

6.1. SCREEN PRINTED INDUCTORS

Conventional screen printing[40] as well as ink jet printing[41] have been used to deposit polymer thick film interconnects and resistors[42] on both rigid and flexible substrates. These technologies enable the incorporation of electronics onto heat-sensitive substrates for a wide range of potential applications, including electronic paper, electronic labels, flexible displays, etc. Screen printing has been used for realization of both the windings and the magnetic core materials.

Low-temperature co-fired ceramics (LTCC) technology[43] served to fabricate integrated magnetic devices for power electronics applications.[44] The following steps have been used to realize circular coil inductors of centimetre-size. Prior to the screen printing of the inner outline of the coil, circular cavities are punched into the different green tape layers. After punching the cavities, via holes that are 200 μm wide are formed to serve as connections for the coils. These via holes are filled with Ag paste; hereafter, silver paste is screen-printed on each layer depending on the inductor design, and then the screen-printed green sheets are laminated together. After the lamination, the sheets are co-fired in a belt furnace at a peak temperature of 850 °C, and then a top conductor of Ag-Pd is post-printed on the co-fired part and post-firing is conducted at a peak temperature of 750 °C. Figure 12 shows the resistance, inductance, and quality factor of a 2-turn 8-layer inductor. The inductance is about 0.8 μH up to 3 MHz. The maximum quality factor of 8.9 is obtained at 20 MHz. The self resonance frequency is around 50 MHz.

Screen printing has also been used to deposit magnetic core materials for inductor applications. A relatively large volume of material for the core is required, necessitating thick films which are difficult to achieve using vacuum deposition and other typical thin film processes. Furthermore, high processing temperatures (often in excess of 900 °C for conventional ceramic films) severely limit the available substrates that can be used and eliminate the potential for integration with other components. Therefore, another approach to the low-temperature deposition of thick, ceramic magnetic films is to use screen- or stencil-printed ceramic–polymer composites, in which ceramic magnetic powders are mixed with a polymer binder. Unlike traditional thick film processes, these polymer films are dried or cured at temperatures less than 200 °C leaving only

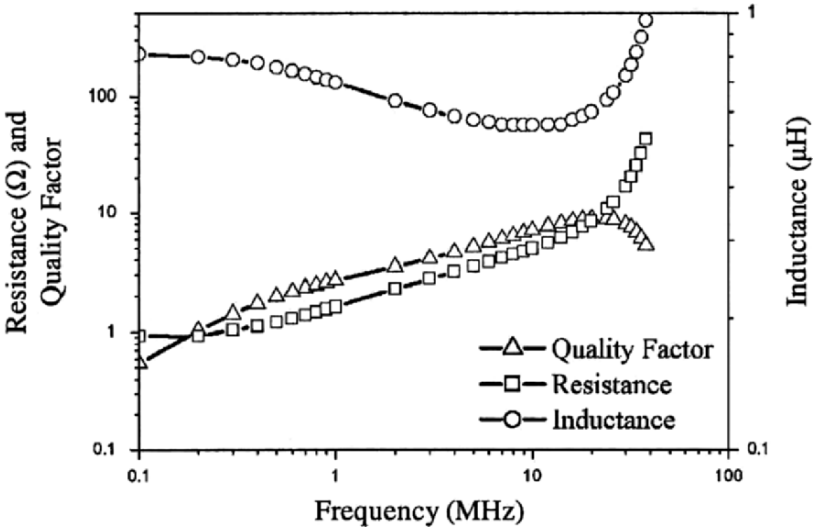

Figure 12. Resistance, inductance and quality factor of a 2-turn 8-layer inductor where the windings are made using low-temperature co-fired ceramics (LTCC) technology. (Reprinted from Kim et al.[44] With permission.)

the magnetic filler and polymer binder. The challenge is to achieve high enough loading fractions of the magnetic ceramic within the diamagnetic polymer binder to achieve sufficient volume magnetization while still maintaining sufficient adhesion to the substrate. Such low-temperature magnetic cores were printed on two sides of 25 μm thick polyimide flexible laminate material carrying a 11-turn square copper coil of 5 mm in size and having a metal thickness of 17.5 μm.[45,46] The inductors had inductance values around 1 μH and showed a peak Q-factor of 20 in the 10–20 MHz range and a self-resonant frequency above 120 MHz.

6.2. MAGNETIC PRINTED CIRCUIT BOARD INDUCTORS

Soft magnetic amorphous magnetic alloys (metallic glasses) are 10–20 μm thick bulk ribbons prepared by casting a molten alloy on a cooled spinning wheel. Due to their amorphous or nanocrystalline structure, the relative magnetic permeability μ_r of these ribbons can be of the order of 10^5–10^6 [47,48] For magnetic induction and current sensing devices, the sensor's response is proportional to the relative permeability of the core material; hence a high μ_r is beneficial, giving these materials a competitive edge at low frequencies ($f < 50$ kHz) where eddy current loss is of little importance. A problem to be solved when using bulk magnetic materials in thin film or PCB applications is how to combine these materials with conventional microfabrication technologies that have a two-dimensional character and therefore are well compatible with sputtering or electroplating methods. We have developed a magnetic PCB technology for the realization of high

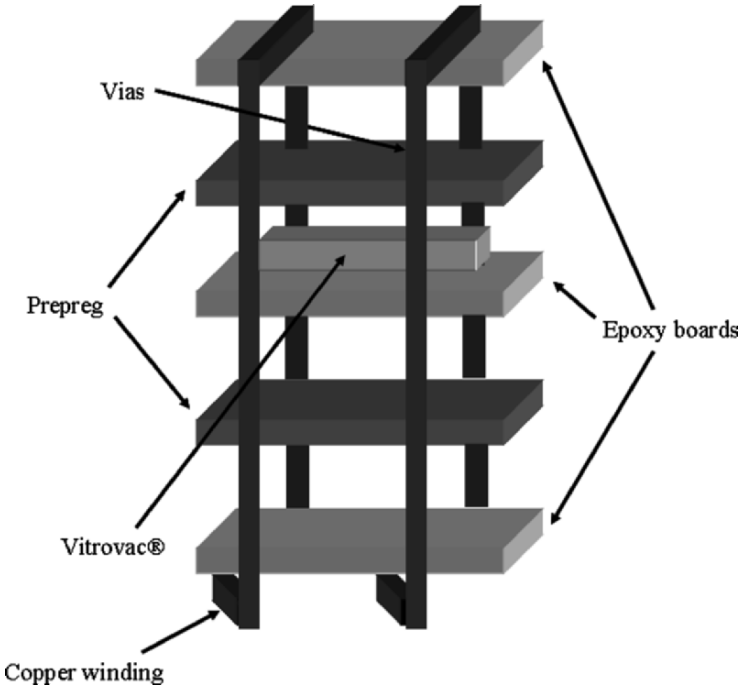

Figure 13. Schematic diagram of a Printed Circuit Board technology with embedded micropatterned magnetic foils. (Reprinted from Belloy et al.[49] With permission.)

inductance transformers[49,50] and for high resolution magnetic sensing devices, based on inductive measurement principles like the fluxgate sensor configuration.[51,52] The magnetic core materials used are Vitrovac 6025 or Metglas 2714A ribbons.[47,48]

A schematic diagram of the inductive device fabrication process is shown in Fig. 13. The proposed method of fabrication is very similar to a conventional PCB process. The devices are based on two epoxy boards (100 μm thick) with copper (35 μm thick) laminated on one side, and by a simple epoxy board (100 μm thick) as a support for the magnetic foil. A liquid epoxy was used to laminate the magnetic foil to the inner epoxy board. Two 100 μm thick sheets of Prepreg solid epoxy were used for bonding the laminates into a stack of five layers. The Vitrovac and Metglas foils were patterned photolithographically by first laminating sheets of solid negative photoresist (Ordyl200) onto degreased foils and then processing according to manufacturer's specifications after pattern transfer. A wet chemical process was developed in-house to etch the magnetic foils.

A layout of a fluxgate type[51,52] of magnetic field sensor, in which the magnetic core material has been patterned into a rectangular-like shape is shown in Fig. 14a. The two excitation coils have been grouped into four clusters of five

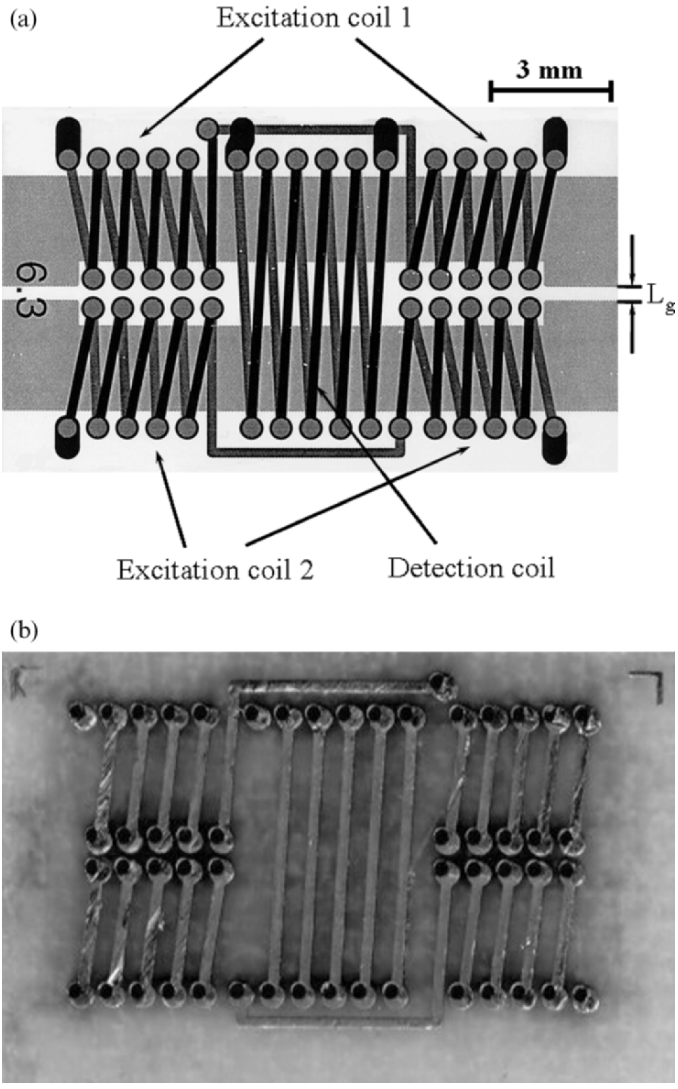

Figure 14. (a) Lay-out of a rectangular fluxgate magnetic field sensor showing the excitation and detection coils and the micropatterned magnetic foil with air gaps L_g. (b) Photograph of a fabricated fluxgate sensor. (Reprinted from Dezuari et al.[51] With permission.)

windings and are symmetrically positioned around the inner five detection coil windings. Moreover, we have introduced air gaps in the magnetic core to tune the magnetic permeability and, hence, the sensitivity of the device. A photograph of the experimental realization of this fluxgate sensor is displayed in Fig. 14b. The detection sensitivity of these magnetic field sensors goes up to 60 V/T.

7. MEMS power inductors

Another field of strong miniaturization is power electronics, where appreciable power is stored/transformed using an inductive circuit. Transformers of 5 mm in size integrated with diodes on a Si wafer were reported by Mino et al.[53,54] These were based on an amorphous magnetic core prepared by sputtering, in the form of three separate layers of CoZrRe, each 5 μm thick, with 0.1 μm SiO_2 spacer layers. This layered configuration was chosen to reduce eddy current losses in the magnetic core. Reported inductance values were in the range of 0.5–1 μH. A specially configured transformer was realized by Yamasawa et al.[55] by sandwiching primary and secondary coils in between two 10 μm thick amorphous CoZr layers. An inductance value of 8.5 μH at 1 MHz was obtained by this rather large planar device of 40 × 30 mm^2.

Besides the development of MEMS inductors based on metallic magnetic materials, also the 'macroscopic' field of power electronics has been subjected to strong miniaturization. An important factor for the size reduction of a power inductor or transformer is its operation frequency (typically 0.1–1 MHz), as with increasing frequency, more power cycles can pass the device. These high frequencies necessitate the use of high-resistivity magnetic core materials, such as ferrites, for reducing eddy current losses. During recent years, a large research effort has been developed in the field of so-called planar magnetics, where one integrates flat three-dimensional (3D) ferrite cores with Cu windings realized in planar PCB technology.[56,57] This device geometry has lead to devices with reduced height and enhanced power density in a vast range of power (few Watt to many kW). However, for special ultra-small low-power applications, such advanced solutions do not exist, as individual component sizes would prevent an easy assembly and handling.

We have therefore proposed a method for the batch-fabrication of 3D inductors and transformers, with which we opened the way to economically feasible ultra-miniaturized ($\leq$1 mm) low-power ($<$1 Watt) applications.[58] Our devices are geometrically similar to larger-size planar magnetic components, and consist of two magnetic ferrite cores and PCB's or flex-foils carrying the electrical windings around the core. The 3D ferrite cores are microstructured out of a 1 mm thick ferrite wafer using a batch-type micro-powder blasting process.[59] The powder, consisting of 30 μm size alumina particles (Al_2O_3) is ejected in a compressed air flux through a rubber tube to a nozzle. Patterning is performed by applying a 0.5 mm thick laser cut stainless steel mask, containing the desired structures, on the ferrite wafer. Scanning the surface of a ferrite wafer along the x and y directions and using the appropriate metallic masks, we obtain an array of very small and identical ferrite E-cores, as shown in Fig. 15a. For the realization of the windings we used a standard PCB process on polyimide flexible substrates. We can realize many cores in parallel and assemble them at wafer-level with the

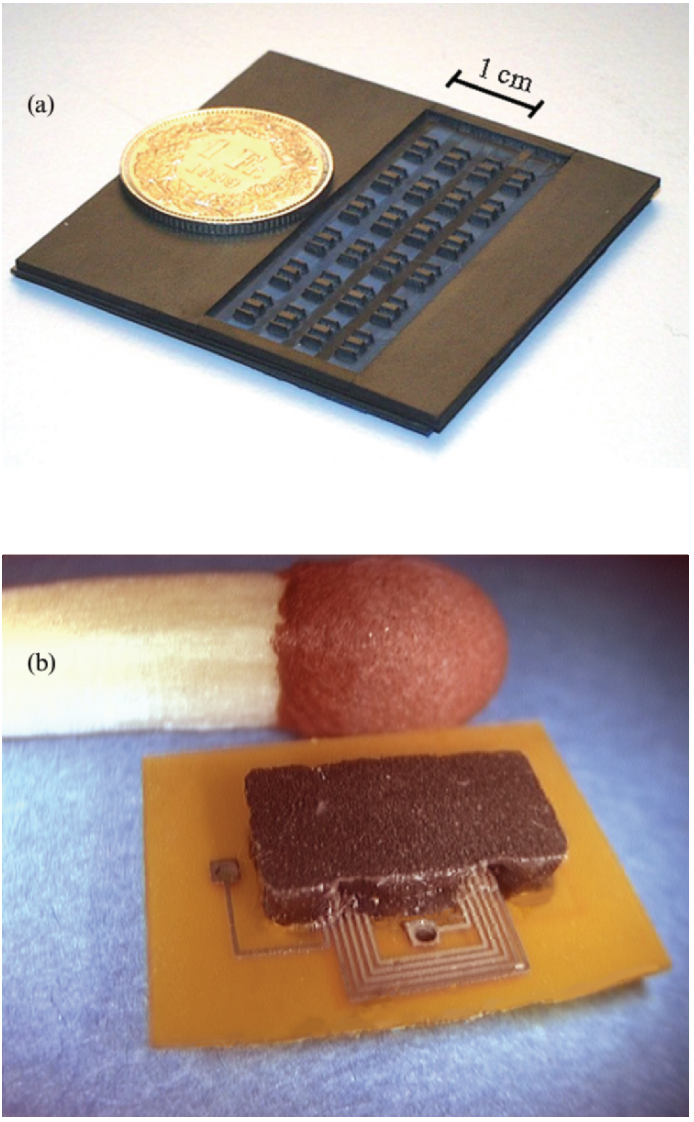

Figure 15. (a) Photograph of an array of identical E-cores patterned into a ferrite wafer by powder blasting. (b) Assembled transformer consisting of two E-cores and windings realized in PCB technology. (Reprinted from Amalou et al.[58] With permission.)

electrical winding patterns; hereafter, complete devices are separated. Figure 15b shows an assembled mini-transformer.

The electrical properties of these devices were measured, such as main inductance, leakage inductance, and resistance, as a function of frequency and device geometry. The conditions for the inductance measurements (see Fig. 16) are the following: a primary coil with $N_p = 12$ turns and a secondary coil with

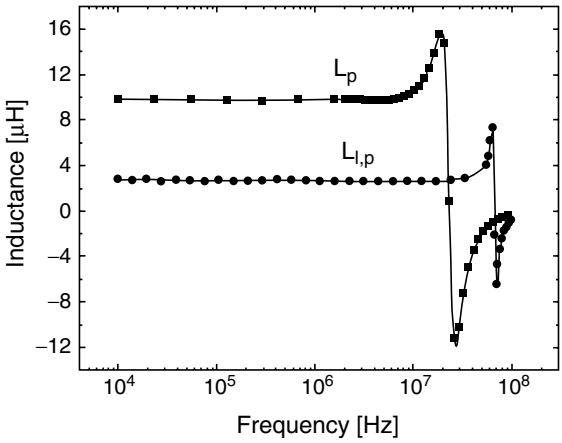

Figure 16. Main (L_p) and leakage ($L_{l,\mathrm{p}}$) inductance of the primary circuit of a minitransformer as a function of frequency

$N_\mathrm{s} = 8$ turns is mounted with two ferrite E-cores and the primary inductance L_p and the leakage inductance $L_{l,\mathrm{p}}$ are measured. The primary inductance is obtained by measuring with the secondary open and the leakage inductance with the secondary short-circuited. Physically, when the secondary is shorted, all flux which is generated by the primary and coupled into the secondary is opposed by the induced secondary current and only that part of the flux, which 'leaks away' elsewhere in space is measured via the remaining inductance $L_{l,\mathrm{p}}$. Negative inductance values in Fig. 16 indicate a capacitive element given by $C = -L^{-1}\omega^{-2}$. The self resonance frequency is about 23.4 MHz and 66.4 MHz for the L_p and $L_{l,\mathrm{p}}$-measurement, respectively. The value of L_p is about 9.9 μH over more than two decades of frequencies and the leakage inductance $L_{l,\mathrm{p}}$ is about 2.7 μH over more than three decades of frequencies.

8. Conclusions

In this chapter, we have exposed the current state-of-the-art of MEMS inductors. Starting from a description of the most commonly developed inductor geometries, i.e. the planar and solenoidal inductors, we have discussed the various techniques to realize RF inductors for operation at GHz frequencies and their integration directly on silicon substrates. Subsequently, we explained how cheap packaging technologies can be used to realize inductive components that interface directly with silicon chips or can be used for high-sensitivity magnetic field sensors. We finally discussed the role of MEMS technologies for the realization of power inductors. We think that, in future, inductive MEMS devices will have a considerable and decisive impact on the miniaturization of a number of industrial applications.

References

1. L. Landau and E. Lifshitz, *Phys. Z. Sowjetunion* 9, 153 (1935).
2. J. Smit and H. P. J. Wijn, *Ferrites*, N.V. Philips' Gloeilampenfabrieken, Eindhoven (1959).
3. E. W. Gorter, Chemistry and Magnetic Properties of Some Ferrimagnetic Oxides Like Those Occurring in Nature, *Advances in Physics* 6(23), 336–361 (1957).
4. J. L. Snoek, Dispersion and absorption in magnetic ferrites at frequencies above one Mc/S, *Physica* 14(4), 207–217 (1948).
5. *Soft Ferrite and Accesories Catalogue*. Available at: http://www.ferroxcube.com (2002).
6. E. van de Riet and F. Roozeboom, Ferromagnetic resonance and eddy currents in high-permeable thin films, *Journal of Applied Physics* 81(1), 350–354 (1997).
7. R. F. Soohoo, Magnetic thin-film inductors for integrated-circuit applications, *IEEE Transactions on Magnetics* 15(6), 1803–1805 (1979).
8. K. Kawabe, H. Koyama, and K. Shirae, Planar inductor, *IEEE Transactions on Magnetics* 20(5), 1804–1806 (1984).
9. O. Oshiro, H. Tsujimoto, and K. Shirae, A novel miniature planar inductor, *IEEE Transactions on Magnetics* 23(5), 3759–3761 (1987).
10. V. Korenivski, GHz magnetic film inductors, *Journal of Magnetism and Magnetic Materials* 215, 800–806 (2000).
11. J. Y. Park and M. G. Allen, A comparison of micromachined inductors with different magnetic core materials, in: *IEEE Electronic Components and Technology Conference*, pp. 375–381 (1996).
12. B. Lochel and A. Maciossek, Electrodeposited magnetic alloys for surface micromachining, *Journal of the Electrochemical Society* 143(10), 3343–3348 (1996).
13. B. Lochel, A. Maciossek, H. J. Quenzer, and B. Wagner, Ultraviolet depth lithography and galvanoforming for micromachining, *Journal of the Electrochemical Society* 143(1), 237–244 (1996).
14. B. Lochel, A. Maciossek, M. Rothe, and W. Windbracke, Microcoils fabricated by UV depth lithography and galvanoplating, *Sensors and Actuators a-Physical* 54(1–3), 663–668 (1996).
15. A. Maciossek, B. Lochel, H. J. Quenzer, B. Wagner, S. Schulze, and J. Noetzel, Galvanoplating and sacrificial layers for surface micromachining, *Microelectronic Engineering* 27(1–4), 503–508 (1995).
16. V. Korenivski and R. B. vanDover, Magnetic film inductors for radio frequency applications, *Journal of Applied Physics* 82(10), 5247–5254 (1997).
17. J. N. Burghartz, D. C. Edelstein, M. Soyuer, H. A. Ainspan, and K. A. Jenkins, RF circuit design aspects of spiral inductors on silicon, *IEEE Journal of Solid-State Circuits* 33(12), 2028–2034 (1998).
18. S. R. Taub and S. A. Alterovitz, Silicon technologies adjust to Rf applications, *Microwaves and Rf* 33(10), 60 (1994).
19. L. E. Larson, Integrated circuit technology options for RFIC's – Present status and future directions, *IEEE Journal of Solid-State Circuits* 33(3), 387–399 (1998).
20. Y. K. Yoon and M. G. Allen, Embedded conductor technology for micromachined RF elements, *Journal of Micromechanics and Microengineering* 15(6), 1317–1326 (2005).

21. Y. K. Yoon, J. W. Park, and M. G. Allen, Polymer-core conductor approaches for RF-MEMS, *Journal of Microelectromechanical Systems* 14(5), 886–894 (2005).

22. J. B. Yoon, B. K. Kim, C. H. Han, E. S. Yoon, and C. K. Kim, Surface micromachined solenoid on-Si and on-glass inductors for RF applications, *IEEE Electron Device Letters* 20(9), 487–489 (1999).

23. V. M. Lubecke, B. Barber, E. Chan, D. Lopez, M. E. Gross, and P. Gammel, Self-assembling MEMS variable and fixed RF inductors, *IEEE Transactions on Microwave Theory and Techniques* 49(11), 2093–2098 (2001).

24. J. H. Chen, J. Zou, C. Liu, J. E. Schutt-Aine, and S. M. Kang, Design and modeling of a micromachined high-Q tunable capacitor with large tuning range and a vertical planar spiral inductor, *IEEE Transactions on Electron Devices* 50(3), 730–739 (2003).

25. J. Zou, C. Liu, D. R. Trainor, J. Chen, J. E. Schutt-Aine, and P. L. Chapman, Development of three-dimensional inductors using plastic deformation magnetic assembly (PDMA), *IEEE Transactions on Microwave Theory and Techniques* 51(4), 1067–1075 (2003).

26. J. Y. C. Chang, A. A. Abidi, and M. Gaitan, Large suspended inductors on silicon and their use in a 2-Mu-M Cmos Rf amplifier, *IEEE Electron Device Letters* 14(5), 246–248 (1993).

27. J. L. A. Yeh, H. R. Jiang, H. P. Neves, and N. C. Tien, Copper-encapsulated silicon micromachined structures, *Journal of Microelectromechanical Systems* 9(3), 281–287 (2000).

28. Z. W. Liu, Y. Ding, L. T. Liu, and Z. J. Li, Fabrication planar coil on oxide membrane hollowed with porous silicon as sacrificial layer, *Sensors and Actuators a-Physical* 108(1–3), 112–116 (2003).

29. C. L. Dai and C. H. Tsai, Fabrication of integrated chip with microinductors and micro-tunable capacitors by complementary metal-oxide-semiconductor postprocess, *Japanese Journal of Applied Physics Part 1-Regular Papers Short Notes and Review Papers* 44(4A), 2032–2038 (2005).

30. X. N. Wang, X. L. Zhao, Y. Zhou, X. H. Dai and B. C. Cai, Fabrication and performance of a novel suspended RF spiral inductor, *IEEE Transactions on Electron Devices* 51(5), 814–816 (2004).

31. Y. Yokoyama, T. Fukushige, S. Hata, K. Masu, and A. Shimokohbe, On-chip variable inductor using microelectromechanical systems technology, *Japanese Journal of Applied Physics Part 1-Regular Papers Short Notes and Review Papers* 42(4B), 2190–2192 (2003).

32. H. R. Jiang, Y. Wang, J. L. A. Yeh, and N. C. Tien, On-chip spiral inductors suspended over deep copper-lined cavities, *IEEE Transactions on Microwave Theory and Techniques* 48(12), 2415–2423 (2000).

33. M. Yamaguchi, K. Suezawa, Y. Takahashi, K. I. Arai, S. Kikuchi, Y. Shimada, S. Tanabe, and K. Ito, Magnetic thin-film inductors for RF-integrated circuits, *Journal of Magnetism and Magnetic Materials* 215, 807–810 (2000).

34. M. Yamaguchi, M. Baba, and K. I. Arai, Sandwich-type ferromagnetic RF integrated inductor, *IEEE Transactions on Microwave Theory and Techniques* 49(12), 2331–2335 (2001).

35. M. Yamaguchi, M. Baba, K. Suezawa, T. Moizumi, K. I. Arai, A. Haga, Y. Shimada, S. Tanabe, and K. Itoh, Improved RF integrated magnetic thin-film inductors by means of micro slits and surface planarization techniques, *IEEE Transactions on Magnetics* 36(5), 3495–3498 (2000).

36. M. Yamaguchi, H. Okuyama, and K. I. Arai, Characteristics of magnetic thin-film inductors at large magnetic-field, *IEEE Transactions on Magnetics* 31(6), 4229–4231 (1995).

37. M. Yamaguchi, K. Suezawa, K. I. Arai, Y. Takahashi, S. Kikuchi, Y. Shimada, W. D. Li, S. Tanabe, and K. Ito, Microfabrication and characteristics of magnetic thin-film inductors in the ultrahigh frequency region, *Journal of Applied Physics* 85(11), 7919–7922 (1999).

38. Y. Suzuki, R. B. vanDover, E. M. Gyorgy, J. M. Phillips, V. Korenivski, D. J. Werder, C. H. Chen, R. J. Felder, R. J. Cava, J. J. Krajewski, and W. F. Peck, Magnetic properties of epitaxial ferrite multilayer films, *Journal of Applied Physics* 79(8), 5923–5925 (1996).

39. M. Saidani and M. A. M. Gijs, High-quality radio-frequency inductors on silicon using a hybrid ferrite technology, *Applied Physics Letters* 84(22), 4496–4498 (2004).

40. T. V. Papakostas and N. M. White, Polymer thick-films on silicon: A route to hybrid microsystems, *IEEE Transactions on Components and Packaging Technologies* 24(1), 67–75 (2001).

41. P. Calvert, Inkjet printing for materials and devices, *Chemistry of Materials* 13(10), 3299–3305 (2001).

42. A. Dziedzic and A. Kolek, 1/f noise in polymer thick-film resistors, *Journal of Physics D-Applied Physics* 31(17), 2091–2097 (1998).

43. L. J. Golonka, A. Dziedzic, J. Kita, and T. Zawada, LTCC in microsystems application, *Informacije Midem-Journal of Microelectronics Electronic Components and Materials* 32(4), 272–279 (2002).

44. C. Y. Kim, H. J. Kim, and J. R. Kim, An integrated LTCC inductor, *IEEE Transactions on Magnetics* 41(10), 3556–3558 (2005).

45. E. J. Brandon, E. Wesseling, V. White, C. Ramsey, L. Del Castillo, and U. Lieneweg, Fabrication and characterization of microinductors for distributed power converters, *IEEE Transactions on Magnetics* 39(4), 2049–2056 (2003).

46. E. J. Brandon, E. E. Wesseling, V. Chang, and W. B. Kuhn, Printed microinductors on flexible substrates for power applications, *IEEE Transactions on Components and Packaging Technologies* 26(3), 517–523 (2003).

47. R. Boll, *Soft Magnetic Materials*, Vacuumschmelze GmbH, Hanau, Germany (1993).

48. Metglas. *Product Literature*, AlliedSignal, Morristown, NJ (1998).

49. E. Belloy, S. E. Gilbert, O. Dezuari, M. Sancho, and M. A. M. Gijs, A hybrid technology for miniaturised inductive device applications, *Sensors and Actuators a-Physical* 85(1–3), 304–309 (2000).

50. O. Dezuari, S. E. Gilbert, E. Belloy, and M. A. M. Gijs, High inductance planar transformers, *Sensors and Actuators a-Physical* 81(1–3), 355–358 (2000).

51. O. Dezuari, E. Belloy, S. E. Gilbert, and M. A. M. Gijs, Printed circuit board integrated fluxgate sensor, *Sensors and Actuators a-Physical* 81(1–3), 200–203 (2000).

52. O. Dezuari, E. Belloy, S. E. Gilbert, and M. A. M. Gijs, New hybrid technology for planar fluxgate sensor fabrication, *IEEE Transactions on Magnetics* 35(4), 2111–2117 (1999).

53. M. Mino, T. Yachi, A. Tago, K. Yanagisawa, and K. Sakakibara, Planar microtransformer with monolithically-integrated rectifier diodes for micro-switching converters, *IEEE Transactions on Magnetics* 32(2), 291–296 (1996).

54. M. Mino, T. Yachi, A. Tago, K. Yanagisawa, and K. Sakakibara, A new planar microtransformer for use in micro-switching converters, *IEEE Transactions on Magnetics* 28(4), 1969–1973 (1992).

55. K. Yamasawa, K. Maruyama, I. Hirohama, and P. P. Biringer, High-frequency operation of a planar-type microtransformer and its application to multilayered switching regulators, *IEEE Transactions on Magnetics* 26(3), 1204–1209 (1990).

56. S. Ben-Yaakov, *The Benefits of Planar Magnetics in HF Power Conversion*, Payton, Rishon-Le Zion, Israel (1996).

57. D. Vanderlinde, C. A. M. Boon, and J. B. Klaassens, Design of a high-frequency planar power transformer in multilayer technology, *IEEE Transactions on Industrial Electronics* 38(2), 135–141 (1991).

58. F. Amalou, E. L. Bornand, and M. A. M. Gijs, Batch-type millimeter-size transformers for miniaturized power applications, *IEEE Transactions on Magnetics* 37(4), 2999–3003 (2001).

59. E. Belloy, S. Thurre, E. Walckiers, A. Sayah, and M. A. M. Gijs, The introduction of powder blasting for sensor and microsystem applications, *Sensors and Actuators a-Physical* 84(3), 330–337 (2000).

MAGNETIC PARTICLE HANDLING IN LAB-ON-A-CHIP MICROSYSTEMS

MARTIN A.M. GIJS
Ecole Polytechnique Fédérale de Lausanne, Institute of Microelectronics and Microsystems, CH-1015 Lausanne, Switzerland

Abstract. We describe recent advances in the handling and manipulation of magnetic particles in microfluidic systems. In particular, we discuss new developments in magnetic manipulation, separation, transport, and detection of magnetic micro- and nanoparticles, pointing out the advantages and prospects of these concepts for future analysis applications.

Keywords: Magnetic particles; beads; magnetic particle separation; magnetic particle transport; magnetic label; giant magnetoresistance; magnetic supraparticle structures; magnetic bio-assay; droplet; microfluidics; lab-on-a-chip

1. Introduction

Well-known advantages of using microfluidic systems of reduced dimension for analytical applications are known to be: (i) the possibility of using minute quantities of sample and reagents (down to picoliters), (ii) relatively fast reaction times, when molecular diffusion lengths are of the order of the microchannel dimension, and (iii) a large surface to volume ratio offering an intrinsic compatibility between the use of a microfluidic system and surface-based assays. Reviews of various fluidic operations in microfluidic systems, like sample preparation, sample injection, sample manipulation, reaction, separation, and detection have been presented.[1–3]

Also nanomaterials and nanoparticles have become a hot topic in research. Functional nano- and micro-particles ('beads') offer a large specific surface for chemical binding and a polymer colloid or microsphere solution has a low viscosity compared to solutions having the same amount of solid, giving it special properties. Such small particles can be advantageously used as a 'mobile substrate' for bio-assays or even for in vivo applications; they can be easily recovered from a dispersion, reversibly re-dispersed, etc. Several reviews on the preparation and use of polymer particles and polymer colloids for medical, biological, and optical applications exist.[4,5]

B. Azzerboni et al. (eds.), Magnetic Nanostructures in Modern Technology, 153–165.

Magnetic nano- and microparticles offer still an additional advantage: having embedded magnetic entities, they can be magnetically manipulated using permanent magnets or electromagnets, independent of normal microfluidic or biological processes. This extra degree of freedom is at the basis of a still improved exposure of the functionalized bead surface to the surrounding liquid and of higher sample pre-concentration efficiencies, due to the increased relative motion of the bead with respect to the fluid. Pankhurst et al.[6] reviewed the applications of magnetic nanoparticles in biomedicine with focus on the underlying physics. Gijs[7] reviewed the handling and manipulation of magnetic particles in microfluidic systems, pointing out the advantages and prospects of these concepts for future analysis applications. The review of Pamme[8] discusses various developments within the field of magnetism and microfluidics. An updated review of analytical applications of magnetic micro- and nanoparticles in microfluidic systems is written by Gijs.[9] In view of the existence and timing of the latter work, the present chapter only intends to present a short overview of the field.

Different types of magnetic beads have their individual advantages and disadvantages. Polystyrene-coated magnetic particles are known for their excellent size distribution and spherical shape.[10,11] However, their hydrophobic surface results in a high amount of unspecific protein and antibody binding on the particle surface, so that it needs to be modified chemically. Magnetic silica particles are very efficient in adsorbing proteins and DNA on their surface, but are hardly available with a small size distribution and an ideal spherical shape.[12,13] Magnetic polysaccharide particles are important for many in vivo applications. They combine biocompatibility with availability in a size range below 300 nm,[14,15] but the particles are irregular in shape and the soft particle matrix causes them to be sensitive to mechanical stress. Also magnetic poly-(lactic acid) particles play an important role in in vivo applications:[16,17] they are biodegradable and their degradation time in the blood can be adjusted by their molecular weight and exact chemical composition.

It is important to recognize that a magnetic field *gradient* is required to exert a translation force. The magnetic force acting on a point-like magnetic dipole or 'magnetic moment' $\mathbf{m}$ can be written as the gradient of the magnetic energy[18,19]

$$\mathbf{F_m} = \frac{1}{\mu_0}\nabla\left(\mathbf{m}\cdot\mathbf{B}\right) \approx \frac{1}{\mu_0}\left(\mathbf{m}\cdot\nabla\right)\mathbf{B} \tag{1}$$

The second part of the equation holds when the magnetic moment of the particle is not varying in space ($\nabla\cdot\mathbf{m}=0$). Note that this is only a correct assumption when the moment is permanent or the magnetic particle is in such large field that its magnetization is completely saturated.

2. Magnetic particle separation

Magnetic separator design can be as simple as the application and removal of a permanent magnet to the wall of a test tube to cause aggregation, followed by removal of the supernatant. However, it is preferable to increase the separator efficiency by producing regions with a high magnetic field gradient to capture the magnetic nanoparticles as they flow by in the carrier medium. For example, the separation can take place within a laminar flow of a carrier fluid along a thin microchannel. A field gradient is imposed across the thin dimension of the channel, perpendicular to the direction of the flow. A division of the flow at the channel outlet using a stream splitter completes the separation into fractions. The perpendicular particle separation velocity is induced by the field gradient. Microfluidic channels made in silicon wafers have been combined with closely positioned permanent magnets to separate magnetic from non-magnetic particles into different output channels.[20] A truly integrated magnetic bead sorter combines micromagnetics with microfluidics and is characterized by a magnetic environment where particles with distinct magnetic properties may be manipulated differently than other particles on the length scale of the microfluidic circuit. The group of Ahn, as one of the first, reported such integrated bead separation systems.[21–23] Such devices can be used, for example, for miniaturized cell sorting, where the magnetic beads are used as magnetic 'label' for actuation, or in a miniaturized bio-reaction system, where the magnetic beads play the role of carrier substrate in an assay.[21,24] Comprehensive theoretical and experimental studies of various types of micro-electromagnets on-chip were presented more recently.[25–30]

In another type of work, a magnetic separation system was realized using an array of 15 μm wide electroplated Ni posts as filtering elements placed inside microfluidic channels made by soft lithography in PDMS.[31] Once magnetized by a magnetic field from an external NdFeB permanent magnet, these Ni posts attracted the magnetic field lines and thereby generated strong magnetic field gradients that efficiently could trap superparamagnetic beads passing them in a flowing stream of water. These Ni post arrays were also used to separate magnetic beads from non-magnetic beads. The idea of integrating an array of integrated soft-magnetic elements embedded beneath or at the side of a microfluidic channel was reported on several occasions in literature.[32,33] Such elements, which are polarized by a moderate bias field provided by an external magnet, produce a non-uniform field distribution characterized by a considerable field gradient.

3. Magnetic particle transport

In magnetic transport, magnetic forces effectively transport the particles: it requires magnetic fields and magnetic forces that act on a larger range than necessary for separation, where magnetic beads approach very closely the magnetic

actuation region by the fluid motion. Manipulation of magnetic beads in general and transport in particular, is a difficult task, as the magnetic susceptibility χ of the magnetic beads is rather weak (typically $\chi \leq 1$), due to the small magnetic volumes of the particles. This explains why mostly the large field of (mechanically moving) permanent magnets has been used for the separation, transport, and positioning of magnetic microbeads.[14] In an approach towards miniaturization and automation of analytical applications, a system has been proposed in which liquid movement is substituted with magnetically induced movement of magnetic particles.[34] In another approach, magnetic particles have been transported over millimetre distances in a microfluidic channel using an array of electromagnets actuated in a four-phase scheme.[35] Also miniaturized magnetic solutions have been proposed for bead transport, thereby taking full profit from batch microfabrication technologies. Typically, the size of the micropatterned magnets determines the spatial range, where appreciable magnetic forces acting on the microbeads exist. Serpentine gold wires micropatterned on silicon substrates, have been combined with microfluidic structures realized in PDMS to transport 4.5 μm polystyrene-coated magnetic beads.[36]

By engineering the magnetic field produced by different current-carrying wires, a microsystem was realized that could generate local magnetic field maxima that trap the magnetic beads. When the field maxima change locations, the microbeads follow those maxima. The device allowed precise positioning and transport over 100 μm distances in a single actuation event, which is partly due to the presence of a permanent magnet placed in proximity of the microfluidic chip, the role of which principally is to enhance the magnetic force by inducing a magnetic moment in the magnetic beads. A micro-electromagnet wire matrix, based on two layers of mutually orthogonal arrays of linear wires, has demonstrated magnetic transport of 1–2 μm size magnetic particles over 20 μm distances in a single actuation event.[37] This is a typical working range for the magnetic force, generated by a current-carrying conductor, when no external permanent magnet is used to induce a magnetic moment to the beads. Transport using current carrying wires or microcoils in combination with a magnetic substrate or film to enhance the magnetic forces has been demonstrated more recently.[27,38]

In another approach, a simple planar coil array-based magnetic transport system has been proposed, in which an individual coil is capable of displacing beads over millimeter distances in a liquid-containing capillary.[39] A drastic increase of the magnetic energy and magnetic forces acting on the beads was obtained by placing the complete coil array in a uniform static magnetic field that imposes a permanent magnetic moment to the microbeads.

An original transporting device consisting of a set of two tapered conductors, shifted linearly over half a period was demonstrated by Wirix-Speetjens et al.[40,41] This device was fabricated using standard semiconductor fabrication and photolithography techniques. The average speed of a magnetic particle is defined as

the distance over which the particle is transported parallel to the conductor edge divided by the minimal time needed to reach the next minimal cross-section and is of the order of several 10 μm/s.

4. Magnetic particles as labels for detection

Detection of biological molecules is usually accomplished using biomolecular recognition between the target molecule and a specific receptor (e.g. an antibody) that is tagged with a label. The label may be a radio-isotope, enzyme, fluorescent molecule, or charged molecule, for example. Recently, also magnetic beads have been used as labels for biosensing. Magnetic labels have several advantages over other labels. The magnetic properties of the beads are stable over time, in particular, because the magnetism is not affected by reagent chemistry or subject to photo-bleaching (a problem with fluorescent labels). There is also no significant magnetic background present in a biological sample and magnetic fields are not screened by aqueous reagents or biomaterials. In addition, magnetism may be used to remotely manipulate the magnetic particles. A number of very sensitive magnetic field detection devices have been developed during recent years, like giant magnetoresistance (GMR)[42] and spin-valve[43,44] magnetic sensors that enable the measurement of extremely weak magnetic fields, for example the magnetic field generated by the magnetization of a magnetic particle.

Researchers at the Naval Research Laboratory,[45–48] followed by others,[49–62] have developed microsystems for the capture and detection of micron-sized, paramagnetic beads on a chip containing GMR or spin-valve sensors. A review of research in this specific area was presented by Graham et al.[63]

Reiss et al.[55,56,58,59,64] developed similar sensors using 0.35 μm magnetic particles. Also a dose-response curve for a real biochemical assay was given and compared with fluorescence detection. The format of the test is rather peculiar, in that the concentration of probe DNA on the surface was varied rather than the concentration of DNA in the incubation step. It is thus more an assay of the likelihood of DNA attachment than of concentration in a test sample.

5. Magnetic supraparticle structures

When placed in a magnetic field, superparamagnetic particles will acquire a magnetic moment and they will start interacting by the magnetic dipole interaction. This interaction induces a spontaneous clustering of the particles into larger, often complicated, structures, sometimes called magnetic supraparticle structures (SPS). The shape of an SPS depends on parameters, like the size of the magnetic moment of the microbeads and the magnetic dipolar interaction between different beads. These properties are dependent on the amplitude and

frequency of the applied magnetic field, the shape and magnetic content of the beads, the concentration of the magnetic particles in the fluid, the temperature, etc. Despite the complexity of the aggregation process of a magnetic fluid into a SPS, the physical effects of a magnetic field on such structure are now very well understood.[65,66]

Self-assembled magnetic SPS have been used for long DNA separation in microfluidic channels. This represents a convenient solution, since no microlithography is required to define geometrical constrictions that are simply defined by the porous magnetic matrix.[67] Experimental separations using the SPS matrix have been combined with theoretical modeling[68] and, recently, computer-piloted flow control and injection of the experiment resulted in a quantitative and reproducible separation of long DNA by a SPS matrix.[69]

Besides the use of magnetic SPS as a static stationary phase for separation in microfluidic channels, researchers have also been investigating the potential of manipulating *dynamically* magnetic particle aggregates for microfluidic applications. Active fluid mixing was demonstrated in microchannels made in a micromachined microfluidic chip of PMMA: mixing was based on the manipulation by a local alternating magnetic field of self-assembled porous structures of magnetic microbeads that are placed over the section of the channel.[70,71]

6. Magnetic particles as substrates for bio-assays

Heterogenous assays, where reactions occur both in solution and in a solid phase, offer the advantage of easy separation of chemical complexes from reactants. Biomolecule immobilization on a solid phase, formed by the surface of micro- or nano-particles, evidently results in a small-volume and localized assay.[72,73] Such solid phase provides a high surface to volume ratio, reducing diffusion times during the microfluidic procedures and increasing the density of binding sites, which is beneficial for a high detection signal and sensitivity. In addition, such assay allows for a rapid regeneration and exchange of the solid support when needed. For example, a small quantity of polystyrene magnetic microbeads containing immobilized biomolecules was injected into a neutral hydrophilic-coated fused-silica capillary.[73] The short plug (2–3 mm) of beads was held fixed by a magnet placed in the cartridge of a Capillary Electrophoresis (CE) system. The microfluidic procedure involved antigen capture from the sample solution to the beads, rinsing, elution, and electrophoretic separation of the sample. The beads could be replaced after each run, eliminating the need to regenerate the solid support.

Choi et al. reported on the development and characterization of an integrated microfluidic biochemical detection system for fast and low-volume immunoassays using magnetic beads.[24] First, antibody-labeled polystyrene magnetic beads were separated from a liquid solution by a set of planar coils. While holding the antibody-coated beads, antigens were injected into the channel. Only target

antigens were immobilized, and thus separated onto the magnetic bead surface due to the specific antibody/antigen reaction. Detection of the target antigen was based on an electrochemical enzymatic reaction in a sandwich immuno-assay.

In another study, a fully integrated biochip cartridge that consists of microfluidic mixers, valves, pumps, channels, chambers, heaters, and DNA micro-array sensors was developed to perform DNA analysis of complex biological sample solutions.[74] Sample preparation (including magnetic bead-based cell capture, cell pre-concentration and purification, and cell lysis), polymerase chain reaction (PCR), DNA hybridization, and electrochemical detection were performed in this fully automated miniature device.

7. Magnetic beads in droplets

An interesting study reported on the magnetic actuation and transport of magnetic beads contained in water droplets that were suspended in a silicone oil solution.[75,76] An aqueous buffer solution containing magnetic beads is dropped into silicone oil on a glass plate, which is made hydrophobic by applying a surface treatment. The droplets that form in the solution are suspended in the oil because of the differences in surface tension between the two liquids and the superior wettability of the oil to the plate. The drops contain magnetic microparticles that serve both as force mediators for the magnetic actuation and as a mobile substrate for the molecules.

Also a magnetic droplet manipulation system in which aqueous droplets are actuated through a multilayer set of coils on a PCB has been presented.[77] The PCB generates a changeable magnetic-field topology over the chip surface that allows variation in the force that acts on the magnetic particles inside the droplets. By combining droplet manipulation steps, a complete DNA-purification procedure was demonstrated. The latter employs six stages of droplet merging, mixing, and splitting. The buffer solutions for binding, washing, and elution are present on the chip in the form of immobilized 10 μL droplets. On-chip DNA purification from whole cell samples down to 10 cells per 10 μL, could be demonstrated.

8. Conclusion

A summary on recent advances in the handling, manipulation, and detection of magnetic beads in microfluidic systems was presented. Some of the classical applications, like magnetic separation, have already found their way down to miniaturized fluidic or ‘lab-on-a-chip’ systems that strongly limit the consumption of samples and reagents; in such systems, magnetic beads effectively provided a chemically active substrate with a large surface to volume ratio. The booming area of miniaturized applications of magnetic beads offers many exciting possibilities

for future developments. Combining magnetic particles and their detection system with the recently developed magnetic manipulation techniques already resulted in highly integrated bio-assay systems, in which all functions (from sample treatment to read-out) could be extremely miniaturized. Droplet-based systems in which aqueous magnetic particle containing droplets are transported in an oil medium are particularly attractive for their simplicity, reconfigurability, self-containment, and the reduction of sample evaporation effects. We therefore think that magnetic particle microsystems will play an important role in future miniaturized analysis techniques.

Acknowledgements

We thank the Swiss National Science Foundation (Grant 200020-107372) for financial support of our research. The author gratefully acknowledges Amar Rida, Victor Fernandez, Hicham Majd, Smail Hadjidj, Ulrike Lehmann, Virendra Parashar, and Caroline Vandevyver for useful discussions and collaboration.

References

1. P.A. Auroux, D. Iossifidis, D.R. Reyes, and A. Manz, Micro total analysis systems. 2. Analytical standard operations and applications, *Analytical Chemistry* 74(12), 2637–2652 (2002).
2. T. Vilkner, D. Janasek, and A. Manz, Micro total analysis systems. Recent developments, *Analytical Chemistry* 76(12), 3373–3385 (2004).
3. P.S. Dittrich, K. Tachikawa, and A. Manz, Micro total analysis systems. Latest advancements and trends, *Analytical Chemistry* 78(12), 3887–3908 (2006).
4. H. Kawaguchi, Functional polymer microspheres, *Progress in Polymer Science* 25(8), 1171–1210 (2000).
5. F.E. Kruis, H. Fissan, and A. Peled, Synthesis of nanoparticles in the gas phase for electronic, optical and magnetic applications - A review, *Journal of Aerosol Science* 29 (5–6), 511–535 (1998).
6. Q.A. Pankhurst, J. Connolly, S.K. Jones, and J. Dobson, Applications of magnetic nanoparticles in biomedicine, *Journal of Physics D-Applied Physics* 36(13), R167–R181 (2003).
7. M.A.M. Gijs, Magnetic bead handling on-chip: new opportunities for analytical applications (review), *Microfluidics and Nanofluidics* 1, 22–40 (2004).
8. N. Pamme, Magnetism and microfluidics, *Lab on a Chip* 6(1), 24–38 (2006).
9. M.A.M. Gijs, Magnetic beads in microfluidic systems - towards new analytical applications, in: S. Hardt and F. Schönfeld (ed.) *Microfluidic Technologies for Miniaturized Analysis Systems*, Springer, New York (2007), pp.
10. J.M. Singer, Future directions in polymer colloids, in: M.S. El-Asser and R.M. Fitch (eds) *NATO ASI series. Series E, Applied Sciences*, 138, Published in cooperation with NATO Scientific Affairs Division by Nijhoff, Dordrecht, The Netherlands (1987), pp. 402.

11. P. Dynal, S.A. Dynal, Oslo, Norway, product catalogue. Available at: http://www.dynal.no

12. J. Kleiber, T. Walter, H. Harttig, C. Lesniak, M. Mennig, M. Riedling, and H. Schmidt, US patent 6255477B1 (2001).

13. Undisclosed_inventors, European patent 1154443A1 (2001).

14. S. Miltenyi, W. Muller, W. Weichel, and A. Radbruch, High-gradient magnetic cell-separation with Macs, *Cytometry* 11(2), 231–238 (1990).

15. C. Gruttner and J. Teller, New types of silica-fortified magnetic nanoparticles as tools for molecular biology applications, *Journal of Magnetism and Magnetic Materials* 194(1–3), 8–15 (1999).

16. U.O. Hafeli, S.M. Sweeney, B.A. Beresford, E.H. Sim, and R.M. Macklis, Magnetically directed poly(lactic acid) Y-90 microspheres – novel agents for targeted intracavitary radiotherapy, *Journal of Biomedical Materials Research* 28(8), 901–908 (1994).

17. U.O. Hafeli and G.J. Pauer, In vitro and in vivo toxicity of magnetic microspheres, *Journal of Magnetism and Magnetic Materials* 194(1–3), 76–82 (1999).

18. M. Zborowski, L.P. Sun, L.R. Moore, P.S. Williams, and J.J. Chalmers, Continuous cell separation using novel magnetic quadrupole flow sorter, *Journal of Magnetism and Magnetic Materials* 194(1–3), 224–230 (1999).

19. S.S. Papell, US patent 3215572 (1965).

20. G. Blankenstein and U.D. Larsen, Modular concept of a laboratory on a chip for chemical and biochemical analysis, *Biosensors and Bioelectronics* 13(3–4), 427–438 (1998).

21. J.W. Choi, C.H. Ahn, S. Bhansali, and H.T. Henderson, A new magnetic bead-based, filterless bio-separator with planar electromagnet surfaces for integrated bio-detection systems, *Sensors and Actuators B-Chemical* 68(1–3), 34–39 (2000).

22. J.W. Choi, T.M. Liakopoulos, and C.H. Ahn, An on-chip magnetic bead separator using spiral electromagnets with semi-encapsulated permalloy, *Biosensors and Bioelectronics* 16(6), 409–416 (2001).

23. C.H. Ahn, M.G. Allen, W. Trimmer, Y.N. Jun, and S. Erramilli, A fully integrated micromachined magnetic particle separator, *Journal of Microelectromechanical Systems* 5(3), 151–158 (1996).

24. J.W. Choi, K.W. Oh, J.H. Thomas, W.R. Heineman, H.B. Halsall, J.H. Nevin, A.J. Helmicki, H.T. Henderson, and C.H. Ahn, An integrated microfluidic biochemical detection system for protein analysis with magnetic bead-based sampling capabilities, *Lab on a Chip* 2(1), 27–30 (2002).

25. Q. Ramadan, V. Samper, D.P. Poenar, and C. Yu, An integrated microfluidic platform for magnetic microbeads separation and confinement, *Biosensors and Bioelectronics* 21(9), 1693–1702 (2006).

26. Q. Ramadan, V. Samper, D. Poenar, Z. Liang, C. Yu, and T.M. Lim, Simultaneous cell lysis and bead trapping in a continuous flow microfluidic device, *Sensors and Actuators B-Chemical* 113(2), 944–955 (2006).

27. Q. Ramadan, C. Yu, V. Samper, and D.P. Poenar, Microcoils for transport of magnetic beads, *Applied Physics Letters* 88(3), (2006).

28. Q. Ramadan, V. Samper, D. Poenar, and C. Yu, On-chip micro-electromagnets for magnetic-based bio-molecules separation, *Journal of Magnetism and Magnetic Materials* 281(2–3), 150–172 (2004).

29. K. Smistrup, P.T. Tang, O. Hansen, and M.F. Hansen, Micro electromagnet for magnetic manipulation in lab-on-a-chip systems, *Journal of Magnetism and Magnetic Materials* 300(2), 418–426 (2006).

30. K. Smistrup, O. Hansen, H. Bruus, and M.F. Hansen, Magnetic separation in microfluidic systems using microfabricated electromagnets-experiments and simulations, *Journal of Magnetism and Magnetic Materials* 293(1), 597–604 (2005).

31. T. Deng, M. Prentiss, and G.M. Whitesides, Fabrication of magnetic microfiltration systems using soft lithography, *Applied Physics Letters* 80(3), 461–463 (2002).

32. E. P. Furlani, Analysis of particle transport in a magnetophoretic microsystem, *Journal of Applied Physics* 99(2), (2006).

33. K. Smistrup, T. Lund-Olesen, M.F. Hansen, and P.T. Tang, Microfluidic magnetic separator using an array of soft magnetic elements, *Journal of Applied Physics* 99(8), (2006).

34. S. Ostergaard, G. Blankenstein, H. Dirac, and O. Leistiko, A novel approach to the automation of clinical chemistry by controlled manipulation of magnetic particles, *Journal of Magnetism and Magnetic Materials* 194(1–3), 156–162 (1999).

35. J. Joung, J. Shen, and P. Grodzinski, Micropumps based on alternating high-gradient magnetic fields, *IEEE Transactions on Magnetics* 36(4), 2012–2014 (2000).

36. T. Deng, G. M. Whitesides, M. Radhakrishnan, G. Zabow, and M. Prentiss, Manipulation of magnetic microbeads in suspension using micromagnetic systems fabricated with soft lithography, *Applied Physics Letters* 78(12), 1775–1777 (2001).

37. C.S. Lee, H. Lee, and R.M. Westervelt, Microelectromagnets for the control of magnetic nanoparticles, *Applied Physics Letters* 79(20), 3308–3310 (2001).

38. Z.H. Wang, W.S. Lew, and J.A.C. Bland, Manipulation of superparamagnetic beads using on-chip current lines placed on a ferrite magnet, *Journal of Applied Physics* 99(8), (2006).

39. A. Rida, V. Fernandez, and M.A.M. Gijs, Long-range transport of magnetic microbeads using simple planar coils placed in a uniform magnetostatic field, *Applied Physics Letters* 83(12), 2396–2398 (2003).

40. R. Wirix-Speetjens, W. Fyen, J. De Boeck, and G. Borghs, Enhanced magnetic particle transport by integration of a magnetic flux guide: experimental verification of simulated behavior, *Journal of Applied Physics* 99(8), (2006).

41. R. Wirix-Speetjens, W. Fyen, K.D. Xu, J. De Boeck, and G. Borghs, A force study of on-chip magnetic particle transport based on tapered conductors, *IEEE Transactions on Magnetics* 41(10), 4128–4133 (2005).

42. M.N. Baibich, J.M. Broto, A. Fert, F.N. Vandau, F. Petroff, P. Eitenne, G. Creuzet, A. Friederich, and J. Chazelas, Giant magnetoresistance of (001)Fe/(001) Cr magnetic superlattices, *Physical Review Letters* 61(21), 2472–2475 (1988).

43. B. Dieny, V.S. Speriosu, S. Metin, S.S.P. Parkin, B.A. Gurney, P. Baumgart, and D.R. Wilhoit, Magnetotransport properties of magnetically soft spin-valve structures, *Journal of Applied Physics* 69(8), 4774–4779 (1991).

44. P.P. Freitas, F. Silva, N.J. Oliveira, L.V. Melo, L. Costa, and N. Almeida, Spin valve sensors, *Sensors and Actuators A-Physical* 81(1–3), 2–8 (2000).

45. D.R. Baselt, G.U. Lee, M. Natesan, S.W. Metzger, P.E. Sheehan, and R.J. Colton, A biosensor based on magnetoresistance technology, *Biosensors and Bioelectronics* 13(7–8), 731–739 (1998).

46. M.M. Miller, P.E. Sheehan, R.L. Edelstein, C.R. Tamanaha, L. Zhong, S. Bounnak, L.J. Whitman, and R.J. Colton, A DNA array sensor utilizing magnetic microbeads and magnetoelectronic detection, *Journal of Magnetism and Magnetic Materials* 225(1–2), 138–144 (2001).

47. J.C. Rife, M.M. Miller, P.E. Sheehan, C.R. Tamanaha, M. Tondra, and L.J. Whitman, Design and performance of GMR sensors for the detection of magnetic microbeads in biosensors, *Sensors and Actuators A-Physical* 107(3), 209–218 (2003).

48. R.L. Edelstein, C.R. Tamanaha, P.E. Sheehan, M.M. Miller, D.R. Baselt, L.J. Whitman, and R.J. Colton, The BARC biosensor applied to the detection of biological warfare agents, *Biosensors and Bioelectronics* 14(10–11), 805–813 (2000).

49. R. Coehoorn and M.W.J. Prins, Patent application WO 03/054523 A2 (2003).

50. D.L. Graham, H.A. Ferreira, P.P. Freitas, and J.M.S. Cabral, High sensitivity detection of molecular recognition using magnetically labelled biomolecules and magnetoresistive sensors, *Biosensors and Bioelectronics* 18(4), 483–488 (2003).

51. H.A. Ferreira, D.L. Graham, N. Feliciano, L.A. Clarke, M.D. Amaral, and P.P. Freitas, Detection of cystic fibrosis related DNA targets using AC field focusing of magnetic labels and spin-valve sensors, *IEEE Transactions on Magnetics* 41(10), 4140–4142 (2005).

52. H.A. Ferreira, N. Feliciano, D.L. Graham, and P.P. Freitas, Effect of spin-valve sensor magnetostatic fields on nanobead detection for biochip applications, *Journal of Applied Physics* 97(10), 10Q904 (2005).

53. H.A. Ferreira, N. Feliciano, D.L. Graham, L.A. Clarke, M.D. Amaral, and P.P. Freitas, Rapid DNA hybridization based on ac field focusing of magnetically labeled target DNA, *Applied Physics Letters* 87(1), (2005).

54. D.L. Graham, H.A. Ferreira, N. Feliciano, P.P. Freitas, L.A. Clarke, and M.D. Amaral, Magnetic field-assisted DNA hybridisation and simultaneous detection using micron-sized spin-valve sensors and magnetic nanoparticles, *Sensors and Actuators B-Chemical* 107(2), 936–944 (2005).

55. G. Reiss, H. Brueckl, A. Huetten, J. Schotter, M. Brzeska, M. Panhorst, D. Sudfeld, A. Becker, P.B. Kamp, A. Puehler, K. Wojczykowski, and P. Jutzi, Magnetoresistive sensors and magnetic nanoparticles for biotechnology, *Journal of Materials Research* 20(12), 3294–3302 (2005).

56. H. Bruckl, M. Brzeska, D. Brinkmann, J. Schotter, G. Reiss, W. Schepper, P.B. Kamp, and A. Becker, Magnetoresistive logic and biochip, *Journal of Magnetism and Magnetic Materials* 282, 219–224 (2004).

57. M. Brzeska, M. Panhorst, P.B. Kamp, J. Schotter, G. Reiss, A. Puhler, A. Becker, and H. Bruckl, Detection and manipulation of biomolecules by magnetic carriers, *Journal of Biotechnology* 112(1–2), 25–33 (2004).

58. J. Schotter, P.B. Kamp, A. Becker, A. Puhler, G. Reiss, and H. Bruckl, Comparison of a prototype magnetoresistive biosensor to standard fluorescent DNA detection, *Biosensors and Bioelectronics* 19(10), 1149–1156 (2004).

59. J. Schotter, P.B. Kamp, A. Becker, A. Puhler, D. Brinkmann, W. Schepper, H. Bruckl, and G. Reiss, A biochip based on magnetoresistive sensors, *IEEE Transactions on Magnetics* 38(5), 3365–3367 (2002).

60. G.X. Li, V. Joshi, R.L. White, S.X. Wang, J.T. Kemp, C. Webb, R.W. Davis, and S.H. Sun, Detection of single micron-sized magnetic bead and magnetic nanoparticles using spin valve sensors for biological applications, *Journal of Applied Physics* 93(10), 7557–7559 (2003).

61. R.L. Millen, T. Kawaguchi, M.C. Granger, M.D. Porter, and M. Tondra, Giant magnetoresistive sensors and superparamagnetic nanoparticles: A chip-scale detection strategy for immunosorbent assays, *Analytical Chemistry* 77(20), 6581–6587 (2005).

62. M. Tondra, A. Popple, A. Jander, R.L. Millen, N. Pekas, and M.D. Porter, Microfabricated tools for manipulation and analysis of magnetic microcarriers, *Journal of Magnetism and Magnetic Materials* 293(1), 725–730 (2005).

63. D.L. Graham, H.A. Ferreira, and P.P. Freitas, Magnetoresistive-based biosensors and biochips, *Trends in Biotechnology* 22(9), 455–462 (2004).

64. W. Schepper, J. Schotter, H. Bruckl, and G. Reiss, A magnetic molecule detection system - A comparison of different setups by computer simulation, *Physica B-Condensed Matter* 372(1–2), 337–340 (2006).

65. J. Liu, M. Lawrence, A. Wu, M.L. Ivey, G.. Flores, K. Javier, J. Bibette, and J. Richard, Field-induced structures in ferrofluid emulsions, *Physical Review Letters* 74(14), 2828–2831 (1995).

66. G.A. Flores, J. Liu, M. Mohebi, and N. Jamasbi, Field-induced columnar and bent-wall-like patterns in a ferrofluid emulsion, *International Journal of Modern Physics B* 13(14–16), 2093–2100 (1999).

67. P.S. Doyle, J. Bibette, A. Bancaud, and J.L. Viovy, Self-assembled magnetic matrices for DNA separation chips, *Science* 295(5563), 2237–2237 (2002).

68. K.D. Dorfman and J.L. Viovy, Semiphenomenological model for the dispersion of DNA during electrophoresis in a microfluidic array of posts, *Physical Review E* 69(1), 011901 (2004).

69. N. Minc, C. Futterer, K.D. Dorfman, A. Bancaud, C. Gosse, C. Goubault, and J.L. Viovy, Quantitative microfluidic separation of DNA in self-assembled magnetic matrixes, *Analytical Chemistry* 76(13), 3770–3776 (2004).

70. A. Rida, T. Lehnert, and M.A.M. Gijs, Microfluidic mixer using magnetic beads, in: *7th International Conference on Miniaturized Chemical and Biochemical Analysis Systems, 5—9 October 2003, Squaw Valley, California USA.*, pp. 579–582 (2003).

71. A. Rida and M.A.M. Gijs, Dynamics of magnetically retained supraparticle structures in a liquid flow, *Applied Physics Letters* 85, 4986–4988 (2004).

72. K. Sato, M. Tokeshi, T. Odake, H. Kimura, T. Ooi, M. Nakao, and T. Kitamori, Integration of an immunosorbent assay system: analysis of secretory human immunoglobulin A on polystyrene beads in a microchip, *Analytical Chemistry* 72(6), 1144–1147 (2000).

73. L.G. Rashkovetsky, Y.V. Lyubarskaya, F. Foret, D.E. Hughes, and B.L. Karger, Automated microanalysis using magnetic beads with commercial capillary electrophoretic instrumentation, *Journal of Chromatography A* 781(1–2), 197–204 (1997).

74. R.H. Liu, J.N. Yang, R. Lenigk, J. Bonanno, and P. Grodzinski, Self-contained, fully integrated biochip for sample preparation, polymerase chain reaction amplification, and DNA microarray detection, *Analytical Chemistry* 76(7), 1824–1831 (2004).

75. M. Shikida, K. Inouchi, H. Honda, and K. Sato, Magnetic handling of droplet in micro chemical analysis system utilizing surface tension and wettability, in: *17th IEEE International Conference on Micro Electro Mechanical Systems (MEMS 2004)*. Maastricht, The Netherlands, pp. 359–362 (2004).

76. M. Shikida, K. Takayanagi, K. Inouchi, H. Honda, and K. Sato, Using wettability and interfacial tension to handle droplets of magnetic beads in a micro-chemical-analysis system, *Sensors and Actuators B-Chemical* 113(1), 563–569 (2006).

77. U. Lehmann, C. Vandevyver, V.K. Parashar, and M.A.M. Gijs, Droplet-based DNA purification in a magnetic lab-on-a-chip, *Angewandte Chemie-International Edition* 45(19), 3062–3067 (2006).

HIGH PERFORMANCE μ-MAGNETS FOR MICROELECTROMECHANICAL SYSTEMS (MEMS)

OLIVER GUTFLEISCH
Leibniz Institute for Solid State and Materials Research, IFW Dresden, Helmholtzstr. 20, D-01069 Dresden, Germany

NORA M. DEMPSEY
Institut Néel, CNRS/UJF, 25 rue des Martyrs, 38042, Grenoble, France

Abstract. This chapter gives an overview of high-performance hard magnetic materials, which have potential applications in microelectromechanical systems (MEMS). It focuses on their fundamental magnetic and non-magnetic properties as well as their preparation routes. The aim of this chapter is to present some key issues concerning the development of μ-magnets such as magnetic performance, mechanical, thermal and chemical compatibility, system integration, and patterning.

Keywords: Permanent magnetism; hard magnetic materials; bulk and thick film magnet preparation routes; mechanical, thermal, and chemical compatibility; system integration; micro-patterning

1. Introduction

Magnetism has fascinated man for millennia. The literature of ancient China and Europe includes many references to the mysterious action at a distance produced by magnetic forces from the first known permanent magnet loadstone (magnetite Fe_3O_4). Originally, the notion of magnetism was identical with that of permanent magnetism and in today's colloquial language permanent magnets are simply called magnets. The last century has been the golden age of permanent magnetism. Permanent magnets are widely used in our daily life and feature in a large variety of products such as quartz analogue watches, earphones, microwaves, cordless tools, mobile phones, voice coil motors, etc. A modern car, for example, contains at least 50 permanent magnets. In this case, most of the magnets are so-called hard ferrites ($BaFe_{12}O_{19}$ and $SrFe_{12}O_{19}$), which generate typically a magnetic field of 0.1 T and are adapted for devices in which weight and space are not a major concern. Hard ferrites are low cost–low performance magnets and have good chemical stability. In more sophisticated applications, where, for example, miniaturization is an issue or completely new or more economical

B. Azzerboni et al. (eds.), Magnetic Nanostructures in Modern Technology, 167–194.

designs are needed, high performance permanent magnets based on rare-earth transition metal (RE-TM) compounds are used. $Nd_2Fe_{14}B$, generating a field of the order of 1 T, is mostly used in computers or portable electronic devices, but also in medicine for (intraoperative) diagnostics using a magnetic resonance imaging apparatus and magnetic navigation of interventional devises such as heart catheters. Other examples for new applications are hybrid electric vehicles (HEV), electronic cyclotronic resonance ion sources, magnetic refrigeration, and wind generators. Modern high-performance magnets are based on compounds of a magnetic light rare earth (Pr, Nd, Sm) for strong magnetic anisotropy and a 3d element (Fe, Co) for large magnetization and high Curie temperature. Permanent magnets based on noble metals such as Pt-Co or Pt-Fe also have excellent hard magnetic properties combined with high corrosion resistance and mechanical strength. However, the high cost of noble metals limits their use to specialized applications such as in biomedicine or in magnetic microelectromechanical systems (MEMS).

MEMS are progressively permeating everyday life, mainly in the form of microsensors: pressure, temperature, contact, chemical, acceleration, gyroscopes, etc. Their impact on automotive, air-and-space, industrial fabrication plants, bio-chemical, and bio-medical equipment is huge, widespread, and growing.

The high efficiency of magnetic interactions involving permanent magnets is the key to their near-universal use in macroscopic electrical actuators and energy converting devices.[1] This is particularly true for magnetic microsystems: energy density and power efficiency are paramount to their portability, compactness, and autonomy. Hybrid actuators incorporating both soft and hard magnetic materials provide a number of advantages over electrostatic actuators, namely low voltage and power consumption, large actuation forces over long distances, and enhanced reliability in adverse operating conditions. Thus, magnetic-MEMS are an emerging new family of devices with a wide range of potential applications in the fields of Bio-Medicine (implantable μ-valves and μ-pumps), Information Technology for both consumer and military applications (addressable RF μ-switches and optic fibre μ-commutators, adaptive optics), as well as Energy Transformation and Management (μ-motors, electrical μ-generators) (for more details see chapter by O. Cugat in this volume).

Magnetic-MEMS need high-performance magnets of thickness in the range of 5–500 μm. The need for both good magnetic properties and an integrated magnet fabrication process has not yet been concurrently fulfilled. Thus there is a real need for interdisciplinary action, bringing together magnetic-MEMS design engineers, permanent magnet material scientists, and microtechnologists.

In this chapter, we will review the basic principles of permanent magnetism. We will present today's high-performance permanent magnets and highlight some of their most pertinent features when prepared in bulk form. We will then describe and compare the various routes, which have been used to prepare permanent

magnets at the scale appropriate for MEMS applications and finally address the important issue of patterning the μ-magnets.

1.1. BASIC PRINCIPLES OF PERMANENT MAGNET MATERIALS

The progress in the field of permanent magnets has been dramatic over the last 35 years. This would have been impossible without a fundamental understanding of the physical phenomena responsible for hard magnet properties, which led to the discovery of new families of permanent magnet materials based on RE-TM compounds.

The search for new materials with superior properties focuses on compounds with high values of Curie temperature ($T_C > 500$ K), high saturation magnetization M_S ($\mu_0 M_S > 1$ T, with μ_0 the permeability of free space ($4\pi * 10^{-7}$ Tm/A)), and high magnetocrystalline anisotropy, H_A. In this section, these intrinsic properties, which depend on crystal structure and chemical composition, will be described and it will be elucidated that a favourable combination of these values does not lead automatically to a good hard magnet material but can only be regarded as a prerequisite (more detailed descriptions can be found in several works.[2–5] The final suitability can only be assessed when the extrinsic properties such as coercive field H_C, remanent magnetization B_r and maximum energy density $(BH)_{max}$, derived from the intrinsic properties by the preparation of appropriate microstructures, fulfill certain criteria.

The crystalline electric field together with the spin-orbit coupling is the main contribution to the *magnetic anisotropy* in permanent magnetic materials. For well-localized electrons (e.g. 4f electrons in rare-earth atoms) it manifests itself as single-ion anisotropy. The atomic moment has local easy directions that reflect the point symmetry of the site. Summing all single-ion contributions results in the overall magnetocrystalline anisotropy of the material. In the case of a hexagonal crystal, the anisotropy energy density E_A is given by

$$E_A = K_1 \sin^2\theta + K_2 \sin^4\theta + K_3 \sin^6\theta + K_3' \sin^6\theta \cos 6\Phi + \ldots \qquad (1)$$

where K_1, K_2, etc. are the so-called anisotropy constants, which vary with temperature and differ for different materials. The direction of the spontaneous magnetization relative to the uniaxial direction (c-axis) and the a-axis is given by the polar angles θ and Φ, respectively. With K_1 dominating and $K_1 > 0$, the equilibrium direction of magnetization will be along the c-axis. Such type of anisotropy is called *easy-axis anisotropy*. It also occurs in other crystallographically uniaxial systems (tetragonal and rhombohedral) where, however, the third and higher order terms in Eq. (1) are different from those of hexagonal systems. Easy-axis anisotropy is beneficial for maintaining the metastable state of magnetized permanent magnets. Therefore all high-performance permanent magnet materials are made of crystallographically uniaxial phases. The anisotropy field

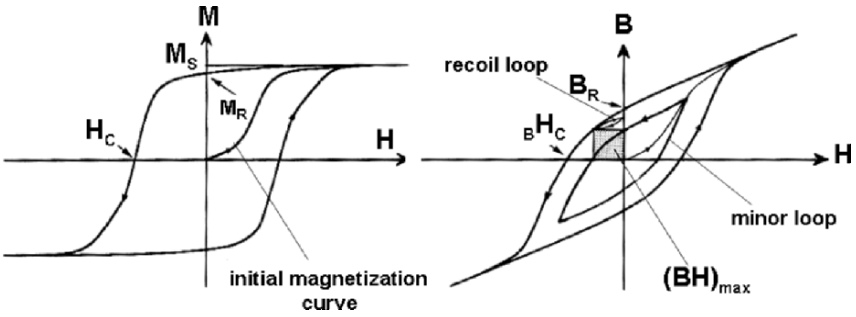

Figure 1. Hysteresis loops for a permanent magnet: (left) M–H loop and (right) B–H loop. The initial magnetization curve after thermal demagnetization starts at the origin; a minor loop arising after the application of fields insufficient for saturation is also shown. The energy product $(BH)_{max}$ is the shaded area in the second quadrant of the B–H loop.

H_A is defined as the intersection of the magnetization curves when measured with the field parallel and perpendicular to the easy magnetization direction and can be used as an estimate for K_1 for materials where K_2 is negligible (this is the case when the magnetization measured with the field applied perpendicular to the easy axis is a straight line, e.g. for tetragonal $Nd_2Fe_{14}B$ at room temperature). H_A is given by

$$H_A = (2K_1 + 4K_2)/\mu_0 M_S \tag{2}$$

The static magnetic properties are described by hysteresis loops as shown in Fig. 1, where either magnetization M or magnetic flux density B is plotted as a function of field H ($M-H$ or $B-H$ curves). Provided the applied field, corrected for the demagnetization effect (the demagnetization factor N is a pure number between 0 and 1 and depends only on sample shape, e.g. one third for spherical particles and the sum of the three orthogonal directions is unity), is sufficient to achieve saturation, one symmetric major loop is traced (the intrinsic property M_S is delineated in the $M - H$ presentation), otherwise minor loops are obtained. In the SI system the relationship between B, M, and H is given by:

$$B = \mu_0(H + M) \tag{3}$$

$M - H$ or $B - H$ loops have different contours, the former more relevant for fundamental aspects, the latter of interest from an application point of view and is usually presented in the magnet data sheets of a magnet producer. The remanence B_r or $\mu_0 M_r$ is the flux density or remanent magnetization that is left after removing the magnetizing field H. Another extrinsic property is given when the loop cuts the field axis, with $M = 0$ the coercivity H_c is obtained (often referred to as 'intrinsic coercivity' which is rather unfortunate because the coercivity is not an intrinsic property but is very much microstructure dependent). The maximum energy density $(BH)_{max}$, or energy product, of permanent magnets, is a measure of the magnetostatic energy stored and thus describes the performance of the magnet

(the shaded area in Fig. 1, right). It is the most widely used figure of merit and is found where the product of B and H is maximized and is equal to twice the potential energy of the magnetic field outside the magnet divided by its volume. $(BH)_{max}$ is limited by the remanence, provided the coercivity has at least half the value of the remanence:

$$(BH)_{max} \leq \mu_0 M_r^2/4 \tag{4}$$

The remanent magnetization M_r is half of the saturation magnetization M_S for an assembly of isotropic non-interacting single domain particles whereas it approaches M_s for textured magnets.

The coercivity is usually approximated by a linear combination of the two characteristic intrinsic fields H_a and $M_s = \mu_0^{-1} J_s$ (J_s – saturation polarization):

$$H_C = \alpha \frac{2K_1}{\mu_0 M_s} - N_{eff} M_s \tag{5}$$

where α and N_{eff} are microstructural parameters, the former ($0 < \alpha < 1$) describing the reduction of the crystal field ('softening') by defects as well as by misaligned grains and the latter, the effective demagnetization factor (note: different from the true demagnetization factor $D_1 + D_2 + D_3 = 1$ and thus not limited to unity), taking into account local stray fields.[6,7] The mechanism by which a permanent magnet is locked in the metastable domain configuration is controlled by many factors; easy-axis anisotropy being an indispensable prerequisite. The particular rare earth needed for uniaxial anisotropy is determined by the symmetry of the site it occupies in the crystal structure. Here we simply state that reverse domain nucleation and domain wall propagation result in $H_c \ll H_A$, which means that the anisotropy field represents an upper limit of the coercivity H_c, but typical coercivities in high-performance magnets do not exceed 20% of H_A. This reduction is principally attributed to microstructural effects.

The critical elementary magnetization reversal processes (CEMRPs), i.e. nucleation and growth of reverse domains from the fully magnetized state, in permanent magnets can be divided into three types. The first one found in microcrystalline magnets such as sintered NdFeB is of the nucleation-type.[8] The wall motion within a grain is relatively easy but the spontaneous nucleation of reverse domains is hindered by an almost defect-free microstructure and smooth surface of the grains, the latter surrounded by a thin paramagnetic boundary phase. In the thermally demagnetized, equilibrium state each individual grain, being much larger than the critical single domain size, contains a classical domain structure. The decoupling of the individual crystallites impedes propagation of reverse domains. Further examples of nucleation-controlled permanent magnets are $SmCo_5$ and bonded $Nd_2Fe_{14}B$ and $Sm_2Fe_{17}N_3$ magnets. In the second type, called pinning-type magnets, the grains are also large and are typified by $Sm_2(Co,Fe,Cu,Zr)_{17}$ magnets.[9] Reverse domains can be easily generated by relatively small reverse fields but here the propagation of these domains is

prevented by pinning the domain walls at inclusions or defects. The pinning mechanism is typical of materials with pronounced nanoscale inhomogeneities. The effectiveness of the pinning will depend on the geometry and spatial distribution of the pinning centers. The pinning will be most pronounced when the thickness or size of the pinning centres is comparable to the domain wall width. Sm_2Co_{17}-based magnets constitute a good example of this type of magnet where the pinning of the domain walls takes place at a $SmCo_5$-type cell boundary phase. The formation of nanometer-sized defects in SmFeN powders by heavy ion irradiation was shown to induce a pinning-type coercivity.[10] The third type is found in fine-grained materials with a grain size in the vicinity of or below the critical single domain particle size.[11] The detailed magnetization reversal behaviour of such materials will depend on the type and the strength of the magnetic interactions. Nucleation and growth of reverse domains, for example, in exchange-coupled magnets consisting of finely dispersed hard and soft magnetic phases ("exchange spring magnets"),[12] have been modelled numerically.[13]

It has been tried to unify the analysis and description of coercivity in the three types of magnets in a "Global model,"[14] which considers explicitly that magnetization reversal develops from an initial "activation volume" v_a.[15] The principal coercivity mechanism can be determined by analyzing initial magnetization curves, after thermal and dc-field demagnetization, and demagnetization curves in the respective hysteresis loops. The nucleation- and pinning-type can be easily recognized from their respective initial magnetization curve, the former showing a large low-field susceptibility whereas the latter is characterized by a small low-field susceptibility.

In thermal equilibrium, a ferromagnetic material consists of magnetic domains,[16] and these find their origin in the lower magnetostatic energy, in comparison to a state where the material has a net magnetization. In a material with sufficiently large grains, the number and the size of domains in the sample is the result of a balance between the domain wall energy produced by the splitting into domains and the lowering of the magnetostatic energy. The change of the spontaneous magnetization from a domain to its neighbour occurs at the domain wall. The spins within the wall ("Bloch wall") are pointing in non-easy directions, so that the anisotropy energy within the wall is higher than in its adjacent domains. While the exchange energy, E_{ex}, tries to make the wall as wide as possible in order to make the angle between adjacent spins as small as possible, the anisotropy energy, E_a, attempts to make the wall thin, i.e. reducing the number of spins pointing in non-easy directions. The result of this competition will be a certain finite width resulting from minimizing the total energy E_{tot} (with further contributions arising from the stray field energy E_{str}, a magnetostrictive term E_{ms} and one due to an applied field E_f):

$$E_{\text{tot}} = E_{\text{ex}} + E_{\text{a}} + E_{\text{str}} + E_{\text{ms}} + E_f \tag{6}$$

The domain wall width δ_w is essentially given by the exchange length l_{ex} and defined as:

$$\delta_w = \pi (A/K_1)^{1/2} \tag{7}$$

with A being the exchange stiffness ($A \propto T_C[J_s(T)/J_s(0)]$; for the materials described here, A is typically around 10^{-11} Jm^{-1} at room temperature). l_{ex} describes the scale of the perturbed area when a spin is unfavourably aligned. The domain wall energy γ is given by:

$$\gamma = 4(A\ K_1)^{1/2} \tag{8}$$

Another characteristic length is the critical single-domain particle size d_c:

$$d_c \approx (A\ K_1)^{1/2}/\mu_0 M_s^2 \tag{9}$$

which describes the size of the largest possible isolated spherical crystallite in which the energy cost for the formation of a domain wall is higher than the gain in magnetostatic energy. In other words, isolated uniaxial spheres with a diameter less than the critical size cannot contain a domain structure but are single domain. Of course, in a compact material the grains are not isolated but magnetically interact with each other and consequently, the approximation (Eq. 9) may be incorrect. Nonetheless, δ_w and d_c are important intrinsic properties of easy-axis magnetic phases. Typically, Fe-based R–T permanent magnets have a domain wall width of $\delta_w = 4$ nm and a critical single domain particle size of $d_c = 200 - 300$ nm.[17]

1.2. HARD MAGNETIC MATERIALS

There are many potential candidate materials for magnet applications, and the choice of material will depend on a number of factors. Here, only high-performance magnet materials are dealt with, and thus no detailed reference to ferrite or alnico magnets will be made, which nevertheless are of great interest and indeed account for a significant slice of the magnet market. An illustrative overview of the intrinsic properties of the most relevant permanent magnet materials is given in Table 1.

A favourable combination of these values is only a prerequisite for a good hard magnet material; the ultimate suitability can only be gauged when coercive field H_C, remanent magnetization B_r and maximum energy density $(BH)_{max}$, fulfill certain criteria. Good extrinsic magnetic properties are achieved by the preparation of appropriate microstructures with typical scale lengths of 1 nm to 100 μm. The interplay between intrinsic and extrinsic magnetic properties is schematized in Fig. 2.

$(BH)_{max}$ has doubled every 12 years during the 20th century and the spectacular development is illustrated in Fig. 3. In 1967, an article by Strnat et al. entitled *A family of new cobalt-base permanent magnetic materials* kicked off the

TABLE 1. Intrinsic magnetic properties (Curie temperature T_C, anisotropy field $\mu_0 H_A$ and saturation magnetization $\mu_0 M_s$), density ρ and a qualitative statement regarding the corrosion resistance of the most important rare-earth transition metal compounds, FePt ($L1_0$), CoPt ($L1_0$) and for comparison $BaFe_{12}O_{19}$ and α-Fe.

Material	$\mu_0 M_S$ (T)	$\mu_0 H_A$ (T)	$(BH)_{max,th}$ kJ/m^3	T_C (K)	ρ (g/cm^3)	Corrosion resistance
$Nd_2Fe_{14}B$	1.61	7.6	514	585	7.6	Poor
$SmCo_5$	1.05	40	220	1000	8.6	Poor
Sm_2Co_{17}	1.30	6.4	333	1173	8.7	Poor
$Sm_2Fe_{17}N_3$	1.54	21	472	749	7.7	Poor
FePt–$L1_0$	1.43	11.6	407	750	15.1	Good
CoPt–$L1_0$	1.00	4.9	200	840	15.2	Good
$\alpha-$Fe	2.16	–	–	1043	7.87	Poor
$BaFe_{12}O_{19}$	0.48	1.8	–	742	5.3	Good

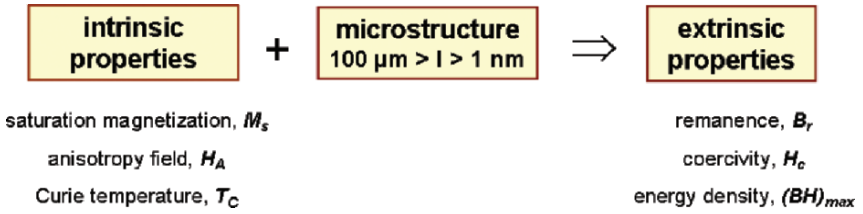

Figure 2. Basic concept: the transfer of intrinsic to extrinsic magnetic properties by the tailoring of the microstructure of rare-earth permanent magnets on a length scale from 1 nm to 100 µm, or in other words, the key to magnet development is the control of hysteresis.

fascinating development of rare-earth magnets.[18] Nowadays, about 95% of the theoretical limit for the energy density $(BH)_{max}$ (based on the $Nd_2Fe_{14}B$ phase) can be achieved in commercially produced sintered Nd-Fe-B grades and the highest attainable coercive fields exceed the practical requirements. At the time of writing, it appears that the search for novel hard magnetic compounds with higher saturation magnetization, as the now relevant parameter, helped by a basic understanding of the crystal field parameters, has somewhat stagnated and no further breakthrough is in sight.

Although the $(BH)_{max}$ is usually considered the most important figure of merit, improvements in other magnetic and non-magnetic figures of merit such as initial magnetization behaviour (1st quadrant), homogeneity of magnetic properties, chemical stability (corrosion), thermal stability (processing and application temperatures), machineability, net-shape processing (geometry), or cost could also have enormous impact.

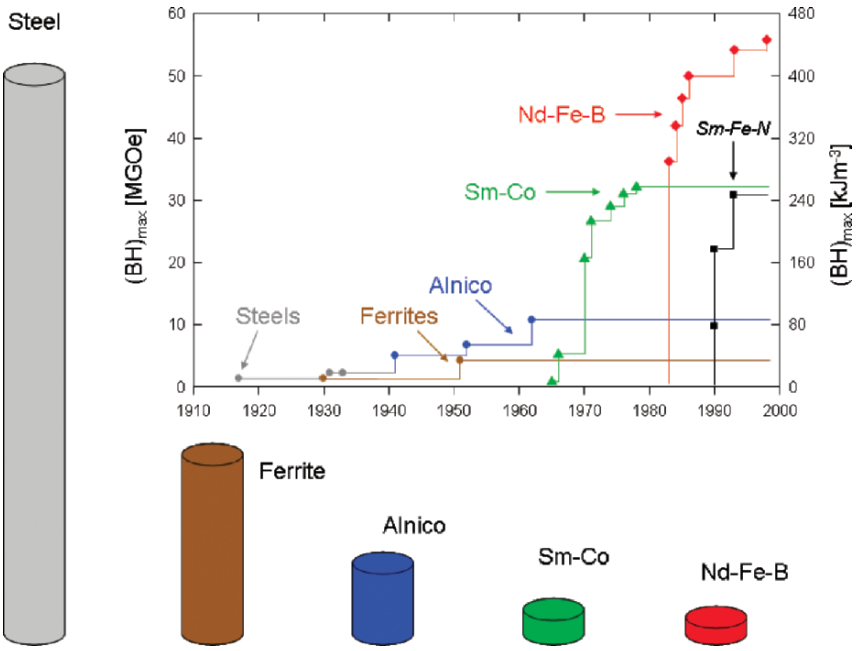

Figure 3. Development in the energy density $(BH)_{max}$ of hard magnetic materials in the 20th century and presentation of different types of materials with comparable energy density (each magnet is designed so that at a reference point 5 mm from the surface of the pole a field of 100 mT is produced).

For most applications in communication and information technologies, in the automotive sector, in medicine, magnetic separation, flywheels, and in the electric and electronic industry, the magnets are required to have stable and uniform magnetic properties from 0°C to 250°C. For even more specialized applications such as magnetic bearings (used in conjunction with high temperature superconductors) or deep sea drill heads, the temperature window needs to be extended to −192°C to 450°C.

An overview of novel developments in the most relevant manufacturing routes of bulk magnets, with special emphasis on nanostructured magnets, is given in the flow chart of Fig. 4.[19–23] This chart illustrates the principal processing routes for rare-earth permanent magnets (RPMs). For the production of high-performance RPMs with a maximized energy density a careful control of low level metallic impurities and non-metallic impurities such as oxygen is pivotal during all processing stages, regardless of which processing route is chosen. Each branch ends by machining and magnetizing the magnet. The left branch represents classical powder-metallurgical processing resulting in monocrystalline particles of around 10 μm in diameter, hence large compared to d_c. The right branch of this

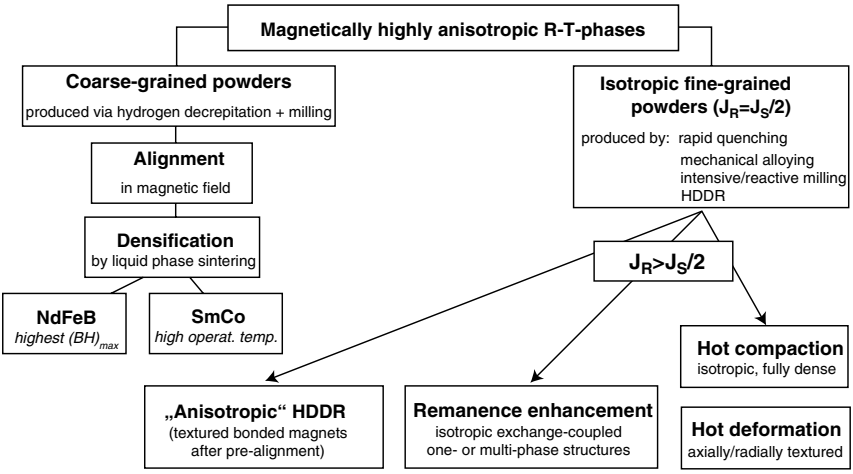

Figure 4. Overview of the main processing routes for high-performance rare-earth bulk magnets.

figure embodies processing routes, which aim at considerably smaller grain sizes somewhere between δ_w and d_c.

1.2.1. $Nd_2Fe_{14}B$

The stoichiometric composition of the magnetically highly anisotropic $Nd_2Fe_{14}B$ compound is $Nd_{11.8}Fe_{82.3}B_{5.9}$. The lattice symmetry is tetragonal (space group $P4_2/mnm$) with 68 atoms per unit cell and a = 0.880 nm and c = 1.221 nm.[17,24,25] There are six crystallographically distinct transition metal sites, two different rare-earth positions, and one boron position. For temperatures above the spin reorientation temperature (which occurs at $T_{SR} = 135$ K for $Nd_2Fe_{14}B$),[26] the easy magnetization direction is the c-axis as can be observed from magnetization curves measured along different crystallographic directions.

Three stable ternary phases can be found in the ternary Nd-Fe-B system: $Nd_2Fe_{14}B$ (Φ), $Nd_{1+\varepsilon}Fe_4B_4$ (η) and $Nd_5Fe_2B_6$ (ρ). The peritectic formation of the Φ–phase at 1180°C will be incomplete in a standard casting process as residues of primary Fe dendrites are left in the Φ–grains, the latter in turn being surrounded by Nd-rich liquid, which will solidify at its eutectic temperature of 630°C.[27,28] The presence of the Fe dendrites is detrimental to the magnets, performance, which has important consequences for the manufacturing of this class of magnets. The orthorhombic η phase is paramagnetic. The Nd-rich phase, also paramagnetic, is not only relevant for the densification during sintering and texturing during hot working, but is also crucial in the improvement of the magnetic properties. It is reported to be of face-centered cubic (fcc) structure and the presence of oxygen might stabilize this structure type as metallic Nd is double hexagonal close packed (dhcp). In sintered (schematic structure shown in Fig. 5) and die-upset NdFeB-type magnets the Nd-rich phase is amorphous if less than 2 nm thick.[29,30]

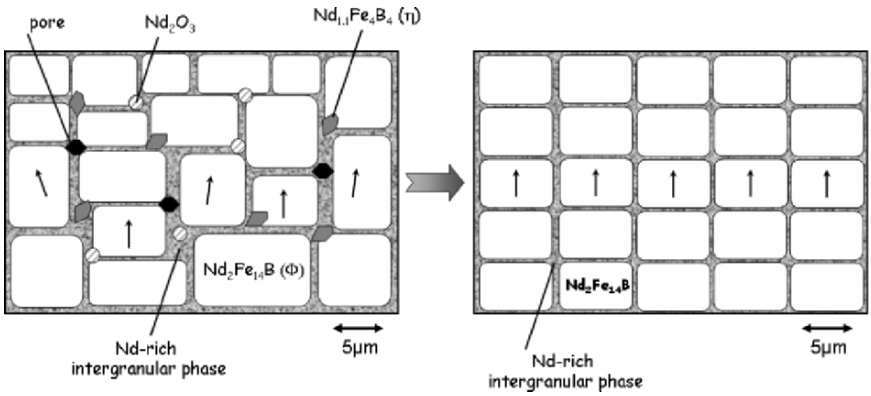

Figure 5. Schematic microstructure of a real (*left*) and an ideal (*right*) sintered NdFeB-magnet.

In order to use RPMs at elevated temperatures and to avoid irreversible flux losses, small temperature coefficients for remanence, $\alpha = (dM_r/dT)$, and coercivity, $\beta = (dH_c/dT)$, and a good stability against corrosion[31] are required. Generally, the coercivity and thus the temperature stability of Nd-Fe-B magnets is increased by a partial substitution of Nd by Dy. However, the anti-ferromagnetic coupling between the Dy- and Fe-sublattices leads to a decreased saturation magnetization and thus remanence. Partial replacement of Fe by Co is used to minimize α and here the consequent loss in coercivity is compensated by the simultaneous addition of Ga, Al, and Cu. The physical properties such as melting point and viscosity of the intergranular phase depend sensitively on composition and small amounts of additives. Ga addition, for example, can decrease the surface energy of this phase, which leads to smooth grain boundaries, and hence reduced R content, and improved corrosion properties. In warm and humid atmosphere, the Nd-rich intergranular phase in conventional Nd-Fe-B sintered magnets tends to form Nd-hydroxides and some free hydrogen, which causes hydrogen embrittlement and, therefore, conventional magnets are usually coated. Another mechanism is electrolytic corrosion, which occurs when water condenses on the magnet surface. In addition to encapsulation, the corrosion properties can also be improved by additions of Co, Cu, Al, and Ga and their main effect is to transform the intergranular phases into more noble compounds.[31–33] More systematically, the additives can be differentiated into type I dopants (Al, Ga, Cu, Sn, Zn) forming additional intergranular phases and type II dopants (Nb, V, Mo, W, Mo, Ti) forming boride precipitates in the intergranular region.[34]

1.2.2. *Sm-Co-type compounds*

Microwave tubes, gyroscopes, and accelerometers, reaction and momentum wheels to control and stabilize satellites, magnetic bearings, sensors, and actuators are examples for applications where high-energy density magnets with magnetic

fields stable over a variety of environmental conditions and wide temperature ranges are required. $SmCo_5$ and Sm_2Co_{17}-type magnets[18,35,36] are ideal for these applications because of their high magnetocrystalline anisotropy and Curie temperature. Standard commercial magnets of these types satisfy these requirements over the temperature range from 50°C to 250°C. In addition, they exhibit an improved corrosion resistance compared to $Nd_2Fe_{14}B$; their disadvantages are the costly raw materials and the difficult magnetization. A slight increase in temperature stability can be achieved when substituting heavy rare-earth elements for Sm. Even better temperature coefficients of remanence and coercivity are required for higher operating temperatures above 450°C, which are needed for RPMs for electric vehicles, hybrid magnetic bearings for turbine engines and advanced power systems.

Unlike the $Nd_2Fe_{14}B$ phase, the hexagonal $SmCo_5$ compound[18] with the $CaCu_5$ structure shows a relatively large homogeneity region in the Sm-Co phase diagram.[37] This region, however, becomes asymmetric when approaching the peritectic melting temperature of 1292°C. The 2:17-type shows currently the best temperature coefficients α and β of all RPMs and its hard magnetic properties are achieved by an elaborate series of heat treatments resulting in a complex microstructure. Commercially produced Sm-Co-type sintered magnets based on the 2:17R-type phase (with the rhombohedral (R) Th_2Zn_{17}-type structure) have usually a composition close to $Sm(Co,Fe,Cu,Zr)_{7.5}$. The homogeneity region of the 2:17R phase narrows with decreasing temperature[37,38] and a fine cellular precipitation structure develops from the single-phase metastable precursor, obtained by solid solution treatment at ~1200°C, quenching and subsequent annealing at ~800°C and slow cooling to 400°C. The 2:17R cells originate from nucleation and growth out of the hexagonal $TbCu_7$-type structure. This induces a related increase of Cu and Sm contents in the surrounding 1:7 matrix, that tends to 1:5 stoichiometry and forms the cell boundaries that have a thickness of 5–10 nm. The rhombohedral structure can be derived from the $SmCo_5$ structure by an ordered substitution of a dumbbell of Co atoms for one third of the Sm atoms. The 2:17R phase is the majority phase of the material. The 1:5 cell-boundary phase is coherent (or at least semi-coherent) with the cell interior. A so-called platelet phase (also referred to as lamellar or Z-phase) rich in Zr is observed additionally parallel to the 2:17R basal plane. In Fig. 6, this Z-phase manifests itself as thin lines extending over many 2:17R cells. The Z-phase, of a thickness ranging from 1 to 3 nm, is considered to stabilize the cellular microstructure and, more importantly, to provide diffusion paths for Cu, Fe, and Co, thereby modifying phase-ordering kinetics.

The subtle changes in microchemistry lead to a heterogeneous system in which the domain wall energy depends on the wall position and in which the walls remain pinned in regions where their energy is reduced. The gradient in Cu across the cell boundaries is facilitated by the presence of the Zr-rich lamellae and coin-

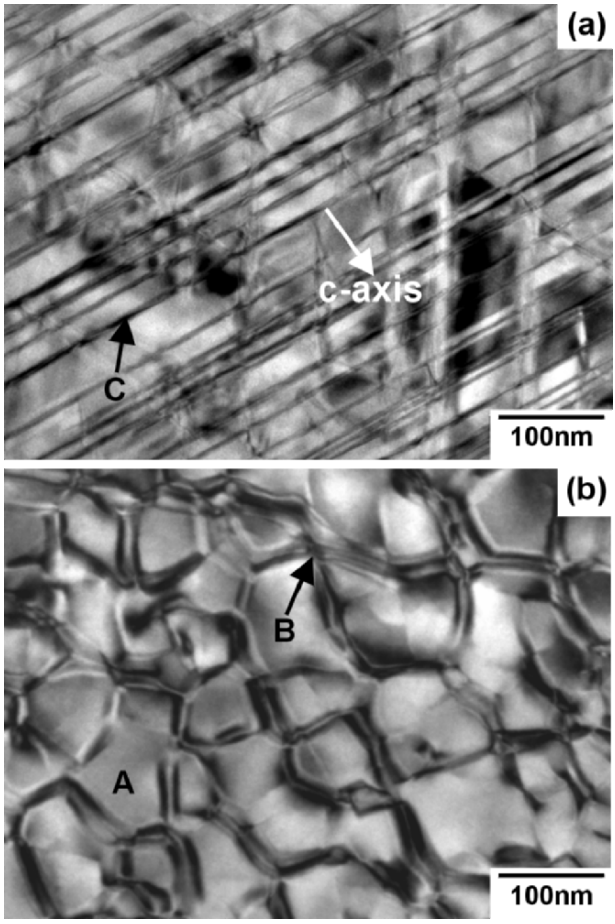

Figure 6. TEM bright field images of a sintered magnet of composition $Sm(Co_{0.784}Fe_{0.100}Cu_{0.088}Zr_{0.028})_{7.19}$ with (a) the nominal c-axis of the 2:17R main phase parallel and (b) perpendicular to the imaging plane (A indicates the 2:17R, B the 1:5-type cell-boundary and C the Z phases).

cides with the gradient in domain wall energy. This pinning-type coercivity mechanism is responsible for the high coercivities in these bulk solid-state precipitation hardened magnets. Due to the large variety in heat treatment and compositional parameters an optimisation of the $Sm(Co_{bal}Fe_wCu_xZr_y)_z$ magnets in terms of high temperature magnetic properties is a complex task (for more details see[21] and references therein).

1.2.3. *$L1_0$ – type intermetallic compounds*

The compounds FePt, FePd, CoPt, and MnAl (with the tetragonal $L1_0$-type (CuAu I) structure; space group $P4/mmm$) are of fundamental interest because

their magnetic anisotropy based on $3d$ and $5d$ electrons is as large as that of the well-known RE-TM high-performance magnets (RPMs) based on the $3d-4f$-systems. The main intrinsic magnetic properties of the itinerant-electron $L1_0$ FePt ferromagnet (see Gutfleisch et al.[39] and references therein) are reported to be $T_c = 750$ K, $J_s = 1.43$ T (at room temperature) and $K_1 = 6.6$ MJ/m^3 (first anisotropy constant at room temperature). The large magnetic anisotropy of the 3d-5d ferromagnets is due to the large spin-orbit coupling in the 5d-element.

Magnets made of the $L1_0$ phase have attracted much attention recently because of their potential usage in ultra high-density data storage[40] and permanent magnets for special applications such as MEMS. Distinct advantages of these compounds are, as opposed to the RPMs, that they are ductile and chemically inert. Self-organized magnetic arrays (SOMA) of dispersed $L1_0$ particles (diameter $\sim$5 nm) are considered as candidates for future thermally stable magnetic recording media with areal densities[41] as high as 1 Tbit/in.^{2} A further size reduction of written bits is hindered by the superparamagnetic limit as thermal fluctuations begin to dominate and spins within the particle begin to randomize in the absence of a field. One possibility to push the superparamagnetism to higher temperatures is to embed the ferromagnetic particles in an anti-ferromagnetic matrix.

Figure 7 shows the demagnetization curves of mechanically milled and heat-treated $Fe_{100-x}Pt_x$ ($x = 40; 45; 50$) powders.[42] The distribution of the chemically highly ordered $L1_0$ FePt and Fe_3Pt phases is sufficiently fine to yield effective exchange interactions between hard and soft magnetic grains. The $Fe_{50}Pt_{50}$

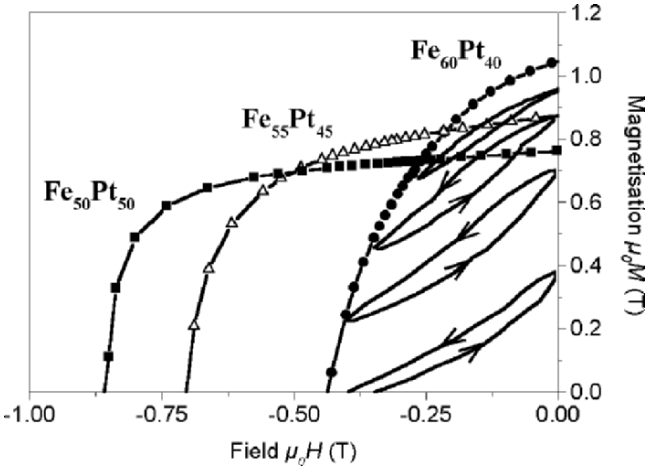

Figure 7. Demagnetization curves of the $Fe_{100-x}Pt_x$ ($x = 40; 45; 50$) powders annealed at 450°C for 48 h in dependence on Pt concentration x. Recoil loops are shown for $Fe_{60}Pt_{40}$. Remanence enhancement, single-phase demagnetization behaviour and steep recoil loops characterized by fair reversibility indicate exchange-spring behaviour.

powder is essentially single-phase. For the Fe-rich samples, a spring-magnet behaviour can be observed and, as a consequence, a higher energy product $(BH)_{max}$ is obtained.[43,44]

2. μ-Permanent magnets

Various routes, which have been used to prepare μ-magnets, are listed in Table 2.

All routes have their advantages and disadvantages. Before discussing each route, we will consider some general issues that will determine which routes will be best adapted for MEMS applications using a certain high-performance permanent magnetic material:

- Process-material-compatibility
- Dimensionality
- Integration into the overall processing of the microsystem
- Compatibility of substrate and buffer/capping layers with microfabrication
- Thermal compatibility
- Mechanical compatibility
- Chemical compatibility

The first point to consider when choosing a suitable preparation technique for μ-magnets is the *process-material-compatibility*. Some of the techniques are only applicable to certain materials, e.g. cold deformation and electro-deposition are presently unsuitable for the preparation of RE-TM compounds. Thickness is not the only film dimension to consider: the *lateral dimensions* of the magnets, as well as the overall magnet shape (disc, ring, wedge), must also be considered. For a particular magnetic material and route to be used, its *integration into the overall processing of the microsystem* has to be considered. This depends on the size and complexity of the microsystem. For relatively simple microsystems, magnets may

TABLE 2. Techniques used to prepare thick film magnets

Top-down routes	**Bottom-up (deposition) routes**
Micromachining of bulk magnets	Electro-deposition
Screen printing, tape casting, and bonding	Plasma spraying
Mechanical deformation	Aerosol
	Pulsed Laser Deposition (PLD)
	Sputtering

be fully processed and then inserted in a "pick-and-place" step, as used today for the assembly of over 600 million wrist watch motors every year. On the other hand, for very small and complex microsystems, it is more realistic to envisage that the magnets are produced and integrated into the microsystem at the same time. The viability of the 'pick and place' route will depend on the ease of magnet fabrication, as well as the possibility to produce magnets in batches. In this respect, the deposition of arrays of individual magnets by screen printing, plasma spraying, sputtering, PLD, or electro-deposition is much better adapted than the mechanical deformation route or the micromachining route.

For deposition routes, it would be preferable to develop processes using *substrates and buffer/capping layers, which are compatible with microfabrication* technology. For this reason Si is an obvious, but not the only choice of substrate. Several ceramics, silica, and alumina among others, can also be considered.

The high-performance magnet materials considered here are all crystalline. When deposited in film form, they must be heated, either during or after deposition, to crystallize ($Nd_2Fe_{14}B$, $SmCo_5$) or order (FePt, CoPt) the required high anisotropy phase, thus *thermal compatibility* becomes an issue. The annealing temperature required will vary from material to material ($Nd_2Fe_{14}B > 580°C$; $SmCo_5 > 400°C$; $FePt > 400°C$). What is more, the extrinsic magnetic properties (coercivity and remanence values) are very dependent on the film microstructure, and thus on annealing conditions. The temperature required for crystallization and microstructure optimization will determine whether the magnet can be deposited onto partially processed substrates, already containing components of the microsystem ('on-chip processing'), or whether the magnet deposition step is the first step of the process. Thanks to wafer bonding, system architectures exist for which complete magnet processing (deposition/annealing/patterning) may be completed before the integration of other components.

Mechanical compatibility is the next critical problem to address. The build up of stress in deposited films will depend on the difference in thermal expansion coefficients of the film and its substrate as well as the film thickness. The problem may be accentuated for NdFeB films, which due to its Invar behaviour, experiences non-monotonous thermal expansion/contraction, with a minimum in thermal expansion/contraction occurring at the material's Curie temperature. The choice of substrate and buffer layer should be tuned to minimize the difference in the thermal expansion coefficients, and thus reduce the risk of explosion or peel-off of the magnetic film. The stress may also be reduced by reducing the surface area of film deposited.

For full integration of the magnet-processing step into the overall microsystem processing scheme, *chemical compatibility* must be considered. Pollution of the other components and of the microtechnology equipment must be avoided, during deposition/patterning/annealing steps.

The various techniques listed in Table 2 will now be described.

2.1. TOP-DOWN PREPARATION TECHNIQUES

2.1.1. *Micromachining of bulk magnets*

This technique is presently used to prepare magnets for application in milli-systems (wrist watches, flip-dot displays, heart catheters, etc.). Spark-cut 0.5 mm thick high quality NdFeB magnets ($\mu_0 H_c = 1.2$ T; $\mu_0 M_r = 1.47$ T; $(BH)_{max} = 424$ kJ/m^3) are used in heart catheters.[45] However, there is a lower limit to the magnet thickness achievable by micromachining (~150 μm for RE-TM magnets). What is more, micromachining of very small, or very large surface areas or complicated shapes would be difficult (mechanical weakness of thin samples), and material wasteful. High quality RE-TM magnets suffer surface-degradation during micromachining, resulting in the loss of coercivity of the surface layer, and thus the overall magnet remanence. The problem is most critical for coarse-grained sintered magnets (NdFeB and to a lesser extent $SmCo_5$) and least critical for nanostructured pinning type Sm_2Co_{17} magnets.[46]

2.1.2. *Screen printing, tape casting, and bonding*

Screen printing and tape casting are well adapted to fabricate isotropic films with thicknesses in the range of 0.1–1 mm.[47–49] In the case of screen printing, the permanent magnetic thick film can be deposited directly onto the microsystem components. Rather limited energy products have been reported (≤40 kJ/m^3), owing to dilution of the magnetic powders in the non-magnetic binder. Anisotopic thick films (hundreds of μm) with energy products of up to 70 kJ/m^3 have been produced by curing PMMA bonded anisotropic NdFeB powders under magnetic field.[50]

2.1.3. *Mechanical deformation*

A novel mechanical deformation process, recently developed to produce FePt foil magnets of typical thickness 100 μm, involves the extensive co-deformation of elemental Fe and Pt foils[51] (Fig. 8). Remanent magnetization values of FePt foils produced by mechanical deformation are so far limited to about 0.75 T as the samples are only weakly textured ($\mu_0 H_c = 0.8$ T, $(BH)_{max} = 76$ kJ/m^3). Some improvement in texture and thus energy product was achieved by annealing under magnetic field ($\mu_0 M_r = 0.82$ T, $(BH)_{max} = 90$ kJ/m^3).[52] Rolling is a mechanical deformation route adapted to the production of thin foils (e.g. 100 μm) of large surface area, though complex (non-rectangular) magnet shapes would lead to material waste, while it may prove difficult to produce magnets of very small surface area. Another approach is the hot-deformation, essentially die-upsetting, of NdFeB-type materials down to thicknesses of several hundreds of microns.[53] This technique provides excellent thick film magnetic properties but is quite laborious.

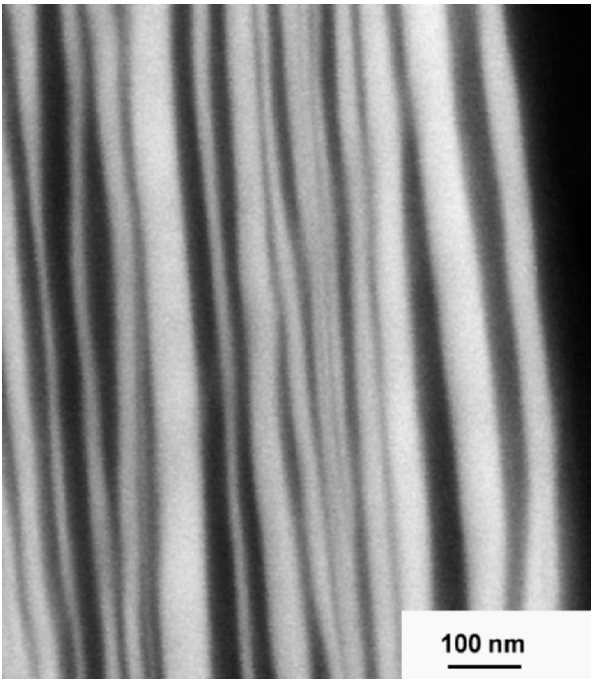

Figure 8. Cross-sectional SEM image of a bulk Fe/Pt nano-structured multilayer produced by cyclic deformation (starting foil thickness in the back scattered electron mode:Fe = 75μm, Pt = 100μm).

2.2. BOTTOM-UP PREPARATION TECHNIQUES

2.2.1. *Electro-deposition*

(Fe,Co)Pt films can be electro-deposited at rates of up to a few μm/h, over large areas.[54] Room temperature electro-deposition has been shown to produce Co_xPt_{100-x} ($x \approx 80$) micromagnets with coercivity of up to 0.5 T and energy products up to[55] 52 kJ/m^3. This is a very important result from the point of view of integration of magnets into magnetic-MEMS, as electro-deposition is ideally compatible with existing MEMS technologies and the low processing temperature allows on-chip processing. The first fully integrated magnetic microswitch has been made with electro-deposited $Co_{80}Pt_{20}$ films with mediocre magnetic properties ($\mu_0 H_c = 0.3$ T, $\mu_0 M_r = 0.32$ T).[56] More recently, high anisotropy $L1_0$ CoPt and FePt alloy films with coercivities of the order of 1.1 T have been prepared by electrodeposition.[57–59]

2.2.2. *Plasma spraying*

Plasma spraying is a rapid solidification technique in which alloy powder is injected into a very high temperature plasma flame and then projected onto a

surface. It is suitable for the preparation of thick films (≤1 mm). It has been used to prepare high coercivity SmCo films ($\mu_0 H_c$ = 6.7 T) with energy products of up to [60]56 kJ/m^3. More recently, it was used to prepare NdFeB films with energy products of up to [61,62]60 kJ/m^3. Limited energy product values in plasma sprayed films are attributed to limited texture development, film porosity, and powder degradation.

2.2.3. *Aerosol*

The main attributes of the aerosol deposition method (ADM), known for the fabrication of fine ceramic films such as PZT, are a high deposition rate (5–50 mm/min) and a high film density. It is based on shock loading solidification due to the impact of ultrafine particles (UFP), which are accelerated by a carrier gas. During impact of the UFP with the substrate, a part of the UFPs' kinetic energy is converted into local thermal energy, promoting bonding between the substrate and the UFPs, as well as between the UFPs themselves. This method has been used to prepare SmFeN and $Nd_2Fe_{14}B/Fe_3B$ thick films,[63,64] however, magnetic properties are so far not competitive.

2.2.4. *Pulsed laser deposition (PLD)*

PLD has been used to prepare high-quality RE-TM and $L1_0$ alloy films.[65–67] However, the majority of papers concern films deposited at low rates which are too thin for MEMS applications (<1 μm). Nakano et al. used high rate (≤72 μm/h) PLD to prepare NdFeB films of up to 120 μm in thickness.[68] However, such rates are only achievable over small surface areas (1 cm^2). The maximum energy product reported (77 kJ/m^3) is limited by the isotropic nature of the films.

2.2.5. *Sputtering*

As for PLD, the majority of papers dealing with sputtered RE-TM films concern thin films deposited at low rates.[69,70] The first report on high rate sputtering (≤50 μm/h) of NdFeB films over large surfaces (5 × 5 cm^2) came from researchers at the Moscow Institute of Steel and Alloys. Excellent extrinsic magnetic properties ($\mu_0 H_c$ = 3.25 T and $(BH)_{max}$ = 195 kJ/m^3 or $\mu_0 H_c$ = 0.8 T and $(BH)_{max}$ = 352 kJ/m^3) were report for films deposited on metallic substrates.[71,72]

Based on these very encouraging results, and the fact that sputtering is one of the most promising routes for the integration of high quality magnets into MEMS, a high rate triode-sputtering chamber was developed at Institut Néel. In our case, Si substrates were chosen for compatibility with microtechnology processing. As a case study, our recent results[73,74] concerning NdFeB films will now be presented.

{Ta (100 nm) / NdFeB (5 μm) / Ta (100 nm)} films were deposited onto 100 mm Si substrates at a rate of 18 μm/h by triode sputtering of targets of surface area 100 × 100 mm. In the as-deposited state, the NdFeB films prepared at

$T_{sub} \leq 450°C$ appeared to be amorphous (no x-ray diffraction peaks are resolved and the films are magnetically soft) while the films deposited at 500°C were crystallized (appearance of $Nd_2Fe_{14}B$ XRD peaks and an out-of-plane coercivity of 0.3 T). All samples were annealed at 750°C for 10 min. Films deposited at $T_{sub} \leq 450°C$ have an equiaxed grain structure while the films deposited at 500°C have a columnar structure. Refinement of the $Nd_2Fe_{14}B$ grain size with increasing deposition temperature up to 450°C was observed, with the average grain size decreasing from a value of the order of 800 nm for the sample deposited on a non-heated substrate to a value of the order of 200 nm for the sample deposited at 450°C. This indicates that the density of $Nd_2Fe_{14}B$ nucleation sites increases with deposition temperature. It is likely that these nucleation sites are also responsible for the development of texture in the films. Though all films showed out-of-plane crystallographic *c*-axis texture, a progressive increase in the degree of texture with increasing deposition temperature was evidenced by a significant sharpening of the (006) x-ray diffraction pole figures shown in the 2nd column of Fig. 9.

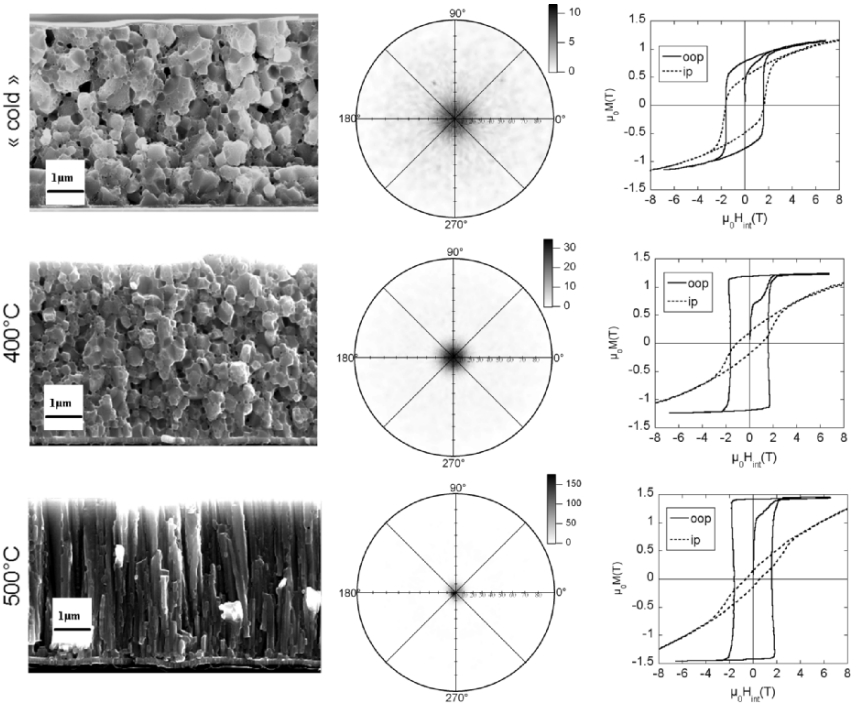

Figure 9. Comparison of the evolution in structural and magnetic properties of sputtered 5 µm thick NdFeB films as a function of deposition temperature (note all films were annealed at 750°C for 10 minutes). Column 1: Fractured cross sections imaged with an in-lens detector; Column 2: XRD pole figure of (006) diffraction peak of $Nd_2Fe_{14}B$; Column 3: In-plane (ip) and out-of-plane (oop) hystersis loops and the initial oop magnetization curves (oop loops were corrected with a demagnetization factor $N = 1$).

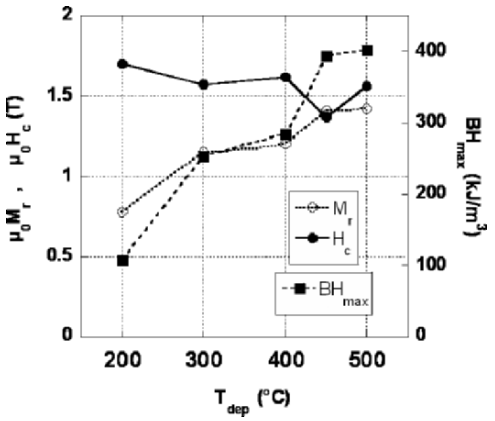

Figure 10. Remanence $\mu_0 M_r$, coercivity $\mu_0 H_c$ and estimated maximum energy product $(BH)_{max}$ as a function of deposition temperature (see Fig. 9).

Correspondingly, an increase in out-of-plane magnetic anisotropy was clearly identified in the 3rd column, in which in-plane and out-of-plane hysteresis curves are compared.

The variation of remanence, coercivity, and energy product of these films with deposition temperature are summarized in Fig. 10. While the remanence increased with deposition temperature, due to the increase in out-of-plane texture, the coercivity varied little ($\mu_0 H_c \approx 1.6$ T). This observation is in contrast to bulk NdFeB samples, in which easy-axis coercivity tends to be reduced as texture is increased.[75] The maximum energy product (400 kJ/m^3), which was achieved for the films deposited at 500°C is comparable to that of high-quality sintered magnets.[19]

All films show a two-stage initial magnetization behaviour in the out-of-plane measurements with a first stage of high susceptibility in low fields (<0.2 T) followed by a second low susceptibility stage. The relative contribution of the former decreases with increasing deposition temperature up to 450°C, and then rises again for a deposition temperature of 500°C. This 2-stage behaviour is attributed to the presence of both multi-domain (high susceptibility) and single-domain (low susceptibility) $Nd_2Fe_{14}B$ grains.

2.3. PATTERNING

A number of different routes, which have been used to pattern permanent magnet films, are schematized in Fig. 11. The patterns produced can be categorized as (i) *topographic* or (ii) *crystallographic*. The topographically patterned films can be further categorized as patterned either *during deposition* or *post-deposition*. Examples of topographic patterning during deposition include electro-deposition or sputtering through a mask and sputtering onto a pre-patterned wafer. $Co_{80}Pt_{20}$ cylindrical magnets (height 2 μm, diameter 5 and 10 μm) with energy products

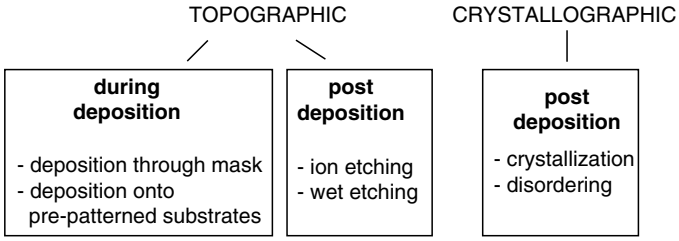

Figure 11. Overview of different routes used to pattern permanent magnet films.

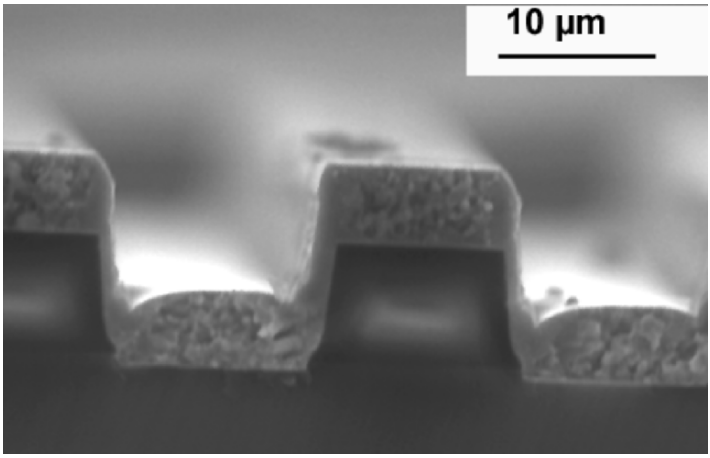

Figure 12. Cross sectional SEM image of Ta(100 nm)/NdFeB (5 µm)/Ta (100 nm) deposited onto a pre-patterned Si/SiO substrate.

of 52 kJ/m^3 and coercivities of 0.5 T have been electro-deposited through a photolithographically defined mask.[76] Out-of-plane textured NdFeB disk magnets ($\mu_0 H_c \approx 1.6$ T, $\mu_0 M_r = 1.1$ T, $(BH)_{max} = 234$ kJ/m^3) with diameters in the range of 2–8 mm and thicknesses of up to 50 µm have been deposited onto Si wafers by sputtered through stainless steel masks (unpublished work from Institut Néel. About 5 µm thick NdFeB films ($\mu_0 H_c \approx 1.6$ T) have been sputtered onto pre-patterned Si/SiO wafers containing 8 µm deep trenches with widths in the range of 5–100 µm and a cross-sectional image of 10 µm wide trenches is shown in Fig. 12 (unpublished work from Institut Néel and CEA-LETI, carried out within the framwork of the ANR "Nanomag2" project). Visualization and field reconstruction of this sample made with a magneto-optic indicator film may be found elsewhere in this book (chapter on *Magnetic Imaging Films*, Fig. 23a). A one-step photolithography process was used to produce arrays of bonded Sm_2Co_{17} magnets (1250 × 1250 × 15 µm) by binding the powders with photoepoxy prior to spin-coating.[77] However dilution of the magnetic power led to rather low energy products (22 kJ/m^3). Post-deposition topographic patterning of

30 μm thick Sm_2Co_{17} sputtered films has been carried out with ion beam etching and wet chemical etching at film removal rates of 1 μm/h and 750 μm/h, respectively.[78] Prior to patterning, the films had maximum energy products of the order of 90 kJ/m^3.

The second, and less conventional type of patterning, involves the local modification of the film's magnetic properties through a change in its crystallographic state. In this case a modulation in the magnetic properties is achieved without a modulation in the film's surface height. The first concrete example concerns the local crystallization of 2 μm thick amorphous NdFeB sputtered films by laser annealing through a mask.[79] This technique was used to produce 100 μm wide strips of hard magnetic NdFeB (crystallized) in a soft magnetic (amorphous) matrix. The irradiated strips showed out-of-plane magnetic anisotropy and coercivities of at least 1.5 T. The second example concerns the local disordering of 40 nm thick $L1_0$ FePt by pulsed laser annealing. This technique was used to produce 10 μm disks of soft magnetic FePt (A_1 – disordered) in a hard magnetic ($L1_0$ – ordered) matrix ($\mu_0 H_c$ = 5.5 T). The applicability of this technique to thicker films remains to be established.

3. Conclusions

Magnetic-MEMS is rich in materials development, design, fabrication, and characterization. The controlled preparation of μ-magnets with microstructures tailored on a level similar to that of bulk permanent magnets will be a challenge for the next years. There is a real need for a systematic microstructural analysis to understand and improve the films' magnetic and non-magnetic (e.g. film adhesion) properties. Tools must be developed for the non-destructive local magnetic characterization of patterned films. The use of magneto-optic imaging films, described elsewhere in this book, is one possibility. Compatibility issues with the design of novel microsystems will need to be taken into account. The progress in magnetic-MEMS will be limited by the capability to prepare 5–500 μm permanently magnetized and magnetically patterned thick films.

References

1. Cugat, O., Delamare, J., and Reyne, G., Magnetic micro-actuators and systems (MAGMAS), *IEEE Trans. Mag.* 39, 3607 (2003).
2. Cullity, B.D., *Introduction to Magnetic Materials*. Addison-Wesley, Reading, MA (1972).
3. Coey, J.M.D. (ed.), *Rare Earth Iron Permanent Magnets*. Clarendon Press, Oxford (1996).
4. Buschow, K.H.J. (ed.), *Handbook of Magnetic Materials*, vol. 10. North Holland/Elsevier, Amsterdam (1997), Chapter 4.
5. Skomski, R. and Coey, J.M.D., *Permanent Magnetism*, Institute of Physics, Bristol (1999).

6. Adler, E. and Hamann, P., A contribution to the understanding of coercivity and its temperature dependence in sintered $SmCo_5$ and $Nd_2Fe_{14}B$ magnets, *Proc. of the 4th Int. Symp. Magn. Anisotropy and Coercivity in RETM Alloys*, Dayton, (1985), pp. 747–760.
7. Durst, K.D. and Kronmüller, H., Magnetic hardening mechanisms in sintered Nd-Fe-B and $Sm(Co,Fe,Cu,Zr)_{7.6}$ permanent magnets, *Proc. of the 4th Int. Symp. Magn. Anisotropy and Coercivity in RETM Alloys*, Dayton (1985), p. 725.
8. Livingston, J.D., Magnetic domains in sintered Fe-Nd-B-magnets, *J. Appl. Phys.* 57, 4137 (1985).
9. Livingston, J.D., Domains in sintered Co-Cu-Fe-Sm magnets, *J. Appl. Phys.* 46, 5259 (1975).
10. Dempsey, N.M., Ghidini, M., Nozières, J.P., Smith, P.A.I., Gervais, B., and Coey, J.M.D., Magnetic hardening of $Sm_2Fe_{17}N_3$ by radiation damage, *Phys. Rev. Lett.* 81, 5652 (1998).
11. Eckert, D., Gutfleisch, O., Kirchner, A., Arnold, K., Grünberger, W., Gebel, B., Handstein, A., Wolf, M., and Müller, K.H., Magnetization processes in different types of fine grained Nd-Fe-B magnets, *Proc. of the 10th Int. Symp. Magn. Anisotropy and Coercivity in RETM*, Dresden (1998), p. 297.
12. Kneller, E.F., and Hawig, R., The exchange-spring magnet: a new material principle for permanent magnets, *IEEE Trans. Magn.* 27, 3588 (1991).
13. Schrefl, T., Finite elements in numerical micromagnetics: Part I: granular hard magnets, *J. Magn. Magn. Mater.* 207, 45 (1999).
14. Givord, D., Rossignol, M., and Barthem, V.M.T.S., The physics of coercivity, *J. Magn. Magn. Mater.* 258–259, 1 (2003).
15. Street, R. and Woolley, J.C., A study of magnetic viscosity, *Proc. Phys. Soc.* A62, 562 (1949).
16. Hubert, A. and Schäfer, R., *Magnetic Domains - The Analysis of Magnetic Microstructures*, Springer-Verlag, Berlin (1998).
17. Herbst, J.F., $R_2Fe_{14}B$ materials: intrinsic properties and technological aspects, *Rev. of Modern Phys.* 63, 819 (1991).
18. Strnat, K.J., Hoffer, G., Olson, J., Ostertag, W., and Becker, J.J., A family of new cobalt-base permanent magnetic materials, *J. Appl. Phys.* 38, 1001 (1967).
19. Gutfleisch, O., Controlling the properties of high density permanent magnetic materials, *J. Phys. D: Appl. Phys.* 33, R157 (2000).
20. Gutfleisch, O., Khlopkov, K., Teresiak, A., Müller, K.H., Drazic, G., Mishima, C., and Honkura, Y., Memory of texture during HDDR processing of NdFeB, *IEEE Trans. on Magn.* 39, 2926 (2003).
21. Gutfleisch, O., Müller, K.-H., Khlopkov, K., Wolf, M., Yan, A., Schäfer, R., Gemming, T., Schultz, L., Evolution of magnetic domain structures and coercivity in high-performance SmCo 2:17 type permanent magnets, *Acta Mat.* 54, 997 (2006).
22. Khlopkov, K., Gutfleisch, O., Eckert, D., Hinz, D., Wall, B., Rodewald, W., Müller, K.-H., Schultz, L., Local texture in Nd-Fe-B sintered magnets with maximised energy density, *J. Alloys Comp.* 365, 259 (2004).
23. Bollero, A., Yan, A., Gutfleisch, O., Müller, K.H., and Schultz, L., Intergrain interactions in nanocrystalline isotropic PrFeB-based magnets, *IEEE Trans. on Magn.* 39, 2944 (2003).
24. Chaban, N.F., Kuz'ma, Yu. B., Bilonizhko, N.S., Kachmar, O.O., and Petriv, N.V., Ternary (Nd, Sm, Gd)-Fe-B-systems, *Deper. Akad. Nank. UKSSR, Ser. A (USSR)* 10, 875 (1979).

25. Herbst, J.F., Croat, J.J., Pinkerton, F.E., and Yelon, W.B., Relationships between crystal structure and magnetic properties in $Nd_2Fe_{14}B$, *Phys. Rev. B* 29, 4176 (1984).

26. Givord, D., Li, H.S., and Perrier de la Bathie, R., Magnetic properties of $Y_2Fe_{14}B$ and $Nd_2Fe_{14}B$ single crystals, *Solid State Comm.* 51, 857 (1984).

27. Schneider, G., Henig, E.T., Petzow, G., and Stadelmaier, H.H., Phase relations in the system Fe-Nd-B, *Z. Metallkd.* **77**, 755 (1986).

28. Knoch, K.G., Reinsch, R., and Petzow, G., The Nd-Fe-B phase diagram and the primary solidification of $Nd_2Fe_{14}B$, *Proc. of the 13th Int. Workshop on RE Magnets and their Appl.*, Birmingham (1994) p. 503.

29. Shinba, Y., Ishikawa, K., Hiraga, K., Konno, T.J., and Sagawa, M., TEM observations on the Nd-rich phase and grain boundary structure of Nd-Fe-B sintered magnets, *Proc. of the 18th Int. Workshop on High Performance Magnets and their Appl.,* Annecy, France (2004), p. 419.

30. Kirchner, A., Thomas, J., Gutfleisch, O., Hinz, D., Müller, K.-H., and Schultz, L., HRTEM studies of grain boundaries in die-upset Nd-Fe-Co-Ga-B magnets, *J. Alloys Comp.* 365, 286 (2004).

31. Grieb, B., New corrosion resistant materials based on Neodym-Iron-Boron, *IEEE Trans. Magn.* 33, 3904 (1997).

32. El-Moneim, A.A., Gebert, A., Uhlemann, M., Gutfleisch, O., and Schultz, L., The influence of Co and Ga additions on the corrosion behavior of nanocrystalline NdFeB magnets, *Corrosion Sci.* 44, 1857 (2002).

33. Rada, M., Gebert, A., Mazilu, I., Khlopkov, K., Gutfleisch, O., Schultz, L., Rodewald, W., Corrosion studies on highly textured Nd–Fe–B sintered magnets, *J. Alloys Comp.* 415, 111 (2006).

34. Fidler, J. and Bernardi, J., in: New aspects of microstructural investigations of rare earth-iron based permanent magnets, S. Zhang (ed.) *Proc. of the 2nd Int. Symp. on Physics of Magn. Mat.*, Int. Academic Publ., Bejing (1992).

35. Ray, A.E., Metallurgical behavior of $Sm(Co,Fe,Cu,Zr)_z$ alloys, *J. Appl. Phys.* 55, 2094 (1984).

36. Kumar, K., $RETM_5$ and RE_2TM_{17} permanent magnets development, *J. Appl. Phys.* R13 (1988).

37. Cataldo, L., Lefevre, A., Ducret, F., Cohen-Adat, M.Th., Allibert, C.H., and Valignat, N., Binary system Sm-Co: revision of the phase diagram in the Co rich field, *J. Alloys Comp.* 241, 216–265 (1996).

38. Perry, A.J., The constitution of copper-hardened samarium-cobalt permanent magnets, *J. Less-Common Met.* 51, 153 (1977).

39. Gutfleisch, O., Lyubina, J., Müller, K.-H., and Schultz, L., FePt hard magnets, *Adv. Eng. Mater.* 7, 208 (2005).

40. Sun, S., Murray, C.B., Weller, D., Folks, L., Moser, A., Monodisperse FePt nanoparticles and ferromagnetic FePt nanocrystal superlattices, *Science* 287, 1989 (2000).

41. Klemmer, T., Liu, C., Shukla, N., Wu, X.W., Weller, D., Tanase, M., Laughlin, D.E., Soffa, W.A., Combined reactions associated with $L1_0$ ordering, *J. Magn. Magn. Mat.* 266, 79 (2003).

42. Lyubina, J., Gutfleisch, O., Müller, K.-H., Schultz, L., Dempsey, N.M., Nanocrystalline hard magnetic FePt powders, *J. Appl. Phys.* 95, 7474 (2004).

43. Lyubina, J., Gutfleisch, O., Müller, K.-H., Schultz, L., Magnetocrystalline anisotropy in $L1_0$ FePt and exchange coupling in FePt/Fe_3Pt nanocomposites, *J. Phys.: Cond. Matter* 17, 4157 (2005).

44. Lyubina, J., Isnard, O., Müller, K.-H., Gutfleisch, O., Schultz, L., Ordering of nanocrystalline Fe-Pt alloys studied by in-situ neutron powder diffraction, *J. Appl. Phys.* 100, 094308 (2006).

45. Vacuumschmelze GmbH, private communication (2006).

46. Katter, M., Ûstüner, K., and Blank, R., Model for calculating J(H) curves of Ni coated Nd-Fe-B magnets, *Proc. of the 19th Int. Workshop on Rare Earth Magnets and their Appl.*, Beijing (2006), p. 87.

47. Pawlowski, B., Rahmig, A., and Töpfer, J., Preparation and properties of NdFeB thick films, *Proc. 15th Int. Workshop on Rare Earth Magnets and their Appl.*, Dresden (1998), p. 1045.

48. Pawlowski, B., Scharzer, S., Rahmig, A., and Töpfer, J., NdFeB thick films prepared by tape casting, *J. Magn. Magn. Mater.* 265, 337 (2003).

49. Rodewald, W., Wall, B., Fernengel, W., and Katter, M., Production of thin flexible RE magnet-foils, *Proc. of the 15th Int. Workshop on Rare Earth Magnets and their Appl.*, Dresden (1998), p. 1021.

50. Romero, J.J., Sastre, R., Palomares, F.J., Pigazo, F., Cuadrado, R., Cebollada, F., Hernando, A., and Gonzalez, J.M., Polymer bonded anisotropic thick films for micromotors /microgenerators, *Proc. of the 19th Int. Workshop on Rare Earth Magnets and their Appl.*, Beijing (2006), p. 240.

51. Hai, N.H., Dempsey, N.M., Veron, M., Verdier, M., and Givord, D., An original route for the preparation of hard FePt, *J. Magn. Magn. Mater.* 257, L139 (2003).

52. Cui, B.Z., Han, K., Li, D.S., Garmestani, H., Liu, J.P., Dempsey, N.M., and Schneider-Muntau, H.J., Magnetic-field-induced crystallographic texture enhancement in cold-deformed FePt nanostructured magnets, *J. Appl. Phys.* 100, 013902 (2006).

53. Hinz, D., Gutfleisch, O., Müller, K.-H., High performance NdFeB magnets with a thickness of some 100 μm for MEMS applications, *Proc. of 18th Intl. Workshop on High Performance Magnets and their Applications*, Annecy (2004), p. 797.

54. Zangari, G., Bucher, P., Lecis, N., Cavallotti, P.L., Callegaro, L., Puppin, E., Magnetic properties of electroplated Co-Pt films, *J. Mag. Mag. Mat.* 157/158, 256 (1996).

55. Zangari, G. and Zana, I., Electrodeposited hard magnetic Co-Pt films and microstructures, *Proc. of the 18th Int. Workshop on High Performance Magnets and their Appl.*, Annecy (2004), p. 817.

56. Dieppedale, C., Desloges, B., Rostaing, H., Delamare, J., Cugat, O., Meunier-Carus, J., Ultra-fast levitating magnetic bistable micro-actuator with integrated permanent magnets, *Proc. of the 18th Int. Workshop on High Performance Magnets and their Appl.* 1, 408 (2004).

57. Rhen, F.M.F., Hinds, G., O'Reilly, C., and Coey, J., Electrodeposited FePt films, *IEEE Trans. Magn.* 39, 2699 (2003).

58. Fujita, N., Maeda, S., Yoshida, S., Takase, M., Nakano, M., Fukunaga, H., Preparation of Co–Pt alloy film magnets by electrodeposition, *J. Magn. Magn. Mater.* 272–276, e1895 (2004).

59. Leistner, K., Backen, E., Schupp, B., Weisheit, M., Schultz, L., Schlörb, H., and Fähler, S., Phase formation, microstructure, and hard magnetic properties of electrodeposited FePt films, *J. Appl. Phys.* 95, 7267 (2004).

60. Kumar, K., Das, D., and Wettstein, E., High coercivity, isotropic plasma sprayed Sm-Co magnets, *J. Appl. Phys.,* 49, 2052 (1978).

61. Overfelt, R.A., Anderson, C.D., and Flanagan, W.F., Plasma sprayed $Fe_{76}Nd_{16}B_8$ permanent magnets, *Appl. Phys. Lett.* 49, 1799 (1986)

62. Rieger, G., Wecker, J., Rodewald, W., Sattler, W., Bach, Fr.-W., Duda, T., and Unterberg, W., Nd–Fe–B permanent magnets (thick films) produced by a vacuum-plasma-spraying process, *J. Appl. Phys.* 87, 5329 (2000).

63. Sugimoto, S., Maki, T., Kagotani, T., Akedo, J., and Inomata, K., Effect of applied field during aerosol deposition on the anisotropy of Sm–Fe–N thick films, *J. Magn. Magn. Mater.* 290–291, 1202 (2005).

64. Sugimoto, S., Nakamura, M., Maki, T., Kagotani, T., Inomata, K., Akedo, J., Hirosawa, S., and Shigemoto, Y., $Nd_2Fe_{14}B/Fe_3B$ nanocomposite film fabricated by aerosol deposition method, *J. Alloys Comp.* 408–412, 1413 (2006).

65. Cadieu, F.J., Rani, R., Qian, X.R., and Chen, Li, High coercivity SmCo based films made by pulsed laser deposition, *J. Appl. Phys.* 83, 6247 (1998).

66. Fähler, S., Neu, V., Weisheit, M., Hannemann, U., Leinert, S., Singh, A., Kwon, A., Melcher, S., Holzapfel, B., and Schultz, L., High performance thin film magnets, *Proc. of the 18th Int. Workshop on High Performance Magnets and their Appl*. Annecy (2004), pp. 566.

67. Hannemann, U., Melcher, S., and Fähler, S., Highly textured Nd–Fe–B films grown on amorphous substrates, *J. Magn. Magn. Mater.* 272–276, e859 (2004).

68. Nakano, M., Katoh, R., Fukunaga, H., Tutumi, S., and Yamashita, F., Fabrication of Nd–Fe–B thick-film magnets by high-speed PLD method, *IEEE Trans. Mag.* 39, 2863 (2003).

69. Cadieu, F.J., Cheung, T.D., and Wickramasekara, L., Magnetic properties of sputtered Nd-Fe-B films, *J. Magn. Magn. Mater.* 54–57, 535 (1986).

70. Cadieu, F.J., Rare earth transition metal film permanent magnets, *Proc. 17th Int. Workshop on Rare Earth Magnets and their Appl.*, Delaware (2002), p. 416.

71. Kapitanov, B.A., Kornilov, N.V., Linetsky, Ya. L, and Tsvetkov, V.Yu., Sputtered permanent Nd-Fe-B magnets, *J. Magn. Magn. Mater.* 127, 289 (1993).

72. Linetsky, Ya.L. and Kornilov, N.V., Structure and Magnetic Properties of Sputtered Nd-Fe-B Alloys, *J. of Mater. Eng. Perform.* 4, 188 (1995).

73. Walter, A., Khlopkov, K., Gutfleisch, O., Givord, D.,and Dempsey, N.M., Evolution of magnetic and microstructural properties of thick sputtered NdFeB films with processing temperature, *J. Magn. Magn. Mater.* (in press).

74. Dempsey, N.M., Walter, A., Givord,D., Khlopkov, K., and Gutfleisch, O., High performance hard magnetic NdFeB thick films for integration into MEMS, *Appl. Phys. Lett.* 90, 92509 (2007).

75. K. Khlopkov, O. Gutfleisch, D. Hinz, K.-M. Müller and L. Schultz, Evolution of interation domains with texture in $Ncl_2Fe_{14}B$ studied with magnetic force microscopy, J. Appl. Phys., accepted.

76. Zana, I., Zangari, G., Park, Jin-Woo , Allen, M. G., Electrodeposited Co–Pt micron-size magnets with strong perpendicular magnetic anisotropy for MEMS applications, *J. Magn. Magn. Mater.* 272–276, e1775 (2004).

77. Dutoit, B., Besse, P.A., Blanchard, H., Guérin, L., and Popovic, R.S., High performance micromachined Sm_2Co_{17} polymer bonded magnets, *Sensors Actuators* A77 178 (1999).

78. Budde, T. and Gatzen, H.H., Thin film SmCo magnets for use in electromagnetic microactuators, *J. Appl. Phys.* 99 08N304 (2006).

79. Okuda, T., Sugimura, A., Eryu, O., Serrona, L.K.E.B., Adachi, N., Sakamoto, I., and Nakanishi, A., Nd–Fe–B thin films with perpendicular magnetic anisotropy and high coercivity prepared by pulsed laser annealing, *Jpn. J. Appl. Phys.* 42, 6859 (2003).

MAGNETIC IMAGING FILMS

ROSTISLAV GRECHISHKIN, SERGEY CHIGIRINSKY
Laboratory of Magnetoelectronics, Tver State University, 170000 Tver, Russia

MIKHAIL GUSEV
Research Institute of Materials Science and Technology, 124460 Zelenograd, Russia

ORPHÉE CUGAT
Laboratoire d'Electrotechnique de Grenoble, LEG-ENSIEG, BP 46, 38402 St Martin d'Hères Cedex, France

NORA M. DEMPSEY
Institut Néel, CNRS/UJF, 25 rue des Martyrs, 38042, Grenoble, France

Abstract. The physical principles behind and various applications of magnetic imaging films are reviewed. The imaging films considered include, liquid and solidified nanoparticle films, thin solid films of bismuth-substituted ferrite garnets, and low- and high-coercivity amorphous films of rare earth–transition metal alloys (Gd-Co, Tb-Fe-Co). Preparation details and properties of uniaxial and planar magneto-optical indicator films (MOIF) are described and discussed alongside the analysis of the conditions for optimal magneto-optic (MO) contrast and experimental setup construction. In addition to this discussion a number of images demonstrating the application of MOIF are shown.

Keywords: Bitter method; ferrite-garnet films; magnetic domain structure; magnetic anisotropy; optical microscopy

1. Introduction

The story of imaging of magnetic objects is an interesting case in point, for the interaction of magnetism with light can be observed by the naked eye only under very special circumstances.[1] The earliest magnetic imaging was of magnetic fringe fields around permanent magnets (PMs) and current-carrying wires revealed with the aid of iron powder (Oersted, Davy, Ampere) (Fig. 1). The modern period of development started with Bitter, Hamos, and Thiessen using Bitter solutions in 1931.[2] Since this time many other powerful techniques have been established,[1–3] which include magneto-optic (MO) microscopy based on Kerr and

B. Azzerboni et al. (eds.), Magnetic Nanostructures in Modern Technology, 195–224.

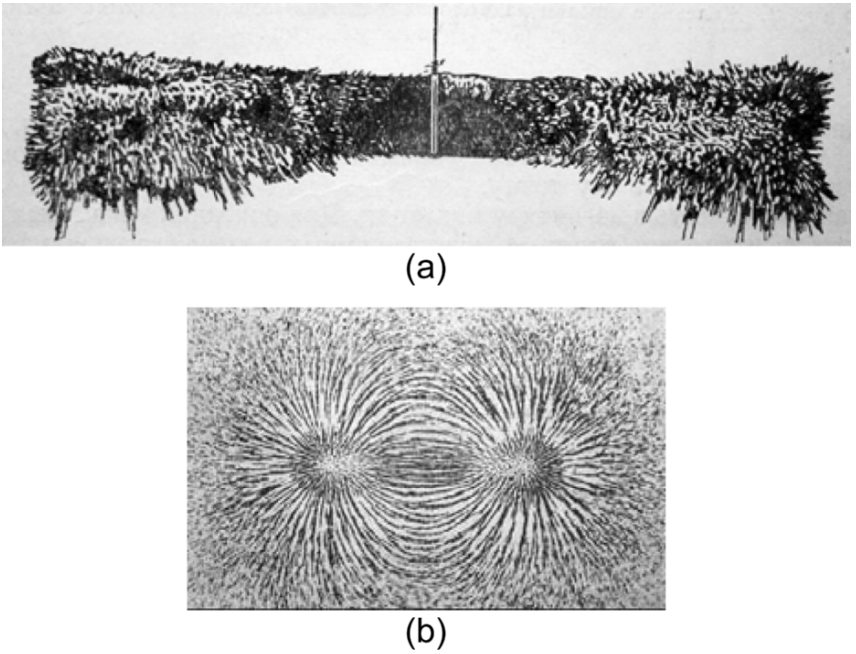

Figure 1. (a) Magnet and free iron powder: 3D visualization. (b) Iron powder distribution around a current loop constrained by a flat sheet of paper: 2D visualization.

Faraday effects, x-ray magnetic circular dichroism (XMCD) microscopy, magnetic force microscopy (MFM), spin-polarized scanning tunneling microscopy (SP-STM), scanners based on SQUID,[4,5] Hall,[6,7] and magnetoresistive[8,9] sensors and many others. All of the above old and new types of microscopy are currently employed by engineers and researchers as each has its own particular advantages for solving particular problems; moreover, in many cases these techniques are complementary.

The imaging methods currently in use may be loosely classified into two groups according to the mechanism of interaction between the probe and sample, i.e. magnetization distribution imaging and stray field imaging.[1] In the present work we will provide an introduction to the technique of magnetic imaging films serving to visualize the stray field distribution at the surface of magnetized objects. This technique is based on the use of two different film types – classical Bitter layers and MO imaging films (MOIF). Relatively slow progress has been made in the development of the Bitter technique based on the use of magnetic nanoparticles, whereas much more interest has been shown in the use of MOIF. The latter were substantially developed during the last decade or two mainly due to their efficiency in the study of high-temperature superconductors. At the same time, MOIF find increasing use in other research areas including materials science, magnetic recording, and magnetic microelectromechanical systems (MEMS).

2. Nanoparticle films (Bitter method)

2.1. LIQUID BITTER FILMS

For a long period, the Bitter method offered the greatest spatial resolution and sensitivity. Progress in the art of obtaining Bitter patterns was related mainly with the magnetic domain structure studies. A comprehensive account of the Bitter method was given recently by Hubert and Schäfer in their book on magnetic domains,[3] so here only an overview and some new details on this technique will be given. Extended bibliography on general properties of magnetic fluids is regularly published by the *Journal of Magnetism and Magnetic Materials* and *IEEE Transactions on Magnetics*.

In the classical Bitter method, the surface of a magnetic material is covered by a thin layer of nanoparticles (size 5–20 nm) suspended in liquid media (water, kerosene, oil). Numerous recipes for preparation and stabilization of magnetic liquids, as well as contrast theory and experimental conditions for the observation of magnetic patterns have been described in detail.[3] The optical contrast arises from the nanoparticle concentration at the places of largest field gradients. Moreover, optical anisotropy may be induced in the magnetic liquid (ferrofluid) by the local field under study; the former produces additional optical contrast owing to the birefringence observed in polarized light[10,11] thus allowing, in principle, a directional map of the stray field pattern to be constructed. Because of this, Bitter layers may be considered as liquid MO films. The resolution of liquid Bitter layers is approximately that of the optical microscope.

2.2. DRIED BITTER FILMS

Thin solid films may be obtained from the ferrofluid if some agents are added to the nanoparticle suspension so that it forms a continuous film on drying. This will increase the resolution, because the dried nanoparticle layer will be thinner than the original ferrofluid. The dried film may be peeled off the sample and examined in greater detail in scanning or tunneling microscopes.[12,13] In this way double advantages of enhanced resolution and large depth of focus, particular to electron microscopes and useful for the study of rough surfaces, is achieved.

2.3. NANOPARTICLE CONDENSATION (“SMOKE” METHOD)

Still another modification of the Bitter method is based on the use of magnetic “smoke” produced by evaporating a magnetic material in a low-pressure gas. During this process single-domain nanoparticles of spherical shape may be formed; the size of these particles is regulated by the gas pressure and conditions of evaporation.[3,14,15] During settling the particles agglomerate in the magnetic stray fields

on the surface of the objects under study. The final decoration is imaged under an optical or electron microscope allowing achieving spatial resolution of the order of 100 nm. Among the recent applications of the Bitter decoration technique are high-resolution studies of vortex structures in superconductors.[16,17] Paramagnetic oxygen particles may be also used to observe the decoration at low temperatures in situ.[18] These particles are readily removed from the sample by heating.

As mentioned by Hubert and Schafer,[3] the contrast mechanism in the smoke method is not quite the same as in Bitter ferrofluids, because the smoke nanoparticles settle in a single trajectory on the surface and do not search equilibrium positions.

2.4. MAGNETOTACTIC BACTERIA

Aquaspirillum magnetotacticum bacteria living in muddy water orient themselves with the aid of the earth's magnetic field to move away from the oxygen-rich surface. This is achieved with the aid of a tiny chain of single-domain magnetite particles inside the cell of the bacterium.[19] The bacteria act as self-propelling north-seeking compasses, so that putting them on a magnetic sample results in their movement along the field vector lines until they reach the northern end of a field line at the surface. This remarkable property of magnetotactic bacteria was applied to the delineation of magnetic domain structure.[3,20] The method is similar to the Bitter method, but the contrast mechanism is somewhat different: the bacteria indicate the positions of the northern footpoints of the field lines rather than the positions of highest absolute values of the field on the surface.

The technique is fast (bacteria velocity is about 30 μm/s) and sensitive. The bacteria survive in a sealed sample for at least 2 years without additional nutrients. Nanoparticles inside the bacterium are single-domain, single-crystalline, and highly monodisperse when compared to synthetically grown nanoparticles of similar sizes. Their extraction and collection is performed with the help of a magnetic field.[21]

2.5. SOLIDIFIED FERROFLUID FILMS

Magnetic nanoparticles may be mixed with a binder (e.g. paraffin) having a solid–liquid transition[22] near the working temperature. In the solidified state the nanoparticles are immobile and insusceptible to external magnetic field. Snapshot sampling may be performed by heat flux pulses fluidizing the binder thus releasing the nanoparticles and permitting them to orient in the magnetic field. This mode may be useful in preventing ferrofluid flocculation in strong external magnetic fields and in conserving the specified patterns for further use.

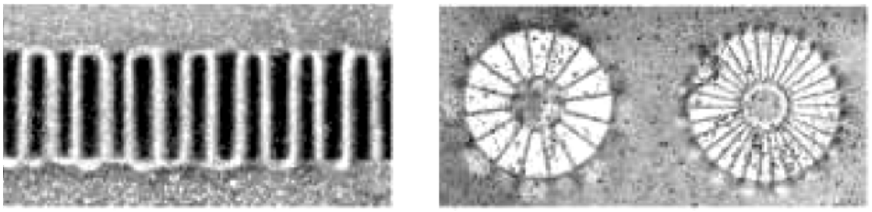

Figure 2. Magnetic field at the surface of a cylindrical radially magnetized multipole rotor (cylinder width 8 mm) and of 8- and 15-pole Ø8 mm axially magnetized Sm-Co rotors observed with the ferrofluid-based viewing film.

2.6. MICRO-ENCAPSULATED FERROFLUID CONTAINING FILMS

The technology of micro-encapsulation which allows a thin 2-mil (≈50 μm) layer of ferrofluid slurry to be bonded to a 5-mil sheet of plastic film was applied to produce a flexible viewing film for dc magnetic fields.[23] In the encapsulation process nickel nanoparticles become engulfed within gelatinous membranes coated onto the plastic film. After complete drying, the nanoparticles maintain freedom of movement within the gelatinous membranes. As for conventional ferrofluids, the viewing film placed on the surface of a magnetic material delineates the regions of largest field gradients, so a particularly useful application is in the identification of changes in magnetic polarity (Fig. 2). The currently available viewing films can detect fields as low as only a few gauss (tenths of millitesla) with a resolution of the order of 0.2 mm.

2.7. RESUME OF AND PROSPECTS FOR NANOPARTICLE FILMS

In spite of its age, the Bitter imaging method, due to its sensitivity, versatility, high resolution, simplicity, and cheapness still finds use in various tasks. New advances should be expected from today's progress in nanotechnology. Of interest are the improvements in the production and stabilization of monodisperse nanoparticle ensembles with uniform properties. Improved sensitivity may be expected with the use of needle-like particles (nanowires) having increased shape anisotropy and microemulsions of the water-in-oil or oil-in-water type with enlarged magnetic moment.[24] Refined visibility may be provided by the ferrofluids containing fluorescent nanobeads or highly reflective metal flakes. A single-component free of phase separation ferrofluid composed solely of ions having an unexpectedly strong response to a magnet was discovered recently.[25] It is of interest to examine the possibility of its use for imaging purposes. One more interesting proposal is to grow magnetic cobalt nanoparticles inside the hollow protein capsid shell derived from the T7 bacteriofhage virus.[26] The resultant "magnetic viruses" are uniform in their properties which may be useful for imaging. And, as a final remark, it is known that ferrofluids may be exploited to control the position of other tiny

objects.[27,28] In this case the imaging properties of ferrofluids may be combined with their use in micromanipulators.

3. Ferrite garnet MO imaging films (MOIF)

3.1. PREPARATION AND PROPERTIES

During the last two decades ferrite garnet single-crystalline films became the de facto material for direct visualization of magnetic field microdistributions. The basics of the method and early works were reviewed in 1995 by Koblischka and Wijngaarden.[29] Since then the interest in the visualization of the microfield distribution of different objects markedly increased.[30–40] In what follows, we present an overview of the state of the art of this technique and discuss how the method can be optimized for various applications.

Ferrite garnets $\{R_3^{3+}\}[Fe_2^{3+}](Fe_3^{3+})O_{12}$ have a cubic structure with rare earth and iron ions occupying different positions ({R} dodecahedral, [Fe] octahedral and (Fe) tetrahedral) between oxygen ions. The uniqueness of this type of ferrites lies in their possibility to produce an endless variety of physical properties by isomorphic substitutions of atoms in the three-sublattice garnet structure; moreover, the properties of ferrite-garnet epitaxial films may be substantially altered by the choice of the substrate and conditions of growth.

High-quality single-crystalline ferrite garnet films are mainly prepared by the method of liquid phase epitaxy (LPE) developed in the 1970s during the era of bubble domain technology.[41–43] An important parameter which is used to characterize the bubble domain materials is the quality factor

$$Q = \frac{2K_{\mathrm{u}}}{\mu_0 M_{\mathrm{s}}^2} \tag{1}$$

where K_{u} is the uniaxial anisotropy constant. The Q-factor defines the ratio between the energy of magnetic (magnetocrystalline or induced) anisotropy and maximum energy density due to shape anisotropy, $\mu_0 M_{\mathrm{s}}^2/2$. The significance of this condition is that for $Q > 1$ the material will be *uniaxial* with the easy axis direction normal to the plane of the film, while for $Q < 1$ the magnetic moments will tend to be oriented in the *plane* of the film due to the effect of the demagnetizing field.

Bismuth-substituted ferrite garnets are high-quality MO materials having specific Faraday rotation an order of magnitude larger than bismuth-free crystals. The optical efficiency is characterized by the MO figure of merit $\Psi = 2\vartheta_F/\alpha$, where α is the optical absorption coefficient. The $\Psi(x)$ compositional dependence has a broad maximum and is practically constant in the x range from 0.8 to 1.1.

Directions of the easy magnetization of the films are determined by the minimum of the anisotropic part of the free energy, including energies of cubic

anisotropy E_c, uniaxial anisotropy E_u, interaction with the external magnetic field $E_m = -\mu_0(\mathbf{M}\cdot\mathbf{H})$ and energy in self demagnetizing field $E_d = -\mu_0(\mathbf{M}\cdot\mathbf{H}_d)/2$. For thin films E_d is maximum when magnetization vector $\mathbf{M}$ is normal to the film plane [$E_d(\max) \cong \mu_0 M_s^2/2$], and it is near zero for $\mathbf{M}$ lying in the film plane. For ferrite garnet films the constant of uniaxial anisotropy K_u is generally represented by magnetoelastic component K_u^s, arising due to differences in the lattice parameters of the film and substrate, and growth component K_u^g, evolving during film crystallization because of nonstatistical ion distribution in garnet magnetic sublattices.

The constants of cubic anisotropy are regulated within broad limits by transition d-metal ion substitutions. The first constant of cubic anisotropy in ferrite-garnet films is always positive, while the second constant may be of any sign. Transition d-metal ions (Co^{2+}, Ru^{3+}, Ru^{4+}, Os^{3+}, Rh^{4+}, and others) give a positive contribution to K_1 and negative one to K_2, thus providing, in principle, a possibility of cubic anisotropy compensation. The constant K_u^s related to mechanical stresses is satisfactorily described with the aid of material elastic constants, film–substrate lattice parameter mismatch $\Delta a/a$ and magnetostriction constants λ:

$$K_u^s = -\frac{3}{2}\frac{E}{(1-\nu)}\frac{\Delta a}{a}\lambda_{hkl}, \tag{2}$$

where E is the Young modulus and ν is the Poisson coefficient. For ferrite garnets E and ν weakly depend on the composition. Maximum K_u^s values are of the order of 10^3 J/m^3 (10^4 erg/cm^3) and are limited by the maximum attainable magnetostriction constants and $\Delta a/a$ mismatch.

Our studies show that the growth anisotropy of Bi-substituted MOIF films depends on the standard controllable technological parameters of LPE (melt-solution composition and supercooling, growth temperature, substrate rotation velocity, etc.). Figure 3a illustrates the variation of the growth anisotropy constant for successive crystallization processes for films of the same composition. It was ascertained that the growth anisotropy depends on such unmanageable parameters as the heat chamber construction, shape and size of the crucible, temperature and time of homogenization, rate of cooling, etc. Figure 3b shows the dependence of K_g on the melt-solution supercooling for epitaxial films of different composition.

The demonstrated variations depend on the melt-solution preparation procedure, particular qualities of the LPE installation, crucibles, and substrates. To take into account these factors one or two reference processes should be made for each new combination of melt-solution–installation–crucible–substrate. This provides a fair degree of predictability (but not controllability) of the growth process.

Operational control of the magnetic anisotropy of MOIF may be performed at the expense of the magnetoelastic contribution. The latter is determined by the

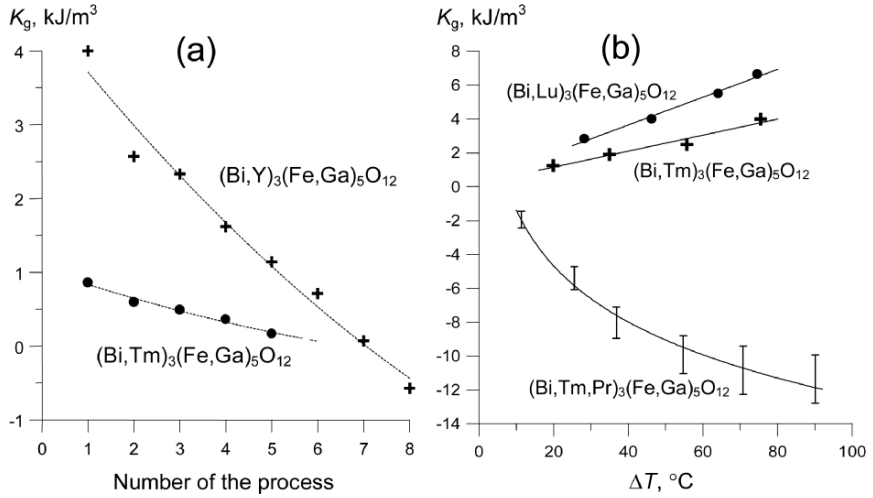

Figure 3. Dependence of the growth-induced anisotropy constant (a) on the number of succesive operations and (b) on the melt-solution supercooling

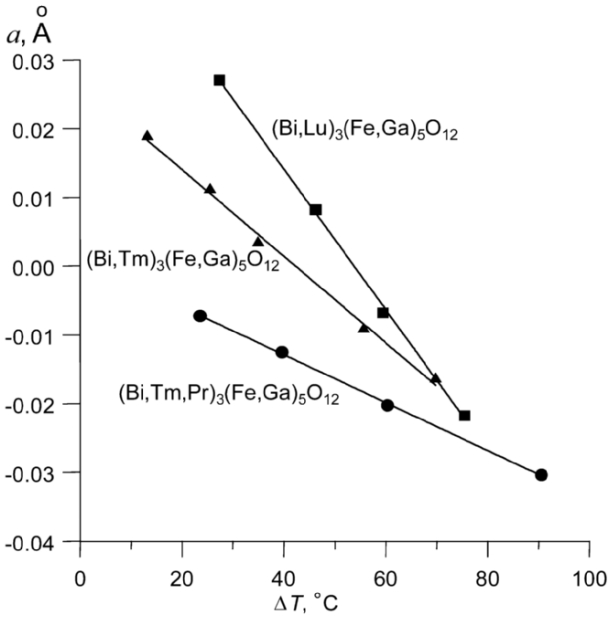

Figure 4. Ferrite garnet MOIF lattice parameter for different solution-melt supercooling

formula (3.2). In the absence of dislocations, the deformation of the epitaxial film is equal to the film–substrate lattice parameter mismatch. The lattice parameter of the substrate is fixed (for gadolinium gallium garnet $a_{GGG} = 1.2383$ nm), whereas for the film it may be regulated by the change of the technological regime (Fig. 4).

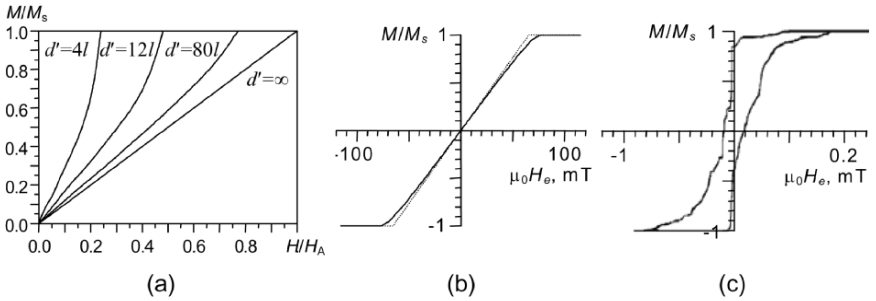

Figure 5. (a) Magnetization curves of uniaxial films along the easy axis for different reduced film thickness $d' = d/l$. (b) Magnetization curve of the film with planar anisotropy along its hard axis (normal to the film plane). Dotted line – theory, solid line – experiment. (c) In-plane hysteresis loop of the planar film (experiment).

Taking into account the above regularities results in a technological process including the following steps: (i) choice of the charge composition with the aid of graphs similar to those of Fig. 4; (ii) refinement of the technological parameters with the help of reference processes; (iii) correction of the melt-solution composition and compensation of the supposed change of the characteristics by the change of the growth parameters.

The easy axis (normal to the plane) magnetization curves of uniaxial films of different thickness may be calculated with good accuracy as described by Kooy and Enz[44] (Fig. 5a). The calculation results are given for the reduced film thickness values, $d' = d/l$, where d is the real thickness of the film, and $1 = \sigma_{\mathrm{dw}} \big/ \mu_0 M_{\mathrm{s}}^2$ ($\sigma_{dw} \big/ 4\pi M_s^2$ in CGS units) is the so-called characteristic length of the material. In the expression for l the surface energy density of the 180° domain wall, σ_{dw}, is compared with the volume density of the demagnetizing field energy. For typical bubble domain materials l is of the order of 180° domain wall width $\delta_{\mathrm{dw}} = \pi \sqrt{A/K_{\mathrm{u}}}$.[41–43]

For uniaxial films of finite thickness the magnetization curves have an initial linear part corresponding to domain wall motion processes followed by a positive curvature $\mathrm{d}^2M/\mathrm{d}H^2$ and quite a sharp approach to saturation characterized by jump-like annihilation of residual domains.

Shown in Fig. 5b are the magnetization curves for the film with "planar" anisotropy, i.e. film with minimized magnetocrystalline cubic and induced uniaxial anisotropy. Here the magnetization in the direction normal to the film plane proceeds by the magnetic moment rotation opposed by the shape anisotropy. The general expression for the shape anisotropy energy is

$$E_{\mathrm{s}} = \frac{\mu_0}{2} \sum_{\mathrm{i,k}=1}^{3} N_{\mathrm{ik}} M_{\mathrm{i}} M_{\mathrm{k}}, \tag{3}$$

where N_{ik} is the tensor of demagnetizing factors. For an infinitely thin film N_{xx} and N_{yy} along x and y axes in the film plane are zero, while N_{zz} factor along the normal is maximum and equals 1 (4π in CGS units), so

$$E_s = \frac{\mu_0 M_s^2}{2} \sin^2 \varphi, \tag{4}$$

where φ is the angle between the $\mathbf{M}_s$ vector and film plane. It is convenient to interprete the coefficient $\mu_0 M_s^2/2$ as a shape anisotropy constant K_s of an infinitely thin film. E_s is zero when $\varphi = 0$, corresponding to the magnetization vectors lying in the film plane ("easy plane" type of anisotropy with a single axis of hard magnetization). The total energy under the action of external magnetic field will be

$$E = E_s + E_H = K_s \sin^2 \varphi - \mu_0 H_e M_s \cos(\theta - \varphi), \tag{5}$$

where θ is the angle between $\mathbf{H}_e$ and the film plane. Stable orientation of $\mathbf{M}_s$ is determined from the minimum condition $\partial E_s/\partial \varphi = 0$.

Solving Eq. (5) enables one to find the angular dependence of the magnetization curves for the case of a reversible rotation process. In particular, for $\theta = \pi/2$ the magnetization z-component is a linear function of the external field ($M_z = \mu_0 M_s^2 H/2K_s$, $M_z \leq M_s$). The optical Faraday rotation is also proportional to the z-component.

In quasi-isotropic samples the experimental magnetization curve is close to the predicted linear variation with field (Fig. 5b); deviations from this behavior are indicative of noncompensated anisotropy contributions. As for the in-plane response, the measurements demonstrate the easiness of the magnetization reversal process with a coercive field as low as 20 μT (Fig. 5c). Large Barkhausen jumps measured during the experiment clearly indicate the domain wall displacement mechanism responsible for the magnetization changes along the in-plane hysteresis loop.

It may be noted that the normal magnetization curve of a planar film (Fig. 5b) coincides with that of an infinitely thick uniaxial film (Fig. 5a). However, the latter situation is ideal. For practical cases of realistic film thickness $d' < 80$ the magnetization curves of uniaxial films are higher than in planar ones, hence higher sensitivity of the former may be expected with other things being equal.

Finalizing this paragraph it should be mentioned that the LPE method of preparing ferrite-garnet MOIF though expensive is well developed, so it is predominantly used by most research groups. At the same time there are a number of attempts to prepare MOIF by other techniques. Pyrolysis,[45] *rf* diode sputtering[46–48] and sol–gel process[49] although not tested yet with respect to MOIF applications, may replace expensive single-crystalline GGG substrates by cheap glasses. There are already positive results in MOIF fabrication by the method of

pulsed laser deposition (PLD);[50–52] however, GGG substrates were still used in this process.

3.2. MO CONTRAST AND EXPERIMENTAL SETUP

Following the analysis given by Scott and Lacklison[53] it is reasonable to consider two modes of possible exploitation of MOIF: the light switch and the modulator. The Malus law for an ideal polarizer/analyzer pair is

$$I_{\pm} = I_0 \exp(-\alpha l) \sin^2(\beta \pm \delta_F l), \tag{6}$$

where β is the angle of polarizer/analyzer uncrossing; I_0 is the incident light intensity; factor $\exp(-\alpha l)$ characterizes the attenuation of the light in the material with an absorption coefficient α and path length l; $\delta_F l$ is the Faraday rotation angle.

For the MO light switch (shutter) β is made equal to $\delta_F l$ and thus for one direction of **M** no light is transmitted ($I_- = 0$); reversal of **M** produces a transmission $I_+ = I_0 \exp(-\alpha l) \sin^2(2\delta_F l)$, so the optical efficiency $\eta_1 \equiv I_+/I_0 = \exp(-\alpha l) \sin^2(2\vartheta_F l)$.

For a MO modulator β is set to $\pi/4$ producing a *difference* in transmitted intrensities of $\Delta I = I_0 \exp(-\alpha l) \sin(2\vartheta_F l)$, resulting in the optical efficiency $\eta_2 \equiv \Delta I / I_0 = \exp(-\alpha l) \sin(2\vartheta_F l)$.

The switch mode corresponds to the condition of maximum contrast of the domain structure of uniaxial films with high enough $Q-$factor. This mode may also be used with planar films for the cases when only qualitative analysis of the field distribution is of interest. However, in planar MOIF the Faraday rotation is a continuous function of the external field; therefore, as distinct from the uniaxial MOIF, the planar ones must be considered as *analog* transducers which in an ideal case are better exploited in the modulator mode.

In practice the implementation of this conclusion is complicated by a number of factors. The main problem is that of the signal/noise ratio and dynamic range of the detector (CCD camera). In addition, the performance of polarization optical microscopes is far from ideal and becomes worse with the increase of the spatial resolution. The degradation of light polarization in an optical system may be described by an extinction factor ξ characterizing the intensity of light transmitted by crossed polarizers. The Malus' law modified for this case may be written as[54]

$$I_{\pm} = (1 - \xi) I_0 \exp(-\alpha l)[\sin^2(\beta \pm \vartheta_F l) + \xi], \tag{7}$$

consequently, the image contrast between two neighboring domains will be

$$C \equiv \frac{I_+ - I_-}{I_+ - I_-} = \frac{(1 - \xi) \sin 2\beta \sin 2\vartheta_F l}{(1 - \xi)(1 - \cos 2\beta \cos 2\vartheta_F l) + 2\xi}. \tag{8}$$

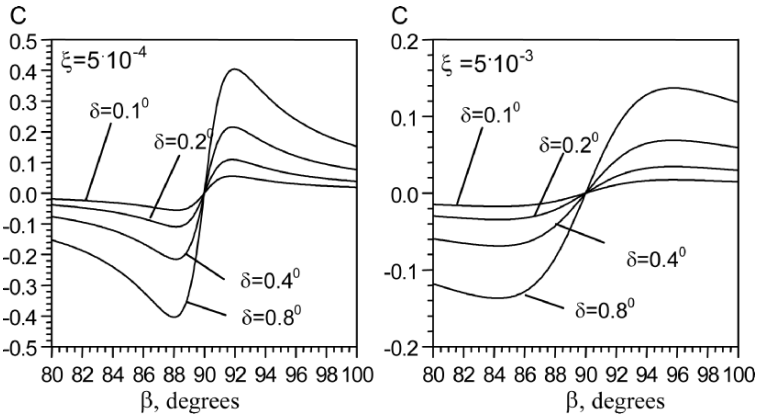

Figure 6. Dependence of the MO contrast on the light depolarization for different Faraday rotation $\delta = \vartheta_F l$. β is the angle of polarizer uncrossing

The angle of uncrossing giving the contrast maximum is found by differentiation of (Eq. 8):

$$\beta = \arccos\left(\frac{\sqrt{(\xi + I_0)(\xi \cos^2\delta + I_0 \sin^2\delta)}}{\xi + I_0}\right), \delta \equiv \vartheta_F l. \tag{9}$$

In the visible the extinction factor ξ of commercially available polarizers is low enough ($10^{-5} \ldots 10^{-6}$). However, due to the light ellipticity and depolarizing effects of various optical elements and the object itself ξ increases by orders of magnitude making it difficult to obtain high contrast C with low $\vartheta_F l$ values. This fact is illustrated for realistic values of ξ and $\vartheta_F l$ by Fig. 6. It is seen that C strongly depends on the polarization quality of the system. For example, for $\xi = 5{\cdot}10^{-3}$ the optical rotation $\delta = 0.4^\circ$ will be hardly observable by naked eye (C = 0.063), while good contrast (C = 0.22) is obtained for the same δ when $\xi = 5 \cdot 10^{-4}$.

Radical improvement of the imaging with the aid of MOIF is obtained making use of the differential regime of image registration and processing as described below.

The intensity of the light registered during observation is described by Eq. (7) and depends on the angle of uncrossing β. Changing the sign of β results in an inversion of the Faraday contrast leaving the optically passive image components (background) unaffected. For $|\beta_1| = |-\beta_2| = \beta$ the corresponding intensities, $I_1 \sim \sin^2(\beta + \vartheta_F l)$ and $I_2 \sim \sin^2(-\beta + \vartheta_F l)$, are proportional to the square sines of the angles $(\pm\beta + \vartheta_F l)$. Element-by-element (pixel-by-pixel) subtraction of the images obtained for $\pm\beta$ provides compensation (leveling) of the background, while the useful polarization signal is

$$\Sigma I(x, y) = I_1(x, y) - I_2(x, y) \sim \sin 2\beta \sin 2\vartheta_F l. \tag{10}$$

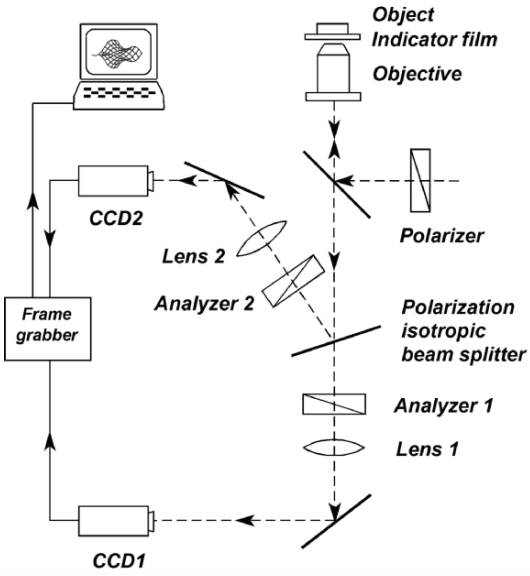

Figure 7. Differential MO setup with independent analyzer settings in both channels

Shown in Fig. 7 is an experimental setup for differential observation of MO images. It was mentioned above that for a MO modulator the largest slope and best linearity of the transfer characteristic occur for the angle $\beta = \pi/4$ between the polarizer and analyzer transmission axes. However for CCD cameras with limited depth of quantization and large intrinsic noise the 45°-geometry may lose its efficiency because of the narrowing of the useful signal dynamic range and increasing of the signal/noise ratio.[55] The scheme of Fig. 7 avoids this problem by providing a flexible setting for optimal polarization geometry. Here the reflected optical beam is split and directed into two registration channels having independent analyzer angle control. The optimal angles of uncrossing in the two channels depend on the characteristics of the image, as well as on the depolarizing effects inevitably present in any microscope;[56] moreover for the same microscope the latter depends on the particular aperture and quality of the changeable objectives, so on-line adjustment appears to be useful. We recall that in the differential mode the transfer function linearity is governed by the factor $\sin(2\vartheta_F l) \approx 2\vartheta_F l$, while the $\sin 2\beta$ value defines its slope (Eq. 9).

This fact is important for the calibration of planar MOIF. It is difficult to perform the calibration in a simple single-channel scheme, because in this case the output light intensity is a nonlinear and, moreover, a nonsingle–valued even function of the Faraday rotation angle (Fig. 8a). By contrast, the differential mode of observation provides a highly linear and single-valued calibration curve (Fig. 8b). In the differential image the defects due to nonuniform illumination are already

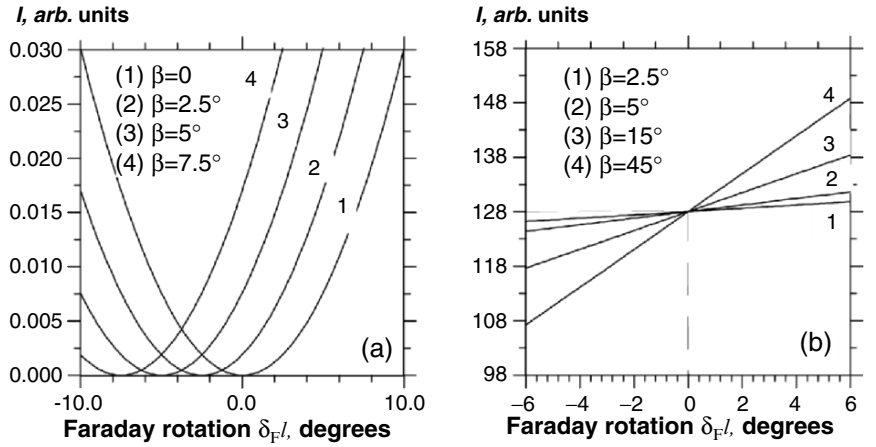

Figure 8. Output light intensity as a function of Faraday rotation angle for different polarizer angles of uncrossing β. (a) Single channel, (b) two-channel differential scheme.

compensated to a large extent. Further improvement is possible by pixel-by-pixel through channel calibration taking into account all systematic errors of the system at the expense of processing time.

A description of the optical part of another experimental MO setup and recommendations on its implementation with a special emphasis on the achievement of maximum polarization sensitivity were given recently by Goa et al.[57] An open modular microscope scheme suitable for experimentation is described. Keeping the microscope as simple as possible avoiding unnecessary optical components is recommended.

A sophisticated imaging polarimeter embodying the differential principle was described by Wijngaarden et al.[58] A Faraday polarization glass rotator controlled by special electronics switches the incident polarization direction during the video blank time between three fixed angle values $-\alpha_0$, 0, and $+\alpha_0$, where α_0 is of the order of a few degrees (maximum rotation due to the sample). Dedicated hardware performs calculations for each pixel in a video stream at an input frame rate of 25 images per second. Excellent sensitivity corresponding to a root-mean-square noise level below 4×10^{-4} degree rotation angle was demonstrated.

Wakabayashi[59] used a garnet film placed before the analyzer instead of glass polarization rotator to invert the contrast of a domain image in real time.

An image processing procedure correcting some defects of the MO image using any MO setup without extensive electronics was proposed by Paturi et al.[60]

3.3. COMPARISON OF UNIAXIAL AND PLANAR MOIF

Images of the domain structure (DS) on the basal plane of a $SmCo_5$ single crystal obtained with a uniaxial MOIF at different distances from the sample surface are

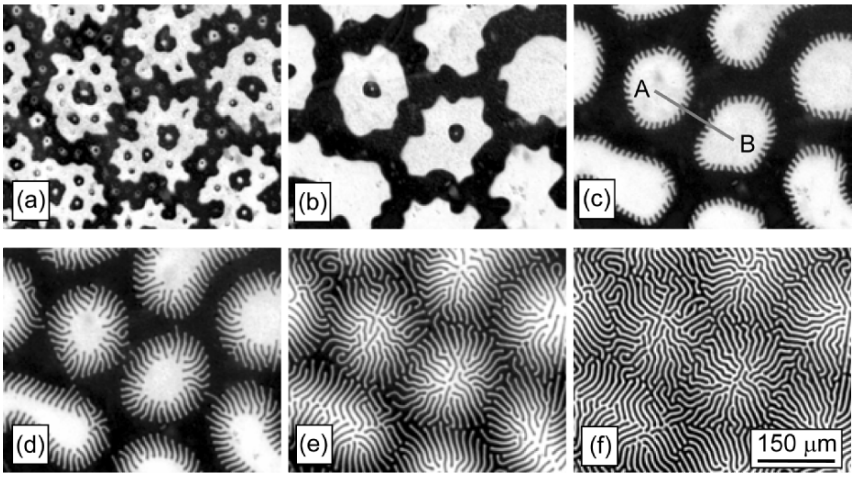

Figure 9. Imaging of the DS of a $SmCo_5$ single crystal by uniaxial MOIF at a distance of (a) 30, (b) 60, (c) 100, (d) 120, (e) 140, and (f) 180 μm from the sample surface

shown in Fig. 9. The $SmCo_5$sample is used in this work as a test sample with well studied DS, which may be independently and directly observed with the aid of polar Kerr effect.

At the shortest distance of $D = 30\mu m$ the field gradient of the sample is high and the MOIF reflects the lines of zero field rather accurately except for the loss of some minute details (Fig. 8a). The short-range fields produced by small domains decay faster with the increase of D than long-range fields from large main domains, so the observed pattern is simplified (Fig. 8b). At the same time specific sinusoidal fringing of domain boundaries develops resulting in continuous patterns corresponding to the initial intrinsic DS of the MOIF. The persistent weak external field manifests itself in a local modulation of the MOIF domain width (Figs. 8e, f).

The behavior of an uniaxial film lying in the xy plane under the action of an external field of the form $H_z(x) = \beta x$ (β constant) was examined by Hagedorn.[61] It was shown that for β exceeding some critical value β_c a flat isolated DW is formed along y-axis. Sinusoidal instability of the DW develops when $\beta < \beta_c$. The critical gradient β_c depends on the magnetization saturation M_s, film thickness d and material characteristic length $1 = \sigma_{dw}/\mu_0 M_s^2$.[61] An example showing the development of sinusoidal instability with the decrease of the field gradient is given in Fig. 10. The parameters of the sinusoid (period and amplitude) may be used to determine the field gradient.

As for the effect of MOIF domain width modulation by the external field it should be noted that it is observed in the region of the magnetization curve below saturation. For small uniaxial MOIF thickness this region is characterized by a sensitivity higher than for planar MOIF. Moreover, the sensitivity increases

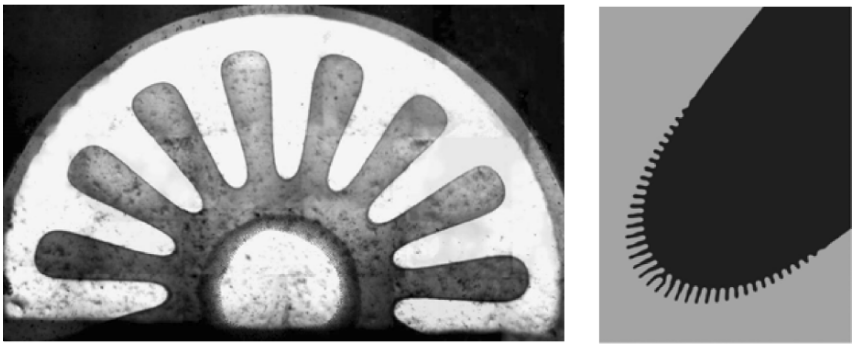

Figure 10. Multipole axially magnetized microrotor (ϕ8 mm) as imaged by an uniaxial MOIF. Enlarged fragment (*right*) shows the DW sinusoidal instability developing with the decrease of the field gradient.

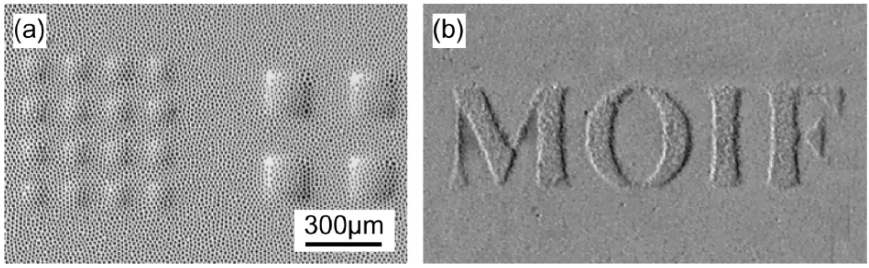

Figure 11. Bubble domain lattice in an uniaxial MOIF modulated by the field of permalloy squares on (a) Si and (b) by standard laser printing (Times 5 pt font) on paper

even more with the approach to saturation, when the stripe domains transform into cylindrical shape[44] (bubbles) (see Fig. 5a). This property may be exploited for producing half-tone images from binary elements (magnetic bubble or stripe domains of opposite polarity) in a fashion similar to the newspaper photo raster having elements small compared with the informative image details (Fig. 11).

The results of the visualization of a field distribution having details comparable with the intrinsic domain width of the uniaxial MOIF may be rather far from the actual pattern (Fig. 12). In addition to wall-pinning by defects the topological hysteresis related to nucleation and collapse field problems[62] affect the patterns formed by uniaxial MOIF. Moreover an effect of period competition in stripe DS occurs when the MOIF is subjected to a periodic field.[63] Magnetic shaking by external periodic fields helps to minimize these artefacts.

Shown in Fig. 13 are the images of the $SmCo_5$ sample obtained with the aid of a planar MOIF. The sample and the field of view are exactly the same as demonstrated above in Fig. 9 for an uniaxial MOIF. For short distances to the sample (micrographs of Figs. 13a and 9a) the images are quite similar. For larger distances the image contours of the planar MOIF start to smear as if the

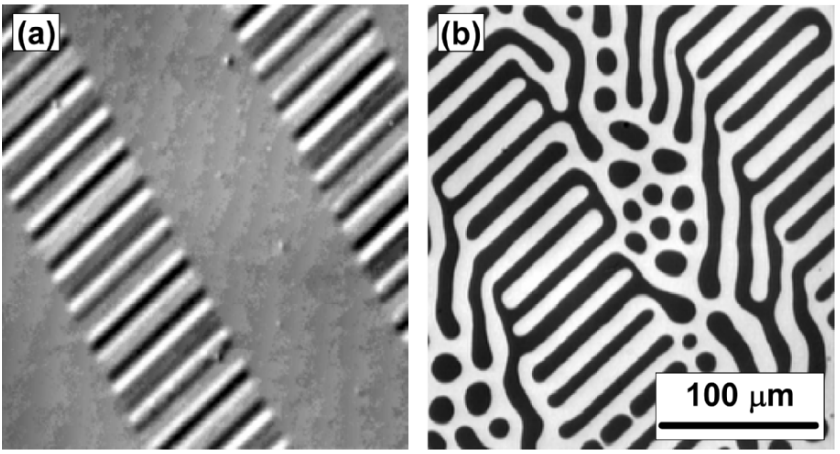

Figure 12. MO images of floppy disk data tracks as depicted by (a) planar and (b) uniaxial MOIF

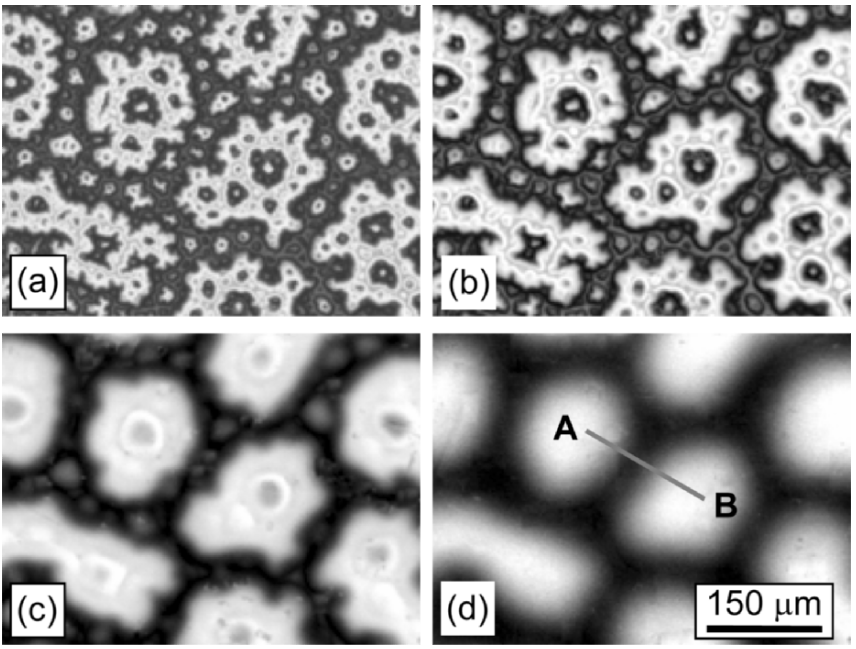

Figure 13. Imaging the DS of a $SmCo_5$ single crystal by planar MOIF at a distance of (a) 10, (b) 40, (c) 60, and (d) 100 μm from the sample surface

sample goes out of focus. At the same time small details (supplementary domains of the $SmCo_5$ structure) having short-range stray fields vanish, whereas main 180° domains producing long-range fields are still visible (Figs. 13c, d).

Figure 14 compares the light intensity distribution for both the uniaxial and planar MOIF measured along AB lines drawn for the same field of view in Figs. 9c

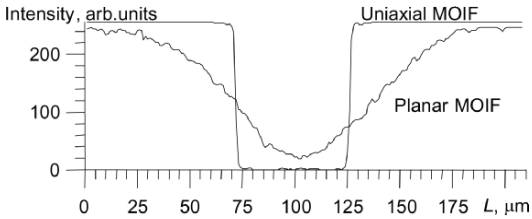

Figure 14. Light intensity profile measured under the same experimental conditions along AB lines shown in Figs. 8 and 12 for uniaxial and planar MOIF

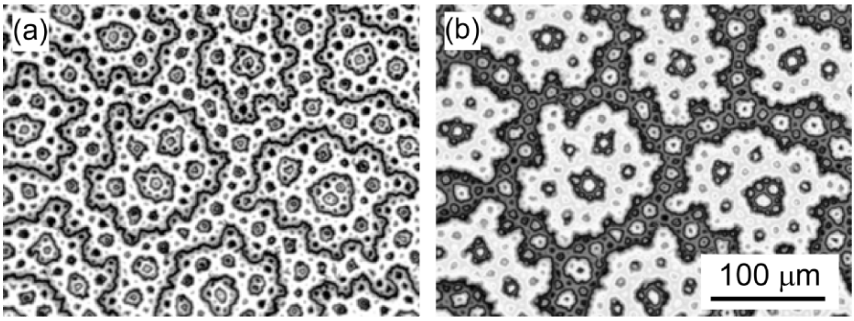

Figure 15. Magnetic DS on the basal plane of a $SmCo_5$ single crystal as revealed with planar MOIF and observed with (a) polarizers crossed and uncrossed by 4° (b) (domain wall and domain contrast modes, respectively).

and 13d. It is seen that the uniaxial MOIF acts as a nearly ideal binarizer because of sharp transitions between the image of oppositely oriented 180° domains having negligible domain wall width. In the planar MOIF the transitions are smooth reflecting gradual changes in the object field distribution thus making possible quantitative field measurements.

It may be added that in the same way as in traditional Faraday MO DS studies both the domain wall and domain contrast modes of observation are feasible with planar MOIF (Fig. 15).

3.4. INTRINSIC DOMAIN STRUCTURE OF PLANAR MOIF

In an ideal case of zero magnetocrystalline and induced magnetic anisotropy planar MOIF should be free of classical magnetic domains with narrow domain walls. Instead some kind of magnetization curling forming closed magnetic fluxes in the film plane minimizing the magnetostatic energy of the sample may be expected. In practice this ideal case seems to be unattainable, because even small magnetic anisotropies will immediately lead to the formation of magnetic DS with domain walls having finite energy and thickness.

The scheme of a simple device for the study of planar magnetization distribution with the aid of the Faraday effect is shown in Fig. 16. The sample is

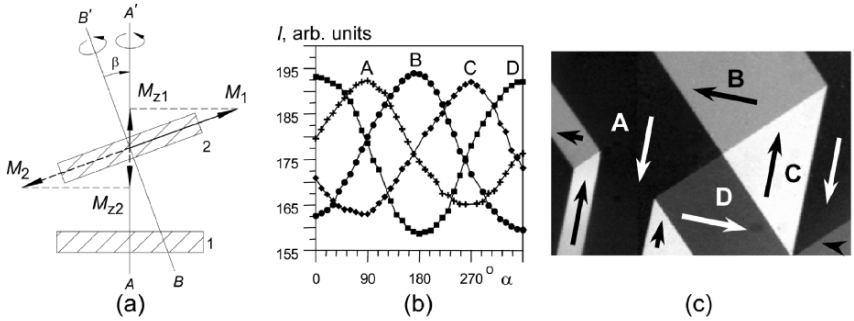

Figure 16. (a) Schematic diagram of a device for the study of planar magnetization distribution with the aid of the Faraday effect. 1 – main rotatable microscope stage, 2 – second rotatable stage with the sample inclined with respect to stage 1. (b) Angular variation of the local light intensity of four selected domains A, B, C, D measured in the course of 360°-rotation of the stage 2. (c) Faraday image and interpretation of the DS of planar MOIF.

inclined by a small angle β with respect to the light propagation direction AA′ thus providing an appearance of nonzero magnetization components in this direction. Rotation of the sample around the inclined BB′ axis provides controllable change of the Faraday component values from positive M_{z1} to negative M_{z2}. This rotation results in a gradual variation of the domain contrast and its inversion after passing through zero point. Angular photometric measurements of the local light intensity for specified domains enables one to find the corresponding directions of magnetization as shown in Figs. 16b, c. The planar DS itself is highly mobile and sensitive even to the weak field of the earth, so screening of the sample during the study of intrinsic DS is necessary.

It should be added that rotation around BB′ has no effect on the image of normal magnetization component distribution in the sample, while the existence of planar components is detected by the angular dependence of the transmitted light intensity. So the extraction of the constant and variable parts of the image by proper processing provides additional information on the magnetization distribution in the planar MOIF.

Manifestations of the intrinsic DS depend on the field distribution under study. In some situations the contrast of the planar domains is low enough so that severe overcontrasting is required to reveal them (Fig. 17). However, in the case of strong field gradients with large horizontal and vertical components zig-zag DS[51] which deteriorate the image may be formed (Fig. 18). As already mentioned by Paturi et al.[60], the zig-zag DS changes with rotation of the MOIF while keeping the arrangement otherwise the same thus showing its relation to the MOIF crystallography.

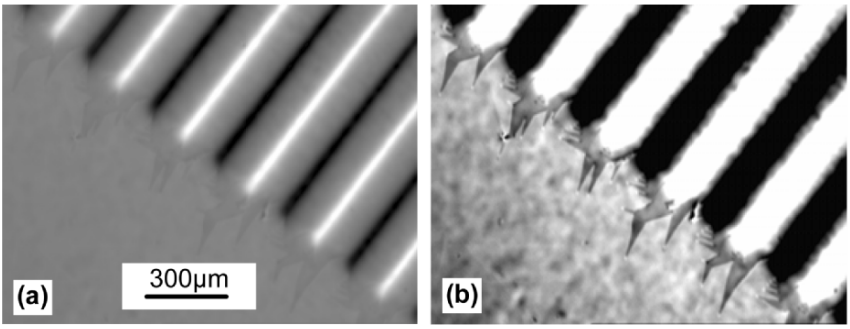

Figure 17. (a) Normal and (b) overcontrasted image of a magnetic card visualized with planar MOIF

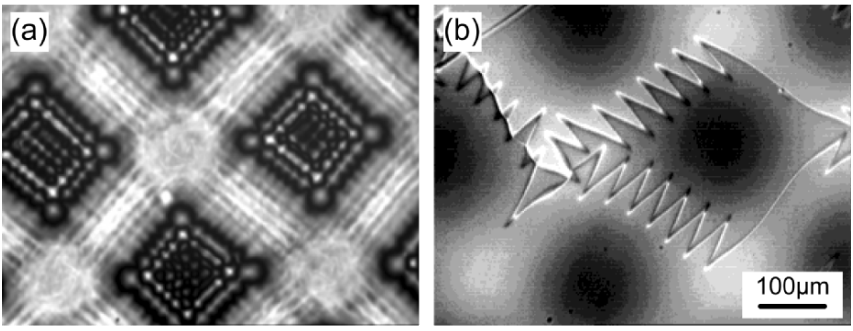

Figure 18. Thermomagnetically written Nd-Fe-B permanent magnet square lattice pattern visualized with the aid of planar MOIF at a distance of (a) 10 μm and (b) 600 μm from the sample surface.

4. Amorphous metallic MOIF

4.1. UNIAXIAL LOW-COERCIVITY FILMS

The methods of preparation of amorphous rare-earth–transition metal thin films with perpendicular uniaxial anisotropy were developed in the past with respect to bubble domain technology and optical storage applications.[41–43] Due to high enough values of MO figure of merit $\Psi = 2\vartheta_F/\alpha$ of amorphous films their DS is easily revealed with the aid of either Kerr (in reflection) or Faraday effect (in transmission). As distinct from ferrite garnet films, amorphous films may be prepared on different types of rigid or flexible substrates including glass, Al_2O_3, Si, polycarbonate, polyimide, etc.

Takahashi et al.[64] in due time mentioned that magneto-optical MnBi metal films may be used for the purpose of magneto-optical visualization. The field distribution of a miniature PM was successfully revealed. However this communication seems to be the only one on imaging with the aid of metallic MOIF. In the present work we prepared metallic magneto-optical $Gd_{1-x}Co_x$ films

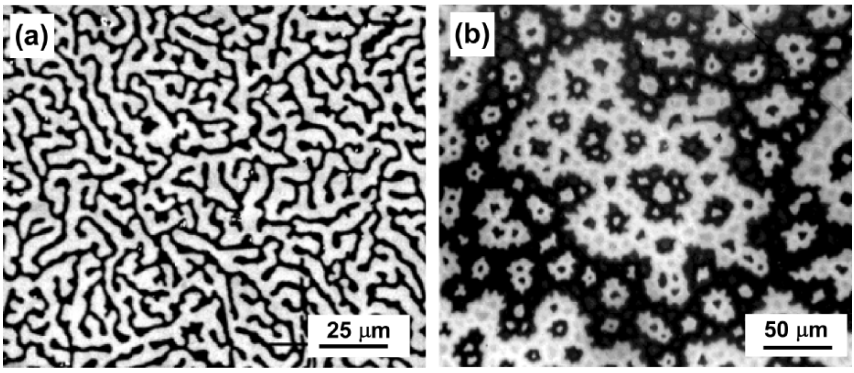

Figure 19. (a) Intrinsic DS of the uniaxial amorphous low-coercivity Gd-Co film on a glass substrate. (b) DS pattern of $SmCo_5$ crystal visualized with the aid of this film.

($0.7 < x < 0.85$) by magnetron sputtering. Typical properties of these films are $\mu_0 M_s = 0.04...0.1$ T, uniaxial anisotropy constant $K_u = (1...7) \cdot 10^4$ J/m^3, quality factor $Q = 1...8$. An illustration of the intrinsic DS of a demagnetized Gd-Co film and its application for the visualization of the DS of the test $SmCo_5$ sample are given in Fig. 19. It is seen that the test DS is reproduced with a high degree of accuracy.

Making a comparison with uniaxial ferrite garnet MOIF (FG MOIF) it should be noted that corrosion stability of amorphous MOIF (AMOIF) is poor so they need to be protected by corrosion-resistant layers. The magnetooptic contrast in AMOIF though satisfactory is lower than in FG MOIF. The geometrical resolutions are practically the same, but significant improvement may be expected for AMOIF because of two factors: (i) AMOIF are much thinner (typically 50–100 nm) than FG MOIF. This improves the resolution in the vertical direction; (ii) AMOIF parameters may be adjusted to obtain the intrinsic DS of submicron size thus improving the lateral resolution. Moreover, the actual resolution of AMOIF may be increased by using flexible substrates allowing more intimate contact with the sample, or, when possible, by direct sputtering the film on the sample under study. Lastly, AMOIF are much cheaper than FG MOIF.

4.2. UNIAXIAL HIGH–COERCIVITY FILMS AND THERMOMAGNETIC IMPRINTING

Amorphous films of Tb-Fe and related alloys such as Tb-Fe-Co are characterized by adequate Kerr rotation and large uniaxial anisotropy. With proper choice of composition the coercivity of these films can rise steeply below the Curie temperature, which allows the stable formation of small domains. These properties are useful for thermomagnetic MO recording.[66] The preparation methods

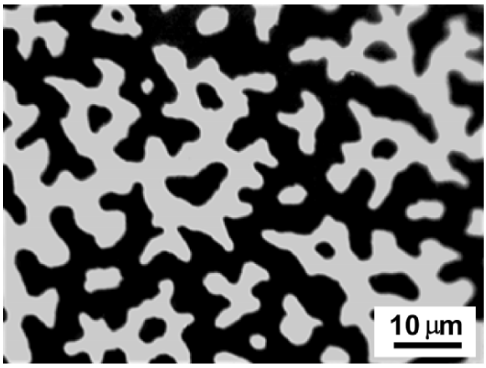

Figure 20. Thermomagnetically imprinted DS pattern of $SmCo_5$ single crystal visualized with the aid of a high-coercivity Tb-Fe-Co amorphous MOIF

for these films are based on standard magnetron sputtering procedures and are well developed.[67]

To investigate the imaging possibilities of this type of material $Tb_{24}Fe_{70}Co_6$ films (T_{comp} = 300 K, T_c = 470 K, RT coercive field 0.6 T) with a SiO_2 quarter-wave antireflection and protective layer on polycarbonate substrates were used. A 10 ms white light pulse from a xenon lamp was employed to realize thermomagnetic imprinting of the test structure of the $SmCo_5$ crystal on the Tb–Fe–Co MOIF (Fig. 20). Alternatively a pulse current may be passed through the MOIF to realize heating by the Joule effect.

The presented image demonstrates excellent contrast and resolution obtainable with thermomagnetic MOIF. Other tests give evidence of high sensitivity of this method down to fields of the order of 10 μT (0.1 Gs).

5. Some application examples

5.1. MAGNETIC RECORDING

Many types of magnetic recording media including cards, analog and digital tapes, and disks may be successfully examined with the aid of uniaxial and planar MOIF. Shown in Fig. 21 are examples of high-resolution images obtained with planar MOIF. Among various tasks related to magnetic recording is data recovery of damaged media, detecting start/stop events in forensic examination, studies of the recording process, magnetic head fields, etc.

5.2. PERMANENT MAGNETS

Shown in Fig. 22 is the calculated and experimental magnetic field distribution of a gradient system comprised of two oppositely magnetized PMs measured with

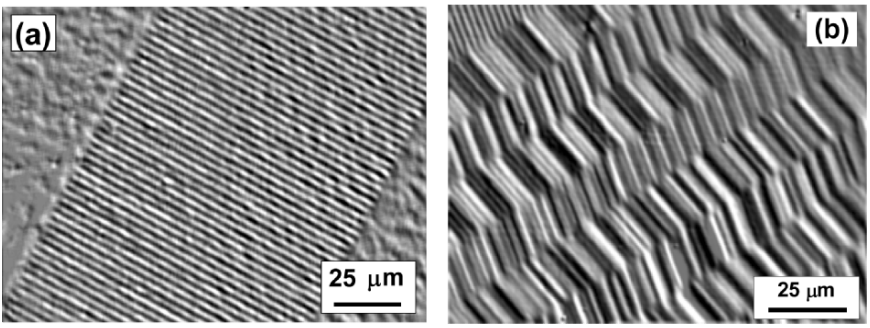

Figure 21. Magnetic recording data tracks of (a) 3.5″ floppy disk and (b) digital audio tape

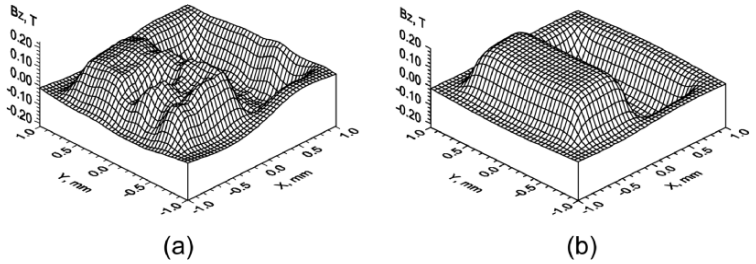

Figure 22. B_Z distribution in the XOY plane at a distance of 0.15 mm from a gradient pair of Sm-Co permanent magnets (1500 × 750 × 250 μm each) with antiparallel magnetization, (a) experiment and (b) calculation

the aid of a calibrated planar MOIF. This comparison serves to characterize both macro- and microuniformity of the PM material. For the given case, large magnetic flux nonuniformities resulting from mechanical damage of the sample during cutting and grinding are revealed by MOIF.

Figure 23 illustrates the results of visualization and field reconstruction of PM structures obtained by sputtering of Nd-Fe-B alloy onto a patterned and a flat substrate. The 1D strip-patterned sample was unidirectionally magnetized normally to the film plane, while a periodic 2D lattice of square islands in an oppositely magnetized matrix was formed in the flat sample by thermomagnetic writing under laser heating. Magnetization modulation inside the square regions is due to light diffraction spots formed in the irradiated regions during writing.

This type of high-coercivity PM films with prescribed magnetic patterns may be successfully used as reference samples for MOIF calibration. Their advantage over NIST imaging reference samples[68] is that due to the rigidly fixed magnetization of the PM, it is easy to calculate accurately the spatial distribution of both horizontal and vertical field components.

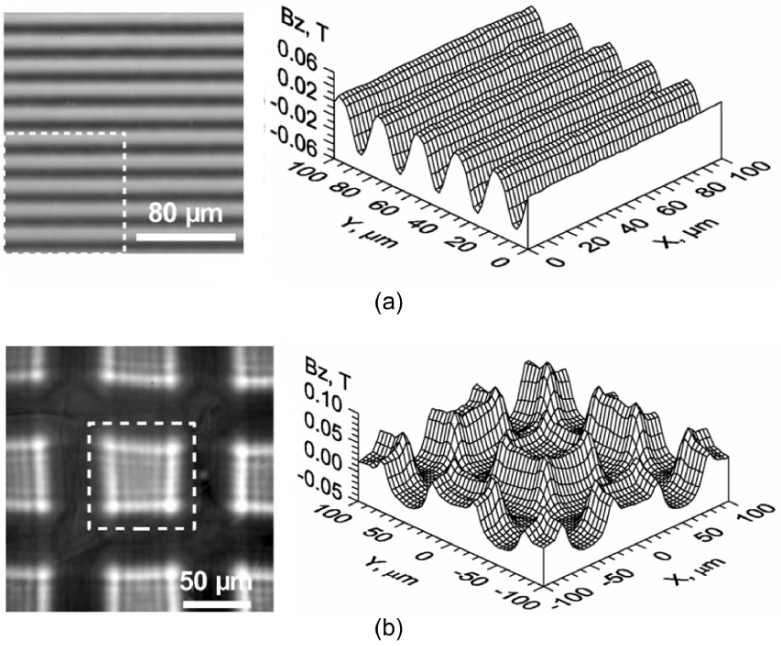

Figure 23. Normal field component distribution of 1D and 2D periodic PM patterns reconstructed from planar MOIF images. (a) NdFeB film sputtered on a patterned substrate (trench width 10 μm). (b) 2D pattern written thermomagnetically on a flat substrate through a mask with 50 μm perforations.

5.3. ELECTRIC CURRENTS

Egorov and Lebedev[69] proposed to use either uniaxial or planar MOIF to study the distribution of electric currents flowing on the surface of integrated circuits (ICs). In particular, the paths of abnormal current due to widespread latchup effect in complementary metal–oxide–semiconductor (CMOS) ICs were visualized. The sensitivity limit (minimal current surface density) of the method was estimated to be 0.1 mA/μm.[69]

5.4. EDDY CURRENT MICROSCOPY

MOIF were successfully applied to visualize the eddy current distributions for nondestructive evaluation of conducting materials.[70,71] In the eddy current microscopes, the induction of eddy currents is conventionally performed by an alternating current excitation coil above the object surface. The magnetic field induced by the eddy currents is visualized with the aid of MOIF. Stroboscopic illumination synchronized with the current in the exciting coil is used to observe the magnetic field distribution at appointed moments. Images of both surface and buried flaws in

aeronautic aluminium structures and steel test samples were successfully obtained and further enhancement of the devices are proposed.[70,71]

5.5. DOMAIN STRUCTURE OF WIRES

Contrary to reasonable doubts, Kabanov et al.[72] were able to show the requirement that the surface of the object under investigation be flat is not mandatory for MOIF application. The DS of amorphous wires with a diameter of 120 μm was successfully revealed with the aid of planar MOIF. Moreover, fine details of the DS were found in the region of an artificial scratch made on the wire along its axis useful in the interpretation of the observed patterns.

5.6. SPIN REORIENTATION TRANSITIONS IN MULTILAYERS

Nikitenko et al.[73] proposed to use the leakage fields around an artificial 400 μm test hole to keep track of the spin configuration during spin reorientation transitions in magnetic multilayers. The idea is to observe the stray field image of the hole with MOIF. The axis of symmetry of this image coincides with the local magnetization direction so the changes of the latter during spin reorientation become visible.

5.7. HIDDEN MAGNETIC IMAGES IN DOCUMENTS

The sensitivity of MOIF with proper use may be high enough to ensure high quality imaging of rather weak hidden magnetic ink patterns of currencies and secure documents (Fig. 24).

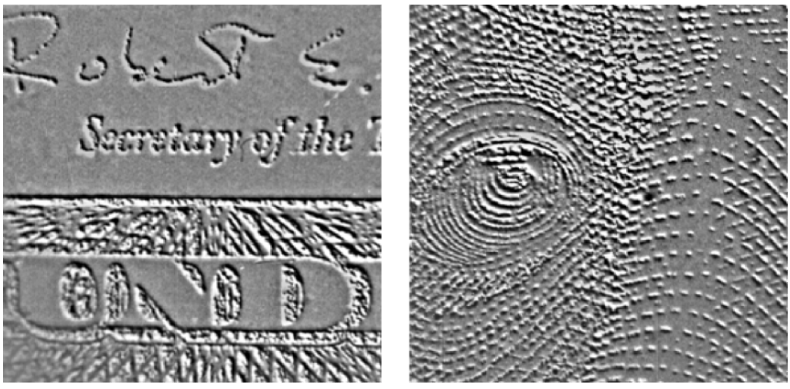

Figure 24. Some details of a banknote's magnetic pattern. Right – the President's eye.

5.8. COMPOSITION-SPREAD STUDIES

Compositional spreads are widely used in combinatorial studies for rapid characterization and mapping composition dependent properties at given external conditions (temperature, electrical, and magnetic fields).[74] Turchinskaya et al.[75] proposed a method of the rapid construction of magnetic phase diagrams in a temperature-composition space using the MOIF technique. The method was applied for mapping the diagram for the $La_{1-x}Ca_xMnO_3$ colossal magneto-resistive oxide films deposited with a compositional spread on a $SrTiO_3$ substrate.

6. Summary

During the last years, the magnetic imaging film technique has developed into a very useful technology with numerous applications. This paper has reviewed this development and discussed emerging trends in this field. Nanoparticle Bitter films are considered along with magnetooptic ferrite garnet and amorphous rare earth – transition metal films with uniaxial and planar anisotropy (MOIF). Nanoparticle films continue to find their wide use in various areas of science and engineering. Uniaxial and planar ferrite garnet MOIF possess complementary properties and differ in sensitivity, pictorial rendition, possibilities of quantification and price, so that each of them should be used in accordance with the aim of the work. Both uniaxial and planar amorphous MOIF possess potentials comparable with ferrite garnet MOIF at a much lower price. We envisage that further progress in magnetic imaging films technology will be connected to the patterned[76] and multilayer[77] MOIF composed of different materials and structures to produce composites with improved properties and enriched functionality.

References

1. M.R. Freeman and B.C. Choi, Advances in magnetic microscopy, *Science* 294, 1484–1488 (2001).
2. E.D. Dahlberg and R. Proksch, Magnetic microscopies: the new addition, *J. Magn. Magn. Mater.* 200, 720–728 (1999).
3. A. Hubert and R. Schäfer, *Magnetic Domains. The Analysis of Magnetic Microstructures*. Berlin, Springer (1998).
4. C. Veauvy, K. Hasselbach, and D. Mailly, Micro-SQUID microscopy of vortices in a perforated superconducting Al film, *Phys. Rev. B* 70, 214513 (2004).
5. M.R. Koblischka, T.H. Johansen, M. Baziljevich, and M. Murakami, SQUID and magneto-optic investigations of flux turbulence in the critical state, *J. Supercond.: Incorp. Novel Magn.*15(2), 153–157 (2002).
6. R.B. Dinner, M.R. Beasley, and K.A. Moler, Cryogenic scanning Hall-probe microscope with centimeter scan range and submicron resolution, *Rev. Sci. Instr.* 76, 103702 (2005).

7. A. Sandhu, H. Masuda, A. Oral, S.J. Bending, Room temperature magnetic imaging of magnetic storage media and garnet epilayers in the presence of external magnetic fields using a sub-micron GaAs SHPM, *J. Crystal Growth* 227–228, 899–905 (2001).
8. R.J. Prance, T.D. Clark, H. Prance, and G. Howells, Imaging of magnetically recorded data using a novel scanning magnetic microscope, *J. Magn. Magn. Mater.* 193, 437–440 (1984).
9. D.P. Pappas, A.V. Nazarov, D. Stevenson, S. Voran, M.E. Read, E.M. Gormley, J. Cash, K. Marr, J.J. Ryan, Second-harmonic magnetoresistive imaging to authenicate and recover data from magnetic storage media, *J. Electr. Imaging* 14(1), 013015 (2005).
10. U. Hartmann and H.H. Mende, The stray-field induced birefringence of ferrofluids applied to the study of magnetic domains, *J. Magn. Magn. Mater.* 41, 244–246 (1984).
11. G.A. Jones, E.T.M. Lacey, and I.B. Puchalska, Bitter patterns in polarized light: a probe for microfields, *J. Appl. Phys.* 53, 7870–7872 (1982).
12. J. Šimšová, R. Gemperle, and J.C. Lodder, The use of colloid-SEM method for domain observation in CoCr films, *J. Magn. Magn. Mater.* 95, 85–94 (1991).
13. P. Rice and J. Moreland, A new look at the Bitter method of magnetic imaging, *Rev. Sci. Instr.* 62, 844–845 (1991).
14. R.I. Hutchinson, P.A. Lavin, and J.R. Moon, A new technique for the study of ferromagnetic domain boundaries, *Rev. Sci. Instr.* 42, 885–886 (1965).
15. T. Sakurai and Y. Shimada, Application of the gas evaporation method to observation of magnetic domains, *Japan. Journ. Appl. Phys.* Pt.1, 31, 1905–1908 (1992).
16. A. Sugimoto, T. Yamaguchi, and I. Iguchi, Direct observation of vortex structure in a high T_c $YBa_2Cu_3O_{7-y}$ thin film by Bitter decoration method, *J. Low Temp. Phys.* 117, 1347–1351 (1999).
17. A. Bezryadin and B. Pannetier, Role of edge superconducting states in trapping of multi-quanta vortices by microholes. Application of the bitter decoration technique, *J. Low Temp. Phys.* 102, 73–94 (1996).
18. A. Szewczyk, K. Piotrowski, and R. Szymczak, A new method for the study of magnetic domains at temperatures below 35 K, *J. Phys. D: Appl. Phys.* 16, 687–696 (1983).
19. R.B. Proksch, T.E. Schaffer, B.M. Moskowitz, E.D. Dahlberg, D.A. Bazylinski, and R.B. Frankel, Magnetic force microscopy of the submicron magnetic assembly in a magnetotactic bacterium, *Appl. Phys. Let.* 66(19), 2582–2584 (1995).
20. G. Harasko, W. Pfützner, and K. Futschik, Domain analysis by means of magnetotactic bacteria, *IEEE Trans. Magn.* 31, 938–949 (1995).
21. A.S. Bahaj, P.A.B. James, and F.D. Moeschler, Continous cultivation and recovery of magnetotactic bacteria, *IEEE Trans. Magn.* 33(5), 4263–4265 (1997).
22. Y.A. Monosov, V.S. Doev, A.F. Kabytchenkov, V.V. Koledov, A.D. Piurbeev, A.A. Tulaikova, V.G. Shavrov, and V.A. Shakhunov, Recording of optical information on magnetic suspension, *IEEE Trans. Magn.* 19(3), 1474–1476 (1983).
23. V.A. Ardizzone, Viewing film for dc magnetic fields. Available at: www.magnerite.com.
24. S. Hayashi, S. Saha, and H. Hamaguchi, A new class of magnetic fluids: bmim[$FeCl_4$] and nbmim[$FeCl_4$] ionic liquids, *IEEE Trans Magn.* 42(1), 12–14 (2006).
25. D.E. Zhang, X.M. Ni, H.G. Zheng, Y. Li, X.J. Zhang, and Z.P. Yang, Synthesis of needle-like nickel nanoparticles in water-in-oil microemulsion, *Mater. Lett.* 59(16), 2011–2014 (2005).

26. C. Liu, S-H. Chung, Q. Jin, A. Sutton, F. Yan, A. Hoffmann, B.K. Kay, S.D. Bader, L. Makowski, and L. Chen, Magnetic viruses via nano-capsid templates, *J. Magn. Magn. Mater.* 302(1), 47–51 (2006).

27. B.B. Yellen and G. Friedman, Programmable assembly of colloidal particles using magnetic microwell templates, *Langmuir* 20, 2553–2559 (2005).

28. L.E. Helseth, Th.M. Fischer, and T.H. Johansen, Magnetic structuring and transport of colloids at interfaces, *J. Magn. Magn. Mater.* 277, 245–250 (2004).

29. M.R. Koblischka and R.J. Wijngaarden, Magnetooptical investigations of superconductors, *Supercond. Sci. Technol.* 8, 199–213 (1995).

30. R.W. Hansen, L.E. Helseth, A. Solovyev, E. Il'yashenko, and T.H. Johansen, Growth and characterization of (100) garnets for imaging, *J. Magn. Magn. Mater.* 272–276, 2247–2249 (2004).

31. V.J. Fratello, I. Mnushkina, S.J. Licht, and R.R. Abbott, Growth and Characterization of Magnetooptic Garnet Films with Planar Uniaxial Anisotropy, *Mater. Res. Soc. Symp. Proc.* 834, J6.2.1–J6.2.12 (2005).

32. I.M. Syvorotka, S.B. Ubizskii, M. Kuĉera, M. Kuhn, and Z. Vértesy, Growth and characterization of Bi, Pr– and Bi, Sc-substituted lutetium iron garnet films with planar magnetization for magneto-optic visualization, *J. Phys. D: Appl. Phys.* 34, 1178–1187 (2001).

33. N. Adachi, T. Yamaguchi, T. Okuda, T. Machi, N. Koshizuka, In-plane magnetic anisotropy of (111) and (100) garnet film prepared for magneto-optical indicator, *J. Magn. Magn. Mater.* 272–276, 2255–2256 (2004).

34. R.M. Grechishkin, M.Yu. Goosev, S.E. Ilyashenko, and N.S. Neustroev, High resolution sensitive magnetooptic ferrite garnet films with planar anisotropy, *J. Magn. Magn. Mater.* 157–158, 305–306 (1996).

35. T.H. Johansen, M. Baziljevich, H. Bratsberg, and Y. Galperin, Direct observation of the current distribution in thin superconducting using magneto-optic imaging, *Phys. Rev.* 54(22), 16264–16269 (1996).

36. L.E. Helseth, R.W. Hansen, E.I. Il'yashenko, M. Baziljevich, and T.H. Johansen, Faraday rotation spectra of bismuth-substituted ferrite garnet films with in-plane magnetization, *Phys. Rev. B* 64, 1744061–1744065 (2001).

37. L.E. Helseth, Model for imaging magnetic fields using a magnetooptic indicator, *J. Magn. Magn. Mater.* 247, 230–236 (2002).

38. L.E. Helseth, A.G. Solovyev, R.W. Hansen, E.I. Il'yashenko, M. Baziljevich, and T.H. Johansen, Faraday rotation and sensitivity of (100) bismuth-substituted ferrite garnet films, *Phys. Rev. B.* 66, 0644051– 0644055 (2002).

39. F. Hansteen, L.E. Helseth, T.H. Johansen, O. Hunderi, A. Kirilyuk, T. Rasing, Optical and magnetooptical properties of bismuth and gallium substituted iron garnet films, *Thin Solid Films* 455–456, 429–432 (2004).

40. C. Jooss, J. Albrecht, H. Kuhn, S. Leonhardt, H. Kronmüller, Magneto-optical studies of current distributions in high-T_c superconductors, *Rep. Prog. Phys.* 65, 651–788 (2002).

41. A.H. Bobeck, E. Della Torre, *Magnetic Bubbles*. Amsterdam, North Holland Publishing (1975).

42. A.H. Eschenfelder, *Magnetic Bubble Technology*. Berlin/Heidelberg/New York, Springer-Verlag, (1981).

43. A.P. Malozemoff and J.C. Slonczewski, *Magnetic Domain Walls in Bubble Domains*. New York, Academic Press (1979).
44. C. Kooy and U. Enz, Experimental and theoretical study of the domain configuration on thin layers of $BaFe_{12}O_{19}$, *Philips Res. Repts* 15, 7–29 (1960).
45. J. Cho, M. Gomi, and M. Abe, Bi-substituted iron garnet films with fine grains prepared by pyrolysis, *J. Appl. Phys.* 70(10), 6301–6303.
46. M. Gomi, T. Tanida, and M. Abe, RF sputtering of highly Bi-substituted garnet films on glass substrates for MO memory, *J. Appl. Phys.* 57(8), 3888–3890 (1985).
47. M. Gomi, K. Satoh, and M. Abe, Improvement in optical and magnetic properties of Bi-substituted garnet sputtered films for MO recording, *J. Appl. Phys.* 63(8), 3642–3644 (1988).
48. M. Abe and M. Gomi, MO recording on garnet films, *J. Magn. Magn. Mater.* 84(3) 222–228 (1990).
49. J.-L. Rehspringer, J. Bursik, D. Niznansky, and A. Klarikova, Characterization of bismuth-doped yttrium iron garnet layers prepared by sol–gel process, *J. Magn. Magn. Mater.* 211(1–3), 291–295 (2000).
50. H. Kidoh, A. Morimoto, and T. Shimizu, Synthesis of ferromagnetic Bi-substituted yttrium iron garnet films by laser ablation, *Appl. Phys. Lett.* 59(2) 237–239 (1991).
51. M. Laulajainen, P. Paturi, J. Raittila, H. Huhtinen, A.B. Abrahamsen, N.H. Andersen, R. Laiho, $Bi_xY_{3-x}Fe_5O_{12}$ thin films prepared by laser ablation for MO imaging of superconducting thin films, *J. Magn. Magn. Mater.* 279, 218–223 (2004).
52. K. Kawano, R.A. Chakalov, G. Kong, J.S. Abell, S. Kahl, A.M. Grishin, BIG films fabricated by PLD for magnetic flux visualization of YBCO, *Physica C* 372–376, 696–699 (2002).
53. G.B. Scott and D.E. Lacklison, Magnetooptic properties and applications of bismuth substituted iron garnets, *IEEE Trans. Magn.* 12(4), 292–311 (1976).
54. W.A. Shurkliff, *Polarized Light.* Cambridge, MA, Harvard University Press (1962).
55. H. Hornauer, T.M. Atmono, and K. Röll, A Kerr magnetometer using Faraday modulation technique, *J. Magn. Magn. Mater.* 83, 551–552 (1990).
56. H. Rohrmann and H. Hoffman, High-resolution Kerr observation of magnetic domains, *Thin Solid Films* 175, 273–279 (1989).
57. P.E. Goa, H. Hauglin, Å.A.F. Olsen, M. Baziljevich, and T.H. Johansen, Magneto-optical setup for single vortex observation, *Rev. Sci. Instrum.* 74(1), 141–146 (2003).
58. R.J. Wijngaarden, K. Heeck, M. Welling, R. Limburg, M. Pannetier, K. Van Zetten, V.L.G. Roorda, and A.R. Voorwinden, *Rev. Sci. Instr.* 72(6), 2661–2664 (2001).
59. K. Wakabayashi, T. Numata, and S. Inokuchi, Garnet film rotator applied in polarizing microscope for domain image modulation, *J. Appl. Phys.* 69(8), 5334 (1991).
60. P. Paturi, B.H. Larsen, B.A. Jacobsen, and N.H. Andersen, Image correction in magneto-optical microscopy, *Rev. Sci. Instr.* 74(6), 2999–3001 (2003).
61. F.B. Hagedorn, Instability of an isolated straight magnetic domain wall, *J. Appl. Phys.* 41(3), 1161–1162 (1970).
62. P. Molho, J.L. Porteseil, Y. Souche, J. Gouzerh, and J.C.S. Levy, Irreversible evolution in the topology of magnetic domains (invited), *J. Appl. Phys.* 61(8), 4188–4193 (1988).
63. P. Molho, J.L. Porteseil, and Y. Souche, Period competition in a stripe domain structure subjected to a periodic field, *J. Appl. Phys.* 63(8), 4327–4329 (1988).

64. S. Takahashi, S. Sawada, and N. Toyama, Application of R-Co permanent magnets to quartz analog watches, *Proceedings of the 3rd International Workshop on RE PM and their Applications*, Dayton (1978), pp. 404–405.

65. Z. Z. Bandić, H. Xu, and T. R. Albrecht, Magnetic lithography using a flexible master: A method for instantaneous magnetic recording on media surfaces with flatness imperfections, *Appl. Phys. Lett.* 82(1), 145–147 (2003).

66. D. Rugar, C.-J. Lin, and R. Geiss, Submicron domains for high density magneto-optic data storage, *IEEE Trans. Magn.* 23(5), 2263–2265 (1987).

67. T.K. Hatwar, High reliability magneto-optic media, *J. Appl. Phys.* 70(10) 6335–6337 (1991).

68. P. Rice, S.E. Russek, J. Hoinville, and M.H. Kelley, Optimizing the NIST magnetic imaging reference sample, *IEEE Trans. Magn.* 33(5), 4065–4067 (1997).

69. A.N. Egorov and S.V. Lebedev, Magneto-optical observation of surface currents in microelectronic circuits, *J. Appl. Phys.* 87(9), 5362–5364 (2000).

70. J. Pinassaud, P.-I. Joubert, and M. Lemistre, Quantitative magneto-optical imager for nondestructive evaluation, *Proc. SPIE,* 5768, 196–203 (2005).

71. U. Radtke, R. Zielke, H.-G. Rademacher, H.-A. Crostack, and R. Hergt, Application of magneto-optical method for real-time visualization of eddy currents with high spatial resolution for nondestructive testing, *Opt. Lasers Engng* 36, 251–268 (2001).

72. Yu. Kabanov, A. Zhukov, V. Zhukova, and J. Gonzalez, Magnetic domain structure of wires studied by using the magneto-optical indicator film method, *Appl. Phys. Lett.* 87, 142507 (2005).

73. V.I. Nikitenko, L.M. Dedukh, V.S. Gornakov, Yu.P. Kabanov, L.H. Bennett, M.J. Donahue, L.J. Swartzendruber, A.J. Shapiro, and H.J. Brown, Spin reorientation transitions and domain structure in magnetic multilayers, *IEEE Trans. Magn.* 33(5), 3661–3663 (1997).

74. I. Takeuchi, O.O. Famodu, J.C. Read, M.A. Aronova, K.-S. Chang, C. Craciunescu, S.E. Lofland, M. Wuttig, F.C. Wellstood, L. Knauss, and A. Orozco, Identification of novel compositions of ferromagnetic shape-memory alloys using compositional spreads, *Nature Mater.* 2, 180–184 (2003).

75. M.J. Turchinskaya, L.A Bendersky, A.J. Shapiro, K.S. Chang, I. Takeuchi, and A.L. Roytburd, Rapid constructing magnetic phase diagrams by magneto-optical imaging of composition spread films, *J. Mater. Sci.* 19(9), 2546–2548 (2004).

76. R.P. Cowburn, D.I. Koltsov, A.O. Adeyeye, and M.E. Welland, Sensing magnetic fields using superparamagnetic nanomagnets, *J. Appl. Phys.* 87(9), 7082–7084 (2000).

77. P. Herget, B. Knight, J.A. Bain, T.E. Schlesinger, and H. Awano, Magnetically defined domain isolation for studies of nucleation and growth coercivities, *IEEE Trans. Magn.* 41(10), 3763–3765 (2005).

ENERGY EXCHANGES OF MAGNETS WITH THE ENVIRONMENT

GIOVANNI ASTI
Dipartimento di Fisica dell'Università di Parma, V.le G.P. Usberti 7, Campus Universitario, 43100 Parma, Italy

Abstract. Magnetic bodies are often employed in modern electromechanical devices as sensors and actuators. Consequently they are subjected to exchange of electromagnetic, mechanical, and thermal energy with the surroundings in a variety of working conditions. Their functioning are here examined by a thermodynamic treatment with the aim of obtaining relations of general validity in the presence of nonuniform magnetic fields. Applications to problems concerning torque magnetometers are presented and discussed in detail.

Keywords: Electromechanical device; magnetic MEMS; free energy; enthalpy; magnetic polarization; magnetic susceptibility; hysteresis

1. Introduction

Energy exchanges of a magnetic body with the surroundings can be of various natures. In what follows we will focus our attention on those exchanges that are typical of a solid ferromagnetic body in a technical device such as a sensor, a transducer, an actuator, or a measuring instrument, i.e. exchanges of electromagnetic, mechanical, and thermal energy. The involved phenomena depend essentially on the physical properties of the material of the body and on its specific working conditions within the device, such as shape of the body, homogeneity of the material, temperature, pressure, support appliances, and so on. The requirement of having optimum performances and the nature itself of a device most often impose working conditions far from idealized situations of simplicity, homogeneity, simple shape, isolation from perturbing actions. The opposite occurs in the case of a measuring or characterization apparatus, where the body is in fact the sample under observation: it should be in the best idealized conditions, so as to reduce at minimum complications due to extrinsic characteristics of the experimental arrangement. However, even in this case one cannot neglect the role of the environmental conditions because they basically dictate the limits of precision and sensitivity of the equipment, which are at the basis of its quality features.

For these reasons the theoretical treatment of the interaction of the magnetic body with external actions should in principle take account of all relevant complications, in particular, the fact that the magnetic fields can be in general very far

B. Azzerboni et al. (eds.), Magnetic Nanostructures in Modern Technology, 225–236.

from uniformity. This is especially important in the design phase and in that of experimental analysis. Despite this, it is obvious that we remain strongly bonded to the necessity to implement the most appropriate approximations, as the best compromise between conflicting demands of which the validity can be mostly evaluated a posteriori.

2. Basic principles

In order to deduce the appropriate equations regarding a magnetic sample in a measuring instrument or a body in an electromechanical device, let us consider the sample/body itself as a physical system exchanging energy with the environment, under the action of a magnetic field. We will neglect changes in size and volume of the body, which could be important for magnetostrictive materials.[6] There are two possible formulations of the problem depending on the way we define the physical system. If we include in it the magnetostatic energy of the magnetic field $\overline{H}_s$ produced by the body itself, then the intensive variable is the external magnetic field $\overline{H}_e$ (extrinsic representation). Instead, if we exclude the magnetostatic energy the relevant magnetic field is the (internal) magnetic field $\overline{H} = \overline{H}_e + \overline{H}_s$ (intrinsic representation).

2.1. EXTRINSIC REPRESENTATION

We have from the first principle of thermodynamics

$$\delta W_{el} + \delta W_m + dU = \delta Q \tag{1}$$

where the first term on the left is the elementary electric work done by the sample on the generators that feed the field coils, the second is the elementary mechanical work done by the sample on the suspension system and mechanical fixtures of the instrument, the third is the infinitesimal increment of body internal energy U, including the magnetostatic energy stored in the magnetic field $\overline{H}_s$ created by it, and δQ is the heat absorbed by the sample in the time dt. The first term is given by the volume integral[1]

$$\delta W_{el} = dt \int \bar{J} \cdot \overline{E}_s dv = dt \int (\nabla \times \overline{H}_e) \cdot \overline{E}_s dv \tag{2}$$

[1] Hereafter the volume integrations are intended in the whole space if not differently specified. Moreover, we are considering in the present context only "slow" processes, that means that we are in the limits of the so-called "slowly varying electromagnetic fields," neglecting displacement currents contributions. Sometimes this condition is more properly described in terms of working frequency range, by saying that the corresponding electromagnetic wavelength is by far larger then the size of the system itself.

where $\overline{E}_s$ is the part of induced electric field generated by the sample alone and $\overline{J}$ is the electric current density in the field coils. The expression can be transformed giving

$$\delta W_{el} = -\int \overline{H}_e \cdot d\overline{B}_s dv = -\int \overline{H}_e \cdot d\bar{I} dv \tag{3}$$

where $\overline{B}_s$ is the magnetic induction generated by the body and $\bar{I} = \mu_0 \overline{M}$ represents its magnetic polarization. Then Eq. (1) becomes

$$-\int \overline{H}_e \cdot d\bar{I} dv + \delta W_m + dU = \delta Q \tag{4}$$

Here U is the sample internal energy including the magnetic dipolar energy

$$U_s = \int \frac{1}{2} \mu_0 H_s^2 dv$$

(here is why we refer to this condition as the extrinsic representation) of its magnetic field $\overline{H}_s$ (the field produced by the free poles of the body: inside it the field is almost opposite to $\bar{I}$ and often called "demagnetizing field"). Note that we have made no limitation on the size and shape of the body. Then the equations are valid in general in the presence of a nonhomogeneous external field. Consequently, $\overline{H}$, $\overline{H}_s$, and $\bar{I}$ are in general nonhomogeneous fields.

2.2. INTRINSIC REPRESENTATION

It is also possible to utilize another system representation that eliminates the dependence on the sample shape. This means that we consider only the intrinsic energy of the sample $U' = U - U_s$, thus excluding the dipolar energy. For this purpose it is easy to decompose the first term in Eq. (4) by expressing the external field $\overline{H}_e$ in terms of the magnetic field $\overline{H}$ and the dipolar field $\overline{H}_s$:

$$\overline{H}_e = \overline{H} - \overline{H}_s \tag{5}$$

Hence Eq. (3) becomes

$$\delta W_{el} = -\int \overline{H} \cdot d\bar{I} dv + \int \overline{H}_s \cdot d\bar{I} dv \tag{6}$$

The second term of the right hand side turns out to be equal to $-dU_s$ that is the differential of the opposite of the dipolar energy of the sample. Then Eq. (4) becomes

$$-\int \overline{H} \cdot d\bar{I} dv + \delta W_m + dU' = \delta Q \tag{7}$$

2.3. THE MECHANICAL ACTIONS ON MAGNETIC BODIES

Depending on the particular problem to be considered the appropriate representation can be the first (extrinsic representation) or the second one (intrinsic representation). For example, if we are interested in calculating the force and torque on a magnetic body under the action of a constant external field $\overline{H}_{\mathrm{e}}$, it is convenient to adopt the extrinsic representation and so to start from Eq. (4). This is in fact the most common situation dealing with ferromagnetic materials, especially in open circuit configuration, because the external field $\overline{H}_{\mathrm{e}}$, and not the magnetic field $\overline{H}$, is the one we can directly control.

2.3.1. *The equilibrium magnetic state*

Within the extrinsic representation we introduce here the free enthalpy (Gibbs free energy)

$$G = F - \int \overline{H}_{\mathrm{e}} \cdot \bar{I} dv = U - TS - \int \overline{H}_{\mathrm{e}} \cdot \bar{I} dv, \tag{8}$$

where F is the free energy (Helmholtz free energy), T is the temperature, and S is the entropy. In general the transformations that the system undergoes include a displacement of the body. This fact implies that, to be rigorous, in the integrals of Eqs. (3), (4), and (8), we should take into account the fact that the volume of the body, V_1, relative to the initial state, and the volume V_2, relative to the final state, are different. We are considering here an infinitesimal transformation and we can separate the overall integration volume $V* = V_1 \cup V_2$ in three parts: $V^+ = V_1 \cap V_2$, $dV_1 = V_1 \backslash V^+$, $dV_2 = V_2 \backslash V^+$. The differential of

$$G = F - \int \overline{H}_{\mathrm{e}} \cdot \bar{I} dv$$

gives

$$dG = dU - TdS - SdT - \left(\int_{V_2} \overline{H}_{\mathrm{e}} \cdot \bar{I} dv - \int_{V_1} \overline{H}_{\mathrm{e}} \cdot \bar{I} dv \right) \tag{9}$$

From the second principle of thermodynamics we have $\delta Q \leq TdS$, the equality being valid for reversible transformations. Substituting $\delta Q = TdS$ from Eq. (4) we obtain

$$dG + SdT + \delta W_{\mathrm{m}} + \int \bar{I} \cdot d\overline{H}_{\mathrm{e}} dv = 0 \tag{10}$$

Correspondingly, for the free energy, using the same *modus operandi*, we obtain

$$dF + SdT + \delta W_m - \int \overline{H}_e \cdot d\bar{I} dv = 0 \tag{10'}$$

In the particular and important case of a homogeneous system with uniform $\bar{I}$, $\overline{H}_e$, and $\overline{H}$, the integrals are substituted with the product by the sample volume V: for instance in the case of ellipsoidal ferromagnet in a uniform $\overline{H}_e$.We can determine the equilibrium polarization vector $\bar{I}$ of a homogeneous system having volume V by writing

$$\frac{1}{V}\frac{\partial G}{\partial \bar{I}} = \frac{\partial g}{\partial \bar{I}} = 0 \tag{11}$$

being g the enthalpy density. These are three scalar equations that allow in principle to obtain[2] $\bar{I}$ as a function of $\overline{H}_e$. For the field and the magnetic polarization we obtain from Eqs (10) and (10') the following expressions:

$$\overline{H}_e = \frac{1}{V}\frac{\partial F}{\partial \bar{I}} \quad \text{and} \quad \bar{I} = -\frac{1}{V}\frac{\partial G}{\partial \overline{H}_e} \tag{12}$$

In the general case $\bar{I}$ is nonuniform so that G includes the exchange energy. Then minimization of G is a variational problem and is achieved through the functional derivative

$$\frac{\delta g}{\delta \bar{I}} = 0 \tag{11'}$$

Note that this functional derivative has the dimension of a magnetic field. In fact in the micromagnetic theory the assumption is made that the magnetization vector has constant modulus M_s. Then the equilibrium condition leads to the Brown equation that merely expresses the fact that the effective field, which is given by

$$\overline{H}_{eff} = \frac{\delta g}{\delta \bar{I}}$$

should be parallel to $\overline{M}_s = \bar{I}_s/\mu_0$. In the present case Eq. (11′) is more general and includes the para-processes. This means that M_s depends on the temperature and the intensity of the effective magnetic field. If the temperature perturbing effect is considered to be equivalent to a counteracting "thermal" magnetic field we can describe Eq. (11′) as the equilibrium condition in terms of a vanishing "total" effective field, including this "thermal" component.

2.3.2. *The mechanical equations*

Even in the general case of a macroscopic body we can always define orientation and position in space of the body through an orientation vector angle $\bar{\vartheta}_0$ and a displacement vector $\bar{r}_0$ denoting the position of a certain point P_0 of the laboratory,

[2] It has to be noted that the expression $\partial G/\partial \bar{I}$ and those of $\bar{f}$ and $\bar{\tau}$ (Eq. (14)) have the meaning of gradients of the scalar function G with respect to variables I_x, I_y, I_z, ϑ_x, ϑ_y,, ϑ_z, and x, y, z, respectively.

with respect to a reference frame fixed with the body. Then the mechanical work can be expressed in terms of the torque $\bar{\tau}$ and force $\bar{f}$ of the magnetic body on the suspension system

$$\delta W_{\mathrm{m}} = \bar{\tau} \cdot d\bar{\vartheta} + \bar{f} \cdot d\bar{r} \tag{13}$$

where $-d\bar{\vartheta}$ and $-d\bar{r}$ are the body infinitesimal rotation and displacement vectors, respectively. Hence the expressions of $\bar{\tau}$ and $\bar{f}$, at constant T and $\overline{H}_{\mathrm{e}}$ turn out to be:

$$\bar{\tau} = -\frac{\partial G}{\partial \bar{\vartheta}}; \qquad \bar{f} = -\frac{\partial G}{\partial \bar{r}} \tag{14}$$

G is a functional given by

$$G = \int g\left[\bar{I}(\bar{\rho}), \nabla\bar{I}, \overline{H}_{\mathrm{e}}(\bar{\rho}), T\right]\ d^3\rho \tag{15}$$

where the enthalpy density g is a known function of $\bar{I}$ and its gradient $\nabla\bar{I}$ (exchange energy), $\overline{H}_{\mathrm{e}}$ and T. Vector $\bar{\rho}$ represents the position of the generic point P in a reference frame fixed with the body and centered at the central point P_0. Then, if we change $\bar{\vartheta}_0$, G changes because $\overline{H}_{\mathrm{e}}$ is rotated with respect to the body. In the case of a nonhomogeneous $\overline{H}_{\mathrm{e}}$, its intensity and orientation is further modified by a change in $\bar{r}_0$. So we can say that in general G is a functional of $\overline{H}_{\mathrm{e}}(\bar{\rho})$, which is also an explicit function of $\bar{\vartheta}_0$ and $\bar{r}_0$. On the other hand, at equilibrium $\bar{I}$ is an implicit function of $\bar{\vartheta}_0$ and $\bar{r}_0$ through Eq. (11′), that plays the role of a state equation for the magnetic system thus allowing in principle to deduce how $\bar{I}$ is changed when $\bar{\vartheta}_0$ and $\bar{r}_0$ vary. Hence we can write

$$G = G\left[\bar{I}(\bar{\rho}), \nabla\bar{I}, \overline{H}_{e}(\bar{\rho}; \bar{\vartheta}_0, \bar{r}_0), T\right] \tag{15′}$$

Actually G is multivalued function of $\overline{H}_{\mathrm{e}}$, due to hysteresis. However, we imagine here to perform a small reversible excursion around a point on a particular branch of the hysteresis loop. The differential of G around point $\bar{\vartheta}_0$ and $\bar{r}_0$, at constant temperature turns out to be

$$\begin{aligned} dG &= \int d^3\rho \left[\frac{\partial g}{\partial \overline{H}_{\mathrm{e}}} \cdot \left(\frac{\partial \overline{H}_{\mathrm{e}}}{\partial \bar{\vartheta}} \cdot d\bar{\vartheta} + \frac{\partial \overline{H}_{\mathrm{e}}}{\partial \bar{r}} \cdot d\bar{r}\right) + \frac{\delta G}{\delta \bar{I}} \cdot d\bar{I}\right] = \\ &= \int d^3\rho \left[\frac{\partial g}{\partial \overline{H}_{\mathrm{e}}} \cdot \left(\frac{\partial \overline{H}_{\mathrm{e}}}{\partial \bar{\vartheta}} \cdot d\bar{\vartheta} + \frac{\partial \overline{H}_{\mathrm{e}}}{\partial \bar{r}} \cdot d\bar{r}\right)\right] \end{aligned} \tag{16}$$

The last term vanishes because of Eq. (11′). Finally, recalling the second of Eq. (12) and utilizing Eq. (14) we obtain

$$\bar{\tau} = \int \bar{I} \cdot \frac{\partial \overline{H}_{\mathrm{e}}}{\partial \bar{\vartheta}} d^3\rho; \qquad \bar{f} = \int \bar{I} \cdot \frac{\partial \overline{H}_{\mathrm{e}}}{\partial \bar{r}} d^3\rho \tag{17}$$

3. Examples

3.1. TORQUE MAGNETOMETER

Let us consider as first example the classic torque magnetometer (Fig. 1). A sample in the form of a disk is suspended horizontally through its center by a thin torque wire (z-axis). An external horizontal magnetic field is applied along y-axis in the plane of the disk. There is a uniaxial anisotropy energy density $e_{\mathrm{k}} = K \sin^2 \varphi$, where φ is the angle between $\bar{I}$ and the easy magnetization axis c and K is the anisotropy constant supposed positive. The c-axis is in the plane of the disk and ϑ is the angle of the external field $\overline{H}_{\mathrm{e}}$ with respect to it. The magnetic field is supposed to have such an intensity to cancel magnetic domains. In these conditions the disk is considered to have a uniform magnetic polarization $\bar{I}$ and we can neglect the dipolar magnetic energy because it is indifferent to the angle φ and small in any case for thin disks. e_k is intended as the gain in potential energy of the unit volume of the sample when $\bar{I}$ is rotated from the easy direction (φ = 0) to a generic angle φ, at constant temperature. Then e_k is the Helmholtz free energy density $F/V = K \sin^2 \varphi$. Hence we have

$$G/V = F/V - \overline{H}_{\mathrm{e}} \cdot \bar{I} = K \sin^2 \varphi - H_e I \cos(\theta - \varphi) \tag{18}$$

and

$$d\overline{H}_{\mathrm{e}} \cdot \bar{I} + \delta W_{\mathrm{m}} + \frac{dG}{V} = 0 \tag{19}$$

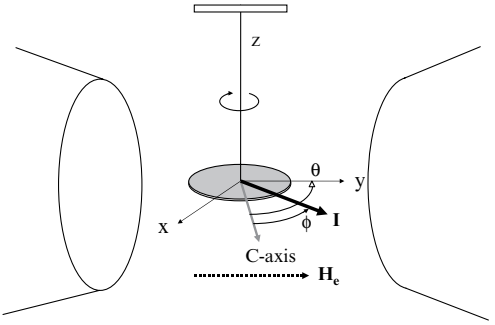

Figure 1. Schematic view of a torque magnetometer. The sample, in the form of an horizontal disk, is suspended by a thin torsion fiber. A horizontal external field is applied to the sample. At equilibrium, the active torque generated by the interaction of the field with the magnetic polarization of the sample is counterbalanced by the elastic torsion of the fiber.

The condition that the system is at thermodynamic equilibrium, once $\overline{H}_{\mathrm{e}}$ and ϑ are fixed, is given by

$$\partial G/\partial\varphi = 0 \tag{20}$$

an equation that allows to determine function $\varphi = \varphi(H_{\mathrm{e}}, \vartheta)$. The torque is given by

$$\tau = -dG/d\vartheta = -\left[\partial G/\partial\vartheta + (\partial G/\partial\varphi)(\partial\varphi/\partial\vartheta)\right] = -\partial G/\partial\vartheta \tag{21}$$

So that τ can be directly calculated from the partial derivative. In the obtained expression we should then substitute the expression of $\varphi = \varphi(H_{\mathrm{e}}, \vartheta)$. In the present case

$$\tau = -V H_{\mathrm{e}} I \sin(\vartheta - \varphi) = -V \left|\bar{I} \times \overline{H}_{\mathrm{e}}\right| \tag{22}$$

Remember here that τ is the torque that the sample exerts on the generator of the field $\overline{H}_{\mathrm{e}}$: that is why there is a minus sign on the right hand expression. We shall now utilize the present example for verification of some of the general expressions previously obtained.

Let us start with the second of Eq. 12. We consider the c-axis as the polar axis of a spherical coordinate system in which $\overline{H}_{\mathrm{e}}$ acts as radius vector and ϑ as colatitude angle. The gradient

$$\bar{I} = -\nabla_{\overline{H}_e} G/V \tag{23}$$

is calculated through the partial derivatives

$$\begin{aligned} I_{H_{\mathrm{e}}} &= -\partial G/V\partial H_{\mathrm{e}} = I\cos(\vartheta - \varphi), \\ I_{\vartheta} &= -\partial G/V H_{\mathrm{e}}\partial\vartheta = -I\sin(\vartheta - \varphi) \end{aligned} \tag{24}$$

The minus sign in the second expression is due to the fact that $\widehat{\vartheta}$ is opposite to x-axis orientation. The relation with the Cartesian reference frame gives $I_{H_{\mathrm{e}}} = I_y$; $I_{\vartheta} = -I_x$. Let us now utilize the general expression (16):

$$dG/V = \frac{\partial G}{V\partial\overline{H}_{\mathrm{e}}} \cdot \left(\frac{\partial\overline{H}_e}{\partial\bar{\vartheta}}.d\bar{\vartheta}\right) = -\bar{I}\cdot\left(\frac{\partial\overline{H}_{\mathrm{e}}}{\partial\bar{\vartheta}}.d\bar{\vartheta}\right) \tag{25}$$

which can be written in the formalism of the ∇ operator as

$$dG/V = \frac{\partial G}{V\partial\overline{H}_{\mathrm{e}}} \cdot \left[\left(d\bar{\vartheta}\cdot\nabla_{\bar{\vartheta}}\right)\overline{H}_{\mathrm{e}}\right] = -\bar{I}\cdot\left[\left(d\bar{\vartheta}\cdot\nabla_{\bar{\vartheta}}\right)\overline{H}_{\mathrm{e}}\right] \tag{26}$$

or

$$dG/V = \frac{\partial G}{V\partial He_k}\cdot\left(d\vartheta_i\frac{\partial He_k}{\partial\vartheta_i}\right) = -I_k\cdot\left(d\vartheta_i\frac{\partial He_k}{\partial\vartheta_i}\right). \tag{26'}$$

The torque is given by

$$\bar{\tau} = -\frac{\partial G}{\partial\bar{\vartheta}} = -\frac{\partial G}{\partial\overline{H}_{\mathrm{e}}}\cdot\frac{\partial\overline{H}_{\mathrm{e}}}{\partial\bar{\vartheta}} = V\bar{I}\cdot\frac{\partial\overline{H}_{\mathrm{e}}}{\partial\bar{\vartheta}} \tag{27}$$

or

$$\tau_i = -\frac{\partial G}{\partial \vartheta_i} = -\frac{\partial G}{\partial He_k}\frac{\partial He_k}{\partial \vartheta_i} = VI_k\frac{\partial He_k}{\partial \vartheta_i} \tag{27'}$$

At this point it is of interest to clarify the meaning of $\partial \overline{H}_e / \partial \bar{\vartheta} (\equiv \partial He_k / \partial \vartheta_i)$. If we consider the space of vector $\bar{\vartheta}$, taken as the radius vector of a reference frame ϑ_x, ϑ_y, ϑ_z, we intend $\bar{\vartheta}$ as a rotation vector through which we rotate $\overline{H}_e$ by the angle ϑ around axis $\bar{\vartheta}$. This is equivalent to say that $\overline{H}_e$ is a vector function in the space of vector $\bar{\vartheta}$. We are interested in the differential of this vector function

$$d\overline{H}_e = d\bar{\vartheta} \times \overline{H}_e \tag{28}$$

Now let us consider the following three vectors corresponding to each component of $d\bar{\vartheta}$:

$$d\overline{H}e_i = d\vartheta_i \hat{u}_i \times \overline{H}_e \tag{29}$$

(with $\hat{u}_i \equiv \hat{i}, \hat{j}, \hat{k}$ for $i = 1, 2, 3$). They represent by definition the tensor-derivative of vector $\overline{H}_e$, in the $\bar{\vartheta}$ space, multiplied by $d\vartheta_i$. Then Eq. (27′) becomes

$$\tau_i = VI_k\frac{\partial He_k}{\partial \vartheta_i} = VI_k \cdot (\hat{u}_i \times \overline{H}_e)_k \tag{30}$$

$$\bar{\tau} = \sum_i V\left[\bar{I} \cdot (\hat{u}_i \times \overline{H}_e)\right]\hat{u}_i = \sum_i V\left[(\overline{H}_e \times \bar{I}) \cdot \hat{u}_i\right]\hat{u}_i = V\overline{H}_e \times \bar{I} \tag{31}$$

As expected we confirm Eq. (22). The above calculation can be performed also using the tensor calculus in the space $\vartheta_i (\equiv \bar{\vartheta})$:

$$d\overline{H}_e = d\bar{\vartheta} \times \overline{H}_e \Rightarrow dHe_r = d\vartheta_s \overline{H}e_t \varepsilon_{rst} \tag{32}$$

The tensor-derivative of vector $\overline{H}_e$ is

$$\frac{\partial He_k}{\partial \vartheta_i} = He_{k/i} = (\hat{u}_i \times \overline{H}_e)_k = u_{ij}He_s\varepsilon_{kjs} \tag{33}$$

Then we can calculate the torque

$$\tau_i = VI_kHe_{k/i} = VI_k\varepsilon_{kjs}u_{ij}He_s \tag{34}$$

and noting that $u_{ij} = \delta_{ij}$ (Kronecker symbol), one gets

$$\tau_i = VI_kHe_s\varepsilon_{kis} = -VI_kHe_s\varepsilon_{iks} (\equiv -V\bar{I} \times \overline{H}_e) \tag{35}$$

3.2. CALCULATION OF THE TORQUE ON A DIAMAGNETIC (OR PARAMAGNETIC) SUBSTRATE

We want to calculate the torque on a typical substrate of a thin film having the form of a square platelet having size $a = b > c$ (Fig. 2). The assumption is made that the platelet is simulated by an ellipsoid having semi-axes proportional to a, b, c, which are parallel to axes x, y, z, respectively. The vertical axis y, is the axis of rotation of the suspension system of the instrument. Then the platelet is free to rotate around y-axis while the external magnetic field $\overline{H}_e$ lies in the xz plane at an angle $\bar{\vartheta}$ with respect to x-axis. Then $\bar{I}$ also lies in the xz plane and form with the a-axis an angle φ. We have from Eq. (10') at constant temperature and $\delta W_m = 0$

$$dF/V = \overline{H}_e \cdot d\bar{I} \tag{36}$$

For a linear material (para- or diamagnetic) $\bar{I} = \mu_0 \overleftrightarrow{\chi}^a \cdot \overline{H}_e$ (or $I_i = \mu_0 \chi^a{}_{ik} He_k$), where $\overleftrightarrow{\chi}^a$ is the apparent susceptibility, a symmetric tensor (see Appendix). Then[3]

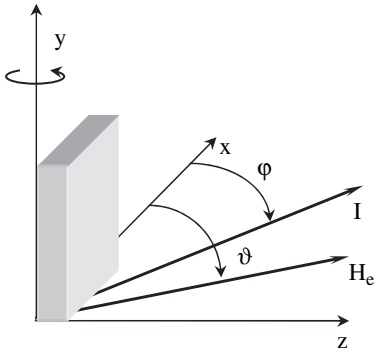

Figure 2. Typical dia- or paramagnetic substrate, utilized for thin film deposition, having the form of a square platelet. It is shown here suspended as an uncovered sample in a torque magnetometer (see Fig. 1), in order to measure its contribution to the torque, under the action of an external field. The torque on the substrate is only due to its shape anisotropy which is reflected in the anisotropy of its apparent susceptibility. In the calculation it is assimilated to an ellipsoid having semi-axes proportional to its dimensions.

[3] This is the integral of vector field $\bar{I}$ in the space $\overline{H}_e$. It is evident that $\bar{I}$ is an irrotational field because $\partial I_k / \partial He_i = \chi a_{ki}$; $\partial I_i / \partial He_k = \chi^a{}_{ik}$. Therefore the integral does not depend on the path. We can take as a path the straight line from the origin $\overline{H}_e = 0$ to the point $\overline{H}_e$: if we denote by $H'e_k = \eta He_k$ the integration variables, with $0 \leq \eta \leq 1$, then we have

$$\int_0^1 \eta He_i \mu_0 \chi^a{}_{ik} He_k d\eta = \frac{1}{2} \mu_0 \chi^a{}_{ik} He_i He_k$$

$$F/V = \int \overline{H}_{\mathrm{e}} \cdot d\bar{I} = \int \overline{H}_{\mathrm{e}} \cdot \mu_0 \overleftrightarrow{\chi}^a d\overline{H}_{\mathrm{e}} \tag{37}$$

$$F/V = \int He_i \mu_0 \chi^a{}_{ik} dHe_k = \frac{1}{2}\mu_0 \chi^a{}_{ik} He_i He_k = \frac{1}{2} He_i I_i = \frac{1}{2}\overline{H}_{\mathrm{e}} \cdot \bar{I}$$

Hence function G turns out to be

$$\frac{G}{V} = \frac{F}{V} - \overline{H}_{\mathrm{e}} \cdot \bar{I} = -\frac{1}{2}\overline{H}_{\mathrm{e}} \cdot \bar{I} \tag{38}$$

or

$$G/V = -\frac{1}{2} He_k I_k = -\frac{1}{2} He_k \mu_0 \chi^a{}_{ki} He_i$$

and $\chi^a{}_{ik} = {}^{-1}(\delta_{ij} + \chi_{il} N_{lj})\chi_{jk}$.

Let us consider for simplicity the case of an isotropic susceptibility $\chi_{ik} = \chi$. The diagonal components of $\overleftrightarrow{N}$ are $N_{xx} = N_a = N_{yy} = N_b$ and $N_{zz} = N_c = 1 - N_a - N_b = 1 - 2N_a$.

Then $a_{kr} = \delta_{kr} + \chi N_{kr}$; $\chi^a{}_{ik} = {}^{-1} a_{ij}\chi_{jk} = {}^{-1} a_{ik}\chi$, so that

$${}^{-1}\overleftrightarrow{a} \equiv \begin{pmatrix} (1+\chi N_{xx})^{-1} & 0 & 0 \\ 0 & (1+\chi N_{yy})^{-1} & 0 \\ 0 & 0 & (1+\chi-2\chi N_{xx})^{-1} \end{pmatrix} \tag{39}$$

and

$$\overleftrightarrow{\chi}_a \equiv \begin{pmatrix} \chi\,(1+\chi N_a)^{-1} & 0 & 0 \\ 0 & \chi\,(1+\chi N_a)^{-1} & 0 \\ 0 & 0 & \chi\,(1+\chi-2\chi N_a)^{-1} \end{pmatrix} \tag{40}$$

Hence

$$G/V = -\frac{\mu_0}{2}\left(He_x^2 \chi^a{}_{xx} + He_z^2 \chi^a{}_{zz}\right)$$

$$G/V = -\frac{\mu_0}{2} H_e^2 \left(\frac{\chi}{1+\chi N_a}\cos^2\vartheta + \frac{\chi}{1+\chi N_c}\sin^2\vartheta\right) \tag{41}$$

Therefore the torque turns out to be

$$\tau = \mu_0 V \chi^2 H_e^2 \frac{N_a - N_c}{(1+\chi N_a)(1+\chi N_c)} \sin\vartheta\cos\vartheta \tag{42}$$

Note the dependence of τ on the square of H_{e} and of χ.

APPENDIX: APPARENT SUSCEPTIBILITY

Let us consider a homogeneous anisotropic ferromagnetic material, of which the macroscopic magnetization state vector $\overline{M} = \overline{M}_0$ corresponds to a given magnetic field vector $\overline{H}_0$ along a certain branch of the hysteresis loop (the description of the macroscopic magnetic state of the ferromagnetic body implies an average of $\overline{M}$ over a volume much larger than the dimensions of the magnetic domains but substantially smaller than the scale of the variations of $\overline{M}$. This choice provides us a vector field $\overline{M}$ which is a regular function of $\overline{H}$). Under the action of a small perturbing field $\bar{h}$, the magnetization vector $\overline{M}$ undergoes a small reversible change $\bar{m}$, so that the resultant $\overline{M} = \overline{M}_0 + \bar{m}$ is a single-valued function of $\overline{H} = \overline{H}_0 + \bar{h}$. The differential reversible susceptibility $\overleftrightarrow{\chi}$ in that particular magnetic state is given by $\bar{m} = \overleftrightarrow{\chi} \cdot \bar{h}$ or $m_i = \chi_{ik} h_k$.

Let us consider a homogeneous body having an ellipsoidal shape characterized by a demagnetizing tensor $\overleftrightarrow{N}$ or N_{ik}. The external applied field is $\overline{He} = \overline{He}_0 + \bar{h}e$ so that $\overline{H} = \overline{He} - \overleftrightarrow{N} \cdot \overline{M}$ or $\overline{H}_0 + \bar{h} = \overline{He}_0 + \bar{h}_e - \overleftrightarrow{N} \cdot \overline{M}_0 - \overleftrightarrow{N} \cdot \bar{m}$.

On the other hand, since $\overline{H}_0 = \overline{He}_0 - \overleftrightarrow{N} \cdot \overline{M}_0$, we have $\bar{h} = \bar{h}_e - \overleftrightarrow{N} \cdot \bar{m}$ or $h_k = he_k - N_{kj} m_j = he_k - N_{kj} \chi_{ji} h_i$. It also follows that $m_i = \chi_{ik} he_k - \chi_{ik} N_{kj} m_j$ and $\left(\delta_{ij} + \chi_{ik} N_{kj}\right) m_j = \chi_{ik} he_k$. Let $a_{ij} = \delta_{ij} + \chi_{ik} N_{kj}$. Now we multiply the last equation on the left by the inverse ${}^{-1}a_{li}$, obtaining

$$ {}^{-1}a_{li} a_{ij} m_j = {}^{-1}a_{li} \chi_{ik} he_k; \; m_l = \chi^a{}_{lk} he_k, $$

where $\chi^a{}_{lk}$ is the apparent susceptibility $\chi^a{}_{lk} = {}^{-1}a_{li} \chi_{ik}$. The susceptibility χ_{ik} is a symmetric tensor because it is a second derivative: χ_{ik} is given by $\partial M_i / \partial H_k$ and $M_i = -\partial G / \partial H_k$. We can see that $\chi^a{}_{lk}$ is also symmetric. In fact it can be transformed on the basis of the symmetry of χ_{ik} and N_{ik}:

$$ \chi^a{}_{ik} = {}^{-1}(\delta_{ij} + \chi_{il} N_{lj}) \chi_{jk} = \chi_{kj} \, {}^{-1}(\delta_{ji} + N_{jl} \chi_{li}) $$

Now we calculate the transpose of $\chi^a{}_{ik}$:

$$ (\chi^a{}_{ik})' = (\chi_{jk})' \left[{}^{-1}(\delta_{ij} + \chi_{il} N_{lj}) \right]' = \chi_{kj} \, {}^{-1}(\delta_{ji} + N_{jl} \chi_{li}) $$

References

1. Landau, L.D. and. Lifshits, E.M., *Electrodynamics of Continuous Media*, Pergamon Press, Oxford (1960)
2. Bertotti, G., *Hysteresis in Magnetism: For Physicists, Materials Scientists, and Engineers,* Academic Press, New York (1998)
3. Brown, W.F., *Magnetostatic Principles in Ferromagnetism*, Interscience, New York (1962).
4. Jackson, J.D. *Electricity and Magnetism*, Wiley, New York (1965)
5. Zijlstra, H., *Experimental Methods in Magnetism*, North Holland, Amsterdam (1967)
6. O'Handley R.C., Modern Magnetic Materials. Principles and Applications, John Wiley & Sons, inc., New York, (2000).

MAGNETIC DATA STORAGE: PAST PRESENT AND FUTURE

THOMAS THOMSON
Hitachi San José Research Center, San José, U.S.A.

LEON ABELMANN, HANS GROENLAND
Systems and Materials for Information Storage Group, MESA + Research Institute, University of Twente, Enschede, The Netherlands

Abstract. The design of media, heads, positioning systems and data detection and coding techniques for various generations of magnetic recording systems are discussed. We will start with current systems, such as longitudinal hard disc and tape. Next we will discuss the immediate future, where perpendicular recording (higher anisotropy, enhanced write fields using a soft underlayer) will address the problem of thermal stability. In the third section we will give an outlook on future developments (patterned media, thermally assisted recording, self assembled arrays of nanoparticles and probe storage).

Keywords: Magnetic data storage; hard disc; tape; probe storage; perpendicular magnetic recording; heat assited magnetic recording; self assembled arrays; patterned media; data detection; coding

1. Introduction

Magnetic recording has existed for over one century (Daniel et al., 1998), and many good review books have been written on the subject. A selection of books published during the last 10 years can be found in the reference list (Hoagland, 1998; Khizroev and Litvinov, 2005; Plumer et al., 2001; Daniel et al., 1998; Jorgensen, 1996; Mee and Daniel, 1996; Comstock, 1999). In short, the basic principle of magnetic recording is that a thin film of ferromagnetic (FM) material is locally magnetised in opposing directions (Figure 1). After removing the write field, the magnetisation persists, and information can be read back, commonly by measuring the stray field variations above the film surface. Based on this simple principle, a staggering technological effort has been achieved. For instance, in hard disc recording, a 10^7 areal density increase and 10^6 volume decrease has been achieved from the first $24''$ hard disc in 1956 Noyes and Dickinson, 2000 (IBM Type 350, Fig. 2), to the $1''$ microdrive in 2000 (Fig. 3). During the last 50 years, the volumetric storage density has increased by factor 10^{14}. There are very few technological systems which have achieved such an increase in performance, just imagine any specification of an automobile improved by a factor 10^7.

B. Azzerboni et al. (eds.), Magnetic Nanostructures in Modern Technology, 237–306.

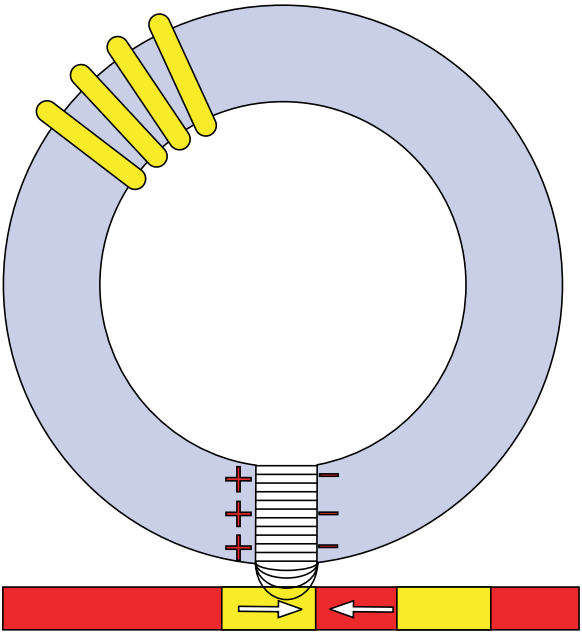

Figure 1. Principle of magnetic recording

Figure 2. IBM Type 350 hard disc, 1956 2 kbit/in^2

Figure 3. IBM microdrive, 2000 15×10^6 kBit/in^2

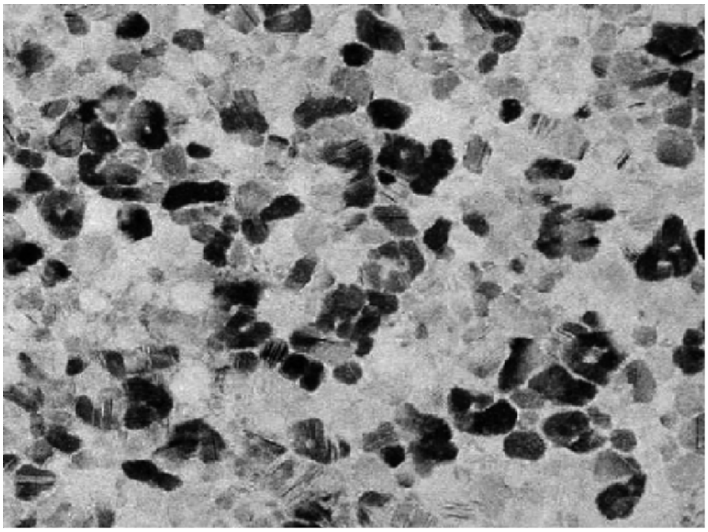

Figure 4. Granular structure of recording materials

Of course, when continuously pushing the boundaries of the design, the more difficult the progress becomes. The major issue in high-density data storage is thermal stability of the data. Hard disc and tape recording media are polycrystalline (Fig. 4). Since the grains are randomly positioned on the substrate, many grains are needed to define a single bit (Fig. 5). As the areal density increases, the grain size should decrease as well. When doing so, the energy stored in a single magnetic grain becomes comparable to the thermal energy present in the system,

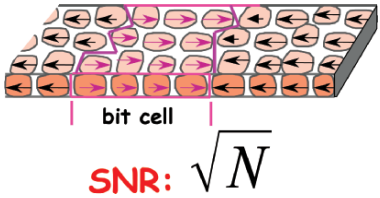

Figure 5. The SNR is determined by the number of grains in a bit

and the decay of stored information becomes unacceptable (the grains become superparamagnetic). Thermal stability, or the superparamagnetic limit, imposes a hard, fundamental limit on achievable areal density. The limit can schematically be expressed as[1]

$$\text{Density} < \frac{\Delta e t}{N 40 k T} \tag{1}$$

where Δe is the energy density in the magnetic material, t the film thickness and N the number of grains in the bit. The problem of thermal stability is addressed in three different areas simultaneously:

- Higher energy densities (Δe), thicker films (t), and lower grains size distribution in the recording medium
- Stronger write heads, either with higher magnetic fields or thermally assisted
- Fewer grains per bit (N) achieved by advanced data coding and detection techniques, and even patterned media

A second major issue in hard disc data storage is the positioning system itself. During the last decades, areal density and data rate have been increased with annual growth rate of 40%–100%. The rotation speed of the disc has however increased with only 7% per year. As a result, the hard disc drive has become relatively slower and slower every year and it is unlikely that rotation speeds will increase with more than a factor four over the years to come. New, MEMS-based, positioning techniques might prove a solution to this problem.

In this chapter, we will discuss the design of media, heads, positioning systems, and data detection and coding for various generations of magnetic recording systems. We will start with current systems such as longitudinal hard disc and tape (Section 2). Next we will discuss the immediate future, where perpendicular recording (higher anisotropy, enhanced write fields using a soft underlayer) will address the problem of thermal stability. In the third, and last section we will give an outlook on future developments.

The purpose of this chapter is not to give a detailed account of all aspects of current and future data storage but rather to provide an overview of the most

[1] A more detailed explanation can be found in Sections 2.1.1 and 4.1

significant developments as they appear to the authors. We provide an in-depth series of references which are intended to provide the reader with a resource for further investigation.

2. Longitudinal recording on hard disc and tape

All magnetic storage systems use a thin film as a medium. The shape of the film will force the magnetisation into the film plane. Therefore, it is convenient to store information by writing in-plane domains, with oppositely magnetised areas (Fig. 5). In the vast majority of systems, the magnetisation is oriented along the writing direction, and we speak about longitudinal recording as opposed to tranversal recording, which never became a commercial system (Atarashi and Shiiki, 1999; Misles et al., 1998; Desserre, 1985; Sauter et al., 1972). In this section we will discuss the different components of longitudinal recording systems, all the way from the recording medium, through heads, positioning systems, and data detection and coding.

2.1. MEDIA

Since the first magnetic recording demonstration in 1898 (Danish, 1898) commercial magnetic recording devices have relied on longitudinal recording media where the magnetisation vector lies within the plane of the medium (Weller and Doerner, 2000). As magnetic recording has evolved, two different classes of media have been developed; one based on a flexible substrate, is used in tape and floppy disc applications and a second is deposited onto either glass or Al/NiP rigid discs with current thicknesses of the order of 1 mm and diameters ranging from 27 to 95 mm. The length of this article precludes discussion on the historical development of these media, so we rather concentrate on giving a brief outline of these media as they appear today.

2.1.1. *HDD Media*

Longitudinal, rigid disc media have developed continuously since the first product was commercialised in 1956 by IBM in the form of the RAMAC data storage and retrieval system (Daniel et al., 1998; Noyes and Dickinson, 2000). However, this development is now at an end with all new media for Hard Disc Drive (HDD) applications being based on materials with perpendicular anisotropy. Current longitudinal media, based on CoCr alloys, are produced by dc sputtering and consist of a number of sequentially deposited thin metallic films together with suitable protective overcoats. Before describing the features of the individual layers it is important to have an understanding of desirable magnetic properties in a high-density granular recording medium. CoCr alloys for HDD media have a hcp structure where the c-axes are random within the plane giving a random in-plane

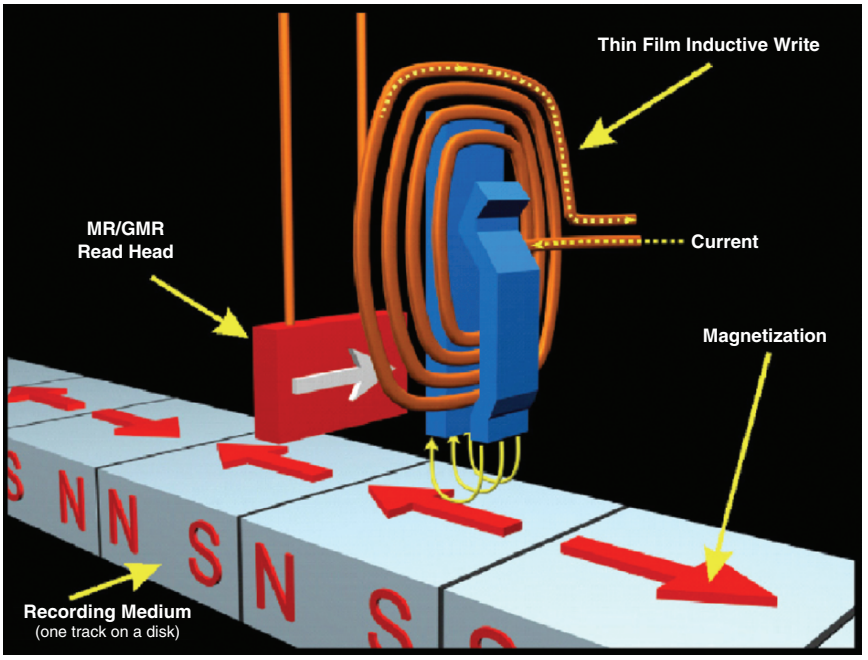

Figure 6. Illustration of longitudinal HDD magnetic recording. (Courtesy of Hitachi GST.)

anisotropy. Some in-plane orientation can be achieved by texturing the substrate prior to film deposition (Tan and Chang, 2005). This texture process uses a fine diamond slurry to create microgrooves in the circumferential direction which assist in grain alignment (Yu et al., 2003; Ajan et al., 2001). In order to record data on a randomly or partially aligned longitudinal medium, the magnetisation of the grains comprising the bit must be switched into one or other circumferential direction as shown schematically in Fig. 6. Figure 7 shows a transition following grain boundaries, which in a granular longitudinal medium with random in-plane anisotropy, and sub-10 nm grains is the narrowest achievable.

Given that the magnetic properties and size of individual grains do not permit a stable multi-domain state, the minimum variance in the transition region between the bits is obtained when the bit boundary follows the grain boundary. Also shown in Fig. 7 is the magnetisation profile and variance for the transition. Since media thin films are densely packed nanomagnetic materials, both exchange and magnetostatic interactions can be significant and hence we need to consider magnetic correlation lengths, rather than the physical grain size, as the important length scale in the recording process. In a recording system where transition noise dominates (the normal situation) and the bit length B is greater than both the downtrack ζ_{down}, and crosstrack ζ_{cross} correlation lengths, then the transition signal to noise ratio (SNR^{tr}) is given by (Tarnopolsky and Pitts, 1997; Bertram et al., 1998; Arnoldussen, 1998)

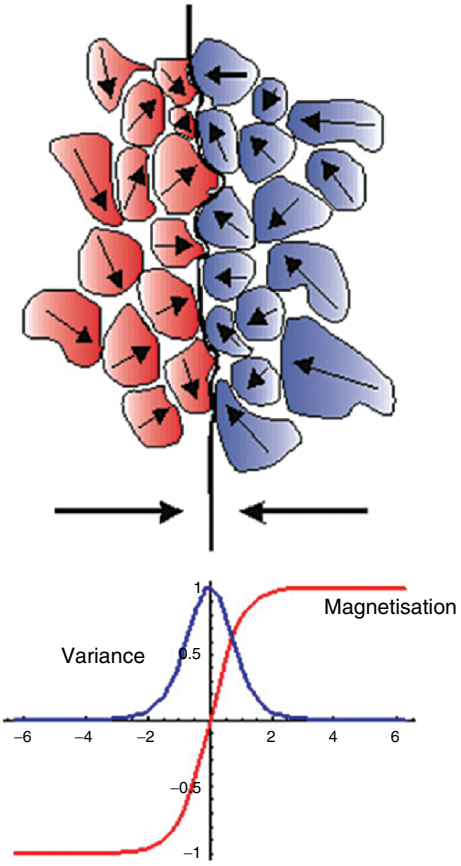

Figure 7. (a) Schematic of longitudinal medium microstructure with random in-plane anisotropy with an ideal transition. (b) Magnetisation profile for the same transition.

$$\mathrm{SNR}^{tr} = \mathrm{const}\frac{W_{\mathrm{read}}}{\zeta_{\mathrm{cross}}}\frac{BPW_{50}}{a^2} \tag{2}$$

where W_{read} is the width of the read head, PW_{50} is the pulse width and a is the Williams and Comstock transition parameter (Williams and Comstock, 1971). It follows that reducing the grain size sharpens (straightens) the transition and improves SNR by reducing the variance and hence the a parameter. This is a particularly effective since SNR $\propto \frac{1}{a^2}$. In real materials there is a distribution of grain sizes, so that larger grains in the distribution give greater transition noise by increasing the magnetic transition variance. However, reducing the grain size too far causes the small grains in the distribution to become thermally unstable, setting a limit on grain size scaling. Thermal instability causes statistical switching of magnetisation and arises when the thermal energy due to the fact that the

medium is at a finite temperature ($k_B T$) becomes competitive with the anisotropy energy of a magnetic grain ($K_u V$). Here k_B is the Boltzmann constant, T is the absolute temperature, K_u is the unaxial anisotropy and V the grain volume. Using Boltzmann statistics and modelling the medium as an assembly of independent switching volumes with energy barriers ΔE, the Arrenhius-Néel probability of not switching, P, is given by[2]:

$$P = \exp(-rt) \tag{3}$$

$$r = \tau^{-1} = f_0 \exp\left(\frac{-\Delta E}{kT}\right) \tag{4}$$

where f_0 is the attempt frequency (often taken as 10^9 Hz). Rearranging these equations to find the probability of switching 10% of the magnetisation after 10 years, a typical magnetic data storage lifetime, gives $\Delta E \approx 40kT$. The switching of magnetic grains in a medium is a complex, incoherent process involving non-uniform intermediate states. Such switching processes cannot be described by simple analytic models. However, since media have small grains and relatively weak exchange interactions it is possible to make progress using the Stoner-Wohlfarth (S-W) model of isolated particles reversing by coherent rotation (Stoner and Wohlfarth, 1948; Stoner and Wohlfarth, 1991). Using the S-W model and assuming only the unaxial anisotropy and Zeeman terms contribute to the energy barrier, ΔE for a di-bit transition is[3]:

$$\Delta E = K_u V - \mu_0 H_d M_r V \cos(21^o) \tag{5}$$

where M_r is the remanent magnetisation, H_d the demagnetising field experienced by the magnetic grain and $\cos(21^o)$ comes from taking the average over grains randomly distributed in the plane of the film (Bertram and Richer, 1999). In practice, values of $\Delta E > 60\, k_B T$ are normally sufficient to ensure that a medium remains sufficiently thermally stable for practical applications. One important aspect that should be mentioned is the role that angular variations of applied field play in the reversal process (Stoner and Wohlfarth, 1948; Kondorsky, 1940; Coffey et al., 2002). In the S-W model, if the field is applied at 45° to the easy axis then the magnitude is exactly half that required for a field applied along the easy axis. This has a significant effect on recording since the field supplied by a write head is three-dimensional in nature. Hence, considering only one component does not adequately describe the forces acting to reverse the medium. This angle effect also modifies the energy barrier to thermally activated reversal as discussed in a series of articles by Pfeiffer (1990). The subject of thermal stability in recording media

[2] Also see Section 4.1

[3] In this chapter, SI units are used where possible. See Table II on p. 56 for a translation between CGS and SI units

has received much attention, particularly, as the practical limits of longitudinal recording became apparent. Although the scope of this article does not allow for a more detailed discussion of the subject, several articles can be recommended (Richter, 1999; Zhang and Bertram, 1998; Moser and Weller, 2001).

This basic understanding of recording physics allows media properties to be defined for high-density longitudinal recording:

- Small grains – but not so small as to be thermal unstable
- Narrow grain size distribution – avoid both very small grains as thermally active and large grains because of transition noise
- Good grain isolation – minimise exchange coupling and keep magnetic correlation length as close as possible to grain size
- High anisotropy – ensure maximum thermal stability but limited by the need to write bits using the available head fields
- Narrow anisotropy distribution – low anisotropy leads to thermal activation whereas high anisotropy grains risk not being written
- Good circumferential alignment – maximise signal and control of angle effects

Magnetically, these physical properties lead to hysteresis loops with narrow switching field distributions (SFD), which is one of the signatures of media suitable for high-density recording. The current generation of longitudinal media, aimed at recording densities of $\backsim 100\,\mathrm{Gbit/in^2}$, have an average grain size of about 8 nm with a distribution of $\sigma/<\mathrm{dia.}> \backsim 0.25$. Anisotropy of $\backsim 0.2\,\mathrm{MJ/m^3}$ and magnetisation of $\backsim 300\,\mathrm{kA/m}$, and an orientation ratio $M_r(\mathrm{circumferential})/M_r(\mathrm{radial})$ $\backsim 2$. The distribution of anisotropy is not well known and has to be implied from modelling since there are no experimental techniques currently available to access the distribution directly. This is because the anisotropy distribution is always convoluted with exchange (and magnetostatic) coupling which obscures the underlaying distribution.

Figure 8 shows a structure that is capable of supporting high-density recording together with a TEM image of the medium grain structure. The various layers in the thin film stack, each of which is of the order of 20 nm, are shown together with a brief description of the layer's function and one of the possible materials choices. The seedlayer and underlayer structure is critical as it is these layers that are responsible for both setting the grain size and providing an epitaxial template to grow grains with an in-plane crystallographic orientation. The underlayer cannot impose an overall Cartesian symmetry; this would lead to variations in magnetic properties as the disc rotates. The growth of each of seed/under layers is carefully tuned through sputtering gas pressure ($\backsim 6$ mTorr) and substrate temperature, typically 200–300 °C, to ensure the greatest possible grain refinement and the best possible lattice matching so that the grain size distribution is

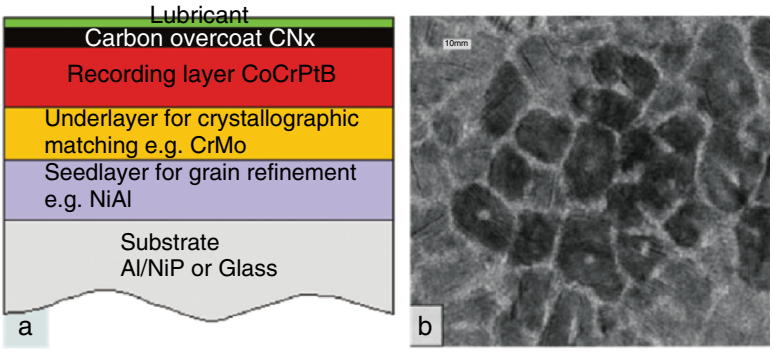

Figure 8. (a) Structure of high-density longitudinal media and (b) TEM image of medium grain structure showing good grain boundary segregation.

kept as narrow as possible and crystallographic defects in the recording layer are minimised. A detailed review of the physical mechanisms and materials used to set the crystallography and microstructure of longitudinal media has been given by Liu and Laughlin (2001). Longitudinal media are typically quaternary alloys of CoCrPtB (Doerner et al., 2001). The exact composition depends on a particular media development programme, but alloys with an approximate composition of $Co_{55}Cr_{20}Pt_{15}B_{10}$ are typically employed where the individual elements are optimized in the range $+/-5\%$. In these alloys Pt is used to control anisotropy since in hcp Co, Pt acts to expand the lattice along the *c*-axis. Media are sputtered at elevated substrate temperatures which causes Cr and B to preferentially segregate at the grain boundaries. It is this mechanism that allows a heterogeneous thin film alloy to form where Co rich grains are separated by Cr and B rich boundaries that are essentially non-magnetic. Hence, the goal of achieving isolated, but densely packed, grains is met by careful control of the CoCrPtB deposition parameters. One additional sophistication used in producing high-performance longitudinal media is that of antiferromagnetically coupling (AFC) two CoCrPtB recording layers using a thin 0.7 nm layer of Ru (Fullerton et al., 2000; Abarra et al., 2000; Bertram, 1994). This AFC structure has the effect of reducing the magnetisation-thickness product ($M_r t$) so that magnetically the media appear thinner. Thin magnetic media, in general, have superior recording performance as the transition *a* parameter (Bertram, 1994) $\propto H_{cr}/M_r t$, leading to enhanced recording performance whilst physically, AFC media are sufficiently thick to resist thermal activation effects.

2.1.2. *Flexible media*

Flexible media have in recent years received much less research attention than media for HDD's. Flexible media discs such as standard floppy (1.4 MB) or higher capacity, i.e. ZIP (100/250 MB) are rapidly being supplanted by a combination

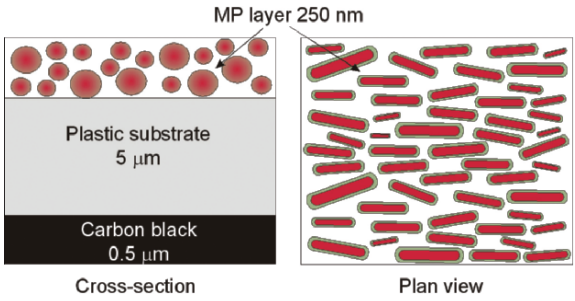

Figure 9. Typical structure of an advanced metal particle tape

of semiconductor flash memory using a USB interface and CD/DVD's. However, tape media continues to be important for archival storage and hence remains commercially significant. Most flexible media consist of magnetic oxide particles suspended in an organic binder and "wet" coated onto a flexible polymer substrate (Köster, 1996). Here, the metal particle pigment consists of super-fine acicular magnetic particles with long axes in the range 0.1–1 μm. The particles have a Fe or a FeCo core surrounded by an few nanometre of oxide. These particles have coercivities of approximately 200 kA/m and saturation magnetisation of 0.15 Am^2/g. A good review of the evolution of magnetic tape pigments has been written by Hisano and Saito (1998). Figure 9 shows the structure of a metal particle (MP) tape together with an indication of thicknesses of the constituent layers.

The MP layer contains the magnetic particles embedded in a specialist resin to produce a coating dispersion which is applied to the flexible plastic substrate. The smoothness of the tape coating can be improved by using a dual-coating approach where an initial layer consisting of a dispersion of TiO_2 particles is used. Physical alignment of the acicular magnetic particles is achieved by passing the wet tape through an electromagnet array. This allows highly oriented magnetic tape to be produced with typical squareness $M_r/M_s \backsim 0.9$. Further details may be found in a review article by O'Grady and Laider (1999).

In addition to MP coating technology, vacuum deposition techniques are also used to produce magnetic tape. See for instance Kawana et al. (1995), Onodera et al. (1996), and references therein.

First, it was attempted to use evaporation onto tape, leading to the metal evaporated product used in for instance Hi8 video cameras. In principle, one could evaporate Co, Fe, or Ni. Due to oxidation problems, Fe is disregarded, and Ni suffers from a very low magnetic moment, so the metal of choice was Co. It turned out, however, that the mechanical properties and oxidation resistance improve substantially when adding Ni. This is only possible since Co and Ni have approximately the same melting point. The commonly used alloy had a composition of $Co_{80}Ni_{20}$. Since the PET tapes used prohibit high temperature deposition, crystal

anisotropy is difficult to obtain. Therefore, anistropy is obtained by deposition under an oblique angle. This causes shadowing effects which enhance the columnar structure of the tape, and introduce a strong shape anisotropy effect which is oriented obliquely with respect to the substrate surface. To separate the columns even more, oxygen is added during deposition (Bijker et al., 1999). Finally, it turned out that the addition of oxygen improved mechanical properties and oxidation resistance as well, and Ni was removed. Modern ME tapes are therefore based on Co/Co-oxide systems.

Next to evaporation, sputtering can also be used for tape production, leading to metal sputtered (MS) tape. The range of alloys that can be used is much larger than for evaporation, and one can "steal" compositions from the hard disc industry. Anisotropy has to be obtained by deposition at elevated temperatures, or by using suitable seed layers (Nguyen et al., 2005, 2004; Bian et al., 2001). High temperatures became available with better tape polymer substrates, such as PEN.

The research on vacuum deposited tapes motivated MP tape manufacturers to improve their products as well, and currently extremely high densities can be obtained (Sekiguchi et al., 2005).

2.2. HEADS

The head illustration in Fig. 6 shows both the read and write elements. The areal density of a HDD is set by the width of the write element, which sets the maximum number of tracks that can be written on a disc of given diameter, and the shortest bit length supported by the writer/medium combination. Typically, the track width is 1.2 times the writer width to allow for effect of crosstrack fringing fields whereas the reader is reduced to 0.6 times the writer width to minimise noise from the track edges. In longitudinal recording, the write field is generated between two poles which extends vertically (y-coordinate) beyond the pole region and it is this field that is responsible for writing bits in the medium. In this brief description of recording heads we shall look at simplified analytic models of the head field as these capture the main features of the writer. The evolution of read elements is described including the latest, advanced tunnelling magnetoresistive devices. It is worth noting that although this section is primarily concerned with read sensors for longitudinal media the same sensors will be used on both perpendicular and patterned media recording systems. Hence this section has direct relevance to both current and future magnetic data storage technology.

2.2.1. *Write element*

Figure 10 shows a simple representation of an inductive write head, sometimes referred to in the literature as a "ring" head. It should be noted that the write elements found in modern HDDs have a significantly more complicated geometry. However, the simple structure shown in Fig. 10 serves to demonstrate the basic

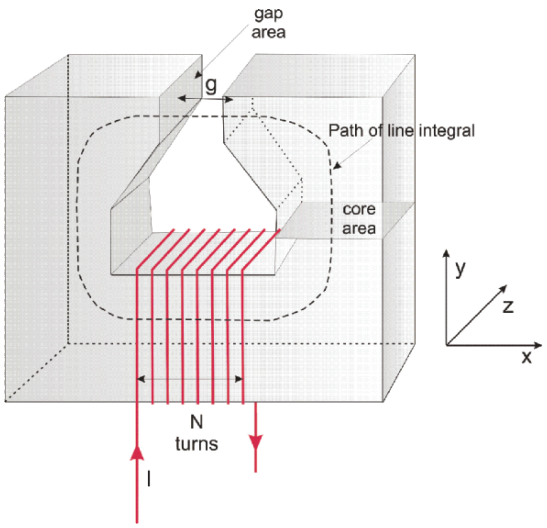

Figure 10. Diagram of a simplified inductive write head. After (Bertram, 1994).

features of all inductive write heads. The field in the middle of the gap (the deep gap field) is found by taking the line integral (shown as a dotted line) around the core and through the coil wound around the body of the head.

The field in the gap can be found in a straightforward manner from the magnetic scalar potentials (Bertram, 1994) and is given by:

$$H_{dg} = \frac{NIE}{g} \tag{6}$$

where N is the number of coil turns, I is the current, E is the head efficiency and g is the gap length (assumed small compared to the gap depth (y-direction)). The head efficiency is defined as the potential drop across the gap relative to the driving magnetomotive force and is given by:

$$E = 1 - \frac{\oint_{\text{core}} H_i \cdot dl}{NI} \tag{7}$$

where the integral includes the total contribution of the internal field in the core. In the case of longitudinal magnetic recording, we are not especially interested in the field in the centre of the gap but rather require knowledge of the field, and how it varies spatially, just outside the immediate gap region. This is because longitudinal recording relies on the so-called fringing field from the head as the medium cannot be placed directly in the space between the poles, as shown illustratively in Fig. 6.

The simplest approximation used to determine the field from a head with finite gap is the far field approximation where the field decreases inversely with distance from the gap. Here it is assumed that the track width (z-direction) is large compared with the gap, g. This immediately reduces the problem to two-dimensions

(2D) allowing the x and y components of the field to be expressed in analytic form (Bertram, 1994). A better approximation is the (Karlqvist, 1954) model where the effects of the finite gap length are included. This is a medium range model that has been used widely where the exact details of the field profile close to the gap corners are not required. As with the far field approximation this is a 2D model where it is assumed that the head is infinitely long (in the x-direction) with an infinitely wide track (z-direction) and with an infinitely deep gap. Hence the gap, g, is the length scale of interest where it is assumed that the potential varies linearly. The x and y field components for this model are:

$$H_x(x, y) = \frac{1}{\pi} H_0 \left(\arctan\left(\frac{(g/2) + x}{y} \right) + \arctan\left(\frac{(g/2) - x}{y} \right) \right) \tag{8}$$

$$H_y(x, y) = \frac{1}{2\pi} H_0 \ln\left(\frac{((g/2) - x)^2 + y^2}{((g/2) + x)^2 + y^2} \right) \tag{9}$$

Figure 11 shows a plot of the x and y components of the field as a function of the downtrack (x-direction) coordinate for a gap length $g = 100$ nm, a head/medium magnetic spacing of 40 nm and a deep gap field $H_0 = 16$ kOe. These parameters are representative of heads designed to record at 100 Gbit/in^2 and give a flavour of the fields from advanced longitudinal ring heads.

The problem of introducing finite head (track) widths to analytical models of head fields has been addressed by Lindholm (1977). Here the approach taken was to produce a closed form solution for the two limiting cases, i.e. infinite head width and zero head width and then to approximate a finite head width by a superposition of these two extrema. The maximum error using this approach was determined

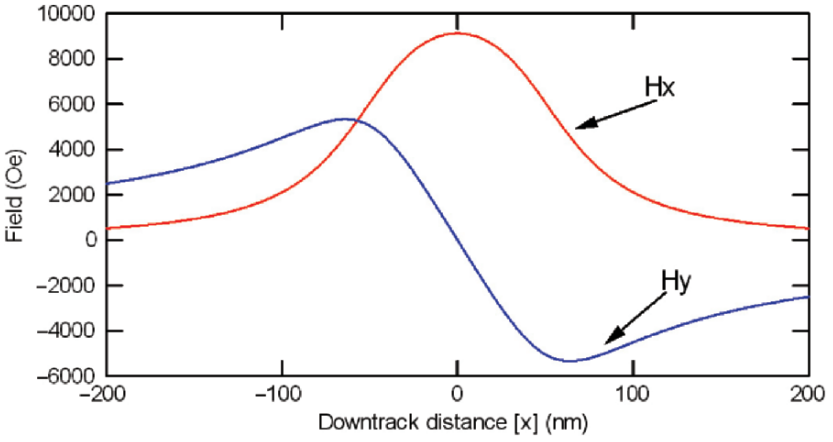

Figure 11. Field components from a Karlqvist head with a 100 nm gap as a function of downtrack coordinate for a magnetic spacing of 40 nm assuming a deep gap field of 16 kOe.

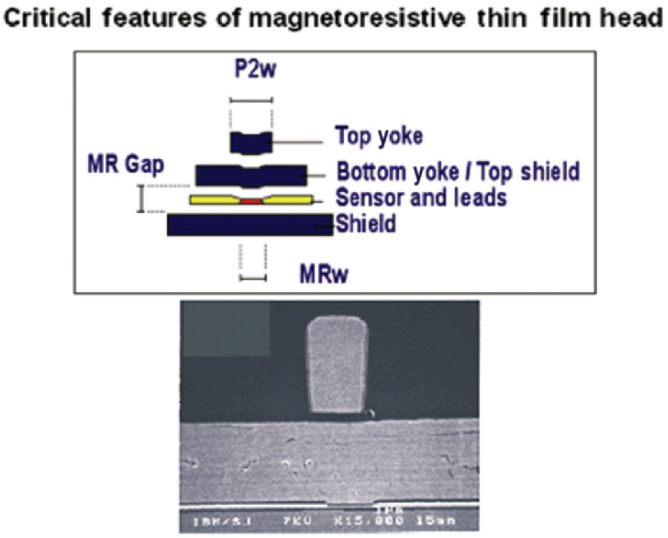

Figure 12. Scanning electron microscopy image and schematic diagram of a longitudinal head viewed from the air bearing surface. Note, the highly asymmetric write poles in contrast to the idealised head shown in Fig. 10.

to be 8% for the case where the magnetic spacing was half the gap length, with the error becoming progressively smaller with increasing head width.

Figure 12 shows a scanning electron microscopy (SEM) image of the poles of a modern longitudinal head. It is apparent that this head is significantly different from the simplified diagram in Fig. 10. The most striking difference is the asymmetric poles where one pole is much wider than the other. Here, the simplified geometry used in analytic models does not properly describe the details of the field emanating from the head. In order to optimise a head for a device, sophisticated finite element models (FEM) are used where the 3D nature of the head structure is properly represented, in order to simulate accurately the 3D field in 3D space. The vector nature of the head field is important in writing transitions since the reversal of the medium depends on both the magnitude of the field and the angle at which it is applied, as mentioned in the previous section. The spatial variation is also critical since the ability to create sharp transitions depends on the head field gradient as well as the SFD of the medium.

In addition to optimizing the shape of the head, the materials have be chosen carefully as well. The material properties necessary to fabricate a successful write head for HDD applications are:

– High saturation magnetisation – in order to obtain the highest possible deep gap field

– A large permeability over a wide frequency range to enable the head to write

at the GHz data rates demanded by modern HDDs. Here, a laminated structure can help to suppress eddy currents although fabrication is more complex. Alternatively, a more resistive material will also act to suppress eddy currents

– Very low anisotropy in order to minimise hysteretic losses and hence avoid excessive power consumption and heating of the element
– Mechanical and chemical stability both initially during high temperature fabrication, and also during the operating lifetime of HDD

Heads are normally electroplated from $Ni_{81}Fe_{19}$ (permalloy), $Ni_{45}Fe_{55}$, or more recently from a higher moment CoFe based alloy. Electroplating is used as it is a highly cost-effective process. However, sputtering offers greater flexibility and more control of the thin film properties which become important as head dimensions shrink. Sputtering can also be used to realize laminated heads. Coil windings are formed from electroplated copper whilst sputtered Al_2O_3 and hard-baked photoresist are used as insulating layers to separate the electrical and magnetic components.

2.2.2. *Read element*

Figure 13 shows a modern "merged" head. A merged head is where the read and write elements share a common shield, so that the second shield of the sensor is also the first pole of the write element.

As HDD capacities have increased so read elements have evolved. Initially, reading bits was accomplished using the same inductive element used for writing. Later in the 1970s a separate element based on anisotropic magnetoresistance (AMR) was introduced in order to increase reader sensitivity (Thompson et al.,

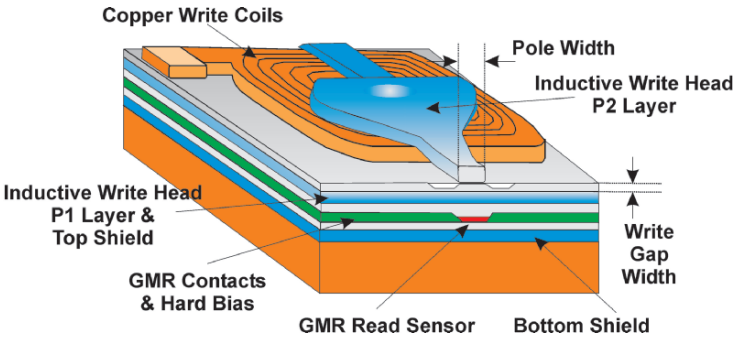

Figure 13. Merged head showing the main features of both write and read elements. (Courtesy of Hitachi GST.)

1975; Rijks et al., 1997). AMR readers use the effect, whereby the electrical resistance of a material depends on the relative orientation of the magnetisation and current flow directions. The thin film resistivity is given by

$$\rho = \rho_{90} + (\rho_0 - \rho_{90}) \cos^2(\theta) \tag{10}$$

where ρ_{90} and ρ_0 are the resistivities when the current and magnetisation are perpendicular and parallel, respectively. The angle θ is the angle between the current and magnetisation. In magnetic metals such as NiFe ($\rho \backsim 20\,\mu$Ohm-cm) the AMR effect $\Delta\rho/\rho \backsim 2\%$, and so whilst there are no special difficulties in scaling AMR devices to smaller dimensions, the AMR effect does not provide sufficient sensitivity to read small bit sizes in HDDs. All readers found in HDDs today are either spin valves which use the giant magnetoresistance (GMR) effect, or tunnelling magnetoresistance (TMR) devices (Childress and Fontana 2005). The exploitation of GMR in real world mass-produced devices is a technological tour-de-force since the time between discovery of the GMR effect and its incorporation into devices was less than 10 years, with IBM introducing the first GMR read sensor in 1997. Since the initial reports of GMR by Grunberg (1986) and by Baibich (1988) an enormous amount of research has been devoted to the subject, including important early work by Parkin et al. (1990). The scope of this article prohibits a detailed discussion of the physics of GMR but many excellent articles are available for the interested reader, e.g. (Heinrich and Bland, 1994; Parkin, 1995; Portier and Petford-Long, 1999; Daughton et al., 1999). The simplest GMR structure consists of two FM thin films separated by a thin non-magnetic layer, for example, Co(3 nm)/Cu(1.9 nm)/Co(4 nm), where the Cu thickness is chosen to ensure that in the absence of applied magnetic fields, RKKY coupling forces the two Co layers to align antiparallel. In an applied field sufficient to overcome the interlayer coupling both Co layers align and as the density of states is different for spin-up and spin-down electrons, there exists a spin-dependent scattering with electrons of one spin strongly scattered whilst electrons of the opposite spin are only weakly scattered. With the field removed and antiparallel alignment of the magnetisation restored, both spin channels undergo the same scattering and hence have the same resistance. The change in resistance due to spin-dependent scattering can be large $\backsim 20\%$ in bilayers at room temperature with values as high as 50% at low temperatures in multilayer stacks, c.f. AMR of $\backsim 2\%$. A spin-valve GMR sensor element is shown in Fig. 14 for a current in-plane (CIP) device where the current flows parallel to the film surface. In addition to the basic GMR structure described above, the spin valve sensor stack includes a thin film antiferromagnet (AFM) which pins one of the ferromagnetic layers through exchange coupling. The second FM layer, in this case NiFe, is able to rotate its magnetisation in response to the magnetic field from a recorded bit.

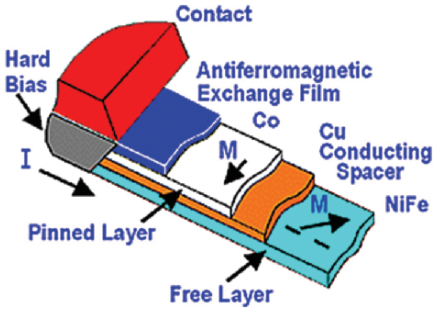

Figure 14. Structure of a GMR spin-value read sensor. (Courtesy of Hitachi GST.)

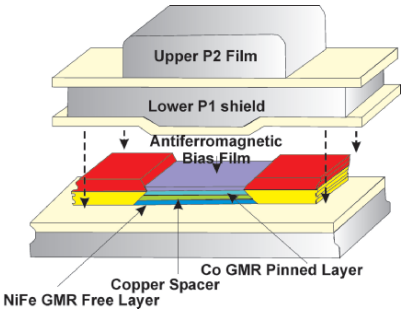

Figure 15. Diagram of GMR-CIP spin valve read sensor as part of a complete merged head. (Courtesy of Hitachi GST.)

The change in magnetoresistance depends on the extent of the rotation and is given by:

$$\frac{\Delta R}{R_0} = \frac{\Delta R_{\max}}{R_0}\left(\frac{1-\cos(\Delta\theta)}{2}\right) \tag{11}$$

where $\Delta\theta$ is the angle between the pinned and free layers, R_0 is the resistance when both layers are parallel and $\Delta R_{\max}$ is the change in resistance between parallel and antiparallel alignment of the pinned and free layers. The voltage output of a GMR-CIP sensor is given by

$$\Delta V = \frac{\Delta R}{R} R_s I E \tag{12}$$

where I is the bias current of a few mA, R_s is the sheet resistance $\backsim$25Ω/square which translates to a device resistance of $\backsim$50Ω and the efficiency E represents the fraction of the available GMR effect that is utilised and is typically in the range 15–30%. The maximum change in resistance of today's GMR-CIP spin valve sensors is $\backsim$20%, a factor of 10 increase over AMR devices. Figure 15 shows how the spin valve sensor is incorporated into the complete head structure. The writer gap is between P1 and P2.

Contact pads are needed to electrically connect the GMR spin valve sensor to the pre-amp circuit. An additional hard magnetic material also forms part of the structure. This hard bias structure is needed to eliminate magnetic domains and provide magnetic stiffness to the free layer, controlling the degree of its rotation. Other structural elements include shields to increase localisation of the field to be sensed allowing smaller bits to be resolved.

Recently, sensors based on TMR have started to become available in products. TMR or magnetic tunnel junction (MTJ) were first described by Julliere (1975) with work prior to 2000 reviewed by Moodera and Mathon (1999). TMR sensors are significantly different from the conventional GMR-CIP devices described previously, and rely on the fact that spin polarised tunnelling can occur when one ferromagnetic metal is separated from another by a thin insulating barrier. Figure 16 shows the important differences between a GMR-CIP and TMR-CPP sensor with spin valve-like properties. Firstly, in TMR devices the current flow is perpendicular to the plane (CPP) rather than parallel to the sensor (track) width. This requires a very different layout in terms of the placement of electrical contacts and correct positioning of insulating layers, shown as white in Fig. 16.

A CPP sensor geometry has important advantages over CIP (Childress and Fontana 2005), (1) the shields can be used as the electrical connections, eliminating the need for separate leads, (2) current shunting in non-active layers is removed, and (3) the sensor dimensions now define the cross-sectional area so that as sensor dimensions are reduced and the device resistance increases. Figure 17 shows the magnetic structure of a TMR sensor in more detail. The magnetic structure has similarities to the GMR sensor in Fig. 15 in that it consists of a FM pinned to an AFM and a second magnetic free layer and associated hard bias structure. The material set used for these layers is also similar, for example, CoFe is often used for the FM layers. A thin ($\backsim$1 nm) insulating layer separates the two FM layers. This layer can be an amorphous insulator such as Al_2O_3 (Sharma et al., 2000)

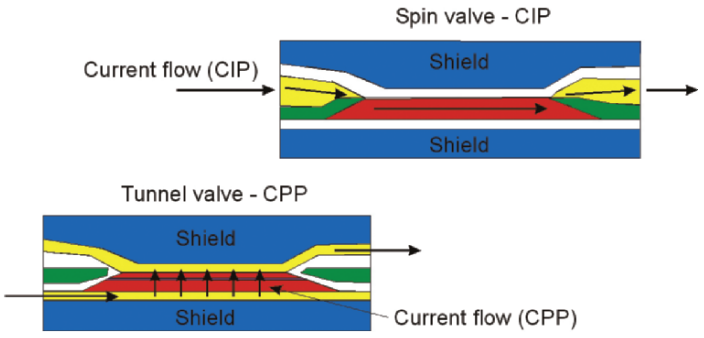

Figure 16. Illustration of differences between GMR-CIP and TMR-CPP read sensors. The white regions show the placement of electrical insulating material, green is the hard bias magnets and yellow the electrical connections. (Redrawn from R.E. Fontana Jr. at Hitachi GST.)

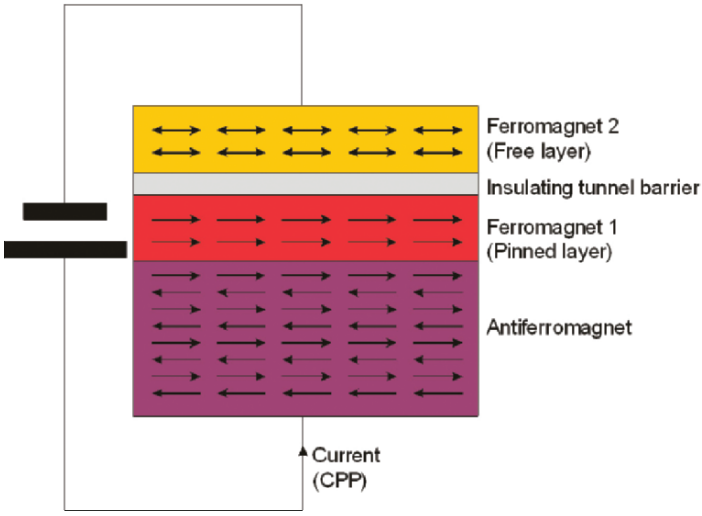

Figure 17. Schematic representation of magnetic structure for a TMR-CPP read sensor.

or a crystalline material such as MgO (Butler et al., 2001). The key manufacturing step is the deposition of a high quality, highly controlled, pin-hole free tunnel barrier in a reliable and reproducible manner (Moodera et al., 1995). Pin holes lead to current shunting and lower MR. There is also a critical need to control the total resistance since the presence of an insulator can lead to devices with far too high resistance for practical applications. Currently, some of the largest measured TMR values in device quality structures are 45–53% at room temperature for a low-resistance CoFeB/MgO/CoFeB MTJ (Tsunekawa et al., 2006). However, values as high as 410% have been reported at room temperature for MBE grown Co(001)/MgO(001)/Co(001) with Co in the metastable bcc phase (Yuasa et al., 2006).

The physics underlying TMR is illustrated in Fig. 18 and arises from spin-polarised tunnelling. Figure 18a shows the difference in density of states (DOS) at the Fermi level of a FM for bulk fcc Co, projected onto the d orbitals (Tsymbal et al., 2003). This difference leads to spin dependent tunnelling (SDT) between two adjacent FM thin films as the tunnelling current carried by spin-up (majority) and spin-down (minority) electrons is different, depending on the relative orientations of the two ferromagnetic layers.

The first reported model used to estimate the magnitude of TMR effects in MTJ was the Julliere model (Julliere, 1975).

$$\mathrm{TMR} = \frac{\Delta R}{R_{\mathrm{P}}} = \frac{R_{\mathrm{AP}} - R_{\mathrm{P}}}{R_{\mathrm{AP}}} = \frac{2P_1P_2}{1 - P_1P_2} \tag{13}$$

where R_{AP} and R_{P} are the junction resistances for the antiparallel and parallel alignment of the two FMs and P_1 and P_2 are the spin polarisations in the two

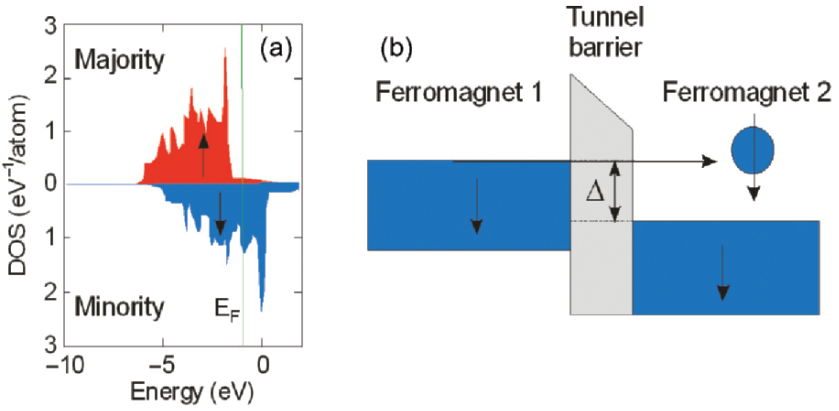

Figure 18. Physics of tunnelling TMR sensors where the differences in density of states (DOS) shown in (a) for bulk fcc Co projected on to the d orbitals (redrawn from Tsymbal et al., 2003) leads to differences in tunnelling conductance for majority and minority spins; (b) shows an electron tunnelling from the first to the second ferromagnetic electrode with an energy gap Δ between the electronic bands.

electrodes. Here it is assumed that electrons tunnelling from a ferromagnet are spin polarised and that the polarisation, P, is related to the spin dependent DOS at the Fermi level, E_F,

$$P = \frac{\text{DOS} \uparrow (E_F) - \text{DOS} \downarrow (E_F)}{\text{DOS} \uparrow (E_F) + \text{DOS} \downarrow (E_F)} \tag{14}$$

with the additional assumption that spin is conserved in the tunnelling process so that the system acts as if the tunnelling current in the spin-up (majority) and spin-down (minority) channels flows in two parallel wires. According to these assumptions, electrons originating from one spin state of the first FM are accepted by unfilled states of the same spin of the second. If the two FM films are magnetized parallel, the minority spins tunnel to the minority states and the majority spins tunnel to the majority states. However, for antiparallel alignment the situation is reversed so the majority spins of the first FM tunnel to the minority states in the second and vice versa. Whilst the Julliere model is successful in predicting TMR ratios from observed values of spin polarisation in a ferromagnet/insulator/superconductor system, it is not able to directly relate the DOS to spin polarisation. It is beyond the scope of this article to adequately cover the new and exciting theoretical and experimental results in SDT. However, a number of excellent reviews have been written including those (Moodera and Mathon, 1999; Tsymbal et al.,2003; Zhang and Bulter, 2003; Zutic et al., 2004).

Concluding this section on read sensors, we note that future read sensors based on GMR but with a CPP electrical configuration have been also proposed (Zhang and Levy, 1991; Pratt et al., 1991), and reviewed by Bass and Parrt (1999).

The advantages of the CPP geometry have already been discussed in the context of TMR sensors and those same advantages apply equally to CPP-GMR devices. The sensor resistance is very different for CPP-GMR since only metallic layers are present and this low resistance means that in order to produce a given output voltage a large sensor current density will be required. This potentially leads to thermal and electromigration problems degrading device performance. However, the lower resistance of GMR as opposed to TMR devices will increase the available bandwidth at the lowest dimensions. Additionally, GMR sensors have only Johnson noise whereas TMR devices, by their nature, have both Johnson and shot noise. Thus, despite the challenges of designing and fabricating GMR-CPP structures, there are advantages which suggest that these devices will be extremely valuable in targeting areal densities $>500\,\mathrm{Gbit/in^2}$.

2.3. POSITIONING

Storage systems can be divided into electrically addressed systems (e.g DRAM, Flash) and mechanically addressed systems (e.g DVD, hard disc, tape). Electrically addressed systems are fast but expensive, mechanically addressed systems are slow but cheap. This is why in computer architectures the various types of storage systems are mixed. A small amount of high-speed DRAM is used for the working memory, whereas large amounts of tape storage are used for backup and archiving. This hierarchy can be represented in the data storage pyramid (Fig. 19). Not all computer systems use all types of memory, we hardly see tape drives in desktop computers, and the first notebooks with Flash drives are entering the market.

When using mechanically addressed storage, one can either use rigid media, or tape. The latter has the huge advantage that it can be wound on a reel. As a

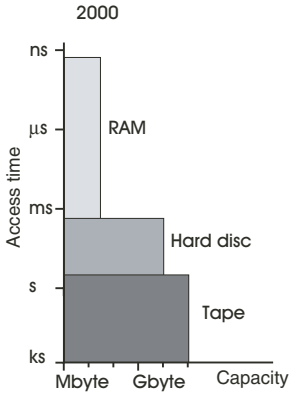

Figure 19. Data Storage Pyramid

result the volumetric data density for tape is quite respectible, even though the areal density is much lower than hard disc (Table I).

The positioning system in tape drives uses two separate mechanisms. The tape is passed by the recording head using an advanced mechanical system which minimizes tape vibrations (Fig. 20, left). The recording head is then positioned across the tape either by a helical scan method, used mainly in video cassette recorders (VCR), or by a linear translation, used in modern tape drives. For an overview of state of the art tape positioning see Childers et al. (2003). The increase of areal density is mainly achieved by reducing the track width. This poses severe demands on the tracking system. Attempts have been made to emboss long wavelength magnetic tracking servo's (Ruigrok et al.,1998), and head actuators become more and more sophisticated (Richards and Sharrock, 1998).

In hard disc systems, positioning along the track is achieved by rotation of the disc, whereas cross-track positioning is realised by a voice-coil actuator under the arm which carries the head (Fig. 21). Tracking is done on pre-written servo tracks on the disc. As in tape recording, the track width is decreasing rapidly, and

TABLE I. Areal versus volumetric data density (Seagate Barracuda 750 GB hard disc versus LTO 3 400 GB tape cartridge)

	Areal density [Gbit/in^2]	Volumetric density [Gbit/cm^3]	Effective storage [0–1]
Hard disc	200	16	$1\ 10^{-5}$
Tape drive	0.3	15	$3\ 10^{-3}$

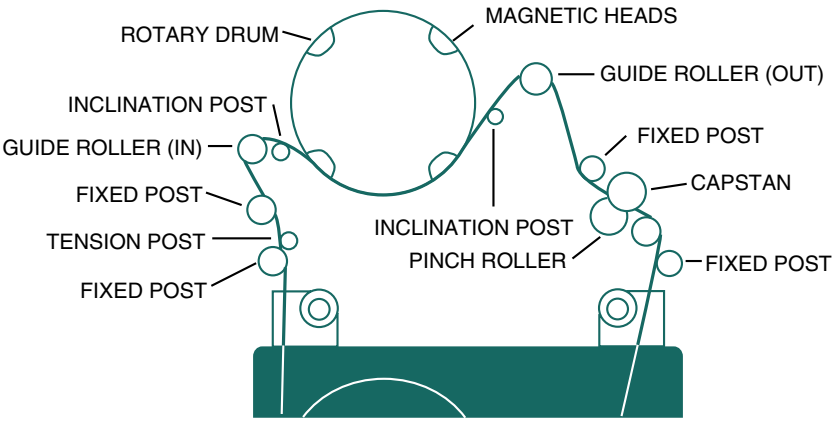

Figure 20. Tape architecture. *Top*: tape transport, *bottom*: movement of head across the tape

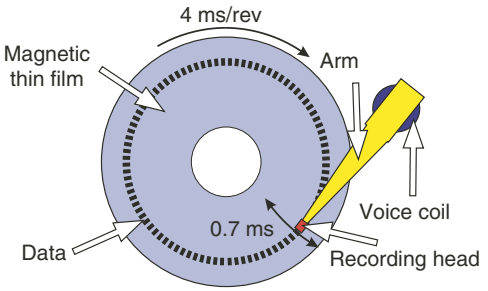

Figure 21. Hard disc architecture

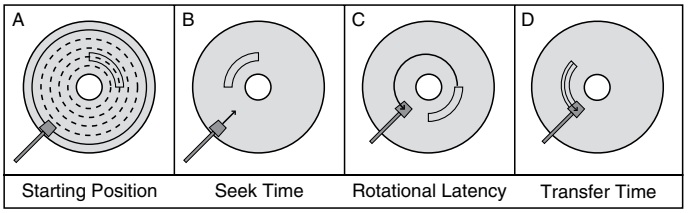

Figure 22. The time to locate a bit is determined by seek time and latency

tracking becomes more and more difficult. Attempts are made to include dual-stage actuators, where the voice coil is used for course positioning, and a small-range actuator is mounted directly behind the head (Mou et al., 2004; Hirano et al., 1998).

The data rate is the product of the bit length and the rotation speed of the disc, possibly multiplied by the number of heads. Since bit length is decreasing rapidly, there is no need to increase the rotation speed. On the contrary, the write frequency of the head is limited by the magneto-dynamics to a few GHz (Batra et al., 2004; Takano, 2004; Bai and Zhu, 2002; Gao and Bertram, 2002; Mao et al., 1999).

The access time before data can be read is determined by the time it takes for the arm to move to a certain track (seek time, Fig. 22) and the time it takes for the disc to rotate with the correct location below the head (latency). The positioning system is designed in such a way that latency is the dominant factor determining the total access time. The average time for the disc to rotate to the correct location is half the rotation cycle, so access times in hard discs are in the order of 60/RPM. Modern hard discs have rotation speeds of 15,000 RPM, which have an average access time of 4 ms.[4] Increasing the rotation speed is extremely difficult. Some progress is made using spindle motors with fluidic dynamic bearings and rotation speeds of 20,000 RPM can be reached (Chen et al., 2001). These speeds have not been commercialised yet because of problems with heat generation and

[4] Seagate Cheetah 15 K.5

vibrations (Sugaya, 2006). Since vibrations can be controlled better for smaller disc diameters, the highest rotation speeds are found in 2.5″ discs for server applications. It can be expected that in the future even smaller discs will be used. The funny situation might emerge that enterprise servers will have 1″ discs! An amusing exercise is to calculate the speed of the outer rim of the disc. A 3.5″ disc running 60,000 RPM will reach the speed of sound! It is difficult to imagine a head running over the disc at a flying height of 5 nm at those speeds.

2.4. SIGNAL PROCESSING/DATA ENCODING

In order to store digital information on a medium and to be able to recover the recorded bit sequence, signal processing and data coding/encoding has to be brought in around the physical write/read process. The basics of these subjects are treated in textbooks like for instance, Hoagland and Monson (1998) and Wang and Taratorin (1999). An overview of modern approaches by a variety of authors is presented in Vasic (2005). Figure 23 shows a conventional basic setup of the so-called magnetic recording channel. Starting with the physical recording interface, the functions of the respective blocks can be described as follows.

The write circuits produce the proper write currents for driving the write heads, while the read front-end and equalizer electronics pre-amplify and equalize (filter) the read-head signals. The "bell shaped" read signal waveforms, either from inductive or shielded GMR heads, result from the magnetic stray fields which are located at the magnetization transitions, and two successive read pulses always show opposite polarities (Fig. 24). Filtering includes narrowing of the read pulses, thereby reducing intersymbol interference (pulse overlap). The data detector has to recover the bit sequence which originally has entered the write circuits. Conventional implementations were based on a peak detector for determination

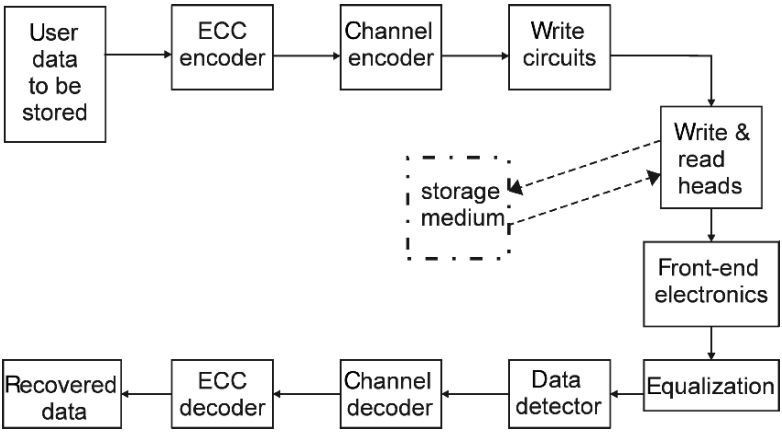

Figure 23. Block schematic of a magnetic recording system

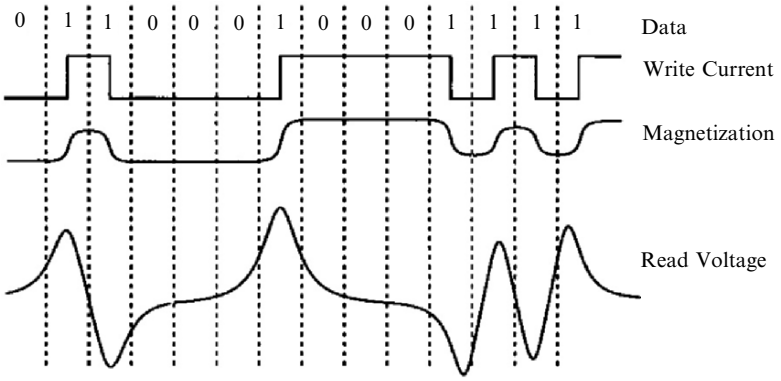

Figure 24. NRZI data '01100010001111' and the corresponding write current, magnetization pattern, and voltage waveform. The dashed lines represent clock windows. (From Wang and Taratorin, 1999.)

of the read-pulse's positions thereby reconstructing the recorded magnetization pattern. From the early 1990s, this simple detection principle was replaced by more advanced and complicated partial-response maximum likelihood (PRML) methods, and other sophisticated techniques.

The channel encoder converts the bit sequence to be recorded into a binary sequence which is better adapted to the physical recording process and, among other things, facilitates clock recovery. The modulation decoder performs the complementary actions.

The error-correction (ECC) encoder basically introduces supplementary (parity) bits into the user-bit sequence for enabling error detection and correction. The ECC encoder and decoder will improve the error rate from 10^{-6} to 10^{-9} at the inner recording channel, to 10^{-10} to 10^{-12} as a result of the outer ECC.

A widely used channel encoder/decoder is the run-length-limited (RLL) "$m/n(d, k)$" code, or modulation code (explained below). A useful feature of this code is its ability to increase the density of user bits on the medium, despite the fact that this code adds extra bits to the data to be recorded. This is illustrated in Fig. 25 showing a bit sequence of 6 user bits (1 1 0 1 0 0) which is coded with a 2/3(1,7) code. Here the bits are displayed following the so-called NRZI convention, with a "1" indicating the position of a magnetization transition, and a "0" the absence of a transition. The applied RLL code scheme (noted in Wang and Taratorin (1999)) converts $m = 2$ input bits into $n = 3$ encoded bits, while in the encoded pattern the minimum number of "0"s between two consecutive "1"s is $d = 1$ (reducing intersymbol interference), and the maximum number of "0"s between two "1"s is $k = 7$ (facilitating clock recovery). In the middle part of Fig. 25 the applied code scheme results an encoded bit sequence of 9 bits. However, because of the minimum distance of two consecutive "1"s $k = 1$,

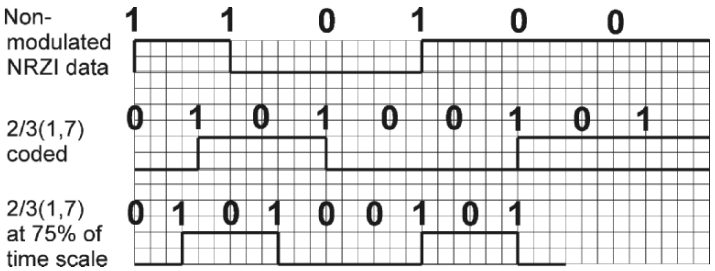

Figure 25. A bit sequence (*upper*) is encoded using an RLL code (*middle*), resulting in reduction of required recording-medium length (*lower*).

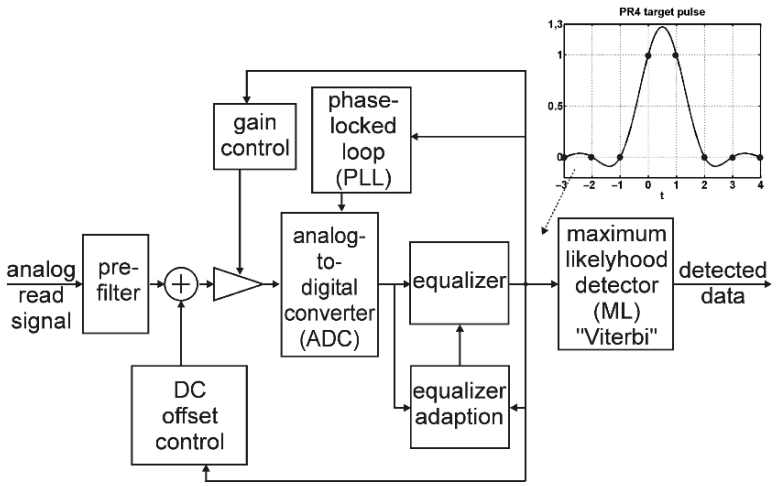

Figure 26. Block schematic of PRML detection. At the equalizer's output the sample values for each read pulse (indicated with dots) should fit the target-pulse form

the encoded pattern could be recorded in a shorter medium segment than the uncoded sequence (lower part in Fig. 25). For RLL codes it can be shown that, principally, the user bit density on the medium actually will be increased with a factor $(d + 1)(m/n)$, here equal to 4/3.

PRML detection methods intentionally introduce an amount of overlap between successive read pulses, and this is essentially different from the approach in more conventional detection systems. Pulse broadening is performed by converting (equalizing) the read-head's pulses to so-called target pulses with a specially designed form (see Fig. 26). Actually the detection process in the maximum likelihood (ML) detector utilizes read-pulse samples, so the equalizer can be supplied with a digital filter. Starting with the known target-pulse form, the ML detector computes the expected read-sample values for different recorded bit combinations, and reconstructs the recorded data by taking the best fit between computed and measured read-sample values.

During the last years coding and detection for digital magnetic recording has developed to new concepts where the coding and detection function blocks indicated in Fig. 23 have merged into new integrated signal and bit processing algorithms (Vasic, 2005; Wu, 2000). Important developments proposed in the mid-1990s are low-density parity-check (LDPC) codes, and turbo codes and turbo equalization. Such methods show the potential of approaching the theoretical limits concerning bit-detection performance, but the complexity of the required electronics impedes a fast introduction.

3. Perpendicular recording

At the time of writing in 2006 HDD manufacturers are in the process of converting from data storage on longitudinal media to storage on perpendicular media. In perpendicular media the easy unaxial anisotropy axis is normal to the plane of the film. The magnetisation vector can therefore be oriented either into or out of the plane of the medium. Figure 27 shows the important magnetic components of a perpendicular HDD.

This is one of the most significant changes to have occurred in the 50-year history (Daniel et al., 1998) of the HDD since up to this point longitudinal media have been employed exclusively. This change in technology has been driven by the economic necessity of producing magnetic storage devices with ever greater capacities and by the technical limitations associated with scaling longitudinal system components beyond $100\,\mathrm{Gbit/in^2}$. These scaling problems were outlined in the previous section on longitudinal recording. Reviews of perpendicular recording have been given by Khizroev and Litvinov, 2004 and Khizroev and Litvinov (2005). Before discussing some of the details of the heads and media for a perpendicular HDD recording system, we note the similarities and differences between longitudinal and perpendicular systems. Superficially, if one were to remove the cover of a HDD it would not be possible to determine if the drive relied on longitudinal or perpendicular recording. The mechanical layout of the drive, spindle motor, head actuator, and printed circuit board are identical, as are the physical appearance of the disc medium and head together with associated suspension. Magnetically, a HDD based on perpendicular recording is substantially different with new requirements placed on both the medium and head, particularly the part of the head responsible for writing. There is also a requirement for the signal processing in the read channel to take account of the difference in the reader output waveform, since the z-component of flux (to which the reader is principally sensitive) is different for longitudinally and perpendicularly magnetised bits.

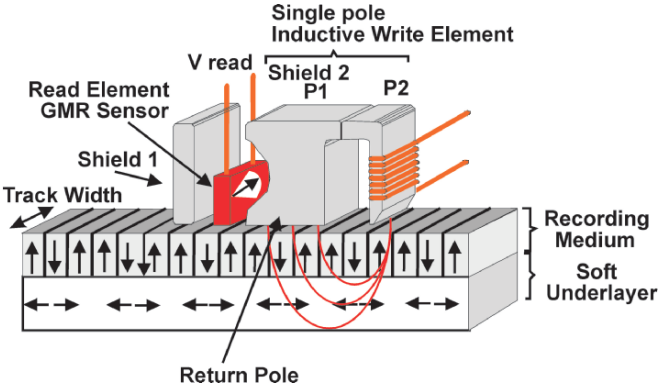

Figure 27. Schematic illustration of the magnetic components of a perpendicular recording system. (Courtesy of Hitachi GST.)

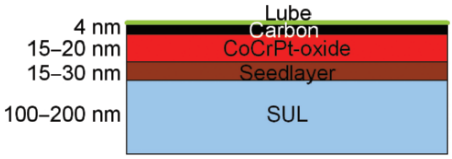

Figure 28. Generic perpendicular medium structure

3.1. MEDIA

The structure of a typical medium for perpendicular HDD recording is shown in Fig. 28. Apart from the change in anisotropy direction, the most significant difference is the inclusion of a thick, magnetically soft, high moment underlayer (SUL).

The SUL is needed to complete the flux circuit between the highly asymmetric poles of the write head, shown schematically in Fig. 27. This highly asymmetric head configuration is often referred to as a "single pole" head and will be discussed in more detail in the next section. As with longitudinal media, the recording performance, that is the ability to write sharp transitions between one magnetic state and the opposite state, depends on the physical and magnetic properties of the recording or data storage layer (in this case CoCrPt-oxide). Hence, we need just the same medium characteristics:

- Small, thermally stable grains
- Narrow grain size and anisotropy distributions
- High anisotropy but not so high that medium is unwritable
- Controlled exchange and magnetostatic coupling to facilitate switching of individual grains
- Well aligned grains

These characteristics are in addition to the obvious requirement of perpendicular anisotropy and the technological challenge of growing such a medium on relatively thin seedlayers. The need for thin seedlayers comes directly from the relation between the deep gap field H_{dg} and the distance l from the write pole to the SUL (Bertram, 1994). The factor of 2 arises from the need to include both the write pole-SUL and SUL-return pole spacings.

$$H_{dg} = \frac{NIE}{2l} \tag{15}$$

Any increase in spacing between the tip of the write pole and the SUL will decrease both the magnitude and the gradient of the field available to write the recording layer. Grain alignment in perpendicular media is controlled by the dispersion of the Co hcp c-axes, typically 2–3°, rather than the 2D random in-plane distribution found in longitudinal media. Hence perpendicular media has a significant orientation advantage, allowing more control over the reversal of grains as a function of applied field angle. The current class of media are based on a CoCrPt-oxide alloy (Oikawa et al., 2002) where Cr and Pt are of the order of 10 at% with the seedlayers chosen to ensure the c-axis of the hcp crystallographic structure is perpendicular to the film plane. A transmission electron micrograph of a typical CoCrPt-oxide perpendicular medium is shown in Fig. 29 and the hysteresis loop from a similar medium in figure 30. Figure 29 shows that in addition to creating a suitable template for perpendicular magnetic anisotropy the seedlayers are also responsible for the creation of small grains, in this case approximately 8 nm, and a reasonably narrow grain size distribution $\sigma/<\text{dia}> \backsim 0.25$. Figure 29 also shows well-separated grains with significant grain boundary material to form a heterogeneous medium. This separation is controlled by sputtering a composite CoCrPt-oxide material under conditions where the oxide forms in the grain boundaries. Since the oxide is non-magnetic, a normal oxide is SiO_2, this helps to achieve the goal of grain isolation through exchange de-coupling.

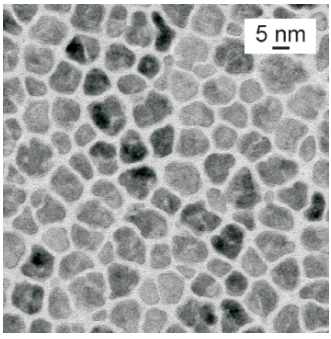

Figure 29. Transmission electron micrograph of a perpendicular medium showing an average grain size of 8 nm and a distribution of $\sigma/<\text{dia}> \backsim 0.25$

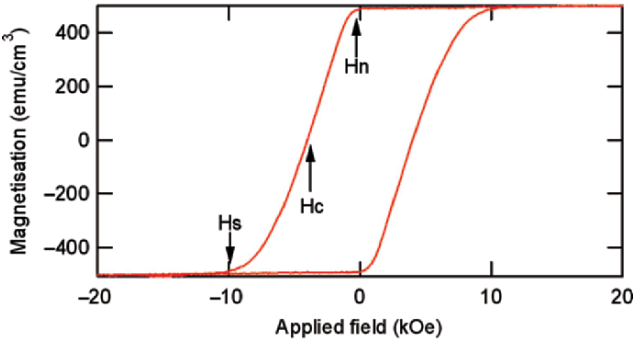

Figure 30. Hysteresis loop measured on a vibrating sample magnetometer at room temperature for a CoCrP-t-oxide perpendicular medium. H_n is the nucleation field, H_c is the coercivity and H_s is field required to saturate the medium.

Figure 30 shows a hysteresis loop from a CoCrPt-SiO_x perpendicular medium. This loop illustrates the important magnetic properties of perpendicular media. Firstly, the loop squareness, remanent magnetisation (M_r) divided by saturation magnetisation (M_s), is unity. This demonstrates that the magnetisation of individual grains is not reversing in the demagnetising field due to the other grains. The nucleation field (H_n) is the minimum applied field required for switching and the saturation field (H_s) sets the maximum field that must be available from the head. It is important to note that switching fields required to reverse a grain depends, at finite temperature, on the length of time for which the field is applied. Hence measurements using a vibrating sample magnetometer where the characteristic time is $\backsim$seconds will give lower switching fields than those required of a recording head where the time available is typically on the order of a nanosecond. H_n must be sufficiently large so that a combination of demagnetising fields and thermal activation of magnetisation reversal do not cause unacceptable degradation of the written bits. H_s must be sufficiently small so that maximum field available from the head is still able to write bits in the medium. Hence the magnetic properties of the medium must be carefully tailored to ensure thermal stability, writability, and have sufficient M_s to generate a signal in the read head.

One variant of perpendicular media that is likely to become important in the future is exchange coupled composite (ECC) media also known as exchange spring media and shown schematically in Fig. 31.

The essential idea of ECC media is to control reversal of the magnetisation through control of the spin structure when the medium is subject to a reverse field. In the simplest implementation, the recording layer of the medium is split into two layers. If we consider one of the grains shown in Fig. 31 then the bottom layer is similar to the conventional perpendicular medium discussed previously. The top layer is a lower anisotropy material which is exchange coupled to the

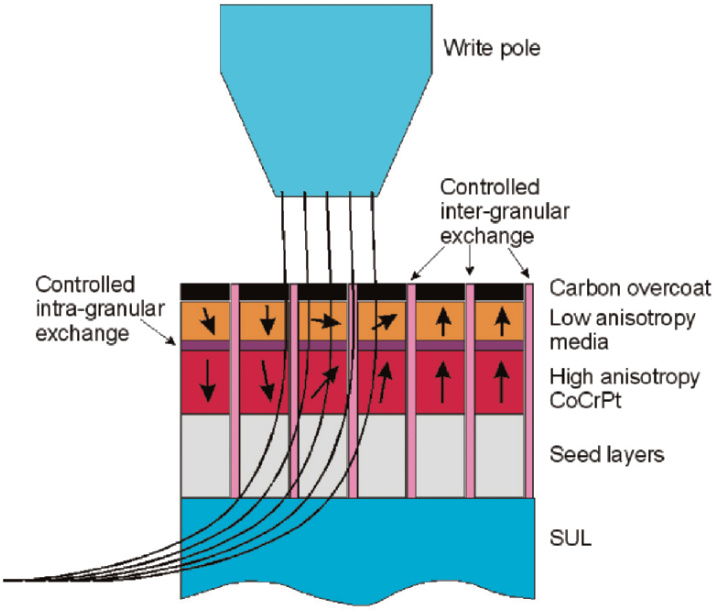

Figure 31. Schematic representation of exchange coupled composite (ECC) media

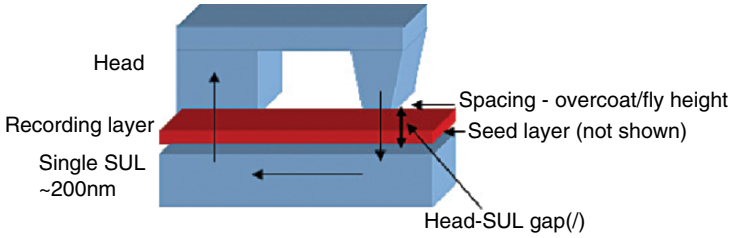

Figure 32. Magnetic circuit for asymmetric pole write head with head-SUL spacing *1*, and the medium recording layer directly in the magnetic circuit

bottom layer to form a single magnetic grain. Applying a field to this structure causes the spins in the top, low anisotropy, layer to *cant*, and increasing the field further then initiates reversal of the entire grain. Thus reversal can be considered as incoherent or as the propagation of a domain wall-like spin structure through the grain. Hence the medium, in response to an applied field, will switch at lower field values allowing the use of a higher anisotropy material in the bottom layer enhancing thermal stability without sacrificing writability. Engineering the spin structure during reversal offers a number of exciting possibilities to increase HDD densities beyond 500 Gbit/in^2 and is likely to make a significant impact to the extendibility of perpendicular recording.

An entirely new feature of a perpendicular medium is the soft underlayer. The SUL forms part of the write head circuit shown schematically in Fig. 32.

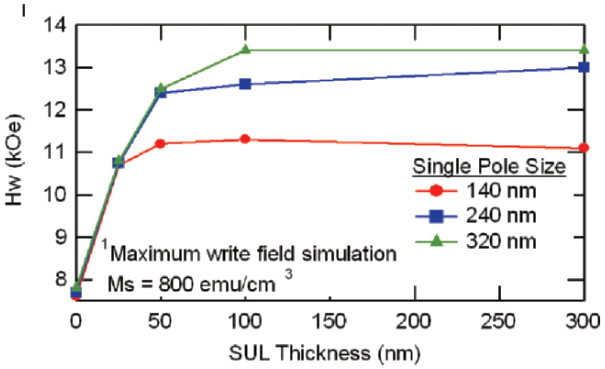

Figure 33. Calculation of the maximum field H_w as a function of SUL thickness for three head sizes with $M_s = 800\,\text{emu/cm}^3$. (From Schabes et al., 2002.)

Ideally, the SUL should be made of exactly the same material as the head since this will provide the greatest fields and field gradients at the medium. Hence a SUL with high M_s, high permeability, and low anisotropy is favoured. The SUL also needs to be capable of carrying all the flux from the writing pole to the return pole without saturating. This requirement places some limitations on the thickness of the SUL which are shown in Fig. 33 where the maximum write field at the recording layer is computed as a function of SUL thickness for various write pole dimensions (Schabes et al., 2002).

A further requirement on SULs is the elimination of domain structures. If a SUL has a domain structure then, by definition, domain walls are also present. A 180° Bloch domain wall gives rise to a large magnetic field perpendicular to the plane of the disc over the width of the wall. When a read sensor encounters such a domain wall it generates a large signal as the remanent magnetisation-thickness ($M_r t$) product of the SUL is much greater than that of the recording layer. This response is known as spike noise and degrades a recording system in an unacceptable way. A further complication that can arise is the formation of a strip domain pattern in the SUL as shown in Fig. 34 (Chang et al., 2002).

Here the periodicity of the strip domain pattern adds noise over a wide spectral range and again unacceptably degrades recording performance. In order to avoid these problems SULs typically have an AFM structure (similar to later generations of longitudinal media), shown in Fig. 35.

Typically SUL materials are FeCoB or CoZrNb which are deposited to induce a radial anisotropy with thicknesses similar to those shown in Fig. 35. These materials have proved successful in suppressing strip and spike noise associated with a domain structure and form the SUL used in the first generation of perpendicular media products.

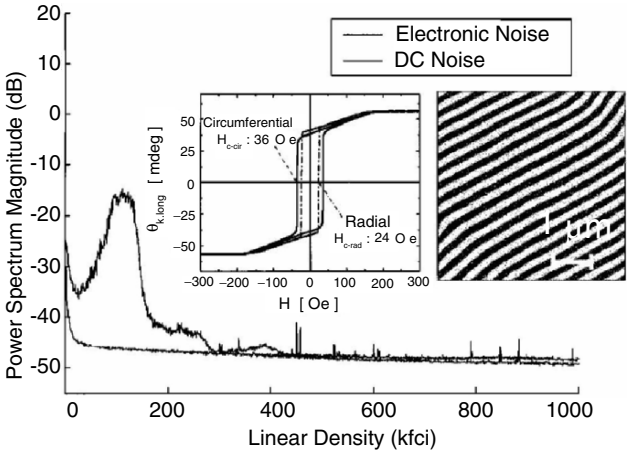

Figure 34. Hysteresis loops, MFM image, and DC noise (*upper*) and electronic noise floor (*lower*) power spectra for an as-deposited FeCoB SUL film. (From Chang et al., 2002.)

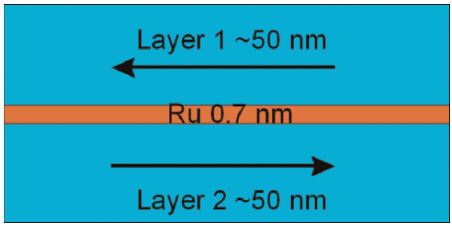

Figure 35. AFC structure for SUL

3.2. HEADS

Figure 27 shows the two elements of a HDD recording head: the write element responsible for creating magnetic bits and the read element used to sense the written bits. In perpendicular recording the read element is essentially the same as for longitudinal recording. The latest developments in GMR, TMR, and geometries where the current travels perpendicular to the GMR stack have already been described in the previous section on longitudinal recording and will not be repeated here. As already mentioned, the writer part of the head is quite different for a perpendicular recording system as is shown schematically in Fig. 36 and reviewed by Mallary (2001). In the previous discussion on the properties of SULs it was shown that unlike longitudinal recording, where the fringing field from a ring head is responsible for writing the medium, for perpendicular recording the head and SUL have to be considered as a single magnetic circuit. The material requirements for perpendicular write elements are very similar to those for longitudinal elements:

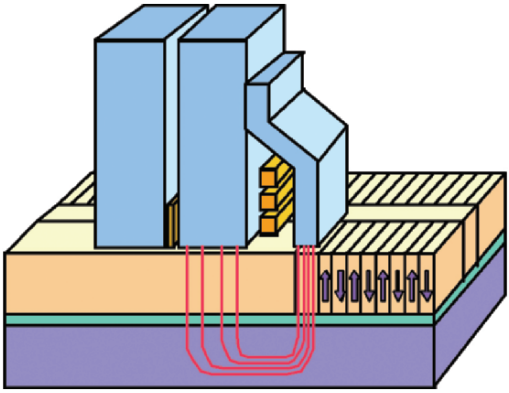

Figure 36. Asymmetric "single pole" write element for perpendicular magnetic recording. (Courtesy of Hitachi GST.)

- High saturation magnetisation – to obtain the highest possible deep gap field
- A large permeability over a wide frequency range to enable the head to write at the GHz data rates
- Very low anisotropy in order to minimise hysteretic losses and hence avoid excessive power consumption and heating of the element
- Mechanical and chemical stability both initially during high temperature fabrication, and also during the operating lifetime of HDD

and hence similar materials based on NiFe or CoFeB are used.

The design of the write pole is a critical feature and a number of requirements are placed on the design:

- Maximise field
- Maximise field gradient
- Allow head to write efficiently over a range of skew angles

The requirement for large fields is easily understood as it allows higher anisotropy material to be used and hence smaller grains of the material to be thermally stable since stability in determined $K_u V$ where K_u is the anisotropy and V the volume of the grain. High field gradients are also critical, since at a transition between bits we require that a grain on one side of the transition is reversed while its neighbour is not affected. This requires very particular pole geometries and shield designs that allow the field to be concentrated over small dimensions and allow field gradients of the order of 10's mT/nm to be realised. The main features of a perpendicular write head are shown in Fig. 37 (Mallary et al., 2002).

The design of the pole must also allow for a range of angles between the track on the disc and the head. This requirement arises from the voice coil motor

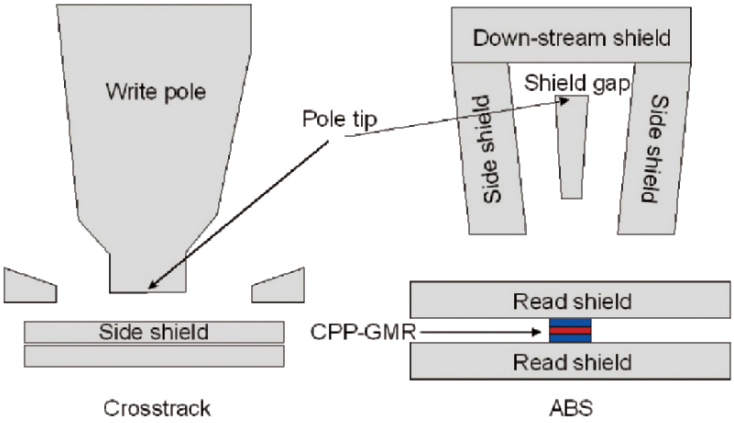

Figure 37. Cross-track and air bearing surface (ABS) views of a perpendicular write head. (after Mallary et al., 2002.)

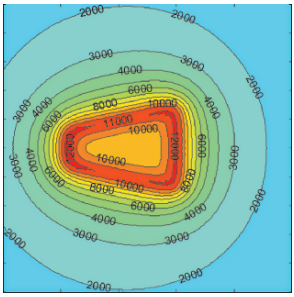

Figure 38. FEM simulation of the field directly below the writing pole of asymmetric perpendicular head (Olson)

(VCM) used to move the head over the disc's surface. The head actuator has a fixed pivot located near to the edge of the disc and the VCM moves the head in an arc across the disc surface giving rise to the range of head/track angles. In order to accomplish these goals, designers of write elements rely on sophisticated FEM. The field at the medium calculated by a FEM model is illustrated in Fig. 38.

The illustration in Fig. 38 shows the trapezoidal shape of the pole needed write over a range of angles relative to the track direction (Mallary et al., 2002; Mallary et al., 1987). The illustration also shows the high field gradients that can be obtained and the magnitude of the field below the pole centre in Oe. In order to continue increasing areal recording density, head designs will evolve. In terms of materials there is little prospect of increasing M_S beyond the $\backsim$1950 emu/cm^3 available from FeCo alloys and this limits the maximum field from write elements (Pan and Du, 2003). Therefore, the challenge will be to increase the field gradient and fabricate ever smaller write poles with close to zero remanence and more elaborate shield designs so that the number of tracks can continue to increase. The

latest laboratory demonstrations of 350 Gbit/in^2 were achieved with track widths of approximately 100 nm and minimum bit lengths close to 20 nm (Seagate 359 Gbit/in^2 demo-presented at TMRC, Pittsburgh 2006). The challenge of reducing these dimensions further in the push to achieve 1 Tbit/in^2 is formidable both for perpendicular recording and for the other potential schemes such as thermally assisted recording and patterned media outlined in the following section. However, the astonishing success of the HDD over the last 50 years suggests that, at least for some time the obstacles will continue to be overcome and storage capacities will continue to increase.

3.3. SIGNAL PROCESSING/DATA ENCODING

A hard disc drive using perpendicular recording can be equipped with a double-layered medium, consisting of a storage layer and a SUL, and also a shielded GMR reader (Sawaguchi et al., 2001). In this configuration, the GMR response to the magnetization pattern corresponds to a low-pass filtered waveform of the originally applied write current (Fig. 39) (Sawaguchi et al., 2001; Vasic, 2005). The response contains a DC component, but application of a differentiator after the GMR head will result in the generation of a voltage pulse for each magnetization transition (Wang and Taratorin, 1999).

The recording-channel properties for perpendicular recording can appear very similar to the longitudinal channel. Therefore, hard discs based on perpendicular

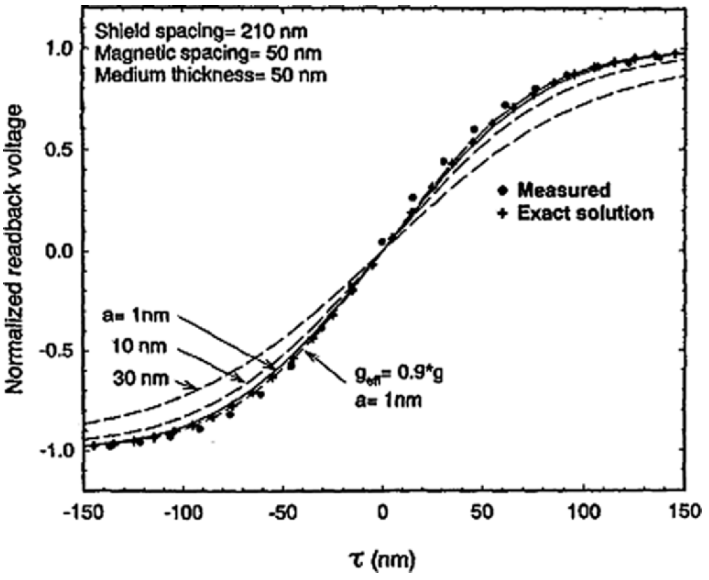

Figure 39. Magnetoresistive-head read signal taken at the position of a magnetization transition of a perpendicularly magnetized medium. (From Hoagland et al., 1998a.)

recording can be drawn up applying the same type of data-detection techniques, including PRML, and error correction electronics still available from conventional longitudinal recording (Tanaka, 2005).

3.4. INTERTRACK INTERFERENCE (ITI)

The introduction of perpendicular recording in HDDs is accompanied with increasing track densities and increasing side-reading, giving rise to a growing importance of the detrimental intertrack interference (ITI). The application of multi-track recording using multi-heads should result in a fixed phase relation between the bit positions in adjacent tracks, enabling the use of dedicated ITI-reduction methods (see for instance, Ahmed et al., 2002). However, in HDDs single recording heads are applied. Due to the minor changes of the HDD rotation velocity, the phases of bit positions in each adjacent track are completely random. Suitable techniques for suppression of the ITI effect of side reading can be found in Tan and Cruz (2005), Wu et al. (2003), and for the case of longitudinal recording in (Singla et al., 2005).

4. Future recording technologies

Looking into the future is quite a hazardous exercise. Still we would like to inform the reader of interesting developments, which may or may not, or at least not in this form, become part of state-of-the art mass storage devices. We restricted ourselves to mechanically addressed magnetic data storage. Many developments are currently in progress, and our selection is heavily baised on our own interest and expertise.

4.1. PATTERNED MEDIA

As was explained in the introduction (Section 1) and in Section 2.1.1, the ultimate limit in data density is determined by the thermal stability of the data. The relaxation time τ of the magnetisation state of a particle can be defined as

$$\tau = \frac{1}{f_0} \exp\left(\frac{\Delta E}{kT}\right) \tag{16}$$

Where ΔE is the energy barrier between the two states of magnetisation in the particle, and f_0 is the frequency at which the particle attempts to change its state. The attempt frequency is related to the Larmor frequency of the magnetisation, and usually taken to be 10^9 Hz. It should be noted that this frequency is material, and field dependent, but since the relaxation time is exponentially dependent on the energy barrier, that does not really matter at this point. The energy barrier is determined by the volume of the particle V, its magnetic anisotropy energy

density K and the switching mechanism. If we assume a (theoretical) coherent rotation mechanism, the energy barrier $\Delta E = KV$. Hard disc system designers are happy when the magnetisation of the bit drops less than 5% within the first 6 months, or approximately 10% after 10 years, which means that ΔE should be higher than 40 kT (Charap et al., 1997). Magnetic energy densities in the best materials known to us today (FePt in $L1_o$ phase, 6.6 MJ/m^3 (Willoughby et al., 2002) therefore limit the crystal grain size to approximately 3 nm for a stabity of 10 years.

A single bit in a polycrystalline recording medium has to be composed of a sufficient number of grains, because of SNR. By simple counting arguments, the SNR is approximately equal to the number of grains in the bit. For a 20 dB SNR, therefore about 100 grains are needed. Modern data detection and error coding techniques can work with lower SNRs, and it is foreseen that in the future one could work with values less than 10 dB, or 5 grains per bit. This will require very fast processors, and one has to add over 35% extra error correction bits (Wood, 2000).

Rather than pushing the data channels for lower and lower SNR, one could also consider the medium. If all grains were positioned at predefined locations, one can envision storing one bit per grain (Fig. 40). This the the concept of a patterned, or discrete, medium (White et al., 1997; Todorovic et al., 1997). Since the grains in the medium are usually defined lithographically, we prefer to call them dots, pillars or islands.

Now it would be naive to assume that the gain which can be made when moving from continuous to patterned media is a factor 5–100. Next to technological problems, there is the fact that a ΔE of 40 kT simply is not sufficient anymore. Just assume that 5% of the bits will have lost their magnetisation after 6 months! Channel coding usually can correct "raw" bit error rates of 10^{-4}. Sufficient thermal stability for patterned media therefore means that only one out of 10,000 dots is allowed to change its magnetisation. This can only be achieved if the energy barrier ΔE is larger than 49 kT, which means a τ of 50,000 years. The situation

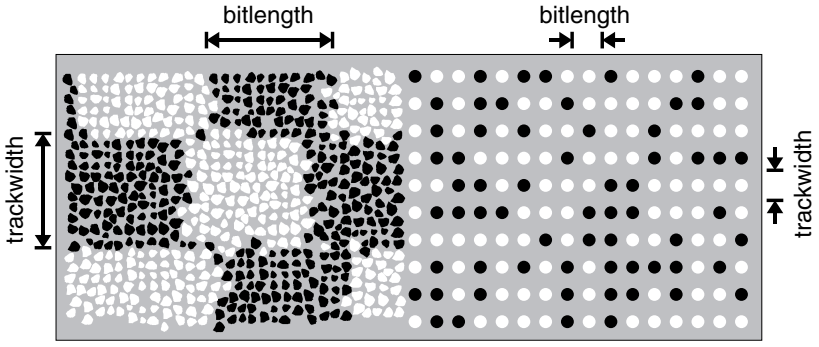

Figure 40. In discrete recording, 1 bit is written per magnetic element

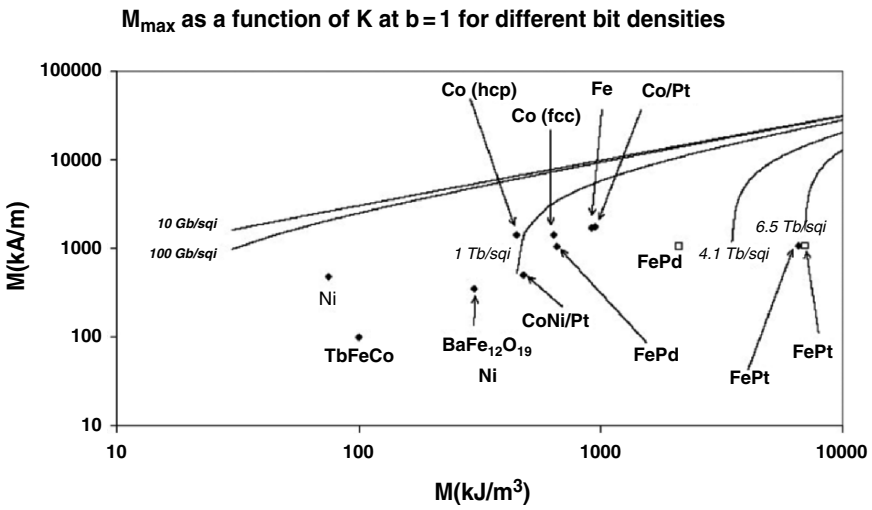

Figure 41. Theoretical upper limits on data density, as function of the saturation magnetisation M_s and anisotropy K

is complicated by the fact that the actual energy barrier of the dots is determined by the stray fields of the surrounding dots. Maximum attainable bit density is therefore a function of both the magnetic energy density in the dots, and the magnetisation. In general, one would like to have dots with a high energy density and low magnetisation. Careful analysis of stray fields and thermal stability results in graphs like Fig. 41 (Murillo-Vallejo, 2006). In this graph the maximum attainable bit density is plotted as a function of magnetisation and energy density. Also shown are various materials found in literature. With the best materials known today, the ultimate density[5] is in the order of 7 TBit/in^2.

An excellent overview of patterned media fabrication techniques can be found in (Terris and Thomson, 2005; Lodder, 2004), and the over 200 references cited therein. In short, there are three main methods to pattern the magnetic film into dots. The fastest method is to locally modify or remove the magnetic layer with a focused ion beam (Fig. 42a). In this way only very small areas can be patterned, and the method is not suitable for mass production. For research purposes the method is applied with great succes, an example is shown in Fig. 43.

The second method is to use high-resolution lithography to pattern a photoresist on the top of the magnetic layer (Fig. 42b), and subsequently modify or remove the exposed magnetic film with an ion beam etch. The resolution of the technique of course depends on the quality of the lithographic step, and is in principle suitable for mass production using for instance nanoimprint techniques.

[5] Which I would like to nickname the "Murillo limit on magnetic data storage", after its proposer. (LA)

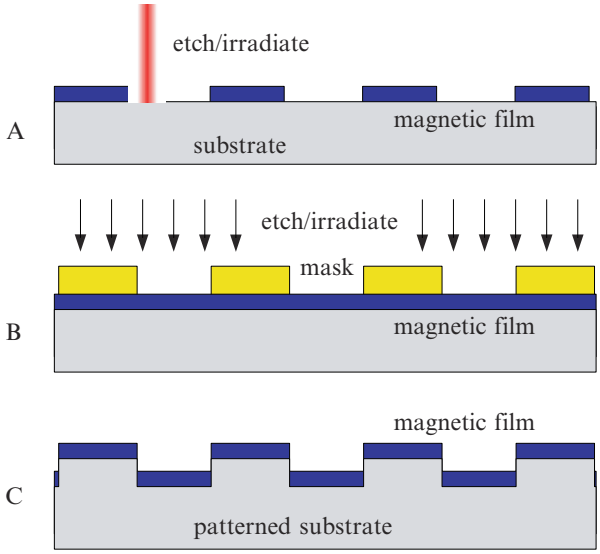

Figure 42. Different routes to pattern magnetic films

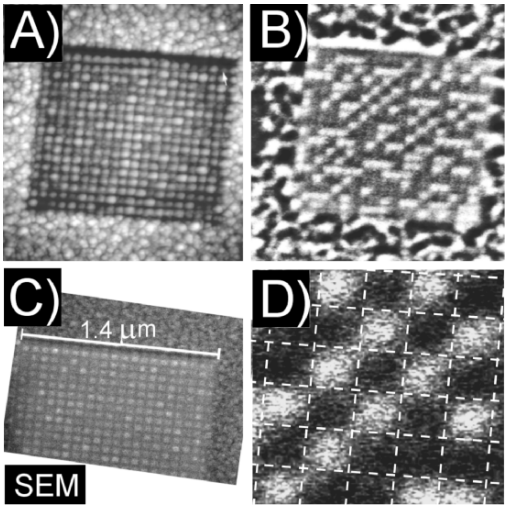

Figure 43. Images of a 1.4×1.2 µm patterned region with a period of ~67 nm. This was patterned by exposure to a 1 pA 30 keV Ga+ beam for 40 s. (A) AFM and (B) MFM images of the same area. (C) portion of an SEM image taken immediately after patterning. (D) Higher magnification MFM image. The dashed line grid has been added as a guide to the eye

In this method a master stamp is realized by e-beam lithography, which is replicated into "daughters" and "sons" in a method similar to the one used in DVD production. The replicas are then used to imprint a thin polymer layer which is spinned on top of the magnetic layer (Fig. 44).

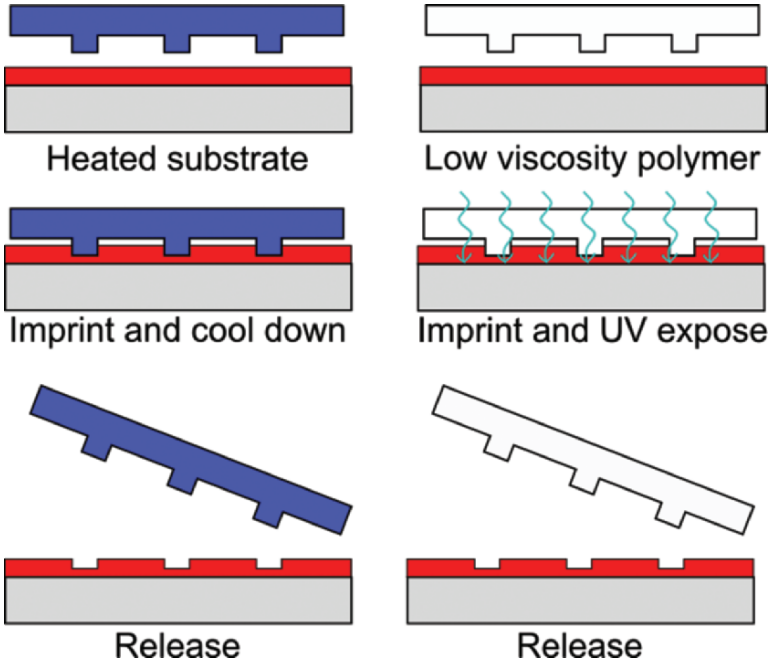

Figure 44. Nano-imprint could be a route to mass production

In general, it is difficult to etch metal films with dry etching techniques. This is especially true for delicate magnetic materials, which are susceptible to oxidation and etch damage. Ion beam etching might cause hardening of the resist and redeposition of etched material. As a result, resist removal becomes very difficult, especially since harsh techniques like plasma oxidation cannot be used because they damage the magnetic layer. Therefore methods where the magnetic film is deposited on a pre-patterned substrate have a big advantage (Fig. 42c). Oblique deposition can be used to magnetically isolate the material in the valleys from the material on top (Landis et al., 2004). An example of such medium is given in Fig. 45.

Patterned media will become interesting when the current technology of polycrystalline media runs out of steam. Since perpendicular media will support areal densities of >500 Gbit/in^2, the first possible use of patterned media will be at densities in excess of 1 Tbit/in^2. The creation patterned media at 1 Tbit/in^2 demands lithography processes with periods less than 25 nm in at least one direction. This is a very small dot periodicity, even for e-beam lithography. Therefore self-assembly techniques are suggested as possible routes to realise media. These techniques are discussed in Section 4.3.

Next to the issue of manufacturability, the second main obstacle in the application of patterned media is the uniformity in the dots. Due to non-uniformities

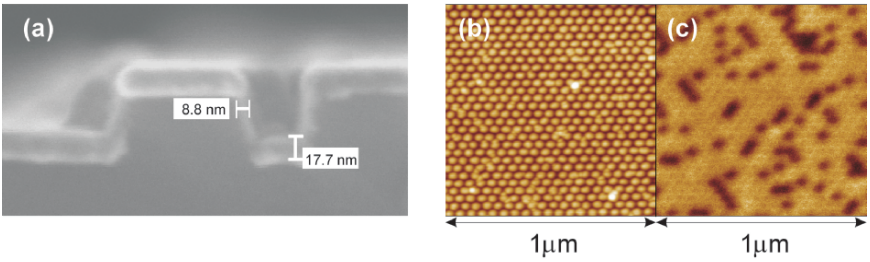

Figure 45. (a) SEM image of lines (100-nm wide) covered by a multilayer of SiO_2/50Å Pd/(3Å Co/8Å Pd)$_{\times 10}$/10Å Pd. (b) AFM image of a 30-nm island array with 60-nm periodicity; (c) MFM image of the same array after ac demagnetization (After Terris et al. 2005b)

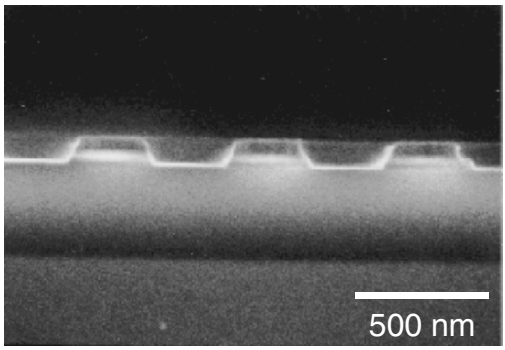

Figure 46. CoNi/Pt multilayered magnetic elements prepared by Laser Interference Lithography with a dot distance of 300 nm. In this image, the resist is still present on the dots, the thin white line is the CoNi/Pt multilayer

in the magnetic layer, the etching process or dot dimensions, every single dot will have a slightly different switching field.

The switching field distribution can be succesfully studied by MFM. As an example, in the authors lab,[6] patterned media are prepared using method b in Fig. 42 using Laser Interference Lithography (LIL) to pattern the resist layer (Vallejo et al., 2006). The magnetic layer is a CoNi/Pt multilayer, which has perpendicular magnetisation from the interface anisotropy between the CoNi and Pt layers. A cross section on a sample with 500 nm distance between the dots is shown in Fig. 46. The LIL technique allows us to go down to 150 nm.

Using in-field Magnetic Force Microscopy (MFM), the array is imaged as a function of the applied field. A measurement at 136 kA/m is shown in Fig. 47. By taking images at various field values, the switching field of the individual dots can be determined. A faster method is to stop the slow scan direction, and image the magnetisation state of a row of dots under increasing field values. This

[6] MESA + Research Institute

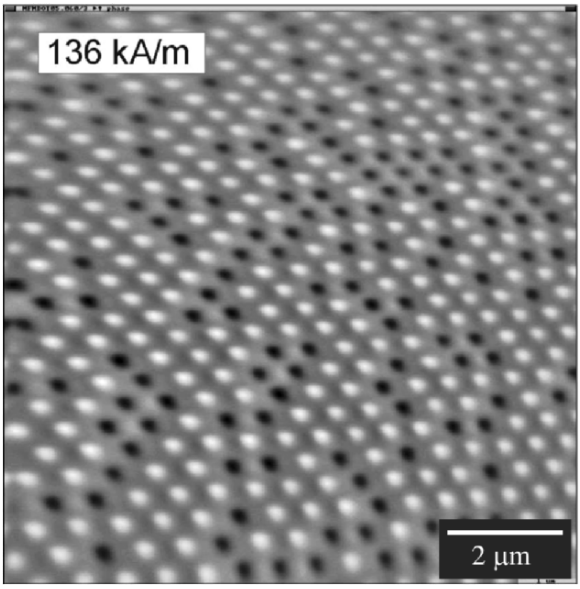

Figure 47. MFM image of patterned medium prepared by Laser Interference Lithography

measurement is shown in Fig. 48. As can be seen, the variation in switching field of neighbouring dots is quite substantial compared to the average switching field. In hard disc recording, this will cause a problem since the trailing fields extend over a certain range, and vary in angle. The field strength of the head has to be adjusted to the dot with the highest switching field. The situation might then occur that a previously written dot with a very low switching field is overwritten. In magnetic probe recording using MFM tips the situation is even worse. Since the field of the MFM tip is low, a background field has to be applied. If the distribution in switching fields between the dots is larger than the field of the MFM tip, the background field will have to be so high that it erases the dots with the lowest switching field.

The reason for the large switching field distribution is unknown. However, several causes can be ruled out. Stray field interaction from neighbouring dots by itself is not sufficient to explain such a large distribution. Calculations indicate that for the dot spacing used, the stray field is at most 7 kA/m. Thermal fluctuations are small for the dot volumes used, and moreover the switching fields are reproducable: the weakest dots always switch first. Etch damage could be a cause of reduction in switching field, but than it is difficult to explain why this damage differs so much for neighbouring dots. So remaining causes will have to do with irregularities in the dots themselves. This could be caused by irregularities in the resist profile, which are transferred into the magnetic material by etching, or in the material of the dots. The latter seems to be the most likely candidate. It is naive

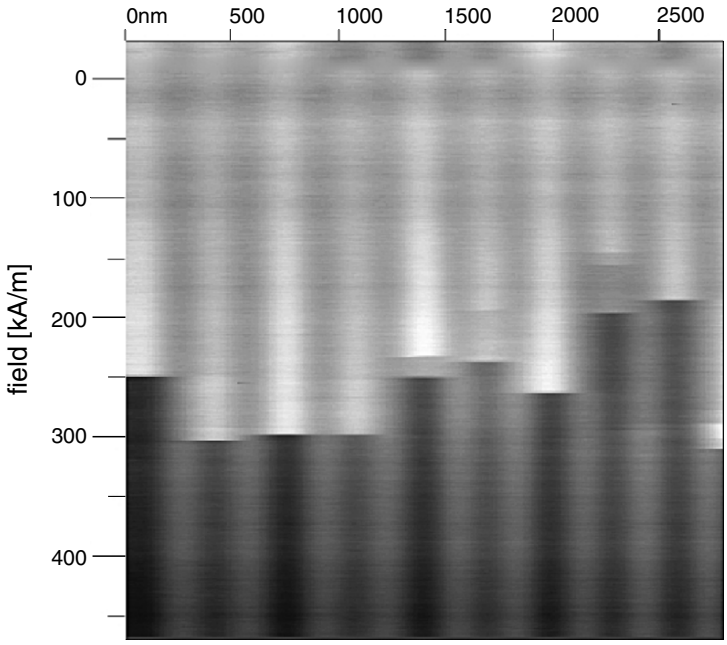

Figure 48. MFM measurement of the reversal of 9 dots as a function of the applied field

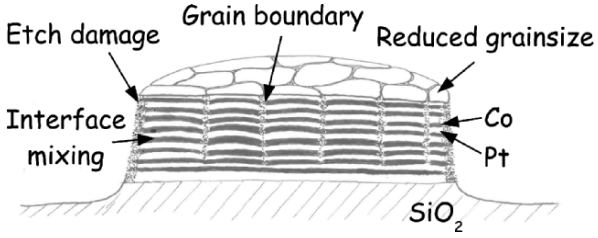

Figure 49. Schematic illustration of non-uniformities in patterned magnetic elements

to assume that dots will be identical when patterning a polycrystalline material with grains in the order of 10 nm into 70 nm dots. The image which emerges is displayed in the cartoon of Fig. 49. Each dot will contain irregularities like a different number of grains, grains cut in half, differences in grain boundaries, etc. So one pre-requisite for low switching field distribution will be to start from an as homogeneous material as possible, preferably an epitaxially grown single crystal film. Whether this is commercially applicable is questionable.

4.1.1. *Two-dimensional intersymbol interference (2D ISI)*

Essentially, the patterned medium consists of a 2D arrangement of rows and columns of magnetized dots (islands) where each dot represents one single data bit. The phenomenon of crosstalk during reading will show itself in both

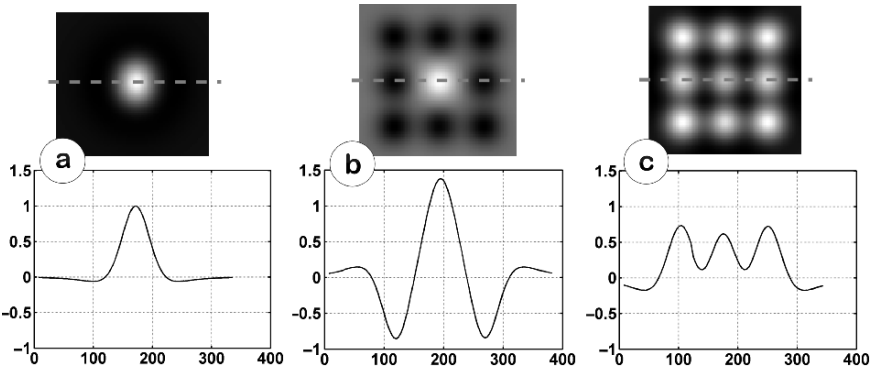

Figure 50. Three configurations of computed magnetic dots scanned by MFM probe (*upper*); Simulated MFM-probe read signals scanned along the dotted lines (*lower*). The x-axes are in nanometers. (a) single bit, (b) "one" bit surrounded by 8 "zero" bits, (c) 9 "one" bits.

directions, and can be taken as a combination of the conventional intersymbol interference (ISI) along the rows, and the so-called ITI along the columns. The difference with continuous media is the occurrence of a predetermined phase relation between the tracks, which can be exploited. In order to combat ITI, extensions of traditional one-dimensional (1D) channel coding and detection methods have been proposed (Ntokas et al., 2005; Vasic, 2005), including RLL codes for two-track systems, 2D partial-response ML, and the application of turbo coding.

Figure 50 displays the simulated read signals of perpendicularly magnetized dots in a patterned medium. The waveforms are typical for both GMR and MFM read-head technologies, in combination with a recording medium with SUL. As a result of 2D ISI, the amplitude of a bit (dot) surrounded by 8 identical bits (Fig. 50c) is seen to be relatively low, and in view of bit-detection reliability such a bit combination can be considered to be a "worst case" pattern.

A simple method to avoid such worst-case patterns when recording using a patterned medium is the application of a geometric 2D channel code. An example of such a code is shown in Fig. 51 where particular bit positions are occupied by fixed bit values (1 of 0), leaving the remaining positions for recording of user bits. This scheme stops the square 9-bit combination of Figure 50c (9 "ones", or 9 "zeros") to occur. Obviously, this coding scheme results in a code rate 7/9 (or redundancy 22%).

The benefit of the introduction of such a fixed bit pattern on bit detection was analysed using a computer simulation programme. This programme incorporates 2D ISI and offers, among other things, facilities for simulation of bit-position jitter. After computation of the read signal for a serpentine scanning trajectory (indicated in Fig. 51), the data bit sequence was reconstructed. Figure 52 shows the number of detection errors in a sequence of 15,876 bits as a function of the

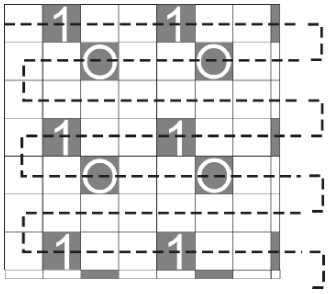

Figure 51. 2D channel code with geometric constraint (fixed "1" and "0" bits) imposed to 2D bit patterns. The empty positions are available for recording of user-data bits

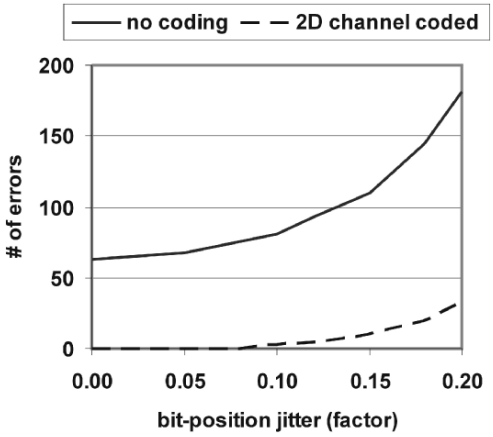

Figure 52. Impact of 2D channel code on bit-detection performance

magnitude of uniformly distributed bit-position jitter. Here the elementary read pulse was taken with a relatively large 16% overshoot in order to investigate the effect of the introduction of the 2D channel code of Fig. 51.

For non-coded data and low jitter levels we found the bit errors generally to occur on medium locations corresponding with the bit pattern of Fig. 50c, i.e. a block of nine (or more) identical bit values. Introduction of the 2D code eliminated this class of errors (Fig. 52). Increasing the jitter magnitude above factor 0.1 resulted in new errors at locations of bits which are surrounded by both "one" and "zero" bits. However, the plotted curves in Fig. 52 suggest that the 2D channel code only modestly combats this second error category.

The code method as depicted in Fig. 51 does not require complicated signal processing. It can be considered as a "brute force" approach, because it claims redundant bit positions on the medium, which are located on fixed positions not correlated to local data content. More research is required for the development of more efficient coding methods in view of the required immunity to 2D ISI and (other) noise effects.

4.2. THERMALLY ASSISTED RECORDING

Thermally assisted recording is considered as one potential method of extending magnetic recording to 1 Tbit/in^2 and beyond. It is currently assumed that perpendicular recording is extendable to between 500 Gbit/in^2 and 1 Tbit/in^2 at which point further grain size reductions will lead to unacceptable thermal activation and bit corruption. Thermally assisted recording, which is also referred to as heat assisted magnetic recording (HAMR) has been reviewed by Mcdaniel et al. (2003); McDaniel, (2005) and Rottmayer et al. (2006). Thermally assisted recording (TAR), as its name implies, requires local heating of the media during the writing process as shown schematically in Fig. 53 where optical power provides the heating.

This heating reduces the anisotropy, and hence coercivity, of the medium locally allowing the magnetisation to be reversed while at elevated temperatures. At all other times, the high anisotropy of the medium protects grains from thermal activation since, as already discussed in the section on longitudinal recording, the energy barrier is related to $K_u V$. Simply put, increasing K_u allows V to be decreased and by lowering K_{u} during writing the medium is still addressable with the available head fields. Following writing, the bit must rapidly return to ambient temperature to prevent significant thermal activation in the grains of the just recorded bit. Figure 54 demonstrates the principle of thermally assisting writing of media and how heating changes coercivity allowing the medium to be reversed by the head field.

At this point, we need to understand the potential gains available from a thermally assisted recording system and to define more precisely what we mean by local heating of the medium. Ruigrok et al., (2000), Ruigrok (2001) made an estimate of potential gain in areal density (AD) from a thermal assisted recording system with a simplified calculation comparing thermal activation of a heated medium with that of same medium at room temperature, Eq. 17.

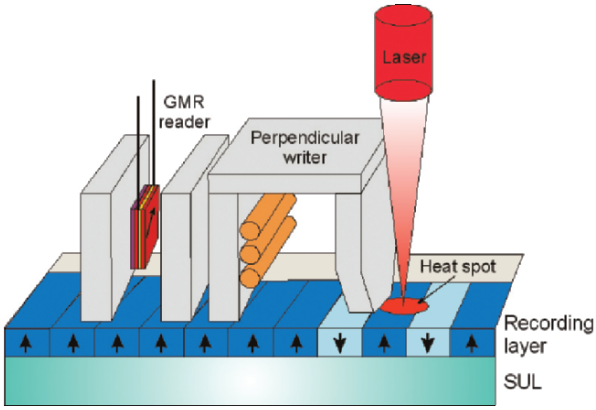

Figure 53. Schematic diagram of head and media for perpendicular thermally assisted recording

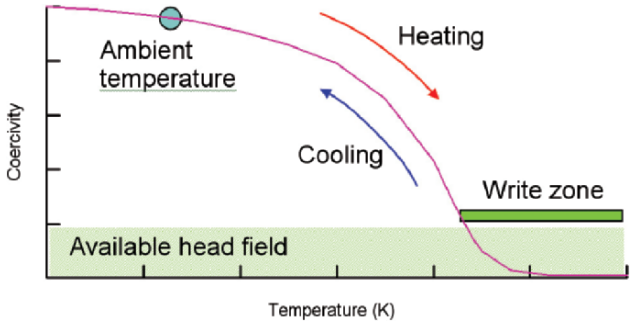

Figure 54. Principal of thermally assisted writing of a medium. (after Rottmayer et al., 2006)

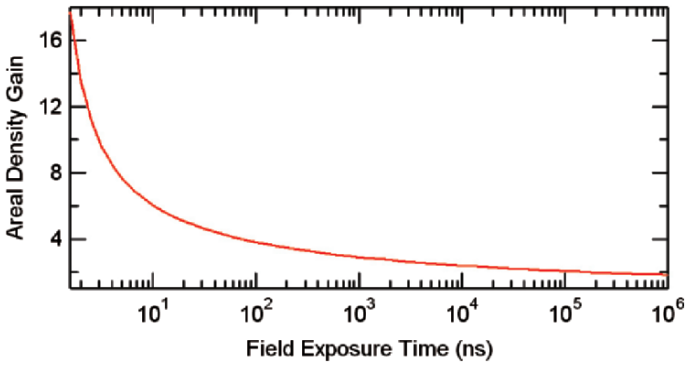

Figure 55. Results from a simplified calculation of potential areal density gain (D_{tar}/D_{con}) for thermally assisted recording using the method of Ruigrok. (From Ruigrok et al., 2000; Ruigrok, 2001.)

$$\frac{D_{\text{tar}}}{D_{\text{con}}} = \left[\left(\frac{T_{\text{amb}}}{T_w}\right)\left(\frac{K_{\text{u}}V_{\text{amb}}}{kV_{\text{amb}}}\right) / \ln\left(\frac{t_w}{\tau_0}\right)\right]^{2/3} \tag{17}$$

where the subscripts w and amb refer to the elevated write temperature and ambient temperature. $D_{\text{tar}}/D_{\text{con}}$ is the AD gain for the thermally assisted medium, K_{u} is the ambient temperature unaxial anisotropy, V is the volume, k is the Boltzmann constant, τ_0 is the reversal attempt time (here taken to be 1×10^{-9} s) and t_w is the time spent at elevated temperature. Taking parameters appropriate for a very high anisotropy medium based on FePt in the $L1_0$ ordered phase and $t_w = 550$ K we can see how the AD gain reduces as the exposure time to elevated temperature increases.

Figure 55 immediately shows two important points. Firstly, heating with a large spot which in this context means a spot greater than the track width provides little AD advantage. The reason for this is quite straightforward, if the area heated during a write cycle exceeds the track width, then the track in question will experience a temperature rise whenever adjacent tracks are written increasing the

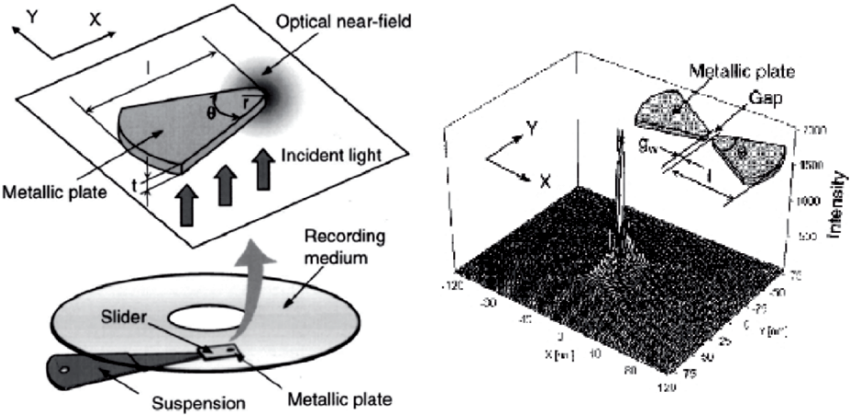

Figure 56. (a) Schematic of a wedge shaped, metallic, near-field optical probe mounted on a HDD slider (b) simulated intensity distribution showing strong enhancement of the optical near-field generated around two metallic plates at a plane 2 nm from the surface. (From Matsumoto et al., 2004.)

probability of thermal activation and bit erasure. Allowing for elevated temperature exposures of 10^2–10^6 ns, due to adjacent track writing, it is apparent that only a small AD gain can be achieved. Figure 55 also shows a potential gain of close to an order of magnitude is possible for a sufficiently confined heat spot. An estimate of heated spot dimensions can now be made, assuming an AD of 1 Tbit/in^2 and a bit aspect ratio of 4:1, an individual bit will need to be 50.8 nm × 12.7 nm so here the track width and hence the spot size will need to be 50 nm. Delivering sufficient power, over these dimensions, in a sufficiently short time to heat the medium by $\backsim$250 K is a formidable challenge.

One possible way of meeting this challenge is to use near-field optics. Recently, it has been discovered that significant enhancements in efficiency can be achieved using near field sources (Shi et al., 2003; Challener et al., 2003; Matsumoto et al., 2004; Jin and Xu, 2005; Matteo et al., 2004). One such source is the bow-tie antenna, similar to wedge-shaped plates shown in Fig. 56b (Matsumoto et al., 2004), where (a) a schematic diagram of a wedge shaped plate mount on the suspension of a HDD with the incident light perpendicular to the plane of the wedge with an intensity enhancement shown at the apex. Figure 56b shows a simulation of the enhancement of the intensity in the gap between two wedge-shaped plates. The simulation assumed that the shape of the metallic silver plates was a sector with gap between the plates $g_w = 5$ nm, apex radius $r = 20$ nm, wedge length $l = 200$ nm, thickness $t = 30$ nm and apex angle $\theta = 60°$. The wavelength of the illumination was taken as 830 nm. A different geometry that has been explored for near-field optical enhancement in thermally assisted recording is the c-aperture (McDaniel, 2005; Jin and Xu, 2005; Matteo et al., 2004) shown in Fig. 57 (McDaniel, 2005). As with the wedge shaped

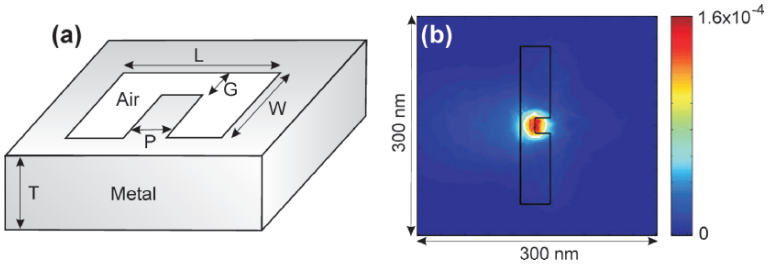

Figure 57. (a) c-aperture for confinement of near-field optical power. (From Mcdaniel, 2005), (b) simulation of a far field focused beam irradiating the top of a waveguide structure with optimised parameters. The computation shows the electromagnetic field emerging below the gap G has characteristic width of ∼31 nm.

structures this geometry shows a strong near field enhancement of intensity. The challenge facing all of these structures is to provide spatial resolution of the order of 50 nm and sufficient intensity to significantly raise the temperature of the medium (McDaniel, 2005).

If we assume that optical confinement capable of delivering sufficient power over very small regions can be achieved, then thermal assisted recording has the potential to create write field gradients that are greater than those available from the head alone, allowing sharper transitions to be written (Thiele et al., 2002; Erden et al., 2005). This enhancement in field gradients arises because the thermal gradient adds to the field gradient

$$\frac{dH_{\text{eff}}}{dx} = \frac{dH_w}{dx} + \frac{dH_k}{dT}\frac{dT}{dx} \tag{18}$$

where dH_{eff}/dx is the total effective gradient, H_w is the normal head field and H_k is the anisotropy field. Hence not only will a well-confined heat spot ensure that adjacent tracks are not erased but will provide extra field gradient compared to a conventional magnetic head. In order to obtain a sharp thermal gradient not only does the delivery of energy to the medium need to be considered, but also its subsequent removal. Incorporating a heat sink into the structure of the medium, as part of the SUL or as a non-magnetic layer allows extremely fast cooling due to vertical heat diffusion. Rottmayer et al. (2006) reported pump-probe reflectivity measurements using a femto-second laser for the medium shown in Fig. 58a for three different interlayer (IL) materials of the same thickness.

The data in Fig. 58b show that the cooling rate of a medium can be significantly changed depending on the choice of IL material as the measured cooling times vary from 100s of ps for IL3 to ns for IL1. Figure 59 shows a simulation of the head field, temperature and medium coercivity needed for successfully writing in a TAR system with a granular medium (Akagi et al., 2004).

As the temperature increases the effective switching field of the medium (H_{ce}) decreases at the trailing edge of the head field (H_h). A transition is created where

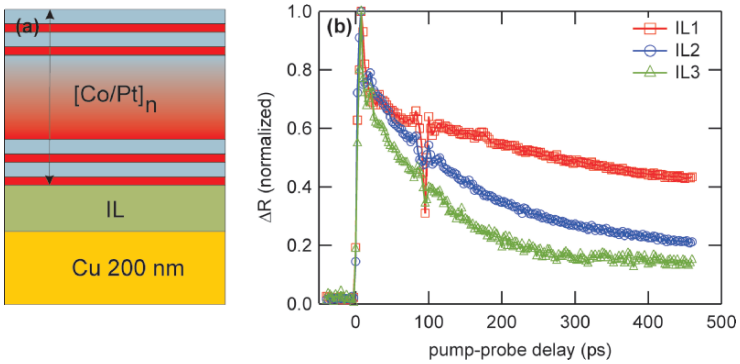

Figure 58. (a) Structure for thermal management of a perpendicular thermally assisted recording medium, (b) thermal decay in a medium with a Cu underlayer and different interlayers (IL) materials, measured by the change in reflectivity (ΔR) using a laser pump-probe technique. (Redrawn from Rottmayer et al., 2006.)

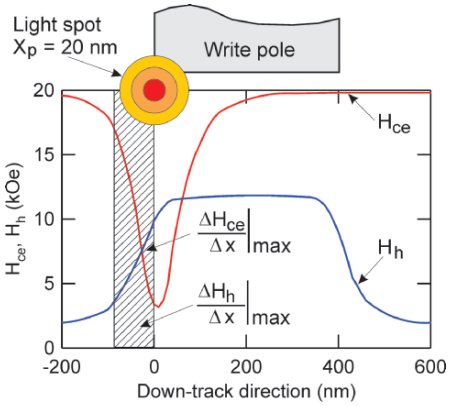

Figure 59. Simulation of the synchronisation of the temperature pulse with the reduction in effective switching field (H_{ce}) and head field (H_h) for a thermal assisted recording system. (Redrawn from Akagi et al., 2004.)

the thermal gradient, and the head-field gradient simultaneously obtain maximum values. Given that this all has to take place in the nanosecond time frame it is clear that designing a head capable of meeting these exacting requirements is a formidable task.

The medium for TAR must have all the properties previously described for longitudinal and perpendicular recording, e.g. small isolated grains, narrow distributions, etc. In addition the medium must have very high anisotropy at ambient temperature, have the appropriate changes in magnetic properties with temperature and be capable of essentially infinite temperature cycling. Figure 60a shows how the anisotropy of ordered FePt in the $L1_0$ phase changes with temperature (Thiele et al., 2002).

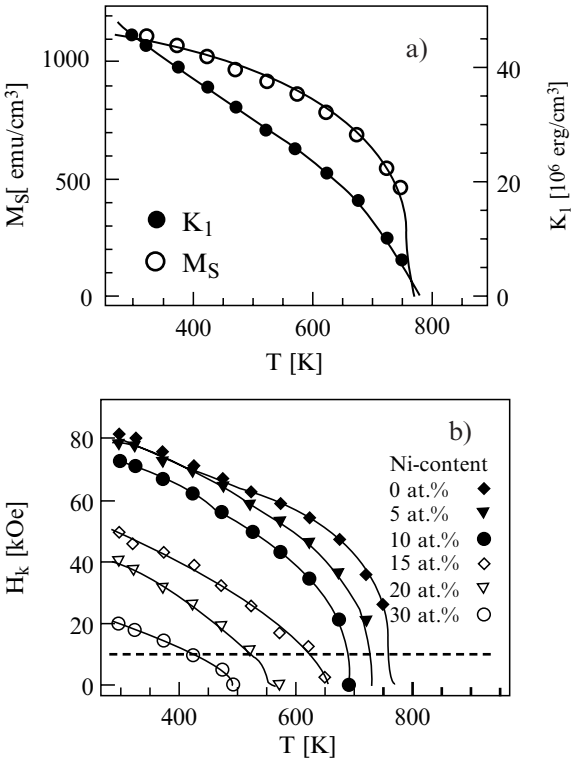

Figure 60. (a) Variation of M_s and anisotropy constant K_1 as a function of temperature for a sputtered $L1_0Fe_{55}Pt_{45}$ thin film, (b) temperature dependence of the anisotropy field, $H_k = K_1/M_s$, for the series of $Fe_{55-x}Ni_xPt_{45}$ films ($x < 30$ at. %). The solid lines are guide lines to the eye. A head field of 1 T is indicated by the horizontal dashed line. (From Thiele et al., 2002.)

This is one potential media choice whose properties can be tailored by including Ni as shown in Fig. 60b (Thiele et al., 2002). The challenge with this media, as with all media, is to produce a sufficiently refined grain structure, grain isolation and the required magnetic properties.

Another potential media path involves using a material that changes magnetic phase with temperature. FeRh is unusual in that it is an AFM below room temperature and a FM above 350 K, Fig. 61 (Kouval and Hartelius, 1962).

Thiele et al. (2003) showed that by creating a AFM/FM bilayer structure using FeRh/FePt it is possible to engineer a thin film with magnetic properties that change dramatically with temperature, Fig. 62.

In conventional media increasing the temperature decreases both saturation magnetisation and anisotropy. In the AFM/FM structure saturation magnetisation increases as anisotropy decreases so that during the writing process the medium has high magnetisation and low anisotropy whilst at all other times the medium has high anisotropy and low magnetisation. Low magnetisation

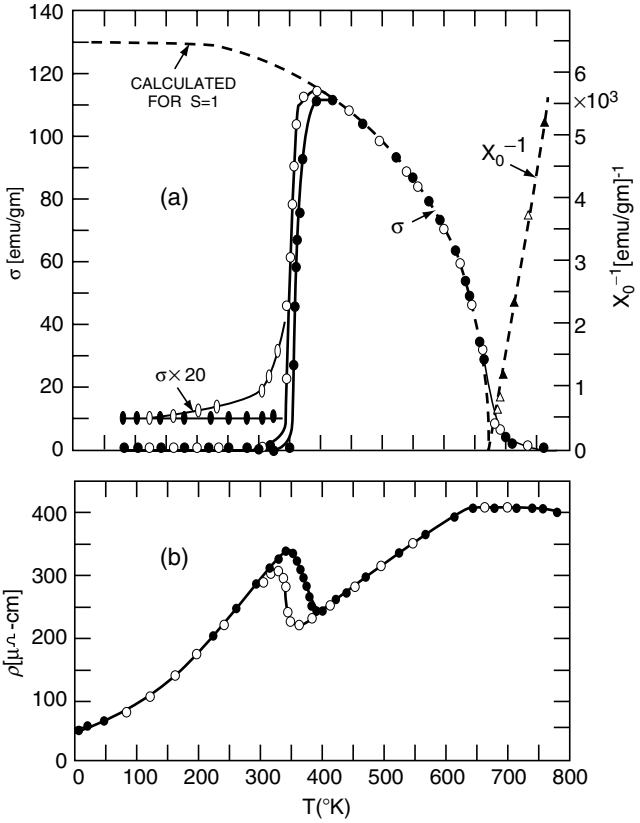

Figure 61. (a) Magnetisation measured at 0.5 T and inverse initial susceptibility as a function of temperature for an induction melted ingot of $Fe_{48}Rh_{52}$, (b) electrical resistivity for increasing temperature (*closed circles*) and decreasing temperature (*open circles*). (From Kouval and Hartelius, 1962.)

reduces demagnetisation effects improving stability. However, a finite remanent magnetisation is required to provide a signal to the read sensor and this can be tailored by adjusting the thickness and composition of the AFM/FM films.

One final requirement of a medium for thermally assisted recording is that of head-disc interface. In thermally assisted recording, constant temperature cycling creates new failure mechanisms where the disc lubricant can degrade, the probability of media delamination is enhanced and surface cracking of head and medium is a possibility. The tribology of thermal-assisted recording has been modelled by Peng et al. (2005) the results of which are used to predict an optimal head-disc interface design.

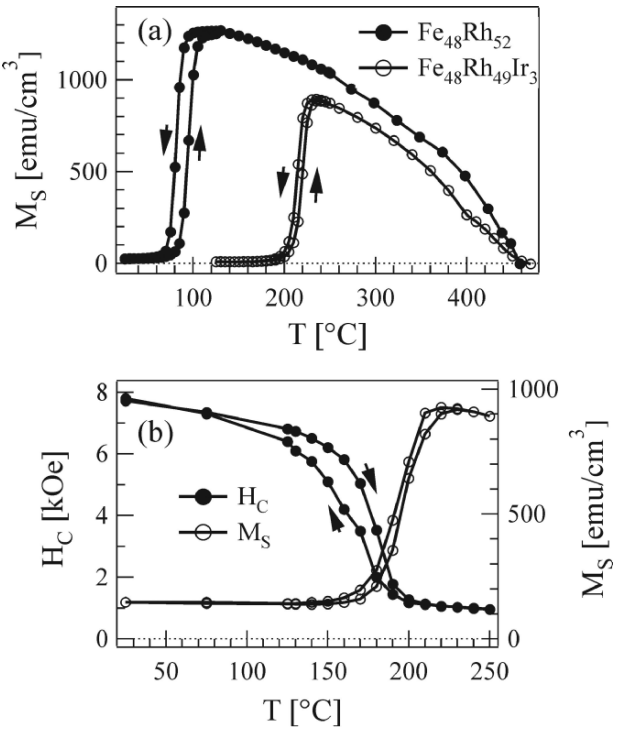

Figure 62. (a) Temperature dependence of the saturation magnetization 70 nm thick single layer $Fe_{48}Rh_{52}$ and $Fe_{48}Rh_{52}Ir_3$ films grown on MgO(100) substrates. (b) Temperature dependence of coercivity and saturation magnetization upon heating and successive cooling of a FePt(25 nm)/$Fe_{48}Rh_{52}Ir_3$ (125 nm) bilayer grown on a SiN coated Si wafer. (From Thiele et al., 2003.)

4.3. NON-CONVENTIONAL MEDIA (NANOPARTICLES)

A number of potential approaches to creating media capable of supporting $>1\,\mathrm{Tbit/in^2}$ recording have been reviewed recently by Terris and Thomson (2005). Of these schemes media based on self-assembled arrays of high anisotropy magnetic nanoparticles has received the most attention. Sun et al. (2000) first demonstrated that FePt nanoparticle assemblies with particles diameters as small as 4 mm and an extremely narrow distribution of sizes (<5%) could be obtained, Fig. 63. FePt is attractive as a nanoparticle recording material (Sun et al., 2001; Harrell et al., 2001; Kodama et al., 2003; Stahl et al., 2003; Christodoulides et al., 2003) since, in the $L1_0$ phase, it is one of a relatively rare class of materials (Weller et al., 2000) that have sufficient magnetocrystalline anisotropy ($K_1 = 7\,\mathrm{MJ/m^3}$, $M_s = 1140\,\mathrm{kA/m}$) to remain magnetically stable at room temperature with diameters of less than 4 nm, i.e. it avoids the effects of superparamagnetism.

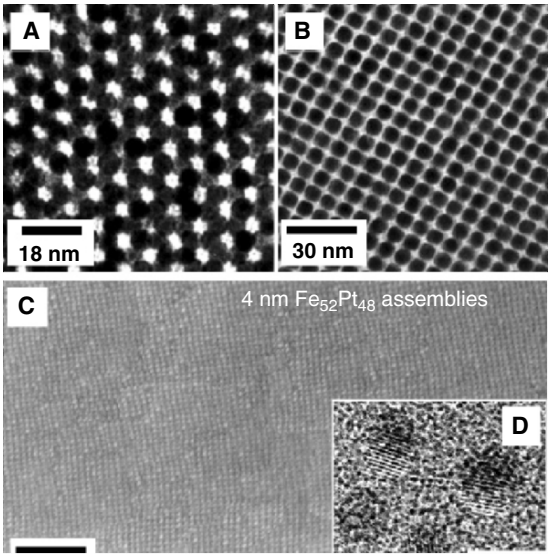

Figure 63. (a) TEM image of a 3D assembly of as deposited 6 nm $Fe_{50}Pt_{50}$ particles, (b) TEM image of as-deposited 6 nm $Fe_{50}Pt_{50}$ particles after replacement of oleic acid/oleyl amine with hexanoic acid/hexylamine, (c) high resistance TEM image of a 180 nm thick, 4 nm $Fe_{52}Pt_{48}$ nanoparticle assembly annealed at 560° C for 30 mins under 1 atm of N_2 gas, (d) high resistance TEM image of 4 nm $Fe_{52}Pt_{48}$ nanoparticles annealed at 560° C for 30 mins on a SiO coated copper grid. (From Sun et al., 2000.)

However, the use FePt nanoparticles as a recording medium presents significant problems many of which remain to be overcome. Obtaining solutions to the difficulties associated with FePt nanoparticles is an active area of research. FePt nanoparticles are typically made using a solution chemistry and arrested precipitation approach, described in detail by Sun et al. (2002, 2003a) and Hyeon (2003) which results in a solution containing particles coated with a surfactant, Fig. 64.

The particles are subsequently deposited on to a substrate by dipping or coating. The surfactant and functionalization of the substrate (Sun et al., 2002) then work under appropriate conditions to form self-assembled layers, Fig. 65.

The particles deposited using this method are nominally in a disordered fcc crystallographic phase and are oriented at random. To use these materials as a recording medium the crystallographic phase must be changed to the high anisotropy $L1_0$ phase. In addition it is highly desirable that the ordered particles have a common magnetic easy axis. The $L1_0$ phase can be created by annealing. However, temperatures in excess of 600° C are required before any significant phase transformation occurs and this leads to particle agglomeration and sintering (Dai et al., 2001; Ding et al., 2003; Klemmer et al., 2003; Thomson et al.,

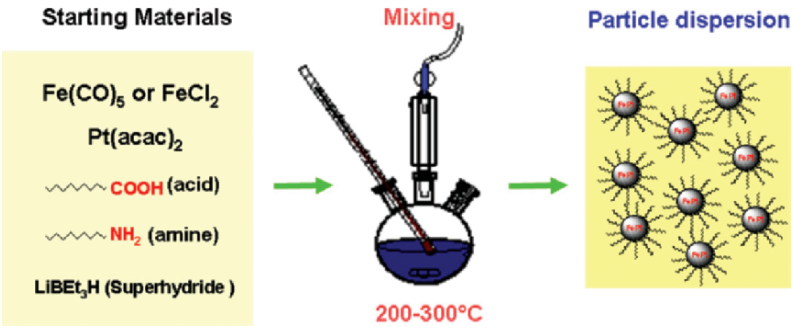

Figure 64. Making surfactant coated FePt nanoparticles using a solution chemistry approach. (From Sun et al., 2003a.)

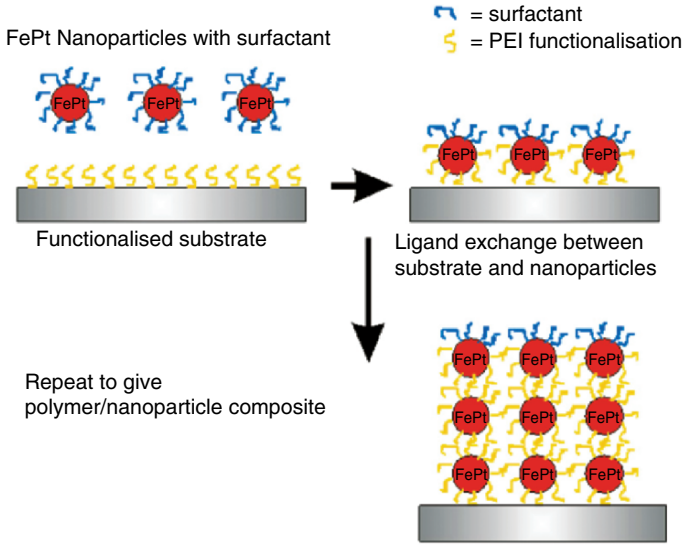

Figure 65. Depositing FePt nanoparticles on functionalised Si substrates using dip coating

2004). Figure 66 shows results from a small angle neutron scattering (SANS) experiment to determine the distribution of particle sizes for a sample of 4 nm FePt nanoparticles deposited onto a Si substrate and annealed at 580° C for 30 mins. Even under these conditions it is clear that larger particles are starting to form although ordering is far from complete (Thomson et al., 2005).

Optimizing the surfactant chemistry can assist in reducing agglomeration (Yu et al., 2003; Momose et al., 2003) as, potentially, can hardening the organic matrix with ion beam irradiation (Baglin et al., 2003). Annealing under different regimes has been attempted including variable times, using a variety of gases, e.g. N_2, Ar, forming gas $Ar_{0.96}H_{0.04}$, He and vacuum, (Klemmer et al., 2003; Thomson

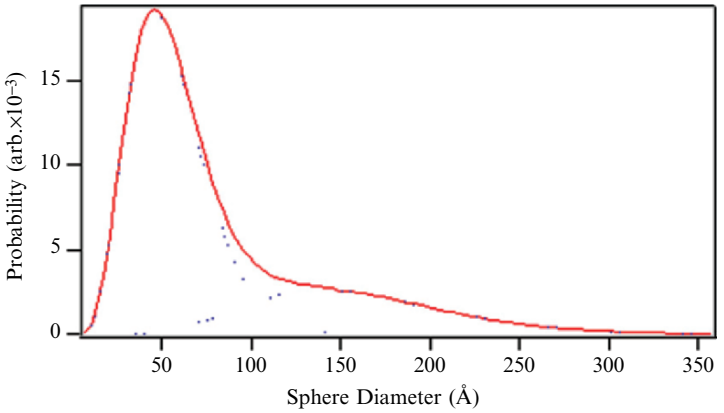

Figure 66. Size distributions determined by simulating SANS data for 3 layers of nominal 4 nm $Fe_{58}Pt_{42}$ nanoparticles deposited onto a Si substrate (Thomson et al., 2005).

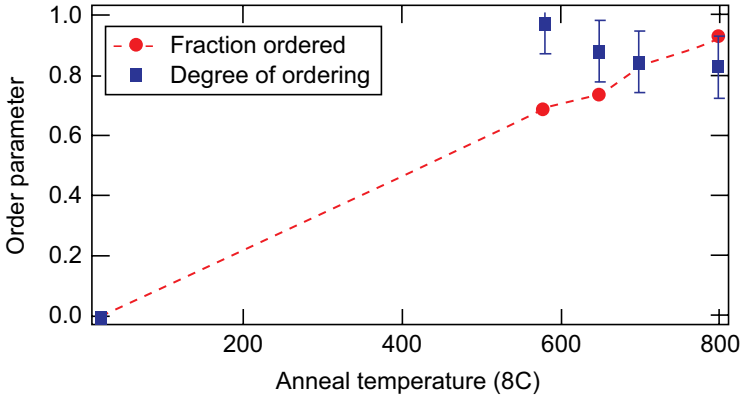

Figure 67. Fraction of particles with $L1_0$ ordering and the degree of ordering within this fraction as a function of anneal temperature. The data show that a two-state model, where particles are either not ordered or are essentially fully ordered should be used to describe these nanoparticle arrays. The dotted lines are included as a guide to the eye. (From (Thomson et al., 2005.)

et al., 2004) rapid thermal annealing (Zeng et al., 2003) and laser annealing. However, despite these advances it is still not clear that the problem of agglomeration has been overcome completely. The problem of orienting the magnetic easy axis has not been solved, and although many attempts at annealing in applied fields have been made, these are to date unsuccessful. An additional concern is that of the uniformity of the chemical ordering induced by annealing (Tanase et al., 2003). Figure 67 shows the results of a careful synchrotron x-ray study to investigate ordering in FePt nanoparticles. Here both the degree of ordering in the ordered regions, and the ordered volume fraction are estimated by fitting the complete x-ray data.

These data show that full ordering is not achieved below annealing temperatures of $\backsim$800° C. In order to avoid the problem of a distribution of anisotropy there is a requirement that all particles have the same degree of ordering. Clearly the medium would have a very wide distribution of anisotropy if some nanoparticles order whilst others remain in the disordered fcc phase (Thomson et al., 2004; Anders et al., 2003; Sakuma et al.,2004). Here the presence of a substantial coercivity does not guarantee that all particles are equally ordered. It has also been suggested (Takahashi et al., 2003) that ordering depends on the particle size with larger particles $\backsim$7 nm ordering more easily than smaller particles $\backsim$4 nm. This would favour an interpretation of agglomeration and ordering where the coalescence of particles is required to achieve chemical ordering. In order to reduce the annealing temperature required for ordering, alloying with a third element such as Au (Kang et al., 2003a), Cu (Sun et al., 2003b) and Ag (Kang et al., 2003b) has been investigated. The most successful approach to date has been the use of Ag where a significant coercivity was measured for samples annealed at 350° C. In order to overcome some of these problems, gas phase based processes have been investigated (Rellinghaus et al., 2003) as have cluster source approaches (Stoyanov et al., 2003) and FePt particles embedded in a sputtered carbon matrix (Christodoulides et al., 2003). The gas phase and cluster methods first seek to form nanoparticles and then accomplish the annealing and hence phase transformation step whilst the particles are still in the gas phase. However, this work is at an early stage and the distribution of particle sizes is typically greater than that found for the arrested precipitation method. If nanoparticles with the correct magnetic and physical properties could be produced then there remains the question of how to uniformly coat a large area, say a 65 nm disc, with perfect registration. One solution proposed is the concept of guided self-assembly (Yang et al., 2004) Here, the idea is to prepattern a substrate into micron sized troughs which then act as containers for local self-assembly. Hence, long range order is imposed by a straightforward lithography process and short range order comes from self-assembly. In summary, although recording media based on assemblies of sub-4 nm high anisotropy nanoparticles offer the possibility of recording densities of up to 40 Tbit/in^2 the practical and scientific challenges of producing these media are very great and solutions to many of the problems have not yet been devised.

4.4. PROBE STORAGE

Since the invention of the hard disc we have seen a gradual decrease of its size, going down from the 24″ IBM 350 to the .85″ Toshiba microdrives of today. Further miniaturisation will inevitably lead to using microsystem technology. One form, which is activily persued by the IBM probe storage team in Switzerland is based on a huge array of read/write probes (Fig. 68), derived from the cantilevers used in scanning probe microscopy (Knoll et al., 2006). Each cantilever has an

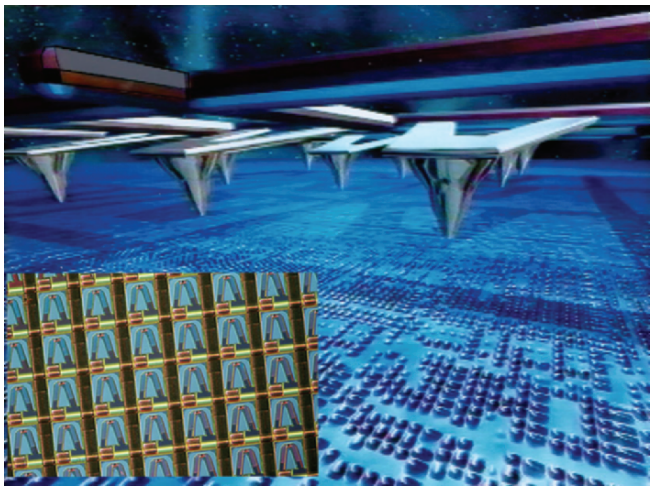

Figure 68. In MEMS based probe storage an array of thousands of read/write probes is used to access data

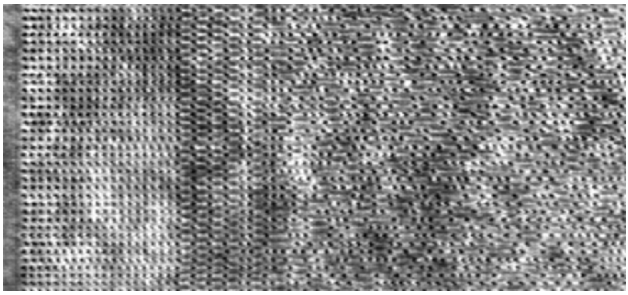

Figure 69. High density recording demonstration in polymer medium. (From IBM website.)

ultrasharp tip which can be heated, and which is used to indent holes. During writing an electrostatic force is applied between cantilever and medium. Read-out of the information is achieved by measuring the height of the cantilever above the medium. Height information is obtained by measuring the temperature of a slightly heated cantilever, which reduces as the tip sinks into a hole. Using this method, extremely high densities (Fig. 69) over 600 GBit/in^2 are demonstrated (Pozidis et al., 2004).

The use of scanning probe techniques opens up a road which might lead to molecular or even atomic storage. That this is not science fiction is demonstrated beautifully by the work of Bennewitz et al. (2002), who positioned Si atoms on a Si surface by means of STM (Fig. 70). Next to moving atoms, one could also modify their charge state (Horn, 2004; Bauschlicher Jr. and So, 2001; Quaade et al., 2001). Of course, data rates are ridiculously low, but using massively parallel arrays this can be circumvented. Still the challenges are tremendous.

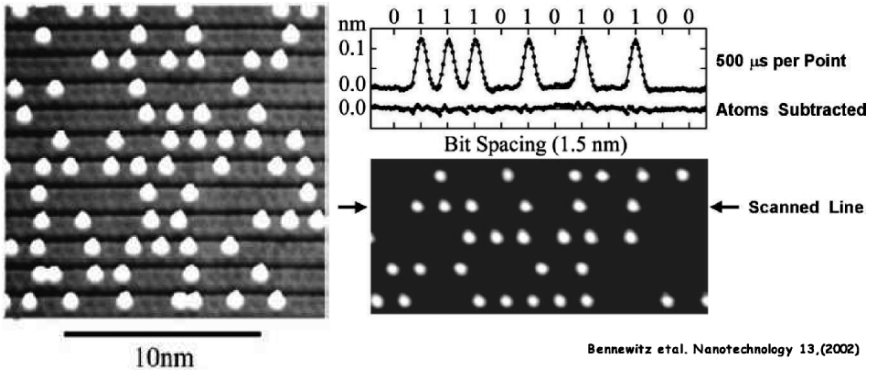

Figure 70. Atomic data storage. Each white dot is a Si atom on a 7 × 7 reconstructed Si surface. (From Bennewitz et al., 2002.)

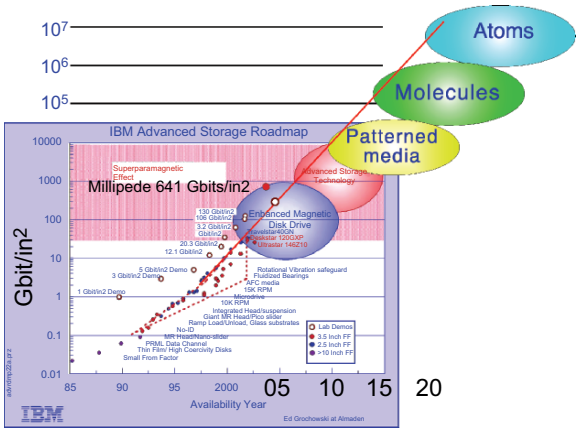

Figure 71. Future recording media will be patterned.

For a workable system, data rates per tip of more than 10 kBit/s are needed, using a square centimetre array of millions of tips. And at an annual density growth rate of 60%, this has to be achieved within 10 years. The road towards this goal (Fig. 71) will at least see the transition from continuous media towards patterned media. The first occurrence of patterned media is in magnetic recording, but soon after single molecular storage will become an option (Cuberes et al., 1996; Stadler et al., 2003). Much could be learned about storage in molecular and atomic patterned media, by studying magnetic patterned media.

The first steps in magnetic probe storage are already taken. One of the first experiments was on continuous media by STM, locally heating the medium and reducing the switching field. The stray field of the surrounding material helps in reversing the magnetisation. Imaging of written bits has to be done by transporting the medium to an MFM, and erasure is not possible (Fig. 72). Erasure becomes

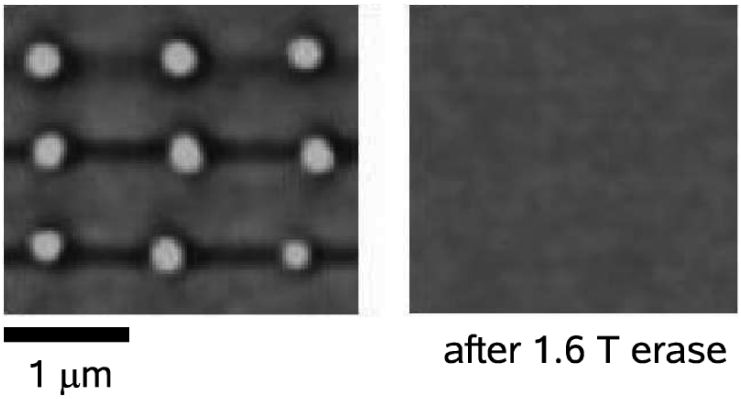

Figure 72. Bits written in a CoNi/Pt multilayer using an STM tip. (From Zhang et al., 2006.)

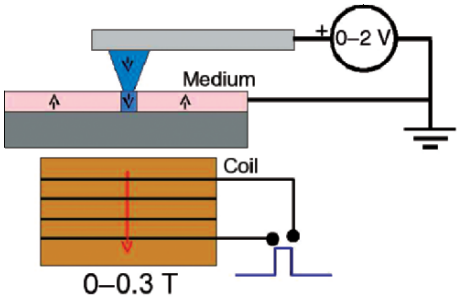

Figure 73. Configuration for magnetic probe recording

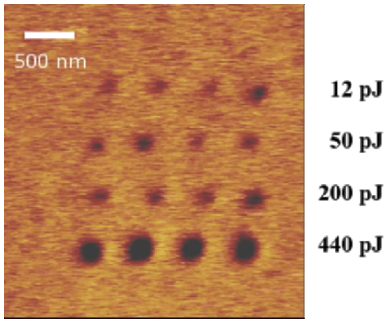

Figure 74. Bits written in a CoNi/Pt multilayer using an MFM tip and induced current. (From Onoue et al., 2005.)

possible with a write assist field (Fig. 73 and 74), and pulsed currents can also be applied from an MFM tip which allows for direct imaging.

Writing without locally heating proved to be impossible on continuous media. Due to inhomogeneities in the medium, reversal starts at an unpredicted place resulting in random nucleation of stripe domains. Also patterned media are subject to inhomogeneities, which express themselves as switching field distributions as

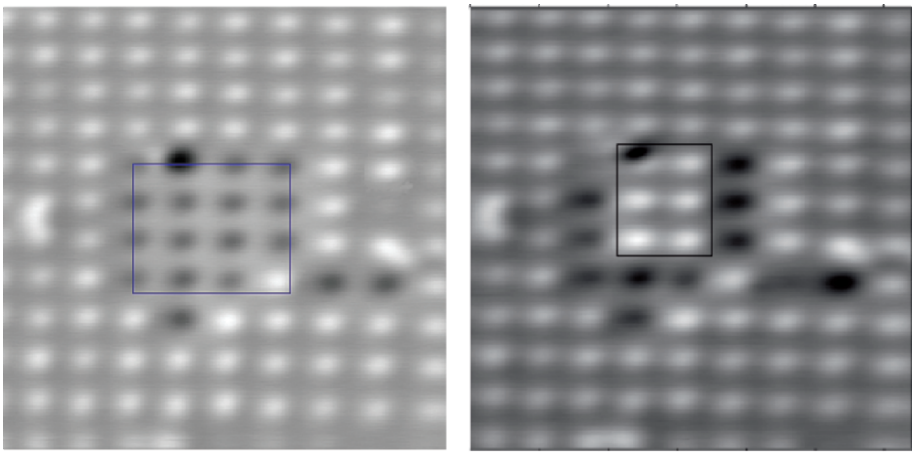

Figure 75. Write experiment. (From Abelmann et al., 2007.)

TABLE II. SI to CGS conversion. To obtain the value in SI units, multiply with the factor

	CGS	SI
Magnetic flux density	Gauss	10^{-4} T
Magnetic field	Oe	$1000/4\pi$ A/m
Magnetic moment	emu	10^{-3} Am^2
Magnetisation	emu/cc	1000 A/m
Energy	erg	10^{-7} J
Energy density	erg/cc	0.1 Jm^{-3}
Length	in	2.54 cm
Bit density	bit/in^2	6.45 bit/cm^2

discussed in Section 4.1. Still, when optimizing the medium and increasing the tip stray field, we could demonstrate writing and erasing data in patterned media produced by Laser Interference Lithography (Fig. 75).

4.5. UNITS

Since this book is primarily meant for (young) researchers in the field, we tried as much as possible to use SI units. We are aware, however, that many researchers in the field are still using CGS units, and *virtually all* magnetic flux meters are indicating in Gauss. We hope these people are aware they are infecting new researchers, and seriously contributing to confusion. If our predecessors agree upon a global standard, who are we to discard it? (Personal opinion LA)

As a result, many of the graphs are in CGS. For your convenience, and for the better of the global community, we provide a short translation table (Table II).

Acknowledgements

The authors wish to thank the many people at the Hitachi San Jose Research Center for their time, effort and helpful comments in preparing this manuscript. In particular, special thanks are due to Jan-Ulrich Thiele, Bruce Terris and Jeff Childress. The group members of the Systems and Materials for Information Storage group of the MESA$^+$ Research Institute of the University of Twente are acknowledged for their contribution, in particular, Martin Siekman and Rogelio Murillo.

References

Seagate-359 Gbit/in^2 demo, Presented at TMRC, Pittsburgh 2006.

Abarra, E., Inomata, A., Sato, H., Okamoto, I., and Mizoshita, Y. (2000) *Appl. Phys. Lett.* **77**, 2581–2583.

Ahmed, M., Davey, P., Donnelly, T., and Clegg, W. (2002) *IEEE Tran. Magn.* **38**, 2331–2333.

Ajan, A., Acharya, B., Abarra, E., and Okamoto, I. (2001) *IEEE Trans. Magn.* **37**, 1508–1511.

Akagi, F., Igarashi, M., Nakamura, A., Mochizuki, M., Saga, H., Matsumoto, T., and Ishikawa, K. (2004) *Jpn. J. Appl. Phys.* **43**, 7483–7488.

Anders, S., Toney, M., Thomson, T., Farrow, R., Thiele, J.-U., Terris, B., Sun, S., and Murray, C. (2003) *J. Appl. Phys.* **93**, 6299.

Arnoldussen, T. (1998), *IEEE Trans. Magn.* **34**, 1851.

Atarashi, E. and Shiiki, K. (1999) *J. Appl. Phy.* **86**, 5780–5787.

Baglin, J., Sun, S., Kellock, A., T.Thomson, Toney, M., Terris, B., and Murray, C. (2003) *Mat. Res. Soc. Symp. Proc.* **777**, T6.5.1.

Bai, D. Z. and Zhu, J. G. (2002) *IEEE Trans. Magn.* **38**, 2240–2242.

Baibich, M., Broto, J., Fert, A., Dau, F. N. V., Petroff, F., Eitenne, P., Cruzet, G., Friederich, A., and Chazelas, J. (1988) *Phys. Rev. Lett.* **61**, 2472–2475.

Bass, J. and Pratt, W. (1999) *J. Magn. Magn. Mater.* **200**, 274–289.

Batra, S., Hannay, J. D., Zhou, H., and Goldberg, J. S. (2004) *IEEE Trans. Magn.* **40**, 319–325.

Bauschlicher Jr., C. W. and So, C. R. (2001) *Chem. Phys. Lett.* **333**, 1–5.

Bennewitz, R., Crain, J. N., Kirakosian, A., Lin, J. L., McChesney, J. L., Petrovykh, D. Y., and Himpsel, F. J. (2002) *Nanotechnol.* **13**, 499–502.

Bertram, H. (1994) *Theory of Magnetic Recording*, Cambridge, Cambridge University Press.

Bertram, H. and Richter, H. (1999) *J. Appl. Phys.* **85**, 4991–4993.

Bertram, H., Zhou, H., and Gustafson, R. (1998) *IEEE Trans. Magn.* **34**, 1845.

Bian, B., Bain, J. A., Kwon, S. J., and Laughlin, D. E. (2001) *IEEE Trans. Magn.* **37**, 1640–1642.

Bijker, M., Abelmann, L., Lodder, J., and Popma, T. (1999) The *J. Magn. Magn. Mater.* **193**, 357–361.

Butler, W., Zhang, X., Schulthess, T., and MacLaren, J. (2001) *Phys. Rev.* **B 63**, 054416.

Challener, W., McDaniel, T., Mihalcea, C., Mountfield, K., Pelhos, K., and Sendur, I. (2003) *Jpn. J. Appl. Phys.* **42**, 981–988.

Chang, C., Plumer, M., Brucker, C., Chen, J.-P., Ranjan, R., van Ek, J., Yu, J., Karns, D., Kubota, Y., Ju, G., and Weller, D. (2002) *IEEE Trans. Magn.* **38**, 1637–1642.

Charap, S. H., Lu, P. L., and He, Y. (1997) *IEEE Trans. Magn.* **33**, 978–983.

Chen, S. X., Zhang, Q. D., Chong, H. C., Komatsu, T., and Kang, C. H. (2001) *IEEE Trans. Magn.* **37**, 805–809.

Childers, E., Imaino, W., Eaton, J., Jaquette, G., Koeppe, P., and Hellman, D. (2003) *IBM J. Res. Develop.* **47**, 471–482.

Childress, J. R., and Fontana Jr., R. E. (2005) *C.R. Physique* **6**, 997–1012.

Christodoulides, J., Bonder, M., Huang, Y., Zhang, Y., Stoyanov, S., Hadjipanayis, G., Simopoulos, A., and Weller, D. (2003) *Phys. Rev. B* **68**, 054428.

Coffey, K., Thomson, T., and Thiele, J.-U. (2002) *J. Appl. Phys.* **92**, 4553–4559.

Comstock, R. L. (1999) *Introduction to Magnetism and Magnetic Recording*, Chichester, Wiley-Interscience.

Cuberes, M. T., Schlittler, R. R., and Gimzewski, J. K. (1996) *Appl. Phys. Lett.* **69**, 3016–3018.

Dai, Z., Sun, S., and Wang, Z. (2001) *Nano Lett.* **1**.

Daniel, E., Mee, C., and Clark, M. (1998) *Magnetic Recording: The First 100 Years*, New York, IEEE Press.

Danish (1898), *Patent* **2653**.

Daughton, J., Pohm, A., Fayfield, R., and Smith, C. (1999), *J. Phys. D. – Appl. Phys.* **32**, R169–R177.

Desserre, J. R. (1985) *IEEE Trans. Magn.* **MAG-21**, 1371–1373.

Ding, Y., Yamamuro, S., Farrell, D., and Majetich, S. (2003) *J. Appl. Phys* **93**, 7411.

Doerner, M., Bian, X., Madison, M., K. Tang, Q. P., Polcyn, T. A., Toney, M., Mirzamaani, M., Takano, K., Fullerton, E., Margulies, D., Schabes, M., Rubin, K., Pinarbasi, M., Yuan, S., Parker, M., and Weller, D. (2001) *IEEE Trans. Magn.* **37**, 1052–1058.

Erden, M., Rausch, T., and Challener, W. (2005) *IEEE Trans. Magn.* **41**, 2189–2194.

Eric D. Daniel, C. Denis Mee (eds), M. H. C. E. (1998) *Magnetic Recording: The First 100 Years*, New-York, Wiley-IEEE press.

Fullerton, E., Margulies, D., Schabes, M., Carey, M., Gurney, B., Moser, A., Best, M., Zeltzer, G., Rubin, K., Rosen, H., and Doerner, M. (2000) *Appl. Phys. Lett.* **77**, 3806–3808.

Gao, K. Z. and Bertram, H. N. (2002) *IEEE Trans. Magn.* **38**, 2063–2065.

Grunberg, P., Schreiber, R., Pang, Y., Brodsky, M., and Sowers, H. (1986) *Phys. Rev. Lett.* **57**, 2442–2445.

Harrell, J., Wang, S., Nikles, D., and Chen, M. (2001) *Appl. Phys. Lett.* **79**, 4393–4395.

Heinrich, B. and Bland, J. (eds.) (1994) *Ultrathin Magnetic Structures II*, Berlin, Springer-Verlag.

Hirano, T., Fan, L. S., Lee, W. Y., Hong, J., Imaino, W., Pattanaik, S., Chan, S., Webb, P., Horowitz, R., Aggarwal, S., and Horsley, D. A. (1998) *IEEE/ASME Trans. Mech.* **3**, 156–165.

Hisano, S. and Saito, K. (1998) *J. Magn. Magn. Mater.* **190**, 371–381.

Hoagland (1998) *Digital Magnetic Recording*, Malabar, FL, Krieger.

Hoagland, A. and Monson, J. (1998) *Digital Magnetic Recording*, Malabar, FL, Krieger Publishing Company.

Horn, K. (2004) *Science* **305**, 483–484.

Hyeon, T. (2003) *Chem. Comm.* pp. 927–934.

Jin, E. and Xu, X. (2005) *Appl. Phys. Lett.* **86**, 111106.

Jorgensen, F. (1996) *The Complete Handbook of Magnetic Recording*, New York, TAB books.

Julliere, M. (1975) *Phys. Lett.* **A 54**, 225.

Kang, S., Jia, Z., Nikles, D., and Harrell, J. (2003a) *IEEE Trans. Magn.* **39**, 2753.

Kang, S., Nikles, D., and Harrell, J. (2003b) *J. Appl. Phys.* **93**, 7178.

Karlqvist, O. (1954) *Trans. Roy. Inst. Technol.* **86**, 3–27.

Kawana, T., Onodera, S., and Samoto, T. (1995) *IEEE Trans. Magn.* **31**, 2865–2870.

Khizroev and Litvinov (2005) *Perpendicular Magnetic Recording*, Berlin, Springer.

Khizroev, S. and Litvinov, D. (2004) *J. Appl. Phys.* **95**, 4521–4537.

Klemmer, T., Liu, C., Shukla, N., Wu, X., Weller, D., Tanase, M., Laughlin, D., and Soffa, W. (2003) *J. Magn. Magn. Mater.* **266**, 79.

Knoll, A., Bachtold, P., Bonan, J., Cherubini, G., Despont, M., Drechsler, U., Durig, U., Gotsmann, B., Haberle, W., Hagleitner, C., Jubin, D., Lantz, M. A., Pantazi, A., Pozidis, H., Rothuizen, H., Sebastian, A., Stutz, R., Vettiger, P., Wiesmann, D., and Eleftheriou, E. S. (2006) *Microelect. Eng.* **83**, 1692–1697.

Kodama, H., Momose, S., Ihara, N., Uzumaki, T., and Tanaka, A. (2003) *Appl. Phys. Lett.* **83**, 5253–5255.

Kondorsky, E. (1940) *J. Phys. (Moscow)* **2**, 161.

Köster, E. (1996) *Magnetic Recording Technology*, New York, McGraw-Hill.

Kouval, J. and Hartelius, C. (1962) *J. Appl. Phys.* **33**, 1343–1344.

Landis, S., Rodmacq, B., Bayle-Guillemaud, P., Baltz, V., and Dieny, B. (2004) *J. J. Appl. Phys., Part 1: Regular Papers Short Notes Rev. Papers* **43**, 3790–3795.

Lindholm, D. (1977), *IEEE Trans. Magn.* **13**, 1460.

Litvinov, D. and Khizroev, S. (2005) *J. Appl. Phys.* **97**, 071101.

Liu, B. and Laughlin, D. (2001) The Physics of High Density Magnetic Recording, pp. 33–80.

Lodder, J. C. (2004) Methods for preparing patterned media for high-density recording, *J. Magn. Magn. Mater.* **272–276**, 1692–1697.

Mallary, M. (1987) *US Patent* **4656546**.

Mallary, M. (2001) *The Physics of High Density Magnetic Recording*, Berlin, Springer.

Mallary, M., Torabi, A., and Benakli, M. (2002) *IEEE Trans. Magn.* **38**, 1719–1724.

Mao, C. Y., Zhu, J. G., White, R. M., and Min, T. (1999) *J. Appl. Phys.* **85**, 5870–5872.

Matsumoto, T., Shimano, T., Saga, H., Sukeda, H., and Kiguchi, M. (2004) *J. Appl. Phys.* **95**, 3901–3906.

Matteo, J., Fromm, D., Yuen, Y., Schuck, P., Moerner, W., and Hesselink, L. (2004) *Appl. Phys. Lett.* **85**, 648–650.

McDaniel, T. (2005) *J. Phys. C: Condens. Mater.* **17**, R315–R332.

McDaniel, T., Challener, W., and Sendur, K. (2003) *IEEE Trans. Magn.* **39**, 1972–1979.

Mee, C. D. and Daniel, E. D. (1996) *Magnetic Recording Technology*, London, McGraw-Hill.

Miles, J., Sivasamy, P., Wdowin, M., Middleton, B., and Casey, S. (1998) *IEEE Trans. Magn.* **34**, 1979–1981.

Momose, S., Kodama, H., Ihara, N., Uzumaki, T., and Tanaka, A. (2003) *Jap. J. Appl. Phys. Part 2-Lett.* **42**, L1252.

Moodera, J., Kinder, L., Wong, T., and Meservey, R. (1995) *Phys. Rev. Lett.* p. 74.

Moodera, J. and Mathon, G. (1999) *J. Magn. Magn. Mater.* **200**, 248–273.

Moser, A. and Weller, D. (2001) *The Physics of High Density Magnetic Recording*, Berlin, Springer.

Mou, J. Q., Lu, Y., Yang, J. P., Li, Q. H., and Guo, G. X. (2004) *J. Micromech. Microengineer.* **14**, 1608–1613.

Murillo-Vallejo, R. (2006) Magnetic media patterned by laser interference lithography, Ph.D. thesis, University of Twente, Enschede, The Netherlands.

Nguyen, L. T., Hozoi, A., and Lodder, J. C. (2004) *IEEE Trans. Magn.* **40**, 2401–2403.

Nguyen, L. T., Tichelaar, F. D., and Lodder, J. C. (2005) *J. Magn. Magn. Mater.* **290–291 PART 2**, 1294–1297.

Noyes, T. and Dickinson, W. E. (2000) The random-access memory accounting machine – II. The magneticdisk, random-access memory (Reprinted from IBM Journal of Research and Development, vol 1, 1957), *IBM J. Res. Develop.* **44**, 16–19.

Ntokas, I., Nutter, P., and Middleton, B. (2005) *J. Magn. Magn. Mater.* **287**, 437–441.

O'Grady, K. and Laidler, H. (1999) *J. Magn. Magn. Mater.* **200**, 616–633.

Oikawa, T., Nakamura, M., Uwazumi, H., Shimatsu, T., Muraoka, H., and Nakamura, Y. (2002) *IEEE Trans. Magn.* **38**, 1976–1978.

Onodera, S., Kondo, H., and Kawana, T. (1996) *MRS Bulletin* **21**, 35–41.

Pan, G. and Du, H. (2003), *J. Appl. Phys.* **93**, 5498–5502.

Parkin, S. (1995), *Annu. Rev. Mater. Sci.* **25**, 357–388.

Parkin, S., More, N., and Roche, K. (1990) *Phys. Rev. Lett.* **64**, 2304–2307.

Peng, W., Hsia, Y., Sendur, K., and McDaniel, T. (2005) *Tribology Int.* **38**, 588–593.

Pfeiffer, H. (1990), *Phys. Stat. Sol.* **118**, 295–306.

Plumer, M., van Ek, J., and Weller, D. (2001) *The Physics of Ultra-High-Density Magnetic Recording*, Berlin, Springer.

Portier, X. and Petford-Long, A. (1999) *J. Phys. D. – Appl. Phys.* **32**, R89–R108.

Pozidis, H., Háberle, W., Wiesmann, D., Drechsler, U., Despont, M., Albrecht, T. R., and Eleftheriou, E. (2004) *IEEE Trans. Magn.* **40**, 2531–2536.

Pratt, W., Jr., Lee, S.-F., Slaughter, J., Loloee, R., Schroeder, P., and Bass, J. (1991) *Phys. Rev. Lett.* **66**, 3060–3063.

Quaade, U. J., Stokbro, K., Lin, R., and Grey, F. (2001) *Nanotech.* **12**, 265–272.

Rellinghaus, B., Stappert, S., Acet, M., and Wassermann, E. (2003), *J. Magn. Magn. Mater.* **266**, 142.

Richards, D. and Sharrock, M. (1998) *IEEE Trans. Magn.* **34**, 1878–82.

Richter, H. (1999) *J. Phys. D-Appl. Phys.* **32**, R147–R168.

Rijks, T. G., Lenczowski, S., Coehoorn, R., and de Jonge, W. (1997) *Phys. Rev.* **B 56**, 362–366.

Rottmayer, R., Batra, S., Buechel, D., Challener, W., Hohlfeld, J., Kubota, Y., Li, L., Lu, B., Mihalcea, C., Mountfield, K., Pelhos, K., Peng, C., Rausch, T., Seigler, M., Weller, D., and Yang, X. (2006) *IEEE Trans. Magn.* 42, 2417–2421.

Ruigrok, J. (2001) *J. Mag. Soc. Japan* **25**, 313–321.

Ruigrok, J., Coehoorn, R., Cumpson, S., and Kesteren, H. (2000) *J. Appl. Phys.* **87**, 5398–5403.

Ruigrok, J., van Kesteren, H., Cumpson, S., Adelerhof, D., Luitjens, S., Draaisma, E., and Hoogendoorn, A. (1998) *IEEE Trans. Magn.* **34**, 1459–61.

Sakuma, H., Taniyama, T., Kitamoto, Y., Yamazaki, Y., Nishio, H., and Yamamoto, H. (2004) *J. Appl. Phys.* **95**, 7261.

Sauter, G. F., Paul, M. C., Oberg, P. E., and Kaske, A. D. (1972) *IEEE Trans. Magn.* **MAG-8**, 194–200.

Sawaguchi, H., Nishida, Y., Takano, H., and Aoi, H. (2001) *J. Magn. Magn. Mater.* **235**, 265–272.

Schabes, M., Lengsfield, B., and Schrefl, T. (2002), *IEEE Trans. Magn.* **38**, 1670–1675.

Sekiguchi, N., Kawakami, K., Ozue, T., Yamaga, M., and Onodera, S. (2005) *IEEE Trans. Magn.* **41**, 3235–3237.

Sharma, M., Nickel, J., Anthony, T., and Wang, S. (2000), *Appl. Phys. Lett.* **77**, 2219–2221.

Shi, X., Hesselink, L., and Thornton, R. (2003) *Optics Lett.* **28**, 1320–1322.

Singla, N., O'Sullivan, J., Miller, C., and Indeck, R. (2005) *IEEE Trans. Magn.* **41**, 2968–2970.

Stadler, R., Forshaw, M., and Joachim, C. (2003) *Nanotechnology* **14**, 138–142.

Stahl, B., Ellrich, J., Theissmann, R., Ghafari, M., Bhattacharya, S., Hahn, H., Gajbhiye, N., Kramer, D., Viswanath, R., Weissmuller, J., and Gleiter, H. (2003) *Phys. Rev. B* **67**, 014422.

Stoner, E. C. and Wohlfarth, E. P. (1948) *Trans. Roy. Soc.* **A240**, 599.

Stoner, E. C. and Wohlfarth, E. P. (1991) A mechanism of magnetic hysteresis in heterogeneous alloys (reprinted from Trans. Roy. Soc. A240), *IEEE Trans. Magn.* **27**, 3475–3518.

Stoyanov, S., Huang, Y., Zhang, Y., Skumryev, V., Hadjipanayis, G., and Weller, D. (2003) *J. Appl. Phys.* **93**, 7190.

Sugaya, S. (2006) *Fujitsu Sci. Tech. J.* **42**, 61–71.

Sun, S., Anders, S., Hamann, H., Thiele, J.-U., Baglin, J., Thomson, T., Fullerton, E., Murray, C., and Terris, B. (2002) *J. Am. Chem. Soc.* **124**, 2884.

Sun, S., Anders, S., Thomson, T., Baglin, J., Toney, M., Hamann, H., Murray, C., and Terris, B. (2003a) *J. Phys. Chem. B* **107**, 5419.

Sun, S., Murray, C., Weller, D., Folks, L., and Moser, A. (2000) *Science* **287**, 1989.

Sun, S., Weller, D., and Murray, C. (2001) *The Physics of High Density Recording*, Berlin, Springer.

Sun, X., Kang, S., Harrell, J., Nikles, D., Dai, Z., Li, J., and Wang Z.L. (2003b), *J. Appl. Phys.* **93**.

Takahashi, Y., Ohkubo, T., Ohnuma, M., and Hono, K. (2003) *J. Appl. Phys.* **93**, 7166.

Takano, K. (2004) *IEEE Trans. Magn.* **40**, 257–262.

Tan, A. and Chang, J. (2005) *Diamond Relat. Mater.*, **14**, 226–231.

Tan, W. and Cruz, J. (2005) *J. Magn. Magn. Mater.* **287**, 397–404.

Tanaka, Y. (2005) *IEEE Trans. Magn.* **41**, 2834–2838.

Tanase, M., Nuhfer, N., Laughlin, D., Klemmer, T., Liu, C., Shukla, N., Wu, X., and Weller, D. (2003), *J. Magn. Magn. Mater.* **266**, 215.

Tarnopolsky, G. and Pitts, P. (1997) *J Appl. Phys.* **81**, 4837.

Terris, B. D. and Thomson, T. (2005) *J. Phys. D: Appl. Phys.* **38**, R199–R222.

Terris, B. D., Albrecht, M., Hu, G., Thomson, T., Rettner, C. T. (2005b) IEEE Trans. Magn. 37, 2822–2827.

Thiele, J.-U., Coffey, K., Toney, M., Hedstrom, J., and Kellock, A. (2002) *J. Appl. Phys.* **91**, 6595–6600.

Thiele, J.-U. and Fullerton, S. M. E. E. (2003) *Appl. Phys. Lett.* **82**, 2859–2861.

Thompson, D., Romankiw, L., and Mayadas, A. (1975) *IEEE Trans. Magn.* **11**, 1039–1050.

Thomson, T., Lee, S., Toney, M., Dewhurst, C., Ogrin, F., Oates, C., and Sun, S. (2005), *Phys. Rev. B* **72**, 064441.

Thomson, T., Toney, M., Raoux, S., Lee, S., Sun, S., Murray, C., and Terris, B. (2004), *J. Appl. Phys.* **96**, 1197.

Todorovic, M., Schultz, S., Wong, J., and Scherer, A. (1997) *Appl. Phys. Lett.* **74**, 2516.

Tsunekawa, K., Djayaprawira, D., Yuasa, S., Nagai, M., Maehara, H., Yamagata, S., Okada, E., Watanabe, N., Suzuki, Y., and Ando, K. (2006) *IEEE Trans. Magn.* **42**, 103–107.

Tsymbal, E., Mryasov, O., and LeClair, P. (2003) *J. Phys. C – Condens. Matter* **15**, R109–R142.

Vallejo, R. M., Siekman, M. H., Bolhuis, T., Abelmann, L., and Lodder, J. C. (2006) *Microsyst. Technol.* 13(12).

Vasic, B. (2005) *Coding and Signal Processing for Magnetic Recording Systems*, Boca Raton, FL, CRC Press.

Wang, S. and Taratorin, A. (1999) *Magnetic Information Storage Technology*, San Diego, CA, Academic Press.

Weller, D. and Doerner, M. (2000) *Annu. Rev. Mater. Sci.* **30**, 611–644.

Weller, D., Moser, A., Folks, L., Best, M., Lee, W., Toney, M., Schwickert, M., Thiele, J.-U., and Doerner, M. (2000) *IEEE Trans. Magn.* **36**, 10–15.

White, R. L., Newt, R., and Pease, R. (1997) *IEEE Trans. Magn.* **33**, 990.

Williams, M. and Comstock, R. (1971) *AIP Conf. Proc.* **5**, 738–742.

Willoughby, S. D., MacLaren, J. M., Ohkubo, T., Jeong, S., McHenry, M., Laughlin, D. E., Choi, S. J., and Kwon, S. J. (2002) *J. Appl. Phys.* **91**, 8822–8824.

Wood, R. (2000) *IEEE Trans. Magn.* **36**, 36–42.

Wu, Y., O'Sullivan, J., Singla, N., and Indeck, R. (2003) *IEEE Trans. Magn.* **39**, 2115–2120.

Wu, Z. (2000) *Coding and Iterative Detection for Magnetic Recording Channels*, Boston, MA, Kluwer Academic.

Yang, X., Liu, C., Ahner, J., Yu, J., Klemmer, T., Johns, E., and Weller, D. (2004) *J. Vac. Phys. B* **22**, 31.

Yu, A., Mizuno, M., Sasaki, Y., Inoue, M., Kondo, H., Ohta, I., Djayaprawira, D., and Takahashi, M. (2003) *Appl. Phys. Lett.* **82**, 4352.

Yu, M., Choe, G., and Johnson, K. (2002) *J. Appl. Phys.* **91**, 7071–7073.

Yuasa, S., Fukushima, A., Kubota, H., Suzuki, Y., and Ando, K. (2006) *Appl. Phys. Lett.* **89**, 042505.

Zeng, H., Sun, S., Sandstrom, R., and Murray, C. (2003) *J. Magn. Magn. Mater.* **266**, 227.

Zhang, S. and Levy, P. (1991) *J. Appl. Phys.* **69**, 4786–4788.

Zhang, X. and Butler, W. (2003) *J. Phys. C – Condens. Matter* **15**, R1603–R1639.

Zhang, Y. and Bertram, H. (1998) *IEEE Trans. Magn.* **34**, 3786–3793.

Zutic, I., Fabian, J., and Sarma, S. D. (2004) *Rev. Mod. Phys.* **76**, 323–410.

QUANTUM EFFECTS IN INTERACTING ELECTRON SYSTEMS: THE ROLE OF SPIN IN THE INTERACTION AND ENTANGLEMENT IN MESOSCOPIC SYSTEMS *

SALVATORE SAVASTA
Dipartimento di Fisica della Materia e Tecnologie Fisiche Avanzate, Università di Messina Salita Sperone 31, I-98166 Messina, Italy

Abstract. A brief introduction to the physics of spin with emphasis on symmetry properties and entanglement is presented. Subsequently to an overview of the linear and nonlinear optical properties of semiconductors and of quantum optical effects in semiconductors and semiconductor microcavities (SMCs) is presented. The recent demonstration of quantum complementarity of optically generated electronic excitations in cavity-embedded quantum wells and the generation of spin-entangled polariton pairs are analyzed and discussed.

Keywords: Spin, excitons, entanglement, polaritons.

1. Introduction

The ability to generate, manipulate, and characterize quantum states is becoming an increasingly important area of physical research, with implications for areas of technology such as computing, quantum cryptography, and communications (Nielsen and Chuang, 2000). Optically active semiconductor quantum structures hold great promise in these areas of technology owing to the possibility of ultrafast optical manipulation (Axt and Kuhn, 2004) the possibility of engineering the valence and conduction electronic states, and thanks to the ease of integration with the present optoelectronic. Owing to the additional possibility of controling the -photon interaction in semiconductor microactivities (SMCs) (Weisbuch et al., 1992), the generation of entangled photon pairs in semiconductor systems (Savasta et al., 2000; Edamatsu et al., 2005; Savasta and DiStefano, 2006) is expected to be promising towards the realization of integrated quantum-optical devices and new sources of entangled light. In contrast to the intuitively plausible assumptions that holds in classical physics, entangled particles, even when isolated, are not allowed to possess definite properties in their own right,

* Footnote to the title with the 'thanks' command.

B. Azzerboni et al. (eds.), Magnetic Nanostructures in Modern Technology, 307–324.

as quantitatively expressed by violations of Bell's inequalities is a key feature of quantum information and communication technology (Nielsen and Chuang, 2000).

A SMC is a photonic structure designed to enhance light–matter interactions. The strong light–matter interaction in these systems gives rise to cavitys which are hybrid quasiparticles consisting of a superposition of cavity photons and quantum well (QW) excitons (Weisbuch et al., 1992). Ultrafast optical spectroscopy of semiconductor and semiconductor quantum structures gives access to the physics of coherences, quantum kinetics, and correlations involving charge, spin, and lattice degrees of freedom (Axt and Kuhn, 2004). Besides interest for applications, the possibilities of quantum state manipulation offered by ultrafast nonlinear optical spectroscopy make these systems a prototypical laboratory for investigating the dynamics of mesoscopic quantum states in complex envronments.

In this paper I will present an overview of semiconductor quantum optics with polaritons with emphasis on spin-dependent nonlinear interactions. Although spontaneous nonlinear processes involving polaritons in bulk semiconductors have been known for decades (Honerlage et al., 1978), the possibility of generating entangled photons by this process was theoretically pointed out only lately (Savasta et al., 2000). This result was based on a microscopic quantum theory of the nonlinear optical response of interacting electron systems relying on the dynamics controlled truncation scheme (Axt and Kuhn, 2004) extended to include light quantization (Savasta and Girlanda, 1996, 1999). The above theory was also applied to the analysis of polariton parametric emission in SMCs (Savasta and Girlanda, 1996; Savasta et al., 1997). The more recent demonstrations of parametric amplification and parametric emission in SMCs (Savvidis et al., 2000; Stevenson et al., 2000) have incresed the interest on the possible realization of nonclassical cavity-polariton states. In 2004, experimental evidence for the generation of ultraviolet polarization-entangled photon pairs by means of biexciton resonant parametric emisison in a single crystal of semiconductor CuCl has been reported (Edamatsu et al., 2005). Short-wavelength entangled photons are desirable for a number of applications as generation of further entanglement between three or four photons. In 2005, an experiment probing quantum correlations of (parametrically pair-emitted) cavity polaritons by exploiting quantum complementarity has been proposed and realized (Savasta et al., 2005).

The paper is organized as follows. In the next section an introduction to the quantum physics of spin and to entanglement is presented. Section III deals with a microscopic quantum description of semiconductor electronic states and their interaction with light. In Section IV the generation of spin-entangled polariton pairs in bulk semiconductors is briefly described. In Section V the quantum complementarity principle for cavity polaritons is discussed. Section VI deals with a very recent proposal for the generation of spin-entangled cavity polaritons (Savasta and DiStefano, 2006).

2. Introduction to spin and entanglement

In this section, I will present a brief introduction to quantum physics, starting from the spin. I will provide a very elementary view where the main puzzling features of quantum mechanics as quantum probabilities, quantum measurements, and entanglement are described without introducing the usual abstract mathematical machine of quantum physics involving Hilbert spaces, Hermitean operators, and so on.

Recently the field of quantum information theory opened up and expanded rapidly. Quantum entanglement began to be seen not only as a puzzle, but also as a resource which can yield new physical effects and techniques, like quantum teleportation, quantum cryptography, and quantum computing (Nielsen and Chuang, 2000). In turn ideas from these fields are beginning to yield new insight into the foundations of quantum physics, suggesting that information should play an essential role in the foundations of any scientific description of nature. In this spirit, I define the spin as a physcal system carrying just one bit of information, e.g. a system that, if asked, can provide only two outcomes. I will also exploit the well known fact that physical quantities have definite transformation properties, which means that they usually are scalars, vectors, or more generally, tensor quantities. So I will try to describe the transformation properties of vector components dealing with just one bit of information. Of course when dealing with only two outcomes, it is not possible to describe deterministically the continuous transformations of vectors under rotations. The only possibility is to require a weaker adherence to them, by asking that they hold at least on the average. It is easy to see that, in order to make this statistical adherence possible, the two outcomes must have equal absolute value (we generically indicate them as $\pm a$ with $a > 0$). Moreover we observe that a must be the maximum value that the expectation value can assume. If not, a rotation could give rise to unattainable expectation values outside the interval between the outcomes. For the same reason, if after a measurement the outcome a is obtained, automatically this implies that the vector is aligned along the measurement axis. Specifically, we assume that, after a measurement along the $\hat{\mathbf{n}}$ axis, outcome $+a$ has been obtained. The system is thus oriented along this axis with positive direction: $\mathbf{J} = a\hat{\mathbf{n}}$. If we perform another measurement along the same $\hat{\mathbf{n}}$ axis without disturbing the system, we will obtain again $\mathbf{J} \cdot \hat{\mathbf{n}} = a$ as it happens to measurements of vector components in classical physics. What happens if we choose a different detection axis $\hat{\mathbf{m}}$? According to the rotation properties of vectors, we obtain $\mathbf{J} \cdot \hat{\mathbf{m}} = a\hat{\mathbf{n}} \cdot \hat{\mathbf{m}} = a \cos\theta$, being θ the angle determined by the two axis. This result is not in $\{\pm a\}$, hence we try to obtain the result statistically (in the mean): $\langle \mathbf{J} \cdot \hat{\mathbf{m}} \rangle_{\hat{\mathbf{n}}+} = a \cos\theta$ and the expectation value can be expressed in terms of probabilities $P(\hat{\mathbf{n}} \pm, \hat{\mathbf{m}} \pm)$ as

$\langle \mathbf{J} \cdot \hat{\mathbf{m}} \rangle_{\hat{\mathbf{n}}+} = a \langle \hat{\mathbf{n}} \cdot \hat{\mathbf{m}} \rangle \equiv a P(\hat{\mathbf{n}}+ : \hat{\mathbf{m}}+) - a P(\hat{\mathbf{n}}+ : \hat{\mathbf{m}}-)$. As a consequence we have the following equation

$$a P(\hat{\mathbf{n}}+ : \hat{\mathbf{m}}+) - a P(\hat{\mathbf{n}}+ : \hat{\mathbf{m}}-) = a \cos\theta \tag{1}$$

By using that probabilities must sum to unity, we obtain:

$$\begin{aligned} P(\hat{\mathbf{n}}+ : \hat{\mathbf{m}}+) &= \cos^2(\theta/2) \\ P(\hat{\mathbf{n}}+ : \hat{\mathbf{m}}-) &= \sin^2(\theta/2) \end{aligned} \tag{2}$$

Analogously, starting from the outcome $-a$, we would obtain $P(\hat{\mathbf{n}}- : \hat{\mathbf{m}}\pm) = P(\hat{\mathbf{n}}+ : \hat{\mathbf{m}}\mp)$. The obtained probabilities coincide with quantum probabilities for the spin $1/2$ system. Once derived probabilities for a measurement of $\mathbf{J}$ along a given axis, it is possible to obtain information about its variance by deriving

$$\langle (\mathbf{J} \cdot \hat{\mathbf{m}})^2 \rangle_{\hat{\mathbf{n}}\beta} = \sum_{\alpha = \pm 1} (\alpha a)^2 P(\hat{\mathbf{n}}\beta : \hat{\mathbf{m}}\alpha) = a^2 \,. \tag{3}$$

As a consequence the expectation value of the square modulus of $\mathbf{J}$ results to be a scalar according to the transformation properties of vectors and in agreement with QM: $\langle \mathbf{J}^2 \rangle = 3a^2$. This elementary derivation just put forward the role of symmetry in driving fundamental quantum features as indeterminacy, when combined with the presence of discrete outcomes. We observe that as predicted by quantum theory, a measurement along the x-axis after a previous measurement along the z-axis results to be completely undetermined: $P(\hat{\mathbf{z}}\beta : \hat{\mathbf{x}}\alpha) = 1/2$. This of different spin components for elementary systems (one of the key features of spin physics), as well as the peculiar features of measurements, here emerge as a straightforward direct consequence of dicotomic oucomes and rotation symmetry, without the need of Hilbert spaces, Hermitian operators, and so on. Of course, the present introduction is not intended to replace the formal construction of quantum mechanics, it just helps to keep a direct contact with the main features of quantum physics suggesting (I hope) that it is not so crazy (Niels Bohr wrote: *Anybody who is not shocked by quantum theory has not understood it*).

In classical physics, we assume that the physical properties of an object have an existence independent from observation. That is, measurements merely act to reveal such physical properties. In quantum physics things are different. As we have just seen, a quantum paricle (e.g. an electron) spin oriented along the $+z$ direction does not possess definite properties (named by Einstein elements of reality) of spin in the x direction, until a measurement along the x direction is actually performed (then definite properties in the z direction are lost). Rather, it provides a set of rules specifying (when the state is known) the probability of obtaining a given outcome when, e.g. a measurement of spin along x is actually performed. Many physicists disliked this state of affairs. The most important

objector was Albert Einstein. He held that quantum mechanics must be incomplete, and produced a series of objections to the theory. The most famous of these was the Einstein Podolsky Rosen (EPR) paradox (Einstein et al., 1935). The EPR paradox was advanced as an argument that quantum mechanics could not be a complete theory but should be supplemented by additional (hidden) variables to restore causality and locality. In 1964, John S. Bell (Bell, 1964) demonstrated (by means of an inequality) that theories satisfying local realism give rise to results in contradiction with predictions from quantum physics. Thus, experimental tests can be performed to verify if nature follows local realism or quantum physics. The Clauser-Horne-Shimony-Holt (CHSH) inequality (Clauser et al., 1969), on which many experimental tests of Einstein *local realism* have been performed, is part of the large set of inequalities known generally as Bell inequalities. It applies to a situation where pairs of particles are sent from a source to two distant observers. It is assumed that it is possible to prepare many identical copies of such a two-particle system so that the two observers may perform many measurements and may share the obtained results. Observer 1 which receives particle 1 can choose to measure one among two physical observables, e.g. two different projections of spin along the axis $\mathbf{n}$ or $\mathbf{n}'$. Analogously observer 2 can perform measurements along $\mathbf{m}$ or $\mathbf{m}'$. In agreement with experiments on single spins, it is also assumed that the measured observables $v_1(\mathbf{n})$, $v_2(\mathbf{n}')$ and $v_2(\mathbf{m})$, $v_2(\mathbf{m}')$ take values only in $\{\pm 1\}$ ($a = 1$). The inequality can be expressed as $|\langle B\rangle| \leq 2$, where

$$B \equiv \left[v_1(\mathbf{n}) + v_1(\mathbf{n}')\right] v_2(\mathbf{m}) + \left[v_1(\mathbf{n}) - v_1(\mathbf{n}')\right] v_2(\mathbf{m}') \tag{4}$$

If the particles are allowed to possess definite properties before measurements and are not influenced by measurements of distant observers, either $v_1(\mathbf{n}) + v_1(\mathbf{n}') = \pm 2$ and thus $v_1(\mathbf{n}) - v_1(\mathbf{n}') = 0$ or $v_1(\mathbf{n}) + v_1(\mathbf{n}') = 0$ and thus $v_1(\mathbf{n}) - v_1(\mathbf{n}') = \pm 2$, resulting in $B = \pm 2$. As a consequence the absolute value of the mean value of B cannot exceed the value of 2. This inequality poses a limit to the degree of correlation permitted by a theory assuming local realism. This derivation is based on two *reasonable* assumptions: (i) the assumption that the physical values $v(\mathbf{n})$ have definite values which exist independent of observation is known as the assumption of realism; (ii) the assumption that observer 1 performing her measurement does not influence the results of observer 2, known as the assumption of locality. These two assumptions together are known as the assumption of *local realism*. In summary dicotomic outcomes plus local realism give rise to a model of physical reality satisfying the CHSH inequality. It can be shown that quantum physics in agreement with experimental tests violate this inequality. This inequality is maximally violated by performing spin measurements on the maximally entangled two-particle state

$$|\psi\rangle = |+\rangle_1 |-\rangle_2 - |-\rangle_1 |+\rangle_2 \tag{5}$$

Instead of deriving the quantum result by using the ordinary machinery of quantum physics and Eq. (5), we try to understand the origin of the violation following a recent analysis presented by Unnikrishnan (Unnikrishnan,2005). Since we are dealing with components of vectors (even if with dicotomic outcomes), we inspect if the mean values of these physical variables satisfy (at least statistically) the rotation properties of vectors. To this aim let us consider a system of two particles with zero total angular momentum. This implies that if we measure projections of total angular momentum along an arbitrary axis $\hat{\mathbf{n}}$, we will find zero, so $\mathbf{J} \cdot \hat{\mathbf{n}}$ and $|\mathbf{J}|$ will be zero. We may assume that total angular momentum is conserved even if the two particles are well separated and have ceased to interact. Since we are assuming that measurements of angular momentum along a given axis take values only in $\{\pm 1\}$, the only possibility for the existence of two particles with zero total angular momentum is that they display perfect anticorrelation for measurements along arbitrary axes. If particle 1 provides the outcome $v_1(\mathbf{n}) = \pm 1$, the other will provide opposite values so that $v_1(\mathbf{n})v_2(\mathbf{n}) = -1$. This kind of anticorrelation, of course, does not imply in itself a violation of local realism. What happens if observer 2 uses a differently oriented apparatus SG $\mathbf{m}$? According to the transformation properties of vectors under rotations (see Fig. 1), from $v_1(\mathbf{n})v_2(\mathbf{n}) = -1$, it results $v_1(\mathbf{n})v_2(\mathbf{m}) = -\mathbf{n} \cdot \mathbf{m}$. In other words, keeping fixed the detection axis of observer 1, the product $v_1(\mathbf{n})v_2(\mathbf{m})$ has the same transformation properties of a vector under rotation, when the detection axis of observer 2 is rotated. Of course theories with discrete outcomes cannot give this result that is not in $\{\pm 1\}$. In analogy with the previous analysis on the single particle, we may require that this result holds in the mean: $\langle v_1(\mathbf{n})v_2(\mathbf{m})\rangle = -\mathbf{n} \cdot \mathbf{m}$. Now we can check it against the CHSH inequality. We consider the usual case where $\mathbf{n}'$, $\mathbf{m}$, $\mathbf{n}$, $\mathbf{m}'$ are coplanar and separated by successive 45°; we obtain $|\langle B\rangle| = 2\sqrt{2}$ in clear violation of the CHSH inequality. Thus the combination of discrete outcomes and classical physics (in a statistical meaning) gives rise to a violation of the CHSH inequality. The following theorem holds: *Local realism, the transformation properties of vectors in classical physics (followed at least in the mean), and dicotomic outcomes cannot hold all together.* The obtained result $\langle v_1(\mathbf{n})v_2(\mathbf{m})\rangle = -\mathbf{n} \cdot \mathbf{m}$ coincides with predictions of ordinary quantum mechanics. Just starting from dicotomic outcomes (the same starting point for the CHSH inequality) and assuming transformation properties of vectors on average we have obtained the violations of the CHSH inequality predicted by quantum theory. According to this analysis, violations of Bell inequalities (usually regarded as the most striking departure of QM from classical physics) is the only possibility for a physical system with zero total angular momentum and with dicotomic outcomes to follow the transformation properties of vectors.

The experimental tests of the CHSH inequalities confirm that nature choose to follow rotation simmetry as far as allowed (in the mean) by the presence of discrete outcomes, giving up local realism (Aspect, 1999) (and refs. cited herein).

The Bell theorem and the experimental tests suggest that quantum particles may have a degree of correlations beyond possiblities of classical physics. A major task of quantum information and computation is to exploit this new resource to perform information procesing tasks more efficiently than allowed by classical resources (Nielsen and Chuang, 2000).

3. Electronic excitations in semiconductors

In semiconductors the many-particle ground state can be approximated by a single Slater-determinant (ensuring antisymmetry) corresponding to filled valence and empty conduction bands separated by a gap (we shall consider direct-gap semiconductors). It is advantageous to describe particles in conduction states by electron Fermi operators $\hat{c}_{\mathbf{k}}^{\dagger}$ ($\hat{c}_{\mathbf{k}}$) and to use hole Fermi operators $\hat{d}_{\mathbf{k}}^{\dagger}$ ($\hat{d}_{\mathbf{k}}$) to represent valence states, i.e. $\hat{c}_{\mathbf{k}}^{\dagger}$ creates ($\hat{c}_{\mathbf{k}}$destroys) an electron in a conduction state, while $\hat{d}_{\mathbf{k}}^{\dagger}$ destroys ($\hat{d}_{\mathbf{k}}$creates) an electron in a valence state. Here $\mathbf{k}$ are 3D wave-vectors in the first Brillouin zone, or when considering electrons in quasi-2D nanostructures () indicates 2D in-plane wave-vectors. More generally this label can be regarded as a collective quantum number specfying single-particle valence and conduction states in semiconductors or semiconductor quantum structures. This electron hole picture has the advantage that the many-particle ground state serves as a vacuum state for electron and hole operators, resulting in particularly simple initial conditions for observables derived from these operators. In particular, when considering undoped semiconductors, the ground state is characterized by filled valence bands and empty conduction bands corresponding to a state with zero holes in valence bands and zero electrons in conduction bands. In the following we consider a zinc blend-like semiconductor band structure. The valence band is made from p-like ($l = 1$) orbital states which, after spin-orbit coupling, give rise to $j = 3/2$ and $j = 1/2$ decoupled states. In materials like bulk CuCl, the upper valence band is twofold degenerate ($j = 1/2$), while in materials like GaAs it is fourfold degenerate ($j = 3/2$). In GaAs-based QWs the valence subbands with $J = 3/2$ are energy splitted into twofold degenerate heavy valence subbands with $m = \pm 3/2$ and lower energy subbands with $m = \pm 1/2$. The conduction band, arising from an s-like orbital state ($\mathrm{l} = 0$), gives rise to $j = 1/2$ twofold states. In the following we will refer to materials like CuCl or GaAs-based QWs and will consider for the sake of simplicity only twofold states from the upper valence band and lower conduction band. As a consequence electrons in a conduction band, as well as holes have an additonal spin-like degree of freedom as electrons in free space. When necessary both heavy and light hole valence bands or subbands can be easily included in the present semiconductor model.

The standard model Hamiltonian near the semiconductor band-edge can thus be written as $\hat{H}_s = \hat{H}_0 + \hat{V}_{Coul}$ (Axt and Kuhn, 2004), which is composed of a

free-particle part $\hat{H}_0$ and the Coulomb interaction $\hat{V}_{Coul}$. $\hat{H}_0$ is given by

$$\hat{H}_0 = \sum_{m,\mathbf{k}} \epsilon^{(e)}_{m,\mathbf{k}} \hat{c}^\dagger_{m,\mathbf{k}} \hat{c}_{m,\mathbf{k}} + \sum_{m,\mathbf{k}} \epsilon^{(h)}_{m,\mathbf{k}} \hat{d}^\dagger_{m,\mathbf{k}} \hat{d}_{m,\mathbf{k}} \tag{6}$$

where $\hat{c}^\dagger$ and $\hat{d}^\dagger$ are the electron (e) and hole (h) creation operators and $\epsilon^{(e)}$ and $\epsilon^{(h)}$ the e and h energies. The Coulomb interaction is given by

$$\begin{aligned} \hat{V}_{Coul} \;=\; & \sum_{\mathbf{q}\neq\mathbf{0}} V_{\mathbf{q}} \sum_{m,\mathbf{k},m',\mathbf{k}'} \Bigg[\frac{1}{2} \hat{c}^\dagger_{m,\mathbf{k}+\mathbf{q}} \hat{c}^\dagger_{m',\mathbf{k}'-\mathbf{q}} \hat{c}_{m',\mathbf{k}'} \hat{c}_{m,\mathbf{k}} \\ & + \frac{1}{2} \hat{d}^\dagger_{m,\mathbf{k}+\mathbf{q}} \hat{d}^\dagger_{m',\mathbf{k}'-\mathbf{q}} \hat{d}_{m',\mathbf{k}'} \hat{d}_{m,\mathbf{k}} - \hat{c}^\dagger_{m,\mathbf{k}+\mathbf{q}} \hat{d}^\dagger_{m',\mathbf{k}'-\mathbf{q}} \hat{c}_{m',\mathbf{k}'} \hat{d}_{m,\mathbf{k}} \Bigg] \end{aligned} \tag{7}$$

where $V_{\mathbf{q}}$ is the Fourier transform of the screened Coulom interaction potential. The first two parts are the repulsive electron–electron and hole–hole interaction terms, while the third one describes the attractive *eh* interaction. The additional label $m = \pm$ indicates the spin degrees of freedom. As we will see the spin degeneracy of the valence and conduction bands (subbands) play a relevant role in the nonlinear optical response of electronic excitations. Only *eh* pairs with total projection of angular momentum angular $\sigma = \pm 1$ are dipole active in optical interband transitions. In CuCl photons with circular polarizations $\sigma = +(-)$ excite e with $m_e = +1/2$ ($m_e = -1/2$) and h with $m_h = +1/2$ ($m_h = -1/2$). In GaAs QWs the situation is analogous: photons with circular polarizations $\sigma = +(-)$ excite e with $m_e = +1/2$ ($m_e = -1/2$) and h with $m_h = -3/2$ ($m_h = 3/2$).

An important feature of $\hat{H}_s$ is that its matrix elements between states with a different number of *eh* pairs are zero. As a consequence it does not couple states with different numbers of *eh* pairs. The eigenstates $|N, \alpha, \mathbf{k}\rangle$ with energy $\omega_{N\alpha\mathbf{k}}$ of $\hat{H}_s$ can be labelled according to the number N of *eh* pairs and the total momentum $\mathbf{k}$. The state with $N = 0$ is the semiconductor ground state and corresponds to the full valence band. The $N = 1$ subspace is the exciton subspace. Optically active exciton states can be labelled with the additional quantum number $\alpha = (n, \sigma)$ where σ indicates the spin projection (e.g. in CuCl $\sigma = +1$ indicates an *eh* pair with $m_e = +1/2$ and $m_h = +1/2$; in GaAs QWs $\sigma = +1$ indicates an *eh* pair with $m_e = -1/2$ and $m_h = 3/2$), and n spans all the exciton levels. Exciton eigenstates can be obtained by requiring that general one *eh* pair states be eigenstates of $\hat{H}_s$:

$$\hat{H}_s |N = 1, n\sigma, \mathbf{k}\rangle = \hbar\omega_{n\sigma}(\mathbf{k}) |N = 1, n\sigma, \mathbf{k}\rangle \tag{8}$$

with $|N = 1, n\sigma, \mathbf{k}\rangle = \hat{B}^\dagger_{n,\sigma,\mathbf{k}} |N = 0\rangle$, being $\hat{B}^\dagger_{n,\sigma,\mathbf{k}}$ the exciton creation operator:

$$\hat{B}^\dagger_{n,\sigma,\mathbf{k}} = \sum_{\mathbf{k}'} \Phi^*_{n,\sigma,\mathbf{k}'} \hat{c}^\dagger_{\sigma,\mathbf{k}'+\mathbf{k}/2} \hat{d}^\dagger_{\sigma,-\mathbf{k}'+\mathbf{k}/2} \tag{9}$$

In order to simplify the notation a bit, the spin notation in Eq. (9) has been changed by using the same label for the exciton spin quantum number and for the spin projections of the electron and hole states forming the exciton. The exciton envelope wave function $\Phi_{n,\sigma\mathbf{k}}$ can be obtained solving the secular equation obtained from Eq. (8). It describes the correlated electron-hole relative motion in k-space. As it results from H_s electrons and holes act as free particles with an effective mass determined by the curvature of the single-particle energies (bands or subbands) interacting via a (screened) Coulomb potential in analogy with an electron and a proton forming the hydrogen atom. Actually, it can be shown that the obtained $\Phi_{n,\sigma\mathbf{k}}$ is the Fourier transform of an hydrogen-like wave-function and the corresponding levels form an hydrogen-like spectrum with bound and unbound states:

$$\hbar\omega_{n\sigma}(\mathbf{k}) = E_n + \frac{\hbar^2}{2M}k^2$$

where E_n describes the hydrogen-like spectrum originating from the electron-hoe relative motion, while the dispersion term describes the center of mass motion of the exciton, being M the sum of the electron and hole effective masses. The set of bound and unbound states with $N = 2$ *eh* pairs, determining the biexciton subspace, can be obtained solving the corresponding secular equation , or by using simpler interaction models. It is interesting to observe that the exciton subspace is spin degenerate. The exciton energy levels do not depend on the spin quantum number, hence the excitonic bands are doubly degenerate. The situation is a little more complex for the biexciton subspace. The structure of biexcitonic states and energies depends strongly on the spin of the involved carriers. In particular, bound biexcitons that are the solid state analogous of the hydrogen molecules arises only when the two electrons and also the two holes have opposite spin. This is a consequence of the Pauli exclusion principle. Bound biexcitons have energies that are usually some meV (or even more in large gap semiconductors) less then twice the energy of excitons. Biexcitonic states made by carriers with the same spin give rise only to a continuum starting at an energy that is twice that of the lowest energy exciton state.

As pointed out, H_s does not couple states with different numbers of *eh* pairs. The transition between the disconnetted subspaces with different N is provided by the interaction with the optical field. Electron-hole pairs are dipoles and give rise to an optical polarization driving the interaction with light. By denoting as μ_σ the interband dipole matrix element between the Bloch states of the valence and conduction bands, the electronic polarization density operator at wave vector $\mathbf{k}$ and with spin σ is given by

$$\hat{P}^+_{\sigma,\mathbf{k}} = \frac{\mu^*_\sigma}{\mathcal{V}} \sum_{\mathbf{k}'} \hat{c}_{\sigma,\mathbf{k}'+\mathbf{k}/2}\hat{d}_{\sigma,-\mathbf{k}'+\mathbf{k}/2}$$

and can be expressed in terms of exciton operators (by using Eq. (Bdag) and completness of the exciton subspace)

$$\hat{P}^{+}_{\sigma,\mathbf{k}} = \frac{\mu^{*}_{\sigma}}{\mathcal{V}} \sum_{n,\mathbf{k}'} \Phi^{*}_{n,\sigma,\mathbf{k}'} \hat{B}_{n,\sigma,\mathbf{k}} = \frac{1}{\sqrt{\mathcal{V}}} \sum_{n} M^{*}_{n\sigma} \hat{B}_{n,\sigma,\mathbf{k}} \equiv \sum_{n} \hat{P}^{+}_{n,\sigma,\mathbf{k}} \,. \qquad (10)$$

The total σ electronic polarization at wave vector $\mathbf{k}$ is $\hat{P}_{\sigma\mathbf{k}} = \hat{P}^{+}_{\sigma\mathbf{k}} + \hat{P}^{(-)}_{\sigma\mathbf{k}}$, being $\hat{P}^{-}$ the Hermitian conjugate of $\hat{P}^{+}$.

In order to analyze the dynamical evolution of the electronic polarization, it is useful to use the projection operators defined by

$$\hat{X}_{N,\alpha,\mathbf{k};N',\alpha',\mathbf{k}'} = \left|N,\alpha,\mathbf{k}\right\rangle\left\langle N',\alpha',\mathbf{k}'\right| \qquad (11)$$

The interaction of the semiconductor with a classical external field $\mathbf{E}(\mathbf{r},t) = \sum_{\sigma,\mathbf{k}} e^{i\mathbf{k}\cdot\mathbf{r}} e^{-i\omega_{\mathbf{k}}t} \mathbf{e}_{\sigma_{\mathbf{k}}} E_{\sigma,\mathbf{k}} + c.c.$ in the usual dipole and rotating wave approximation is given by

$$\hat{H}_{i} = -\mathcal{V} \sum_{\sigma} \hat{P}^{+}_{\sigma,0} E^{*}_{\sigma}(t) + H.c.\,, \qquad (12)$$

where $E_{\sigma}(t) = \sum_{\mathbf{k}} E_{\sigma,\mathbf{k}}(t)$. The total Hamiltonian $\hat{H}_{s} + \hat{H}_{i}$ governs the dynamics of the electron system interacting with an external classical light field. The interaction Hamiltonian H_{i} is essentially given by the light field times the polarization density operator. The latter can be expanded in terms of transition operators as $\left|N \pm 1,\alpha,\mathbf{k}\right\rangle\left\langle N,\alpha',\mathbf{k}'\right|$. As a consequence, when applied to an electronic state with N *eh* pairs, it can induce upward or downward transitions to the nearest neighbor subspaces. For example, by exploiting the scheme of time-dependent perturbation theory it is easy to see that at first order the interction with a light field can induce a transition from the ground state ($N = 0$) to the exciton subspace ($N = 1$). A second order process is needed to reach the biexciton sbspace ($N = 2$).

The interaction Hamiltonian (12) is suitable for the description of many linear and nonlinear optical processes involving interband electronic excitations in semiconductors. However, there are quantum optically processes involving spontaneous decay processes that cannot be described without taking into account the quantization of the light field. This can be essntially accomplished by expanding the electric field in (12) in terms of photon destruction and creation Bose operators. In this case it can be seen that, for reasons of energy conservation, an upward transition $N \rightarrow N+1$ comes with the destruction of one photon. In many cases it can be useful to keep the semiclassical Hamiltonian (Eq. 12) describing the effect of a classical light beam sent to excite the medium and at the same time to add a further term H_{iq} with photon operators to describe quantum optical processes in semiconductors.

In order to calculate the dynamical evolution of the σ electronic polarization in a photon field, ones considers the Heisenberg equation of motion, governed by $\hat{H}_s + \hat{H}_i + H_{iq}$, for the exciton operators $\hat{B}_{\alpha,\mathbf{k}}$. However, this equation contains general projection-operators terms whose dynamics should be calculated by new Heisenberg equations. Taking the expectation values of all the operator terms in the equations one finally obtains an open set of equations for the relavant dynamical quantities. Whenever one is dealing with an open hierarchy of dynamical objects, one is facing the problem of finding an appropriate termination procedure. The truncation of the hierarchy of equations can be achieved using a classification according to powers in the driving field (Savasta and Girlanda, 1996; Axt and Kuhn, 2004). Such truncation scheme is analogous to the classification scheme of nonlinear optical processes, where the input light beam represents the expansion parameter. Once fixed to the perturbative order, the Coulomb interaction between electrons (Eq. 7) is exactly taken into account up to the prescribed order in the excitation strength (Axt and Kuhn, 2004). For example, it can be demonstrated that if one is interested to nonlinearities up to the third order in the driving field, only subspaces with N up to 2 (ground state, exciton subspace, biexciton subspace) have to be included. Linear optical processes can be described by considering only the ground state and the exciton subspace.

4. Of bulk excitonic-

In the present section the polariton concept will be briefly introduced, then the theoretical framework presented in the previous section will be exploited to describe a nonlinear optical process able to generate spin-entangled polariton pairs. The recent realization of the first source of ultraviolet entangled photons was based on this process (Edamatsu et al., 2005).

Let us consider a bulk semiconductor, e.g. a CuCl crystal slab. If we illuminate the slab with photons at frequency close to its energy gap and with a given wavevector, photons will be absorbed by the medium giving rise to excitons with the same wavevector. The generated *eh* pairs during their propagation will in turn recombine giving rise to photons with the same wavevector, the resulting photons will be absorbed again giving rise to excitons and so on until the end of the slab. So the presence of a strong interaction described by H_i together with the conservation of wavevectors during transitions ensure a peculiar strongly coupled exciton–photon propagation inside the slab. This coupled propagation gives rise to new propagation modes known as polaritons with dispersion curves $\omega(\mathbf{k})$ (allowed frequencies versus wavevectors) that close to resonance (energy of incident photons close to the energy of excitons) differ significantly from that of bare photons and excitons. The new dispersion curves can be obtained by simply solving the Maxwell equations including the excitonic polarization. In particular,

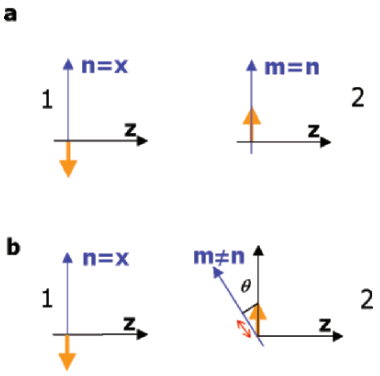

Figure 1. Scheme describing measurements for two particles with dicotomic outcomes and with null total angular momentum: (a) View of one of the two possible results when the two observers choose the same axis. (b) What happens when observer 2 chooses a different rotation axis, according to the transformation properties of vectors under rotation. Panel (b) is based on the assumption that observer 1 performs the measurement just before 2: the red line indicates the value that would be measured according to the rotation properties of classical vectors. The converse assumption (2 just before 1) would not modify the result $v_1(\mathbf{n})v_2(\mathbf{m}) = -\mathbf{n}\cdot\mathbf{m}$.

the condition in order to obtain nontrivial transverse solutions of the Maxwell equations is

$$k^2 = \frac{\omega^2}{k^2}\varepsilon(\mathbf{k},\omega) \tag{13}$$

where $\varepsilon(\mathbf{k},\omega)$ is the dielectric function of the medium containing the contribution from resonant excitons. By writing down the Heisenberg equation of motion for the excitonic polarization in the linear response regime and considering explicitly only the lowest exciton band ($1s$ excitons labelled with n = 1), one obtains

$$\varepsilon(\mathbf{k},\omega) = \varepsilon_\infty + \frac{2\pi}{\hbar}\frac{\omega_1(\mathbf{k})\,|\mu F_1(0)|^2}{\omega_1^2(\mathbf{k}) - \omega^2} \tag{14}$$

In this equation ε_∞ takes into account the influence of out-of-resonance excitations at higher energies (e.g. higher excitonic bands) and $F_1(0)$ is the real space exciton envelope function calculated at $\mathbf{r} = 0$, being $\mathbf{r}$ the coordinate describing the electron-hole relative motion. $|F_1(0)|^2$ provides the probability of finding the electron and the hole at the same place. Solving Eq. (13) after inserting Eq. (14) gives rise to two polariton dispersion curves $\omega_j(\mathbf{k})$ ($j = 1, 2$) named lower and upper dispersion branches (see Fig. 1).

The process that we are going to describe is known as hyper-Raman scattering (HRS) or two-photon Raman scattering. HRS can be schematically described as follows: A first photon induces a transition from the ground state to the excitonic subspace, the second photon induces a further transition from the exciton to the

biexciton subspace, then the excited biexciton may decay spontaneously into an exciton and a photon such that total energy and wave vectors are preserved. However we have just mentioned that the allowed propagating modes inside the crystal slab are polaritons. The above picture should be modified accordingly: a pair of incident photons of given wavevector and energy propagate inside the crystal as polaritons of given energy $\hbar\omega(\mathbf{k}_i)$ and may give rise (according to the hierarcy of dynamic equations) to a biexciton excitation, such excitation can finally decay into a pair of final polaritons. Total energy and momentum are conserved in the whole process :

$$\omega(\mathbf{k}_1) + \omega(\mathbf{k}_2) = 2\omega(\mathbf{k}_i)$$
$$\mathbf{k}_1 + \mathbf{k}_2 = 2\mathbf{k}_i$$

where final polariton states have been labelled with 1 and 2. The determination of the polariton dispersion has successfully been accomplished by HRS in several large-gap bulk semiconductors (Honerlage et al., 1978). HRS is a process related to the third-order nonlinear susceptibility and can be considered as a spontaneous resonant nondegenerate four-wave mixing (FWM). In FWM, the optical decay of the coherently excited biexcitons is stimulated by sending an additional light beam, while in HRS the decay is determined by intrinsic quantum fluctuations. This subtle difference imply that HRS is a quantum optical process that cannot be described properly without including the quantization of the light field (Savasta and Girlanda, 1999). The scattering process largely increases when a bound biexciton state is resonantlly excited by the two polariton process. The final result of the scattering process is the generation of polaritons with slightly different wavevectors and energy displaying pair quantum correlations. If the two final quanta are polaritons with a significant photon component, at the end of the slab they can escape the semiconductor as photons and both can be detected. Being the bound biexciton formed by carriers with oppisite spin, the resulting polariton pairs will be composed by polaritons of opposite spin, which will give rise to photons with opposite circular polarization, corresponding to the following polarization entangled quantum state:

$$|\Psi\rangle = \frac{1}{\sqrt{2}} \left(|+\rangle_1 |-\rangle_2 + |-\rangle_1 |+\rangle_2\right) \tag{15}$$

In 2004, experimental evidence for the generation of ultraviolet polarization-entangled photon pairs by means of biexciton resonant parametric emisison in a single crystal of semiconductor CuCl has been reported (Edamatsu et al., 2005).

5. Quantum complementarity of cavity polaritons

With the devolopment of accurate growth and nanofabrication techniques, it has been possible to confine electrons and holes (and hence excitons) along one (QWs) or more directions (quantum wires and quantum dots). By constructing

artificial semiconductor nanostructures, it has been possible to modify and control the optical and transport properties of electrons. The QW is obtained by sandwitching by means of epitaxial growth technique one layer of semiconductor (a few nanometers thick) between two barriers of a different material with larger gap and analogous lattice constants. In this way the wave functions of the first excited electronic states results to be confined along the growth (z) direction inside the lower-gap layer, while they are of Bloch-type in the orthogonal plane. This electronic confinement enhances optical interactions and modify the polariton concept. The confinement determines the breaking of translation symmetry in the growth direction and thus only the in-plane component of the crystl pseudo-momentum is conserved. As a consequence, an optically active exciton with a given in-plane wavevector can interact with a continuum of light modes with the same in-plane vector but with generic k_z. Thus the 2D excitons of a QW show a radiative decay analogous to the spontaneous emission of the atomic electronic states. In this case, the energy does not oscillate between the photon and the exciton, but it decays either by nonradiative processes or by the interaction of the available continuum of light modes. In this case, the strong coupling between exciton and photons can be established by confining the light modes interacting with the QW excitons in a planar microcavity. This can be achieved by growing a multilayer structure in which one or more QWs results to be embedded in a planar dielectric cavity of the order of the optical wavelength able to confine light. In this case it is possible to achieve a strong-coupling regime and consequently an energy splitting between the cavity–polariton modes. This regime is achieved when the exciton-photon coupling rate is larger than the radiative and nonradiative decay processes. This effect is the solid state analogous of the Rabi splitting observed in cavity quantum electrodynamics experiments on atoms in single-mode cavities. Cavity-polaritons are 2D quasiparticle whose dispersion depends on the in-plane wavevector orthogonal to the growth directions. These modes can be directly excited by illuminating the structure with a ligh beam with resonant frequency. The incidence angle fix the in-plane wave vector of generated polaritons. In the following section we briefly discuss the quantum complemantarity of these hybrid quasiparticles (Savasta et al., 2005).

When two physical observables are complementary, the precise knowledge of one of them makes the other unpredictable. The most known manifestation of this principle is the ability of quantum-mechanical entities to behave as particles or waves under different experimental conditions. For example, in the famous double-slit experiment, a single electron can apparently pass through both apertures simultaneously, forming an interference pattern. But if a "which-way" detector is employed to determine the particle's path, the particle-like behavior takes over and an interference pattern is no longer observed. The link between quantum correlations, quantum nonlocality, and Bohr's complementarity principle was

established in a series of "which-way" experiments using quantum-correlated photon pairs emitted via parametric down-conversion (see e.g. Mandel, 1999). These experiments inequivocably showed that the quantum-mechanical correlation between two different light modes is able to store the "which-way" information, so affecting the interference pattern. These results at the same time help a fundamental understanding of the features of pair quantum states and constitute an elegant demonstration of nonclassical correlations between the photons emitted in parametric down conversion.

Here we report on the theoretical and experimental investigation of quantum complementarity in SCM. Experimental results provide evidence for quantum correlations of emitted polariton pairs. Excitons exhibit strong nonlinearities due to saturation effects (phase space filling) and to Coulomb interaction. The latter enforces exciton–exciton scattering and determines many-body correlations including biexciton effects. Polariton-polariton interactions are determined by their exciton content. Owing to these interactions, pump polaritons generated by a resonant optical excitation can scatter into pairs of polaritons (the signal and the idler modes) according to total momentum and energy conservation criteria (see e.g. Savasta et al., 2003). Cavity-polariton parametric emission has been recently observed (Stevenson et al., 2000). In the low excitation limit it is a spontaneous process driven by vacuum-field fluctuations (Savasta and Girlanda, 1996).

We adress a two-pump scheme with partially degenerate modes. Within this two-pump scheme, pairs of parametric processes with different idlers and sharing the same signal mode are allowed. As a direct quantum mechanical calculation demonstrates[1], the presence or absence of interference is thus implicitly related to the quantum correlation between signal and idler modes. In particular, when detecting a polariton at the signal mode, a coincidence detection at one of the two idlers would in principle say which of the two parametric processes produced the signal-idler polariton pair. The two paths are therefore distinguishable and, according to quantum complementarity, no interference can occur. When instead the two idlers are superimposed at the detection apparatus, interference occurs because the two idler modes are pair-correlated with the same signal mode. Even by means of a signal-idler coincidence measurement, no "which-way" information could be retrieved. Hence the presence or absence of interference is a direct consequence of the complementarity principle enforced by the pair-correlation between signal and idler modes.

The coherence properties of the polaritons are stored in the emitted photons, thus making it possible to carry out the devised "which-way" measurement within a standard optical spectroscopy setup. The measured visibility for the parametricprocess is given in Figure 2, showing that interference is actually observed at and only at the expected region in **k** space. The measured interference between

[1] Savasta et al., 2005

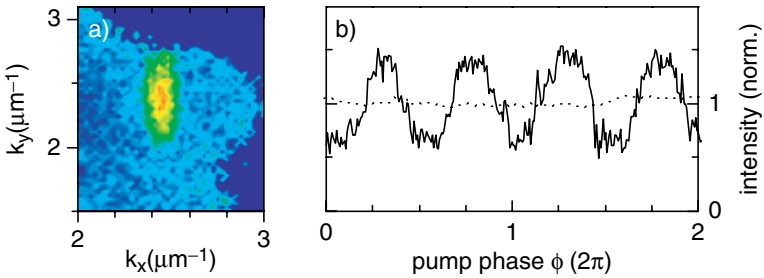

Figure 2. Measured interference. a) $\mathbf{k}$ resolved idler interference visibility (color scale 0 to 0.5). b) Measured $\tilde{I}_{\mathbf{k}}$ at $\mathbf{k} = (2.4, 2.4)\mu m^{-1}$ (full) and at $\mathbf{k} = (0.0, 1.0)\mu m^{-1}$ (dotted) (corresponding to the common signal) versus pump phase ϕ.

the two idler polaritons shows a $\cos(2\phi)$ dependence (see Fig. 2b), in perfect agreement with theory. Additionally, in agreement with the above analysis, the signal at $k_x = 0$ (dotted) displays no interference, even though it is created by a superposition of contributions from both pumps.

These experimental results prove the existence of polariton pair correlations that store the which-way information. This interpretation was confirmed by a theoretical analysis of the measured interference visibility in terms of quantum Langevin equations (Savasta et al., 2005). This result opens the possibility of producing many-particle entangled states of light-matter waves in a semiconductor, extending further the perspective of using solid-state microdevices for the implementation of quantum information technology.

6. Spin entangled cavity polaritons

Cavity polaritons can be optically excited at the desired energy and momentum by tuning the incidence angle and the frequency of the exciting laser. Let us analyze again spontaneous parametric emission in SMCs. We neglect the effects of energy splitting between TE an TM polariton modes . This effect is relevant only at quite high angles and can be prevented by using a scheme with two energy degenerate pumps ($\omega_{\mathbf{k}_p}$) at quite small angles. In this case parametric processes from only one pump are not allowed by energy and momentum conservations, but mixed processes involving both pumps are allowed. We also neglect bound biexciton effects. This last effect is expected to be negligible if the energy of pump polaritons is lower than half the biexciton energy. This can be easily ensured setting the SMC at negative exciton-cavity detuning. With the above assumptions, the polariton parametric scattering preserves the spin orientation, e.g. clockwise polarized pump beams give rise to two clockwise copolarized signal and idler beams with total energy an momentum conservation, as observed experimentally at low excitation density even with less stringent conditions.

In the following we adress calculations within a single pump, generalization to a two-pump scheme is straightforward. Let us consider a **linearly polarized** (along the direction $\tilde{e}_p$) pump laser beam of given in-plane momentum $\mathbf{k}_p$ and energy $\omega_{\mathbf{k}_p}$. The interaction Hamiltonian describing the process for a signal-idler pair is given by

$$\hat{H} = \frac{g P_p^2}{2}[\hat{P}_{s+}^{\dagger}\hat{P}_{i+}^{\dagger} + \hat{P}_{s-}^{\dagger}\hat{P}_{i-}^{\dagger}] + H.c. \tag{16}$$

where P_p^2 represent the classical amplitude of pump polaritons (we also assume the undepleted pump approximation which is a good approximation in the low excitation density regime), $\hat{P}_s$, $\hat{P}_i$ are the operators describing respectively the signal and idler polariton pairs produced by the scattering process with momenta $\mathbf{k}_s$, $\mathbf{k}_i$. The Hamiltonian describes two phase coherent twin-beam sources corresponding to the pairs of modes $\hat{P}_{s+}^{\dagger}$, $\hat{P}_{i+}^{\dagger}$ and $\hat{P}_{s-}^{\dagger}$, $\hat{P}_{i-}^{\dagger}$. The two different sources arise from the decomposition of the linear pump polarization $\hat{e}_p$ in the two indipendent left and right circular components $\hat{e}_-$, $\hat{e}_+$:

$$\tilde{e}_p = \frac{1}{\sqrt{2}}(\tilde{e}_- + \tilde{e}_+)$$

Solving the corresponding Heisenberg-Langevin equations in the low excitation density regime, one finds that the signal and idler emission results to be completely unpolarized. On the contrary, a calculation of signal-idler coincidence displays important polarization effects. This is due to the fact that + and − polarized polaritons are emitted with the same intensity, but polaritons are emitted in pairs that are co-circularly polarized. They are spin-entangled. Neglecting losses and noise, in the limit of low excitation intensity, Hamiltonian (Eq. 16) gives rise to the following spin-entangled polariton quantum state:

$$|\Psi\rangle = \frac{1}{\sqrt{2}}\left(|+\rangle_s|+\rangle_i + |-\rangle_s|-\rangle_i\right) \tag{17}$$

Since this entanglement origins from mean-field scattering, without biexcitons that can give rise to undesired effects like spin-flips and noise, and since photoluminescence within the suggested configuration is negligible, we expect that a quite high degree of entanglement can be produced within this scheme.

References

Aspect, A. (1999) Bells inequality test: more ideal than ever, *Nature* **398**, 189–190.

Axt, V.M. and Kuhn, T. (2004) Femtosecond spectroscopy in semiconductors: a key to coherences, correlations and quantum kinetics, *Reports on Progress in Physics* **67**, 433–512.

Bell, J.S. (1964) On the Einstein-Podolsky-Rosen paradox, *Physics* **1**, 195–200.

Clauser, J.F., Horne, M.A., Shimony, A., and Holt, R.A. (1969) Proposed experiment to test local hidden-variables theories, *Physical Review Letters* **49**, 1804–1807.

Edamatsu, K., Oohata, G., Shimizu, R., and Itoh4, T. (2005) Generation of ultraviolet entangled photons in a semiconductor, *Nature* **243**, 2322–2330.

Einstein, A., Podolsky, B., and Rosen, N. (1935) Can quantum-mechanical description of physical reality be considered complete? *Physical Review* **47**, 777–780.

Honerlage, Bivas, A., and Phach, V.D. (1978) Determination of the excitonic polariton dispersion in CuCl two-photon Raman scattering, *Physical Review Letters* **41**, 49–52.

Mandel, L. (1999) Quantum effects in one-photon and two-photon interference, *Review of Modern Physics* **71**, 274–282.

Nielsen, M.A. and Chuang, I.L. (2000) *Quantum Computation and Quantum Information*, Cambridge University press, Cambridge.

Savasta, S. and DiStefano, O. (2006) Quantum optics with interacting polaritons, *Physica Status Solidi (b)* **111**, 495–500.

Savasta, S., DiStefano, O., and Girlanda, R. (2003) Many-body and correlation effects on parametric polariton amplification in semiconductor microcavities, *Physical Review Letter* **90**, 096403–1–096403–4.

Savasta, S., DiStefano, O., Savona, V., and Langbein, W. (2005) Quantum complementarity of cavity polaritons, *Physical Review Letter* **94**, 246401–1–246401–4.

Savasta, S. and Girlanda, R. (1996) Quantum optical effects and nonlinear dynamics in interacting electron systems, *Physical Review Letters* **77**, 4736–4739.

Savasta, S. and Girlanda, R. (1999) Hyper-Raman scattering in semiconductors: a quantum optical process in the strong-coupling regime, *Physical Review B* **59**, 15409–15421.

Savasta, S., Martino, G., and Girlanda, R. (1996) Hyper Raman scattering in microcavity quantum wells: a quantum optical process in the strong coupling regime, *Physica Status Solidi (a)* **164**, 85–89.

Savasta, S., Martino, G., and Girlanda, R. (2000) Entangled photon pairs from the optical decay of excitons, *Solid State Communications* **111**, 495–500.

Savvidis, P.G., Baumberg, J.J., Stevenson, R.M., Skolnick, M.S., Whittaker, D.M., and Roberts, J.S. (2000) Many-body and correlation effects on parametric polariton amplification in semiconductor microcavities, *Physical Review Letters* **84**, 1547–1550.

Stevenson, R.M., Astratov, V.N., Skolnick, M.S., Whittaker, D.M., Emam-Ismail, M., Tartakovskii, A.I., Savvidis, P.G., Baumberg, J.J., and Roberts, J.S. (2000) Continuous wave observation of massive polariton redistribution by stimulated scattering in semiconductor microcavities s, *Physical Review Letters* **85**, 3680–3683.

Unnikrishnan, C.S. (2005) Correlation functions, Bell's inequalities and the fundamental conservation laws, *Europhysics Letters* **69**, 489–495.

Weisbuch, C., Nishioka, M., Ishikawa, A., and Arakawa, Y. (1992) Observation of the coupled exciton-photon mode splitting in a semiconductor microcavity, *Physical Review Letters* **69**, 3314–3317.

MAGNETISM IN ONE-DIMENSIONAL METAL SYSTEMS

PIETRO GAMBARDELLA
Institució Catalana de Recerca i Estudis Avançats (ICREA) and Centre d'Investigacions en Nanociència i Nanotecnologia (CSIC-ICN) UAB Campus, E-08193 Bellaterra (Barcelona), Spain.

Abstract. We introduce the magnetic properties of finite-sized one-dimensional (1D) systems in the framework of the Heisenberg model and a superparamagnetic spin block model. We further analyze the experimental observation of short- and long-range ferromagnetic (FM) order in epitaxial 1D Co monatomic chains supported on a Pt substrate. Finally, we discuss changes in the local magnetic moments and anisotropy associated with the low coordination of the magnetic atoms in 1D metallic nanostructures.

Keywords: Low-dimensional magnetism, Heisenberg model, magnetic anisotropy, nanowires.

1. Introduction

According to statistical mechanics, the tendency to magnetic order reduces as thermal fluctuations become more disruptive with decreasing dimensionality. As a result, magnetism in two-dimensional (2D) ultrathin films is more sensitive to temperature effects compared to three-dimensional (3D) systems (Gradmann,1993). Indeed, owing to the reduced number of neighbors contributing to the exchange interaction, rigourous results for the isotropic Heisenberg model rule out ferromagnetic (FM), antiferromagnetic (AFM), as well as oscillatory long-range order in 2D and 1D (Mermin and Wagner, 1966; Bruno, 2001). However, in 2D the introduction of dipolar coupling or of an arbitrarily small anisotropy of spin-orbit origin is sufficient to establish long-range magnetic order (Bander and Mills, 1988). In the last two decades, progress in the preparation and characterization techniques of epitaxial metal films has enabled to confirm and elaborate such predictions experimentally in 2D films down to monolayer thickness (Dürr et al., 1989; Gradmann et al., 1989; Poulopoulos and Baberschke, 1999). In 1D, on the other hand, spin wave excitations, i.e., fluctuations in the relative alignment of adjacent spins, cost less energy compared to 2D and are more effective in breaking long-range order for obvious topological reasons. Indeed, even in the 1D Ising model, i.e. the extreme anisotropic limit of the Heisenberg Hamiltonian, magnetic disorder is predicted in the absence of an external field for any temperature $T > 0$. A simple thermodynamic argument due to Landau exemplifies this very clearly as a function of the system size (Landau and Lifshitz, 1959). Consider

B. Azzerboni et al. (eds.), Magnetic Nanostructures in Modern Technology, 325–342.

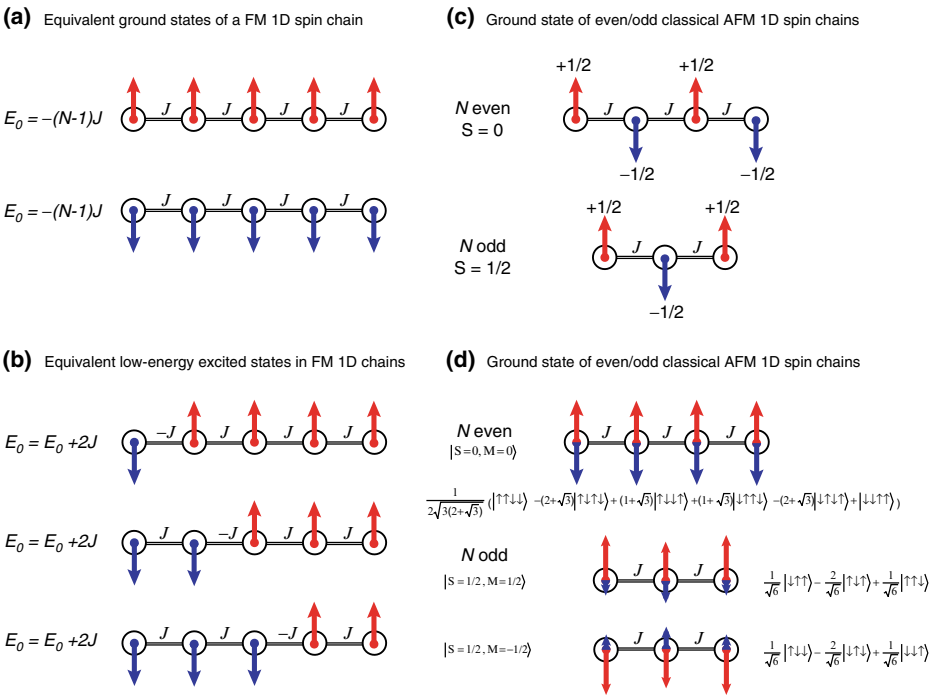

Figure 1. (a) Equivalent ground state configurations (at $T = 0$ K) of a FM spin chain in zero applied magnetic field. (b) Equivalent lowest-energy excited states states. (c) Néel ground state of AFM classical spin chains with $N = 3, 4$ atoms. (d) Ground state of AFM quantum chains with spin $1/2$. The length of the arrows represents the relative probability for each spin to point up or down. The corresponding wavefunctions are also given.

a chain consisting of N magnetic moments described by the Ising Hamiltonian $H = -J \sum_{i=1}^{N-1} S_{z\,i} S_{z\,i+1}$, with nearest-neighbor exchange coupling energy $J > 0$ (FM interaction). The ground state energy of the system is $E_0 = -J(N-1)$ and corresponds to the situation where all the moments are aligned, as shown in Fig. 1a. The lowest lying excitations are those in which a single break occurs at any one of the N sites. There are $N-1$ equivalent to such excited states, all with the same energy $E = E_0 + 2J$, shown in Fig. 1b. At a given temperature T the change in free energy due to these excitations is $\Delta G = 2J - k_B T \ln(N-1)$. For $N \to \infty$ the entropy term prevails and we have $\Delta G < 0$ at any finite temperature. The FM state becomes unstable against thermal fluctuations. For chains of finite length, however, if $(N-1) < \mathrm{e}^{2J/k_B T}$, FM order is energetically stable. Assuming $2J = 10\,(20)$ meV, we get an upper limit of $N \approx 10\,(100)$ atoms at $T = 50$ K. Such conclusions apply to an ideal 1D lattice of spin point vectors in both the FM and AFM case, for which $J < 0$. An AFM system, however, present additional complications. If the spins in the Heisenberg Hamiltonian are

considered as classical vectors, then the ground state of a 1D chain is easily found to be the alternate up-down configuration shown in Fig. 1c, the so-called Néel state. Note that depending on odd/even N, the chain might or might not have a net magnetization. When the quantum nature of the spins is considered, the situation is radically different. The eigenstates of the quantum AFM Heisenberg Hamiltonian are then given by a superposition of states, each representing a classical spin configuration (Fig. 1d). As a consequence, contrary to the FM case, we cannot assign a well-defined orientation to individual atomic spins in the ground state of an AFM quantum system; the spins are entangled, inseparable from each other. Such an effect, which is well-known for the wavefunctions describing the triplet singlet pair $1/\sqrt{2}(|\uparrow\downarrow\rangle \pm |\downarrow\uparrow\rangle)$ of a two-electron molecular bond, is generally present in AFM 2D and 1D low-dimensional magnetic systems and discussed more at length by de Jongh and Miedema (1974) and Welz (1993). A very recent demonstration of the entangled nature of AFM spin chains has been given for Mn monatomic chains assembled on a CuN substrate by Hirjibehedin and coworkers using scanning tunneling microscopy (STM) (Hirjibehedin et al., 2006).

Most experimental investigations on 1D magnetic systems have concentrated on insulating crystals consisting of arrays of linear chains of exchange-coupled transition-metal ions separated by nonmagnetic atom spacers and characterized by weak interchain interactions (de Jongh and Miedema, 1974; Hone and Richards 1974; Caneschi et al., 2001). One example is tetramethyl ammonium manganese chloride, which typically exhibits AFM coupling and 1D paramagnetic behavior down to about $T = 1$ K (Dingle et al., 1969). More recently, investigations have focused on pure metal chains, whose thickness and spatial separation can be independently controlled. The atomic steps of a nonmagnetic vicinal surface are used as deposition template for TM atoms, thus producing a large number of nanowires in a parallel process. A small cost is due in terms of the finite size distribution of the wires with respect to, e.g. atom manipulation by scanning probes (Hirjibehedin et al., 2006), but the large wire density allows us to use spatially integrating techniques with magnetic sensitivity such as Kerr magnetometry and x-ray magnetic circular dichroism (XMCD). This approach was first explored by Elmers et al. (1994) in the study of Fe wires on vicinal W(110), which show in-plane anisotropy and a relaxation-free FM phase transition due to dipolar-induced coupling across adjacent stripes (Hauschild et al., 1998; Pietzsch et al., 2000; Pratzer et al., 2001). Shen et al. (1997a,b) found a pronounced temperature- and time-dependent magnetic relaxation for Fe stripes on stepped Cu(111) with out-of-plane anisotropy, due to the formation of 1D Ising-coupled spin blocks. Fe and Co stripes on Pd(110) (Li et al., 2001; Yu et al., 2005) and Pt(997) (Dallmeyer et al., 2000; Gambardella et al., 2002a; Gambardella, 2003; Gambardella et al., 2004; Vindigni et al., 2006; Repetto et al., 2006) have also been studied, as well as Fe on Au(778) (Fujisawa et al., 2005).

In this chapter, we present a survey of the magnetic properties of 1D metallic atomic chains of varying thickness for the model case of Co grown on a single-crystal Pt substrate. In Section 2, we present the self-assembly approach that allows to produce uniform arrays of 1D chains by molecular beam epitaxy. We then address the magnetic behavior of Co chains in the monatomic limit by combining XMCD experiments with theoretical models apt at describing strongly anisotropic FM systems. Finally, we discuss the effects of dimensionality on properties other than magnetic order, such as the local magnetization and magnetic anisotropy, which are also very important in metallic systems.

2. Epitaxial growth of one-dimensional atomic chains

Progress in heteroepitaxial growth methods today allows to fabricate arrays of continuous, 1D mono- or bilayer stripes of a magnetic metal on top of a nonmagnetic substrate (Himpsel et al., 1998), where the control of the system size can be pushed down to the monatomic limit (Gambardella et al., 2000a,b; Gambardella and Kern, 2001; Gambardella et al., 2006). Nucleation and diffusion of metals on densely stepped substrates can be exploited to grow arrays of 1D atomic chains by step decoration. Depending on the surface temperature, adatoms on vicinal surfaces tend to self-assemble into chain-like structures at the lower side of the step edges (Gambardella et al., 2001a; Gambardella et al., 2006). This is simply due to the increase of binding energy at step sites (Gambardella et al., 2001a; Picaud et al., 2000) and is, of course, a general phenomenon that holds for metals (Mundschau et al., 1989; Himpsel et al., 2001; Himpsel and Ortega, 1994; Gambardella et al., 2000a; Gambardella et al., 2000b; Gambardella and Kern, 2001), as well as for gas species (Marsico et al., 1997; Gambardella et al., 2001b). An advantage of this growth method is that by adjusting the adatom coverage and the average step spacing one can independently control the chain width and separation, respectively. Growth proceeds either as a smooth step-wetting process (Himpsel et al., 2001; Himpsel and Ortega, 1994; Gambardella et al., 2000a,b) or as nucleation of 2D islands at the step edges (de la Figuera et al., 1995), provided that the adatom deplacement prior to nucleation is larger than the terrace width of the substrate. In Fig. 2 we show different scenarios of heteroepitaxy on a stepped substrate. We distinguish (i) the ideal case of row-by-row growth, (ii) chains of different widths due to interlayer crossing of the adatoms, (iii) formation of irregular 2D islands at the step edges, (iv) alloying, (v) formation of double layer-thick stripes. In preparing arrays of 1D chains for spectroscopic investigation with spatially-integrating probes, we must focus on the conditions that favor the ideal case (i). As a general trend we find that 1D chain formation is limited at low temperature by slow edge-diffusion processes and at high temperature by interlayer diffusion and, eventually, by alloying between the metal adspecies and the substrate.

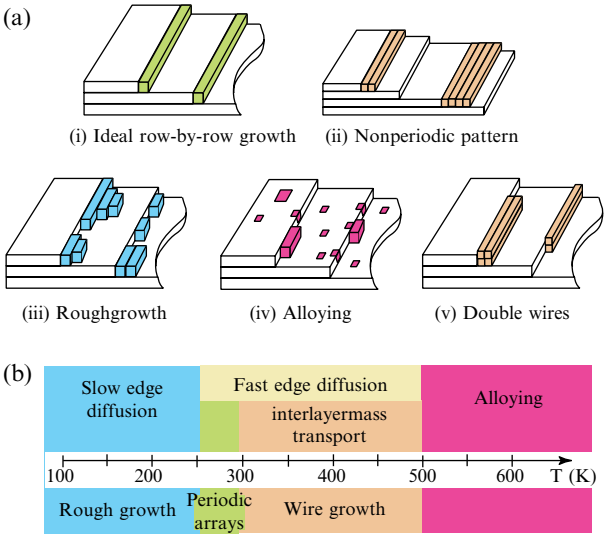

Figure 2. (a) Epitaxial growth modes on a stepped substrate. (b) Co growth modes on Pt(997) as a function of the substrate temperature. (From Gambardella, 2003.)

The basic requirement to grow self-assembled patterns of regular chains by step decoration is a suitable substrate template. By this we mean a sample whose steps are as straight and as evenly spaced as possible. We have chosen to work with Pt vicinal surfaces since repulsive interactions between adjacent steps suppress step meandering (Papadia et al., 1996), resulting in remarkably straight steps and in a narrow terrace width distribution, as shown in the STM image in Fig. 3a. The average step separation as well as the kink density along the steps are determined by the crystal miscut. In the Pt(997) case, the average terrace width is 20.2 Å (Fig. 3b,c) with standard deviation $\sigma = 2.9$ Å (Hahn et al., 1994), which allows us to obtain a density of 5×10^6 atomic chains per cm^{-1}. Below 250 K the chain formation is kinetically hindered by slow edge- and corner-diffusion processes. Regular Co chains grow only above 250 K (Gambardella et al., 2000b). A monatomic chain array is obtained as the coverage equals the inverse of the number of atomic rows in the substrate terraces, i.e. 0.13 ML (1 monolayer = 1.5×10^{-15} atoms/cm^2) for Pt(997). The average length of a continuous Co chain is estimated to be about 80 atoms from the average kink density per Pt step obtained by STM. As the coverage increases to more than a single monatomic chain per terrace, Co grows row-by-row (Fig. 3d and e) up to $T = 290$ K. At $T > 290$ K, interlayer diffusion, i.e., the diffusion of adatoms across adjacent terraces, sets in. This implies that the proportionality between adlayer coverage on each terrace and terrace width is no longer valid, resulting in either or both (ii) and (v), shown in Fig. 2a. At $T > 500$ K significant Co-Pt alloying takes place. The temperature window for the growth of a regular periodic array of Co atomic chains is therefore

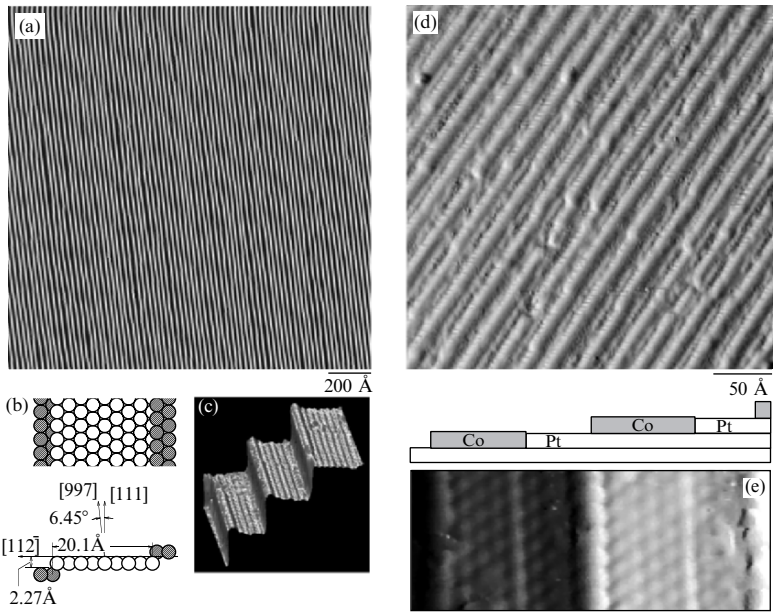

Figure 3. The Pt(997) surface. (a) STM topographs of the periodic step structure (each white line represents a monatomic Pt step). Step down direction is from right to left. (b) Diagram of the surface lattice. (c) 3D STM image of the Pt steps (the vertical scale has been enhanced for better rendering). (d) STM image of 0.6 monolayer Co deposited at $T = 250$ K on Pt(997); step down direction is from right to left. Row-by-row growth conserves the original step pattern, forming regular stripes that run parallel to the Pt steps. (e) Detail of two adjacent terraces, as shown in the diagram, showing atomically resolved Co chains and Pt terraces.

limited to a narrow interval between 250 and 300 K, as edge diffusion is fast enough to have row-by-row growth and interlayer diffusion and intermixing are still inhibited.

3. Short- and long-range ferromagnetic order in one-dimension

3.1. EXPERIMENT

The magnetic behavior of the 1D Co chains has been investigated by XMCD, i.e., the absorption of circularly polarized x-rays in the soft x-ray energy range ($2p \rightarrow 3d$ transitions) (Schütz et al., 1987; Chen et al., 1990). XMCD is defined as the difference in the absorption coefficients for parallel and antiparallel orientation of the helicity of the incident light with respect to the magnetization direction of the sample. Because of its element-selectivity and surface sensitivity (reaching down to 3×10^{12} atoms cm^{-2} (Gambardella et al., 2002b), XMCD represents one of the most powerful magnetic probes available to date. The technique allows to identify the magnetization direction and strength and to separately determine

the spin (m_S) and orbital (m_L) magnetic moment of a given element by means of dipole sum rules (Thole et al., 1992; Carra et al., 1993; Chen et al., 1995). The XMCD measurements were performed at beamline ID12B of the European Synchrotron Radiation Facility (ESRF) in Grenoble, where samples were prepared in-situ at $T = 260$ K according to the procedure described in Section 2. The Co coverage was controlled by cross-checking the coercive field of Co ultrathin films with that obtained by means of combined Kerr effect (MOKE)-STM experiments. This method gave consistent results with the yield of a quartz microbalance and is extremely precise since the coercive field of Co on Pt depends critically on the Co coverage (McGee et al., 1993). XMCD spectra were taken at the $L_{2,3}$ absorption edges of Co in the electron yield mode by measuring the drain current of the photoexposed sample for parallel and antiparallel alignment of the applied magnetic field **B** with the incident light direction. The sample was rotated about its polar and azimuthal axes with respect to the light beam in order to measure the XMCD for different orientations of the chains relative to **B**. The XMCD spectra so obtained are reported by Gambardella et al. (2002a), Gambardella et al. (2003), Vindigni et al. (2006). Here we show the magnetization curves obtained at fixed photon energy by recording the L_3 XMCD maximum intensity as a function of **B**. These allow us to analyze the magnetization measured at different angles with respect to the chain axis and to compare it as a function of chain thickness.

3.2. MAGNETIC BEHAVIOR OF CO MONATOMIC CHAINS

The magnetic response of a set of monatomic Co wires at $T = 45$ K is shown in Fig. 4a. The zero remanent magnetization reveals the absence of long-range FM

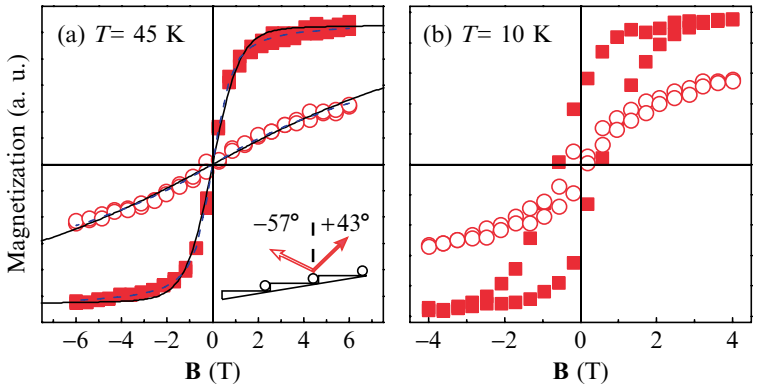

Figure 4. Magnetization of a monatomic chain array as a function of the applied field **B**. (a) Magnetization at $T = 45$ K, easy direction (solid squares, $+43°$) and $80°$ away from the easy direction (empty circles, $-57°$) in the plane perpendicular to the wire axis (see inset). The solid lines are fits to the data according to the spin block model (1), dotted lines are fits according to the Heisenberg model (3). (b) Magnetization at $T = 10$ K, same geometry as (a). (Adapted from Gambardella et al., 2002a and Vindigni et al., 2006.)

order. However, the shape of the magnetization curve indicates the presence of short-range order, i.e., of significant interatomic exchange coupling in the chains. For noninteracting paramagnetic moments, the magnetization expected in the present experimental conditions would be significantly smaller and nearly linear up to 6 T. Moreover, we observe a remarkable dependence of the magnetization on the direction of the applied field. The strongest magnetic response is found in the plane perpendicular to the chain axis, tilted by $+43^\circ$ with respect to the (111) surface normal, where the positive sign indicates the step-up direction. This large magnetic anisotropy plays a major role in stabilizing FM order in the 1D chains. As in bulk FM systems, anisotropy energy barriers can effectively pin the magnetization along a fixed direction in space. By lowering the sample temperature below 15 ± 5 K, we observe a transition to a long-range FM ordered state with finite remanence (Fig. 4b), which is extended over the whole sample. The reduced remanent magnetization relative to the saturation magnetization is due to inhomogeneities in the chain growth (Gambardella et al., 2000b), with chains of different length or thickness having different magnetic behavior (Gambardella et al., 2004). The observation of long-range FM order might appear in clear contrast with its predicted absence discussed in Section 1 for long 1D chains. However, one must note that such an anisotropy-stabilized FM state does not necessarily represent the thermodynamic limit of the system, but rather a metastable state that allows FM to exist over timescales equal or longer than the measurement time.

3.3. SPIN BLOCK MODEL

There are two models that can be employed to analyze the chain magnetization. The first is that of a 1D superparamagnetic system, i.e. a system composed by segments, or spin blocks, each containing N_c exchange-coupled Co atoms, whose resultant magnetization orientation is not stable at high temperature due to thermal fluctuations. The curvature of the superparamagnetic magnetization *vs.* $\mathbf{B}$ depends on N_c times the magnetic moment per Co atom as well as on the magnetic anisotropy energy of each spin block $N_c D$, where D is a uniaxial magnetic anisotropy energy constant. Below a threshold temperature, the so-called blocking temperature, the magnetization of each spin-block aligns along the common easy axis direction and the whole system becomes FM. The magnetic energy of the system is given by the sum of a Zeeman and uniaxial anisotropy energy terms:

$$E = -N_c \mathbf{m} \cdot \mathbf{B} - N_c D(\hat{\mathbf{m}} \cdot \hat{\mathbf{e}})^2, \tag{1}$$

where $\mathbf{m}$ is the magnetic moment per Co atom ($3.8\ \mu_B$/atom in monatomic chains, including the spin and orbital contributions as well as the induced magnetization on the first and second nearest Pt neighbors (Ferrer et al., 1997)), and $\hat{\mathbf{e}}$ the unit vector representing the easy axis direction. According to Boltzmann statistics, the

magnetization of an assembly of aligned chains with the easy axis oriented at an angle θ_0 with respect to **B** is given by

$$M = M_s \frac{\int_0^{2\pi} d\phi \int_0^{\pi} d\theta \ \sin\theta\cos\theta \ \exp\left[-E(\theta_0,\theta,\phi)/kT\right]}{\int_0^{2\pi} d\phi \int_0^{\pi} d\theta \ \sin\theta \ \exp\left[-E(\theta_0,\theta,\phi)/kT\right]}, \tag{2}$$

where θ and ϕ are the polar and azimuthal spherical coordinates in the reference system defined by **B**, and M_s the saturation magnetization. The simultaneous numerical fit of the easy and hard axis magnetization according to Eq. (2) (solid lines in Fig. 4a) allows to obtain both N_c and D (Gambardella et al., 2002a; Gambardella et al., 2004). We find $N_c = 15$ atoms, giving an average estimate of the extent of short-range FM order at 45 K, and $D = 2.0 \pm 0.2$ meV/Co atom. The total anisotropy energy of a spin block is thus $N_c D = 31$ meV. According to the Néel-Brown model of magnetization reversal (Wernsdorfer et al., 1997), this allows us to estimate the blocking temperature separating the paramagnetic to FM transition. If the relaxation time of a single spin block is expressed by an Arrhenius law of the form $\tau = \tau_0 \exp(\frac{D}{kT})$, where τ_0 is a prefactor of the order of 10^{-9} s, we find that FM order should be present below 15 K over timescales of the order of $\tau \geq 10^2$ s, in agreement with our observations.

3.4. HEISENBERG MODEL

The spin block model described in the previous paragraph considers the individual spins in each block as rigidly aligned. In general, however, the relative alignment between adjacent spins may vary depending on competing interactions: exchange, local magnetic anisotropy, dipolar, and external fields. If the magnetic moments of individual Co atoms in a chain are assumed to be separable, then we can employ a 1D Heisenberg model to study the correlation between the atomic moments at different positions along the chain. The model Hamiltonian in the present case is:

$$\mathcal{H} = -\sum_{i=1}^{N-1} J\vec{S}_i \cdot \vec{S}_{i+1} - \sum_{i=1}^{N} \left[D\left(S_i^z\right)^2 + g_{Co-Pt}\mu_B \vec{\mathrm{B}} \cdot \vec{S}_i \right], \tag{3}$$

where J is the exchange coupling constant and $|\vec{S}_i|^2 = 1$. The gyromagnetic factor g_{Co-Pt} has been set equal to 3.8 to take into account the Co spin and orbital atomic moment as well as the induced moment on Pt, as in the previous paragraph. The Hamiltonian (Eq. 3) describes linear atomic chains of finite length N, with no periodic boundary conditions. Here we have set $N = 80$ as suggested by the structural analysis of our sample. The magnetization of Heisenberg chains can now be calculated from Eq. (3) using a finite-size transfer matrix algorithm described by Vindigni et al. (2006), and a fit is performed on the monatomic chain data of Fig. 4a. The free parameters in the fit are the J and D constants and a rescaling factor for the magnetization, since the XMCD curves in Fig. 4 are

given in arbitrary units. The dotted lines in Fig. 4a represent the fit performed on the magnetization data measured along both the easy and hard directions at $T = 45$ K. For the two parameters of the spin Hamiltonian we obtain $J = 228.7$ K (20 meV) and $D = 38.3$ K (3.3 meV). The value of J is in good agreement with first-principles calculations of the interatomic exchange interaction in bulk and monolayer Co structures, ranging from 15 to 40 meV (van Schilfgaarde and Antropov, 1999; Frôta-Pessoa and Kudrnovský, 2000; Pajda et al., 2000), and slightly larger than that (14 meV) estimated for a Fe monolayer on a W(110) surface based on the analysis of domain walls (Pratzer et al., 2001; Pratzer and Elmers, 2003). Notably, despite the conceptual differences between the spin block model and the present calculation, we find consistent results for the uniaxial magnetic anisotropy energy term. Electronic structure calculations for Co monatomic chains deposited on Pt (Hong and Wu, 2004; Lazarovits et al., 2003 ; Hong and Wu, 2003; Újfalussy et al., 2004; Shick et al., 2004; Baud et al., 2006; Komelj et al.,2006) also agree with our results. The smaller D found for the spin block atoms can be easily rationalized by the fact that a relatively large number of rigidly coupled atoms aligns more readily to the external field.

Using the fit parameters derived above, we can now investigate magnetic correlation effects along our model Co chains at different temperatures. The spin–spin correlation function depends on sites i and $i + r$ in chains of finite length. This function can be conveniently represented by means of the matrix (Vindigni et al., 2006):

$$\mathcal{C}^{\alpha\gamma}_{i,i+r} = \left\langle S^{\alpha}_{i} S^{\gamma}_{i+r} \right\rangle , \tag{4}$$

which is real and symmetric in the exchange $i \leftrightarrow i + r$ and $i \leftrightarrow N - i$. Here $\alpha, \gamma = x, y, z$ represent orthogonal directions, with z set parallel to the easy axis. Figures 5a and b show the correlation matrices $\mathcal{C}^{zz}_{i,j}$ and $\mathcal{C}^{xx}_{i,j}$ for the Hamiltonian (Eq. 3) in zero field at $T = 45$ K. The zz-correlation at this temperature is already quite strong between all the spins of the chain, as the matrix values are rather detached from the zero plane away from the diagonal terms. One can also notice that the FWHM of the correlation function cut across the diagonal corresponds to the average size of the spin block estimated in Section 3.3. Excluding the end spins, the spin-spin diagonal correlation for the easy axis matrix $\mathcal{C}^{zz}_{i,j}$ is about three times larger compared to $\mathcal{C}^{xx}_{i,j}$, reflecting the anisotropy of the system. Also, the hard plane correlation (the results obtained for $\mathcal{C}^{xx}_{i,j}$ and $\mathcal{C}^{yy}_{i,j}$ are identical thanks to the symmetry about the z-axis of the Hamiltonian (Eq. 3)) vanishes faster compared to the correlation between the easy axis components. Typically related to the finite size of the chains is the smoothing of the diagonal maxima curve of the $\mathcal{C}^{zz}_{i,j}$ matrix in the vicinity of the end points. The zz-autocorrelation function ($\mathcal{C}^{zz}_{i,i}$) is in fact expected to be smaller for the spins at the chain edges, as they miss one magnetic neighbor and can fluctuate more freely. Through the constraint given by the norm of each spin vector this effect reflects on the hard

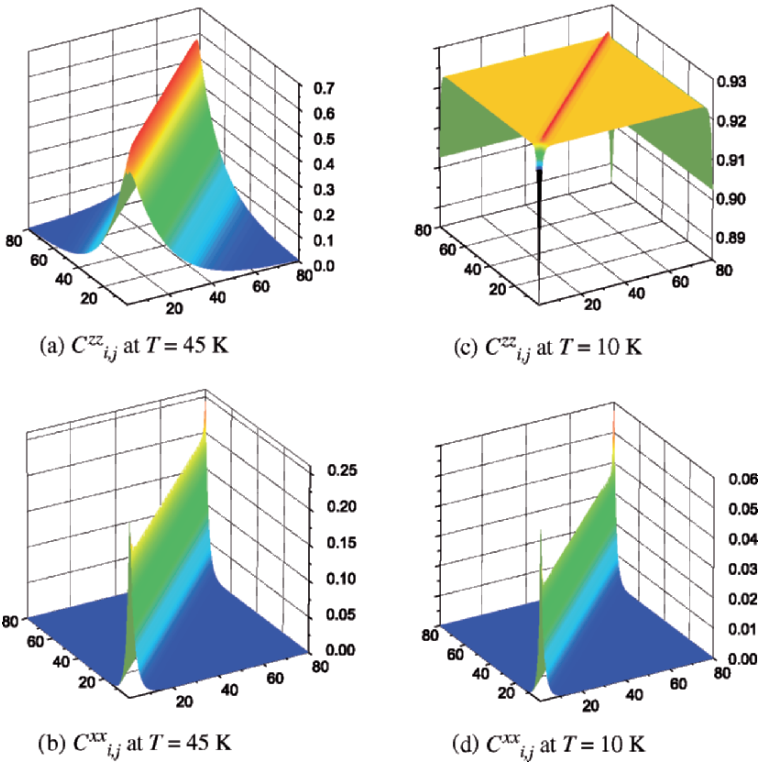

Figure 5. Correlation matrix of the Hamiltonian (3) computed using the fit parameters for the two experimental temperatures $T = 45$, 10 K. The basal plane represents the considered couples of spin (i, j); the correlation functions $\mathcal{C}^{zz}_{i,j}$, (a) and (c), and $\mathcal{C}^{xx}_{i,j}$, (b) and (d), are reported on the vertical axes. (From Vindigni et al., 2006.)

plane autocorrelation functions ($\mathcal{C}^{xx}_{i,i}$ and $\mathcal{C}^{yy}_{i,i}$) too: their values increase in the vicinity of the edges (see spikes in Fig. 6b) in order to satisfy the relationship $\langle S^x_i S^x_i \rangle + \langle S^y_i S^y_i \rangle + \langle S^z_i S^z_i \rangle = 1$. The same effect does not occur in the isotropic Heisenberg model because the symmetry of the Hamiltonian forces the spin-spin correlation function to contribute to the same level to the unitary norm $|\vec{S}_i|^2$ and $\langle S^x_i S^x_i \rangle = \langle S^y_i S^y_i \rangle = \langle S^z_i S^z_i \rangle = \frac{1}{3}$ for any temperature and at any site. We can conclude that the localization of disorder is enhanced by the anisotropy term D, while it completely disappears in the isotropic Heisenberg limit.

At T=10 K the correlation between the spins along the easy axis (Fig. 5c) is much stronger compared to 45 K. It is interesting to observe that the correlation of the first (not evident from the picture) and the last spin with all the others is significantly weaker than between the middle spins; this is again consistent with the confinement of entropy close to the end spins. The relationship between the autocorrelation function along the easy axis and those of the hard plane (Fig. 5d)

is similar to that described above for $T = 45$K. The analysis of the correlation matrix in terms of the plot of Fig. 5 reveals, even at first sight, that the physics of the system at the two considered temperatures may be very different, and supports the experimental observation of FM order in the monatomic Co chains.

As the diagonal terms of the correlation matrix are directly related to the susceptibility, the localization of disorder at the end spins indicates that these will respond to an applied field differently from the "internal" spins. It is therefore possible that, depending on the length of the chains (Hinzke and Nowak, 2000), thermally activated magnetization reversal will proceed in a nonuniform way from the end points towards the center of the chains (Bogani et al., 2004; Braun, 1994, 1999).

4. Dependence of the magnetic moment and anisotropy on the atomic coordination

In studies concerned with insulating or molecular magnetic compounds (de Jongh and Miedema, 1974; Welz, 1993; Hone and Richards, 1974; Caneschi et al., 2001; Dingle et al., 1969), the use of the Heisenberg and Ising models to reproduce the experimental behavior can be justified under the assumption of well-localized magnetic moments. On the other hand, 1D-like metallic systems are characterized by a larger degree of electron delocalization because of the direct interaction between metal atoms and the presence of a nonmagnetic but metallic substrate. Apart from magnetic order, fundamental intrinsic magnetic properties like the magnitude of m_S and m_L, as well as the magnetocrystalline anisotropy (the equivalent of *single ion anisotropy* in molecular compounds) depend strongly on the dimensionality of a given system (Gradmann et al., 1993; Schneider and Krischner, 2000; Himpsel et al., 1998; Gambardella et al., 2002b). It is known that the reduced atomic coordination in thin films (Gradmann et al.,1993; Tischer et al., 1995; Weller et al., 1995; Ohresser et al., 2000) and small particles (Billas et al., 1994; Dürr et al., 1999; Gambardella et al., 2002b; Gambardella et al., 2003) significantly alters such quantities. In 1D, depending on the substrate chosen as a support, even stronger changes in m_S, m_L, and D are expected. Theoretical calculations (Lazarovits et al., 2003; Baud et al., 2006) and photoemission experiments (Dallmeyer et al., 2000; Gambardella, 2003) show that m_S changes from about 1.6 to 2.1 μ_B/atom from bulk Co to a 1D chain. Changes with respect to the atomic coordination, however, are even more evident for m_L. With respect to the 0.15 μ_B/atom bulk value, monatomic Co chains show almost a fivefold enhancement, an effect due to the narrowing of the Co 3$d$band in 1D structures. Figure 6 shows the strong dependence of m_L on the chain lateral thickness measured by XMCD, with the strongest differences occurring for the least coordinated Co atoms in the monatomic 1D limit.

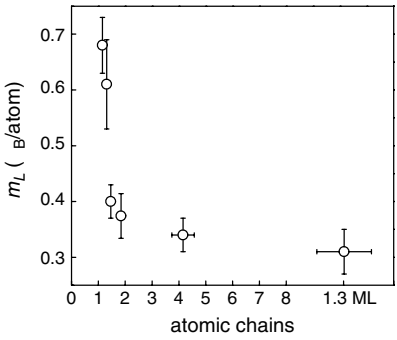

Figure 6. Orbital magnetic moment measured by XMCD as a function of the number of atomic rows in Co chains on Pt(997). The data have been measured at $T = 10$ K parallel to the easy axis direction

Theoretical models (Bruno, 1989; van der Laan, 1998) show that the magnetocrystalline anisotropy is connected via m_L and the spin–orbit interaction to the atomic structure of a magnetic material. From the decreased symmetry and coordination of monatomic chains we expect significantly larger values of the magnetic anisotropy energy compared to the bulk and even 2D films. The fits in the previous sections show that the magnetic anisotropy energy D of monatomic 1D chains is one to two orders of magnitude larger compared to typical values in 2D films (Gradmann et al., 1993; Sander, 2004), as a consequence of the reduced coordination and unquenched orbital magnetization of the Co atoms in the chains (Gambardella et al., 2003). A fit of the magnetization of multiple atomic chains according to the spin block model shows that D reduces abruptly to 0.33 ± 0.04 meV/atom in double chains (Fig. 7a, top panel). The anisotropy reduction is such that the low-temperature hysteretic behavior vanishes at low temperature going from single to double chains (Fig. 7a, bottom panel). As the system evolves towards a 2D film and the number of exchange-coupled Co atoms increases, we would on the other hand expect a stronger tendency towards magnetic order. Evidently, the tendency towards order is counteracted by the drastic reduction of the magnetic anisotropy energy per Co atom. Therefore, one might paradoxically conclude that the 1D character of the monatomic chains favors rather than disrupts FM order owing to the minimal coordination of the Co atoms and related enhanced magnetic anisotropy energy.

Despite the general trend with atomic coordination, the magnetic anisotropy of Co chains might vary in a nontrivial way for chains composed of an increasing number of atomic rows. In triple chains, D shows a significant and unexpected 35% increment, up to 0.45 ± 0.06 meV/atom (Fig. 7b), before decreasing further in a continuous monolayer film (Fig. 7c). In concomitance with the increased size of the spin-blocks in triple chains, such increment favors again FM order at low temperature (Fig. 7b). This D upturn is opposite to that expected for the increasing average coordination of Co atoms going from double to triple chains.

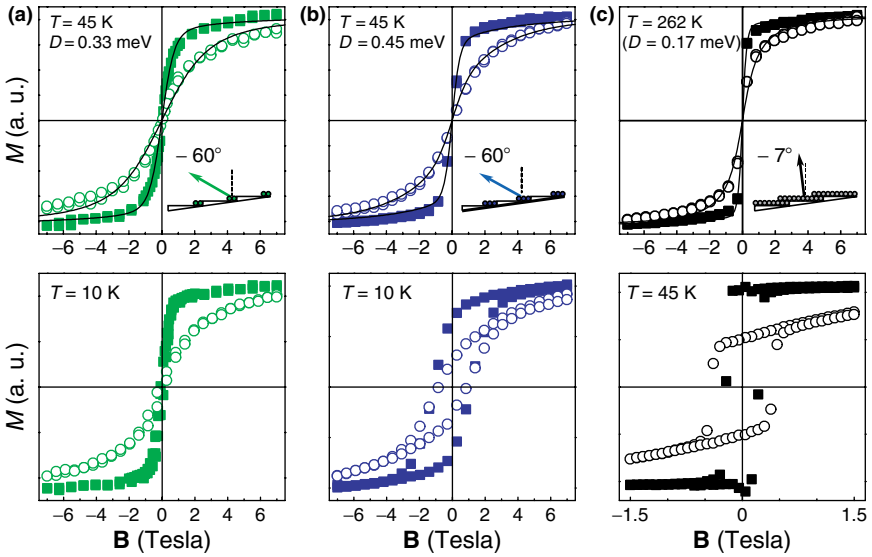

Figure 7. Magnetization of (a) biatomic (b) triatomic chains, and (c) 1.3 monolayers of Co on Pt(997) along the easy and hard directions (filled and open symbols, respectively). Top panel, above and, bottom panel, below the blocking temperature. The easy axis is indicated by the arrows in the insets. Solid lines are fits to the data according to the spin block model (1). (Adapted from Gambardella et al., 2004.)

Tight-binding calculations have revealed analog D oscillations for free-standing 1D wires, suggesting that the observed effect is related to the specific electronic configuration of multiple chains (Dorantes- Dávila and Pastor, 1998). Epitaxial strain, which results in fcc-hcp dislocations at 1 monolayer coverage (Gambardella et al., 2000b), is also liable to influence D, although it is unlikely a cause for the anisotropy oscillations.

Modifications of the electronic structure of the chains, such as in the relative filling of d orbitals with different symmetry (Wang et al., 1993), also reflect in oscillations of the easy magnetization direction (Gambardella et al., 2004). This is found at $\Phi = +43°$ (step-up direction) for the monatomic wires, $-60°$ from biatomic to quadruple wires, and finally at $-7°$ for the monolayer film, close to the (111) direction expected for ultrathin Co films on Pt(111) (McGee et al., 1993).

5. Conclusions

1D models have long been praised for their role in exemplifying and analyzing many-body problems that are common to physics, chemistry, and statistics. It is only recently, however, that 1D systems made of real atoms have become the object of experiments. Arrays of parallel monatomic Co chains can be constructed on a Pt vicinal surface whose steps serve as a deposition template. A narrow

temperature range exists where the Co chains grow row by row. Taking advantage of the uniformity and elevated density of the chain arrays, integral spectroscopic methods can be used to address the electronic and magnetic structure in 1D–2D systems. Owing to large magnetic anisotropy energy barriers and related slow magnetic relaxation, FM can be observed in linear monatomic chains without contradicting thermodynamic restrictions to long-range magnetic order in 1D. These results have been interpreted on the basis of a spin block model and the 1D anisotropic Heisenberg model, which allowed us to estimate quantitatively the anisotropy energy and exchange coupling constants, as well as finite-size correlation effects. The analysis of XMCD data permits to elucidate the dependence of local, intrinsic magnetization parameters on the atomic coordination typical of metallic systems. The magnitude of the atomic orbital magnetic moments of Co increases significantly with decreasing thickness of the chains. The magnetic anisotropy energy as well as the easy axis of magnetization oscillate with chain thickness demonstrating the influence of microscopic structural effects on macroscopic magnetization properties.

Acknowledgments

A. Dallmeyer, K. Maiti, M.C. Malagoli, W. Eberhardt, C. Carbone (Forschungszentrum Jülich), P. Ohresser, S.S. Dhesi, N.B. Brookes, and K. Larsson (ESRF), K. Kern (MPI Stuttgart), C. Hirjibehedin, A. Heinrich (IBM Almaden), A. Vindigni, A. Rettori (Universitá di Firenze), and M.G. Pini (CNR Firenze) are gratefully acknowledged for their contributions to the results reported here.

References

Bander, M. and Mills, D. (1988), *Phys. Rev. B* **38**, 12015.

Baud, S., Ramseyer, C., Bihlmayer, G., and Blügel, S. (2006), *Phys. Rev. B* **73**, 104427.

Billas, I. M. L., Châtelain, A., and de Heer, W. A. (1994), *Science* **265**, 1682.

Bogani, L., Caneschi, A., Fedi, M., Gatteschi, D., Massi, M., Novak, M. A., Pini, M. G., Rettori, A., Sessoli, R., and Vindigni, A. (2004), *Phys. Rev. Lett.* **92**, 207204.

Braun, H. -B. (1994), *Phys. Rev. B* **50**, 16501.

Braun, H. -B. (1999), *J. Appl. Phys.* **85**, 6172.

Bruno, P. (1989), *Phys. Rev. B* **39**, 865.

Bruno, P. (2001), *Phys. Rev. Lett.* **87**, 137203.

Caneschi, A., Gatteschi, D., Lalioti, N., Sangregorio, C., Sessoli, R., Venturi, G., Vindigni, A., Rettori, A., Pini, M., and Novak, M. (2001), *Angew. Chem. Int. Ed.* **40**, 1760.

Carra, P., Thole, B., Altarelli, M., and Wang, X. (1993), *Phys. Rev. Lett.* **70**, 694.

Chen, C. T., Idzerda, Y. U., Lin, H. -J., Smith, N. V., Meigs, G., Chaban, E., Ho, G. H., Pellegrin, E., and Sette, F. (1995), *Phys. Rev. Lett.* **75**, 152.

Chen, C. T., Sette, F., Ma, Y., and Modesti, S. (1990), *Phys. Rev. B* **42**, 7262.

Dallmeyer, A., Carbone, C., Eberhardt, W., Pampuch, C., Rader, O., Gudat, W., Gambardella, P., and Kern, K. (2000), *Phys. Rev. B* **61**, R5133.

de Jongh, L. and Miedema, A. (1974), *Adv. Phys.* **23**, 1.

de la Figuera, J., Huerta-Garnica, M., Prieto, J., Ocal, C., and Miranda, R. (1995), *Appl. Phys. Lett.* **66**, 1006.

Dingle, R., Lines, M., and Holt, S. (1969), *Phys. Rev.* **187**, 643.

Dorantes-Dávila, J. and Pastor, G. M. (1998), *Phys. Rev. Lett.* **81**, 208.

Dürr, H. A., Dhesi, S. S., Dudzik, E., Knabben, D., van der Laan, G., B. Goedkoop, J., and Hillebrecht, F. U. (1999), *Phys. Rev. B* **59**, R701.

Dürr, W., Taborelli, M., Paul, O., Germar, R., Gudat, W., Pescia, D., and Landolt, M. (1989), *Phys. Rev. Lett.* **62**, 206.

Elmers, H., Hauschild, J., Höche, H., Gradmann, U., Bethge, H., Heuer, D., and Köhler, U. (1994), *Phys. Rev. Lett.* **73**, 898.

Ferrer, S., Alvarez, J., Lundgren, F., Torrelles, X., Fajardo, P., and Boscherini, F. (1997), *Phys. Rev. B* **56**, 9848.

Frôta-Pessoa, S. and Kudrnovský, R. M. J. (2000), *Phys. Rev. B* **62**, 5293.

Fujisawa, H., Shiraki, S., Furukawa, M., Nantoh, M., Kawai, M., Nakamura, T., and Muro, T. (2005), *J. El. Spectr. Rel. Phen.* **144**, 519.

Gambardella, P. (2003), *J. Phys.: Condens. Matter* **15**, S2533.

Gambardella, P., Blanc, M., Brune, H., Kuhnke, K., and Kern, K. (2000a), *Phys. Rev. B* **61**, 2254.

Gambardella, P., Blanc, M., Bürgi, L., Kuhnke, K., and Kern, K. (2000b), *Surf. Sci.* **449**, 93.

Gambardella, P., Blanc, M., Kuhnke, K., Kern, K., Picaud, F., Ramseyer, C., Girardet, C., Barreteau, C., Spanjaard, D., and Desjonquères, M. (2001a), *Phys. Rev. B* **64**, 045404.

Gambardella, P., Brune, H., Kern, K., and Marchenko, V. (2006), *Phys. Rev. B* **73**, 245425.

Gambardella, P., Dallmeyer, A., Maiti, K., Malagoli, M., Eberhardt, W., Kern, K., and Carbone, C. (2002a), *Nature* **416**, 301.

Gambardella, P., Dallmeyer, A., Maiti, K., Malagoli, M., Rusponi, S., Ohresser, P., Eberhardt, W., Carbone, C., and Kern, K. (2004), *Phys. Rev. Lett.* **93**, 077203.

Gambardella, P., Dhesi, S., Gardonio, S., Grazioli, C., Ohresser, P., and Carbone, C. (2002b), *Phys. Rev. Lett.* **88**, 047202.

Gambardella, P. and Kern, K. (2001), *Surf. Sci.* **475**, L229.

Gambardella, P., Rusponi, S., Veronese, M., Dhesi, S., Grazioli, C., Dallmeyer, A., Cabria, I., Zeller, R., Dederichs, P., Kern, K., Carbone, C., and Brune, H. (2003), *Science* **300**, 1130.

Gambardella, P., Šljivancanin, Z., Hammer, B., Blanc, M., Kuhnke, K., and Kern, K. (2001b), *Phys. Rev. Lett.* **87**, 056103.

Gradmann, U. (1993), *Handbook of Magnetic Materials*, Amsterdam, Elsevier, Vol. 7/1 pp. 1–96.

Gradmann, U., Przybylski, M., Elmers, H., and Liu, G. (1989), *Appl. Phys. A* **49**, 563.

Hahn, E., Schief, H., Marsico, V., Fricke, A., and Kern, K. (1994), *Phys. Rev. Lett.* **72**, 3378.

Hauschild, J., Elmers, H., and Gradmann, U. (1998), *Phys. Rev. B* **57**, R677.

Himpsel, F., Altmann, K., Bennewitz, R., Crain, J., Kirakosian, A., Lin, J. -L., and McChesney, J. (2001), *J. Phys.: Condens. Matter* **13**, 11097.

Himpsel, F. J. and Ortega, J. E. (1994), *Phys. Rev. B* **50**, 4992.

Himpsel, F. J., Ortega, J. E., Mankey, G. J., and Willis, R. F. (1998), *Adv. in Phys.* **47**, 511, and references therein.

Hinzke, D. and Nowak, U. (2000), *Phys. Rev. B* **61**, 6734.

Hirjibehedin, C., Lutz, C., and Heinrich, A. (2006), *Science* **312**, 5776.

Hone, D. and Richards, P. (1974), *Ann. Rev. Mat. Sci.* **4**, 337.

Hong, J. and Wu, R. (2003), *Phys. Rev. B* **67**, 020406(R).

Hong, J. and Wu, R. (2004), *Phys. Rev. B* **70**, 060406.

Komelj, M., Steiauf, D., and Fähnle, M. (2006), *Phys. Rev. B* **73**, 134428.

Landau, L. and Lifshitz, E. (1959) *Statistical Physics*, Vol. 5, Pergamon, London.

Lazarovits, B., Szunyogh, L., and Weinberger, P. (2003), *Phys. Rev. B* **67**, 024415.

Li, D., Cuenya, B. R., Pearson, J., Bader, S., and Keune, W. (2001), *Phys. Rev. B* **64**, 144410.

Marsico, V. E., Blanc, M., Kuhnke, K., and Kern, K. (1997), *Phys. Rev. Lett.* **78**, 94.

McGee, N., Johnson, M., de Vries, J., and aan de Stegge, J. (1993), *J. Appl. Phys.* **73**, 3418.

Mermin, N. D. and Wagner, H. (1966), *Phys. Rev. Lett.* **17**, 1133.

Mundschau, M., Bauer, E., and Swiech, W. (1989), *J. Appl. Phys.* **65**, 581.

Ohresser, P., Ghiringhelli, G., Tjernberg, O., and Brookes, N. (2000), *Phys. Rev. B* **62**, 5803.

Pajda, M., Kudrnovský, J., Turek, I., Drchal, V., and Bruno, P. (2000), *Phys. Rev. Lett.* **85**, 5424.

Papadia, S., Desjonquères, M., and Spanjaard, D. (1996), *Phys. Rev. B* **51**, 4083.

Picaud, F., Ramseyer, C., Girardet, C., and Jensen, P. (2000), *Phys. Rev. B* **61**, 16154.

Pietzsch, O., Kubetzka, A., Bode, M., and Wiesendanger, R. (2000), *Phys. Rev. Lett.* **84**, 5212.

Poulopoulos, P. and Baberschke, K. (1999), *J. Phys.: Condens. Matter* **11**, 9495.

Pratzer, M. and Elmers, H. (2003), *Phys. Rev. B* **67**, 094416.

Pratzer, M., Elmers, H., Bode, M., Pietzsch, O., Kubetzka, A., and Wiesendanger, R. (2001), *Phys. Rev. Lett.* **87**, 127201.

Repetto, D., Lee, T. Y., Rusponi, S., Honolka, J., Kuhnke, K., Sessi, V., Starke, U., Brune, H., Gambardella, P., Carbone, C., Enders, A., and Kern, K. (2006), *Phys. Rev. B.* **74**, 054408.

Sander, D. (2004), *J. Phys.: Condens. Matter* **16**, R603.

Schneider, C. M. and Kirschner, J. (2000) K. Horn and M. Scheffler (eds.), *Handbook of Surface Science*, Amsterdam, Elsevier, pp. 511–668.

Schütz, G., Wagner, W., Wilhelm, W., Kienle, P., Zeller, R., Frahm, R., and Materlik, G. (1987), *Phys. Rev. Lett.* **58**, 737.

Shen, J., Klaua, M., Ohresser, P., Jenniches, H., Barthel, J., Mohan, C., and Kirschner, J. (1997a), *Phys. Rev. B* **56**, 11134.

Shen, J., Skomski, R., Klaua, M., Jenniches, H., Manoharan, S. S., and Kirschner, J. (1997b), *Phys. Rev. B* **56**, 2340.

Shick, A., Máca, F., and Oppeneer, P. (2004), *Phys. Rev. B* **69**, 212410.

Thole, B., Carra, P., Sette, F., and van der Laan, G. (1992), *Phys. Rev. Lett.* **68**, 1943.

Tischer, M., Hjortstam, O., Arvanitis, D., Dunn, J. H., May, F., Baberschke, K., Trygg, J., and Wills, J. (1995), *Phys. Rev. Lett.* **75**, 1602.

Újfalussy, B., Lazarovits, B., Szunyogh, L., Stocks, G., and Weinberger, P. (2004), *Phys. Rev. B* **70**, 100404.

van der Laan, G. (1998), *J. Phys.: Condens. Matter* **10**, 3239.

van Schilfgaarde, M. and Antropov, V. (1999), *J. Appl. Phys.* **85**, 4827.

Vindigni, A., Rettori, A., Pini, M. G., Carbone, C., and Gambardella, P. (2006), *Appl. Phys. A* **82**, 385.

Wang, D., Wu, R., and Freeman, A. (1993), *Phys. Rev. B* **47**, 14932.

Weller, D., Stöhr, J., Nakajima, R., Carl, A., Samant, M. G., Chappert, C., Mégy, R., Beauvillain, P., Veillet, P., and Held, G. (1995), *Phys. Rev. Lett.* **75**, 3752.

Welz, D. (1993), *J. Phys.: Condens. Matter* **5**, 3643–3652.

Wernsdorfer, W., Orozco, E. B., Hasselbach, K., Benoit, A., Barbara, B., Demoncy, N., Loiseau, A., Pascard, H., and Mailly, D. (1997), *Phys. Rev. Lett.* **78**, 1791.

Yan, L., Przybylski, M., Lu, Y., Wang, W. H., Barthel, J., and Kirschner, J. (2005), *Appl. Phys. Lett.* **86**, 102503.

Yu, C., Li, D., Pearson, J., and Bader, S. (2001), *Appl. Phys. Lett.* **79**, 3848.

INDEX

anisotropy, *see* magnetic anisotropy
Ampère 64, 77, 80–83
anisotropic 113, 176, 183, 200, 236, 252, 325, 328, 339
antiferromagnetic 61, 325

bifurcation 37, 41, 44, 45, 51, 55–57
bi-stability 114, 115, 118, 121
Bitter method 197, 198

constrictions 85, 98–101, 158
correlation length 245
current density 2, 9, 14, 25, 26, 29–31, 37, 40, 45, 62, 63, 71, 107–112, 227, 258
diamagnetism 109
diffusion length 4
dissipation 42, 47, 70, 72
domain wall 85
  head-to-head 85–87, 89, 90, 94, 99
  coupling 94
  geometrically confined 86
  motion 62, 78, 80, 87, 203
  phase diagram 90
  propagation 171
  spin structure 91, 92
  stray field 95, 96
  transformations 91, 93
  transverse 98
  vortex 86, 89–101
droplet 159, 160
dynamical system 37, 41, 42
electron holography 85, 88, 95, 96, 99, 101
energy
  dipolar 227
  mechanical 105
  thermal 92, 185, 225, 239, 243
entanglement 307–309, 323
enthalpy 228–230
epitaxial growth 86, 320, 328, 329
exciton 315–318, 320–322
exotic materials 106, 113
FePt 174, 179, 180, 182–184, 189, 275, 276, 285, 290–295

ferrite
  cores 146
  films 141
  garnet 200–202, 204, 214, 215, 220
  wafer 146
ferromagnet 3, 4, 7, 8, 12–14, 38, 40, 61, 62, 69, 131, 180, 229, 257
fluxgate 144, 145
Fokker-Planck equation 37, 39, 47, 49, 50, 52, 66
functional 229, 230

hard magnetic materials 167, 168, 173, 175
Heisenberg model 325, 331, 334, 336, 339
hysteresis 129, 130, 170, 172, 174, 187, 203, 204, 210, 231, 236, 245, 266, 267, 270

induction 88, 96, 98, 109, 111, 129–131, 143, 218, 227, 290
Ising model 325
lab-on-a-chip 153, 159
Landau-Lifshitz equation 1, 3, 13, 15, 18, 130
Landau-Lifshitz-Gilbert equation 39, 62, 65, 70
Langevin equation 37, 39, 46, 65, 322, 323
levitation 105, 106, 109, 113
lithography 1, 86, 87, 155, 278, 280, 296, 299, 379
  magnetic anisotropy 130, 141, 168, 169, 180, 187, 189, 201, 212, 266, 328, 332, 334, 337–339
  magnetic beads 154–159
  magnetic domain 86, 197, 198
  magnetic field sensor 144, 145
magnetic interactions 105–107, 109, 111, 115, 168, 172
magnetic moment 41, 69, 77, 108, 154, 156, 157, 199, 203, 247, 300, 331, 332, 335, 336
magnetic particle separation 155
magnetic particle transport 155
magnetic rings 85, 87
magnetic supraparticle structure 157

magnetization
  dynamics 51, 64
  oscillations 38, 41, 42, 52
  precession 46, 72, 73
  switching 46
magnetoresistance 2, 7, 14, 15, 17, 26, 40, 87, 99, 252–254
  giant 157, 253
magnetostatic coupling 64, 77, 78, 82, 95, 245, 266
Melnikov function 44, 45, 50
Melnikov theory 43, 45, 46
microcoils 156
microfluidics 154, 155
micromagnetic computations 80–82
micromagnetic model 70, 71, 79, 83
micromagnetic modelling 61, 62, 69, 71
micromagnetic simulations 65, 70, 71, 78, 85, 86, 90, 100
micromagnets 184
microwave oscillations 37, 44, 78
MOIF 195, 196, 200–220
MRAM 61, 78, 80
MTJ 24, 25, 28–30, 32, 33, 63, 66, 255, 256
nanocontact 38
nanopillar 38, 53, 57, 69, 78, 80
NdFeB 113, 117, 155, 171, 176, 177, 182, 183, 185–189, 218
nonlinear dynamical system 37, 41
notches 98
patterning 86, 112, 146, 167, 169, 182, 187–189, 281
permanent forces 114
permanent magnetism 167, 168
permeability 127, 128, 130–132, 143, 145, 169, 251, 269, 271
pinning 98
  strength 100
Poincaré-Melnikov theory 43, 45, 46
point contact 38, 41, 62, 69, 71
polaritons 308, 317, 319–323
polarization function 63, 64, 72, 82, 83
power inductor 146
printed circuit board 142–144, 264
prototypes 105, 115, 116, 118–120
quality factor 127, 131, 134, 135, 139, 141–143, 200, 215
quantum complementarity 307, 308, 319, 321
quantum wells 307, 308
remote actuation 105, 114, 124
scale reduction laws 105–107, 110
self-assembly 279, 295, 328
self-oscillation 44, 81
semiconductor microcavities 307
SmCo 116, 171, 172, 174, 176, 178, 182, 183, 185, 208–212, 215, 216
spatial distribution 79, 80, 172, 217
spectral mapping 80
spin polarized current 1, 2, 8, 42, 47, 61, 69, 77, 81, 87
spin transfer 1, 2, 7, 37–44, 46, 49–53, 62, 69, 72
spin waves 1, 70, 71
spin-channel 2, 3, 15, 24
sputtering 5, 28, 112, 113, 141, 143, 146, 181, 182, 185, 187, 204, 215–217, 241, 245, 248, 252, 266
stability diagram 44, 81, 82
stationary mode 42
STM 196, 296, 298, 327, 329–331
stochastic differential equation 39, 46
stray field 85, 88, 89, 95–98, 100, 101, 172, 196, 197, 219, 237, 281, 298, 299
  see also domain wall
superparamagnetism 180, 292
susceptibility 156, 172, 187, 234–236, 290, 319, 336
suspensions 109, 114, 115
tensor 233, 234, 309
  anisotropy 40
  derivative 233
  demagnetizing 204, 236
thermal excitations 85, 91
thermal field 65
thermal fluctuations 37, 38, 46, 49, 50, 52, 66, 180, 281, 325, 326, 332
thick film 106, 113, 115, 121, 142, 181, 183, 185, 189
three-layer structure 37, 38, 40
threshold current 20, 70
transverse wall 85, 86, 89–101, *see also* domain wall
tunneling (in-)elastic 2, 29–33
tunnel junction 29
tunneling 2, 21–23, 26–33, 196, 197, 327
  polarized 28
  quantum 21
  rate 22

uniaxial symmetry 37, 50–53
vortex core 85, 89, 91, 96, 97, 101
vortex wall, *see* domain wall
wireless actuation 114
XMCD 88, 91, 94–96, 101, 196, 327, 328, 330, 331, 334, 335, 337, 339